

NASA CONTRACTOR REPORT



NASA CR-121

NASA CR-121

FACILITY FORM 1002	165 11865	
	(ACCESSION NUMBER)	(TRF#)
	319	1
	(PAGES)	(CODE)
	CR-121	31
	(NASA CR OR TMX OR AD NUMBER)	(CATEGORY)

DEVELOPMENT AND EVALUATION OF THE ELASTIC RECOVERY CONCEPT FOR EXPANDABLE SPACE STRUCTURES

by N. O. Brink, B. C. Anderson, C. E. Thompson, and C. E. Wolcott

GPO PRICE \$ _____

OTS PRICE(S) \$ _____

Prepared under Contract No. NASw-661 by
WHITTAKER CORPORATION
San Diego, Calif.

Hard copy (HC) _____

Microfiche (MF) _____

for

NATIONAL AERONAUTICS AND SPACE ADMINISTRATION • WASHINGTON, D. C. • DECEMBER 1964

DEVELOPMENT AND EVALUATION OF THE
ELASTIC RECOVERY CONCEPT FOR
EXPANDABLE SPACE STRUCTURES

By N. O. Brink, B. C. Anderson, C. E. Thompson,
and C. E. Wolcott

Distribution of this report is provided in the interest of
information exchange. Responsibility for the contents
resides in the author or organization that prepared it.

Prepared under Contract No. NASw-661 by
WHITTAKER CORPORATION
San Diego, Calif.

for

NATIONAL AERONAUTICS AND SPACE ADMINISTRATION

ABSTRACT

11865

The purpose of this program was to investigate the feasibility of using elastic recovery for expandable structures. The elastic recovery concept is a mechanism in which the stored potential energy in a packaged structure expands the structure to the original full-sized configuration. The study determined the structural characteristics, thermal insulative characteristics, meteoroid penetration resistance, and radiation protection for the elastic recovery composite materials. The investigation determined the type of elastic recovery composite which could be applied to manned space stations or shelters, storage tanks, antennas, and secondary structures. The results of the study indicate that the elastic recovery expandable compares favorably, on the basis of weight, with other types of expandable structures.

author

TABLE OF CONTENTS

<u>Section</u>	<u>Page</u>
I	Introduction 1
II	Structural Loading and Environmental Design Criteria 4
	A. Range of Applied Loads 4
	B. Range of Permissible Leak Rates 10
	C. Range of Thermal Effects 12
	D. Requirements for Protection from Meteoroid Impact 14
	E. Requirements for Protection from Radiation 16
	F. Structural Requirements of Solar Collectors and Space Antennas 19
III	Material and Composite Studies 25
	A. Materials 25
	B. Composites 35
	C. Conclusions 44
IV	Parametric Evaluation of the Elastic Recovery Concept 48
	A. Structural Capabilities 48
	B. Thermal Characteristics 56
	C. Meteoroid Protection 56
	D. Radiation Protection 60
	E. Packaging of Elastic Recovery Composites 63
	F. Comparison and Application of Different Elastic Recovery Wall Concepts 66
	G. Conclusions from the Parametric Evaluation 76
V	Comparison of Elastic Recovery, Inflatable, and Telescoping Types of Expandable Structures 77

TABLE OF CONTENTS (Continued)

<u>Section</u>	<u>Page</u>
VI	Conclusions and Recommendations for Further Investigation 84
	A. Materials and Composites 84
	B. Structural Capabilities 84
	C. Thermal Characteristics 84
	D. Meteoroid Protection 84
	E. Radiation Resistance 85
	F. Applications of Elastic Recovery Structures 85
	G. Recommendations for Further Investigations 85
	Appendix A - Geometrical Studies of Expandable Structures 87
	Appendix B - Structural Analysis of the Elastic Recovery Concept 98
	Appendix C - Thermal Analysis of Elastic Recovery Composites 147
	Appendix D - An Analysis for the Meteoroid Protection of Spacecraft Utilizing the Elastic Recovery Sandwich Composite Wall Concepts 171
	Appendix E - Evaluation of Space Radiation Shielding Properties for Elastic Recovery Expandable Materials 214
	Appendix F - A State-of-the-Art Review and a Concept for Large, Expandable Space Antennas Employing Elastic Recovery Materials 292
	References 348

LIST OF FIGURES

<u>Figure</u>		<u>Page</u>
1	Expansion Sequence of an Elastic Recovery Model	2
2	Internal Pressure vs. Space Configuration	5
3	Estimated of Docking Loads Range Projected vs. Space Vehicle Weight (Docking dec = 1 to 3 ft/sec ²)	7
4	Impact Kinetic Energy vs. Space Vehicle Weight	8
5	External Pressure Envelope vs. Space Vehicle Configurations	9
6	Predicted Leakage Rate vs. Spacecraft Volume	11
7	Heat Flux from Sun Across the Planetary System	13
8	Meteoroid Flux Near Earth vs. Mass	15
9	Effect of Earth's Atmosphere on Cosmic Radiation	18
10	Spectral Energy Curve Related to the Sun	20
11	Contour Surface Accuracy Required for Communication and Telemetry Antennas (UHF to Microwave)	23
12	Contour Surface Accuracy Required for Communication Antennas (Microwave)	24
13	Experimental Semirigid Core of Polyvinyl Chloride Reinforced with Regenerated Cellulose Fiber Cloth	33
14	Experimental Natural Rubber Semirigid Core	33
15	Experimental Flexible Chloroprene Rubber Core Material	34
16	Wall Concepts for Expandable Space Structures	36
17	Time of Erection Under Different Conditions	39
18	Composite Sample for Compression Test	40
19	Load Deformation Characteristics, Long-Term Compressive Loading	41
20	Maximum Load-Weight Ratio vs. Foam Thickness for Various Laminate Thicknesses	43

LIST OF FIGURES (Continued)

<u>Figure</u>		<u>Page</u>
21	Foam Thickness vs. Number of Laminate Plies	45
22	Foam Weight vs. Laminate Weight	46
23	Strength-to-Weight Ratio of Internally Pressurized Single Face Sandwich Cylinder	49
24	Strength-to-Weight Ratio of Internally Pressurized Sandwich Cylinder	50
25	Strength-to-Weight Ratio of Internally Pressurized Sandwich Cylinder	51
26	Strength-to-Weight Ratio of Axially Compressed Cylinder	53
27	Strength-to-Weight Ratio of Axially Compressed Cylinder	54
28	Strain Energy per Unit Cylinder Length at Buckling	55
29	Equilibrium Temperature vs. Absorptivity-to- Emissivity Ratio for a Rotating Cylinder	57
30	Thermal Efficiency Parameter vs. Flexible Foam Core Thickness for a Rotating Cylinder	58
31	Thermal Efficiency Parameter vs. Flexible Foam Core Thickness for a Rotating Cylinder	59
32	Estimate of Weight Required for Meteoroid Protection Using "Best" Elastic Recovery Wall Concept vs. Exposed Area (ft ²) of Spacecraft x Time of Mission (hr)	61
33	Test Instrumentation Arrangement	62
34	Close-up of Reduced Pressure Chamber	64
35	Volume Ratio vs. Effective Diameter to Thickness Ratio Cylindrical Shape	67
36	Effect of Package L/D on Expanded Volume to Packaged Volume Ratio, $\frac{V_e}{V_p}$	68
37	Typical Elastic Recovery Composite Wall Sections	71

LIST OF FIGURES (Continued)

<u>Figure</u>		<u>Page</u>
38	Elastic Recovery Expandable Antenna Configuration	74
39	Elastic Recovery Airlock Design	75
40	"Sine-wave" Core Configuration	88
41	Length Contraction vs. Amplitude-Length Ratio, Sine Wave Core	92
42	Rectangular Core Configuration	93
43	Area-side Ratio vs. Angular Deflection of Core	94
44	Expansion-to-Contraction Ratio vs. the Angular Deflection of Core	96
45	Tensile Load Distribution Between Unequal Faces of a Sandwich Loaded by Internal Pressure	118
46	Tensile Load Distribution Between Equal Faces of a Sandwich Loaded by Internal Pressure	119
47	Sandwich Cylinder Under Axial Compression-Isotropic Core	120
48	Chart for Determining Stress at which Dimpling of Sandwich Facing will Occur	121
49	Buckling Pressure of Cylinder with Finite E_{core} Under External Pressure	122
50	Buckling Pressure of Cylinder Under External Pressure with Infinite E_{core}	123
51	Facing Stress Ratio of Internally Pressurized Sandwich Cylinder (Foam and Honeycomb Core)	124
52	Ultimate Internal Pressure of Sandwich Cylinder (Foam Core; R = 40 in.)	125
53	Ultimate Internal Pressure of Sandwich Cylinder (Foam Core; R = 80 in.)	126
54	Ultimate Internal Pressure of Sandwich Cylinder (Honeycomb Core; R = 40 in.)	127

LIST OF FIGURES (Continued)

<u>Figure</u>		<u>Page</u>
55	Ultimate Internal Pressure of Sandwich Cylinder (Honeycomb Core; R = 80 in.)	128
56	Strength-to-Weight Ratio of Internally Pressurized Sandwich Cylinder (Foam Core; R = 40 in.)	129
57	Strength-to-Weight Ratio of Internally Pressurized Sandwich Cylinder (Foam Core; R = 80 in.)	130
58	Strength-to-Weight Ratio of Internally Pressurized Single Face "Sandwich" Cylinder (Foam Core; R = 40 in.) . .	131
59	Strength-to-Weight Ratio of Internally Pressurized Single Face "Sandwich" Cylinder (Foam Core; R = 80 in.) . .	132
60	Strength-to-Weight Ratio of Internally Pressurized Sandwich Cylinder (Honeycomb Core; R = 40 in.)	133
61	Strength-to-Weight Ratio of Internally Pressurized Sandwich Cylinder (Honeycomb Core; R = 80 in.)	134
62	Strength vs. Weight Diagram - Internally Pressurized Sandwich Cylinder Foam Core	135
63	Strength vs. Weight Diagram - Internally Pressurized Single Facing Sandwich Cylinder Foam Core	136
64	Strength vs. Weight Diagram - Internally Pressurized Sandwich Cylinder Honeycomb Core	137
65	Buckling Stress of Axially Compressed Cylinder, Foam and Honeycomb Cores	138
66	Strength-to-Weight Ratio of Axially Compressed Cylinder (Foam and Honeycomb Cores; R = 40 in.)	139
67	Strength-to-Weight Ratio of Axially Compressed Cylinder (Foam and Honeycomb Cores; R = 80 in.)	140
68	Strength-to-Weight Ratio of Axially Compressed Cylinder (2-lb/ft ³ Polyurethane Foam Core; R = 40 in.) . .	141
69	Strength-to-Weight Ratio of Axially Compressed Cylinder (2-lb/ft ³ Polyurethane Foam Core; R = 80 in.) . .	142

LIST OF FIGURES (Continued)

<u>Figure</u>		<u>Page</u>
70	Compressive Strength vs. Weight/Length (2-lb/ft ³ Paper or Fiberglass Honeycomb Core with a Thickness Range of 0.5 in. to 6.0 in. Polyurethane - 181 Regenerated Cellu- lose Fiber Cloth Facings).	143
71	Strain Energy per Unit Cylinder Length at Buckling (2-lb/ft ³ Paper or Fiberglass Honeycomb Core with Polyurethane - 181 Regenerated Cellulose Fiber Cloth Facings)	144
72	Equilibrium Temperature vs. Absorptivity-to- Emissivity Ratio for a Rotating Cylinder	157
73	Generalized Composite Configuration for Thermal Evaluation	158
74	Heat Transfer Rate vs. Inner Facing Temperature for a Rotating Cylinder	159
75	Heat Transfer Rate vs. Inner Facing Temperature for a Rotating Cylinder	160
76	Heat Transfer Rate vs. Inner Facing Temperature for a Rotating Cylinder	161
77	Heat Transfer Rate vs. Inner Facing Temperature for a Rotating Cylinder	162
78	Heat Transfer Rate vs. Inner Facing Temperature for a Rotating Cylinder	163
79	Temperature Distribution Within Sandwich for a Rotating Cylinder	164
80	Temperature Distribution Within Sandwich for a Rotating Cylinder	165
81	Temperature Distribution Within Sandwich for a Rotating Cylinder	166
82	Temperature Distribution Within Sandwich for a Rotating Cylinder	167
83	Thermal Efficiency Parameter vs. Flexible Foam Core Thickness for a Rotating Cylinder	168

LIST OF FIGURES (Continued)

<u>Figure</u>		<u>Page</u>
84	Thermal Efficiency Parameter vs. Flexible Foam Core Thickness for a Rotating Cylinder	169
85	Heat Transfer Rate vs. Weight per Unit Area for a Rotating Cylinder	170
86	Possible Failure Modes of Shield under Projectile Impact	176
87	Possible Mode of Failure for Inner Layer of an Elastic Recovery Composite under Projectile Impact	177
88	Typical Elastic Recovery Wall Concept Impacted by a Hypervelocity Particle (Penetration Mode Only)	178
89	Idealized Model of Impact Penetration by a Hypervelocity Particle in an Elastic Recovery Sandwich Composite	180
90	Idealized Model for Spallation/Delamination Analysis of a Sandwich Composite	182
91	Ratio of Bumper Thickness to $\frac{t_f}{t_p}$ Break Up Meteoroid to Thin Plate Penetration Depth (For Estimation of Required Meteoroid Fracture Thickness (t_f))	186
92	Velocity Ratio vs. Shield/Projectile Weight	188
93	Estimated Variation of \bar{V}_f vs. Bumper Parameter (Z)	191
94	$\frac{t_F}{L} \frac{\bar{V}_s}{\bar{V}_f}$ vs. Z as Determined from Table 16	195
95	Wall Concepts for Expandable Space Structures	196
96	Two Basic Narmco Elastic Recovery Wall Concepts for Meteoroid Protection	197
97	Basic Idea X ₁ and Weight Required for Meteoroid Penetration	201
98	Basic Idea X ₂ and Weight Required for Meteoroid Penetration	204

LIST OF FIGURES (Continued)

<u>Figure</u>		<u>Page</u>
99	Estimate of Weight Required for Meteoroid Protection Using "Best" Elastic Recovery Wall Concept vs. Exposed Area (ft ²) of Spacecraft x Time of Mission (hr)	211
100	Weight of Single-Sheet Aluminum Required for Meteoroid Protection vs. Area of Spacecraft (ft ²) x Time Mission (hr) Using Eichelberger and Gehring Formulas	212
101	Typical Space Radiation Flux Magnitude	252
102	Test Instrumentation Arrangement	253
103	α Radiation Source	254
104	β Radiation Source	254
105	γ Radiation Source	255
106	Test Chamber Background Setting at Atmospheric Pressure	255
107	Video-Monitored Radiation Level at 15-in. Vacuum	256
108	Video-Monitored Radiation Level at 25-in. Vacuum	256
109	Vacuum Environment During Calibration and Material Tests	257
110	Video-Monitored Radiation Level at 29.5-in. Vacuum	257
111	Aluminum Index Reference Standard	258
112	Video-Monitored Radiation Level	258
113	Test Sample of Aluminum Deposited on Polyester Terephthalate	259
114	Video-Monitored Radiation Level	259
115	Test Sample of Polyurethane Elastic Foam	260
116	Video-Monitored Radiation Level	260

LIST OF FIGURES (Continued)

<u>Figure</u>		<u>Page</u>
117	Test Sample of DuPont Type 46971 Adhesive on 1.5-mil Cellophane Base	261
118	Video-Monitored Radiation Level	261
119	Test Sample of Laminate (PK-1044 resin and 181 glass fabric)	262
120	Video-Monitored Radiation Level	262
121	Test Sample of Laminate (PK-1044 resin and regenerated cellulose fiber fabric)	263
122	Video-Monitored Radiation Level	263
123	Test Sample of Laminate (PK-1044 resin with 20% by weight carbon loading and type 181 glass fabric)	264
124	Video-Monitored Radiation Level	264
125	Test Sample of Laminate (PK-1044 resin with 20% by weight carbon loading and regenerated cellulose fiber fabric)	265
126	Video-Monitored Radiation Level	265
127	Carbon-Saturated Polyurethane Elastic Foam	266
128	Video-Monitored Radiation Level	266
129	Gamma Ray Shielding Material Coefficients NOMOGRAM	267
130	Total Mass Attenuation Coefficient μ_0/ρ for γ Radiation	268
131	Total Mass Attenuation Coefficient μ_0/ρ for γ Radiation	269
132	Total Mass Attenuation Coefficient μ_0/ρ for γ Radiation	270
133	Total Mass Attenuation Coefficient μ_0/ρ for γ Radiation	271
134	Total Mass Attenuation Coefficient μ_0/ρ for γ Radiation	272

LIST OF FIGURES (Continued)

<u>Figure</u>		<u>Page</u>
135	Total Mass Attenuation Coefficient μ_0/ρ for γ Radiation	273
136	Total Mass Attenuation Coefficient μ_0/ρ for γ Radiation	274
137	Total Mass Attenuation Coefficient μ_0/ρ for γ Radiation	275
138A	Proton Shielding Extrapolation	276
138B	Proton Shielding Extrapolation Aluminum Deposited on Mylar	277
139A	Proton Shielding Extrapolation	278
139B	Proton Shielding Extrapolation	279
140A	Proton Shielding Extrapolation	280
140B	Proton Shielding Extrapolation	281
141A	Proton Shielding Extrapolation	282
141B	Polyurethane Foam Test Sample 1.9 lb/ft ³ Proton Shielding Extrapolation	283
142A	Proton Shielding Extrapolation	284
142B	Proton Shielding Extrapolation	285
143A	Proton Shielding Extrapolation	286
143B	Proton Shielding Extrapolation Polyurethane Foam Test Sample 1.9 lb/ft ³ Carbon Saturated	287
144A	Proton Shielding Extrapolation	288
144B	Proton Shielding Extrapolation	289
145A	Proton Shielding Extrapolation	290
145B	Proton Shielding Extrapolation Adhesive Type 46971	291
146	Petal Deflection Test Fixture	298

LIST OF FIGURES (Continued)

<u>Figure</u>		<u>Page</u>
147	Illustration Showing Petal Segment Location in Parabola of Revolution Arrangement	300
148	Precision 12-ft K-Band Antenna Reflector with Contour Check Template Installed for Test	306
149	Cassegrain Antenna Employing Segment Petal Concept	308
150	Parabolascope Rangefinder	312
151	Air-Inflatable Enclosure	314
152	X-Band Reflector (60-ft Diameter)	317
153	Thermal Gradient Deflection Test; Dial Gage Locations, Top View of Panel. Supports Fixed	318
154	Thermal Gradient Deflection Tests; Dial Gage Locations, Top View of Panel, Simply Supported	319
155	Thermocouple Probe Locations, Both Sides of Panel	320
156	Data Comparison Curves	324
157	Centerline Deflection for Various Temperature Gradients (Supports Infinitely Fixed; Concave Side Up and Heated; Panel No. 1)	325
158	Centerline Deflection for Various Temperature Gradients (Supports Infinitely Fixed; Concave Side Up and Heated; Panel No. 2)	326
159	Centerline Deflection for Various Temperature Gradients (Simply Supported; Concave Side Up and Heated; Panel No. 1)	328
160	Centerline Deflection for Various Temperature Gradients (Simply Supported; Concave Side Up and Heated; Panel No. 2)	329
161	Thermal Distortion of a Sphere Due to Incident Solar Radiation	332
162	Total Thermal Distortion of a Sphere Due to Incident Solar Radiation and Shadow Areas	333

LIST OF FIGURES (Continued)

<u>Figure</u>		<u>Page</u>
163	Coordinate Relationship Between a Curve of Constant Radius and a Parabolic Curve of F/D = 0.225	334
164	Method to Electromagnetically Change a Spherical Reflecting Surface to an Equivalent Parabolic Reflecting Surface	337
165	Newtonian Antenna Arrangement Shown With Electronic Equipment Housed in the Spherical Radome Structure	345
166	Expandable Cassegrain Antenna Arrangement	346
167	Expandable Newtonian Antenna Arrangement	347

LIST OF TABLES

<u>Table</u>		<u>Page</u>
1	Strength Properties of Typical Film Materials	27
2	Permeability of Film Materials	28
3	Results of Flexible Laminate Tests	29
4	Typical Core Materials for Expandable Structures	32
5	Effective Atomic Number and Density of Elastic Recovery Materials	65
6	Parametric Study of Design Requirements for Elastic Recovery Expandable Structures	69
7	Weight of a Telescoping Expandable Structure Case 1	78
8	Weight of Inflatable Space Structure Case II	79
9	Section Weight Analysis for Elastic Recovery Composite	80
10	Comparison of Unit Weights	82
11	Summary of Meteoroid Protection Weight	83
12	Buckling Equations for Certain Limiting Cases	145
13	Materials Used in the Structural Analysis	146
14	Sandwich Constructions Considered for Thermal Evaluation	152
15	Material Properties for Thermal Calculations	152
16	Summary of Data and Calculations for Points on Figure 93	190
17	Summary of Experimental and Calculated Data* to Estimate \bar{V}_s	194
18	Data for Final Weight Estimate for Meteoroid Protection of a Spacecraft	210
19	Effective Atomic Number and Density of Elastic Recovery Materials	248
20	Maximum Deflection Data Summary ⁽⁶⁴⁾	322
21	Heat and Temperature Data Summary	323

I. INTRODUCTION

The purpose of this program was to provide the National Aeronautics and Space Administration with information on the feasibility and applicability of the elastic recovery concept to expandable structures. This program was performed to determine the load capabilities, the effect of the space environment, and possible areas of application for elastic recovery composite sections.

The elastic recovery concept is a mechanism by which a packaged flexible structure may be erected in space. The erection of the structure takes place from the stored potential energy within the compressed composite wall. Basically, the composite consists of flexible facings and a compressible core. The structure is packaged into a small volume by alternately folding and compressing the composite wall section. Upon release from the package in space, the stored potential energy is sufficient to erect and cause the structure to be self-supporting without any external influences. Figure 1 shows a model cylinder being released from its package and expanding to the full size. This particular sequence was taken in a vacuum chamber.

In order to determine the feasibility of employing the elastic recovery concept in space structures, the program included the following main study areas:

1. Determination of structural loading and environmental conditions to be expected for different types of structures. The possible applications of the structure, such as for space stations, planetary shelters, cryogenic fuel storage tanks, solar collectors, antennas, and secondary structures, were taken into account for this study.
2. Investigation of candidate materials for both the facings and the cores of the elastic recovery composite.
3. A parametric study to determine the effect of the loading and environmental conditions upon the elastic recovery composite. This area of investigation made up the bulk of the program effort. The parametric studies determined the weight of elastic recovery composite sections for structural requirements, thermal control, meteoroid protection, and radiation resistance. Each of these areas of study was conducted in as great a detail as possible to determine the requirements. However, it was often necessary to limit the study or make admittedly simplifying assumptions in order to keep the study from dwelling on details which were unknown and/or beyond the general scope of the program.
4. The major area of study for this program also included an analysis to determine the best type of elastic recovery concept for a particular application. Consideration was given to the type of loading on the structure and the environment in which the structure was placed for determining the weight of wall required.



(a) Packed Cylinder in Vacuum Prior to Opening



(b) Opening of Package and Cylinder Beginning to Unfold



(c) Time at +2 sec After Opening



(d) Time at 1 min After Opening: Unfolding is Complete



(e) Time at 10 min After Opening. Note Change in Surface Condition

Figure 1. Expansion Sequence of an Elastic Recovery Model

5. The last area of study was the comparison by weight of a typical elastic recovery composite wall expandable structure with other types of expandable structures. Due to the small amount of data available on the different expandable structures, this study was rather limited in scope.

These five major areas of study determined the possible areas of application for the elastic recovery concept.

II. STRUCTURAL LOADING AND ENVIRONMENTAL DESIGN CRITERIA

To determine the types of loads and environments a space structure would encounter required a rather extensive review of the current and past literature. To accomplish this task, the design criteria for expandable space structures were divided into the following groups:

1. Range of applied loads
2. Range of permissible leak rates
3. Range of thermal environments
4. Requirements for protection from meteoroid impact
5. Requirements for protection from radiation
6. Structural requirements for solar reflectors and space antennas

The first five items are the results of information gained from many sources. The results are either summarized at the end of each of the subsequent sections or shown as envelopes on curves. The information represents the state-of-the-art studies and, in some cases, are estimates only. The sixth item presents general information required for the design of solar reflectors and space antennas and indicates the criteria required for surface accuracy of each.

A. Range of Applied Loads

The applied loads on a space or planetary structure result from the following conditions:

Internal pressure

Docking loads

Impact loads

External pressure

These loading spectrums have been selected from the anticipated end applications of expandable structures.

1. Internal Pressure

The range of internal pressures anticipated for various types of structures are shown in Figure 2. The pressure data for the manned space station and lunar shelters are from References 1, 2, and 3. The pressure ranges for the tank assumed the storage of cryogenic fluids and are taken from References 4 and 5. The pressure in the storage tank as described in section II.B (Permissible Leakage Rates) could be increased beyond the critical pressure of the cryogenic fluid if desired. This, of course, is dependent upon the design and the structural application.

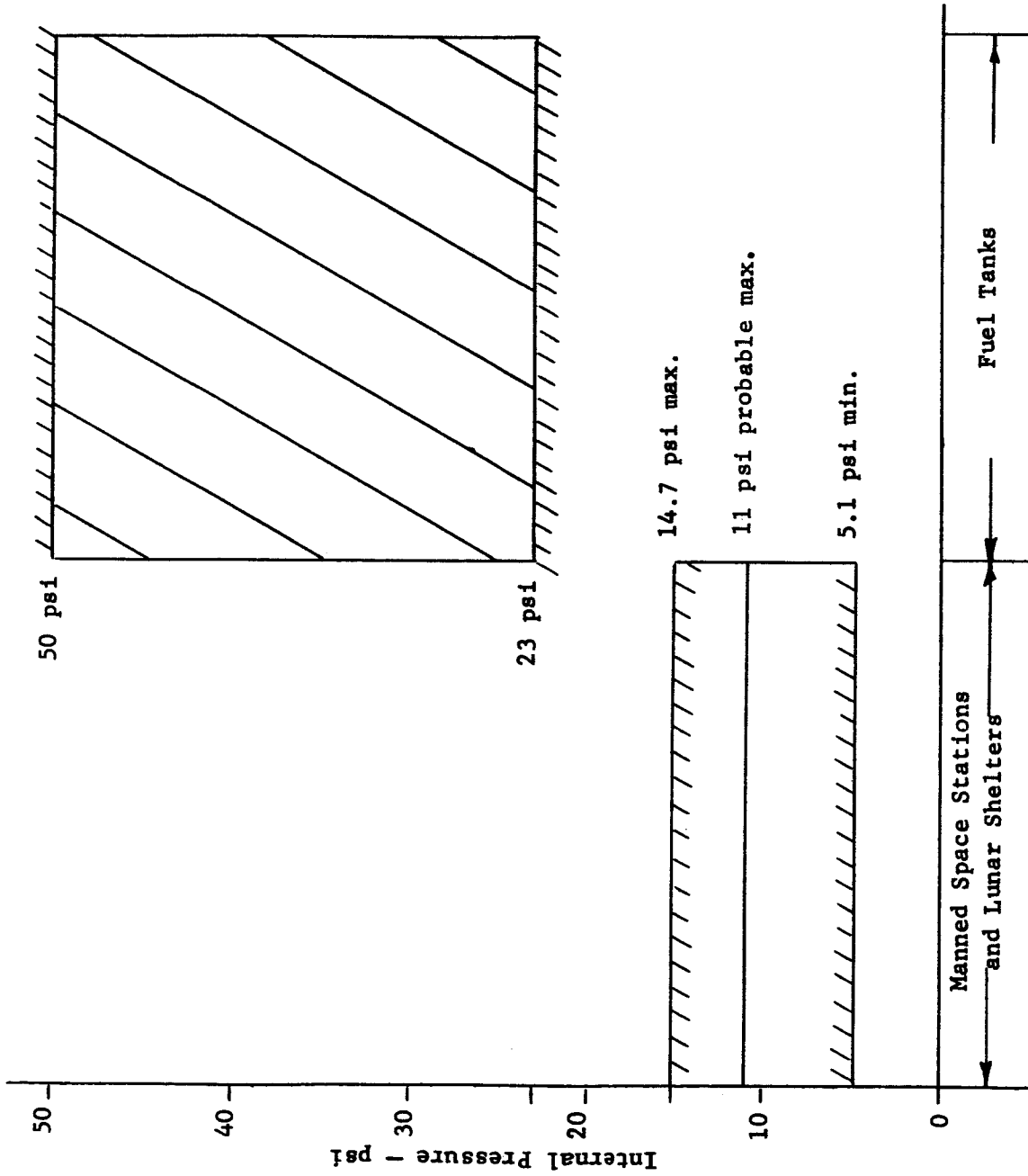


Figure 2. Internal Pressure vs. Space Configuration

2. Docking Loads

The range of docking loads vs. space vehicle weight is given in Figure 3. The docking load was based on a deceleration of 1 to 3 ft/sec² (Reference 6). Further information indicated that the closing velocity would range from 0.1 to 3.0 ft/sec. The space vehicle weight is obtained from Reference 7 and represented a vehicle docking into a larger space station. The docking loads would require sufficient stiffness of the space station to prevent excessive deformation surrounding the immediate docking area.

3. Impact Energy

The impact energy criteria presented herein determined the effect of landing on a lunar or planetary surface. This type of loading would not be applied directly to an expandable structure since a lunar shelter would probably be packaged during impact. The energy, however, would have to be absorbed by various means to reduce the landing shock. The range of possible impact energy for different weight space vehicles is shown in Figure 4. The impact velocity for different types of vehicles was found to range from 3 ft/sec (Reference 6) to a maximum of 30 ft/sec (Reference 8). The impact energy was computed from $KE = 1/2 M V^2$ and weight was assumed to be acting on earth; hence, $g = 32.2 \text{ ft/sec}^2$.

4. External Pressure

The effect of external pressure upon lunar or planetary shelters is shown in Figure 5. The external pressures shown were estimates based upon possible conditions a structure may encounter on various planetary surfaces. The external pressure for the lunar mobile vehicle tires was obtained by assuming a tire contact area for various sized lunar vehicles (Reference 9). The vehicle weight ranged from 6000 to 20,000 earth pounds. The studies indicate that the wheeled lunar vehicles would have large-diameter, low-pressure type tires. The present study assumed that a conservative 10% of the projected tire area was in contact with the lunar surface.

The second external load condition (Figure 5) applies to antennas and shelters required for communications and logistics from planetary exploration on Mars or Venus. The wind pressure on an antenna dish was determined by assuming a coefficient of drag (C_D) of 1.5. The Venian atmospheric characteristics were obtained from Reference 10. The wind pressure on an antenna was found from $P = \frac{F}{A} = C_D q$, where $q = 1/2 \rho V^2$. For this study, a maximum wind of 100 mph was assumed.

The third external loading condition in Figure 5 applies to underground lunar shelters. It was found that a lunar shelter would be buried for protection from meteoroids. Several sources have indicated that the shelter would be under lunar soil ranging from a few inches to many feet in depth. The plot of external pressure on the shelter wall was determined for a 40-ft diameter in both cases. The pressure was based upon a soil density of 125 lb/ft³, but the gravity field on each planet was assumed.

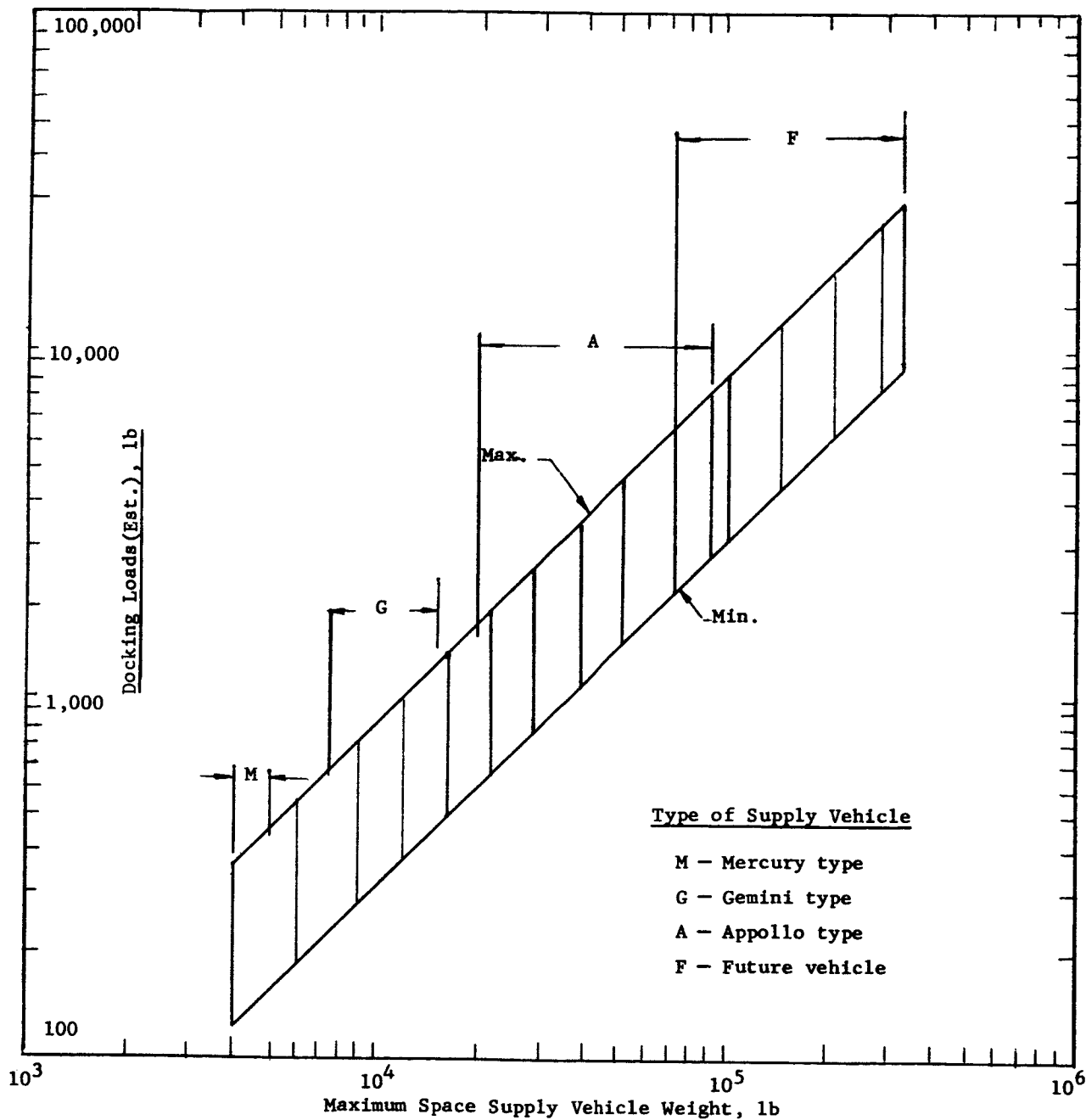


Figure 3. Estimated of Docking Loads Range Projected vs. Space Vehicle Weight (Docking dec = 1 to 3 ft/sec²)

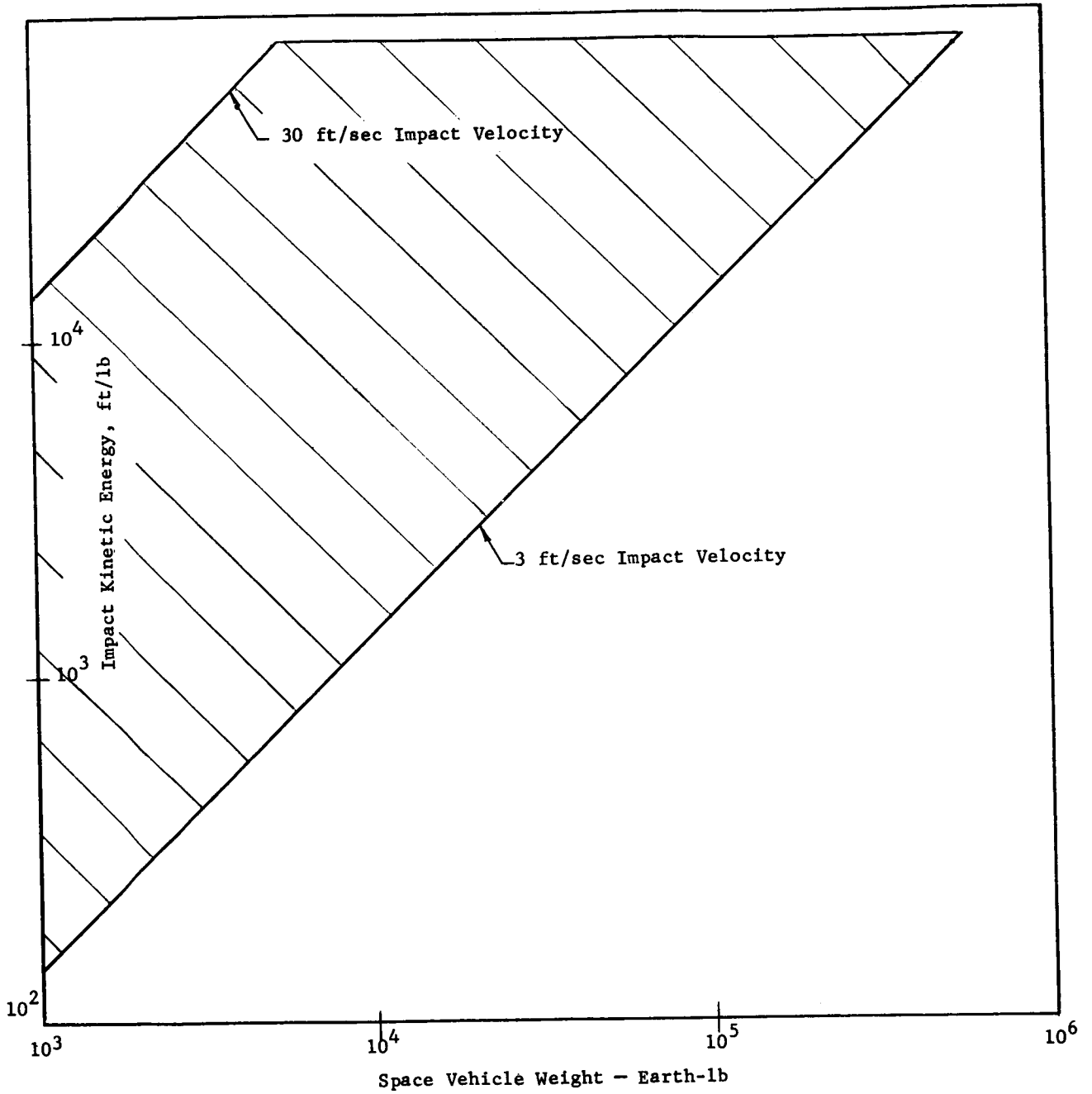


Figure 4. Impact Kinetic Energy vs. Space Vehicle Weight
 (Note: Weight based upon earth gravity)

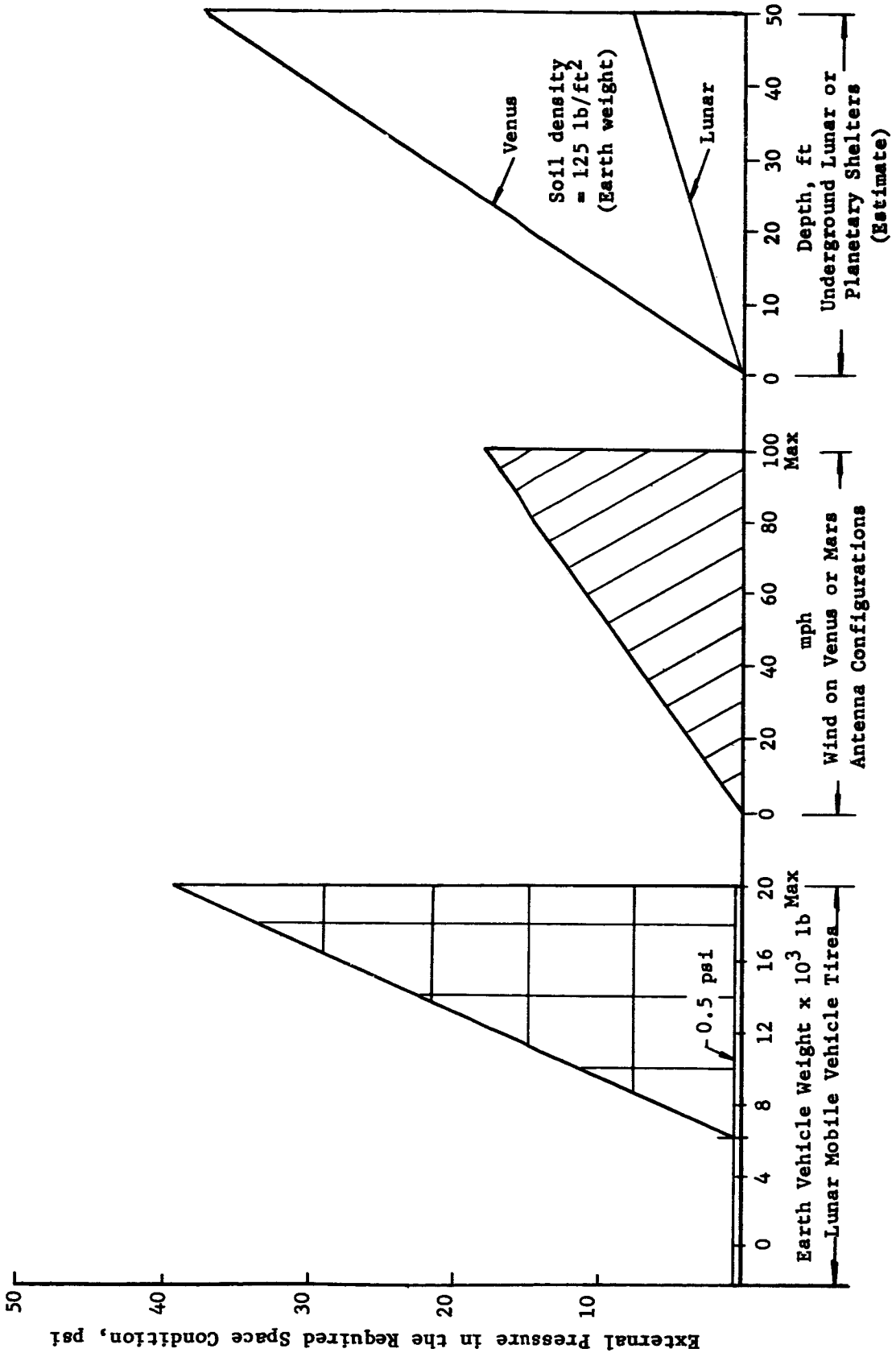


Figure 5. External Pressure Envelope vs. Space Vehicle Configurations

B. Range of Permissible Leak Rates

The leakage rate requirements were, in general, divided into two areas: the leakage requirement for manned vehicles, and the leakage requirement for cryogenic fluid storage vessels.

1. Requirements for Manned Vehicles

The leakage rate for manned vehicles or shelters depends upon many factors, including internal pressure, material permeability, joints, and hatch seals. A higher internal pressure would, of course, cause higher leakage rates. Since the pressure in the space vehicle ranged from 5 to 11 psi (References 7 and 11), the leakage rate is approximately proportional to these pressures. The Mercury capsule, which operates at a pressure of 5.1 psi, had a design leakage rate of 300 cc/min. However, the actual leakage rate was found to be 650 and 1000 cc/min (Reference 3). This leakage was apparently due primarily to the difficulties in sealing around the hatches, etc. Reference 11 determined the leakage rate of a large space station. Based on the results of the Mercury leakage, it would be a minimum of 36,000 lb/yr, and could possibly be 72,000 lb/yr. The resupply requirements for these leakage rates would be prohibitive. It has been estimated that the leakage could be reduced to 3600 lb/yr by improved design. Figure 6 shows the range of leakage based upon station volume.

The predicted leakage rates given above are based upon a complete station, with its leakage through the seals, joints, and in some cases, materials. The seal and joint leakage is primarily a design problem, with material choice for gasket a limiting factor. The wall permeability, on the other hand, is basically a problem for the flexible materials. The use of a flexible, relatively impervious film can reduce the leakage of air through the cabin wall.

2. Requirements for Cryogenic Fluid Storage Vessels

The second area of leakage was the loss of fuel in space storage tanks. The loss is a function of material permeability and, in the case of cryogenic fluids, solar radiation. The wall permeability is again the function of the wall material. To minimize the loss due to boiloff from external heat sources, insulation would be required. The present investigation has shown that a liquid hydrogen tank in a circular orbit would have a mean skin temperature of -100°F and would lose 0.32% to 0.4%/day of liquid hydrogen (Reference 12). These losses were for tanks having a combination of insulation and vacuum, and insulation alone, respectively.

Other methods of reducing losses of cryogenic fluids include the use of internal pressure, tank orientation in space, and shielding. The concept of using pressure reduces the losses, because pressure is allowed to build up when the tank is exposed to a heat input. Reference 12 also shows this effect of increased tank pressure. The storage time at no loss can be increased from 0 to 40 days if the pressure is increased from

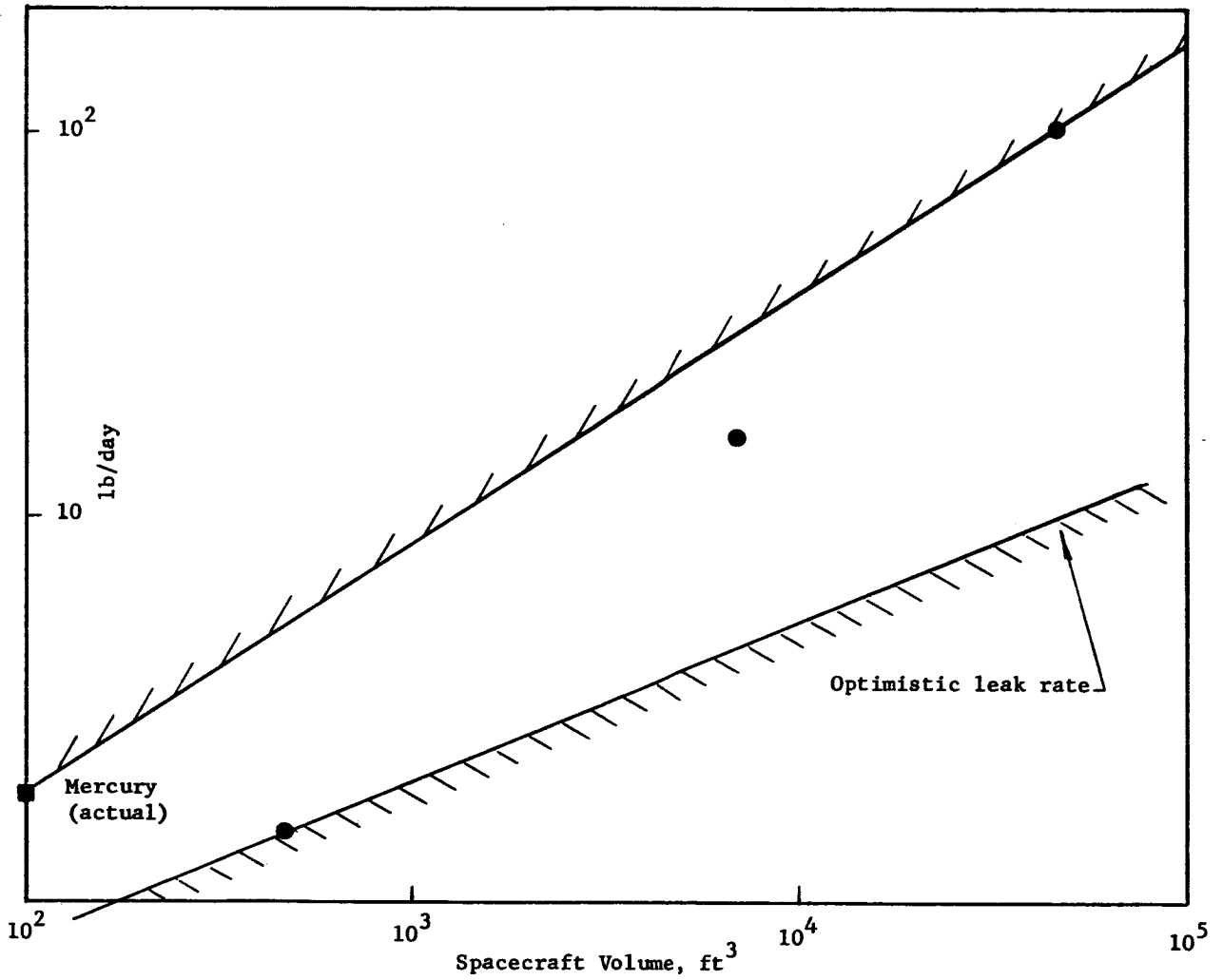


Figure 6. Predicted Leakage Rate vs. Spacecraft Volume

14.7 to 80 psi, assuming the same tank is used in each case. The use of pressure, however, will have to be limited with the use of flexible materials, due to elongation and tensile strength.

The other methods of reducing fluid losses in a cryogenic tankage include orientation and/or shielding. Both these methods minimize the heat flux into the tank, thereby reducing fluid loss. The first method orientates the tank so that the smallest area is always presented to the heat source. This will restrict the heat input into the tank, since the input is a function of the projected area. The second method of minimizing heat input is by the use of shielding, which casts a shadow upon the tank. This method also requires tank orientation.

Use of the following leakage ranges, based on state-of-the-art information, is indicated:

Manned Shelters:

0.002 to 0.021 lb/day/cu ft of shelter volume

Storage Tanks for Earth Orbit:

Liquid hydrogen - 0.32% to 0.40%/day for large tanks

Liquid oxygen - 0.08%/day for large tanks

C. Range of Thermal Effects

The vehicle in space is subjected to varying heat fluxes. These fluxes originate from the sun and either radiate directly or reflect from the planets. For this initial study, only the direct radiation from the sun was considered. The solar heat flux at the earth is 440 Btu/sq ft-hr (Reference 7). The heat flux throughout the solar system is shown in Figure 7 (Reference 13).

In an earth orbit, the temperature may vary from -150°F to +400°F (Reference 11), depending upon the orbit, orientation, heat capacity, skin thickness, and α_s/ϵ ratio, which indicates the ability of a skin to absorb high-temperature radiation and reradiate at a lower temperature. The higher the α_s/ϵ ratio, the higher the structure temperature will be.

The thermal radiation load has different effects on different types of space structures. For example, the thermal gradients on a solar collector could cause sufficient deviation in the mirror's surface to degrade its efficiency. The skin of a space station, lunar shelter, or tank will have to include insulation to reduce the inside steady state temperature. As the structural wall temperature is lowered, the requirement for space radiators for structural cooling is reduced. Lower internal temperature will also reduce the boiloff of cryogenic fluid.

The primary thermal effect for evaluating an expandable structure will be solar radiation. The heat flux on the structure will be dependent upon orbital location, orientation, and vehicle shape. The heat flux will be determined from Figure 7.

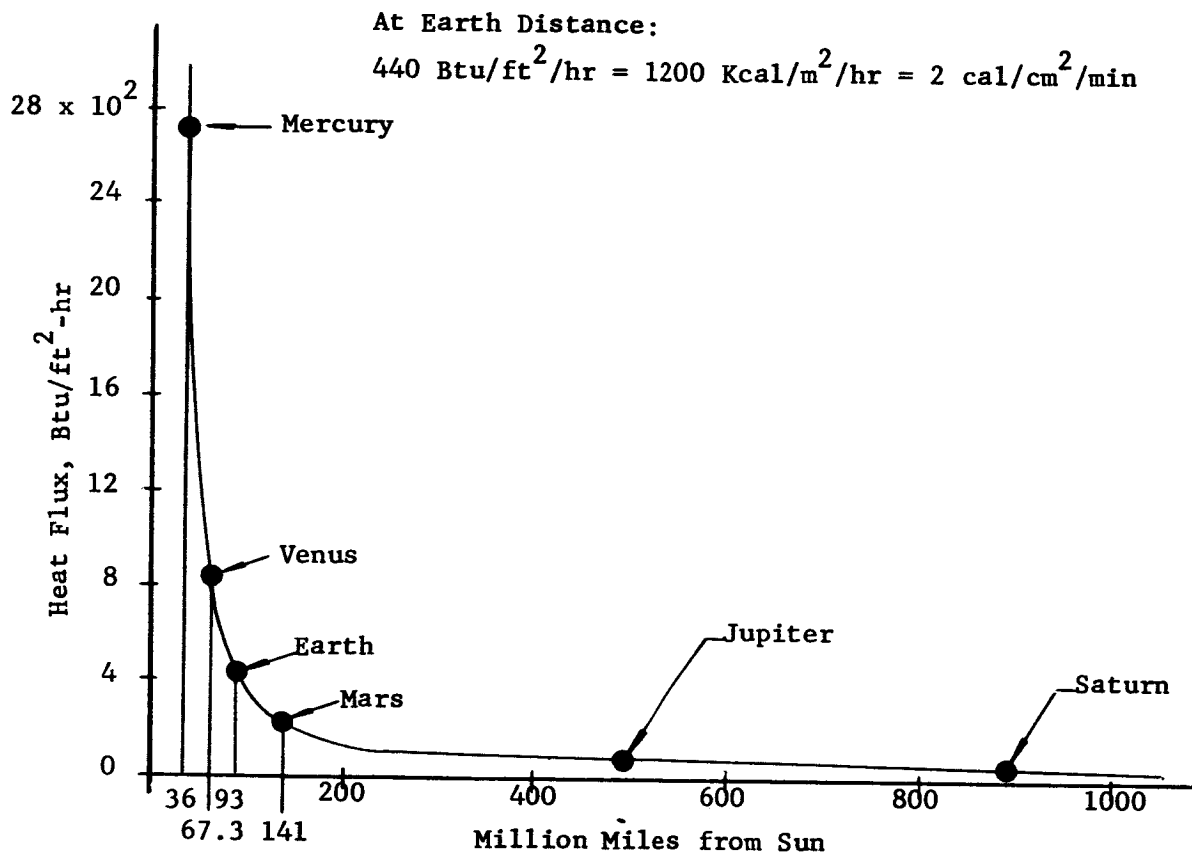


Figure 7. Heat Flux from Sun Across the Planetary System (13)

D. Requirements for Protection from Meteoroid Impact

It has become increasingly apparent from astronomical observations and the continuing exploration of terrestrial space that the hazard of meteoroids impinging the surface of space vehicles is real. However, data obtained from Explorer VIII (Reference 14) and Explorer XVI (Reference 15) indicate that the influx of the more massive particles may be less severe than previously expected.

The possible effects of hypervelocity impacts upon the surface of a space vehicle include puncture or spalling of the vehicle wall. This can result in loss of air pressure, direct injury to the inhabitants, or damage to equipment. Adequate protection for the astronauts and the interior of the vehicle must therefore be provided. Hypervelocity impact of micrometeoroids also can cause an erosion of the exterior surface, thus changing its optical properties.

1. Meteoroid Impact Flux

The first step in assessing the danger of meteoroid impact on the hull of a space structure is to estimate the frequency of these impacts per unit area. If the effect of the individual particles can then be determined, an estimate can be made of the total damage to be expected over a given time period.

Photographs of meteors (particles visible to the naked eye as they enter the atmosphere and burn-up), radio-echo and radar techniques, and actual satellite impact data are the sources from which the particle flux surrounding the earth is estimated. In the photographic and radio-echo methods, large areas of the sky are constantly surveyed, although detection is limited to the relatively infrequent particles of mass greater than 0.001 g for radio-echo methods and 0.25 g for photographic methods. On the other hand, those satellites containing instruments to register particle impacts can sample only a comparatively small region of space. Therefore, these instruments must be sensitive enough to detect the impacts of very small particles, since only the small meteoroids are found in abundance (References 14, 16, and 17). Thus, at present, such rocket and satellite measurements are limited to data on particles having masses of about 10^{-7} g, or less. This limitation is responsible for the gap in information between the radio-echo and satellite data (see Figure 8).

The method by which these data are put into meaningful terms is by showing the variation of the average rate of influx of meteoroid particles as a function of particle mass. The flux, ϕ , is the number of particles, per unit area, per unit time, of a mass greater than (m). However, this concept of flux is an oversimplification of the real environment, since it is subject to transient variations, such as showers as the earth passes through the orbit of a comet, and spatial variations (e.g., greater flux on the morning side of earth). These data must be reduced to manageable proportions so that space vehicle designers can establish design procedures having some semblance of order and accuracy.

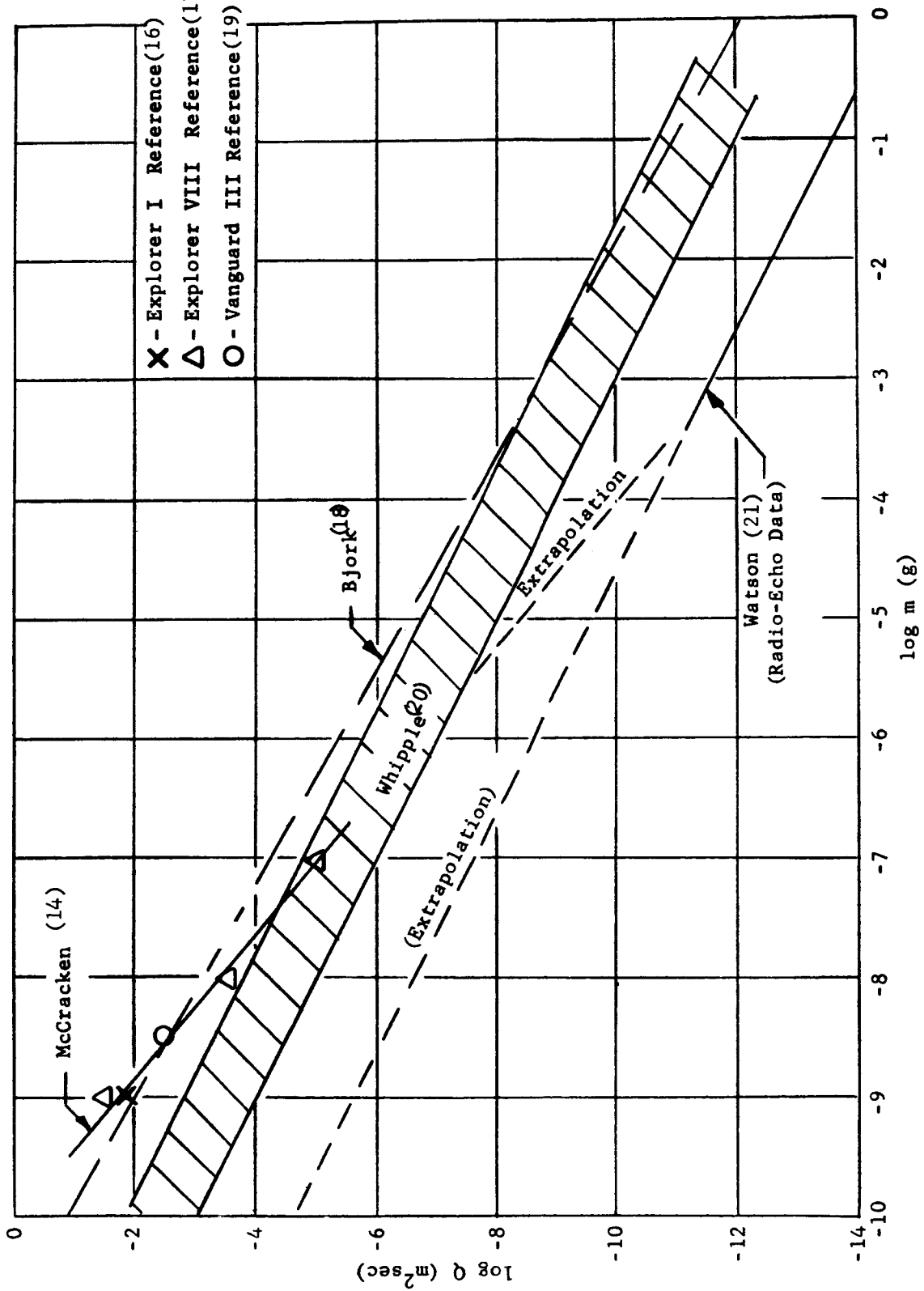


Figure 8. Meteoroid Flux Near Earth vs. Mass

Figure 7 presents the data obtained from various satellites and rockets, radio-echo results, and assumed and extrapolated distributions from a number of investigators (References 14 and 16 through 21). These distributions have the form:

$$\phi = \frac{K}{m^a} \quad (1)$$

where ϕ is usually given the units of particles/meter²sec and (m) in grams. The constants used by various authors range from 10^{-17} to 10^{-12} for (K) and from 1.0 to 1.7 for (a). For the purpose of assuring that meteoroid damage is not underestimated, the more conservative distribution used by Bjork (Reference 18) will be employed:

$$\phi = \frac{10^{-12}}{m^{10/9}} \quad (2)$$

The problem of determining the damage caused by a given meteor does not lend itself to theoretical analysis, and to date it has not been possible to experimentally accelerate particles of well-defined mass to meteoric velocities. Hence, extrapolations of lower velocity data must be used.

The range of meteor velocities is from 11 km/sec to 72 km/sec. The lower limit is equal to the Earth's escape velocity. This is the velocity that a particle at rest, with respect to Earth, would attain after falling several Earth radii to the sensible atmosphere. The upper limit is that of closed solar orbital velocities (parabolic orbit velocity) at Earth.

2. Erosion

Erosion of the surface was also listed as another possible hazard of meteoroid impacts. However, Jaffe (Reference 22) has indicated that this erosion results in a volume loss of less than 1 Å/year far from the earth and about 200 Å/year close to the earth. This has been verified by examination of meteorites picked up on the Earth whose ages were measured by isotope analysis (References 23 and 24). Erosion of these pieces by smaller meteoroids and other sources while far from earth was less than 30 Å/year. Jaffe concludes that the amount of dust erosion expected is thus so small that the effect (if any) on engineering properties will probably be limited to degradation of optical properties of exposed lenses, mirrors, and windows.

Figure 8 summarizes the information gained on meteoroid impact flux. The results of the latter portion of the investigation indicate that erosion will not cause structural damage but might degrade optical surfaces.

E. Requirements for Protection from Radiation

1. Ionizing Radiation Environment (Unshielded)

Beyond the protective blanket of the Earth's atmosphere, an environment of particulate and electromagnetic radiation exists which can damage and

kill living cells. Man has never had to adapt himself to survive and procreate in such an environment. Thus, astronauts embarking upon space exploration must be protected and radiation damage minimized. In regions far from the Earth and in the radiation belts around the Earth, this hazard is formidable; consequently, very heavy shielding is required for protection (Reference 25).

The hazard of electromagnetic radiation at lower altitudes (less than 500 miles) in reference to the Earth is insignificant, as this is just below the lower radiation belt. In these regions, only high-energy protons will pass through the wall of a space vehicle and threaten damage to the astronauts and the vehicle's contents (Reference 2). Such high-energy protons are in evidence, however, when sporadic giant solar flares cause an influx of high-intensity, high-energy radiation. Periods when the solar activity is at a minimum will allow relatively safe habitation of the orbiting vehicle for 5 to 30 days. Emergency procedures and equipment, including warning devices, however, are required for solar flare protection.

The hazard of electrons is considered to be insignificant for these altitudes also. Generally, the electrons will be stopped in the outer skin of the space vehicle. Secondary radiation produced when electrons are decelerated (bremstrahlung), have a much greater penetrating power than the electrons causing them. For the lower altitudes, however, the bremstrahlung intensity is also considered to be insignificant.

Further, the only ionizing radiation to contend with below the 500 miles altitude, in the absence of solar flares, is the solar and intergalactic background flux of protons (References 2, 26, and 27) with the possible exception of artificial radiation belts. The following information is taken from Reference 2, and presents a limited description of the energy distribution of these protons.

PROTON SPECTRUM AT 500 km (310 mi) ABOVE THE
EARTH AT 30 DEGREES GEOMAGNETIC NORTH
(Reference 2)

<u>Energy Range, MeV</u>	<u>Proton Flux, cm⁻² sec⁻¹</u>
23	--
23 - 52	10
52	1

Figure 9 gives the variation of cosmic radiation dose with altitude. (28)
The peak dosage between 10 and 15 miles is due to interaction of the cosmic primaries with the atmosphere, resulting in a large flux of secondary radiation. Subsequently, the dose gradually rises with altitude, due to the decreasing shadow effect of the Earth.

The complete spectrum of types and levels of radiation have not been fully determined as yet. Hence, it is extremely difficult to accurately predict radiation levels for a specific mission. The approach to be taken in this program will be therefore, to determine material capabilities.

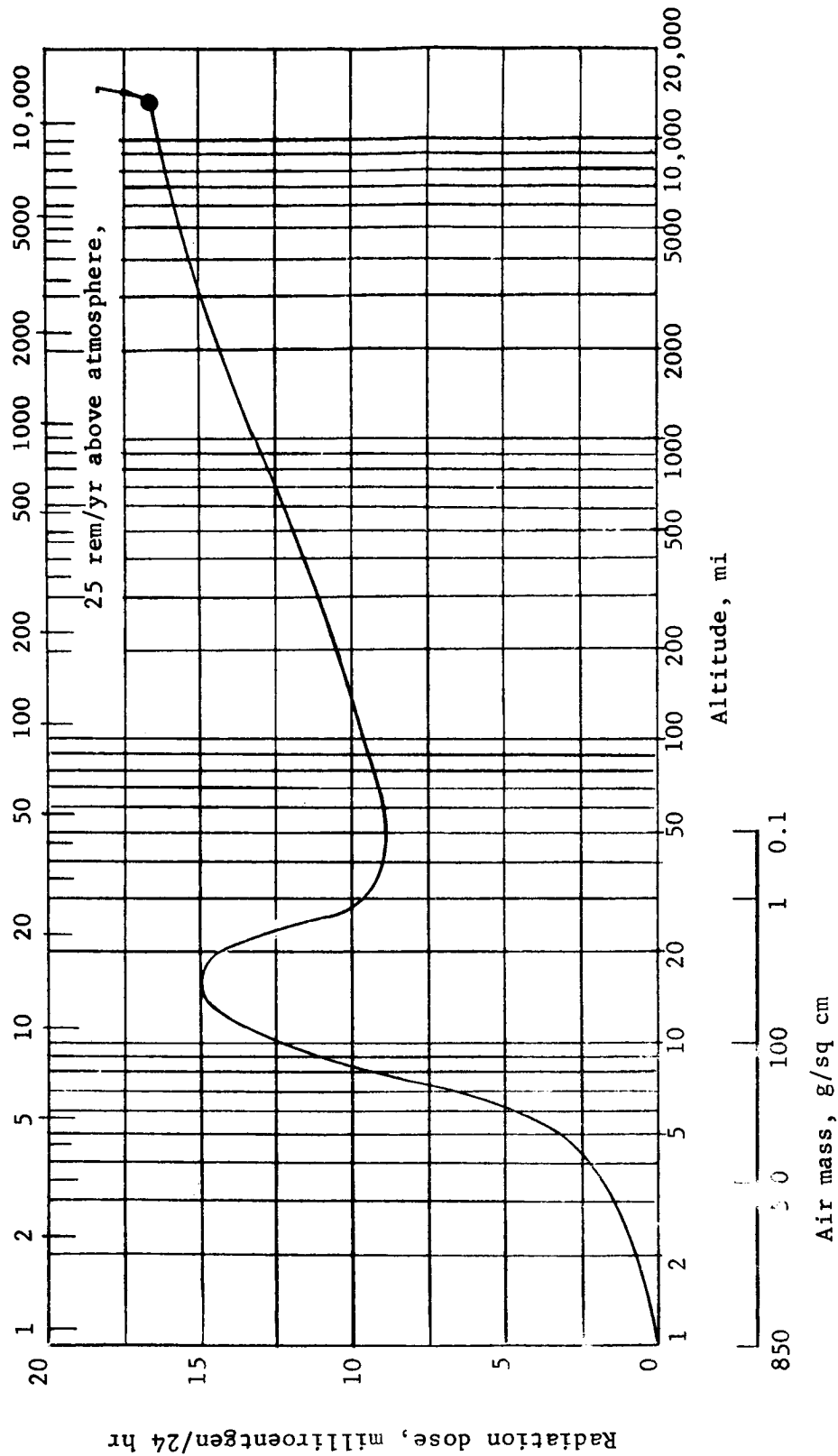


Figure 9. Effect of Earth's Atmosphere on Cosmic Radiation (Reference 28)

F. Structural Requirements of Solar Collectors and Space Antennas

1. Loads

The primary loads imposed upon a solar collector or antenna in space result from the sun. The sun as a source of energy is the subject of constant investigation. Because of the influence of the earth's atmosphere upon these investigations, many observations are made at high altitudes, in aircraft, and from high-altitude balloons. Thus, the sun is generally considered to approximate a blackbody radiator at a temperature of 6000°K, having its radiant energy peak at 0.5 μ as shown in Figure 10. The solar radiant power occurs in the following ranges: 50% in the infrared wavelengths longer than 0.7 μ, 25% of the energy at wavelengths longer than 1.0 μ, and 2% of its energy in wavelengths longer than 3.0 μ.

The loads imposed when utilized on planetary surfaces will be similar to those outlined in Section II.A. Therefore, it is possible that load combinations with thermal conditions can be imposed.

2. Solar Collectors

The energy density used to evaluate solar mirrors for space applications is based upon the solar constant at the earth's orbital radius and taken to be 130 watts/sq ft; or, power radiated from the sun and intercepted by a receptor may be approximated from the blackbody law as

$$P = \frac{A_s A_d T^4 \sigma}{\pi D^2}$$

where

σ = Stephan-Boltzmann constant

A_s = Area of sun

A_d = Area of receptor

T = Temperature of sun

D = Distance from sun

P = Power in watts

The obvious value of this approximation lies in its use when the solar collector is used on a mission in which the figure of merit is different from that at the earth's solar constant. The power received by the collector is then directed to an energy convertor.

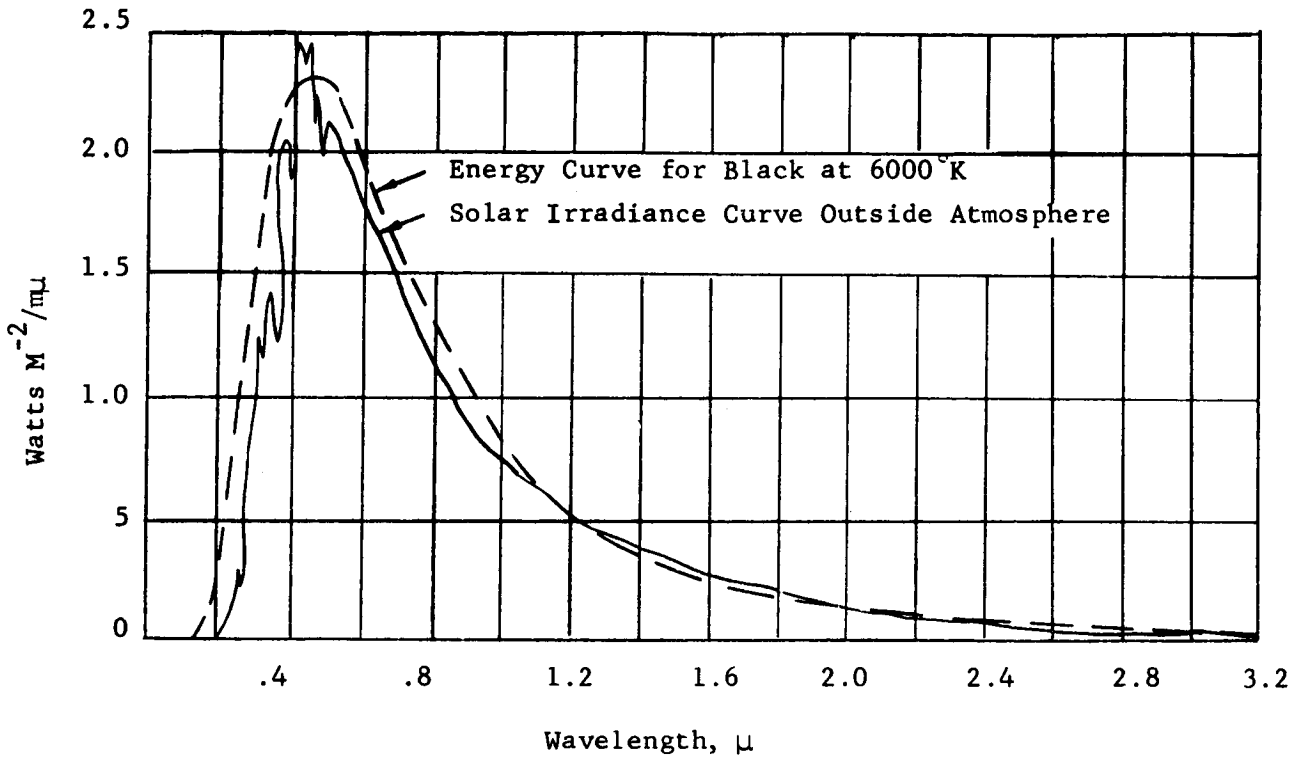


Figure 10. Spectral Energy Curve Related to the Sun¹³

The efficiency of the collector is a function of the wavelength of the reflective medium. Due to the short wavelengths involved, the surface tolerance for the solar collector must be small. If a parabolic solar mirror could be constructed having some arbitrary surface accuracy, the energy concentration would be contained in a relatively large density area, and at a low intensity. As the surface accuracy of the reflector increases, the area of concentration decreases and the intensity increases. If the function of the solar reflector is to concentrate energy, then the active area of solar intensity required for conversion must be taken into consideration. Energy outside this area would be classified as spillover energy and would be lost, thus reducing efficiency.

The maximum theoretical efficiency of a parabola to provide the maximum collimation of spectral energy, assuming a perfect parabola, is 55%. The 55% efficiency also assumes a perfect reflecting surface which cannot be achieved. Some of the energy incident upon the reflecting surface is lost by diffusion, and some is lost as heat due to the surface being a sink. The maximum reflectance obtainable, therefore, would be somewhat less than 90%. The optimum theoretical efficiency is less than 50% at wavelengths in the $1\ \mu$ region. One micron corresponds to a frequency of 10^{14} cycles, so the wavelength λ is slightly greater than 0.0001 in. To achieve the theoretical efficiency for optimum energy concentration, the mirror surface accuracy should be maintained accurate to $1/8$ wavelength or 0.0000147 in., obviously an impossible case regardless of the technique of reflector construction. However, degrading the mirror surface contour defocuses the mirror for those points of discontinuity and, in addition to increasing the phase error, enlarges the area of collimated energy. Since this results in a reduction of intensity, the mirror collimating efficiency has been reduced.

The solar energy has been defined as a power spectrum and, therefore, the energy is dispersed over this spectrum, although only 2% of this energy exists at wavelengths longer than $3\ \mu$. Consider the mirror designed for a wavelength in the far-infrared which may possibly be feasible within near-future manufacturing technology: If the wavelength is assumed to be $10\ \mu$, then the wavelength will be approximately 0.001 in. The efficient mirror surface, therefore, would be accurate to 0.000125 in. and with a 3-sigma Gaussian distribution; i.e., 99.97% of the surface shall be within 0.0008 in. To maintain the contour accuracy such that a 1-sigma distribution is achieved at $1\ \mu$, maintaining 68.27% of the surface within an rms deviation of 0.0000147 in. is required. Assuming that the above contour accuracies are achieved on a 5-ft diameter parabolic mirror with 90% reflectance efficiency and that the mirror is oriented to the sun at the earth's orbital radius, the energy incident upon the mirror will be 2554.5 watts. The collimated energy of the parabola focal point, maximum intensity concentration, will be 753 watts.

If the mirror contour is degraded further, so that the 1-sigma distribution is 0.0008 in., the energy intensity at focus will be reduced to approximately 93 watts. Although the energy density appears small, its concentration is very high (about 0.8 milliradians), and therefore, the concentration temperature is very high.

If the solar loading effects upon a mirror are considered with the limitations of achieving an optical surface, large diameter mirrors apparently would degrade in contour as the diameter is increased. The collimating efficiency would reduce to the extent where increasing the diameter could contribute to phase error, which results in a further efficiency reduction. Therefore, the most efficient collector would be a number of small-diameter, high-precision mirrors with their attached energy convertors connected in series.

3. Antennas

The tolerance of the surface contour of an antenna is not nearly as critical as the collector. The permissible surface deviations peak to peak for communication and telemetry antennas, where frequencies range up to 1000 Mc, are shown in Figure 11. Figure 12 presents those for microwave communication antennas, where frequencies range from 2000 to 15000 Mc.

The following summarizes the conclusions reached during this phase of the study:

Loads: Those of primary concern are thermal stresses. However, the loads as outlined in Section II.A also apply.

Collectors: Required surface accuracies are such that the use of large, stationary collectors is precluded. Multiple small collectors appear to be the most efficient approach.

Antennas: Permissible surface deviations are given in Figures 11 and 12.

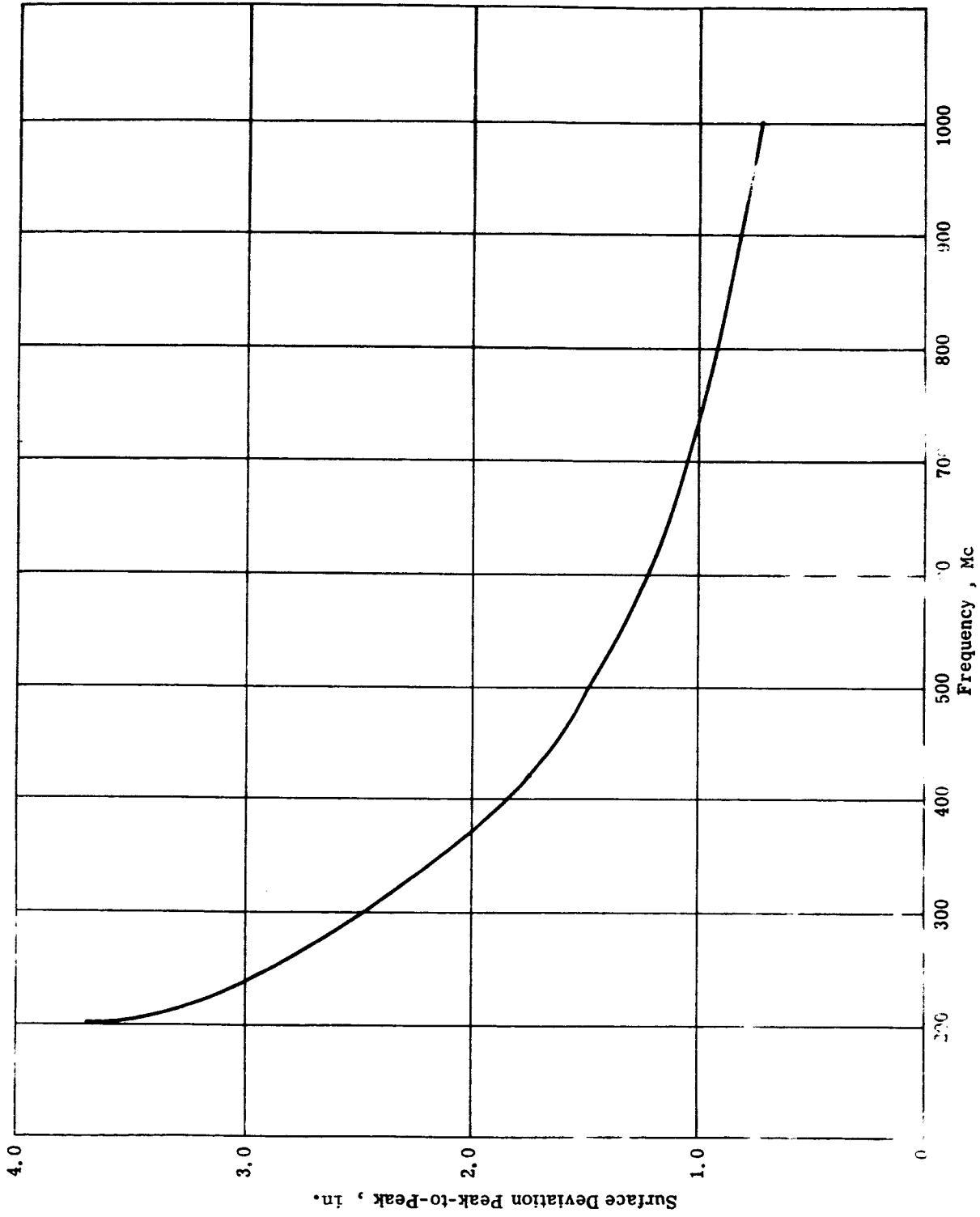


Figure 11. Contour Surface Accuracy Required for Communication and Telemetry Antennas (UHF to Microwave)

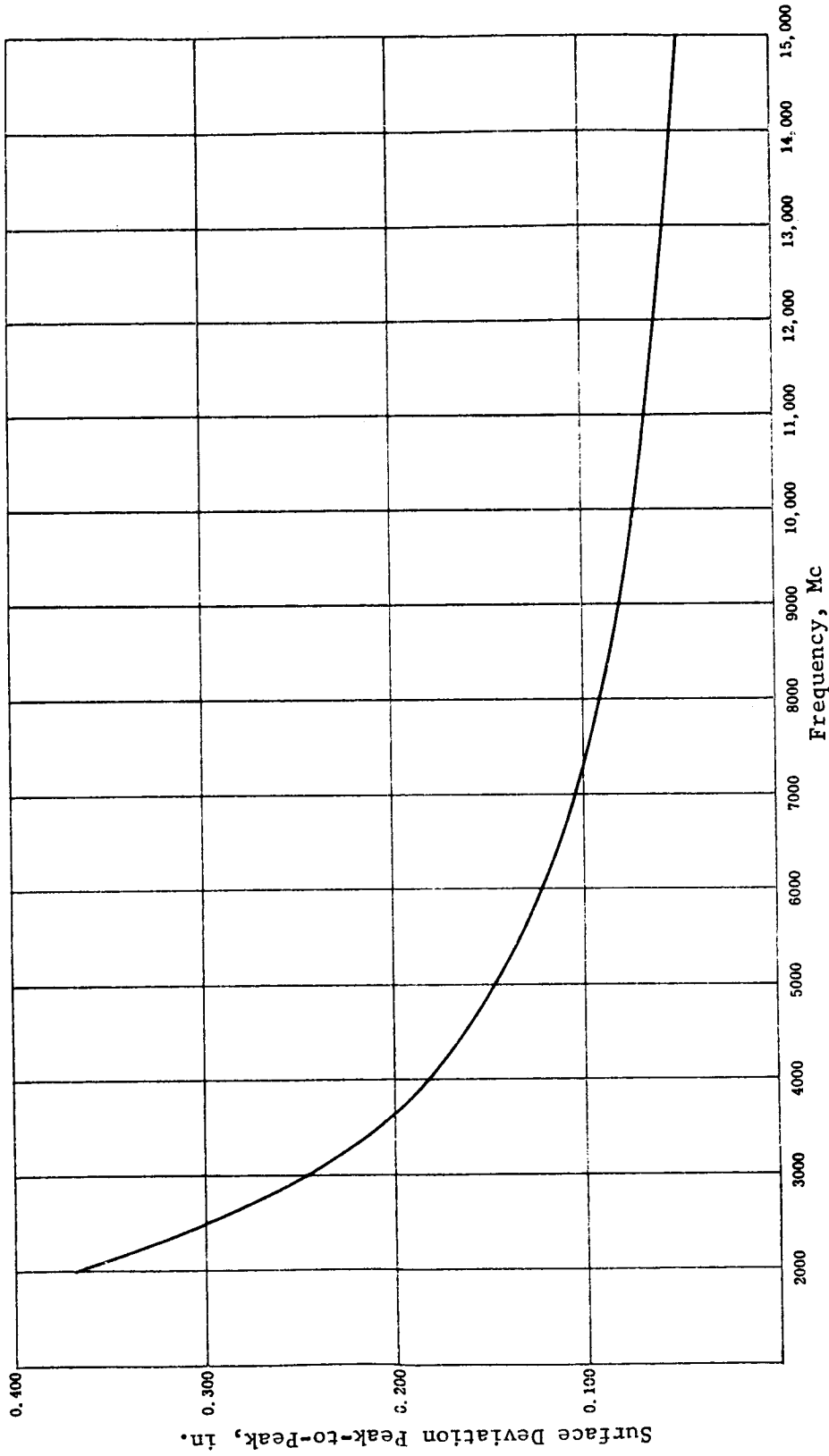


Figure 12. Contour Surface Accuracy Required for Communication Antennas (Microwave)

III. MATERIAL AND COMPOSITE STUDIES

The application of the elastic recovery to space structures is dependent upon the materials used in the composite. For this program, the materials of the elastic recovery composite were divided into the following three general classes:

1. Film: The material represented the material needed for either outer surface thermal control or internal impervious gas barriers.
2. Laminate: The laminate material was required for the primary structural skin and also to provide the necessary protective layers.
3. Core: The core performs the expansion function through its memory and recovery phenomenon, besides offering protection from meteoroids.

The most efficient way of determining the feasibility of the application of elastic recovery concept to space structures was considered to be an evaluation of materials both separately and combined into composite sections. Consequently, this portion of the report is separated into these two general areas. The first portion presents the individual material characteristics, while the second portion describes the different studies performed upon sections of the elastic recovery composite. These studies investigated the compressibility, recovery, and expansion characteristics of the elastic recovery concept.

A. Materials

Section III is concerned only with the basic structural requirements for elastic recovery materials; the specific requirements (e.g., the material needed for the structural requirements, thermal, meteoroid, and radiation protection) are discussed in Section IV and in the Appendixes.

The effect of the space environment was not investigated in detail for this initial study since only limited data are available from literature. To fully determine the effect of the space environment, the combination of vacuum, ultraviolet and solar radiations was beyond the scope of this program. However, the effect of the space environment is recognized upon certain materials which would have application to the elastic recovery composite.

1. Film Material

The film materials are used for either outer surface thermal control or an inner wall gas barrier. The thermal control aspects of the film surface are discussed in detail in Appendix C. The general requirement for the thermal control surface coating depended upon the orientation of the space structure to the sun. It was assumed that the coating material would be applied to a carrier film by either painting or vapor deposition. The strength of the carrier film material was of particular

interest. The literature was surveyed in order to determine the strength characteristics of different film materials. Table 1 summarizes the data available; i.e., the area factor, specific gravity, tensile strength, tensile modulus, elongation, and tear strength for several representative film materials. The range of strength levels for the individual film materials apparently is the result of different methods of forming. The other main function for a film material would be the retention of gas; consequently, the permeability to gases was also determined for the selected materials (see Table 2). This information was obtained from several literary sources. The data were reduced to common units for the basis of comparing the different materials. The results indicate that the polyvinylidene chloride (e.g., Saran) maintained the lowest gas permeability of all the materials and would probably be the material used for this purpose. It should be noted that the water vapor permeability of those materials listed was for the 100% humidity condition. The figure appears to be high; however, in an actual atmosphere, the water vapor would be a smaller portion of the total atmosphere.

The use of a film gas barrier will be required for the weight studies of the application of the elastic recovery concept to a space vehicle design. Possibly, however, the resin used in the impervious film may also be used in the laminate. If the resin-reinforcement interface has a high-strength bond, then perhaps the additional material required for the impervious layer would not be required.

2. Laminate Materials

It was originally planned to use data from literature for the strength characteristics of the flexible laminate materials, but as the study progressed, it was apparent that information was not available on laminates made with flexible resins and synthetic cloths. In order to obtain the required data, a limited test program was initiated for several combinations of flexible resins and reinforcements.

The evaluation of the different laminate combinations was accomplished by fabricating 12-in. square panels. The various combinations of resins and reinforcements used in the laminates along with the cure process and test results are listed in Table 3. The last two laminate combinations listed were not tested, as fabrication difficulties occurred and a good quality laminate could not be made. Since it was beyond the scope of this program to develop process techniques for laminates, the results probably represent values from nonoptimum processing for each panel. The relatively high resin content substantiates the fact that the laminates were not of high-strength quality. However, a laminate with high resin content may have a higher degree of flexibility than a typical laminate with low resin content.

The completed laminates were machined into tensile specimens and tested at room temperature. The tensile tests were conducted by using Federal Test Methods Standard No. 406, Method 1011, "Plastics: Methods of Testing." This test was chosen since the tensile strength is of primary interest in an expandable structure. The tensile modulus was also determined and will be used in the stiffness studies. It was assumed that the compressive modulus of elasticity will closely match that of the tensile modulus.

TABLE 1

STRENGTH PROPERTIES OF TYPICAL FILM MATERIALS

Material	Area Factor, in. ² /lb/mil	Specific Gravity	Tensile Strength, psi	Tensile Modulus, psi	Elongation, %	Tear Strength, lb/in.
Polyvinylidene Chloride*	16,000-23,000	1.20-1.68	8,000-20,000	-	20-140	80-465
Polyester Terephthalate*	20,000	1.38-1.395	23,000	550,000	100	-
Polyvinyl Chloride* (PVC)	20,000-23,000	1.20-1.45	7,000-10,000	-	150-500	110-490
Polytetrafluoroethylene*	12,800	2.1-2.2	1,500-4,000	-	100-350	-
Polyimide film**	19,500	1.40	25,000	430,000	70	-
Polyurethane Rubber***	-	-	6,000	1,700 @ 300%	550	430

* From Modern Plastics Encyclopedia: 1963 Issue

** E. I. du Pont de Nemours & Co., Film Dept. information

*** BF Goodrich Chemical Company information

TABLE 2
PERMEABILITY OF FILM MATERIALS

Material	Permeability to Gases, $\frac{\text{cc-mil}}{100 \text{ in.}^2/24 \text{ hr/atm}}$			
	Nitrogen	Oxygen	Carbon Dioxide	Water Vapor @ 100% Humidity
Polyvinylidene Chloride	0.86**	3.0*	9.0***	11.5**
Polyester Terephthalate	1.2*	5.6*	27**	1485**
Polyvinyl Chloride (PVC)	43***	123*	58***	-
Polytetrafluoroethylene	9.5*	30*	-	-
Polyimide film	5.8****	24.5****	-	-
Polyethylene	210***	655***	2240***	-

* From Modern Plastics Encyclopedia: 1963 Issue
(31)

** Goodyear information

*** C. J. Major and K. Kammermeyer, "Gas Permeability in Plastics," Modern Plastics, July 1962

**** E. I. du Pont de Nemours & Co., Film Dept. information

TABLE 3

RESULTS OF FLEXIBLE LAMINATE TESTS

Panel	Resin & Reinforcement	Cure Process Time @ Press Temperature @ Press Pressure	Specific Gravity	% Resin	Av. Ultimate Tensile Strength, x 10 ³ psi	Av. Tensile Modulus, x 10 ⁶ psi
A	RTV Silicone, 181 style glass cloth	16 hr @ 200°F @ 40 psi pressure Postcure: 8 hr @ 300°F	1.37	43.7	N.A.**	0.158
B	RTV Silicone, 181 style regenerated cellulose fiber cloth	16 hr @ 200°F @ 40 psi pressure Postcure: 8 hr @ 300°F	1.00	56.9	N.A.**	N.A.**
C	Polyvinyl Chloride, 181 style glass cloth	5 min @ 310°F @ 100 psi; increased pressure to 200 psi; cooled press	1.71	39.0	14.85	0.202
D	Polyvinyl Chloride, 181 style regenerated cellulose fiber cloth	Same as Panel C	1.29	41.0	17.15	0.403
E	Polyvinyl Chloride, 112 style glass cloth	Same as Panel C	1.48	61.6	14.84	0.567
F	Polyurethane, 181 style glass cloth	1 hr @ 300°F @ 150 psi; cooled under pressure	1.83	18.5	15.44	1.34
G	Polyurethane, 181 style regenerated cellulose fiber cloth	Same as Panel F	1.41	45.8	33.32	1.35
H	Polyvinylidenechloride, 181 style glass cloth	Not Processed	-	-	-	-
J	Polyvinylidenechloride, 181 style regenerated cellulose fiber cloth	Not Processed	-	-	-	-

* Not available - test specimens failed in grips

** Not available - test specimens degraded

The results of these tests (summarized in Table 3) show that there is an extreme range of values for different combinations of materials. Again, the range of the strengths shown may be attributable to the processing of the laminate. Table 3 also gives the specific gravity and resin content for the laminates tested. The specific gravity and percent resin for the glass fabric laminates were obtained by using Federal Test Methods Standard No. 406, Methods 5012 and 7061 respectively. The resin percentage for regenerated cellulose fiber cloth (e.g., Fortisan) laminates was approximately obtained by determining the weight increase of the cloth due to the resin impregnation.

Some difficulties were incurred in the processing of laminates, particularly with the flexible RTV silicone and polyvinylidene chloride resins. The use of RTV silicone as a laminating resin was doubtful, but the inherent flexibility of the material made it seem attractive as a material for the elastic recovery concept. This material did not impregnate the reinforcement as a typical resin; instead, the resulting laminate consisted of distinct layers of reinforcement and resin matrix. This no doubt contributed to the flexibility of the material, but also made testing impossible since the test specimens could not be gripped satisfactorily. The glass cloth specimen failed by interlaminar shear in the grip area.

The laminates which were to be made with the polyvinylidene chloride resin could not be processed, although several attempts were made with different process parameters. However, this material still seemed promising as an expandable structure material since the resin has good strength as a film.

The results of this laminate test program indicate the following general trends:

- a. The test laminates were more flexible than general reinforced plastic laminates. Based upon the stiffness, the flexibility of the materials ranged from approximately the same as the films up to approximately one-quarter that of the typical reinforced plastics. Hence, the laminates did have the higher modulus required for stiffness when compared with nonreinforced film materials.
- b. These materials were not made with laminate optimization in mind, since this would have been beyond the scope of this feasibility study.
- c. The strength ranged from values approximately the same as films and rubber-coated fabrics up to the typical strength of structural laminates.
- d. The effect of cryogenic temperature upon these laminates is not completely known at this time.*

* Previous experience as given in ASD-TDR-62-794 Part II, Determination of the Performance of Plastic Laminates at Cryogenic Temperature, indicates that the strength of flexible laminates increases appreciably as the temperature decreases, while the modulus exhibits a slight increase.

3. Core Materials

An investigation was made into the types of flexible and compressible core which would be applicable to the elastic recovery concept. The work included the fabrication of core samples from different materials to determine their degrees of flexibility and strength. The flexible cores included foams and cellular cores. An example of the cellular core would be one which compresses in one direction. This core type is fabricated with flat strips, then expanded to form the cell size. The foam materials are, of course, compressible in all directions. In general, the shear strength and modulus of the compressible cores ranged from a few hundred to the order of a thousand pounds per square inch. The strengths for lightweight paper and fiber glass-reinforced plastics are given in Table 4. The lightweight paper core may have an application for expandable structures, providing the space environment does not degrade the materials.

For supplemental information, Narmco fabricated and evaluated semirigid cores by using flexible materials. The materials included regenerated cellulose fiber-reinforced polyvinyl chloride and different types of rubbers; samples of these cores are shown in Figures 13 and 14 respectively. These cores were made with the Multiwave pattern for ease of fabrication. The pieces were subsequently tested for core shear modulus and flatwise compression. The results of these tests also are shown in Table 4. Interestingly, the weight of these developmental cores are on an order of magnitude higher than the lightweight honeycomb and foam cores.

One of the most interesting developmental cores was one made with 1/64-in. thick chloroprene (e.g., Neoprene) rubber. This semirigid core was not only compressible but was flexible enough to be folded upon itself. The sample of this core is shown in both the normal and folded position in Figure 15. The core shear modulus and compressive strength of this sample as shown in Table 4 appeared to be extremely low for its weight.

The results of this limited evaluation of core materials indicate their low core properties and relatively high density may rule out use of this type of core material. However, the strength characteristics of core materials can be improved not only by using different materials but also by different core cell geometry. A different cell geometry would allow for better utilization of the low-modulus material and still have the necessary compressibility for an expandable structure. A further investigation of the core materials applicable to the elastic recovery concept provided the determination of the area expansion rates and the expansion-to-contraction ratio for flexible honeycomb type cores. Three types of cores were investigated: "sine wave," square, and rectangular. Results indicated that when a flexible honeycomb core configuration will be required in an elastic recovery expandable structure, it will have to be in "underexpanded" condition, in order to minimize the Poisson distortion of cells. It also appears that a square cell configuration would not be efficient, due to excessive distortion and limited node bond area. The complete study is given in Appendix A to this report.

TABLE 4
TYPICAL CORE MATERIALS FOR EXPANDABLE STRUCTURES

Material	Density, lb/ft ³	Flat Compressive Strength, psi	Shear Strength, psi	Shear Modulus, psi	Compressive Modulus, psi
Paper Honeycomb (Douglas Aircomb- Style 60-20 Type 40) *	2.6	103 TYP	42 TYP	1-in. Thick 3500	-
1-2 lb/ft ³ Urethane foam **	1.35	-	1.8	-	-
Natural Rubber "Multiwave" **	24.7	24	4.5	19.7	165
Neoprene Rubber "Multiwave" **	14.7	5.0	2.5	10	65
Fortisan - Plastisol Fabric "Multiwave" **	14.3	52	32	142	519
Fiberglass Honeycomb Hexcel NP 3/8-21-2.5 ***	2.5	180	70	4500	15,500

* Data from Douglas Aircraft Co. "Aircomb" brochure

** Test data results

*** Data from "Honeycomb Sandwich Design Data and Test Methods,"
Hexcel Products Inc.

Note: All tests conducted on 1/2-in. thick specimens except where noted.

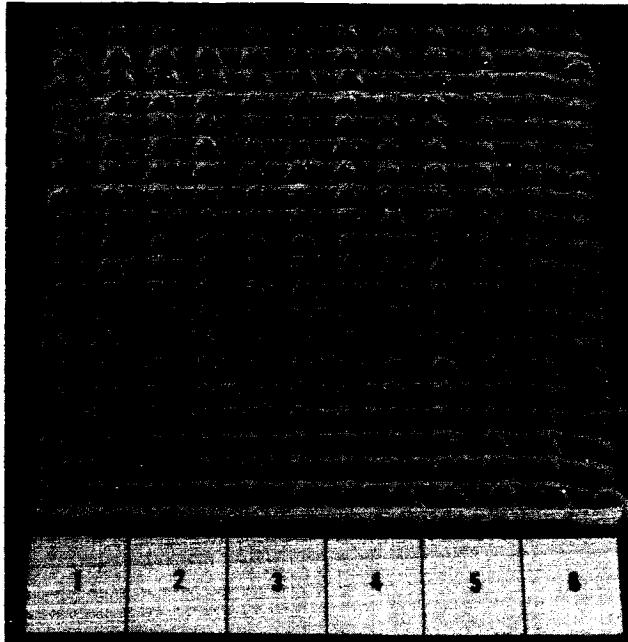


Figure 13. Experimental Semirigid Core of Polyvinyl Chloride Reinforced with Regenerated Cellulose Fiber Cloth

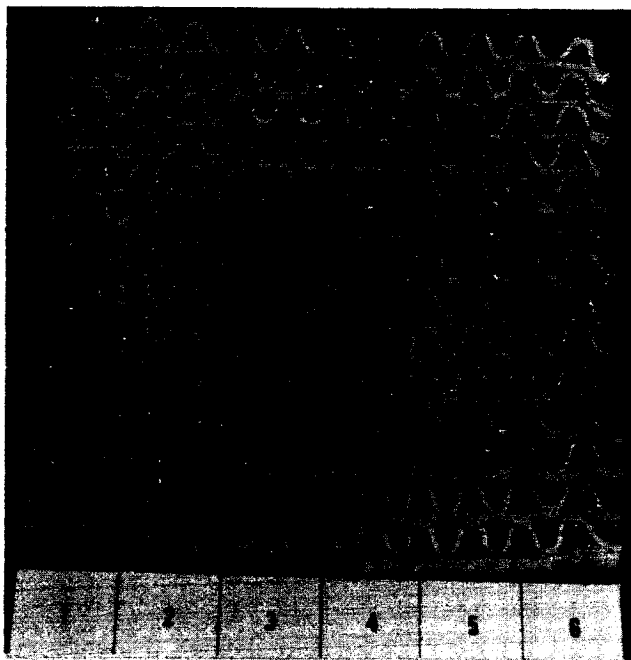
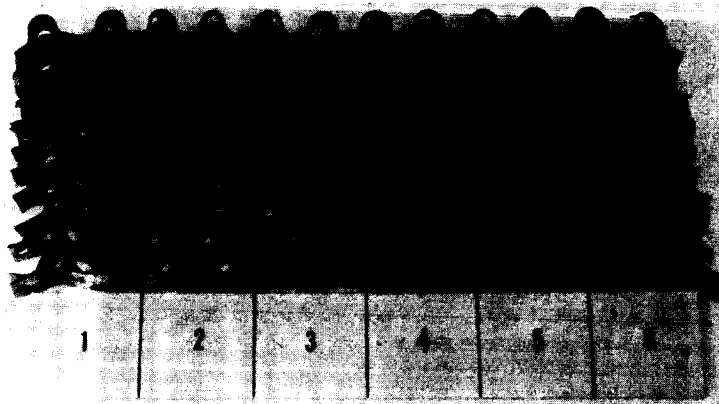


Figure 14. Experimental Natural Rubber Semirigid Core



Normal Expanded Position



Folded Position

Figure 15. Experimental Flexible Chloroprene Rubber Material

B. Composites

The second portion of the material studies was to determine the behavior of the elastic recovery composites. These studies were set up to ascertain the effect of different environments on the expansion characteristics, the load-deformation behavior, and load-carrying ability of typical elastic recovery composites.

1. Composite Wall Concepts

The starting point for this series of composite studies was the determination of typical wall configurations which would be applicable to the elastic recovery concept. The end use, or application, of the expandable structure will essentially determine the type of composite required. For example, the expandable structure subjected to an internal pressure will have tensile stress induced in the composite wall. On the other hand, the structure subjected to either external pressure or impact loads will have to be designed with the stability criteria in mind. The load conditions greatly affect the type of wall concept which may apply to expandable structures. The requirement for storage of energy for expansion of the structure is also of prime importance. Other equally important requirements include protection from radiation and micrometeoroids.

The different types of wall concepts were determined by assuming the different loading requirements. The simplest concept (Figure 16a) consists of a primary load-carrying inner facing, compressible core material for micrometeoroid or radiation protection, and a surface film for the thermal control. Since this wall concept uses only the inner facing for the structural portion, the intended use would be for tensile applications, based upon the assumption that the core material has such a low core shear modulus and compressive modulus that it is not capable of transferring load to other facings in the composite.

The second wall concept for the elastic energy concept is a modification of the previous one. This concept (Figure 16b) has additional layers of material within the core material. It was assumed that an additional material would be required to provide more protection from the space environment. The layer would consist of either impregnated or plain cloth, and would be nonstructural.

The third concept (Figure 16c) would be used where additional stiffness is required for the wall of the expandable structure. For example, the stiffness would be required to prevent deformation of the structural wall. The semirigid core would be needed in this case to stiffen and transfer the load from the inner facing to the second load-carrying face. The proportion of the load transferred to the second facing would be dependent upon the properties of the core; that is, the higher the compressive modulus of the core, the higher the proportion of load transferred.

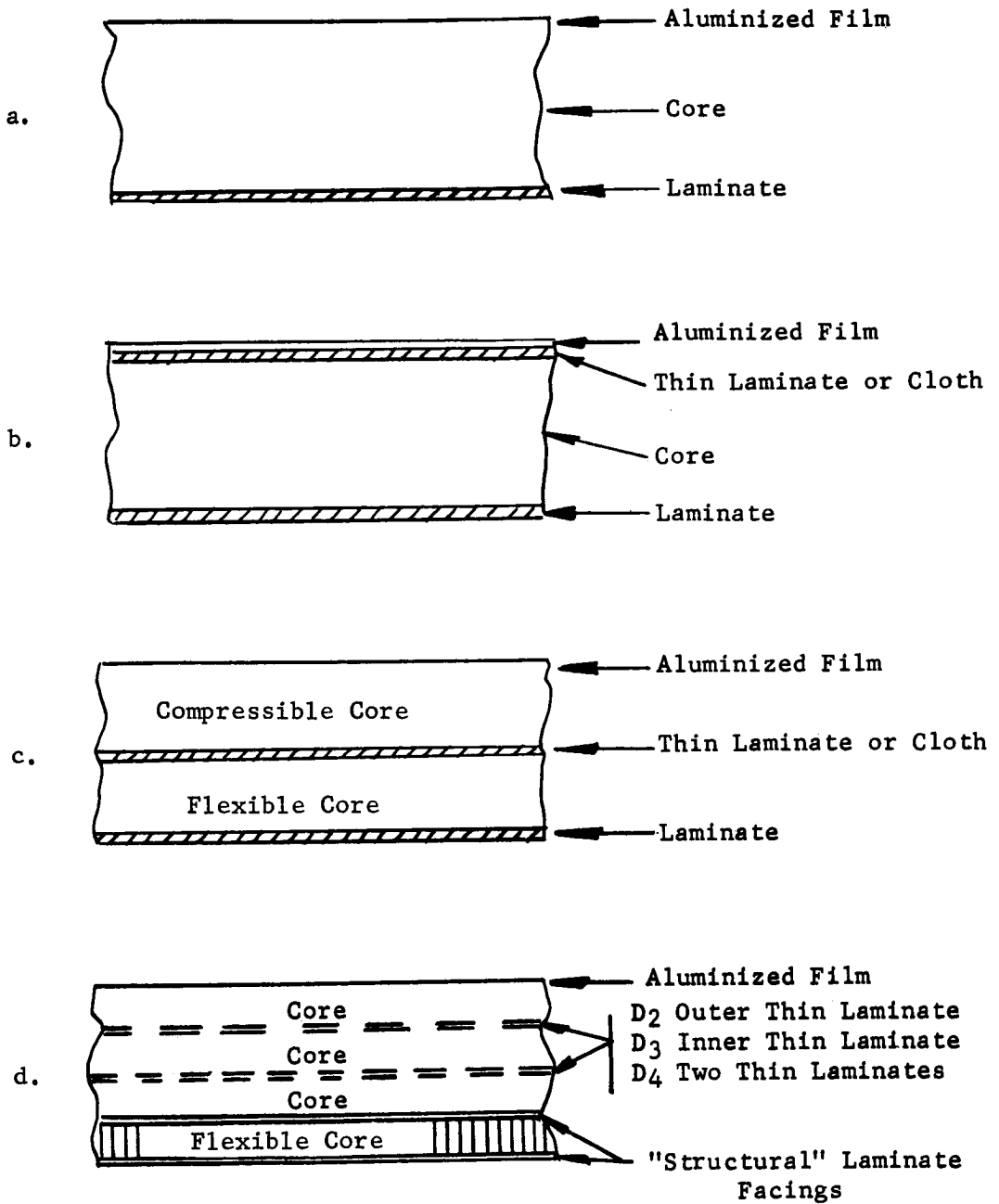


Figure 16. Wall Concepts for Expandable Space Structures

The fourth concept (Figure 16d) is a modification of the third concept wherein additional layers of cloth were included in the composite. The purpose of the cloth is again to improve the protection against the space environment. As with the second concept, the cloth would or would not be impregnated with a flexible resin in order to achieve the maximum protection.

The four main classes of wall concepts were used throughout the remainder of the study to determine which one will be the best wall for a particular space structure application. By using these general wall concepts for the different areas of investigation (i.e., structural, thermal, meteoroid, or radiation), a measure of consistency was available. As each of the major areas of study progressed, the general wall concept was modified to improve its characteristics. These changes will be noted in the discussion of the results of the studies.

2. Composite Expansion Characteristics

This study was performed with models to determine the expansion characteristics of an elastic recovery composite in different environments. The simulated environments used were

- a. Room temperature and atmospheric pressure
- b. Room temperature and vacuum
- c. Long-term compression at room temperature
- d. Cryogenic temperature

Under these conditions, the time for erection of a package cylinder was observed.

In all the tests, a cylinder with a 10-in. inside diameter and a 10-in. length was packaged into an approximately spherical container with a radius of 2.5 in. Different identical cylinders which consisted of a 1-ply laminate inner skin, 1 in. of 1.5 lb/ft³-foam, and aluminized polyester terephthalate (specifically, Mylar) outer skin were used for the tests. The expanded-to-package ratio based upon volume was approximately 22, which does not represent an optimized ratio because the container was not packed full. Two of the tests were run at room temperature: one at atmospheric pressure, and one under a vacuum of 5×10^{-5} torr. Erection time for the cylinders was 10 minutes for the vacuum test and 12 minutes for the atmospheric test. This indicates that there is little difference in the time in which the structure regained its original shape for the two environments. The time could not be accurately measured to complete erection, because final changes in shape of the structure are difficult to determine. The erection sequence for the packaged cylinder in the vacuum was shown in Figure 1.

The third test was to determine the effect of long-term compression upon the packaged cylinder. The test cylinder was packaged into the container for a period of 6 weeks. The container was released and the erection of

the cylinder took place over a period of 2 hours. Although the time for recovery was longer for this cylinder, this test indicated that the elastic recovery concept will still perform its primary function; i.e., causing the structure to regain its original shape.

The fourth and final test in this series was to cold-soak the packaged cylinder and observe the recovery time. The packaged cylinder was put into a dry-ice storage box for 2 hours, then taken out and allowed to expand at room temperature. Room temperature expansion was necessary, as no large-volume cold facility was available in the laboratory; this also took 2 hours.

The results of all of these tests are summarized graphically in Figure 17.

3. Composite Compressibility

A parallel study to the long-term packaged test discussed above was performed. In this study, however, the effect of long-term loading upon the compressibility or load deformation characteristics upon a typical section of the elastic recovery concept was investigated. This specimen was compressed for a 3-month period; the load deformation characteristics were studied. The sample, shown in Figure 18, was 4-in. square and approximately 2-in. thick. The composite consisted of a 3-ply inner laminate, and an outer skin of aluminized polyester terephthalate. The laminate consisted of regenerated cellulose fiber cloth impregnated with a polyvinyl chloride (PVC) resin.

The foam of the composite was compressed with sufficient load to cause it to "bottom out," which would represent the compressed condition of a folded elastic recovery structure. For greater simplicity, the test was performed at room temperature and atmospheric pressure. The load deformation characteristics of the composite were determined prior to the test, immediately after removal of the weight (after 3 months of compression), and again 5 days after the weight removal. The load deformation curves were plotted as shown in Figure 19. This test showed that although there were gross changes in the deformation characteristics of the composite or, more correctly, of the foam, there was also an adequate recovery of the foam (i.e., the primary erection function of the foam was not impaired, even though it was slowed down). It was also interesting to note that after a period of 5 days, the foam appeared to have recovered a large portion of its original load deformation characteristics.

4. Composite Load-Carrying Capability

The last major area of investigation of composite sections of the elastic recovery concept was to determine the load-carrying capabilities and also the thickness of foam required for erection of the laminate. These areas of investigation were determined empirically since no theoretical solution for the composite construction was available. Samples representing the elastic recovery concept were fabricated with varying foam

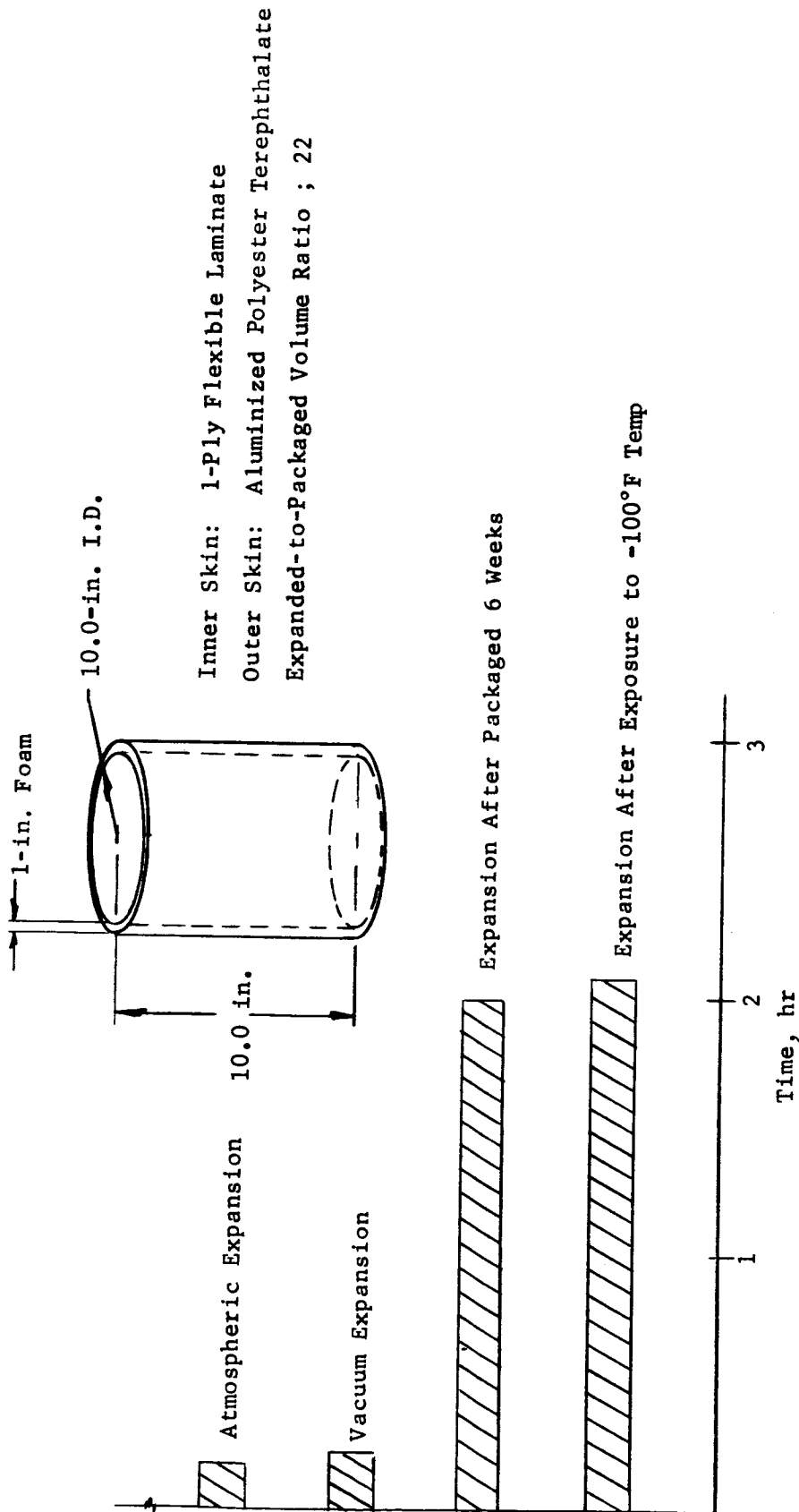


Figure 17. Time of Erection Under Different Conditions

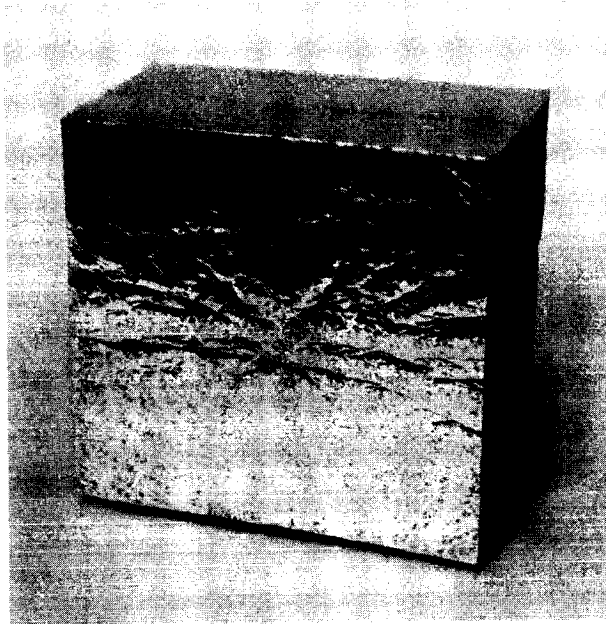


Figure 18. Composite Sample for
Compression Test

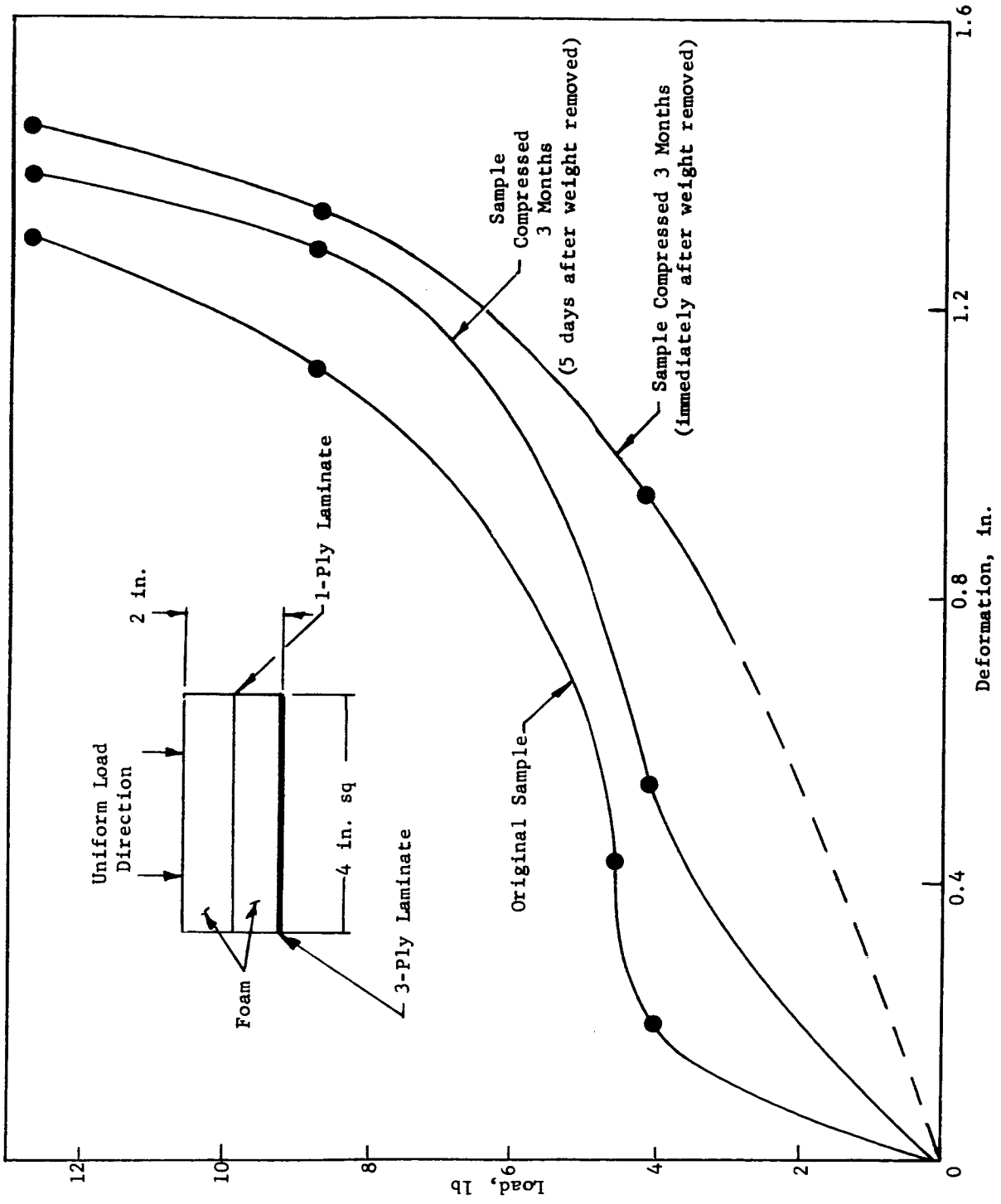


Figure 19. Load Deformation Characteristics, Long-Term Compressive Loading

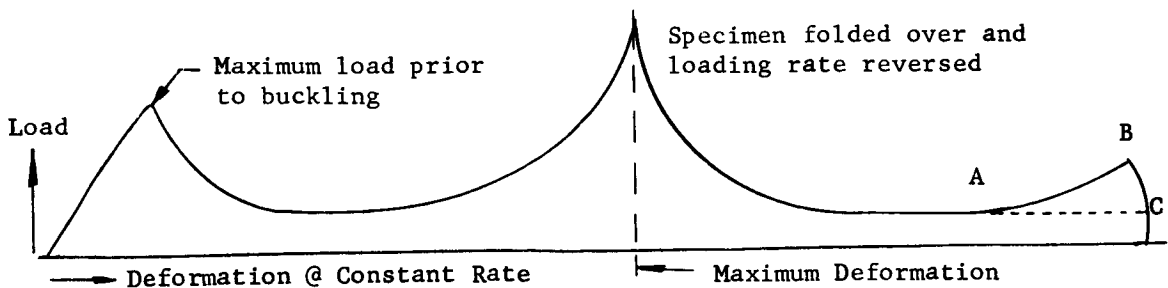
and laminate thicknesses. A simple, single test was devised to estimate both the maximum load and recovery characteristics for the test samples. The 4-in. square test samples, which varied in foam thickness from 1/2 in. to 3 in., were loaded in compression with an Instron Universal Test Machine, Model TM. A constant loading rate of 1.0 in./min was applied beyond the initial buckle until the sample was completely folded over on itself. The constant loading rate was then reversed and the sample was allowed to return to its normal position. The load-deformation was recorded throughout the test.

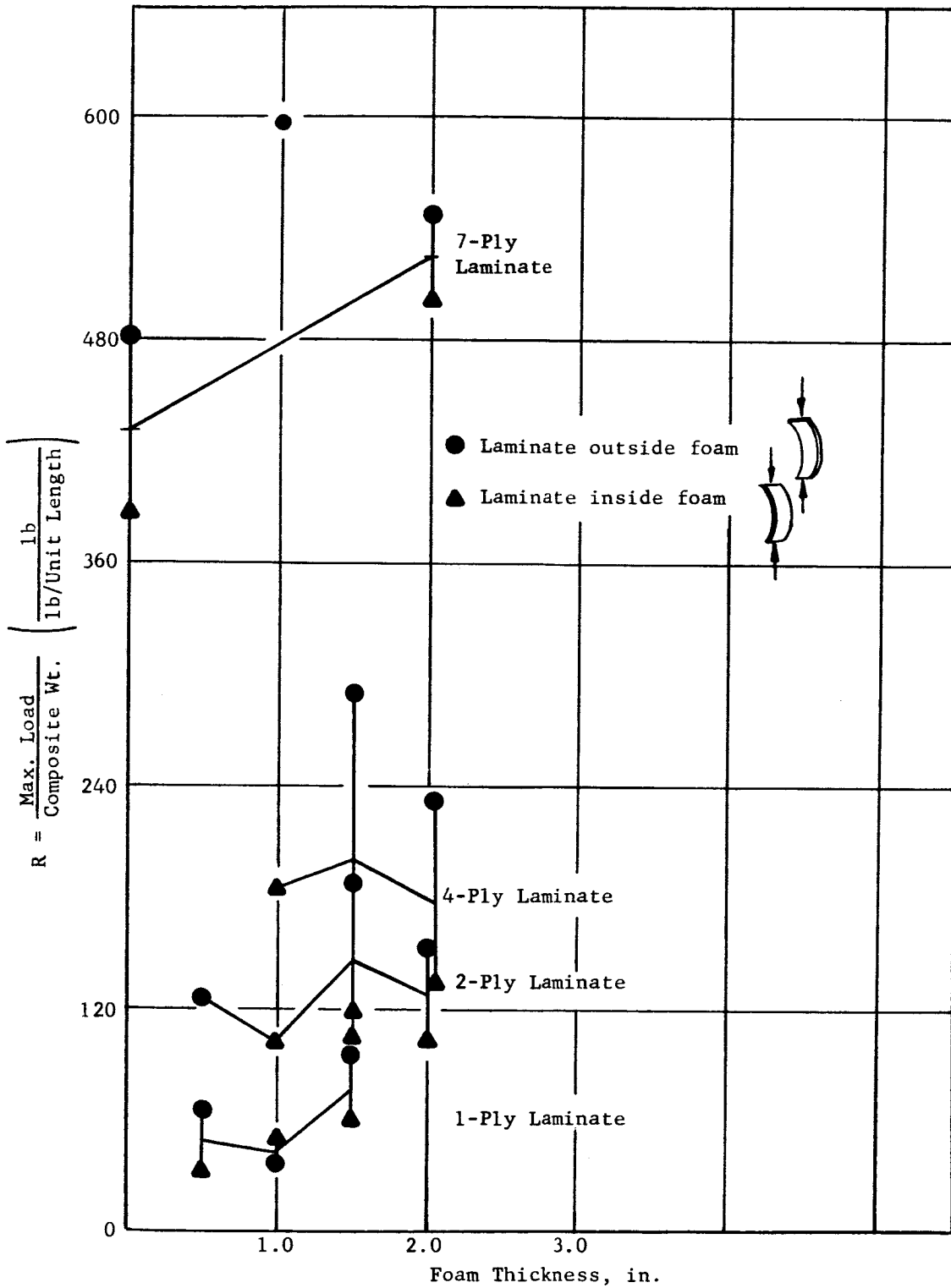
Two test runs were made upon each sample. In one test, the sample buckled with the foam on the outside of the laminate, while in the second test, the foam was inside the folded skin. The desired direction of the fold was forced into the sample at the beginning of each test.

The maximum load that each composite section would support was determined from the load deformation curves. The maximum load was defined as the load the composite supported just prior to buckling. In order to use a common parameter, the ratio of maximum load in pounds over the weight of a unit length of the composite section was used.

The results of this series of tests are shown in Figure 20, where the maximum load-over-composite weight ratio was plotted against the foam thickness for the different laminate thicknesses. The test points were connected at the average values in order to determine the trends. Reliable test data were not obtained and therefore were not plotted for the 3-in. foam thickness composite since they were too bulky in thickness for the size of specimen. It must be pointed out that according to these tests, the laminate thickness was the factor which determined the load the composite could support. However, despite the wide range in test points, the slight influence of foam thickness on the maximum load supporting capabilities can be noted.

The second series of data obtained from these tests was the effect of the foam thickness upon the recovery of various laminate thickness. It was originally planned to obtain this information by analytical means. However, the development of the equations was found to be extremely complex due to the composite construction of the sections; consequently, these tests had to be performed. The results were taken from the same tests in which the maximum load data were obtained. For these tests, the information from the portion of the load-deformation curves in which the loading rate was reversed was used. A typical load-deformation curve obtained for a test was shown in the following sketch.





NOTE: Lines connect av. values of 2 tests

Figure 20. Maximum Load-Weight Ratio vs. Foam Thickness for Various Laminate Thicknesses

The first peak was the maximum load prior to the initial buckle. The second peak occurred when the sample was folded over and the foam was being compressed. At this point, the loading rate was reversed and the load deformation curve was used to determine the recovery characteristics of the composite. All test specimens showed the initial tendency to decrease in load as the deformation. However, after the minimum point was reached (point A on the sketch), the different tests separated into two characteristics. The first group of tests followed the curve shown as "A to B" in the sketch, which indicated an increasing load for the reduction in deformation. The second group of tests followed the curve "A to C" in the sketch. For this analysis, it was assumed that the samples which caused the increasing curve "A to B" would recover at a greater rate than the unloading rate of the test machine (1.0 in./min). On the other hand, the tests which caused a decreasing load recovered at a rate slower than the unloading ratio of the test machine.

On this basis, the results of these tests were plotted as shown in Figures 21 and 22.

In Figure 21, the thickness of foam was plotted vs. the number of plies in the laminate. Based upon these data, the area above the dash line represents the range of foam thickness which would provide the greatest assistance in expanding an elastic recovery composite.

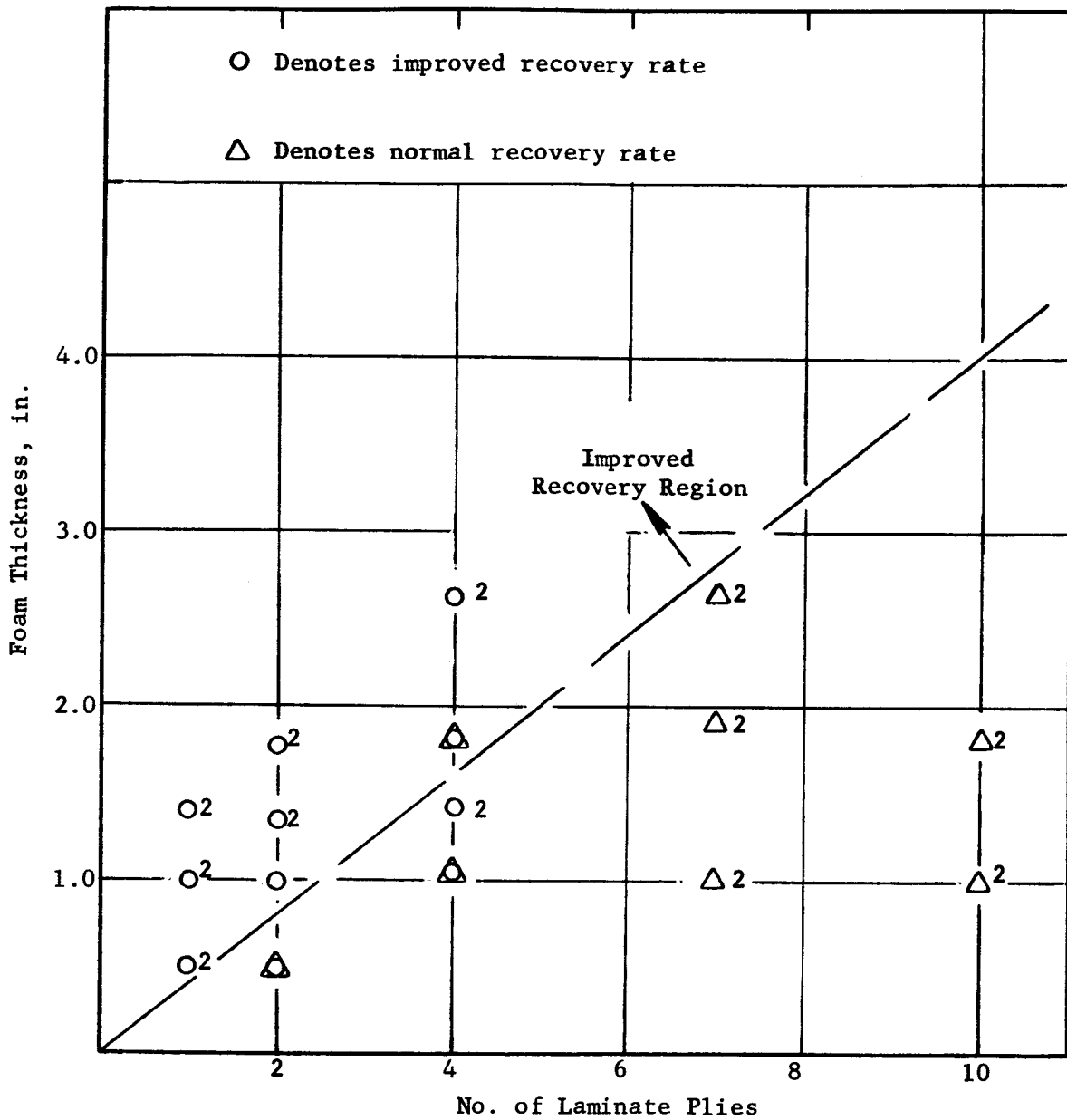
These data were also plotted to present the weight of foam per square inch of area vs. the weight of laminate per square inch of area as shown in Figure 22. Again, the dash line represents the division of the tests which indicated an increasing load on the load deformation curves.

The erection mechanism of an elastic recovery composite results from the combination of stored energy in the composite foam and laminate wall of the structure. This test showed only relative effect of the foam component of composite. If the test could have been performed in such a manner such that the load was held constant and the unloading rate varied, then more information upon the recovery characteristics of the composite sections would have been available. This constant load and a recording variable unloading rate was, however, beyond the range of the test equipment.

C. Conclusions

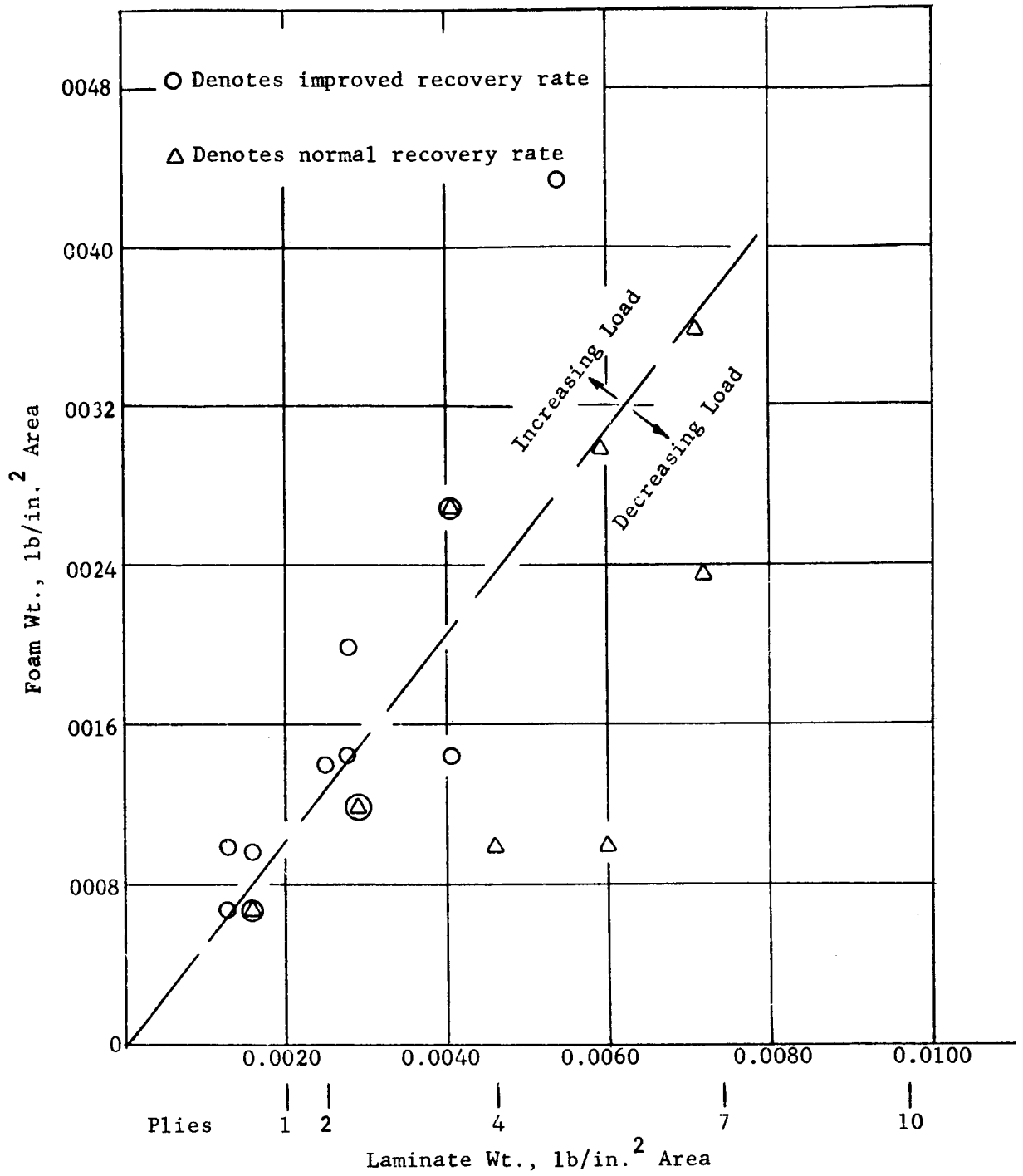
The results of these investigations were to determine the trends in the strength of different materials applicable to elastic recovery composite sections. The strength characteristics of different materials indicate that a wide range of strength levels is available in the flexible materials ranging from the films up to the reinforced laminates.

The studies upon the composite sections representing typical elastic recovery wall of an expandable indicated that erection will take place under different environmental conditions such as vacuum, low temperature, and in the package condition for long periods of time.



NOTE: Each point represents 2 tests.

Figure 21. Foam Thickness vs. Number of Laminate Plies



NOTE: Each point represents 2 tests.

Total number of plies includes laminate and layers between foam.

Figure 22. Foam Weight vs. Laminate Weight

It must be noted that all these studies were performed to give the general characteristics of the elastic recovery composite. The studies were kept general in order to provide a wide range of possible behavior characteristics for the elastic recovery concept. The results of these studies were used to study and evaluate the effect of structural and environmental conditions on the composite. These studies and possible applications for the elastic recovery concept will be discussed in detail in the subsequent sections.

IV. PARAMETRIC EVALUATION OF THE ELASTIC RECOVERY CONCEPT

In order to fully determine the capabilities of the elastic recovery concept for use in expandable space structures, several investigations in different areas were made. The detailed studies were made to determine the load-carrying or structural capabilities, and the degree of thermal insulation available of typical elastic recovery composites. Further studies were made to determine the degree of protection available for the space environments of radiation and meteoroids. Only the summary of these four studies will be presented in this section; however, the details for the analytical approach will be found in Appendixes B through E. The individual appendixes give details on the assumptions and the analytical methods used in the studies.

The results of each area are presented in the form of a parameter based upon either the composite weight or weight of the core. Thus, in this manner, the four major areas of study (i.e., structural, thermal, meteoroid, and radiation) will have a common basis upon which the different types of elastic recovery composites may be compared. The characteristic of an elastic recovery composite required for a specific application dependent upon these individual studies will then be discussed in this section.

A. Structural Capabilities

To determine the structural capabilities of elastic recovery composites, the investigation was divided into the different primary loading conditions of internal pressure (tension), axial compression, and energy absorption. The details of this study are found in Appendix B. In general, the analysis assumed a composite or sandwich construction for the evaluation. The use of the particular design loading condition rather than the stress condition will provide a designer with a better understanding of the structural requirements; e.g., the ultimate internal pressure acting on a particular cylinder size was used to determine the effect of tensile stresses within the composite.

The parameter chosen for the tensile loading condition was the ultimate internal pressure over the unit weight of composite ($\frac{P_{ult}}{w}$). The parameter was plotted for various strength levels representing the laminate materials and varying foam core thickness. The summary curves of the strength-to-weight ratio for a cylinder of 40-in. radius under the internal pressure condition are shown in Figures 23, 24, and 25. These curves show the effect of the different typical elastic recovery facing material for different composite configurations including foam core sandwich, single facing combined with foam, and a compressible honeycomb core sandwich.

From these curves, it appears that on the basis of internal pressure-to-weight parameter, elastic recovery composites with foam on the outer surface or a honeycomb type sandwich would be approximately equivalent. Taking into consideration other design criteria (e.g., the elastic recovery mechanism), the single skin would be the better concept for internal pressure.

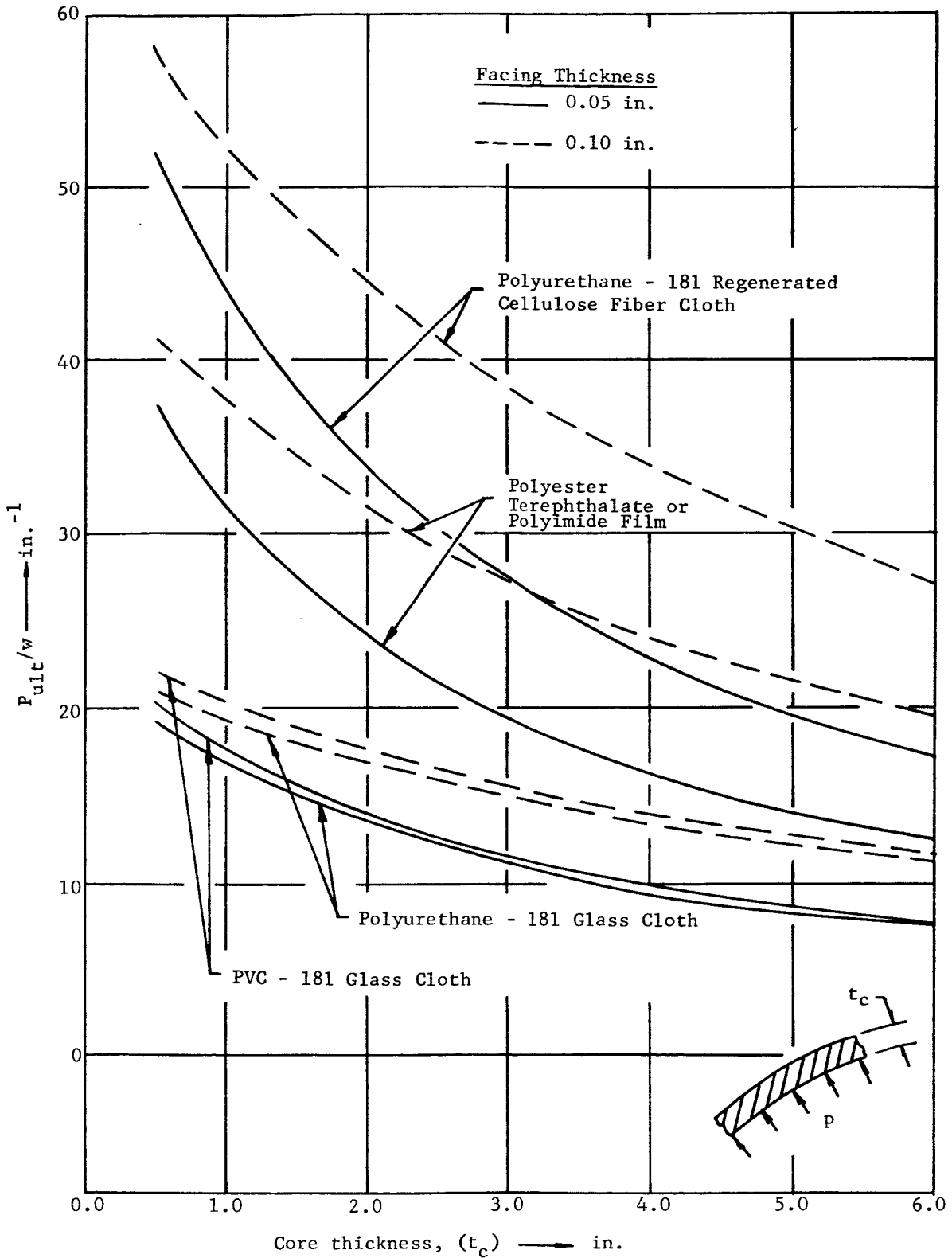


Figure 23. Strength-to-Weight Ratio of Internally Pressurized Single Face "Sandwich" Cylinder (Foam Core; $R = 40$ in.)

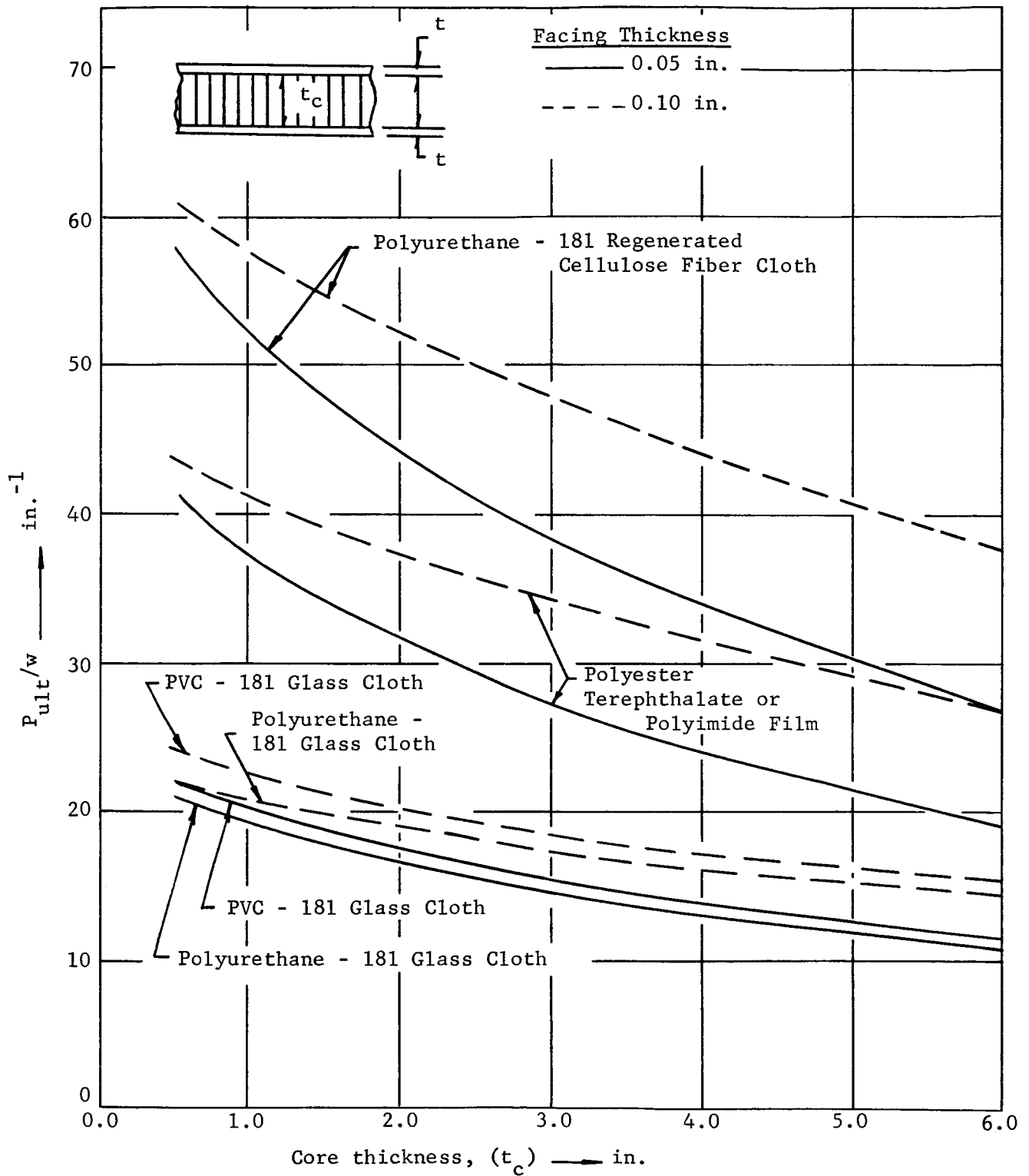


Figure 24. Strength-to-Weight Ratio of Internally Pressurized Sandwich Cylinder (Honeycomb Core; $R = 40$ in.)

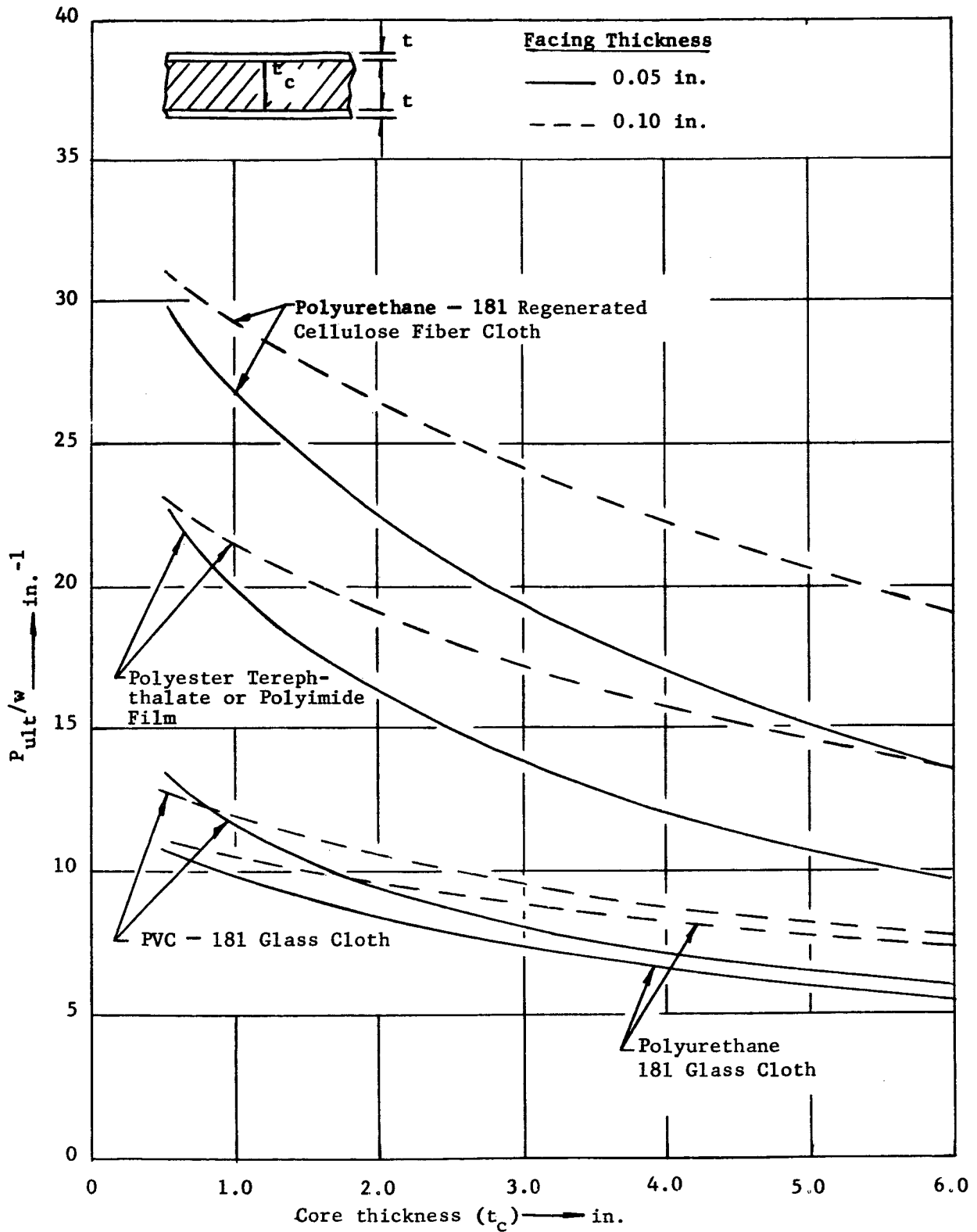


Figure 25. Strength-to-Weight Ratio of Internally Pressurized Sandwich Cylinder (Foam Core; $R = 40$ in.)

The second primary loading condition investigated was axial compression. The loading of an elastic recovery structure or any other structure was a complex condition, due to the cylinder buckling.

Figures 26 and 27 present the strength-to-weight ratio as a function of core thickness (t_c) and based upon a unit cylinder length. The first figure indicates the relative efficiencies of the facing materials when combined with the honeycomb core for a 40-in. radius cylinder. The latter figure shows the much lower strength-to-weight ratios of the same facing materials when combined with foam core for the same cylinder size. The low shear modulus of the foam allows each facing to behave as if it were an individual shell subjected to axial compression; hence the lower weight ratio. The polyurethane resin, regenerated cellulose fiber cloth laminate facings, when combined with the honeycomb core, result in the most efficient composite sandwich cylinder for supporting a compressive axial load.

The composite section utilizing the flexible honeycomb core materials exhibited maximum points for the axial load to weight per unit length parameter, particularly for the flexible honeycomb type of cores (Figure 26). The maximum point represents an optimum condition; i.e., the maximum strength of the facing material was reached prior to the buckling of the cylinder. As the core thickness increased, the P_{cr}/w parameter decreases because the core weight of the composite increased. The composite sections with the foam core did not exhibit this maximum as shown in Figure 27.

Since the elastic recovery structure is capable of storing energy for erection from the packaged condition, the section would also be capable of acting as an energy absorber. In order to evaluate the elastic recovery composite for its ability to act as an energy absorber, it is assumed that the strain energy available will act as a figure of merit. The strain energy per unit length was determined from the following equation:

$$U/L = \frac{P^2}{2AE} = \frac{F_{cr}^2 A}{2E} = \frac{2 \pi R t_s F_{cr}}{E}$$

The strain energy per unit cylinder length was determined as a function of sandwich core thickness (t_c) for a honeycomb type core with flexible laminate facings. The strain energy of a sandwich with polyurethane resin-regenerated cellulose fiber cloth reinforced laminate facings is presented in Figure 28. Since the strain energy was assumed to be a function of the critical stress, only the elastic recovery concept which gave the highest critical stress was plotted. It should be noted from the equation that the strain energy per unit length would be a function of the material characteristics $\frac{F_{cr}^2}{E}$ for the same cylinder geometry.

The leveling off of the curves in Figure 28 indicates the maximum laminate strength has been reached.

From this study, it could be concluded that the flexible laminate composite with a high strength would be needed for the maximum energy required for the docking of large ferry vehicle.

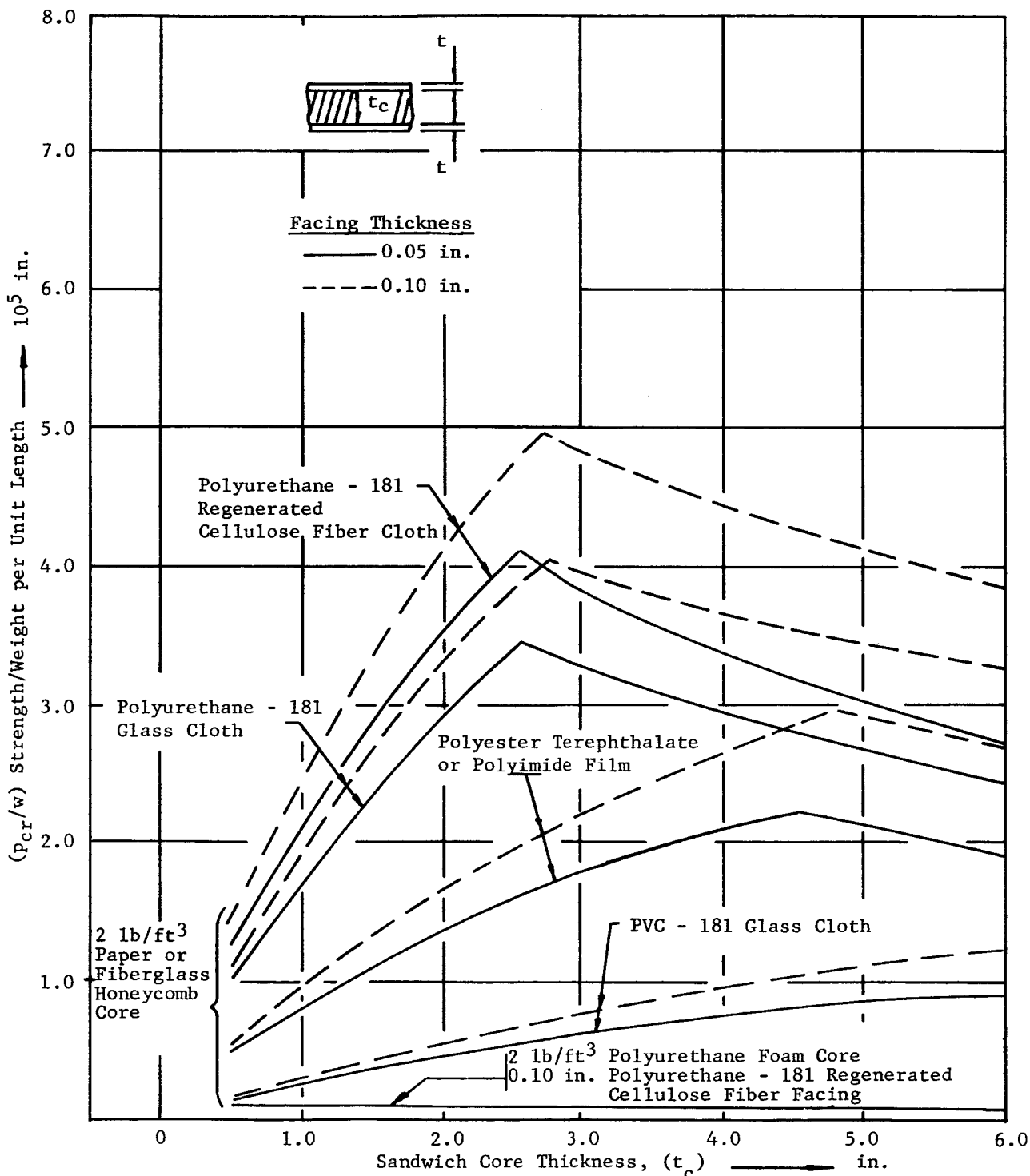


Figure 26. Strength-to-Weight Ratio of Axially Compressed Cylinder (Foam and Honeycomb Cores; $R = 40 \text{ in.}$)

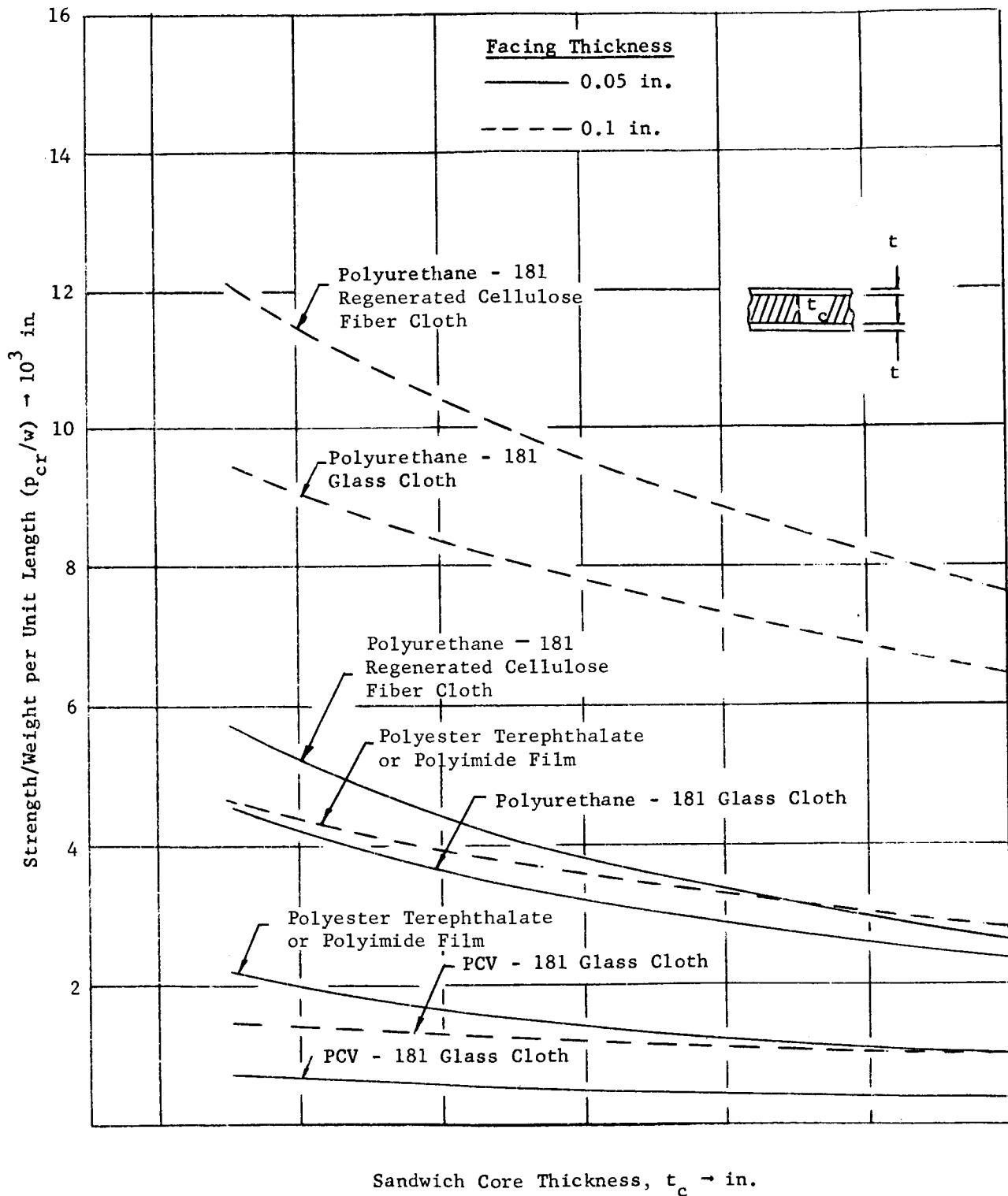


Figure 27. Strength-to-Weight Ratio of Axially Compressed Cylinder (2-lb/ft³ Polyurethane Foam Core; R = 40 in.)

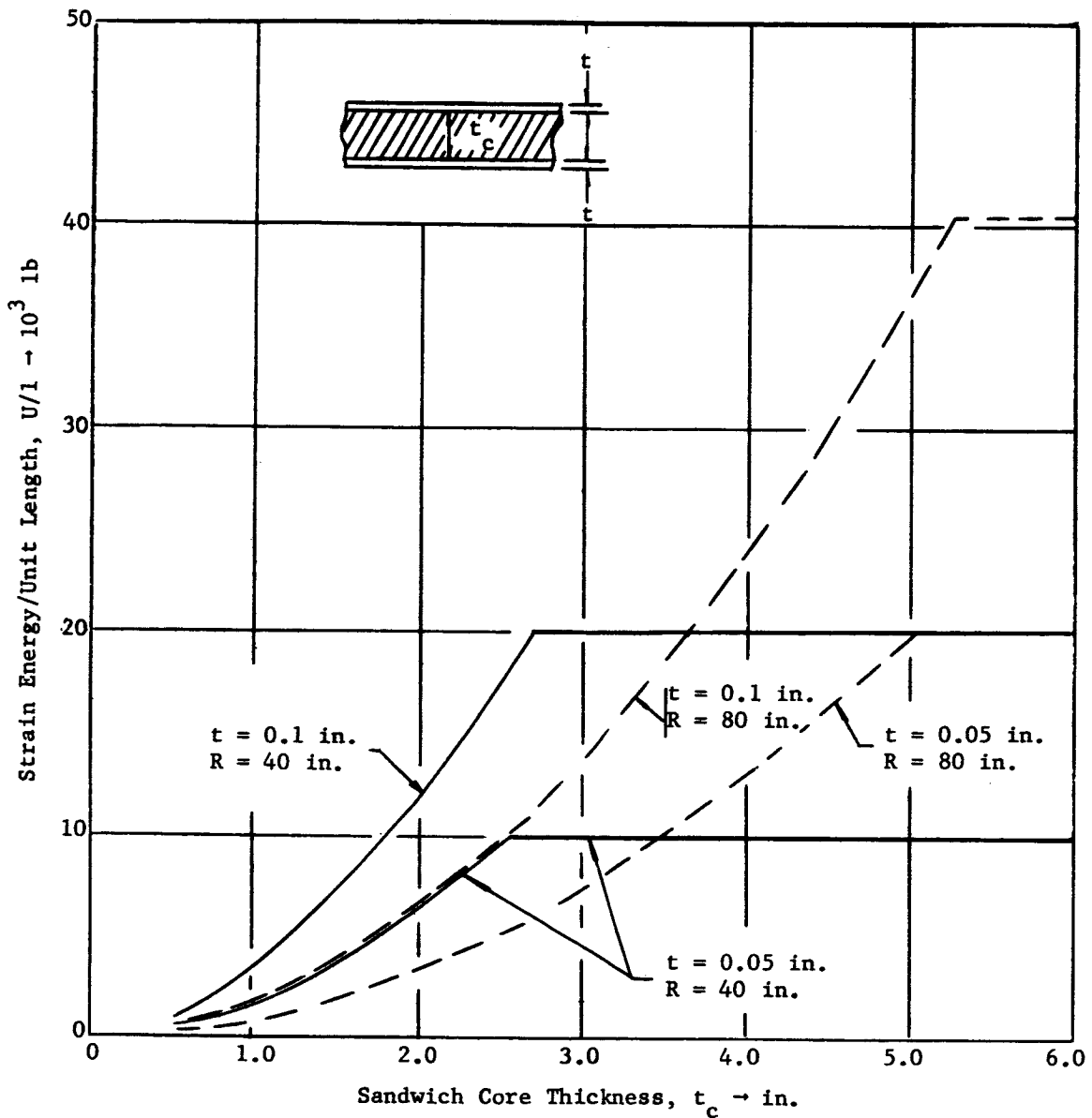


Figure 28. Strain Energy per Unit Cylinder Length at Buckling (2-lb/ft³ Paper or Fiberglass Honeycomb Core with Polyurethane - 181 Regenerated Cellulose Fiber Cloth Facings)

B. Thermal Characteristics

The second major area of evaluation for the elastic recovery concept was that of thermal characteristics. (This investigation is discussed in detail in Appendix C.) In order to evaluate the thermal characteristics of the elastic recovery concept, typical composite sections, including compressible honeycomb, foam, and combination of the two types of cores, were assumed. The investigation assumed a one-dimensional heat conduction through the composite wall in order to reduce the complexity of the calculations. However, a good estimate of the temperature profile and the heat flux through the composite wall was obtained since the composite materials have low thermal conductivities. The solar radiation constant at the Earth was assumed to be the only source of radiation for this study.

The temperature condition inside a vehicle depends primarily upon the conductivity of the core thickness and the outer surface absorptivity and emissivity conditions when subjected to a radiant heating flux; hence, these characteristics of the composite were the ones which were varied in the analysis. The effect of different surface conditions on the equilibrium temperature is shown in Figure 29. The results of the evaluation were plotted with an effective thermal efficiency parameter against the foam thickness. The parameter includes the total composite thermal conductivity and the composite weight ($K_c w$). These summary curves from Appendix C are presented herein as Figures 30 and 31. The curves show the effect of the two chosen surface conditions and the foam thickness. The results of this investigation show the profound effect that results when foam alone is used for insulation of the interior of the structure. The curve shows the effect of the assumed two interior temperatures of 160°R and 525°R ; the former temperature represents that for a cryogenic storage tank, while the latter is for a manned vehicle. The lower the parameter, $K_c w$, the better the insulative characteristics.

C. Meteoroid Protection

The third area of investigation for determining the capabilities of the elastic recovery concept was the protection afforded by the composite against meteoroids. This work was of an analytical nature, and the details are presented in Appendix D. One of the goals of this investigation was to obtain a procedure in which the protective characteristics of a composite section could be determined. This work required the use of many assumptions, particularly in the area of material and meteoroid properties. The investigation included the effects of both the impacting and spallation phenomena on the elastic recovery composite.

The elastic recovery concept has excellent potential for meteoroid protection because of its layered or composite construction. The state-of-the-art configurations are based upon the meteoroid bumper which serves to break up the incoming meteoroid. The elastic recovery composite not only has the outer bumper, but also has the foam core, which helps to absorb the fragments and reduce the stress pulse. The mechanism of stopping the particles in the foam involves the fanning or coning action. The impacted particles divide into two groups: the faster group (which is absorbed by the foam) and the slower group (which loses energy but must be stopped by the next composite layer).

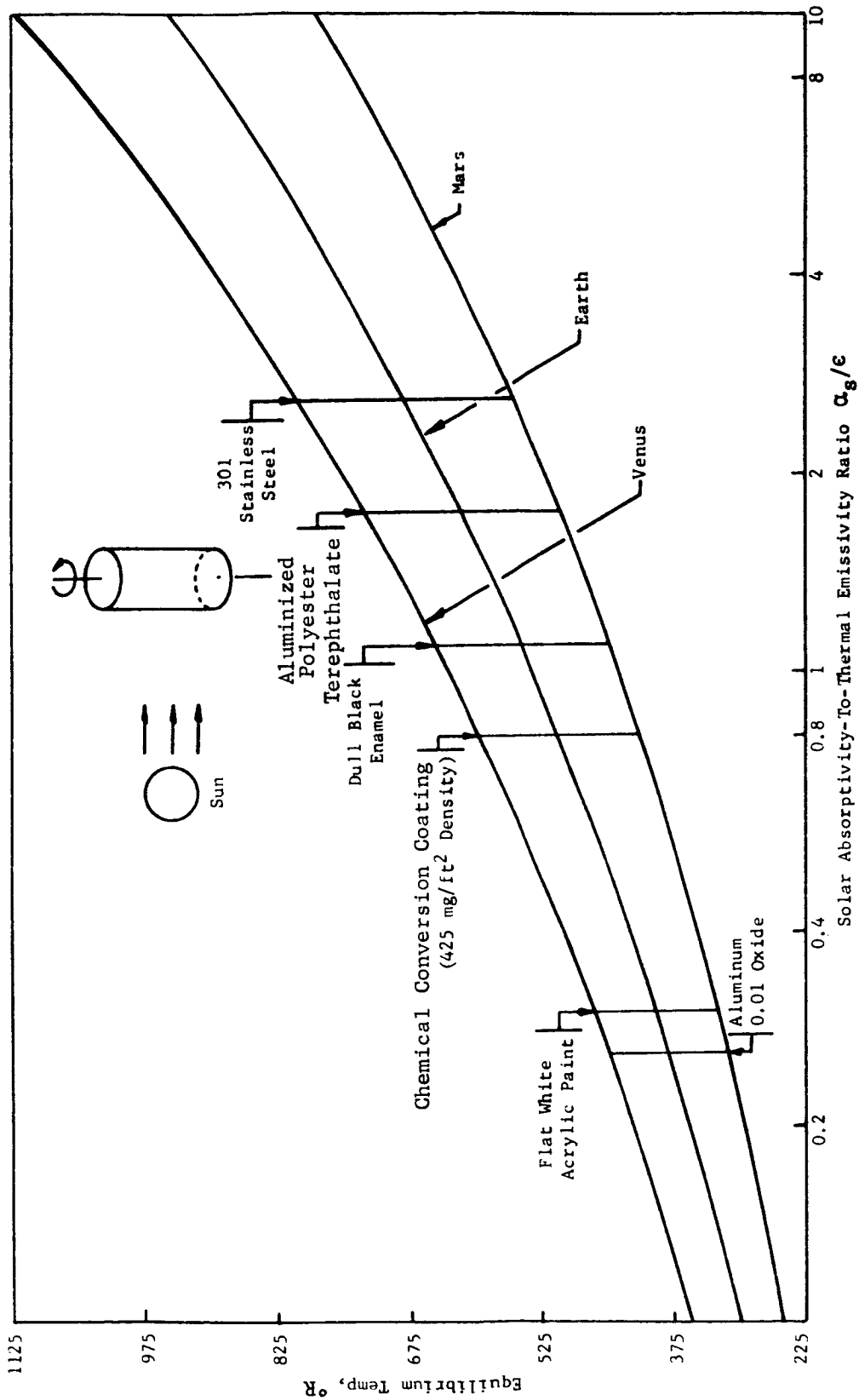


Figure 29. Equilibrium Temperature vs. Absorptivity-to-Emissivity Ratio for a Rotating Cylinder

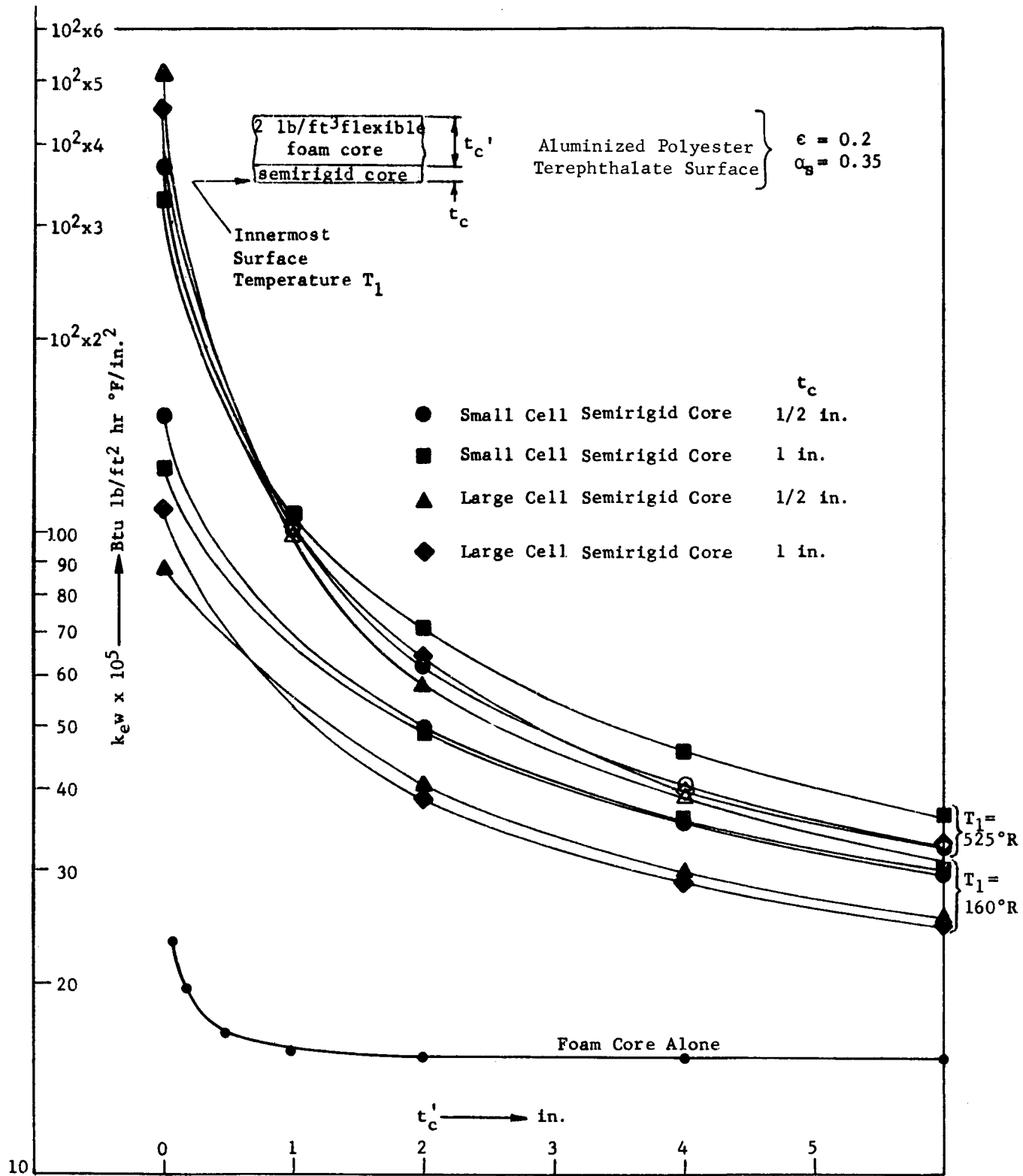


Figure 30. Thermal Efficiency Parameter vs. Flexible Foam Core Thickness For a Rotating Cylinder

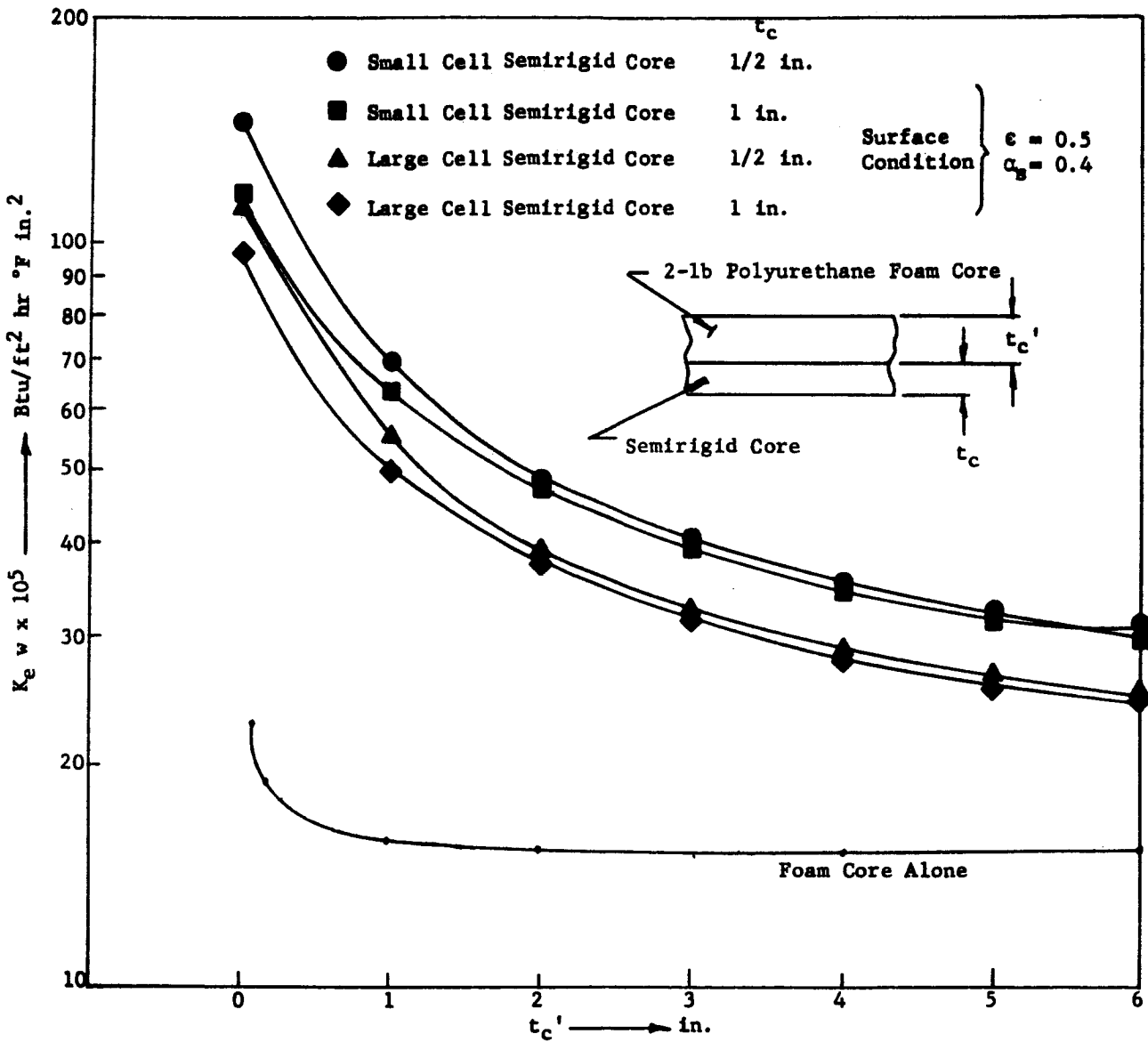


Figure 31. Thermal Efficiency Parameter vs. Flexible Foam Core Thickness for a Rotating Cylinder

Through the use of this method of analysis, the weight of composite required to prevent penetration was determined on the basis of the product of unit surface area of vehicle and the length of the mission, as shown in Figure 32. The weight curves were derived for two probabilities, 0.999 and 0.90, for no penetration of the composite wall.

The results of this analysis indicated that an outer skin or bumper, as shown in Figure 16(b), would be required on the composite to effectively fragmentize the impacting particle. The foam layers would then be capable of stopping the smaller fragments. The resulting theory from this analysis also indicated that spallation would probably not occur with the laminated materials. From early tests, it appeared that the laminate would tend to separate (delaminate) from the core due to the shock waves set up during the impact. The determination as to whether a delamination would be catastrophic depends upon the design conditions imposed upon the inner wall. The results of this study indicated that the elastic recovery composite would be lighter and more efficient than single sheet aluminum shields in preventing a puncture from a critical mass meteoroid.

D. Radiation Protection

In order to evaluate the radiation protective characteristics of the elastic recovery composite materials, a test evaluation was developed rather than using a theoretical treatment. The reason for this method of evaluation concerns itself with the very nature of radiation effects. The space radiation is so complex, due to the many types of radiation, that there appeared to be no simple method by which the stopping or absorptive protection could be analytically treated. As a result of the different types of radiation and also because of the unknown radiation levels, it was planned early in the program to set up monitoring equipment which would measure the decrease radiation level through the typical elastic recovery materials.

The investigation of the radiation protective characteristics resolved into three major areas, which are discussed in detail in Appendix E. The areas detailed in this appendix include: radiation environment, development of the test equipment, and results of tests on the typical elastic recovery materials. The first section of the discussions deals with the types of radiation and how to classify their effects on the composite materials. The development of the "effective atomic number" for composite materials is discussed in this section.

The second section of Appendix E details the instrumentation set up to monitor the radiation stopping effects of the elastic recovery materials. The equipment utilized included the low-pressure chamber, the radiation detectors, and readout equipment (see Figure 33).

The three types of isotopic radiation used for calibration and tests included:

- α - emitter providing 14,400 disintegrations/min
- β - emitter providing 32,900 disintegrations/min
- γ - radiation from 3.22 mg of radium

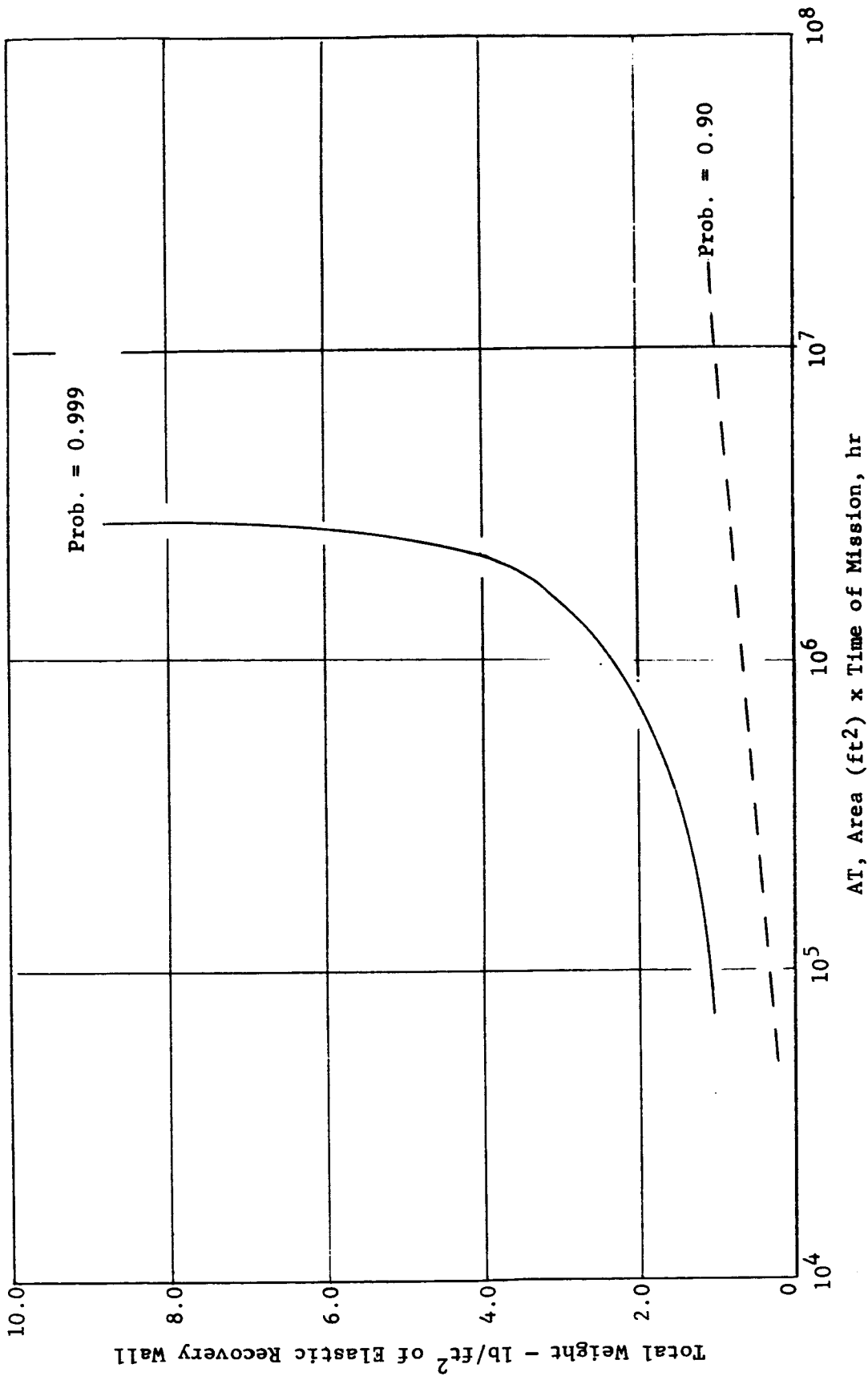


Figure 32. Estimate of Weight Required for Meteoroid Protection Using "Best" Elastic Recovery Wall Concept vs. Exposed Area (ft²) of Spacecraft x Time of Mission (hr)

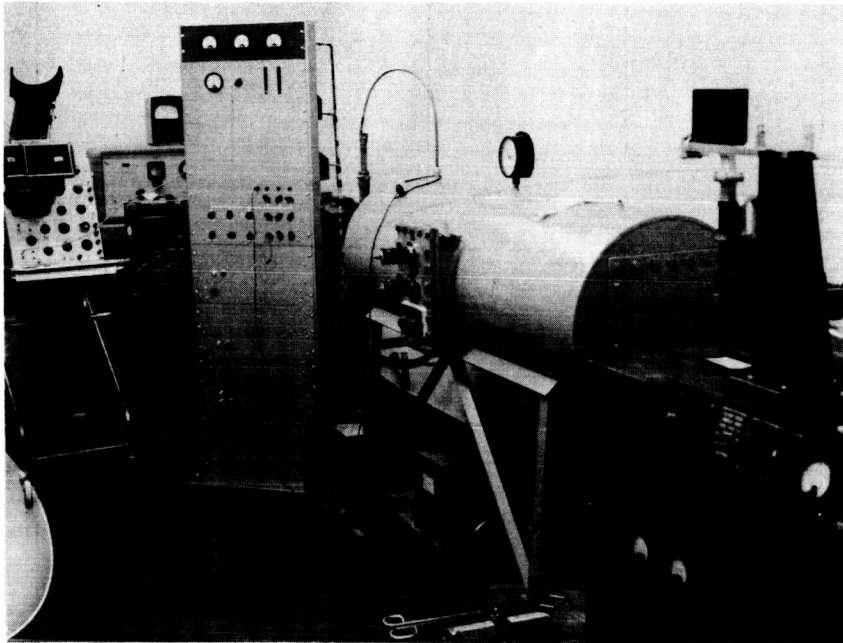


Figure 33. Test Instrumentation Arrangement

The isotopic radiation sources were chosen because of the relative ease with which they can be used as compared with the particle accelerators. The primary disadvantage for these sources, however, was the limited types of radiation available, particularly the high-energy electrons and protons. This disadvantage was more than compensated for by the economy and the manageability of the isotopes for the preliminary evaluation of the component materials in the elastic recovery concept. The isotopic sources for radiation were particularly easy to use in the reduced pressure chamber shown in Figure 34.

The radioactive sources were used to determine, by test, a figure of merit for the composite materials. The basis of comparison was aluminum. The elastic recovery materials tested included those representing the cloth, adhesive, resin, and foam components. The figure of merit was based upon the Effective Atomic Number of the materials, and is summarized in Table 5. The lower the Effective Atomic Number, the more effective the material will be for shielding against corpuscular radiation. From these tests, all the elastic recovery materials with a lower density offered superior shielding to that of aluminum. Note the decrease in effective atomic number when carbon was added to the material. This indicates that the addition of carbon to the foam and/or resin would improve the Van Allen radiation protective characteristics of the elastic recovery composite. The addition of carbon to the resin or the foam does not appear to impair the flexibility or expandability of the materials.

E. Packaging of Elastic Recovery Composites

The effective packaging ratios of an elastic recovery composite were found to be dependent primarily upon the application or structure. Several basic model and analytical studies were made during the program. The model studies described in the composite material investigations (Section III) required the study of packaging procedures. The analytical studies determined actual packaging ratios based upon the expanded and packaged volumes.

Since the mechanism for erection of the composite wall section comes from elastic recovery, the folding procedures affect the speed of unfurling. The work performed with models indicated the best folding characteristics appeared to put many minor folds rather than a few major folds. (The typical unfurling sequence of a model cylinder is shown in Figure 1.) The number of folds depends upon the thickness of the core and laminate. Figure 1(b) shows the folds in the composite. The folding procedure is important since it imparts the potential energy to the section besides reducing volume. The greater the folding that can be accomplished, the greater will be the potential energy available for a faster erection of the structure. The folding procedure, however, is not a characteristic which would be easily treated as an independent study, since it is dependent upon the type of wall construction required for the space structure and the packaged volume.

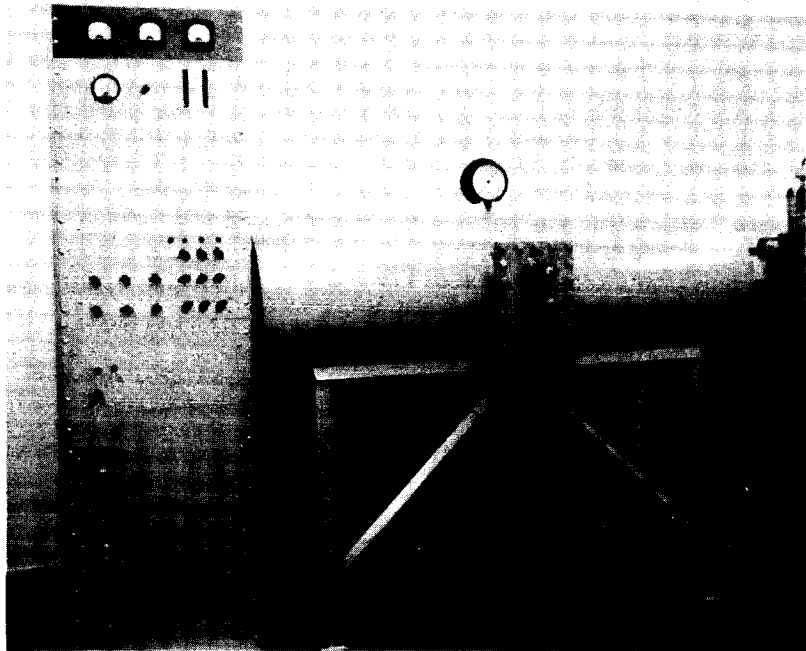


Figure 34. Close-up of Reduced Pressure Chamber

TABLE 5

EFFECTIVE ATOMIC NUMBER AND DENSITY OF
ELASTIC RECOVERY MATERIALS

Material	Relative \bar{Z}^*	ρ g/cm ^{3**}
Index reference standard aluminum	13.00	2.700
Aluminum on polyester terephthalate	12.23	1.315
PVC resin/181 glass fabric	11.34	1.680
PVC resin/regenerated cellulose fiber cloth fabric	10.24	1.380
Polyurethane foam	9.13	0.237
PVC resin-carbon/181 glass fabric	8.80	1.395
Polyurethane foam-carbon	8.24	0.356
PVC resin-carbon/regenerated cellulose fiber cloth fabric	8.02	1.280
DuPont type 46971 polyester adhesive	6.92	1.240

* Effective Atomic Number

** Density

In determining the packaging ratio of an elastic recovery composite structure, the compressibility of the foam core material was taken into account. A study was made upon the effect of cylinder length and foam compressibility. With this study, the ratio of expanded volume to possible packaged volume was determined. The compressibility of the foam core was accounted for by allowing the wall thickness to decrease to one-quarter its original thickness when in the packed conditions. This average compressibility for the foam was found to be typical from compressibility tests for the 1 to 2 lb/ft³ density range. The ratio of the expanded to packaged volume was found for the effective, or compressed, diameter to thickness ratio, $(D/t)_{eff.}$, for different lengths. The results of the study are shown in Figure 35. The compressed volume was based upon the volume of the wall or the surface area of the cylinder times the compressed thickness. This study did not optimize the shape of the container but rather determined the volume required for packaging a given expanded volume.

The effect of the package shape upon the expanded-to-package volume ratio can be seen in Figure 36. The length over diameter ratio (L/D) of the package determined the shape. The L/D ratio greater than 1.5 would appear to give the better capabilities for packaging. The cylindrical shape would also offer a better package since it would be geometrically similar to the expanded structure.

F. Comparison and Application of Different Elastic Recovery Wall Concepts

The comparison of the different types of wall concepts applicable to an elastic recovery expandable space structure requires knowledge of both the vehicle shape and the anticipated mission. For this portion of the study, a specific vehicle was not assumed but rather a general characteristic or a requirement from the mission was used. To completely definitize the design requirements of a specific vehicle for a mission was beyond the scope of this feasibility program. However, the general requirements such as temperature, structural loading, etc. are known; hence, the type of elastic recovery wall which would be needed could be obtained.

The type of loads and environments required for different space applications are shown in Table 6. The parameter which must be investigated includes both structural and environmental conditions. The types of possible space applications are grouped as follows:

1. Space Shelters - These structures include the space stations in which a large volume would be needed to give astronauts "elbow room." The primary loading condition is from internal pressure plus the environmental conditions.
2. Space Storage Tanks - This class of structures would solve the requirement for large volume storage capabilities. The requirements include insulation for cryogenic fuel storage.

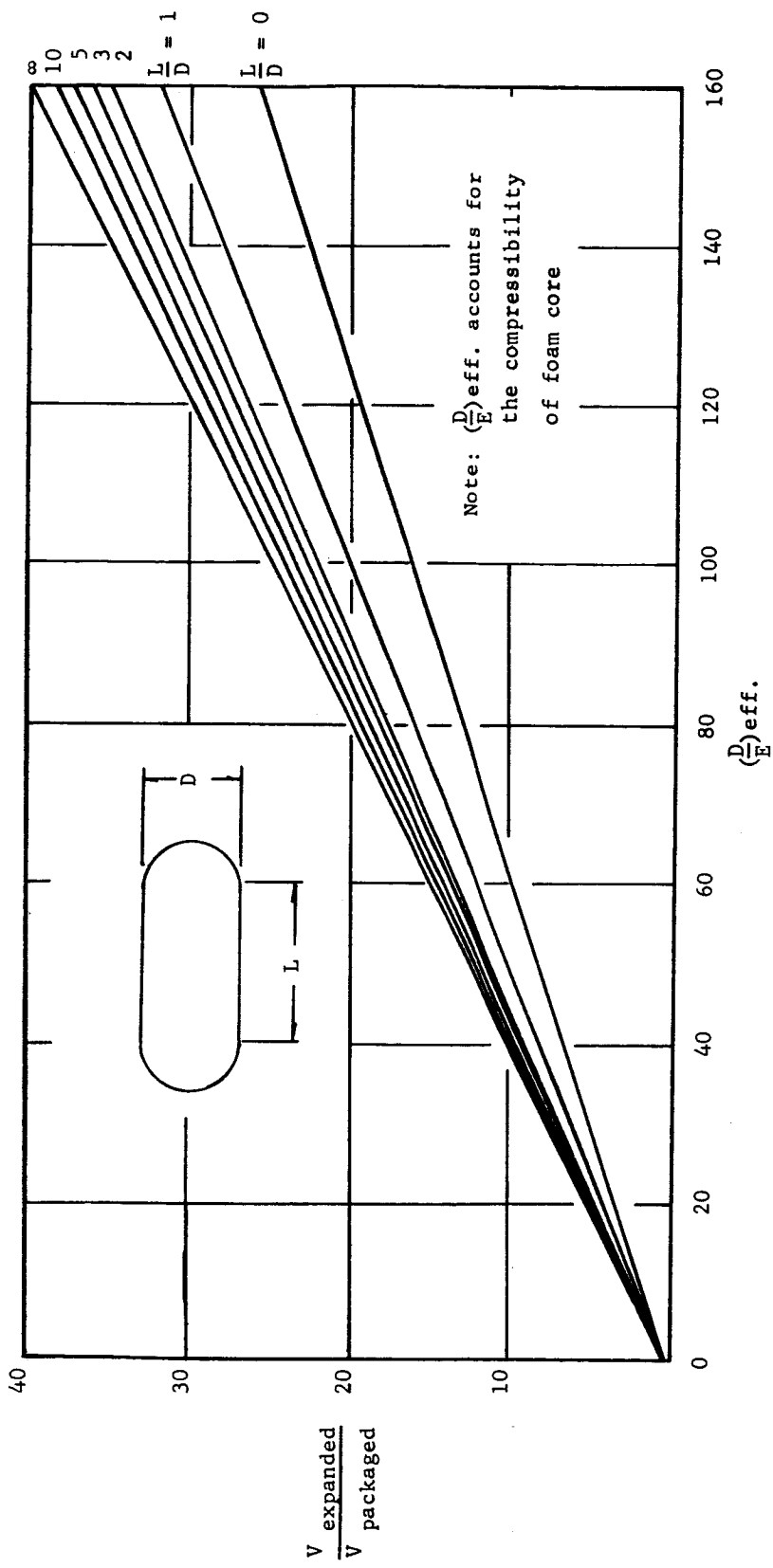


Figure 35. Volume Ratio vs. Effective Diameter to Thickness Ratio Cylindrical Shape

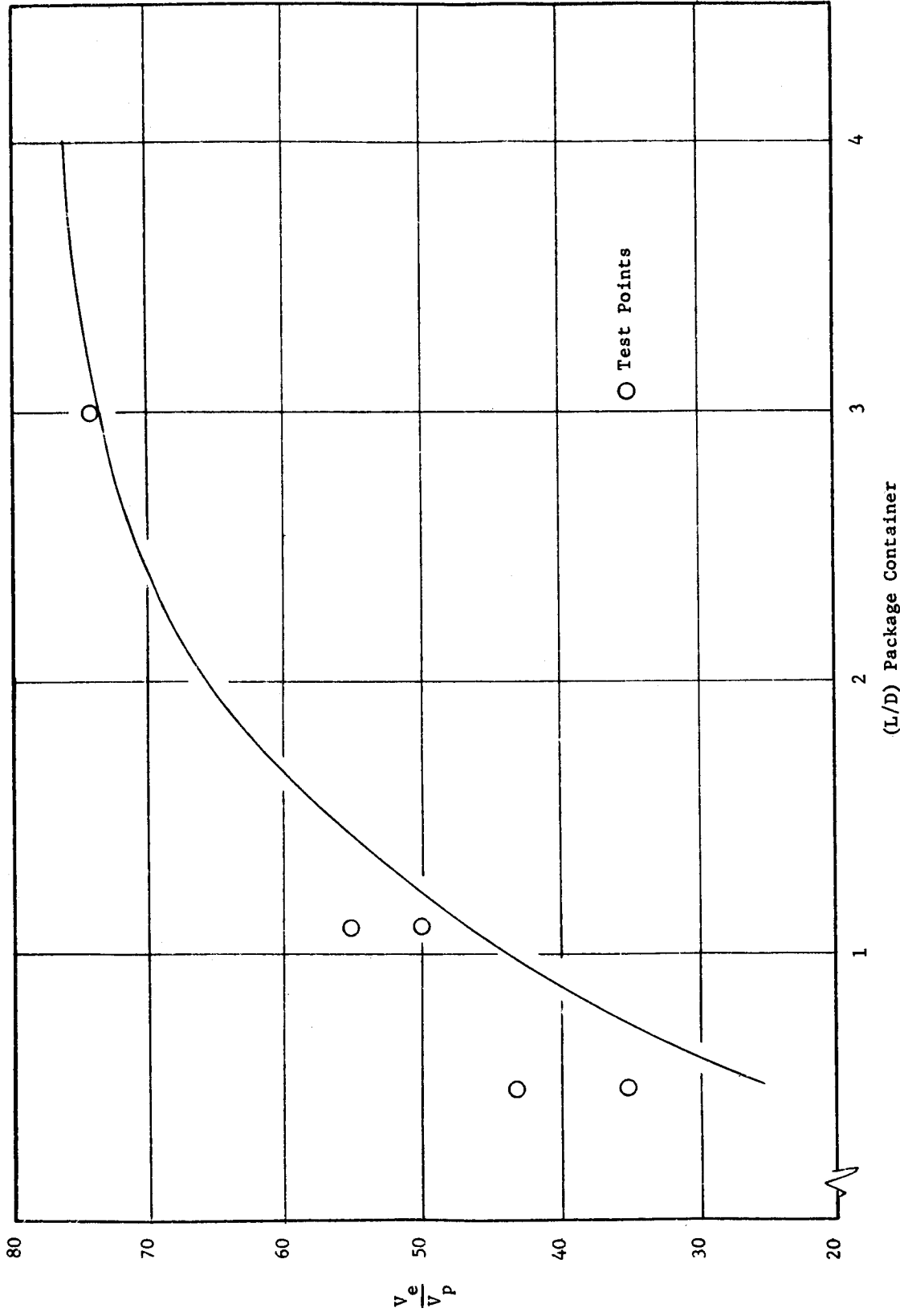


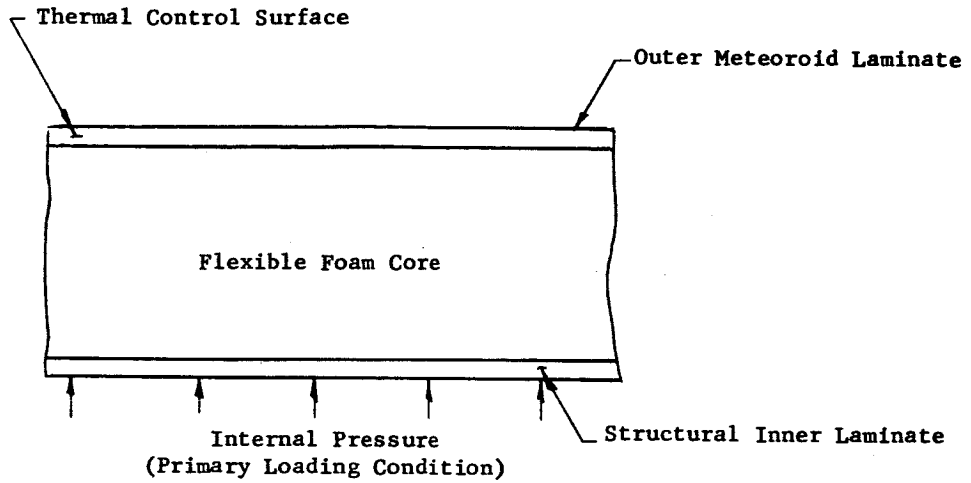
Figure 36. Effect of Package L/D on Expanded Volume to Packaged Volume Ratio, $\frac{V_e}{V_p}$

TABLE 6
PARAMETRIC STUDY OF DESIGN REQUIREMENTS FOR ELASTIC RECOVERY EXPANDABLE STRUCTURES

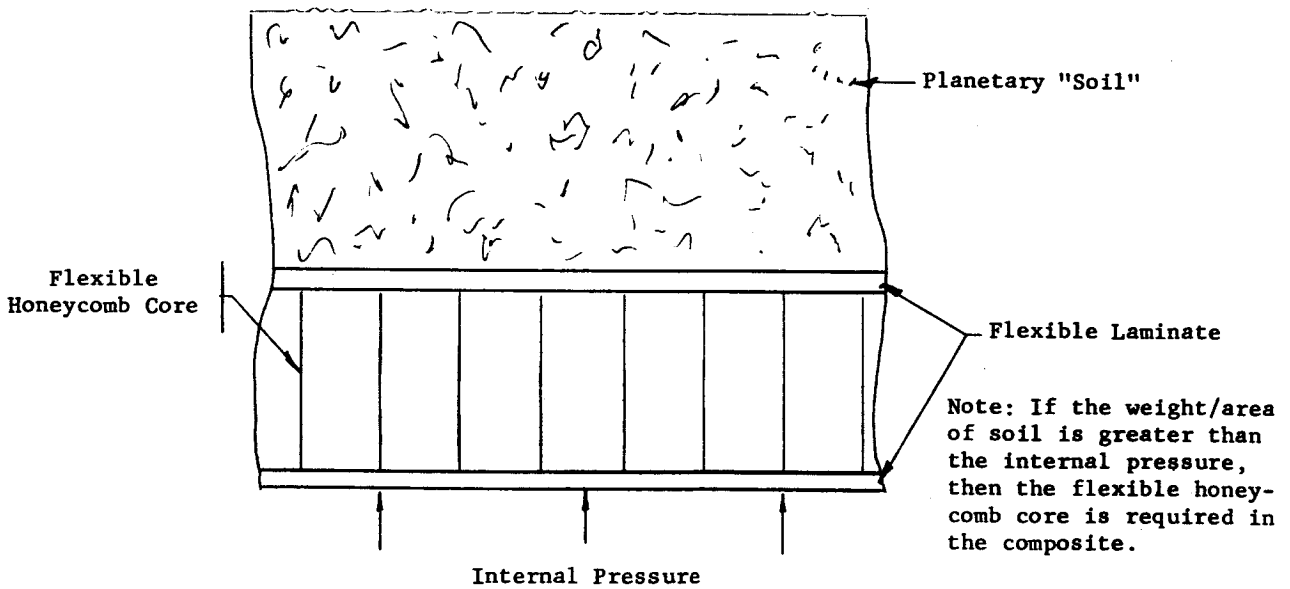
Parametric Requirement	Application							
	Space Shelters	Space Storage Tanks	Planetary Shelters	Planetary Storage Tanks	Planetary Vehicles	Solar Reflectors	Space Antennas	Airlocks or Interconnectors
<u>Structural</u>								
Tension (internal pressure)	X	X	X	X				X
Axial Compression	X	X	X	X	X			
Compression (external pressure)					X			
Stiffness						X	X	X
<u>Thermal</u>								
Heat flux	X	X	X	X				X
Temp	X	X	X	X	X		X	X
Deformation								X
<u>Radiation Resistance</u>	X		X		X			X
<u>Meteoroid Protection</u>	X	X	X	X	X			X
<u>Permeability</u>	X	X	X	X	X			X
<u>Surface Accuracy</u>							X	
<u>Packageability</u>	X	X	X	X	X		X	X

3. Planetary Shelters - This design requirement is essentially the same as that for the space shelters except for the planetary location. The shelter may also be buried, which results in the external pressure loading condition.
4. Planetary Storage Tanks - These are the companion structures to the shelter with the same requirement.
5. Planetary Vehicles - This application of elastic recovery includes several components of a planetary or lunar vehicle. Components such as wheels and panels could utilize the erection characteristics of an elastic recovery composite. Included in this class of structures would be planks which could be used for bridging gaps in the surface of the planets.
6. Solar Collectors - These structures require an accurate surface contour in order to achieve a high degree of efficiency. Hence, dimensional stability after erection would be required to minimize the distortion.
7. Space Antennas - The design requirement for antennas would be similar to the solar reflectors.
8. Airlocks or Interconnectors - These structures represent a secondary class of designs. The design requirements are similar to the space shelter. The additional requirements include possible repeated cyclic expansion and repackaging and also possible energy absorption; i.e., a load from a docking collar.

The first four types of structures have internal pressure as the primary loading condition. Since this results in a tensile stress in the composite, either the single skin or a compressible honeycomb sandwich wall section would be the most efficient based upon weight. The structural analysis of this loading condition (see Appendix B) indicated these types of elastic recovery composites had almost equivalent weight. The requirements for the meteoroid protection will further dictate the complete thickness requirement of the wall. It must be pointed out, however, that from discussion on meteoroid protection in Appendix D, the compressible honeycomb sandwich would not be as effective at stopping the particle as the foam core. This analysis of a meteoroid penetration indicated that for a high probability of no penetration for a large particle, the composite will need a laminate layer at the outer surface. The resulting elastic recovery composite section for these applications is shown typically in Figure 37a. The outer composite layer also has the reflective surface to control the internal temperature. The foam core would also provide thermal control due to its low conductivity through the section. The internal temperature requirement will dictate the thermal characteristics of the composite wall. For example, the cryogenic storage tank requires a wall with greater insulation than the manned shelters to prevent excessive fluid boiloff.



a. Space Structure



b. Buried Shelter

Figure 37. Typical Elastic Recovery Composite Wall Sections

The planetary shelter will have the same loading requirements as the space shelters plus a possible external pressure condition. In order to remain stable, the buried shelter with an external pressure loading greater than the internal pressure will require additional stiffness above the normal self-supporting characteristics of elastic recovery composite. The structural study indicated that for a compressive load in the composite wall, a compressible honeycomb core would be needed for the stiffness. A typical cross section of the composite for this application is shown in Figure 37b. The additional stiffness needed for a buried shelter could also be obtained by the use of foam ribs. The buried shelters would not need the degree of protection from the meteoroids or radiation that an orbiting station would require, since the planet's soil would be capable of some shielding. The thermal control requirements would also be less severe than for an orbiting station since the temperature extremes for the buried shelter would not be too great. The thermal problem would be one in which the heat conduction out of the shelter is minimized.

The planetary storage tank would have the same environmental design conditions as the planetary shelter and the requirements for wall stiffness would be identical. The storage tank would also have slightly different thermal insulation properties. The buried tank would not require the protection from direct solar radiation but will require insulation to prevent heat conduction from the surrounding soil.

The application of the elastic recovery composite to planetary vehicle components would allow the use of flexible materials in the design. The wheeled components, for example, require a flexible composite which would act as a spring and yet would not have too large a contact area. The area of the wheel print would determine the contact pressure on the surface and also the size of the wheel. The self-supporting capabilities of a wheel fabricated with an elastic recovery composite would allow for a design that is compatible with the vehicle and the soil conditions encountered on the planet. Such a wheel fabricated from elastic recovery materials would behave similarly to a low-pressure automotive tire. The wheel would also be capable of being packaged for transport to the planet surface then expanded when the vehicle was needed.

The application of the elastic recovery concept to solar collectors requires a complete system analysis. The primary requirements for the design of an efficient solar collection system include very low deviations from the surface tolerances and also stiffness to prevent distortion of collector wall. The required surface tolerance for an efficient collector was discussed in detail in the section on space environments (Section II). From this previous discussion, it would appear that the elastic recovery concept would only have a limited use as a solar collector mirror because of the stringent requirement for surface accuracy. However, alternative methods of designs may utilize the elastic recovery concept.

The system designs to which the elastic recovery concept could be adapted include those which use a relatively large area cavity absorber as a boiler to heat a fluid for the turbogenerator. This system would be similar to the NASA "Sunflower" solar-dynamic system (Reference 29).

A use of the elastic recovery concept in conjunction with direct solar conversion would also be feasible. Several of the direct solar conversion schemes are inherently flexible. In these systems, the elastic recovery mechanism would be used to expand the solar conversion array to its large operating area after it were in space.

The detailed system analysis for the use of the elastic recovery concept for solar conversion to power would require use of parameters such as overall power efficiency, collector area, surface characteristics, weight, and packing capabilities. The additional analysis would have to include the effects of the combined space environment upon the materials used in the composite.

Another area of possible application for the elastic recovery concept would be for space antennas. The antenna has design requirements similar to the solar collector (i.e., shape stability is the primary design criteria). The space antennas, also have contour accuracy requirements, particularly for large sizes. The problems of antenna design are discussed in Appendix F.

The application of elastic recovery to a spherical antenna system concept is illustrated by Figure 38. This figure shows the use of graded dielectric foam materials to obtain a large antenna aperture with a spherical surface. Further background on the requirements for antenna design in general are also discussed in Appendix F.

Secondary structures represent another area of possible application of the elastic recovery concept. The flexible composite would be used in structures such as airlocks, docking rings, and module interconnectors. A possible airlock structure is shown in Figure 39. The use of elastic recovery composite sections has excellent potential in these smaller structures. The general design requirements for these structures include the internal operating pressure and providing protection from the space environment. The secondary structures constructed with the elastic recovery composite also have the desirable capability of being repackaged.

The repackaging capabilities of an elastic recovery composite is a distinct advantage over other types of airlock since it would allow for reducing the volume. The composite would have the self-erecting characteristics which would not require external forces. The elastic recovery composite used in a secondary structure would also be self-supporting after expansion, which means the structure would not collapse with the release of the internal pressure. However, provisions will have to be made to apply forces to the structure to repack it. The repackaging capabilities of a foldable airlock would be especially desirable on a small station to minimize the shift of the mass moment of inertia and drag.

The investigations of the possible application for the elastic recovery concept have shown its possibilities. Without going into complete design studies, the characteristics of the elastic recovery composite appear to be applicable to different types of expandable structures. The design of the future space structures will be dependent upon the missions and the booster sizes available.

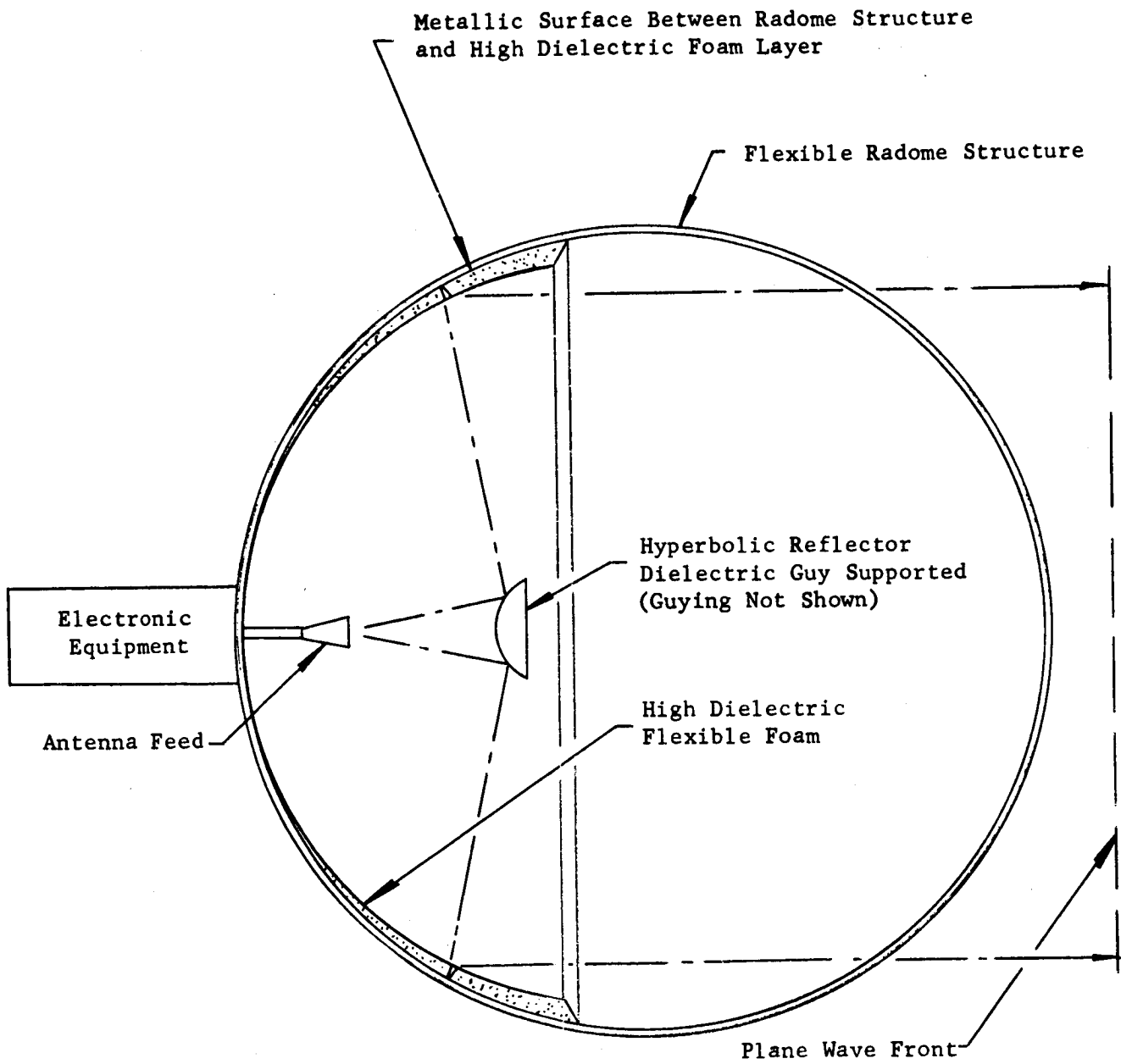


Figure 38. Elastic Recovery Expandable Antenna Configuration

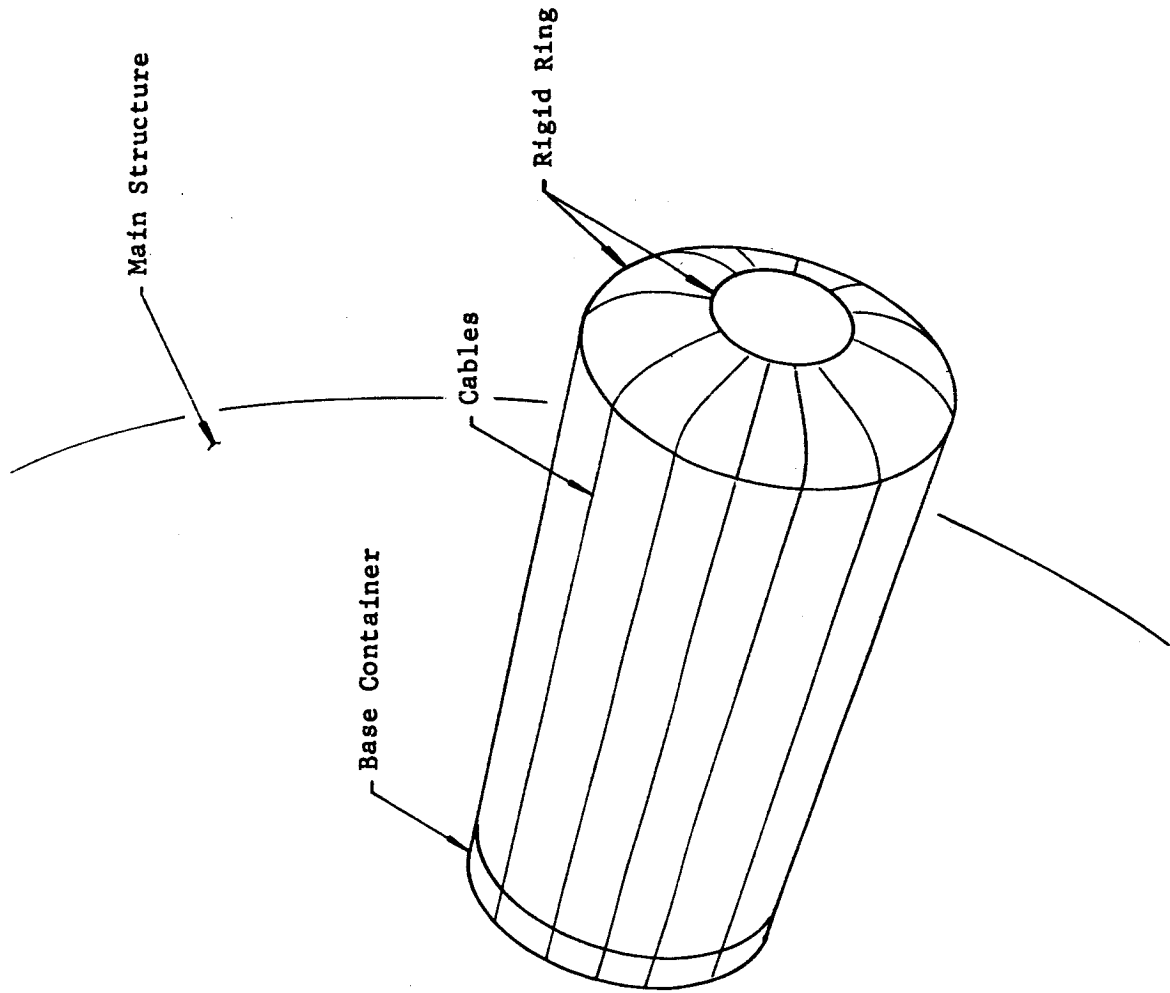


Figure 39. Elastic Recovery Airlock Design

G. Conclusions From the Parametric Evaluation

From this parametric investigation of the elastic recovery concept, several trends in the types of composite construction and possible applications were determined. The general requirements for use of the elastic recovery composite in the space environment dictated some of the characteristics, such as:

1. The loading condition of the structural wall (tension or compressive stresses) determine the type of wall. In other words, if the load was compressive, the stability of a sandwich composite would be needed.
2. The thermal evaluation indicated that a foam core in an elastic recovery composite resulted in the least heat conduction through the section.
3. The meteoroid protection required for the space environment was found to be a composite consisting of a foam core and an outer laminate. The outer laminate would break up the impacting meteoroid and the core would act as the absorbing material so that the inner wall would not be penetrated by the fragments.
4. For the protection from the space radiation, the materials which make up the elastic recovery composite were tested in the low-pressure chamber. The results of this evaluation indicated that each of the elastic recovery composite materials had an improved effective atomic number than aluminum for stopping charged particles. The loading of the material with carbon improved the stopping power of the laminates against corpuscular radiation.
5. The elastic recovery composite for space structures appears to be most useful for secondary structures such as tankage, airlocks, docking areas, or module interconnectors. The use of elastic recovery is feasible for spherical communication antennas.

V. COMPARISON OF ELASTIC RECOVERY, INFLATABLE, AND TELESCOPING TYPES OF EXPANDABLE STRUCTURES

In order to accomplish a comparative study of the different types of expandable structures, the literature was surveyed to determine the weights of the common types of expandable structure. The purpose of this study was to compare the three different types of expandable structures including elastic recovery, inflatable, and semirigid telescoping on the basis of weight per unit area. The latter two types of expandable structures were chosen because the most information on the structural weight was available. The weight summary for the semirigid expandable structure was taken from Reference 30. Reference 31 was used for the summary of weight for the type of inflatable structure. The weights were obtained for a particular size structure representing a small space station. The design size for the two space stations was different; hence, in order to compare the three different expandable structures, the weight was reduced to a unit surface area for the basis of comparison. The component weight for the two types of expandables are presented in Tables 7 and 8.

Table 7 records the weight data from Reference 30 for the telescoping expandable structure, and includes the weight of the structure, meteoroid bumper, insulation, and internal sealing bladder. The structural weight includes the primary pressure skin, the frames for the ends of each telescoping section, and the guide rails for the telescoping mechanism. The meteoroid bumper consists of a thin aluminum bumper separated from the main skin by 3 lb/ft² polyurethane foam. The shield weight was based upon a 99.9% probability of one puncture. The expandable structure consists of five telescoping sections, with one end domed and the other end flat. The expanded size is approximately 15-ft overall length and 8 ft in diameter. The weights given for this structure represent a nonflight test item designed for state-of-the-art manufacturing techniques; hence, the weights were not fully optimized.

The second expandable structure was the inflatable type (the weight is summarized in Table 8). The weight of this structure was given in Reference 31 for a square-woven polyethylene terephthalate fiber (e.g., Dacron) cloth with chloroprene rubber which closely matches the elastic recovery laminate. The weight was given for only the structural shell and the pressurization systems. The shape of this space station design was a cylinder with hemispherical ends 8 ft in diameter with a 25-ft overall length. No weight was given for the meteoroid protection of this design; however, other space structure designs (given in Reference 31) assumed a meteoroid protection weight of 0.25 lb/ft². The probability and number of punctures were not given for this weight. The weight breakdown does not reflect the weight of the container for the inflatable structure.

The best method of comparing the unit weight of the different types of expandable structures would be to determine the unit weight for the elastic recovery composite designed to the requirements given in Tables 7 and 8. The weights could then be compared between the different types of expandable structures. The weight of the elastic recovery composite will be based primarily upon weight required for the structural (or pressure wall) laminate, the foam weight required for erection of the composite section, and the weight necessary for meteoroid protection. The summary of the section unit weight is given in Table 9. The first six items review the size of the two elastic recovery structures and are directly comparable with the sizes of the telescoping and inflatable expandable designs listed in Tables 7 and 8 respectively.

TABLE 7

WEIGHT OF A TELESCOPING EXPANDABLE STRUCTURE CASE I

Total surface area: 378 ft²
 Internal volume: 510 ft³

Wt. Breakdown	Wt., lb	Wt./Unit Surface Area, lb/ft ²
Frames	370	
Pressure skin & associated structure	269	
Guide rails & shoes	<u>69</u>	
<u>Total structural wt.</u>	708	1.87
Insulation	53	0.140
Thermal control	15	0.040
Internal bladder	<u>104</u>	<u>0.275</u>
<u>Total cylindrical wt.</u> (less meteoroid bumper)	880	2.325
<u>Meteoroid bumper wt.</u> (99.9% probability of one puncture)	<u>174</u>	<u>0.460</u>
<u>Total wt.</u>	1054	2.785
Wt. of end closures	<u>356</u>	
<u>Total design wt.</u>	1410	

NOTE: Weight for cylindrical portion of vehicle approximate length 12-1/2 ft, nominal 8-ft diameter.

TABLE 8

WEIGHT OF INFLATABLE SPACE STRUCTURE CASE II

Surface area: 628 ft²
 Internal volume: 1123 ft³
 Internal operating pressure: 7 psi
 Factor of safety: 3.0

Material Component	Square Woven Polyethylene Terephthalate Chloroprene Rubber	
	Wt., lb	Wt./Unit Area, lb/ft ²
Pressurization system	123	0.195
Cutout reinforcement	19	0.030
Partitions	91	0.145
Total shell wt.	<u>286</u>	0.455
<u>Total wt.</u>	519	0.827
Meteoroid protection wt./unit area (assumed probability not known)		0.250
<u>Total wt./unit area</u>		1.077

NOTE: Weights for a cylindrical vehicle 25-ft total length with hemispherical ends.

TABLE 9

SECTION WEIGHT ANALYSIS FOR ELASTIC RECOVERY COMPOSITE

Items	Case I	Case II
1. Surface area, ft ²	378	628
2. Internal volume, ft ³	510	1123
3. Diameter of cylinder, ft	8	8
4. Total length of cylinder, ft	12.5	25
5. Internal operating pressure, psi	11	7
6. Factor of safety	3.0	3.0
7. Material (Regenerated cellulose fiber cloth reinforced polyurethane resin), design tensile strength, psi	25,000	25,000
8. Wt. of structural wall, lb/ft ²	0.553	0.352
9. Wt. of foam for erection, lb/ft ² (from Figure 22)	0.257	0.173
10. Wt. for meteoroid protection		
a. 99.9% probability of <u>no</u> punctures, lb/ft ²	1.40	1.70
b. 90% probability of <u>no</u> punctures, lb/ft ²	0.50	0.60
11. Wt. for thermal or permeability control film, lb/ft ²	0.043	0.043
12. Summation of Items 8, 9, 11	0.853	0.568

Item 7 in Table 9 shows the design tensile strength used for the weight calculations. This assumed tensile strength level of 25,000 psi was taken as design strength for regenerated cellulose fiber cloth reinforced polyurethane resin. The assumed strength level was reduced from the ultimate strength of 33,000 psi given in Table 3 (Section III) which was derived from the test program described in that section. The density of the laminate material was approximately 0.060 lb/in³.

To find weight per unit surface area as given in Item 8 of Table 9, the familiar pressure vessel formula of $f = \frac{pRn}{t}$; where f = composite stress, p = internal pressure, R = radius of the cylinders, and n = factor of safety, was used to determine the skin thickness. Then the weight/unit area was determined by multiplying the thickness by the density and area.

In order to estimate the weight of foam required to erect a structural laminate, Figure 22 was used. These data for this curve were developed by tests as were described in Section III. This weight per unit surface area is given in Item 9 of Table 9.

The next area of weight for the elastic recovery composite is that necessary for meteoroid protection. The weight per unit surface area was established from the method developed in Appendix D (Meteoroid Protection). The weight was determined for a 30-day mission with no-puncture probabilities of 99.9% and 90%. The protection required was based upon an earth orbit for both cases. This timespan in earth orbit agrees with the design philosophies of both the telescoping and inflatable expandable structures. The weight for the meteoroid protection includes both the outer laminate and the foam. The outer laminate skin fragments the incoming particle with the shear strength determining the thickness. The foam absorbs the fragments and attenuates the shock wave. This weight per unit surface area is given in Item 10 of Table 9 for both cases.

The last component of weight for the elastic recovery composite was that of the thermal control and the internal impervious coating. For this weight study, it was assumed that these film materials would weigh the same. The weight per unit surface area for these coatings was given in Item 11 of Table 9 and was based upon a 3-mil thickness for each coating. From Table 1 of Section III, the area factor for the two materials could be taken as approximately 20,000 in.²/lb/mil. For both films, the area factor reduces to a total of 0.043 lb/ft².

The summation of the important weight items is given in the last item for the two designs. The comparison with the unit weight is also shown in Table 10. For this study, the following items should be noted when drawing the comparison:

1. The weight of the container was not included in the total weight estimate for the elastic recovery and inflatable expandable structures. Since the sections of the telescoping structure nest inside each other, the container weight is included in the total weight for this type of expandable structure.

TABLE 10

COMPARISON OF UNIT WEIGHTS

Type of Expandable Structure	Structural Wt./Unit Area, lb/ft ²	
	Case I	Case II
Telescoping	1.87	-
Inflatable	-	0.827
Elastic Recovery	0.853	0.568

NOTE: This summary does not include the weight for meteoroid protection.

- The weight per unit area for meteoroid protection shows a wide variation between the three types of expandable structures. This could be due to the use of different mission puncture probabilities. The telescoping expandable structure was designed for a 99.9% probability of one puncture during the mission and is based upon empirical data. The weight of meteoroid protection for the inflatable structure was given as typical for other types of inflatable structure discussed in Reference 31; no information was available on the probability or number of punctures. The meteoroid weight for the elastic recovery concept was based upon the material shear strength of the outer laminate and two probabilities of no puncture. Weight improvements in the meteoroid protection could be obtained by using higher shear strength material. A summary of the meteoroid weights is given in Table 11.
- The three types of expandable structures were not optimized in weight with regard to material strength and wall configuration.

From this preliminary study, the weight of an elastic recovery expandable structure would be less than the weight for an equivalent size structure utilizing either the telescoping or inflatable types of expansion. A direct comparison of weight was difficult because of the wide variation in weight for meteoroid protection. However, a comparison can be drawn on the structural weight/unit surface area as shown in Table 10. These data were taken from Tables 7, 8, and 9. The weights for the structure and erection mechanism were included in this summary.

It would be expected that the telescoping type of expandable structures would have a different weight since its expansion characteristics are different from either the inflatable or elastic recovery types. The telescoping structure, once expanded, is basically a rigid structure. On the other hand, the inflatable structure is flexible, but requires an internal pressure to maintain its shape. The elastic recovery expandable structure is also a flexible structure but the wall will maintain its shape without an internal pressure.

TABLE 11

SUMMARY OF METEOROID PROTECTION WEIGHT

Type of Expandable Structure	Probability, %	No. of Punctures	Wt., lb/ft ²	
			Case I	Case II
Telescoping	99.9	One	0.46	
Inflatable	--	--	--	0.25
Elastic recovery	99.9	None	1.40	1.70
Elastic recovery	90.0	None	0.50	0.60

VI. CONCLUSIONS AND RECOMMENDATIONS FOR FURTHER INVESTIGATION

The conclusions drawn from work under this program were given at the end of each section or appendix. However, major conclusions are repeated here for convenience.

A. Materials and Composites

1. Flexible laminates exhibited higher modulus levels than film materials. The strength ranged from an equivalent level to a greater level than that of the film materials.
2. The flexible foam core is more amenable to the elastic recovery composite, under normal loading conditions, than compressible honeycomb core.
3. The elastic recovery composite will erect itself when under the influence of vacuum or cryogenic temperature. Model studies also indicated that the composite will also erect after being packaged for long periods.

B. Structural Capabilities

1. For the internal pressure loading condition, the single facing or compressible honeycomb sandwich composites were almost equivalent on the basis of weight. However, the single skin with the foam erecting mechanism would be easier to package.
2. For the axial compression loading condition, the compressive honeycomb core sandwich was required to prevent buckling of the structure. An elastic recovery or composite with a foam core did not react the load as a unit, but rather as separate facings.

C. Thermal Characteristics

1. The effective thermal conductivity of a foam core elastic recovery composite was much lower than the composites with a honeycomb core.
2. The surface coating for radiant heat control was found to have a profound effect on the heat transfer through the composite.

D. Meteoroid Protection

1. The analytical treatment of impact on an elastic recovery composite indicated the most effective protection would be obtained from an outer skin laminate and a foam core.

2. The outer skin breaks up the particle, with the material's shear strength determining the thickness.
3. The foam core acts as an absorber for the fragments.
4. From limited test data, it appears that spallation does not occur on the inner laminate skin of the elastic recovery composite. Delamination of the inner skin, from the core, however, might occur.

E. Radiation Resistance

1. The radiation tests indicated that the components of the elastic recovery composite had better absorption characteristics than the aluminum standard.
2. The addition of carbon particles to the composite components further improved the material's radiation "Figure of Merit."

F. Applications of Elastic Recovery Structures

1. The elastic recovery concept appears to be feasible for a structure which is capable of being expanded when in orbit. These structures include space stations and storage tanks. One of the limiting factors for an expandable space station, however, will be the psychological aspects of the astronaut of being confined by a flexible wall.
2. It appears that the current designs for a solar collector structure would not employ the elastic recovery concept because of the stringent surface smoothness requirements.
3. The use of elastic recovery would be feasible, however, when used as the expansion mechanism of a flexible direct solar conversion system in space.
4. The use of elastic recovery to expand antennas in space would be feasible, particularly if the large-aperture, spherical type of antenna is utilized.
5. The elastic recovery expandable structure would be especially useful for secondary space structures such as airlocks, interconnectors, and space environment protective devices for rigid space structures. The smaller structures could be repeatedly cycled through the expanded and packaged conditions. The elastic recovery composite wall for these structures would also be self-supporting.

G. Recommendations for Further Investigations

The following items suggest areas for further investigations which could not be studied in detail or had to be assumed during this feasibility program:

1. The design properties of the elastic recovery materials must be more fully determined. The properties requiring investigation include

effects of repeated loading and folding and also the effect of space environment upon the strength.

2. A larger range of surface thermal control coatings applicable to the flexible elastic recovery composite must be determined.
3. A detailed analysis must be made of the transient thermal characteristics on the composite for the elastic recovery materials.
4. The analytical treatment of meteoroid penetration of the composite must be further refined. Experimental verification of the developed theory is also necessary.
5. The effect of hypervelocity impact on the elastic recovery composite materials requires further analysis. The material shear strength was one of the criteria used for determining penetration.
6. Further radiation tests must be performed upon a wider range of materials applicable to expandable structures. One such material possibility would be a polyethylene foam for the core material. This material, in bulk form, acts as an excellent, corpuscular shield.
7. The application of the elastic recovery to an expandable large-aperture spherical antenna shows promise and warrants further investigation.
8. The next step in developing the elastic recovery concept should be its application to an actual design, which is now recommended. A small, secondary structure such as an airlock is suggested since it could be completely evaluated in the space chambers currently available.

APPENDIX A

GEOMETRICAL STUDIES OF EXPANDABLE STRUCTURES

by

Victor Grinius

This study encompasses expandable structures consisting of honeycomb material. Originally, the core is in a compressed state, and then is left to expand to an optimum position.

The main purpose of this study is to determine the Poisson's ratio effect as the core expands. In the compressed state, the width of the structure is the summation of the individual thicknesses of the ribbons in the core. The structure is then expanded to a position in which the expansion in the direction perpendicular to the ribbons is maximum, and the contraction in the direction parallel to the ribbons is minimum; i.e., an optimum position.

Curves are shown for angular deflection of core vs. area of core, and angular deflection of core vs. the overall dimensions of the core.

The three types of core configurations used in this study are "sine wave," rectangular, and hexagonal.

Nomenclature used herein is as follows:

- a = amplitude of sine wave core
- A = cell cross-sectional area
- b,k = constants for elliptic integral
- e = sine wave "chord" length
- l = side length of rectangular or hexagonal core
- h = expansion amplitude for rectangular or hexagonal core
- d = core length
- S = perimeter of core cells
- θ = angle of expansion of core

1. "Sine-Wave" Core

The behavior of the "sine wave" core is the most general of all cases. The hexagonal and rectangular cores are just particular cases of the "sine wave" core, the main difference being the length of the bonding surface of the ribbons.

The calculations that follow show how the plot for the "sine-wave" core was obtained. The rectangular and the hexagonal core calculations are a simplified form of the "sine-wave" core calculations.

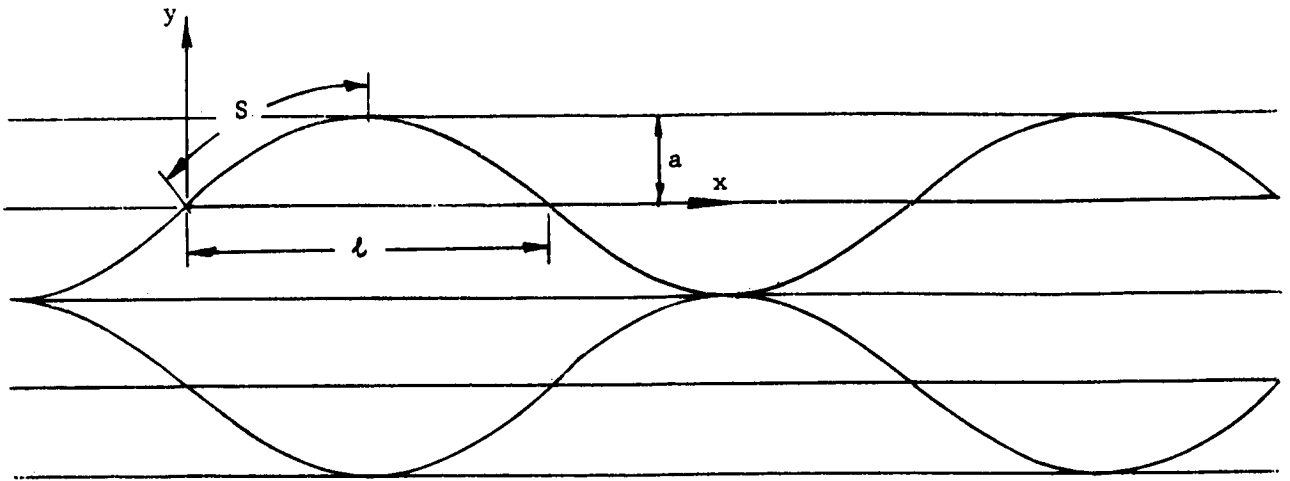


Figure 40. "Sine-wave" Core Configuration

Arc length of sine wave remains constant as "l" and "a" vary.

$S = \text{Arc length} = \text{constant.}$

$$dS = \sqrt{1 + \left(\frac{dy}{dx}\right)^2} \quad (1)$$

$$y = a \sin \frac{x\pi}{l} \quad (2)$$

$$\frac{dy}{dx} = a \frac{\pi}{l} \cos \frac{x\pi}{l} \quad (3)$$

$$S = \int_0^{l/2} \sqrt{1 + \left(\frac{a\pi}{l}\right)^2 \cos^2\left(\frac{\pi x}{l}\right)} dx \quad (4)$$

The above is an elliptic integral, and the limits have to be changed for convenient evaluation.

Let: $\frac{\pi x}{l} = z$ and $dz = \frac{\pi}{l} dx$

Then:

$$S = \int_0^{\pi/2} \sqrt{1 + \left(\frac{a\pi}{l}\right)^2 \cos^2 z} \frac{l}{\pi} dz \quad (5)$$

$$S = \frac{l}{\pi} \int_0^{\pi/2} \sqrt{1 + \left(\frac{a\pi}{l}\right)^2 - \left(\frac{a\pi}{l}\right)^2 \sin^2 z} dz \quad (6)$$

$$S = \frac{l}{\pi} \sqrt{1 + \left(\frac{a\pi}{l}\right)^2} \int_0^{\pi/2} \sqrt{1 - \frac{(a\pi)^2}{l^2 \left[1 + \left(\frac{a\pi}{l}\right)^2\right]} \sin^2 z} dz \quad (7)$$

Equation (7) is an elliptic integral of the form:

$$S = b \int_0^{\pi/2} \sqrt{1 - k^2 \sin^2 z} dz \quad (8)$$

where:

$$b = \frac{l}{\pi} \sqrt{1 + \left(\frac{a\pi}{l}\right)^2} \quad \text{and} \quad k^2 = \frac{(a\pi)^2}{l^2 \left[1 + \left(\frac{a\pi}{l}\right)^2\right]}$$

Now taking different values of $\frac{a}{l}$; "S" is obtained from Equation (8) as a function of l :

$$\frac{a}{l} = 0$$

$$S \Big|_{a=0} = \frac{l}{\pi} \int_{z=0}^{z=\pi/2} 1 dz = \frac{l}{\pi} \left[z \right]_0^{\pi/2} = \frac{l}{\pi} \cdot \frac{\pi}{2} = \underline{0.5 l}$$

$$\underline{a/l = 0.25}$$

$$S \Big|_{a=l/4} = \frac{l}{\pi} \sqrt{1 + \left(\frac{\pi}{4}\right)^2} \int_0^{\pi/2} \sqrt{1 - \frac{\left(\frac{l\pi}{4}\right)^2}{l^2 \left[1 + \left(\frac{\pi}{4}\right)^2\right]} \sin^2 z \, dz$$

$$= \frac{l}{\pi} \sqrt{1 + \frac{\pi^2}{16}} \int_0^{\pi/2} \sqrt{1 - 0.383 \sin^2 z} \, dz$$

$$b = 1.27, \quad k^2 = 0.383, \quad k = 0.62, \quad \sin^{-1} k = 38^\circ$$

From the elliptic integral tables:

$$E = 1.4092$$

$$S \Big|_{a=l/4} = \frac{l}{\pi} \cdot 1.27 \cdot 1.4092 = \underline{0.569 \, l}$$

$$\underline{a/l = 0.50}$$

$$S \Big|_{a=l/2} = \frac{l}{\pi} \sqrt{1 + \frac{l\pi^2}{4l}} \int_0^{\pi/2} \sqrt{1 - \frac{\pi^2}{4 \left[1 + \frac{\pi^2}{4}\right]} \sin^2 z} \, dz$$

$$= \frac{l}{\pi} \sqrt{1 + \frac{\pi^2}{4}} \int_0^{\pi/2} \sqrt{1 - \frac{\pi^2}{4 + \pi^2} \sin^2 z} \, dz$$

$$= \frac{l}{\pi} 1.862 \int_0^{\pi/2} \sqrt{1 - 0.711 \sin^2 z} \, dz$$

$$k^2 = 0.711, \quad k = 0.845, \quad \sin^{-1} k = 58^\circ, \quad E = 1.2301$$

$$\therefore S \Big|_{a=l/4} = \frac{l}{\pi} \cdot 1.862 \cdot 1.2301 = \underline{0.73 \, l}$$

$$\underline{a/l = 0.75}$$

$$S \Big|_{a=\frac{3l}{4}} = \frac{l}{\pi} \sqrt{1 + \frac{9\pi^2}{16}} \int_0^{\pi/2} \sqrt{1 - \frac{9\pi^2}{16 \left[1 + \frac{9\pi^2}{16}\right]} \sin^2 z} \, dz$$

$$= \frac{l}{\pi} 2.56 \int_0^{\pi/2} \sqrt{1 - 0.849 \sin^2 z} \, dz$$

$$k^2 = 0.849, \quad k = 0.921, \quad \sin^{-1} k = 67^\circ, \quad E = 1.1453$$

$$S = \frac{l}{\pi} \times 2.54 \times 1.1453$$

$$S = \underline{0.926 \, l}$$

$$\underline{a/l = 1.0}$$

$$S \Big|_{a=l} = \frac{l}{\pi} \sqrt{1 + \pi^2} \int_0^{\pi/2} \sqrt{1 - \frac{\pi^2}{1 + \pi^2} \sin^2 z} \, dz$$

$$= \frac{l}{\pi} 3.3 \int_0^{\pi/2} \sqrt{1 - 0.91 \sin^2 z} \, dz$$

$$k^2 = 0.91, \quad k = 0.955, \quad \sin^{-1} k = 73^\circ, \quad E = 1.0927$$

$$S = \frac{l}{\pi} \times 3.3 \times 1.0927$$

$$S = \underline{1.149 \, l}$$

The results are tabulated on page 92 and plotted in Figure 41.

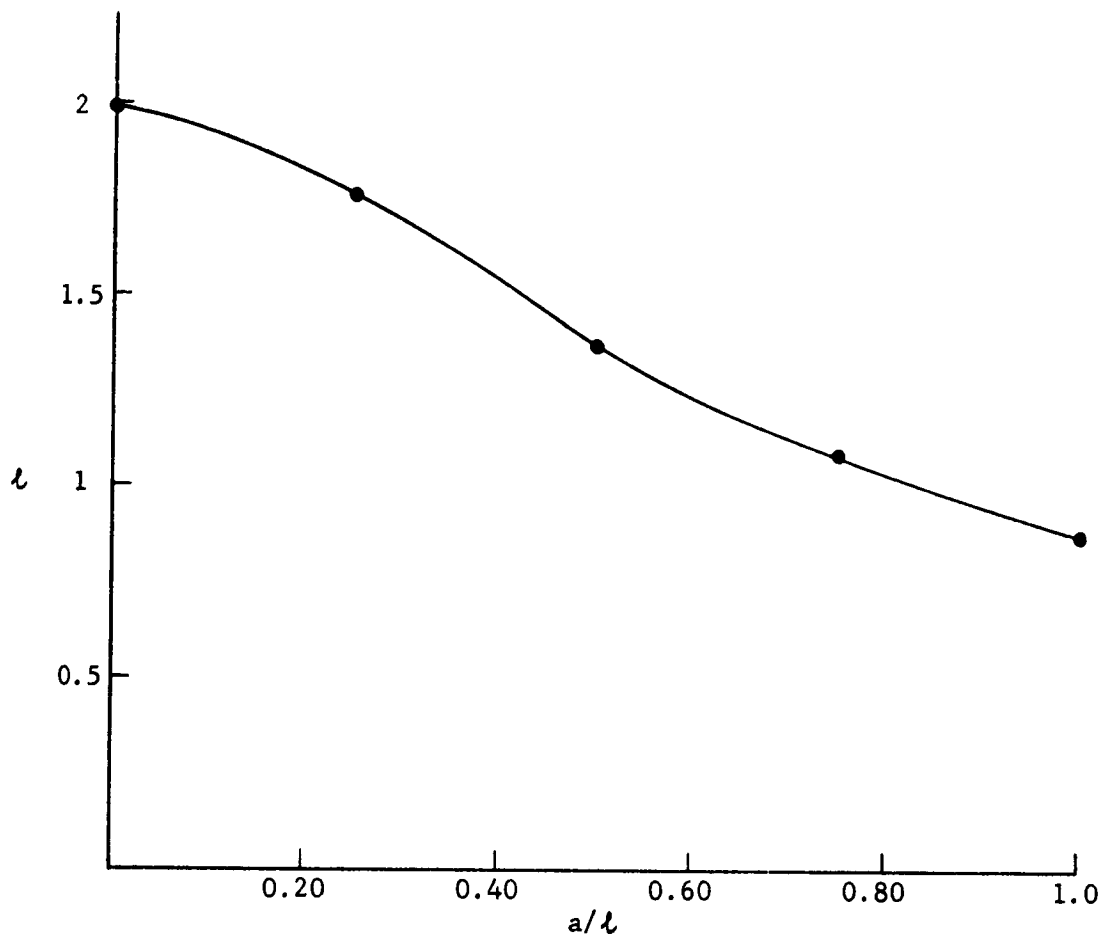


Figure 41. Length Contraction vs. Amplitude-Length Ratio,
Sine Wave Core

a/l	S	l
0	$0.5 l$	$2 S$
0.25	$0.569 l$	$1.76 S$
0.50	$0.73 l$	$1.37 S$
0.75	$0.926 l$	$1.08 S$
1.00	$1.149 l$	$0.872 S$

2. Rectangular Core

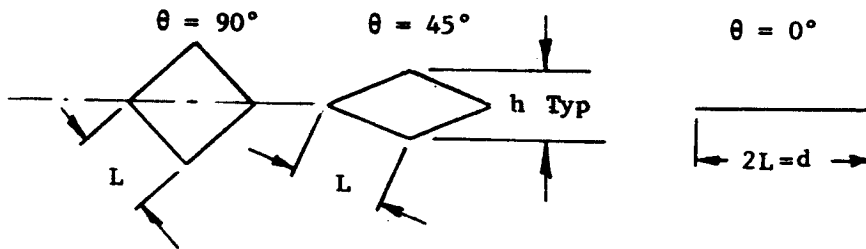


Figure 42. Rectangular Core Configuration

The variables are x and y . L stays constant.

$$x = L \cos \frac{\theta}{2}, \quad y = L \sin \frac{\theta}{2}$$

$$\text{Perimeter} = 4L = S$$

$$A_{\text{total}} = 2 \left[2x \frac{y}{2} \right] = 2xy = 2 \left[L \sin \frac{\theta}{2} \right] \left[L \cos \frac{\theta}{2} \right] \quad (9)$$

$$= 2 L^2 \sin \frac{\theta}{2} \cos \frac{\theta}{2} \quad (9a)$$

$$\text{now: } 2 \sin \frac{\theta}{2} \cos \frac{\theta}{2} = \sin \theta$$

$$\text{Therefore: } \underline{\underline{A_{\text{tot}} = L^2 \sin \theta}} \quad \text{or} \quad \frac{A}{L^2} = \sin \theta. \quad (10)$$

Equation (10) is plotted in Figure 43.

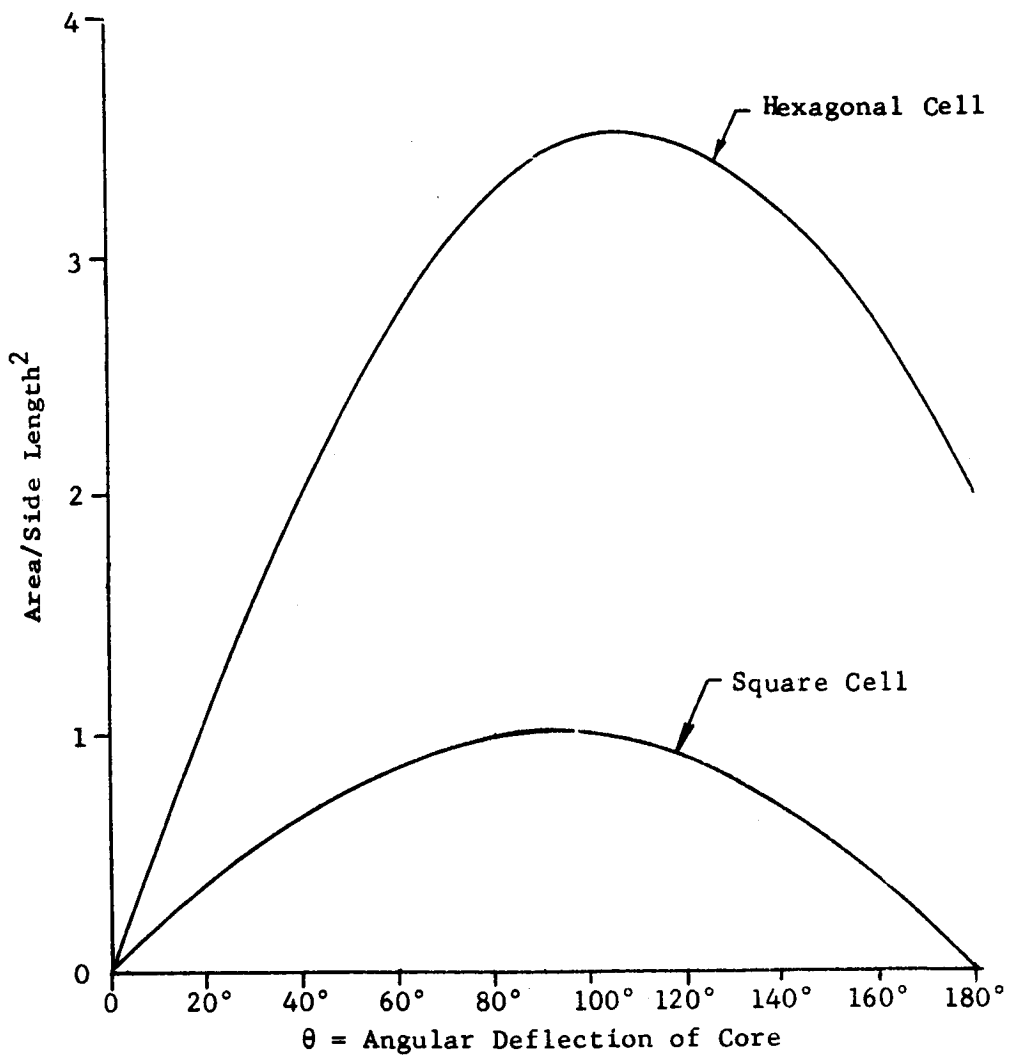


Figure 43. Area-side Ratio vs. Angular Deflection of Core

The parameter h/d was determined next. This ratio (refer to Figure 42) shows the rate of expansion to contraction as the core expands.

Boundary Conditions:

$$\begin{aligned} \theta &= 0 & A &= 2L & B &= 0 \\ \theta &= 90^\circ & A &= & B &= \\ \theta &= 180^\circ & A &= 0 & B &= 2L \end{aligned}$$

$$\begin{aligned} x &= L \cos \frac{\theta}{2} & y &= L \sin \frac{\theta}{2} \\ d &= 2x & h &= 2y \\ d &= 2L \cos \frac{\theta}{2} & h &= 2L \sin \frac{\theta}{2} \end{aligned}$$

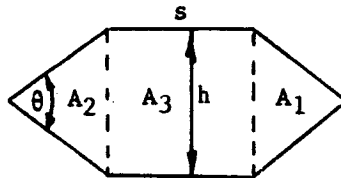
Taking parameter h/d vs. angle θ :

$$\frac{h}{d} = \frac{2L \sin \frac{\theta}{2}}{2L \cos \frac{\theta}{2}} = \frac{\sin \frac{\theta}{2}}{\cos \frac{\theta}{2}} = \underline{\underline{\tan \frac{\theta}{2}}} \quad (11)$$

This ratio is plotted vs. the angle θ in Figure 44.

3. Hexagonal Core

Cell area



$$A_3 = hs$$

$$A_1 + A_2 = 2 \left[2 \left(\frac{h}{2} s \cos \alpha \right) \right]$$

$$A_{\text{tot}} = A_1 + A_2 + A_3 = hs + 2hs \cos \frac{\theta}{2} \quad (12)$$

$$= hs \left(1 + 2 \cos \frac{\theta}{2} \right)$$

where:

$$h = 2s \sin \frac{\theta}{2}$$

$$A_{\text{tot}} = 2s^2 \sin \frac{\theta}{2} \left(1 + 2 \cos \frac{\theta}{2} \right) \quad (13)$$

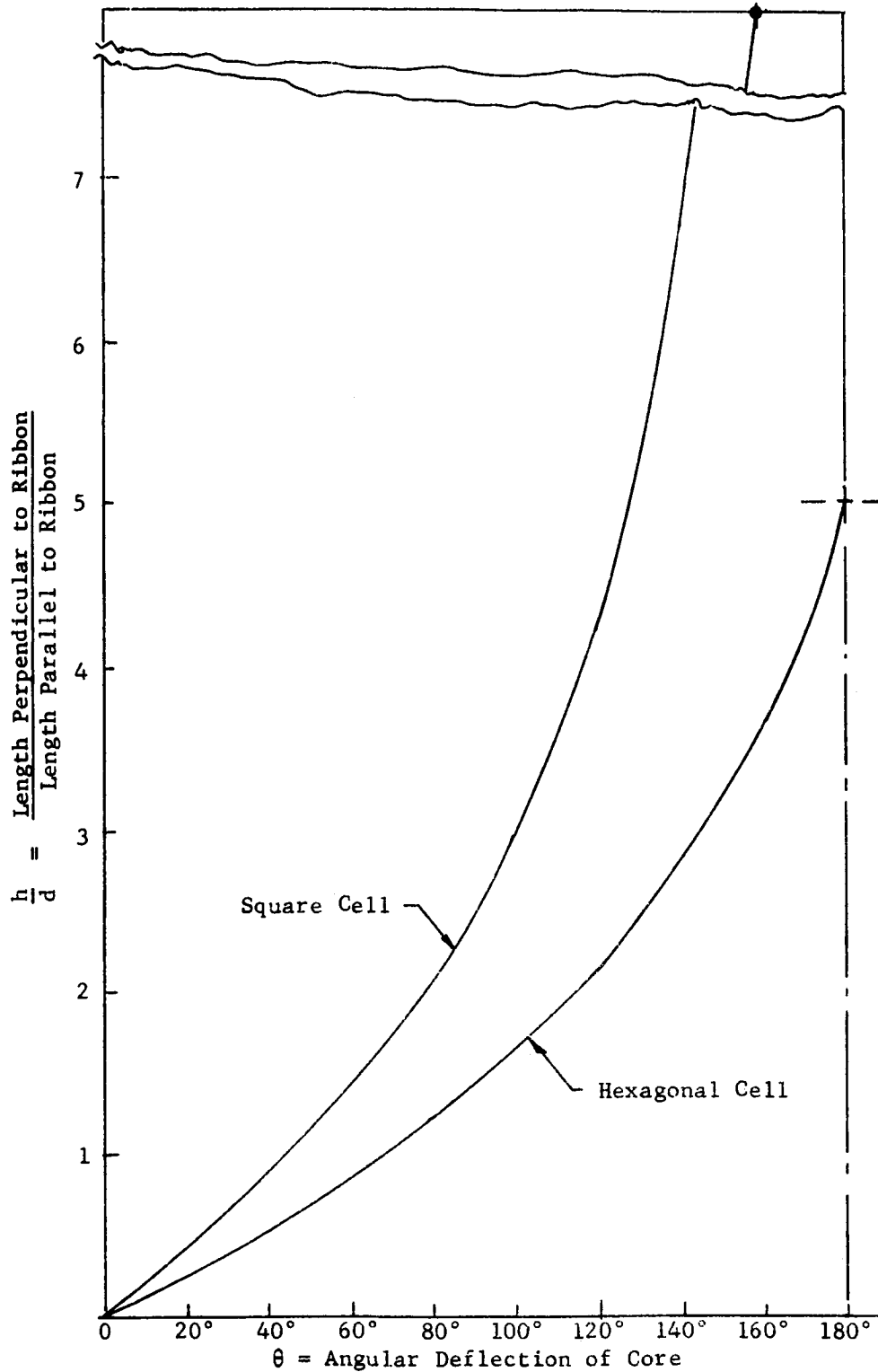


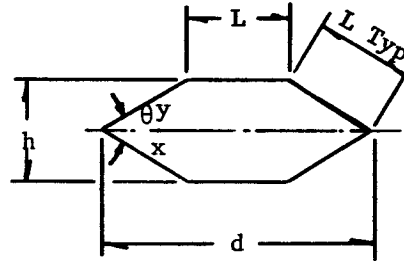
Figure 44. Expansion-to-Contraction Ratio vs. the Angular Deflection of Core

$$\therefore \frac{A}{s} = 2 \sin \frac{\theta}{2} \left(1 + 2 \cos \frac{\theta}{2} \right) \quad (14)$$

This parameter is also plotted vs. angle θ in Figure 43.

Cell change in dimensions.

$$\text{Perimeter} = 6 L$$



Boundary conditions

$$\begin{aligned} \theta = 0 & \quad d = 3 L & \quad h = 0 \\ \theta = 180^\circ & \quad d = L & \quad h = 2 L \\ x & = L \cos \frac{\theta}{2} & \quad y = L \sin \frac{\theta}{2} \end{aligned}$$

Assume perimeter $\frac{h}{d}$ vs. angle θ

$$\frac{h}{d} = \frac{2 L \sin \frac{\theta}{2}}{L \left(2 \cos \frac{\theta}{2} + 1 \right)} = \frac{2 \sin \frac{\theta}{2}}{2 \cos \frac{\theta}{2} + 1} \quad (15)$$

Equation (15) was also plotted in Figure 44.

Conclusions:

From the previous curves, the optimum expansion can be determined. A regime of core expansion has to be determined in order to keep the area of the structure at a maximum. Examination of the curves indicate that for a core to be useful for an expandable structure, it must be in the underexpanded condition. This condition will minimize the distortion of the structure.

The rectangular-shaped core does not appear to be feasible as the length of the bonding surface will have to be very small, which would diminish the strength of the core. On the other hand, the hexagonal core would be better since a large node bond area would be available.

APPENDIX B

STRUCTURAL ANALYSIS OF THE ELASTIC RECOVERY CONCEPT

Abstract

The purpose of this report was to determine the structural potential of the elastic recovery concept. The methods of analysis were developed after generally accepted methods used for sandwich construction. The primary deviation in the analysis was to account for a core material with a very low modulus.

The major loading conditions of internal pressure and axial compression were assumed to be imposed upon cylinders with elastic recovery wall sections. For the different material strengths, the ultimate internal and critical buckling pressures were used as the parameters. Other loading conditions investigated in this report included external pressure and energy absorption.

The results of this investigation indicated that on the basis of the ultimate internal pressure to weight ratio, a single inner skin foam core composite and a flexible honeycomb core sandwich would be the most efficient concepts. For the axial compression loading condition, the flexible honeycomb sandwich was the most efficient based upon a unit weight.

APPENDIX B

STRUCTURAL ANALYSIS OF THE ELASTIC RECOVERY COMPOSITE

by

Byron Anderson

I. INTRODUCTION

The following study details the approach taken to determine the structural potential of the elastic recovery concept. This is a general analysis only, so that the entire range of loading conditions an elastic recovery composite structure might encounter will be covered.

This analysis is divided into two general sections. The first section develops the methods of analysis to determine the effect of the different loading conditions, primarily composite tension and compression, on elastic recovery composites. This section also discusses the assumptions required for the development of the equations.

The second section of the report presents the results of the tension, or internal pressure, loading condition. A cylindrical section is assumed to be the general shape. This section also presents the results of the axial compression loading condition. The effect of energy absorption of the elastic recovery composite is also discussed in the second section.

II. SECTION I - METHODS OF ANALYSIS

General Assumptions: This section presents the basic analytical tools required to make the calculations of load distribution within sandwich cylinders due to internal pressure and to establish buckling loads for the conditions of external pressure and axial compression.

The specific wall concepts evaluated fall into two general classifications for expandable structures: (1) high-modulus core, and (2) low-modulus core. The former is characterized by a flexible honeycomb type of core that distributes pressure loading fairly equally between skins and results in buckling of the sandwich as a unit when loaded in compression. If the second

type of core consisted of flexible polyurethane foam or some other extremely low-modulus material, pressure loads would be carried entirely by a single facing. When a buckling load is applied to a composite with the second type of core, failure takes the form of individual thin shell failure.

Techniques presented herein consider these two types of sandwich core, but are preliminary in nature since an exhaustive treatment of the subject was not attempted at this time. As future studies will be required to more thoroughly evaluate such factors as the buckling characteristics, effect of initial imperfections, and foldability, these characteristics will be evaluated both on an individual basis and by the influence they have on one another.

Nomenclature: The following symbols and nomenclature are used for the structural analysis:

d	-	The total sandwich wall thickness
E	-	Elastic modulus for facings of equal thickness
E_1, E_2	-	Elastic modulus of the individual facings
E_c	-	Compressive modulus of the core
G_c	-	Shear modulus of the core
f_1, f_2, f_3	-	Stresses in the individual facings
f_{av}	-	Average stress in facings
f_{cr}	-	Critical buckling stress
h	-	Distance between facing centroids for sandwich constructions
K_1, K_2	-	Proportionality coefficients
L	-	Length of cylinder
P	-	Load
p	-	Applied internal pressure
P_{cr}	-	Critical external pressure (buckling)
P_{ult}	-	Internal pressure corresponding to ultimate strength of material

- R - Mean radius of sandwich cylinder
- t - Facing thickness for symmetrical sandwich ($t = t_i = t_o$)
- t_i, t_o - Inner and outer facing thickness for structural sandwich constructions
- t_1, t_2, t_3 - Facing thickness for multilayer composite constructions
- t_c - Core thickness
- U - Strain energy
- w - Composite weight per unit length, lb/unit in.
- λ - $\sqrt{1 - \nu^2}$
- ν - Poisson's ratio
- ρ - Density

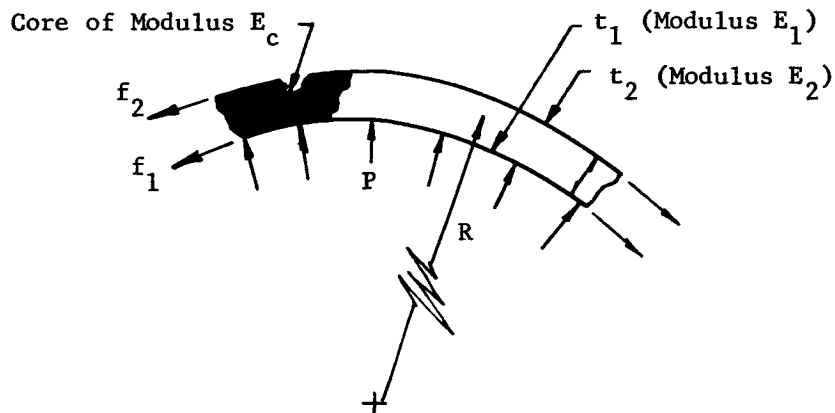
A. Internal Pressurization of Pressure Vessels

In any multiple skin-core structure subjected to an internal pressure, the effectiveness of each skin in resisting load is a function of core stiffness as well as skin modulus.

It was assumed that this analysis would be applicable for external pressure on the sandwich structure, providing the load was below the critical buckling pressure.

1. Typical Sandwich Structure

The following is a schematic drawing of a single layer sandwich cylinder showing the relationship of the facing and core geometries:



From static equilibrium conditions,

$$f_1 = \frac{K_1 pR}{t_1}$$

$$f_2 = \frac{K_2 pR}{t_2}$$

Where: K_1 and K_2 are proportionality coefficients

$$pR = K_1 pR + K_2 pR$$

$$K = 1 - K_2$$

Strain continuity in the radial direction* is expressed as follows:

$$\frac{K_1 pR^2}{t_1 E_1} - \frac{K_2 pR^2}{t_2 E_2} = \frac{K_2 p h}{E_c}$$

$$\frac{K_1 R^2}{t_1 E_1} - \frac{(1-K_1)R^2}{t_2 E_2} = \frac{(1-K_1)h}{E_c}$$

Solving for K_1

$$\frac{K_1 R^2}{t_1 E_1} + \frac{K_1 R^2}{t_2 E_2} + \frac{K_1 h}{E_c} = \frac{h}{E_c} + \frac{R^2}{t_2 E_2}$$

$$K_1 \left(\frac{R^2}{t_1 E_1} + \frac{R^2}{t_2 E_2} + \frac{h}{E_c} \right) = \frac{h}{E_c} + \frac{R^2}{t_2 E_2}$$

$$K_1 = \frac{\frac{h}{E_c} + \frac{R^2}{t_2 E_2}}{\left[R^2 \left(\frac{1}{t_1 E_1} + \frac{1}{t_2 E_2} \right) + \frac{h}{E_c} \right]}$$

* The growth of the outer shell minus the growth of the inner shell is equal to the deformation of the core.

$$K_2 = 1 - K_1$$

$$= \frac{R^2}{t_1 E_1 \left[R^2 \left(\frac{1}{t_1 E_1} + \frac{1}{t_2 E_2} \right) + \frac{h}{E_c} \right]}$$

The stress in each facing can then be written as:

$$f_1 = \frac{pR \left(t_2 E_2 h + R^2 E_c \right)}{t_1 t_2 E_c E_2 \left[R^2 \left(\frac{1}{t_1 E_1} + \frac{1}{t_2 E_2} \right) + \frac{h}{E_c} \right]}$$

$$f_2 = \frac{p R^3}{t_1 t_2 E_1 \left[R^2 \left(\frac{1}{t_1 E_1} + \frac{1}{t_2 E_2} \right) + \frac{h}{E_c} \right]}$$

For the general case, the ratio of the facing stresses had to be used.

$$\frac{f_2}{f_1} = \frac{R^2 E_2 E_c}{t_2 E_1 E_2 h + R^2 E_1 E_c}$$

The stress ratio reduces to the following:

$$\frac{f_2}{f_1} = \frac{R^2 E_c}{t_2 h} \left(\frac{1}{E_1 + \frac{R^2 E_c}{t_2 h} \left(\frac{E_1}{E_2} \right)} \right)$$

This equation is plotted in Figure 45 for the range of sandwich constructions. The average stress for the sandwich construction can be found by combining the individual facing stresses. The stress is shown as:

$$2 f_{av} = \frac{pR \left(t_2 E_2 h + R^2 E_c \right) + pR^3 E_2}{t_1 t_2 E_1 E_2 \left[R^2 \left(\frac{1}{t_1 E_1} + \frac{1}{t_2 E_2} \right) + \frac{h}{E_c} \right]}$$

$$2 f_{av} = \frac{pR^3(E_c + E_2) + pRt_2E_2h}{R^2t_2E_2 + R^2t_1E_1 + \frac{t_1t_2E_1E_2h}{E_c}}$$

$$\frac{2 f_{av}}{pR} = \frac{R^2E_c(E_c + E_2) + t_2E_2E_ch}{R^2t_2E_2E_c + R^2t_1E_1E_c + t_1t_2E_1E_2h}$$

For the special case of equal skin thicknesses and the same material, the constants are rewritten as:

$$K_1 = \frac{\frac{tEh + R^2E_c}{E_c tE}}{\frac{2R^2E_c + htE}{E_c tE}} = \frac{tEh + R^2E_c}{2R^2E_c + htE}$$

$$K_2 = \frac{R^2E_c}{2R^2E_c + htE}$$

The facing stresses are simplified to the following:

$$f_1 = \frac{pR(tEh + R^2E_c)}{t(2R^2E_c + htE)}$$

$$f_2 = \frac{pR^3E_c}{t(2R^2E_c + htE)}, \quad f_{av} = \frac{pR}{2t}$$

The ratio of the outer facing stress to the average stress is found to be

$$\frac{f_2}{f_{av}} = \frac{2K_2}{K_1 + K_2} = \frac{2R^2E_c}{tEh + 2R^2E_c}$$

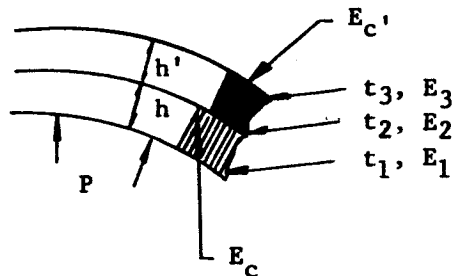
$$\frac{f_2}{f_{av}} = \frac{R^2 E_c}{tEh} \left(\frac{2tEh}{tEh + 2R^2 E_c} \right)$$

$$= \frac{R^2 E_c}{tEh} \left(\frac{2}{1 + \frac{2R^2 E_c}{tEh}} \right) = g \left(\frac{R^2 E_c}{tEh} \right) \quad \text{where } g \text{ denotes function}$$

This relationship is plotted in Figure 46 for the full range of construction, including that for conventional structural sandwich.

2. Multilayer Sandwich Structure

For this section, a composite was assumed to consist of three facings (t_1, t_2 , and t_3) and separated by two core spacings.



By writing the basic equations of strain continuity, the distribution of stress between skins is obtained as follows:

$$\frac{K_1 p R^2}{t_1 E_1} - \frac{K_2 p R^2}{t_2 E_2} = \frac{K_2 p h}{E_c} \quad (1)$$

$$\frac{K_2 p R^2}{t_2 E_2} - \frac{K_3 p R^2}{t_3 E_3} = \frac{K_3 p h'}{E_c'} \quad (2)$$

$$K_1 + K_2 + K_3 = 1 \quad (3)$$

$$(2) \text{ and } (3) \quad \frac{K_2 R^2}{t_2 E_2} - \frac{(1 - K_1 - K_2) R^2}{t_3 E_3} = \frac{(1 - K_1 - K_2) h'}{E_c}$$

$$\frac{K_2 R^2}{t_2 E_2} - \frac{R^2}{t_3 E_3} + \frac{K_1 R^2}{t_3 E_3} + \frac{K_2 R^2}{t_3 E_3} = \frac{h'}{E_c} - \frac{K_1 h'}{E_c} - \frac{K_2 h'}{E_c} \quad (4)$$

$$(4) \text{ and } (1) \quad \frac{K_2 R^2}{t_2 E_2} - \frac{R^2}{t_3 E_3} + \frac{\left(\frac{K_2 h}{E_c} + \frac{K_2 R^2}{t_2 E_2}\right) t_1 E_1}{t_3 E_3} + \frac{K_2 R^2}{t_3 E_3}$$

$$= \frac{\left(\frac{K_2 h}{E_c} + \frac{K_2 R^2}{t_2 E_2}\right) \left(\frac{t_1 E_1}{R^2}\right) h'}{E_c} - \frac{K_2 h'}{E_c}$$

$$\therefore K_2 = \frac{\left(\frac{h'}{E_c} + \frac{R^2}{t_3 E_3}\right)}{\frac{R^2}{t_2 E_2} + \frac{\left(\frac{h}{E_c} + \frac{R^2}{t_2 E_2}\right) R^2}{t_3 E_3} + \frac{R^2}{t_3 E_3} + \frac{\left(\frac{h}{E_c} + \frac{R^2}{t_2 E_2}\right) \left(\frac{t_1 E_1 h'}{R^2}\right)}{E_c} + \frac{h'}{E_c}}$$

$$K_2 = \frac{\left(\frac{h'}{E_c} + \frac{R^2}{t_3 E_3}\right)}{\left(\frac{h}{E_c} + \frac{R^2}{t_2 E_2}\right) \left(\frac{R^2}{t_3 E_3} + \frac{t_1 E_1 h'}{R^2 E_c}\right) + \frac{R^2}{t_2 E_2} + \frac{R^2}{t_3 E_3} + \frac{h'}{E_c}}$$

Similarly, K_3 and K_1 can be solved, but due to the complexity of the solutions, the work will be postponed until the need is established.

3. Comments on Stress Curves

For the case of a sandwich with two equal skins, f_2/f_{av} is plotted versus a stiffness parameter. Here, the closer the stress ratio approaches one, the more efficient the sandwich becomes. Because of the low-core modulus of polyurethane foam, a more efficient stress distribution is obtained when a relatively low-modulus material is used as the facing material. With the stress ratio equal to one, the two skins would theoretically fail at the same internal pressure, corresponding to the material strength.

The general case of a pressurized sandwich with differing face materials and thicknesses is treated somewhat differently. In this case, f_2/f_1 is plotted as a family of curves of varying stiffness parameter versus a second stiffness parameter. Here, the closer the stress ratio approaches the ratio of the respective material strengths, the more efficient the sandwich becomes. With the stress ratio equal to the strength ratio, failure of both skins would theoretically occur simultaneously. As previously mentioned, relatively low-modulus facing materials are required for an efficient polyurethane foam core expandable sandwich.

It should be again noted that the stress functions presented hold true for an external pressure loading up to initial buckling as well as for an internal pressure loading.

B. Cylinder Buckling; Axial Compression

The discussion on the buckling of sandwich cylinders under axial load is divided into two classifications: (1) a sandwich having a core possessing sufficiently high shear modulus and modulus of elasticity to prevent wrinkling of the skins and buckling of the individual sandwich walls; and (2) a sandwich having a core of very low modulus and, therefore, one that behaves as two independent cylinders. The low-density polyurethane foam cores are examples of this second classification. Rigid and flexible honeycomb type cores fall into the first classification. Methods of analysis for the two types of core in a sandwich have been determined separately.

1. High-Modulus Core

Methods of analysis presented in MIL-HDBK-23: Part III⁽³²⁾ apply to this type of core. Section 4.3 of this reference presents a method of establishing minimum core thickness and core shear modulus to prevent overall buckling of the sandwich walls. Furthermore, design charts are presented to aid in the determination of minimum core thickness and modulus. The use of these charts, which are rather extensive, is suggested for design work.

A curve (Figure 47) is included which presents the buckling stress, F_{cr} , as a function of sandwich dimensions, modulus, etc. Because of assumptions made in the design charts, a final check using this curve is required to establish true buckling stress.

In the case of a very long cylinder, buckling as a column should also be checked.

If the core is of a cellular (honeycomb) material, dimpling of the facings into the spacing between cell walls can occur. Dimpling of the facings may not lead to failure unless the amplitude of the dimples becomes large enough to cause the buckles to grow across core cell walls and result in wrinkling of the facings. Chapter 5 of MIL-HDBK-23 presents equations for determining dimpling stress level. Figure 48 has been directly reproduced from this source and is included as a means of establishing dimpling stress as a function of cell size. Because of the expandable criteria of this program, intracell dimpling should be avoided.

It should be noted that the probability of initial imperfections is much less in a more rigid sandwich as contrasted with a low-density sandwich. The presence of imperfections does influence buckling strength. However, this is not expected to result in anywhere near the reduction that would be experienced in a low-modulus sandwich having the same imperfection, because of the shear path between skins.

2. Low-Modulus Core

When a low-modulus core material such as polyurethane foam is used in a sandwich construction, the relationships set forth in MIL-HDBK-23 no longer apply. Failure occurs in the skins with very little additional strength contribution from the core.

The buckling relationships found in Theory of Elastic Stability⁽³³⁾ for thin cylindrical shells can be assumed to apply to each of the two sandwich skins and the total allowable compressive load obtained by adding the loads carried by each skin.

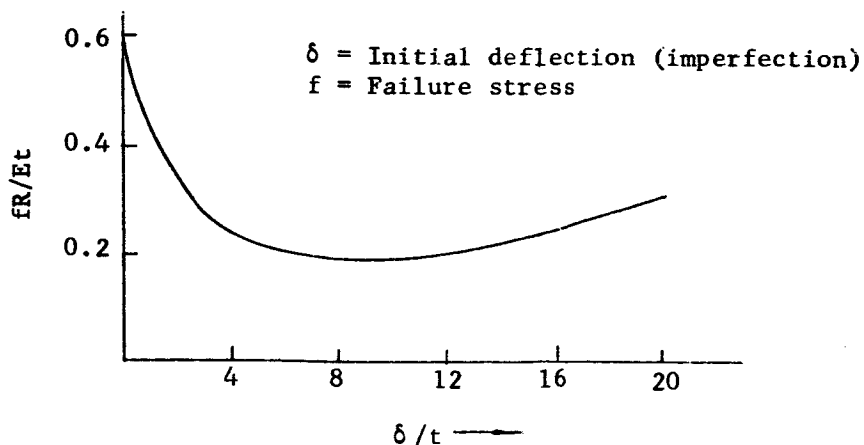
Equation (a) assumes a perfect cylindrical surface.

$$f_{cr} = \frac{Et}{r\sqrt{3(1-\nu^2)}} \quad (a)$$

Experiments made by several researchers have revealed that the discrepancy between the actual and theoretical buckling strengths of thin cylindrical shells is very large.

A curve presented in Theory of Elastic Stability and reproduced below is indicative of the effects of imperfections. As δ/t approaches 0,

$$\left(\frac{fR}{Et}\right) = \frac{1}{\sqrt{3(1-\nu^2)}} \quad (b)$$



Thus, equation (b) agrees with equation (a), which assumed a perfect surface. It can be seen that the lowest value of buckling stress corresponds to a value equal to one-third that of equation (b). Therefore, the following design equation in view of the numerous initial skin deformations associated with a low core density sandwich structure is presented:

$$\left(f_{cr}\right)_{\text{design}} = \frac{E t}{5.2 R \sqrt{1-\nu^2}}$$

Finally, it should be mentioned that this discussion on buckling of cylinders is intended only to provide basic design relationships. In order to accomplish this task, the foregoing study assumes that the composite materials behave as isotropic materials. An exhaustive treatment of the subject is beyond the scope of the present study. A series of compressive tests will be most informative in regard to the specific buckling characteristics associated with sandwich structures.

C. Cylinder Buckling; External Pressure

Some work on the buckling problem of externally pressurized sandwich cylinders has been done by the Forest Products Laboratory. (34)(35)(36) The included curves and equations were based essentially upon the theory presented in these three references. The sandwich cylinders were assumed to have isotropic facings and orthotropic or isotropic cores. The natural axes of the orthotropic cores are axial, tangential, and radial.

The curves in Figures 49 and 50 present specific solutions to the buckling equations which by no means cover the range of geometries and materials that could be considered for elastic recovery expandable structures, but do provide design information that is valuable. Unfortunately, solutions for a sandwich core possessing a finite modulus are excessively complex, and a family of curves would be required for each specific ratio of $E_c/G_{R\theta}$ and E_c/G_{RZ} . Actually, for most core materials (with the exception of very low-density foams, which are important from the standpoint

of the elastic recovery concept), E_c is sufficiently large so that the assumption of infinite E_c yields values of the critical pressure that are only slightly too great; Figure 50 applies to this case. For the case of a sandwich having a foam core, buckling stress is closely approximated by equation (3), Table 12.

For certain limiting cases, the basically complex 4X4 determinant that expresses the buckling pressure reduces to a relatively simple equation. Table 12 notes the critical pressure for various material combinations (E_c and $G_{R\theta}$) and sandwich geometrics (t_o, t_i).

III. SECTION II - ELASTIC RECOVERY CONCEPT EVALUATION

A. Internal Pressure

In Section I.A, the theoretical effectiveness of each sandwich facing in resisting an internal pressure as a function of core stiffness and facing modulus was developed.

For the present analysis, two types of core are considered: a 2-lb/ft³ polyurethane foam with a compressive modulus of approximately 1 psi and a 2-lb/ft³ paper or fiberglass honeycomb core with a compressive modulus of 15,000 psi. An extensive material evaluation and development program would undoubtedly reveal a wider range of efficient and compressible flexible core materials other than the paper and fiberglass cores. These core materials, however, represent a reasonable choice for evaluation. Temperature effects upon the composite materials may limit core and face materials for the space application being considered; these thermal effects, however, are fully discussed in Narmco Engineering Report 64-E14.⁽³⁷⁾ It should be noted that any reduction in core density below 2 lb/ft³ for the flexible honeycomb type core results in a proportionately greater reduction in core properties.

Figure 51 presents the facing stress ratio, f_2/f_{av} , as a function of the facing-geometry parameter R^2/E for foam core thicknesses up to 3 in. in increments of 1/2 in. and for facing thicknesses of 0.05 and 0.10 in. For all practical purposes, the f_2/f_{av} ratio for the two honeycomb core

materials remains constant at 1.0, independent of both core thickness and facing thickness.

The most efficient facing materials (presented in Table 13) were chosen for evaluation. The vertical lines in Figure 51 represent specific stress ratios for the following facing materials and cylinder radii of 40 and 80 in. It should be noted that the material ultimate strengths presented in the materials section were used without incorporating a factor of safety throughout this investigation. It is felt that appropriate factors of safety can be best incorporated on the basis of the specific mission requirements of a particular application.

Inspection of Figure 51 reveals that for form, there is considerable variation in the f_2/f_{av} stress ratio, not only with the R^2/E parameter but with core thickness and facing thickness as well. Because of the low core modulus of polyurethane foam, a more efficient stress distribution is obtained when a relatively low-modulus material is used as the sandwich facing. Similarly, thinner sandwiches of foam result in a more equitable distribution of load between facings than do the thicker sandwiches. This is true because of the smaller deformation per unit load associated with the thinner sections of polyurethane foam core. The vertical lines on Figure 45 also indicate that the f_2/f_{av} increases with increasing cylinder radius, corresponding to the higher stresses associated with the larger size.

Of the facing materials considered, polyvinyl chloride resin - 181 style glass cloth results in the most efficient distribution of load between facings of a sandwich, utilizing a polyurethane foam core. Because of its lower ultimate strength, however, the polyvinyl chloride - 181 style glass cloth laminate does not result in the most efficient foam core sandwich construction.

Figures 52 through 55 present the ultimate internal pressure that can be supported by sandwich cylinders of both foam and honeycomb core construction as a function of core thickness for the facing materials considered. Ultimate internal pressure is defined as that internal

pressure which results in a tensile stress in the inner facing equal to the ultimate strength of the material. Obviously, the higher the f_2/f_{av} ratio, the more efficient the structural sandwich will be. With the f_2/f_{av} stress ratio equal to one, the two skins would theoretically fail at the same internal pressure and corresponding to the ultimate material tensile strength.

The next step in the analysis is to determine the efficiency of the composite sections. The efficiency parameter used to compare the effectivity of the various composites is the ultimate internal pressure to composite weight ratio. This ratio is plotted as a function of core thickness (t_c) in Figures 56 through 61. From Figures 52 and 53 it is apparent that the single face-foam core composite has a strength-to-weight ratio advantage over a typical sandwich with two facings with the same core and facing materials. The honeycomb core sandwiches (Figures 54 and 55) possess the highest strength-to-weight ratios due primarily to the load transferral between the facings.

Figures 62 through 64 present ultimate pressure as a function of unit length cylinder weight. These figures dramatically emphasize the ineffectivity of increasing core thickness for an internal pressure application. In these figures, the facing composite was assumed to be polyurethane resin and regenerated cellulose fiber cloth. The honeycomb core sandwich ranked the highest in structural efficiency, followed by the foam sandwich with a single facing and foam sandwich with two facings, in that order.

Conclusions (internal pressure evaluation): It should be emphasized that the structural efficiency of a foam sandwich subjected to internal pressure can be significantly increased by choosing each facing of a different flexible, high-strength material having moduli such that a more equitable distribution of load between facings is obtained. Thickness of the individual facings can also be varied, the one relative to the other, in order to increase the efficiency of a foam sandwich. The basic load distribution equations will serve as guides for design efforts in this direction.

From the developed curves, it appears that on the basis of internal pressure-to-weight parameter, elastic recovery composites consisting of either a single inner skin with foam on the outer surface or a honeycomb type sandwich would be desirable. Taking into consideration other design criteria (e.g., the elastic recovery mechanism), the single skin would be the better concept for internal pressure.

B. Concept Evaluation - Axial Compression

The theoretical basis for evaluating sandwich cylinders subjected to axial compression is presented in Section I.B of this report.

For purposes of this portion of the structural study, a cylinder of composite wall construction representing the elastic recovery concept is considered. Curves are presented for the buckling stress of a 2 lb/ft³-density polyurethane foam flexible core and a 2-lb/ft³ paper of fiberglass honeycomb semirigid core. Shear moduli of the two honeycomb core materials are almost identical and, therefore, dictate essentially identical buckling characteristics.

Figure 65 presents the buckling stress as a function of the facing-geometry parameter $\lambda R/E$ for honeycomb core thicknesses up to 3 in. in increments of 1/2 in. The buckling stress for a foam core sandwich is also presented. Buckling of the foam sandwich is relatively independent of core thickness because of the extremely low compression modulus of the flexible low-density foam.

As in the case for the internal pressure condition, two cylinder sizes of 40 and 80 in. radii have been chosen for analysis. The same types of materials as used in the internal pressure have also been used to determine the critical axial load; Poisson's ratio is taken at 0.1 for all of the facing materials.

It should be noted that the buckling stresses indicated on Figure 65 are ultimate, with no factor of safety. The cylinder length is assumed to be less than the respective critical column length. For the present,

the ultimate strength in compression has been taken equal to the ultimate strength in tension. For this study, this assumption was reasonable, since, in general, the ultimate compressive strength of reinforced plastics approaches the ultimate tensile strength. One reason for this characteristic is the lack of any definite yield point for reinforced plastics which occurs in metallic materials.

Intercell buckling is not a problem over the stress range indicated in Figure 65 and for the facing materials considered. Cell size of the honeycomb is approximately 0.3 in. (diameter of inscribed circle). A thorough investigation into wrinkling of individual sandwich facings involves elastic foundation considerations and involves work beyond that warranted in the present evaluation. For the sandwich composites evaluated, however, problems in this area are not anticipated.

A study of Figure 65 reveals several interesting and important trends. One of the first obvious factors noted was that little change in the buckling stress occurred as facing thickness increased from 0.05 in. to 0.10 in., which is to be expected. The large difference between the buckling strength of foam core sandwich and the more rigid paper or fiberglass honeycomb cores sandwich is also apparent.

Considering an elastic recovery composite sandwich structure fabricated from either of the two types of honeycomb cores, it is worth noting that a 3-in. core will develop a 31,000-psi stress in a glass or regenerated cellulose fiber cloth reinforced polyurethane facing but only a 6,000 psi stress in a PVC-glass laminate, based on a cylinder of 40-in. radius. Thus, a 1-in. core will develop the ultimate strength of polyurethane glass facings while a 3-1/2 in. core is required for developing the much higher strength of polyurethane-regenerated cellulose fiber cloth facings, and a core of approximately 4-in. thickness is required to develop the in-between ultimate strength of polyester terephthalate polyimide film (e.g., H-film) facings, again based upon a 40-in. radius. Facing modulus, of course, is the controlling material property.

Figures 66 through 69 present the strength-to-weight ratio as a function of core thickness (t_c) and based upon a unit cylinder length. The first two figures indicate the relative efficiencies of the facing materials when combined with the honeycomb core, while the last two figures present the much lower strength-to-weight ratios of the same facing materials when combined with foam core. As previously explained, the low shear modulus of the foam allows each facing to behave as if it were an individual shell subjected to axial compression. The polyurethane resin regenerated cellulose fiber cloth laminate facings, when combined with the honeycomb core, result in the most efficient composite sandwich cylinder for supporting a compressive axial load.

The composite section utilizing the flexible honeycomb core materials exhibited maximum points for the axial load to weight per unit length parameter, particularly for the flexible honeycomb type of cores (Figures 66 and 67). The maximum point represents an optimum condition; i.e., the maximum strength of the facing material coincides with the buckling strength of the cylinder. As the core thickness increases, the P_{cr}/w parameter decreases because the core weight of the composite increased. The composite sections with the foam core did not exhibit this maximum as shown in Figures 68 and 69.

The maximum compressive strength is presented in Figure 70 as a function of weight per unit length. These curves were established to serve as a quick design reference in establishing the weight requirements for a cylinder length under an axial loading condition. Note that the curves denote the maximum stress up to the point of the ultimate material strength. Since the load would have to remain constant at this maximum stress condition, the weight/unit cylinder would remain constant as the composite thickness increased. It can be concluded from the axial compression study that for an elastic recovery composite to be stressed to a level near the ultimate, a core with a finite core modulus would be required. The compressible honeycomb type of cores would be required for the higher core modulus. When a foam core composite was used for an axial compression application, the facings would each act essentially as independent concentric shells.

C. Concept Evaluation; Energy Absorption

In order to evaluate the elastic recovery composite for its ability to act as an energy absorber, it is assumed that the strain energy available will act as a figure of merit. The strain energy per unit length was determined from the following equation:

$$\frac{U}{L} = \frac{F_{cr}^2 A}{2AE} = \frac{2 \pi R t_s F_{cr}^2}{E}$$

The strain energy per unit cylinder length was determined as a function of sandwich core thickness (t_c) for a honeycomb type core with flexible laminate facings. The results using a polyurethane resin-regenerated cellulose fiber cloth reinforced laminate are presented in Figure 71. Since the strain energy was assumed to be a function of the critical stress, only the elastic recovery concept which gave the highest critical stress was plotted. It should be noted from the equation that the strain energy per unit length would be a function of the material characteristic F_{cr}^2/E for the same cylinder geometry.

From this study, it could be concluded that the flexible laminate composite with a high strength would be needed for the maximum energy required for the docking of a large ferry vehicle.

D. Concept Evaluation; External Pressure

The method of analysis for external pressure was developed in Section I.C. Since this analysis reveals that the prevention of a stability failure is the primary design problem, the elastic recovery composite with a finite core modulus which was required for axial compression would also be needed for external pressure.

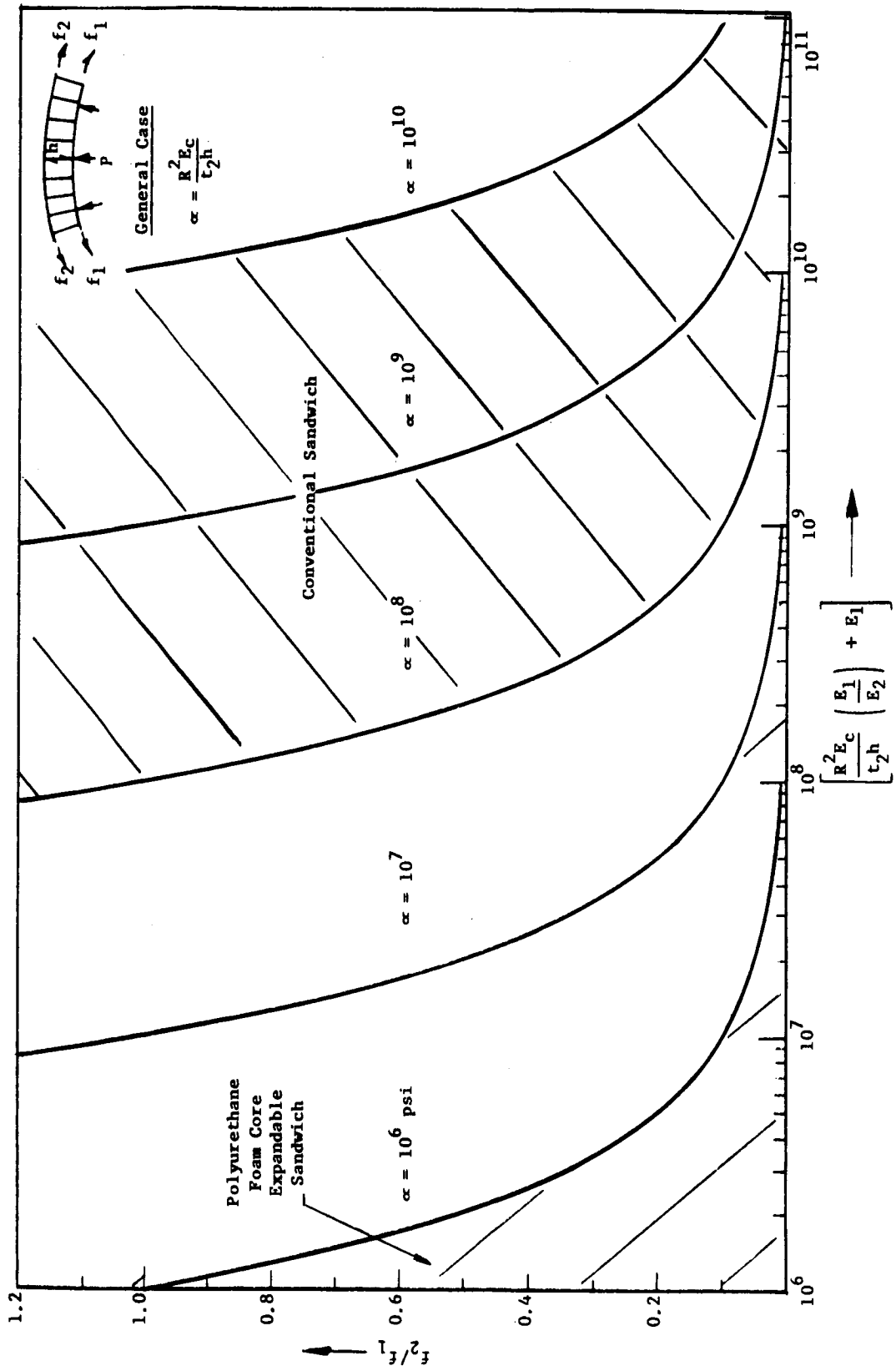


Figure 45. Tensile Load Distribution Between Unequal Faces of a Sandwich Loaded by Internal Pressure

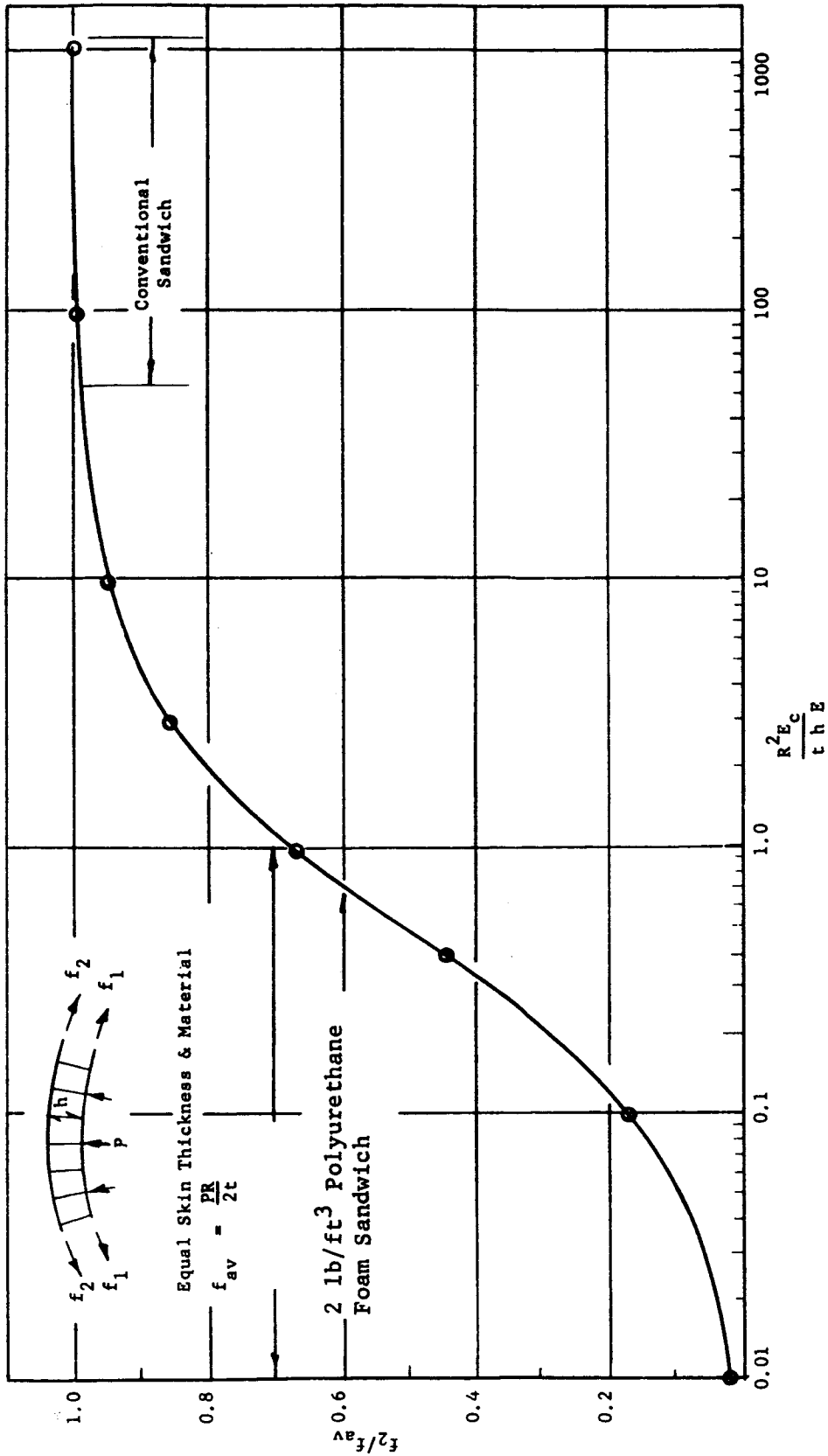


Figure 46. Tensile Load Distribution Between Equal Faces of a Sandwich Loaded by Internal Pressure

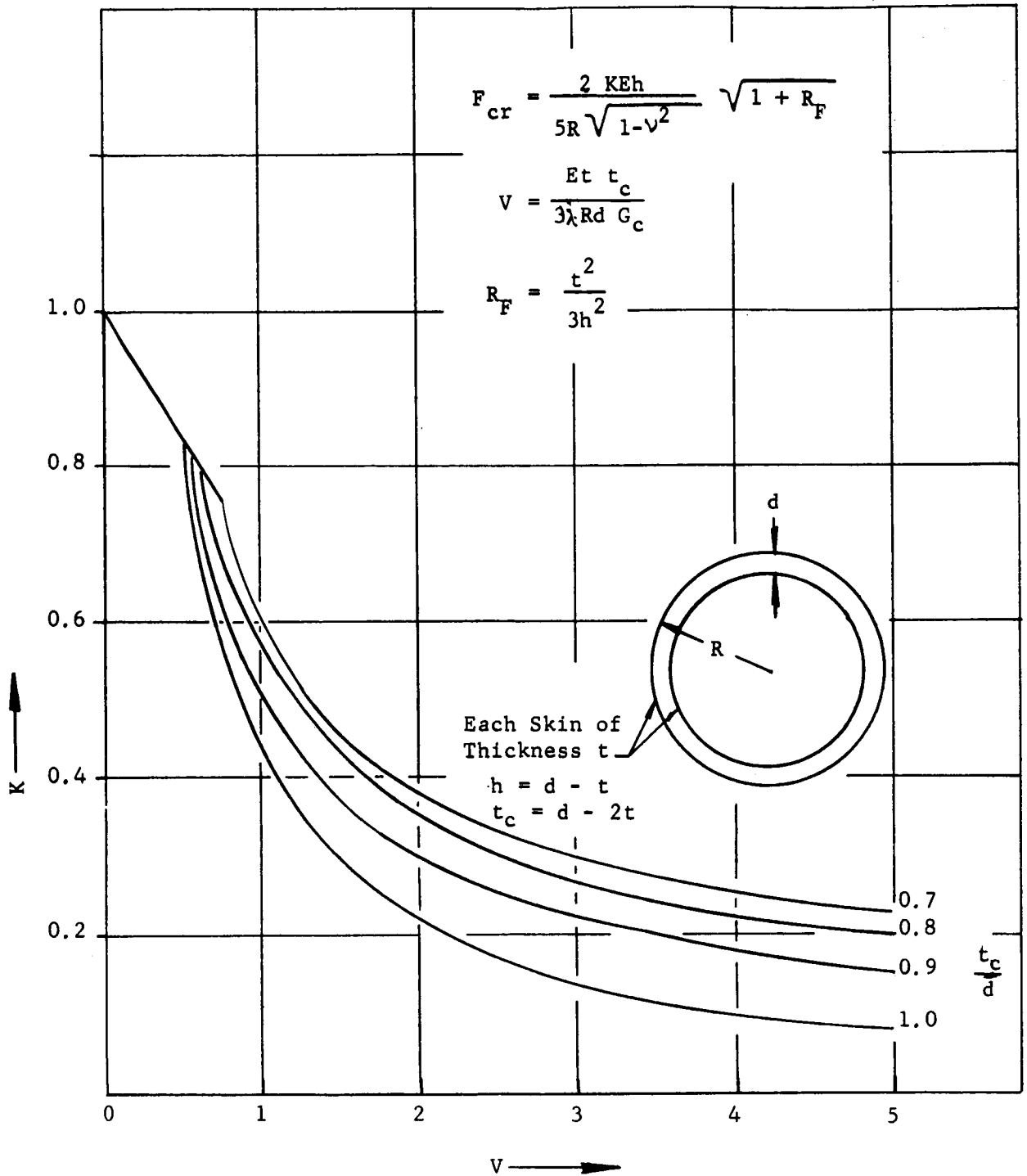


Figure 47. Sandwich Cylinder Under Axial Compression-Isotropic Core
 (Reference: MIL-HDBK-23; Part III)

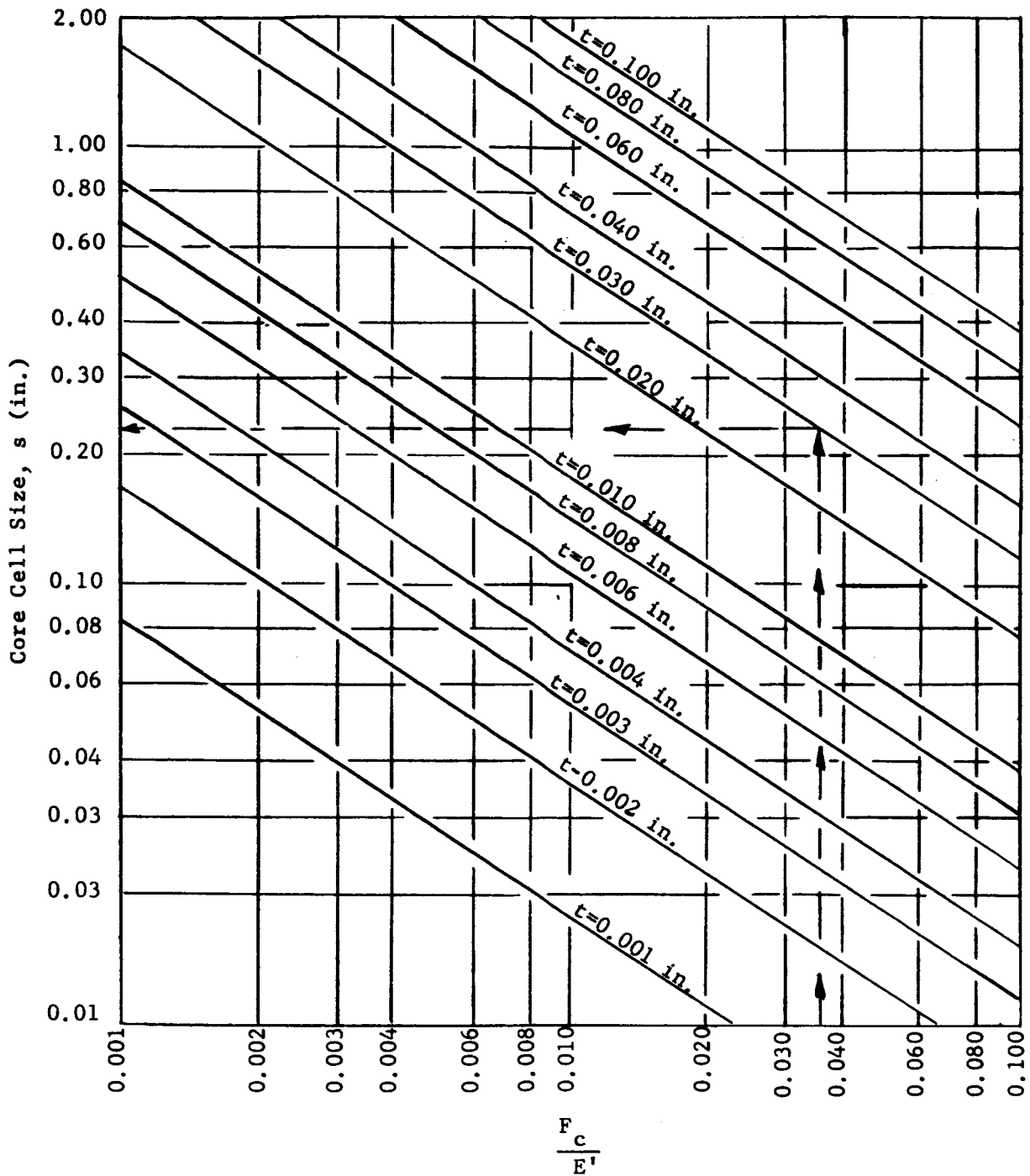


Figure 48. Chart for Determining Stress at which Dimpling of Sandwich Facing will Occur

(s = Diam. of Circle Inscribed Within Cell)

(Ref: MIL-HHBK-23: Part III)

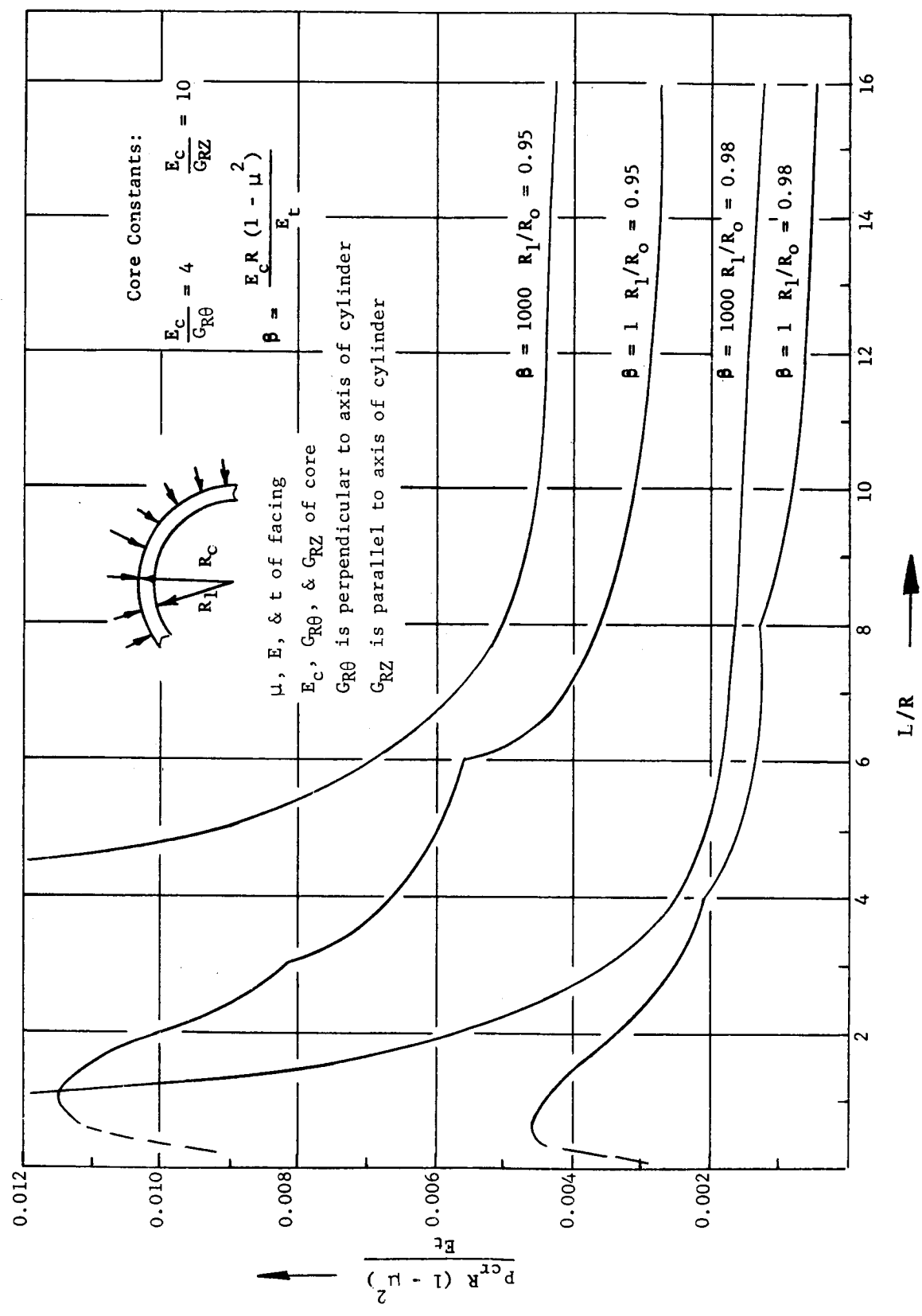


Figure 49. Buckling Pressure of Cylinder with Finite E_{core} Under External Pressure

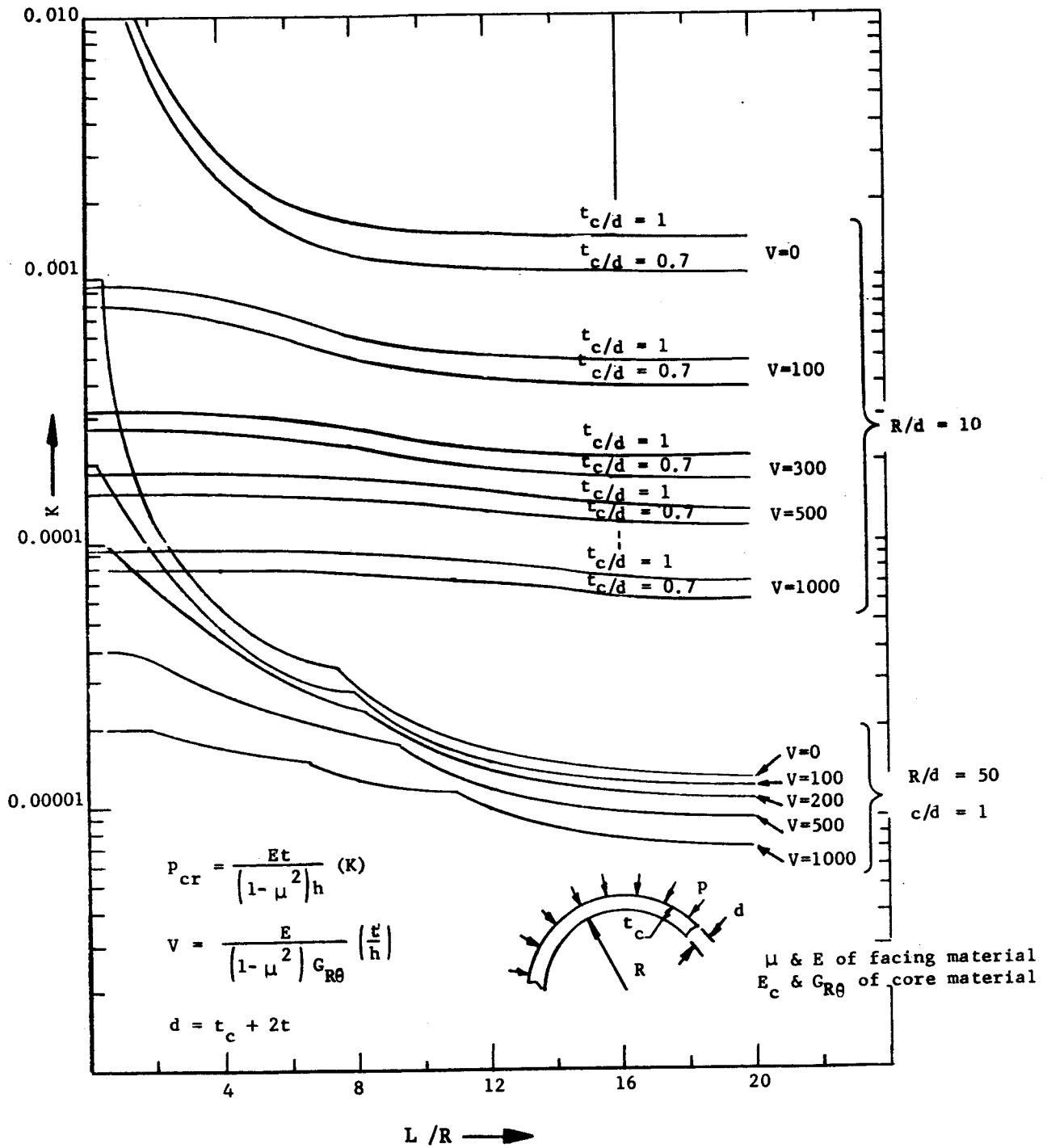


Figure 50. Buckling Pressure of Cylinder Under External Pressure with Infinite E_{core}

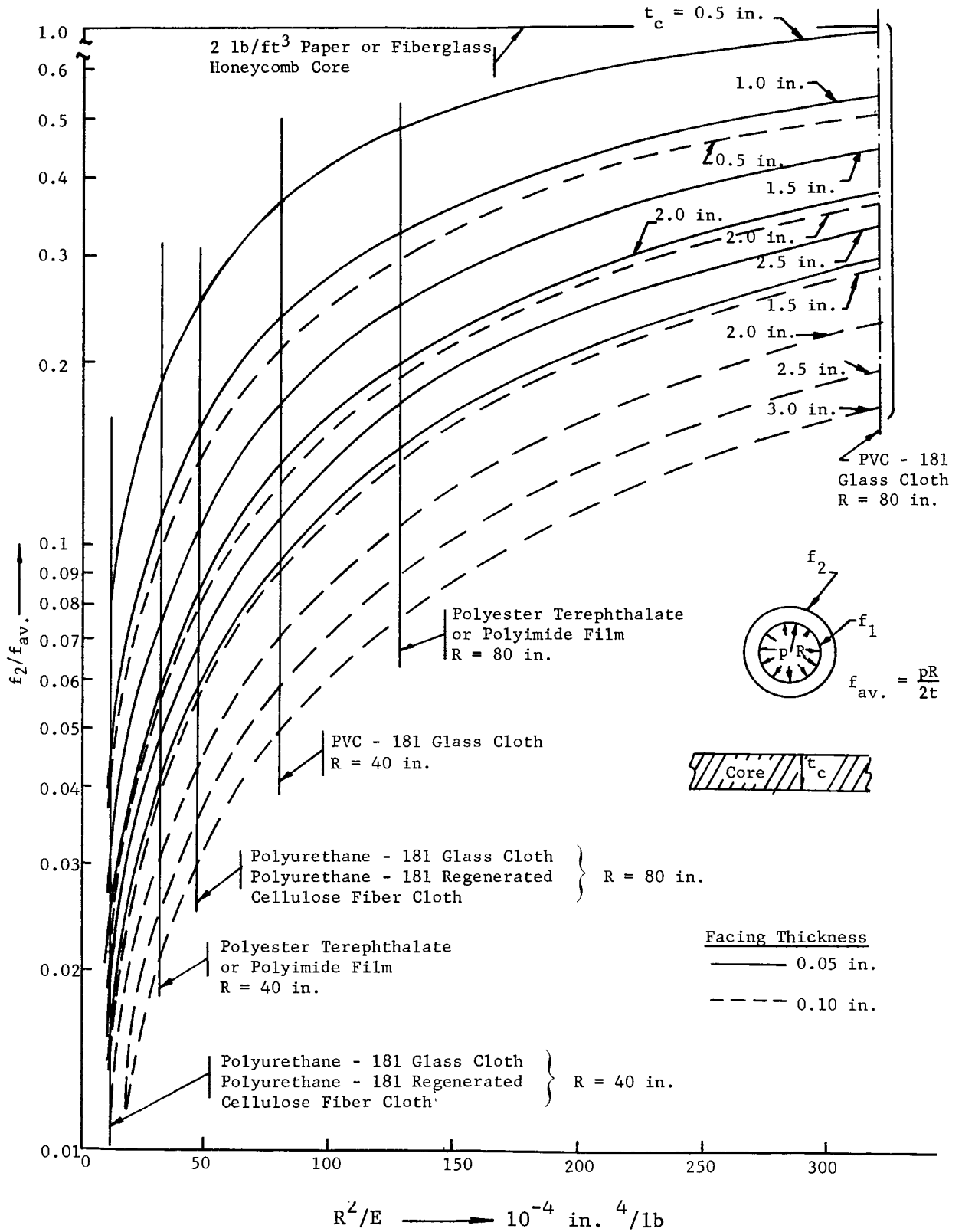


Figure 51. Facing Stress Ratio of Internally Pressurized Sandwich Cylinder (Foam and Honeycomb Core)

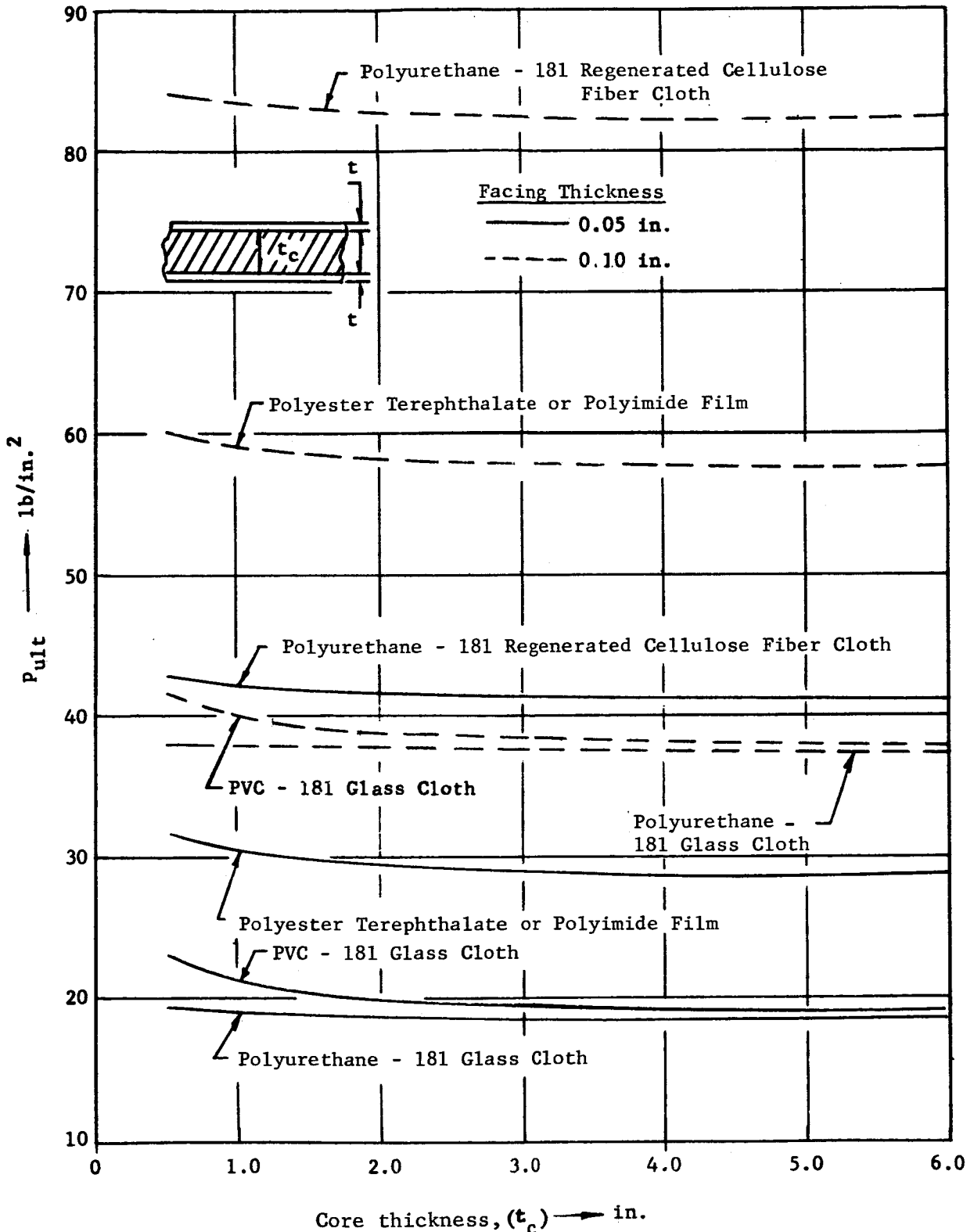


Figure 52. Ultimate Internal Pressure of Sandwich Cylinder
 (Foam Core; $R = 40$ in.)

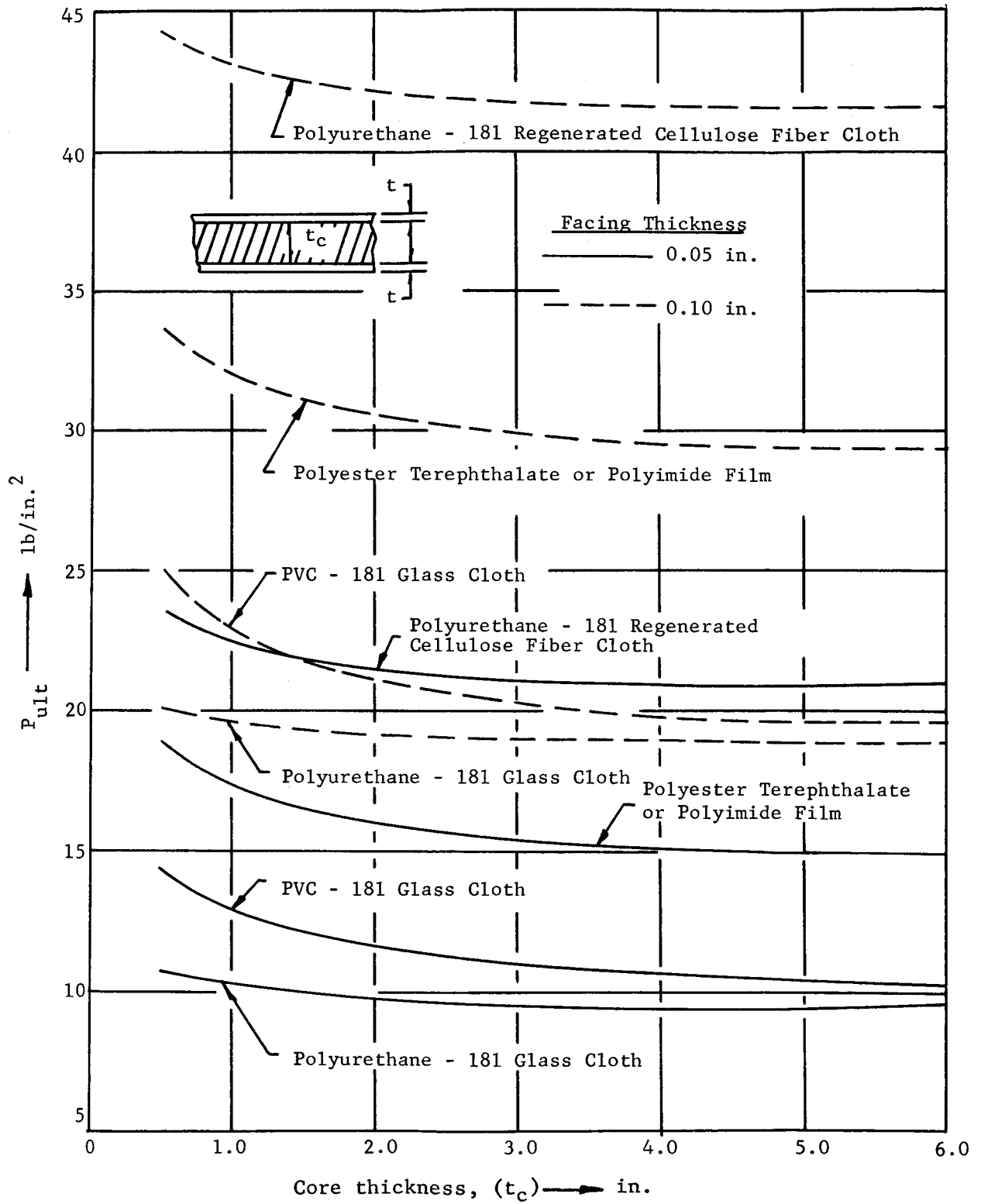


Figure 53. Ultimate Internal Pressure of Sandwich Cylinder (Foam Core; $R = 80$ in.)

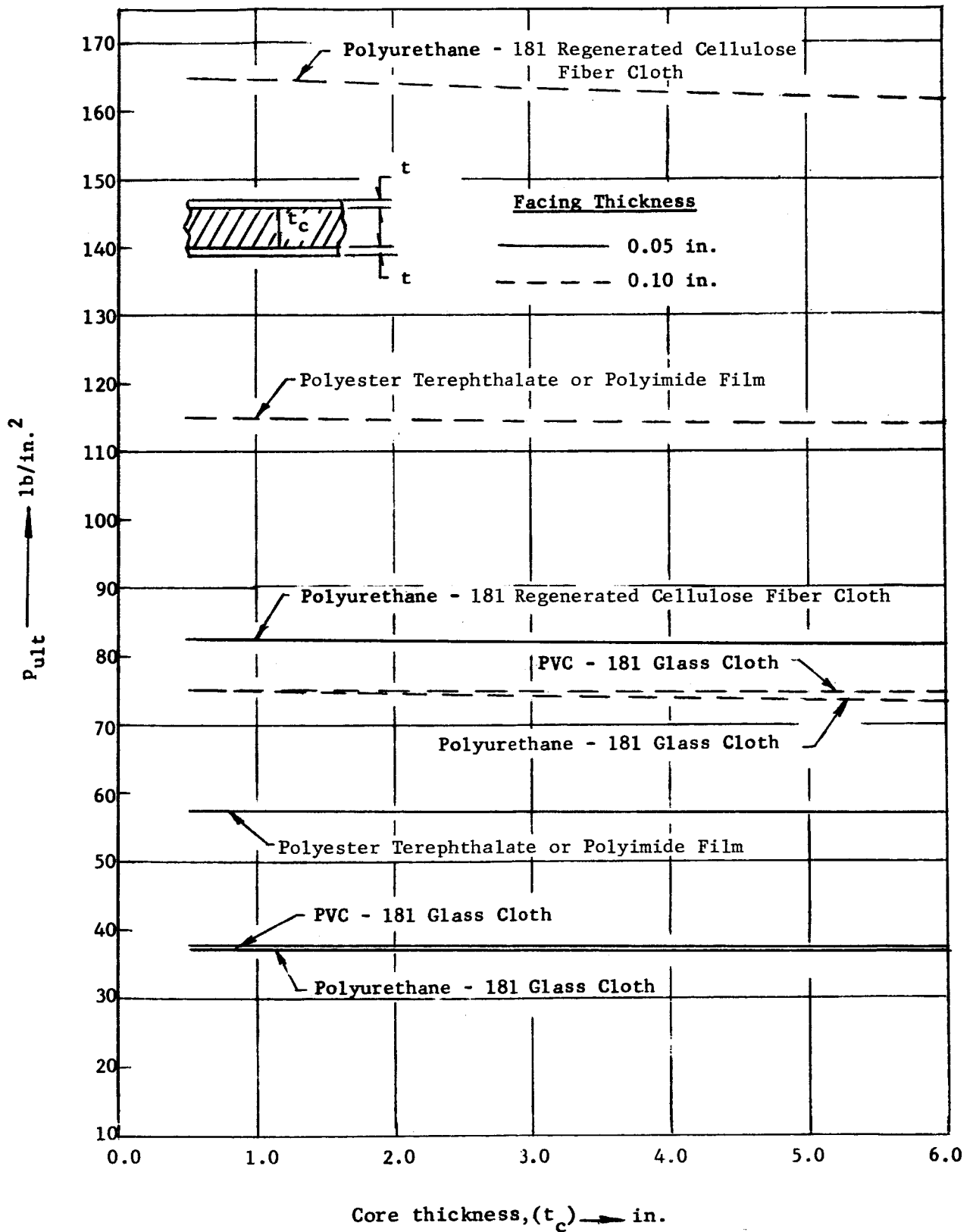


Figure 54. Ultimate Internal Pressure of Sandwich Cylinder (Honeycomb Core; $R = 40$ in.)

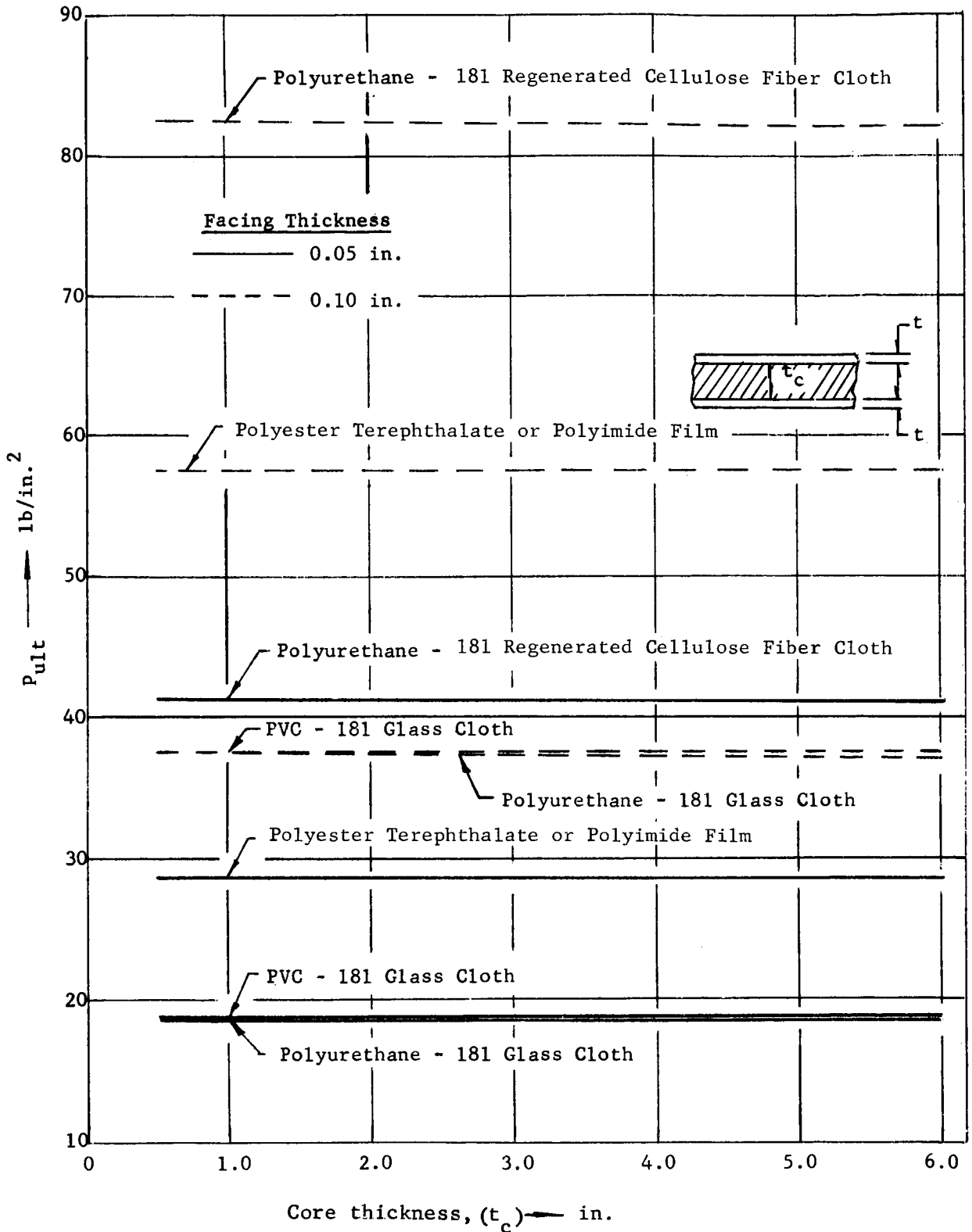


Figure 55. Ultimate Internal Pressure of Sandwich Cylinder (Honeycomb Core; $R = 80$ in.)

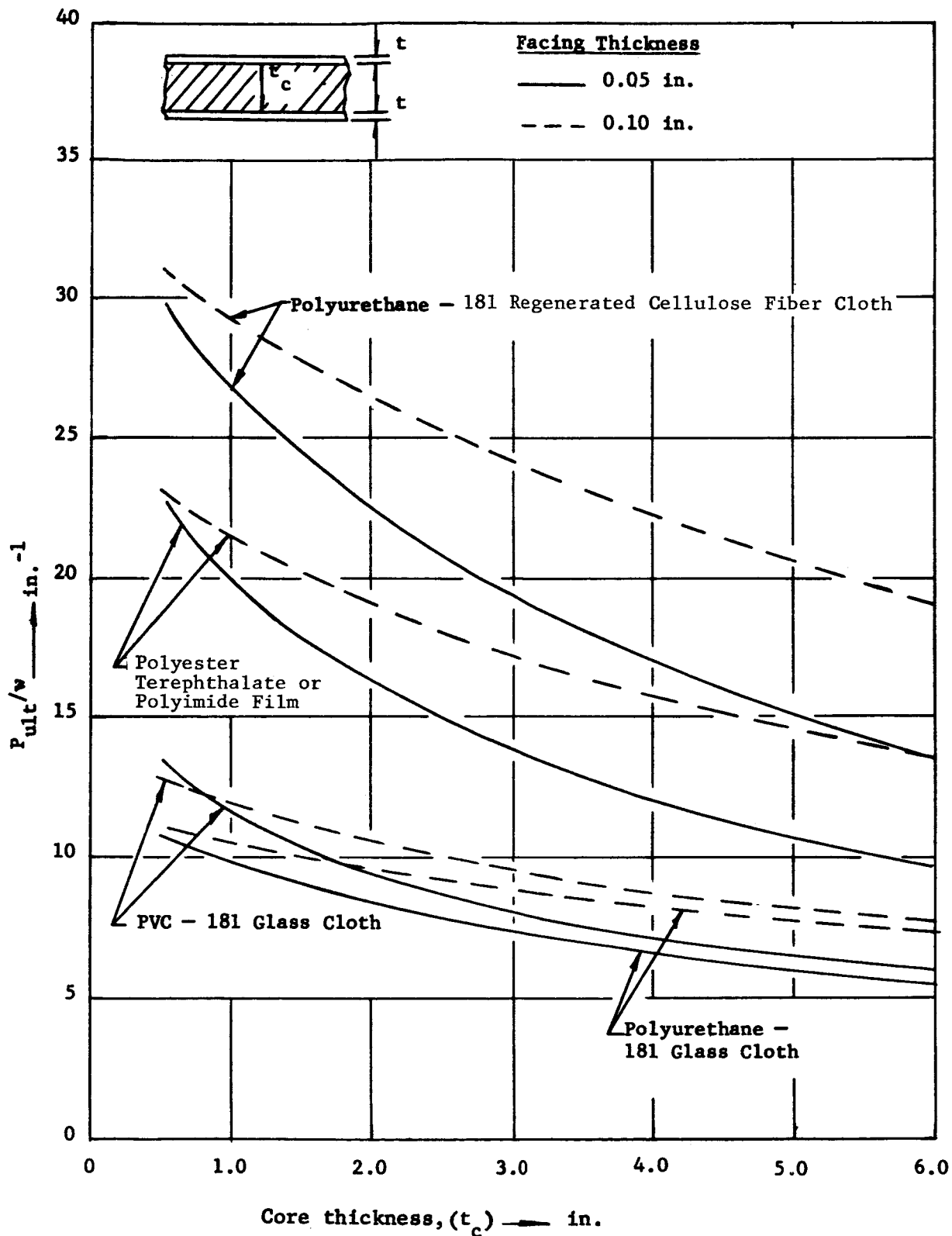


Figure 56. Strength-to-Weight Ratio of Internally Pressurized Sandwich Cylinder (Foam Core; $R = 40$ in.)

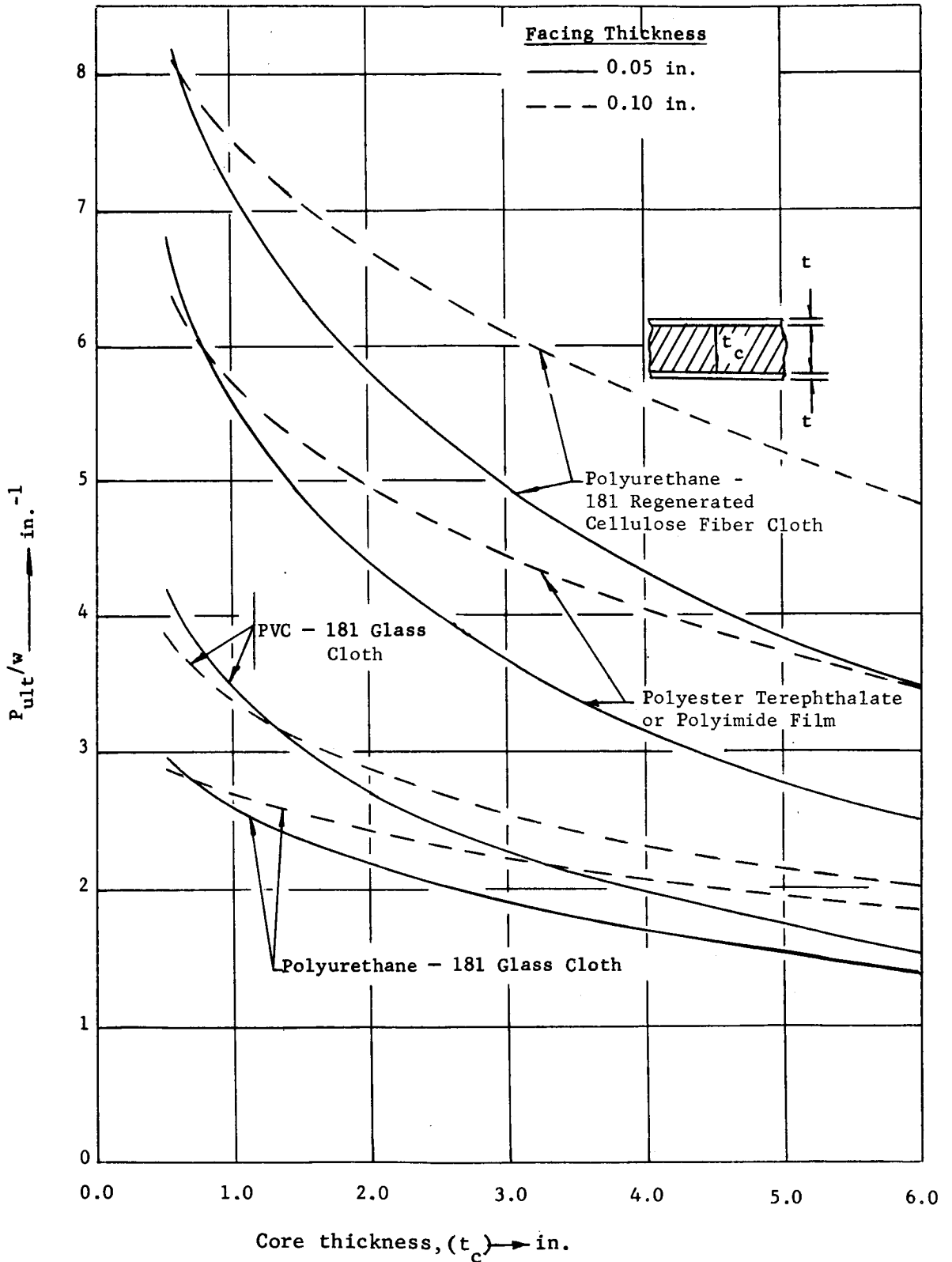


Figure 57. Strength-to-Weight Ratio of Internally Pressurized Sandwich Cylinder (Foam Core; $R = 80$ in.)

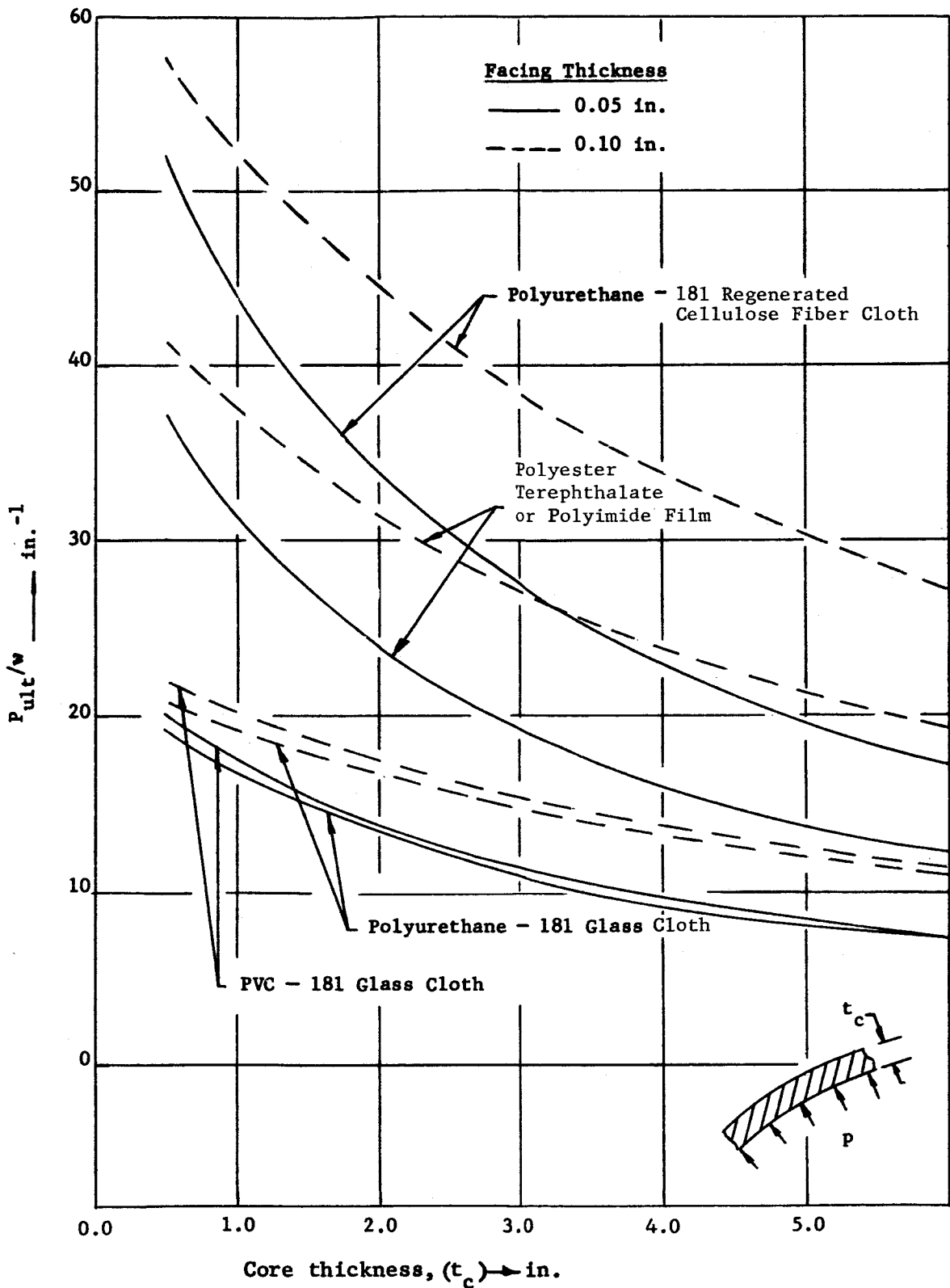


Figure 58. Strength-to-Weight Ratio of Internally Pressurized Single Face "Sandwich" Cylinder (Foam Core; $R = 40$ in.)

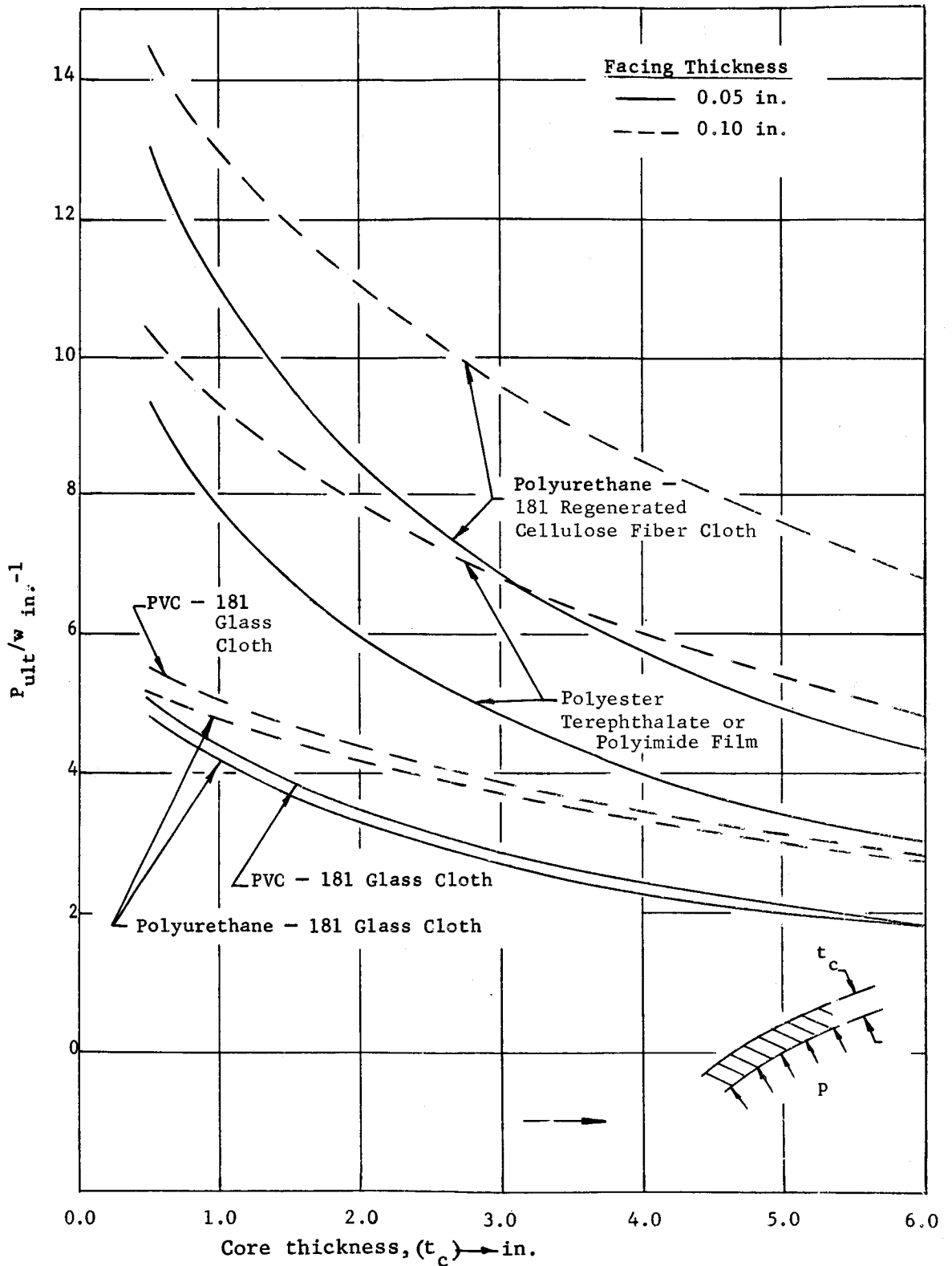


Figure 59. Strength-to-Weight Ratio of Internally Pressurized Single Face "Sandwich" Cylinder (Foam Core; $R = 80$ in.)

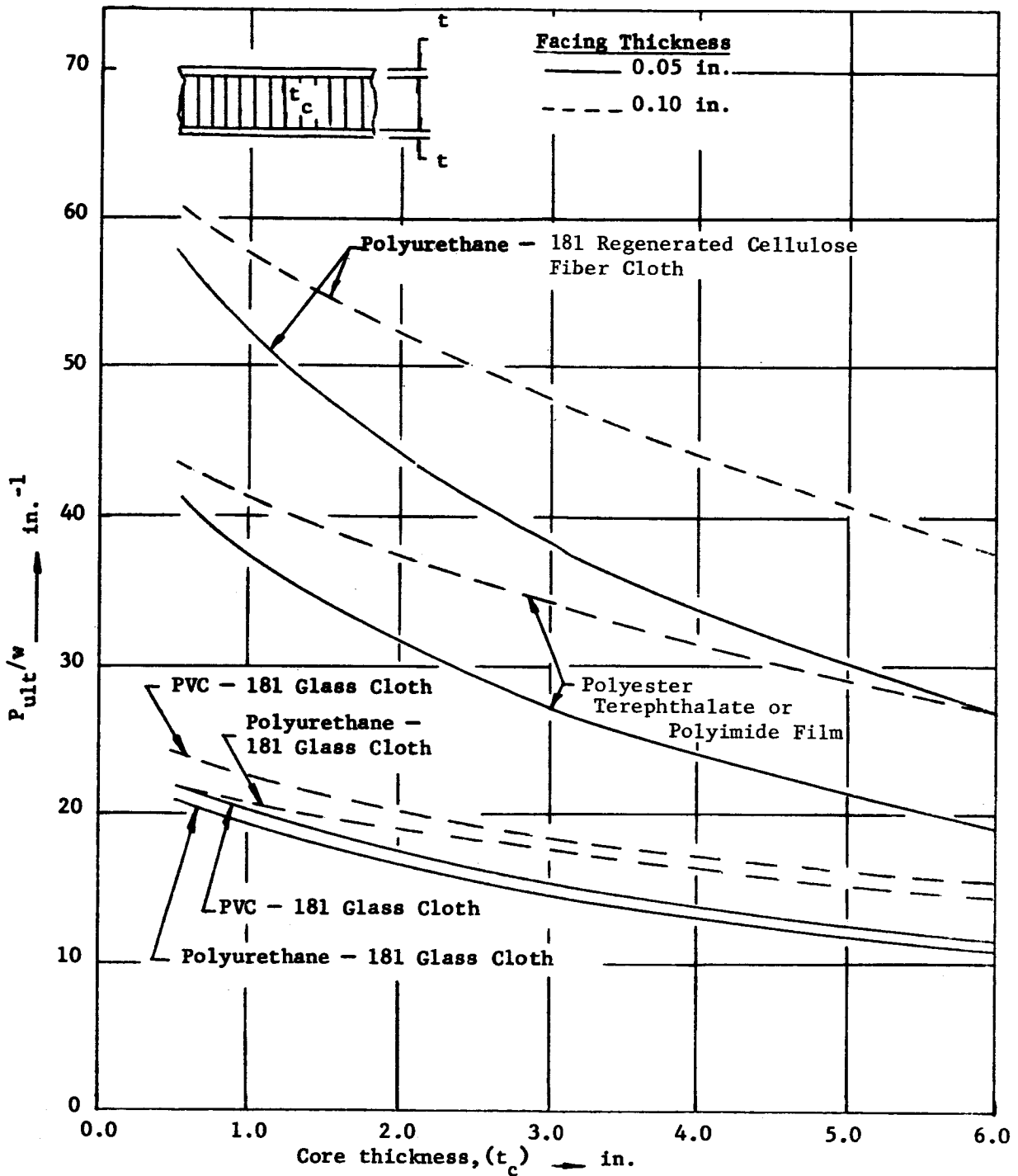


Figure 60. Strength-to-Weight Ratio of Internally Pressurized Sandwich Cylinder (Honeycomb Core; $R = 40$ in.)

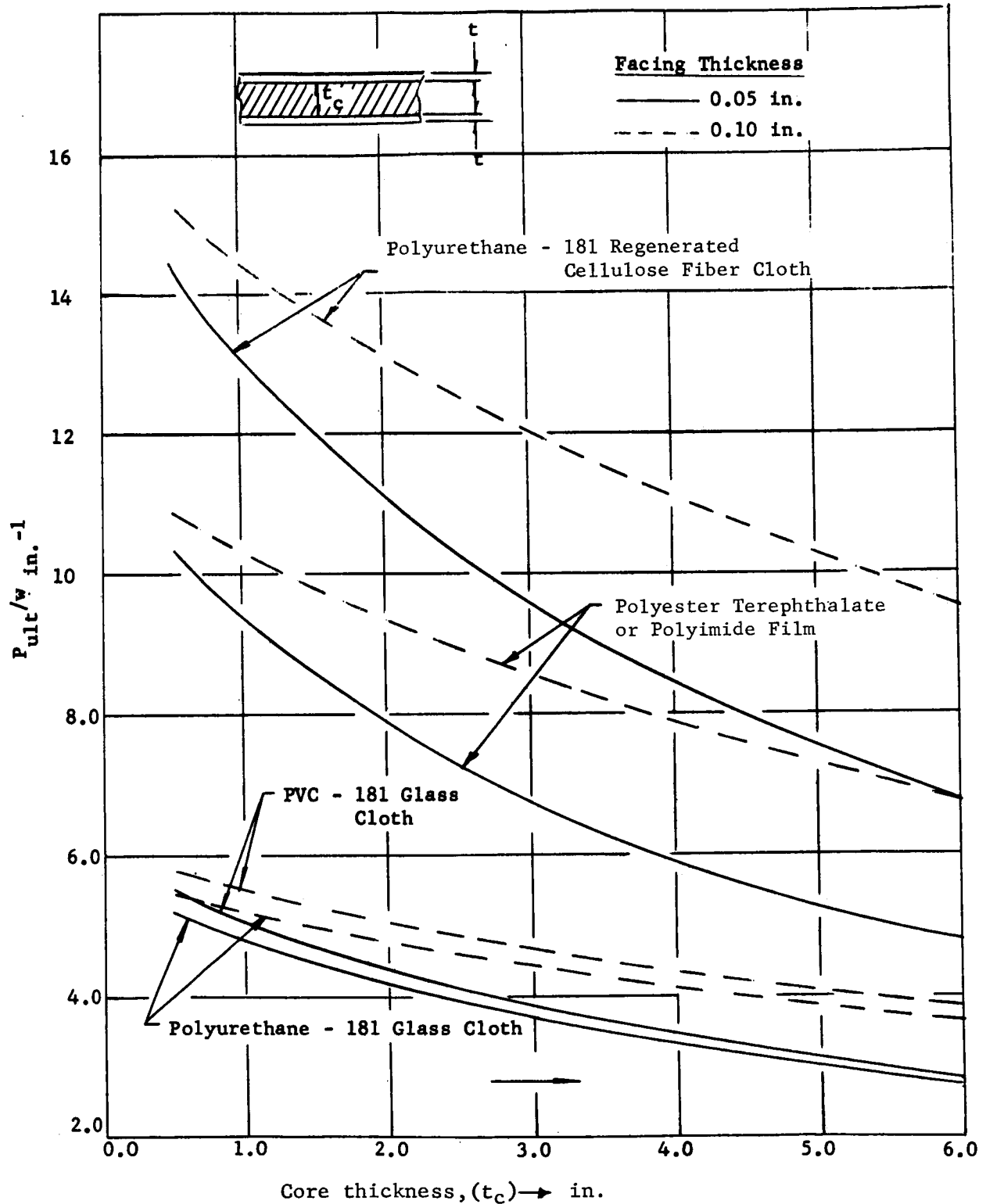


Figure 61. Strength-to-Weight Ratio of Internally Pressurized Sandwich Cylinder (Honeycomb Core; $R = 80$ in.)

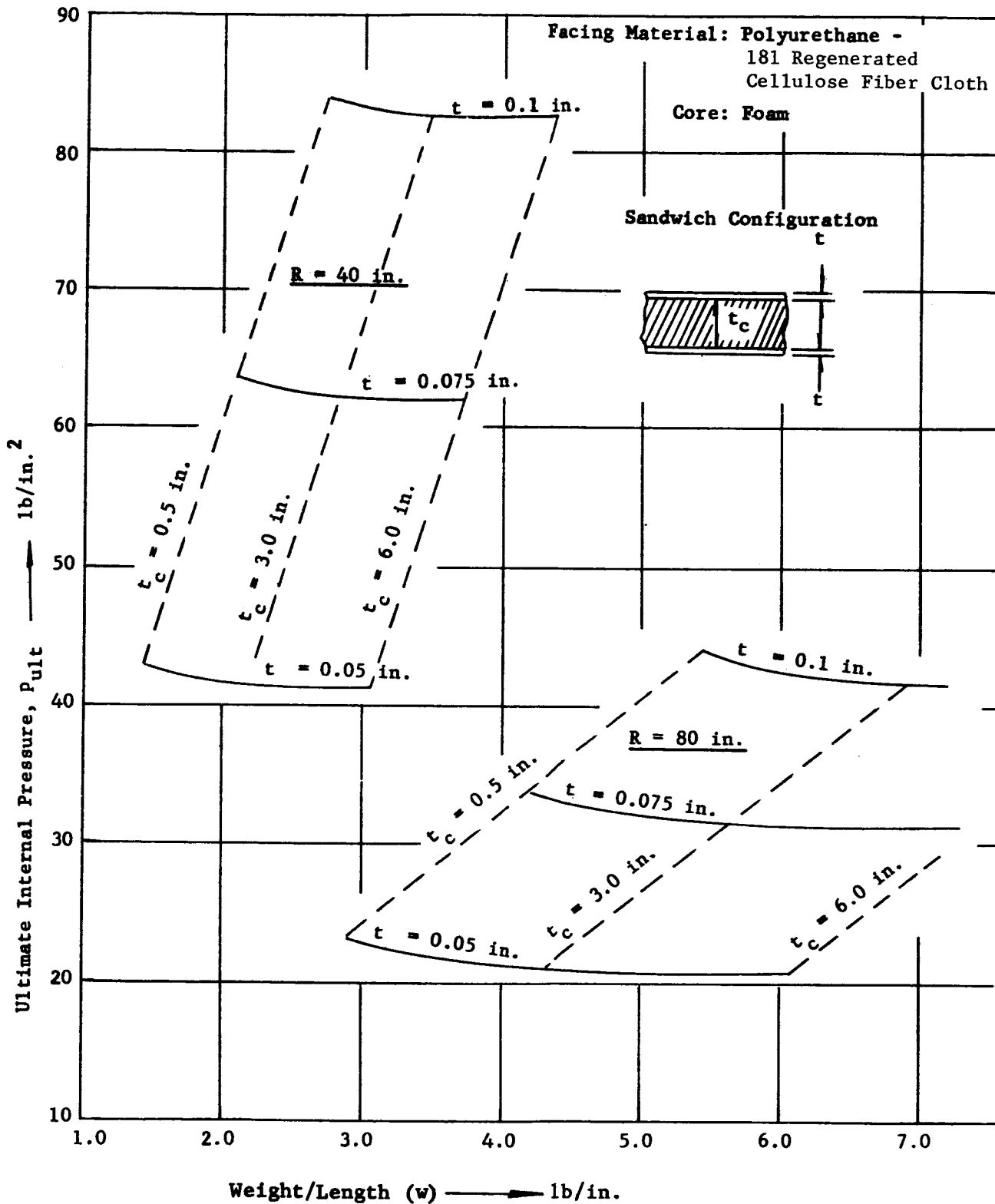


Figure 62. Strength vs. Weight Diagram - Internally Pressurized Sandwich Cylinder Foam Core

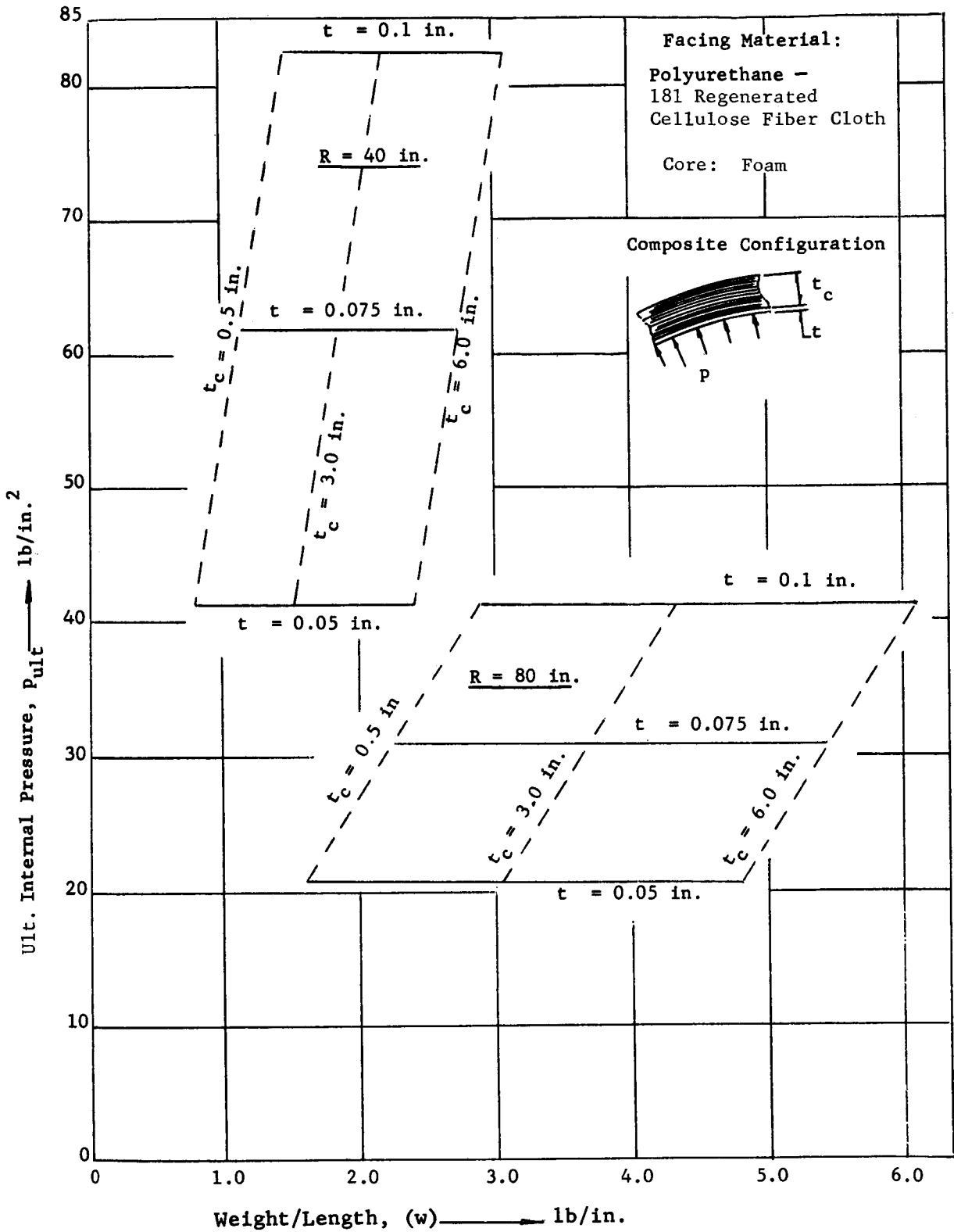


Figure 63. Strength vs. Weight Diagram - Internally Pressurized Single Facing Sandwich Cylinder Foam Core

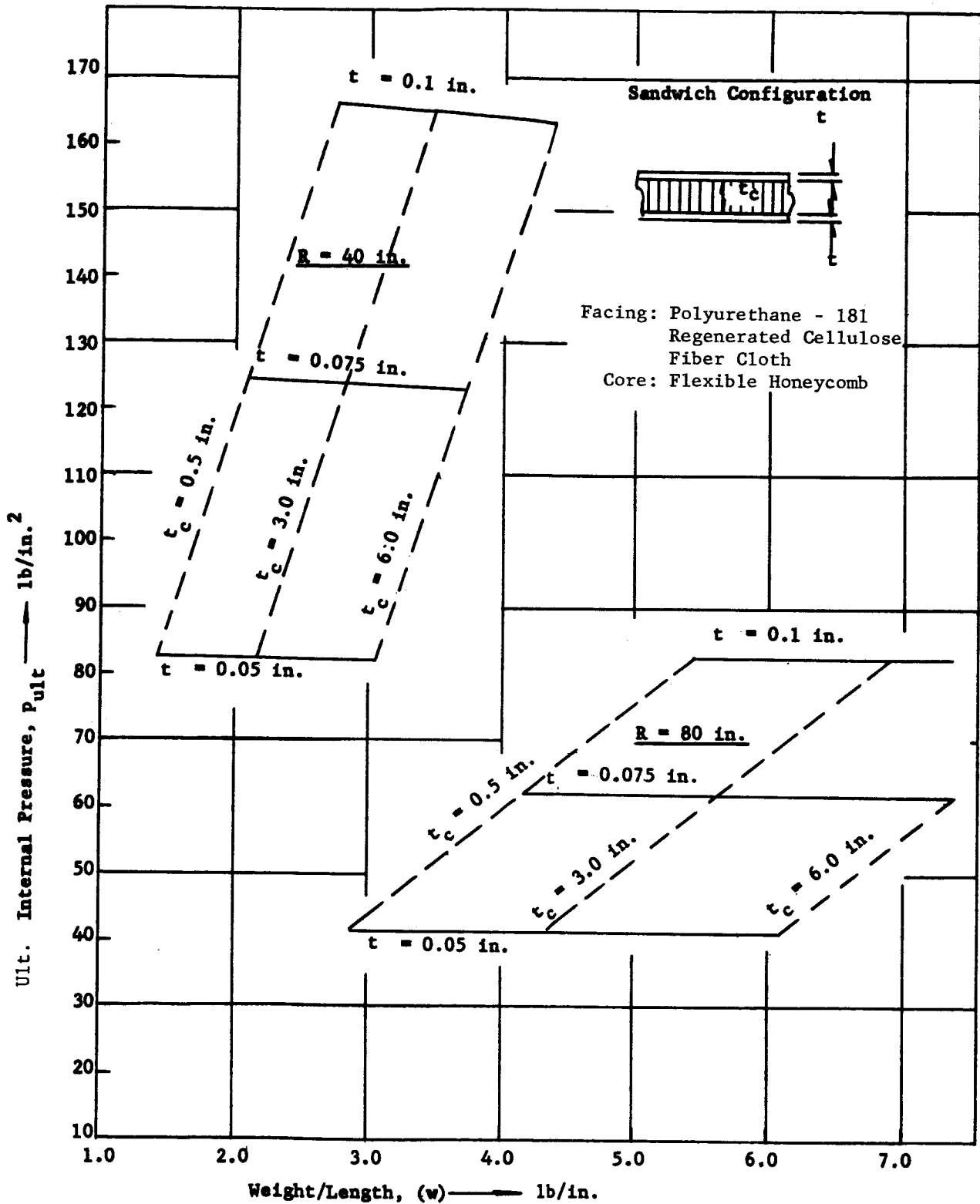


Figure 64. Strength vs. Weight Diagram - Internally Pressurized Sandwich Cylinder Honeycomb Core

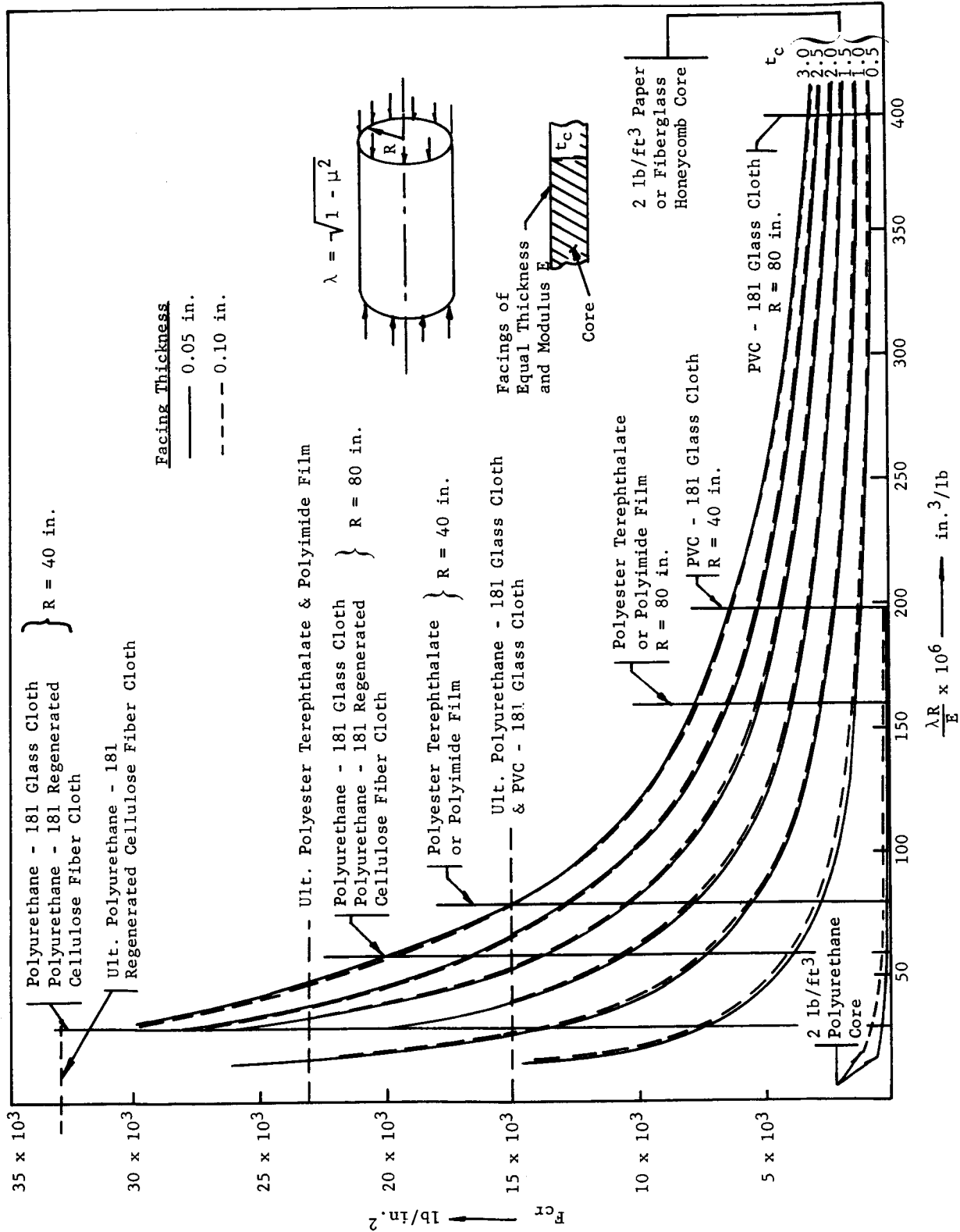


Figure 65. Buckling Stress of Axially Compressed Cylinder, Foam and Honeycomb Cores

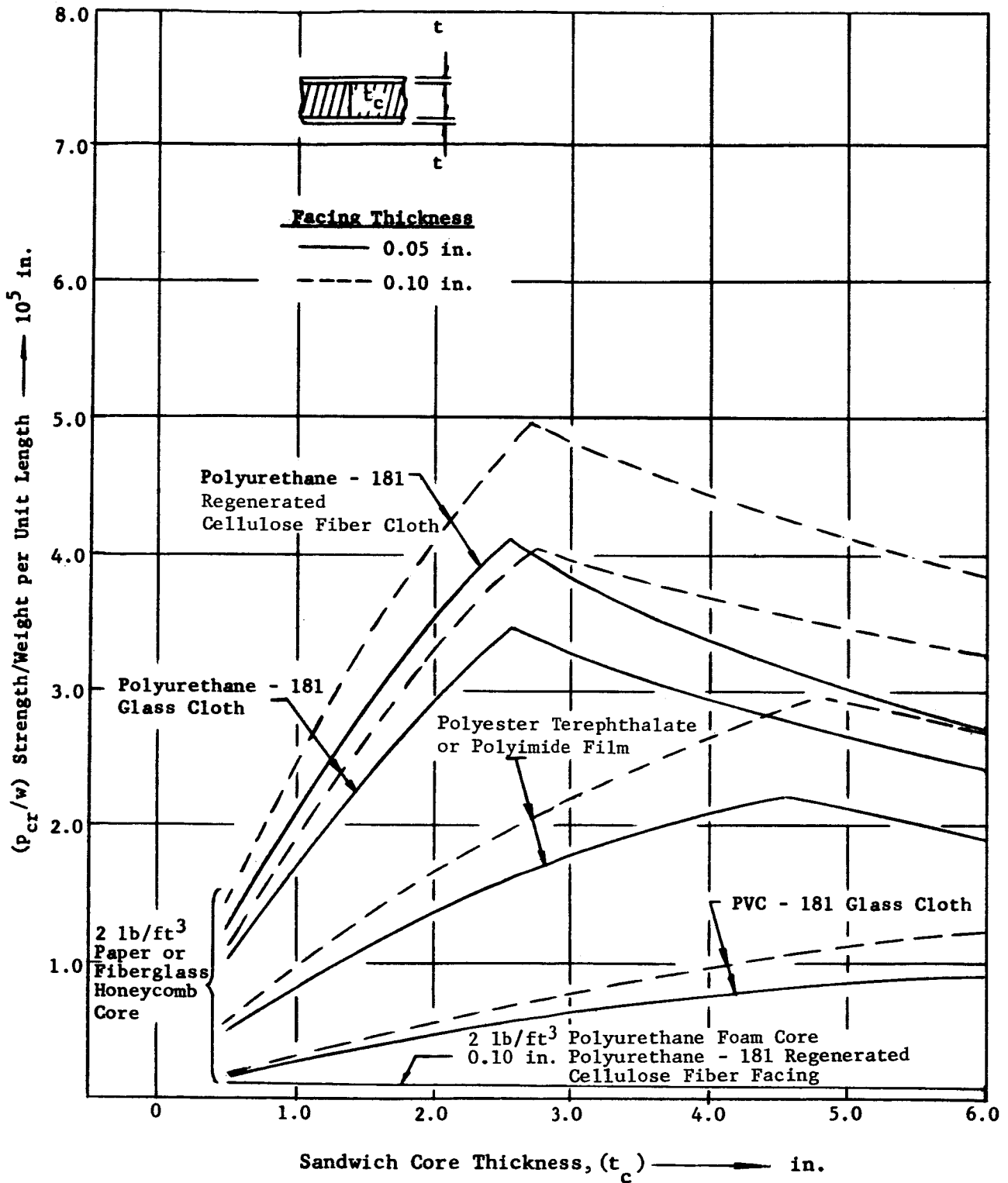


Figure 66. Strength-to-Weight Ratio of Axially Compressed Cylinder (Foam and Honeycomb Cores; $R = 40$ in.)

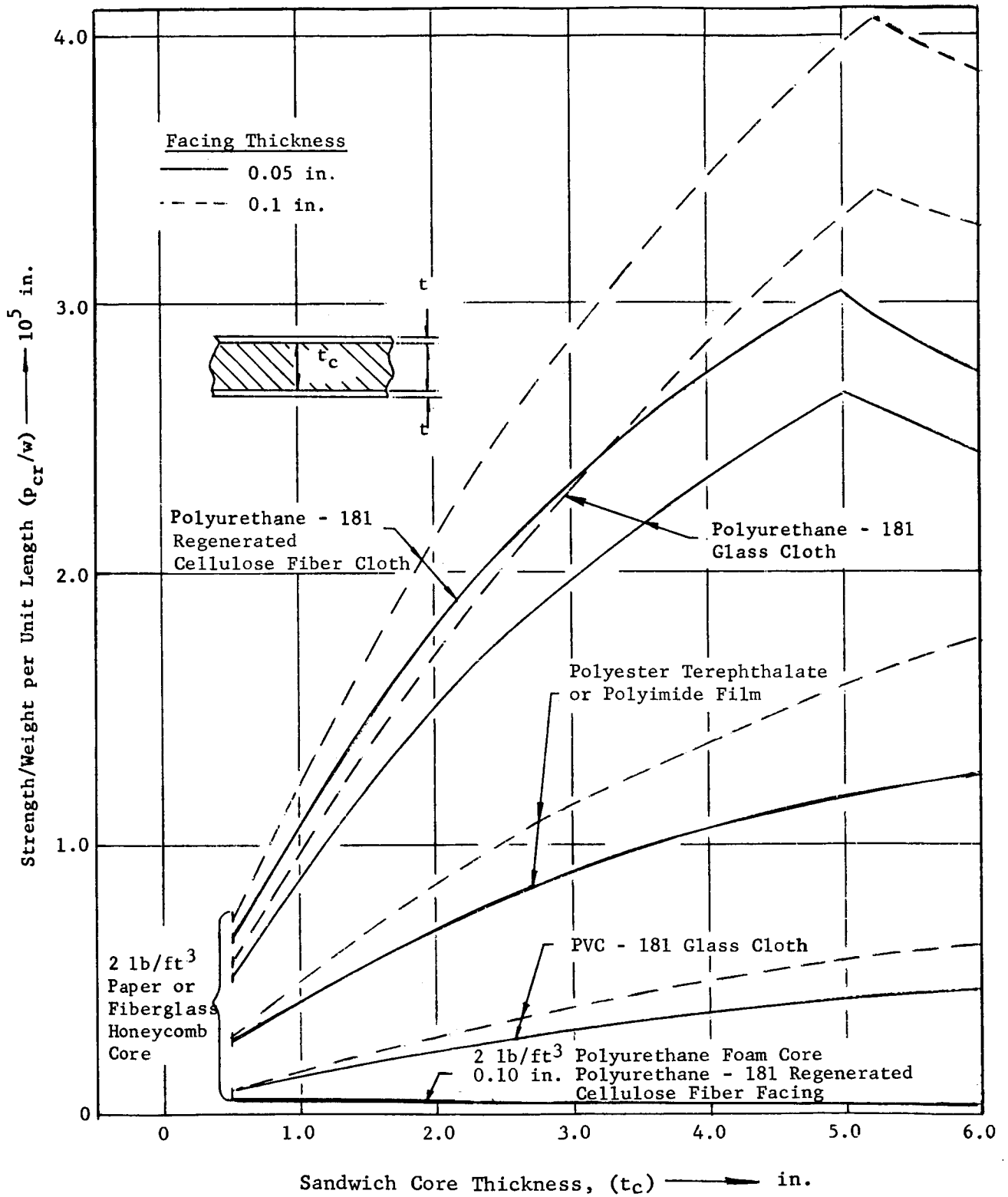


Figure 67. Strength-to-Weight Ratio of Axially Compressed Cylinder (Foam and Honeycomb Cores; $R = 80$ in.)

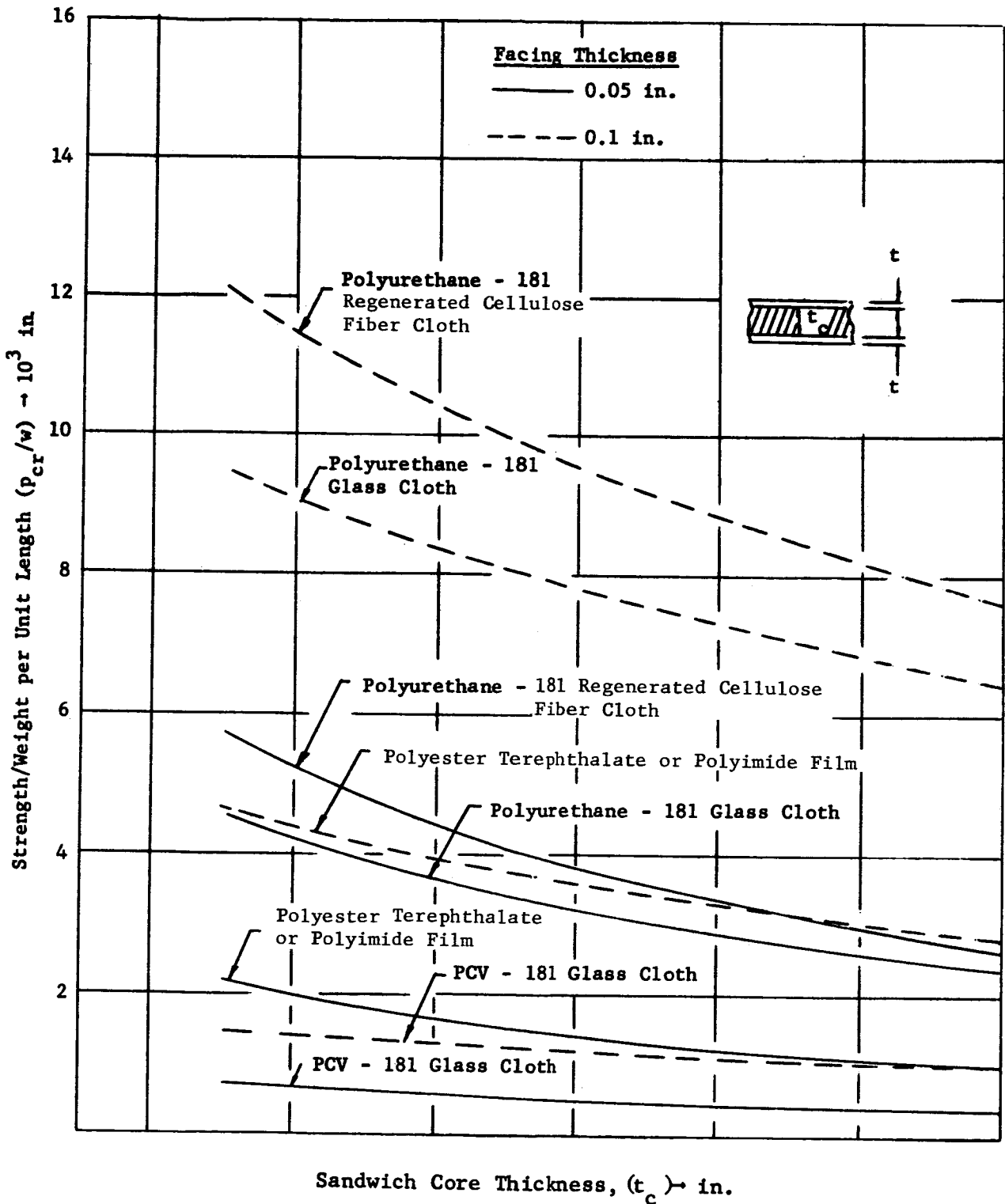


Figure 68. Strength-to-Weight Ratio of Axially Compressed Cylinder (2-lb/ft³ Polyurethane Foam Core; R = 40 in.)

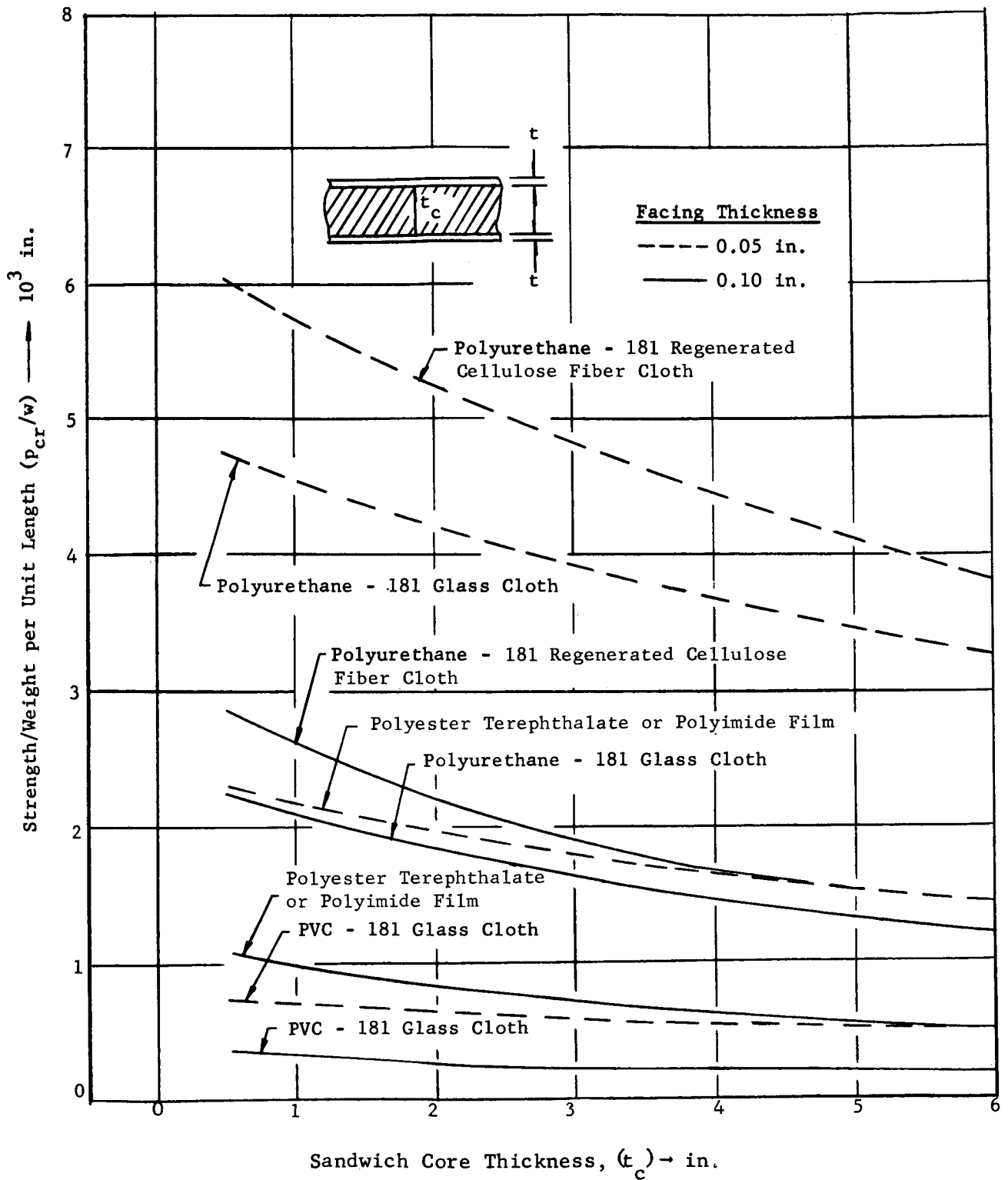


Figure 69. Strength-to-Weight Ratio of Axially Compressed Cylinder (2-lb/ft³ Polyurethane Foam Core; R = 80 in.)

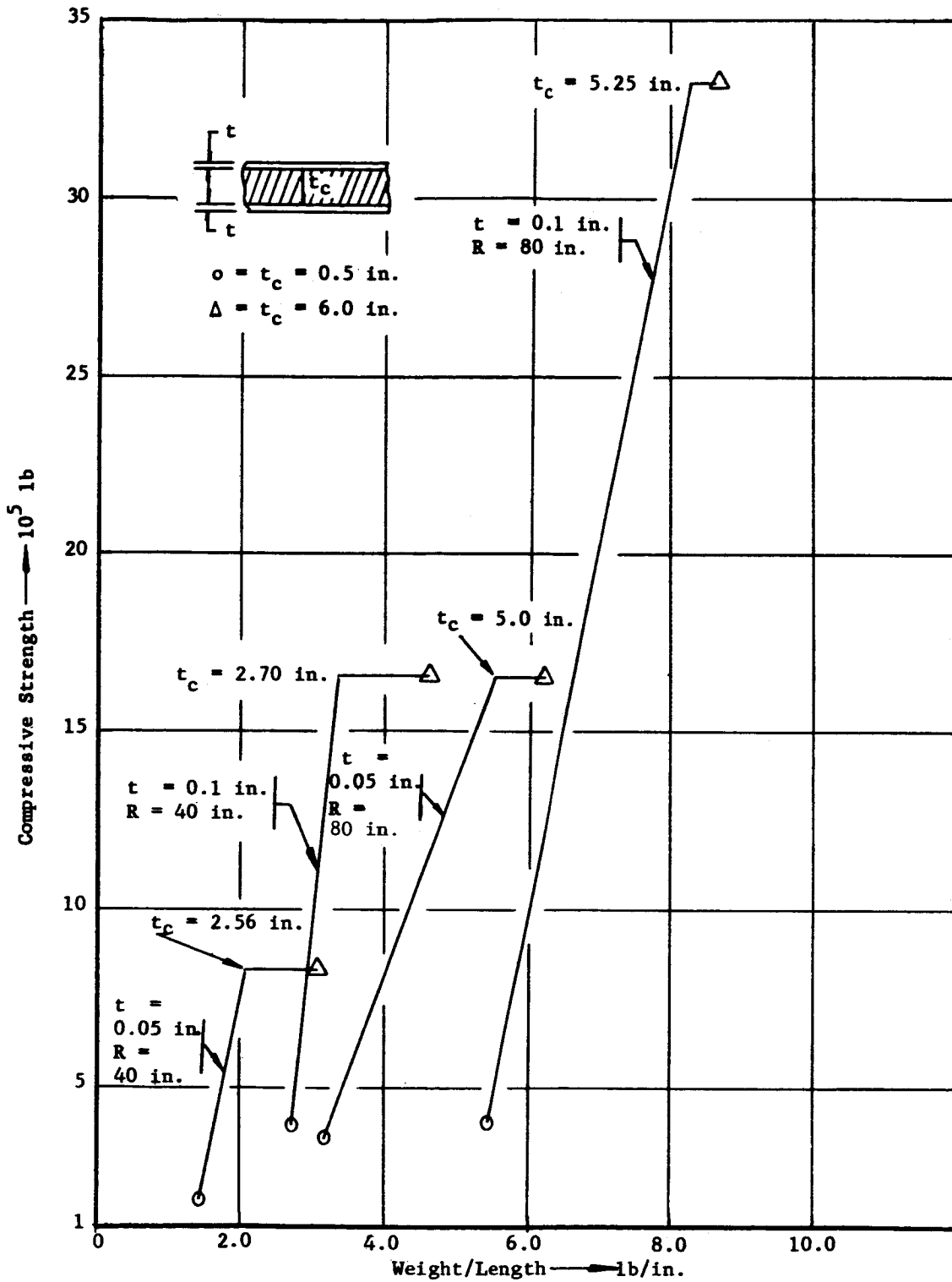


Figure 70. Compressive Strength vs. Weight/Length (2-lb/ft³ Paper or Fiberglass Honeycomb Core with a Thickness Range of 0.5 in. to 6.0 in. Polyurethane - 181 Regenerated Cellulose Fiber Cloth Facings)

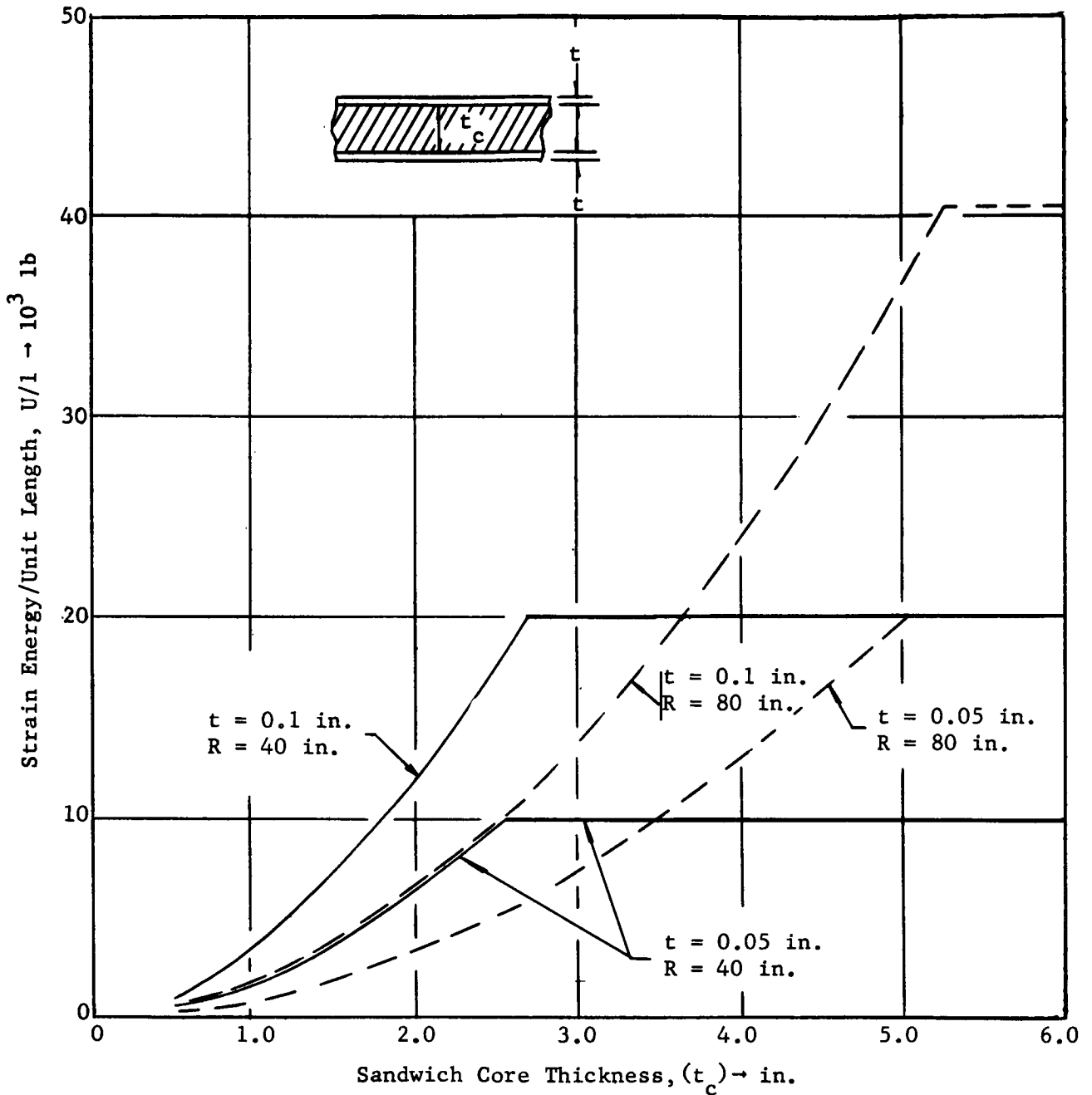


Figure 71. Strain Energy per Unit Cylinder Length at Buckling (2-lb/ft³ Paper or Fiberglass Honeycomb Core with Polyurethane - 181 Regenerated Cellulose Fiber Cloth Facings)

TABLE 12

BUCKLING EQUATIONS FOR CERTAIN LIMITING CASES

Equation	E_c	$G_{R\theta}$	t_o	t_i	P_{cr}
1	E_c	$G_{R\theta}$	0	t_i	$\frac{Et_1^3}{4(1-\mu^2)R_i^3} \left(\frac{R_i}{R_o} \right)$
2	E_c	$G_{R\theta}$	t_o	0	$\frac{Et_o^3}{4(1-\mu^2)R_o^3}$
3	0	$G_{R\theta}$	t_o	t_i	$\frac{Et_o^3}{4(1-\mu^2)R_o^3}$
4	∞	0	t_o	t_i	$3 \frac{Et_o}{R_o(1-\mu^2)} \left(\frac{1 + \frac{R_i}{R_o} \frac{t_o}{t_i}}{1 + \frac{R_i^2}{R_o^2} \frac{t_o}{t_i}} \right) \left(\phi_o \frac{R_i}{R_o} + \phi_i \frac{t_i}{t_o} \right)$
5	∞	∞	t	t	$3 \frac{Et}{R_o(1-\mu^2)} \left[\frac{\left(1 - \frac{R_i}{R_o} \right)^2 + \frac{t^2}{12R_i R_o} \left(1 + \frac{R_i}{R_o} \right)^2}{1 + \frac{R_i^2}{R_o^2}} \right]$

where $\phi_o = \frac{t_o^2}{12 R_o^2}$ and $\phi_i = \frac{t_i^2}{12 R_i^2}$

TABLE 13

MATERIALS USED IN THE STRUCTURAL ANALYSIS

Polyurethane resin reinforced with 181 style glass cloth

Polyurethane resin reinforced with 181 style, regenerated
cellulose fiber cloth

Polyvinyl chloride resin reinforced with 181 style glass cloth

Polyester terephthalate

Polyimide film

APPENDIX C

THERMAL ANALYSIS OF ELASTIC RECOVERY COMPOSITES

Abstract

The purpose of this investigation was to determine the heat flux and temperature profile through typical elastic recovery composite wall sections. The method of analysis assumed a one-dimensional heat flow and incident solar radiation at an earth orbit for the primary heat flux.

The heat transfer analysis accounted for both honeycomb type and foam cores as well as their combination. Two different thermal coatings were used in the analysis to determine this effect upon the heat transfer through the elastic recovery composite. The heat flux and the temperature distribution through the composite were determined for the varying core thickness.

The results of this study indicated that for maximum thermal efficiency the use of foam alone in the elastic recovery composite would be required. A thermal efficiency parameter - defined as the product of the thermal conductivity and the weight per unit area of the wall composite - was defined and its minimization noted to confirm maximum thermal efficiency in a composite.

APPENDIX C

THERMAL ANALYSIS OF ELASTIC RECOVERY COMPOSITES

by

Byron Anderson

I. INTRODUCTION

In a space environment, an expandable structure is exposed to thermal loads in the form of impinging thermal radiation fluxes. These fluxes originate from the sun and either radiate directly or reflect from the planets.

Once outside the atmosphere, direct solar radiation becomes the predominant source of heat. The maximum amount of heat impinging upon a body at Earth's distance from the sun is 440 Btu/hr ft². All analytical calculations and structural comparisons for this study of elastic recovery are based upon this value of solar flux. The actual net amount of heat absorbed by a body is a function of the projected area, surface area, solar absorptivity, thermal emissivity, temperature, and orientation.

Planetary or albedo radiation results from reflected solar radiation and direct thermal radiation from the planets. The planetary radiation reaching a vehicle is a function of the altitude above the planet, night or day position with respect to the planet, and the geometry of the body in consideration. At altitudes greater than 10 planet radii, planetary radiation becomes negligible. For Narmco's present analytical purposes, planetary radiation is not considered.

Heating from internal sources generally results from radiation and solid conduction from adjacent components: payloads, engines, etc. The existing condition of internal heating, or the lack of it, along with the heat dissipation apparatus available for a given mission envelope establishes, for the most part, the insulation and/or other thermal control techniques that are required.

Obviously, thermal protection from the sun must be provided for missions of any significant duration. Protection for cryogenic structures must

also be considered; e.g., if a 10-ft diameter spherical tank of stainless steel were filled with liquid hydrogen and located at Earth's distance from the sun, heating from the sun alone would result in a 100% boiloff per day (vented at 14.7 psia). With liquid oxygen, the tank would boil off 13% per day. (38)

There are many methods available to control heat input or output, ranging from simple insulation techniques to the more complex refrigeration concepts. Weight and complexity (reliability) requirements are of paramount importance in establishing thermal requirements. In general, thermal control systems can be classified as either passive or active. The passive systems include surface coatings, insulations, and shadow shields. Active systems include tank heaters, refrigeration systems, reliquification circuits, etc. Passive methods ordinarily provide the lightest weight and the least complex systems for short and intermediate missions. Active systems may be required for cryogenic and storable propellant tanks or where extended planetary missions are being made.

Coatings, as a form of surface treatment, can be effectively used to alter the absorptivity and emissivity characteristics of a surface. Thermal coatings is a vast field of study in itself, involving organic as well as inorganic materials. Since many organic compounds may be adversely affected by extended exposure to ultraviolet and ionizing radiation, inorganic coatings that possess good stability to these conditions must be considered for application to the expandable structures concept. It is not the intention of this report to exhaustively evaluate coatings in this area of study, but rather to indicate the range of control that can be expected.

The following is a list of symbols used throughout this thermal analysis:

a = shape factor, $1/\pi$

A = area, in.²

ΔA = cross-sectional area of conduction path through core

c = isotropic plate half thickness

- d = diameter of inscribed circle in a core cell configuration
 E = modulus of elasticity
 f = stress
 H = solar radiation flux, 440 Btu/hr ft²
 K = thermal conductivity of core material
 K_e = equivalent thermal conductivity of sandwich
 Q = heat transfer rate
 T = temperature
 \bar{T} = dimensionless temperature, $\left(\frac{\sigma t_c A_1}{K \Delta A} \right)^{1/3} T$
 t = facing thickness
 t_c = core thickness; (t_c') denotes foam core
 w' = weight per unit area
 α_s = solar absorptivity
 ϵ = emissivity of surface
 ν = Poisson's ratio
 σ = Stefan Boltzmann constant
 λ = $\frac{t_c}{d}$

Subscripts 1, 2, 3 refer to inner, middle, and outer skins respectively

A series of chemical conversion coatings for aluminum (e.g., the alodine coatings*) can be used for thermal control. A surface density of 425 mg/ft² of one chemical conversion coating (specifically, Alodine 401-41) results in an absorptivity of 0.4 and an emissivity of 0.5. Figure 72 indicates the equilibrium temperature of a perfectly insulated cylindrical surface rotating about its own axis in the sun as a function of the solar absorptivity-to-thermal emissivity ratio, α_s/ϵ .

* Produced by Amchem Products, Inc.

Temperatures are given at Venus, Earth, and Mars distances from the sun. Vertical lines indicate the α_s/ϵ ratio of various metallic and painted surfaces.

II. METHOD OF ANALYSIS

A one-dimensional heat conduction analysis has been used herein to determine the effect of solar radiation upon elastic recovery concepts. It should be noted that the effect of shape has been considered, by the use of the cylindrical surface, which has notably reduced equilibrium temperatures (i.e., 25%). Hopefully, future studies will permit an evaluation of two-dimensional heat transfer conditions. This more complex heat transfer problem is encountered when the cylinder is not rotating about its axis.

Although coatings provide a relatively lightweight approach to thermal control, coatings alone can seldom provide sufficient protection. The most practical approach is to insulate the structure and to apply the coating on the outer surface of the insulation.

The present thermal evaluation of the elastic recovery concept of expandable structures includes the application of a foam layer to a flexible sandwich core as one approach. The foam functions as the expanding medium for the structure and also provides meteoroid and radiation protection as well as thermal insulation. The generalized elastic recovery composite used in this investigation is shown in Figure 73. The external skin is polyester terephthalate with a vapor-deposited surface of aluminum. Two surface conditions are considered: (1) an absorptivity of 0.35 and emissivity of 0.20, representative of the untreated aluminized surface and (2) an absorptivity of 0.40 and emissivity of 0.50, corresponding to a 425 mg/ft² density of the chemical conversion coating. Both large- and small-cell flexible honeycomb type cores are considered.

Calculations have been made to establish rate of heat transfer per unit area as a function of internal temperature and also of temperature distribution for the sandwich constructions indicated in Table 14. Again, all calculations consider a cylindrical structure rotating about its axis in the sun.

TABLE 14

SANDWICH CONSTRUCTIONS CONSIDERED FOR THERMAL EVALUATION

	Flexible Foam Core Only	Foam Core with Small Cell Semirigid Core* (d = $\frac{1}{4}$ in.)		Foam Core with Large Cell Semirigid Core** (d = 1 in.)	
		0	0.5	1.0	0.5
$t_c' =$	1.0	0	0	0	0
Foam thickness	2.0	1.0	1.0	1.0	1.0
	4.0	2.0	2.0	2.0	2.0
	6.0	4.0	4.0	4.0	4.0
		6.0	6.0	6.0	6.0

* 7.67 lb/ft³ density** 3.31 lb/ft³ density

The semirigid core and facings are assumed to be a polyester-181 glass cloth laminate. This choice was made for the reason that the thermal properties of this material are fairly well documented and are reasonably representative of the types of materials that can be considered for the elastic recovery application. The thermal properties used in this analysis are listed in Table 15. Thickness of core material was assumed to be 0.01 in.

TABLE 15

MATERIAL PROPERTIES FOR THERMAL CALCULATIONS

Material	Thermal Conductivity Btu/hr ft ² °F/in.	Emissivity	Density
Polyester terephthalate	----	----	0.05 lb/in. ³
Polyester-181 style glass cloth	0.85*	0.82*	0.065
Polyurethane foam	0.13**	----	2.0 lb/ft ³

* From MIL-HDBK-17

** From the Lewis Research Center, "Report on Research of Interest to the NASA Committee on Missile and Space Vehicle Structures," 8-10 Oct 1963 (for vacuum condition)

NOTE: Material properties are conservatively taken at room temperature.

III. HEAT TRANSFER THEORY

A method of determining an effective thermal conductivity for a sandwich panel, considering radiation within the sandwich as well as conduction, is presented in NASA TN D-714⁽³⁹⁾ and provides the basis for the following theoretical treatment. One-dimensional heat transfer is assumed.

$$\frac{K_e}{K} \left(\frac{A_1}{\Delta A} \right) = 1 + 0.664 (\lambda + 0.3)^{-0.69} e^{1.63 (\lambda + 1)^{-0.89}} \times \left(\bar{T}_1^2 + \bar{T}_2^2 \right) \left(\bar{T}_1 + \bar{T}_2 \right) \dots \dots \dots (1)$$

The heat flux transferred through the sandwich can then be expressed as follows:

$$Q = \left[\left(\frac{K \Delta A}{\sigma t_c A_1} \right)^{1/3} \right] \left[\frac{K_e}{t_c} \left(\bar{T}_2 - \bar{T}_1 \right) \right] \dots \dots \dots (2)$$

This is true, since K_e can be defined from the following:

$$Q_{12} = \frac{K_e}{t_c} \left(T_2 - T_1 \right) \dots \dots \dots (3)$$

For outer space considerations, air is not present within the cells to function as an additional term in the overall thermal conductivity relationship.

The heat transfer flux (Q_{12}) must be equal to the net radiative heat input, which is written as follows:

$$Q_{12} = \alpha_s a H - \epsilon \sigma T_3^4 \dots \dots \dots (4)$$

Shape factor derivation:

$$2\pi R \ell a \alpha_{sH} - \epsilon \sigma T_3^4 = \left[2R \ell (\alpha_{sH}) \right] - \left[2\pi R \ell (\epsilon \sigma T_3^4) \right]$$

\uparrow Surface absorbs over projected surface on one side \uparrow Surface radiates over entire surface

$$\therefore a = \frac{1}{\pi}$$

Heat transfer through the polyurethane foam portion of the composite structure resolves itself to a process of simple conduction, and the corresponding temperature drop across the foam is readily calculated.

IV. DISCUSSION OF HEAT TRANSFER CURVES

From the heat transfer theory, the heat flux and temperature distribution through the wall was obtained. Figures 74 through 78 show the heat flux vs. the internal temperature for the two assumed flexible honeycomb core thicknesses and the outer skin surface conditions. Figure 74 shows the heat flux rate for a composite with a core of 2 lb/ft³ foam alone of different thicknesses. Figures 75 and 76 indicate the effect on the heat transfer rate of a 1-in. flexible honeycomb core with various thicknesses of foam for the two surface conditions. The surface condition with the lower absorptivity-to-emissivity ratio ($\alpha_s = 0.40$, $\epsilon = 0.50$) showed less heat through the composite. The calculations for the heat transfer rate were repeated for a flexible honeycomb thickness of $\frac{1}{2}$ in. (Figures 77 and 78 show these results.)

The temperature distribution through the composite wall was similarly determined for the two surface conditions and core thicknesses. The outer surface and intermediate temperatures (T_3 and T_2 respectively) were plotted against the inside temperature, T_1 , as shown in Figures 79 through 82. Comparison of Figures 79 and 80 show the effect of the lower solar absorptivity-to-emissivity ratio in the decrease in temperature. When compared with Figures 79 and 80, Figures 81 and 82 show the relatively small influence the thickness of the honeycomb type of core had on the outer temperature distribution of the composite.

The effect of the chemical conversion surface coating, as previously discussed, has been to reduce the α_s/ϵ ratio for the exterior surface and thus to reduce the thermal flux and external temperature for a given internal temperature.

The small cell honeycomb is obviously more inefficient than the large cell, from a heat transfer standpoint, and this fact is substantiated by the curves.

Foam was a far more efficient core material for insulation than honeycomb. In Figures 83 and 84, the insulation efficiency vs. foam core thickness

indicated this superiority of foam very dramatically. The thermal efficiency parameter, $K_e w'$, is the product of the equivalent thermal conductivity and the weight per unit area of the wall concept. Since the desirable trend, from a heat transfer standpoint, is the minimization of heat flux through the composite on a per unit weight basis, the smaller the $K_e w'$ product, the more efficient the composite will be.

Heat transfer rate vs. composite weight, plotted in Figure 85, serves as a design curve and at the same time indicates relative composite efficiency. The most effective configuration is represented by the lowest unit weight for a given heat transfer rate.

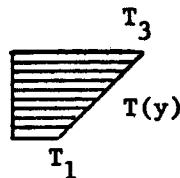
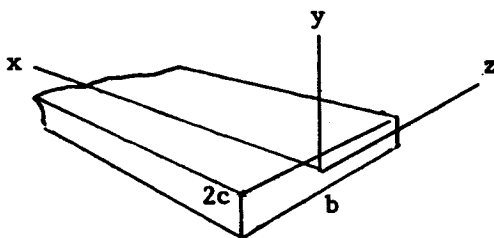
Thermal efficiency for a honeycomb sandwich is, of course, a function of temperature and becomes more efficient with decreasing temperature. Foam sandwich efficiency remains independent of temperature. The temperature chosen for evaluation, 525°R and 160°R , reflect a shirt sleeve environment and a liquid oxygen cryogenic environment, respectively.

It should be noted that if means are not provided for the internal dissipation of heat in a given cylindrical application of expandable structure, and the equilibrium temperatures of Figure 72 are attained, material temperature limitations will not be exceeded.

The general thermal stress equation for one-dimensional temperature distribution is found in Thermal Stresses by B. E. Gatewood:⁽⁴⁰⁾

$$f_x = f_z = -\frac{\gamma E T(y)}{1-\nu} + \frac{1}{2c(1-\nu)} \int_{-c}^c \gamma E T(y) dy + \frac{3y}{2c^3(1-\nu)} \int_{-c}^c E T(y) y dy \quad (5)$$

where γ = coefficient of linear thermal expansion



$$E = f(y)$$

This equation is based upon an isotropic plate; however, it gives a qualitative insight into what occurs within a sandwich cylinder having a linear temperature distribution $T(y)$. Because E is a function of y and very small across the depth of the foam core, the thermal stress function indicates a relatively unhindered linear growth of each facing. The low modulus of the core in the x and z directions, therefore, allows the two facings to grow differentially with very little restraint or thermal stress. Another way of looking at the thermal stress condition is to realize that equation (5) reduces essentially to the stress across two very thin plates (the facings), and that each facing is essentially a uniform temperature.

It has been impossible to analyze the effects of creep and related phenomena on pressurized cylinders in the thermal environment because of the lack of material information on applicable materials.

V. CONCLUSIONS

Based upon this one-dimensional heat conduction analysis, the elastic recovery composite with the foam core appears to minimize the heat conduction through the section. This conclusion was based upon the weight of composite per unit area. The thermal stresses in this composite would be minimal since the relatively weak core would allow for differential growth of the skins.

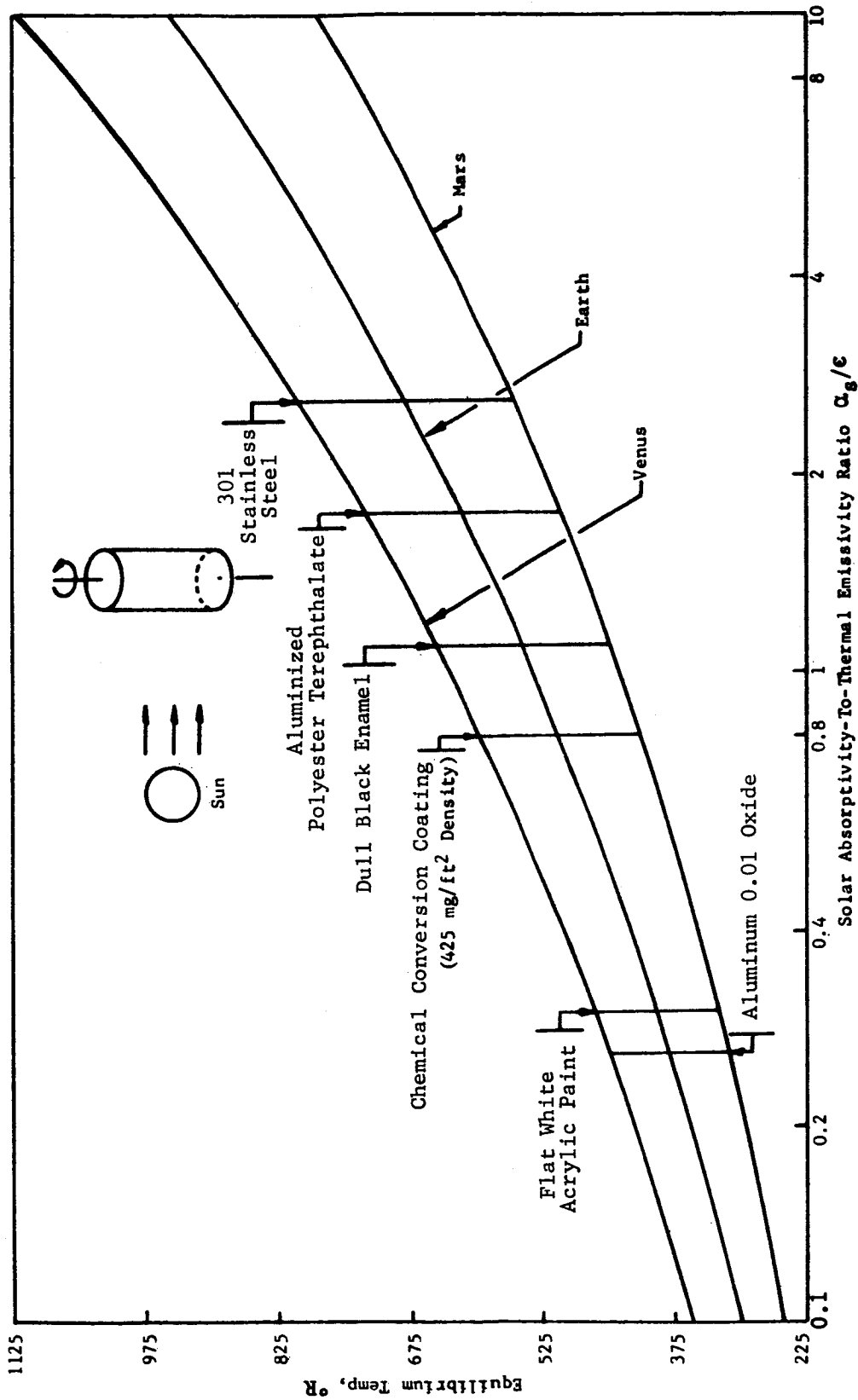


Figure 72. Equilibrium Temperature vs. Absorptivity-to-Emissivity Ratio for a Rotating Cylinder

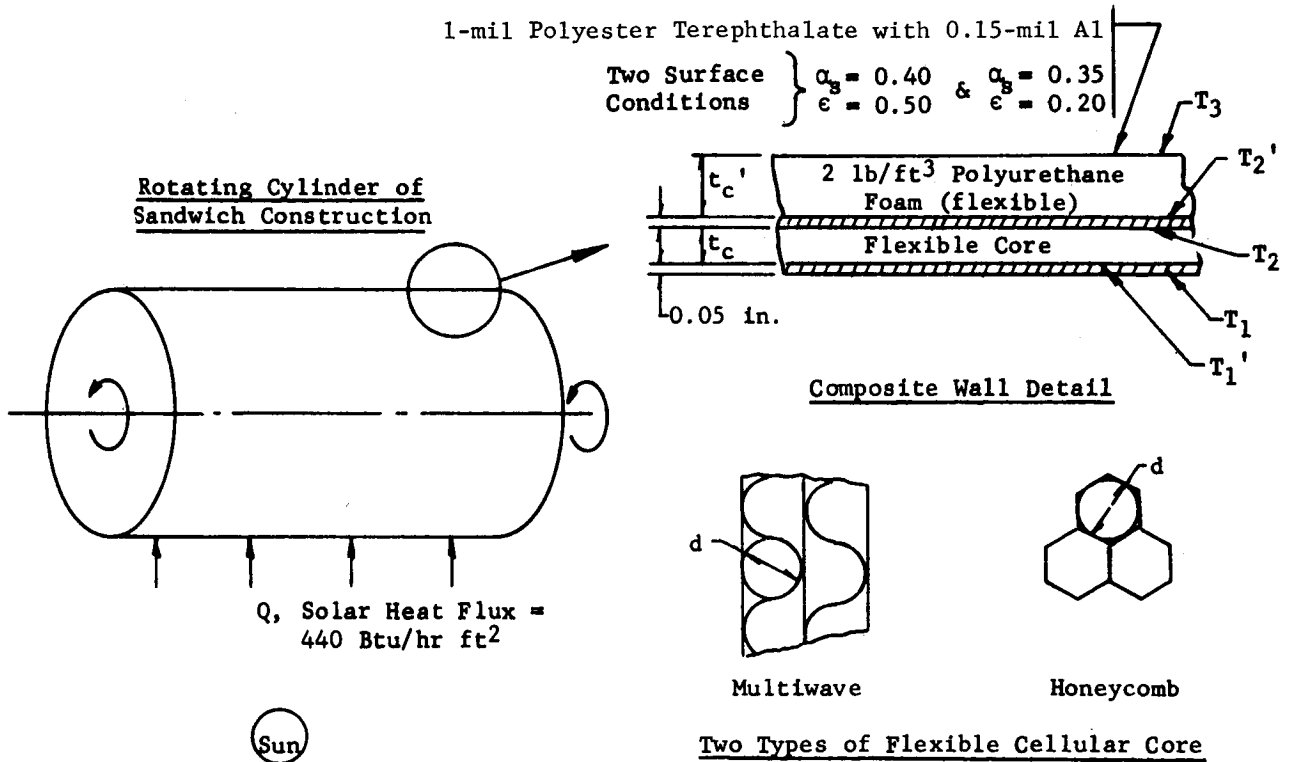


Figure 73. Generalized Composite Configuration for Thermal Evaluation

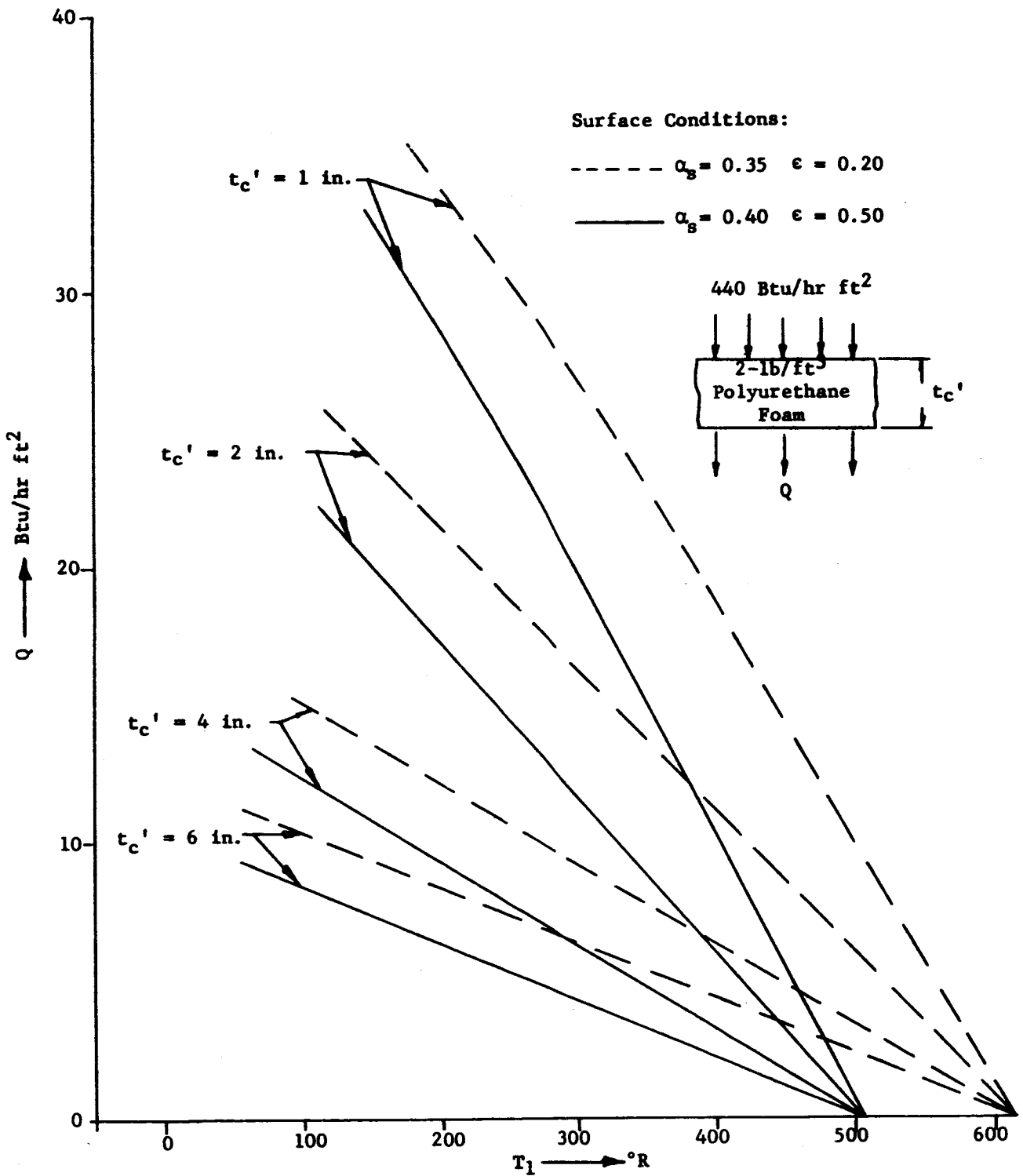


Figure 74. Heat Transfer Rate vs. Inner Facing Temperature for a Rotating Cylinder

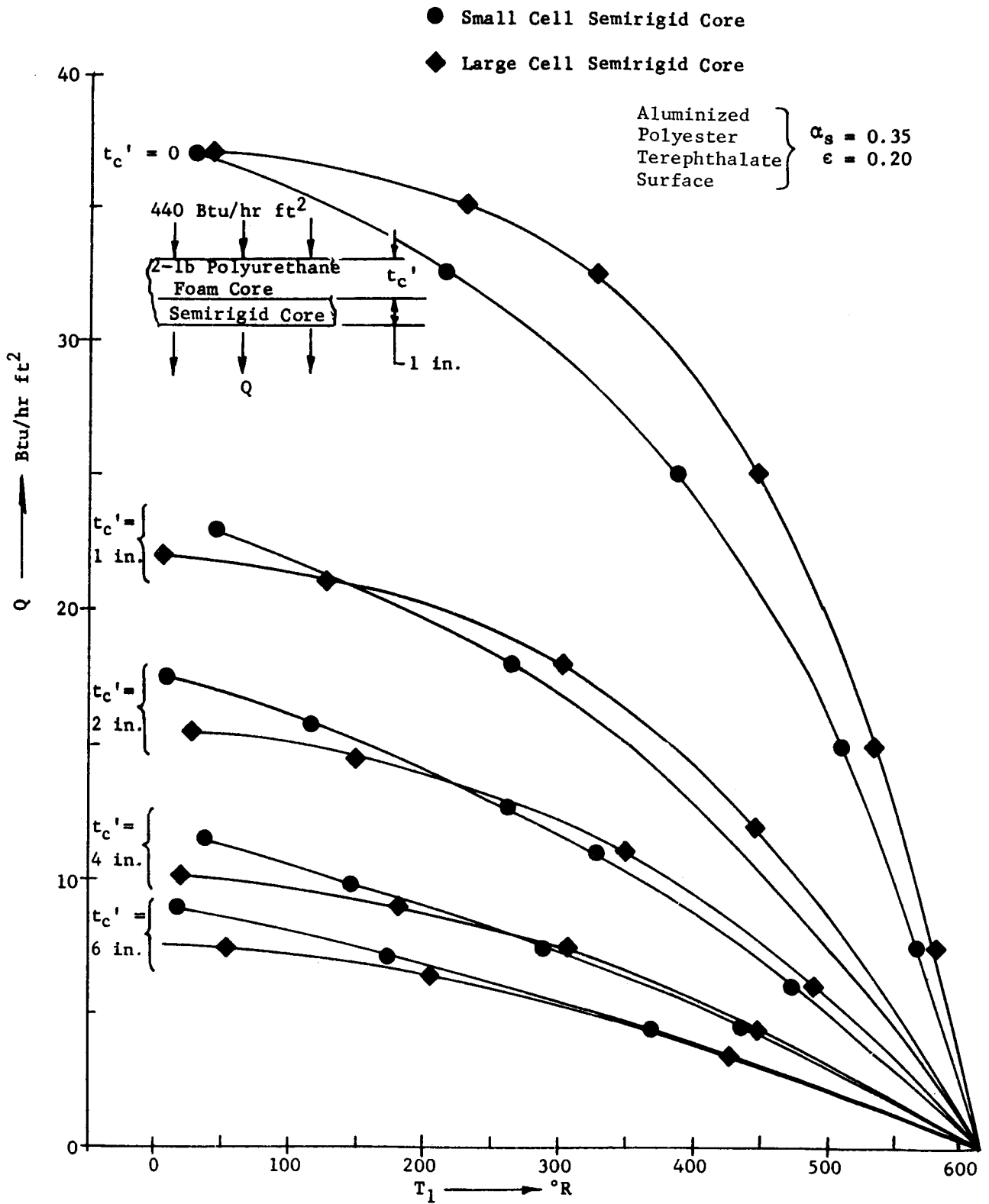


Figure 75. Heat Transfer Rate vs. Inner Facing Temperature for a Rotating Cylinder

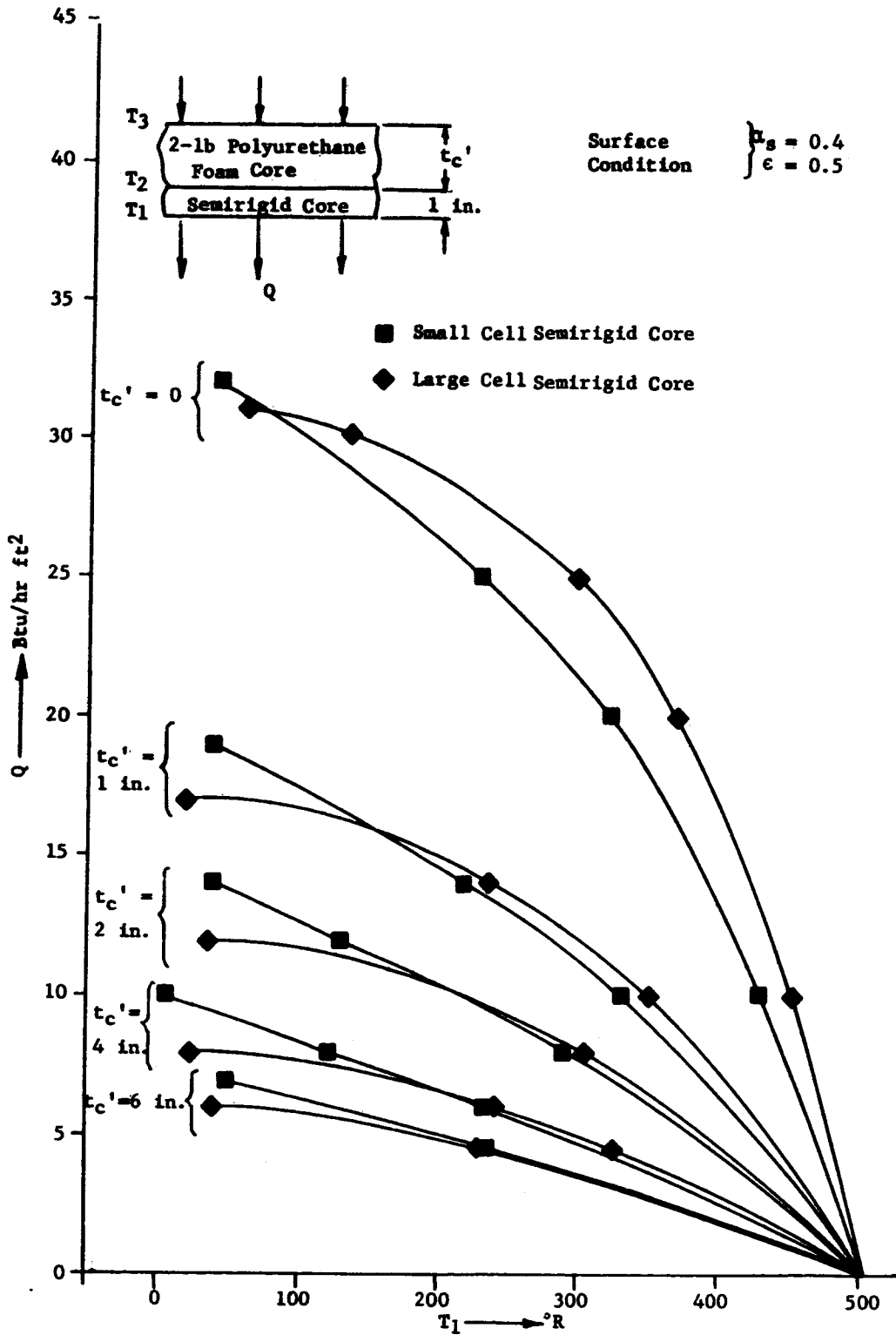


Figure 76. Heat Transfer Rate vs. Inner Facing Temperature for a Rotating Cylinder

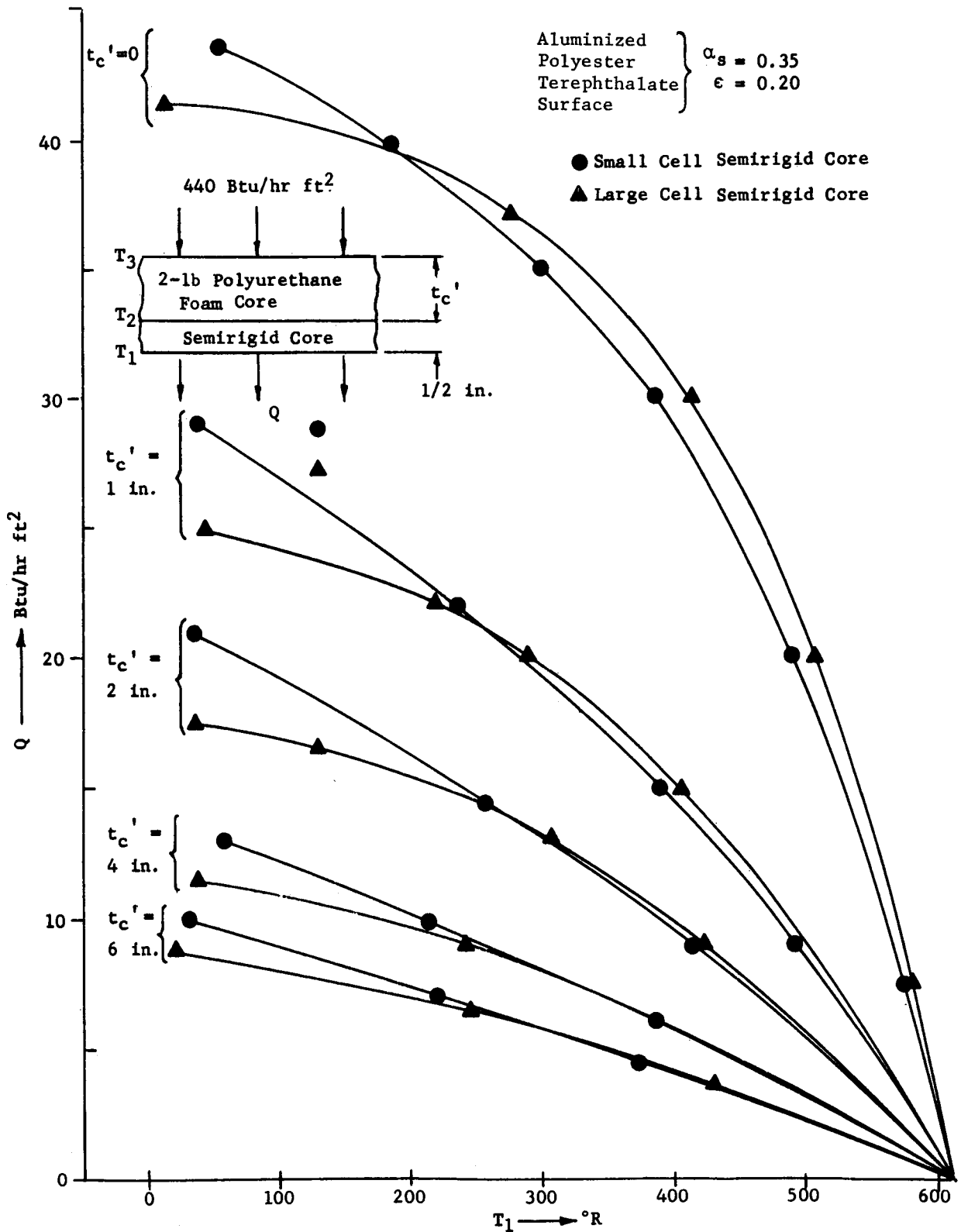


Figure 77. Heat Transfer Rate vs. Inner Facing Temperature for a Rotating Cylinder

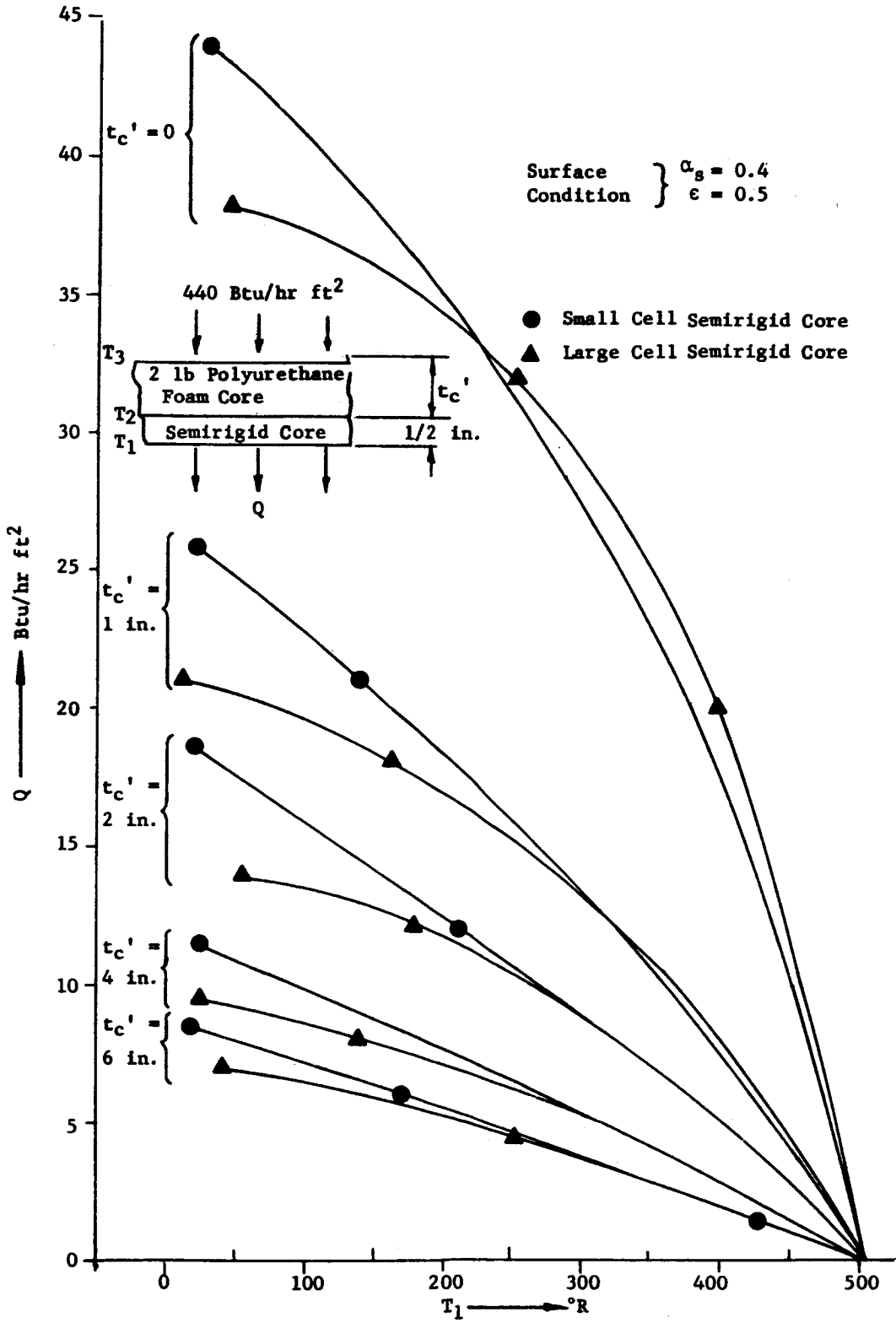


Figure 78. Heat Transfer Rate vs. Inner Facing Temperature for a Rotating Cylinder

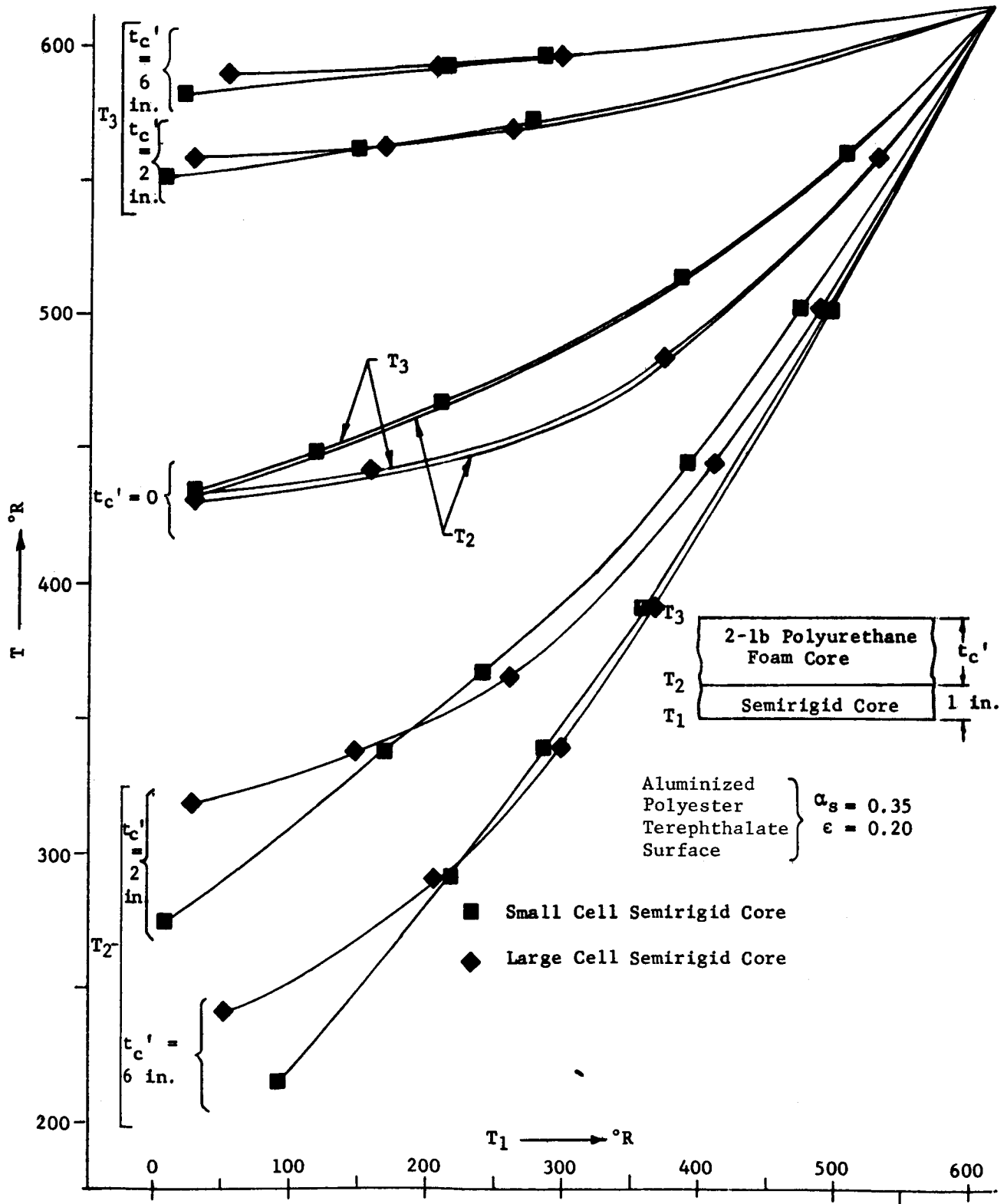


Figure 79. Temperature Distribution Within Sandwich for a Rotating Cylinder

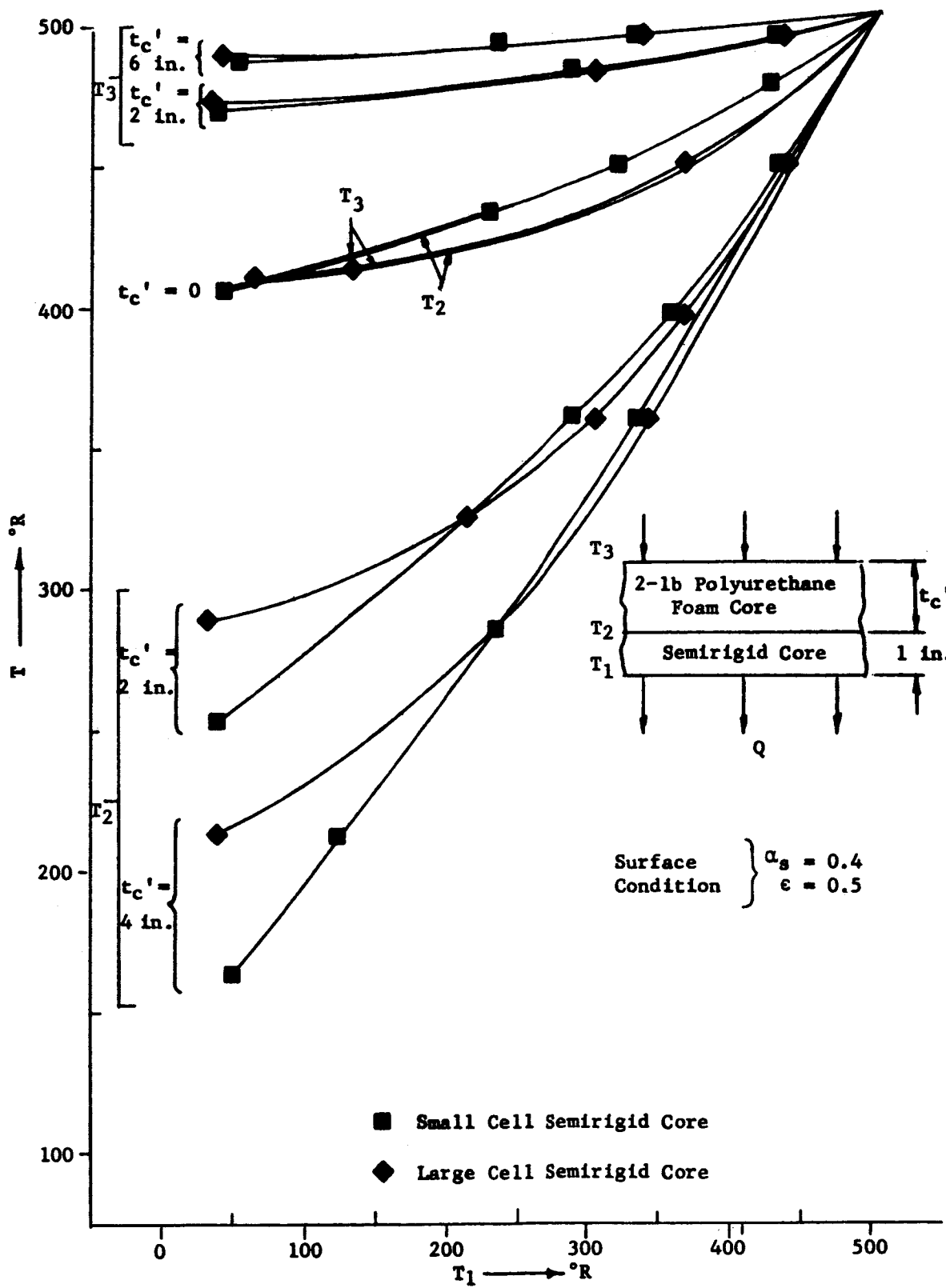


Figure 80. Temperature Distribution Within Sandwich for a Rotating Cylinder

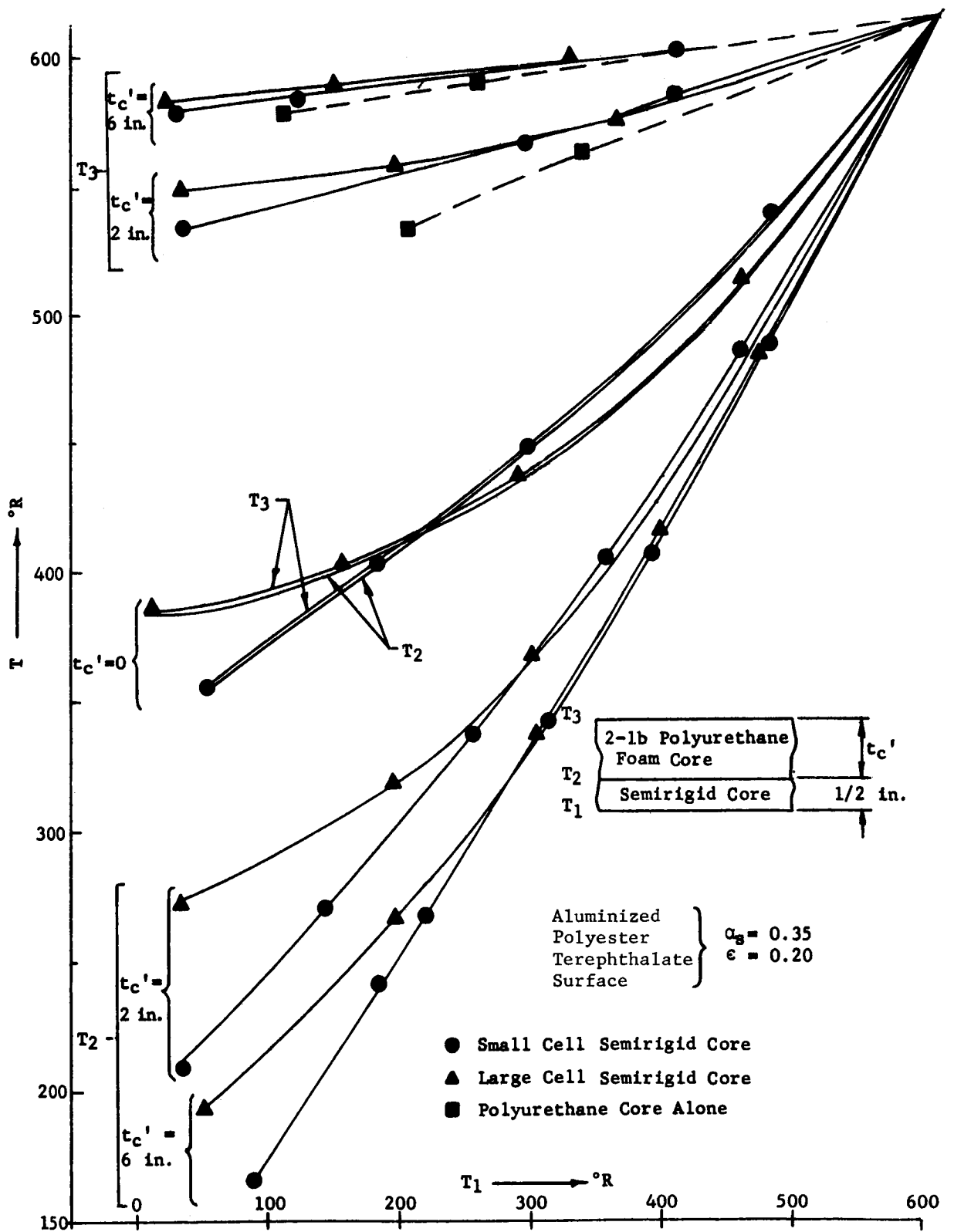


Figure 81. Temperature Distribution Within Sandwich for a Rotating Cylinder

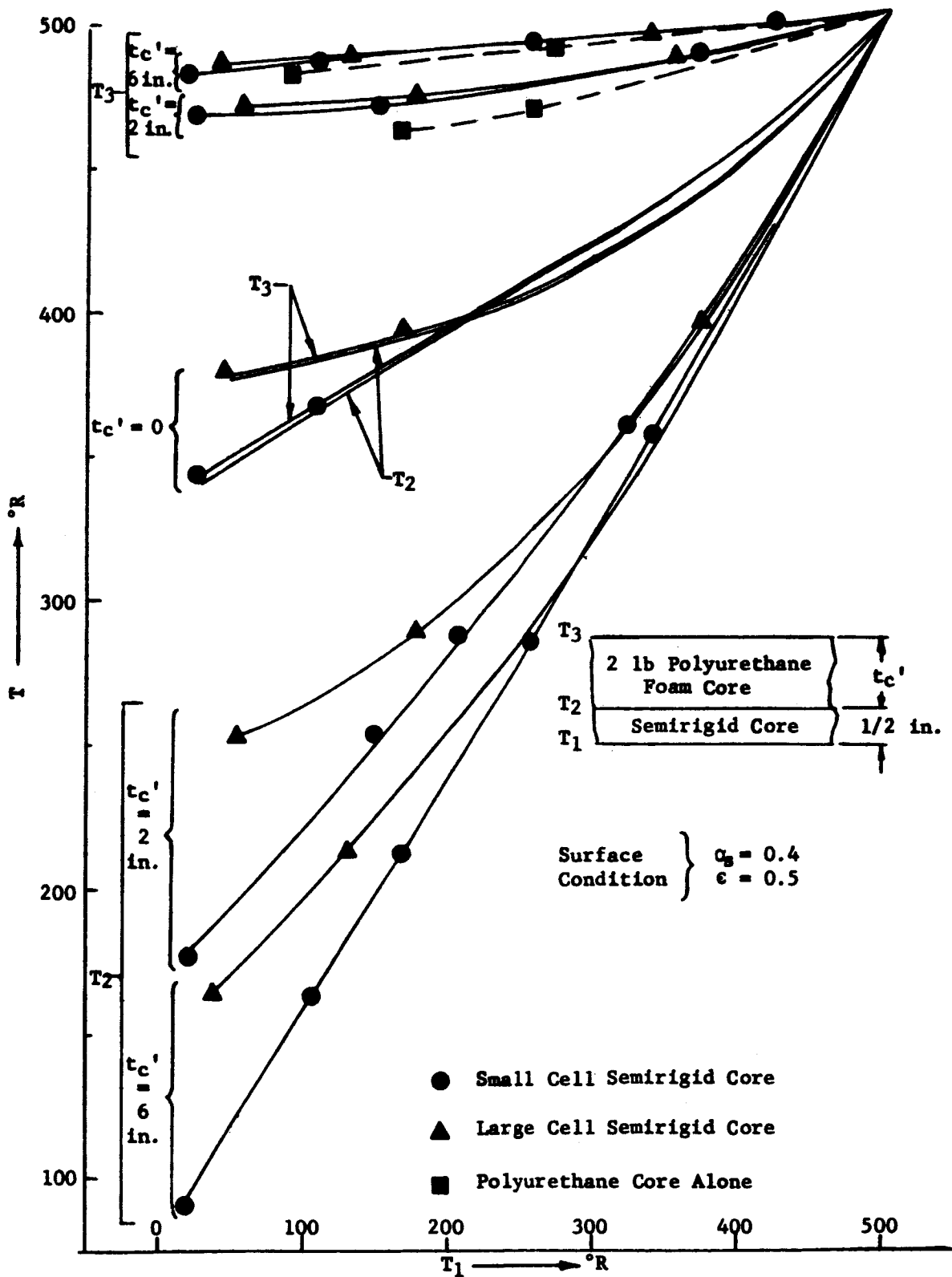


Figure 82. Temperature Distribution Within Sandwich for a Rotating Cylinder

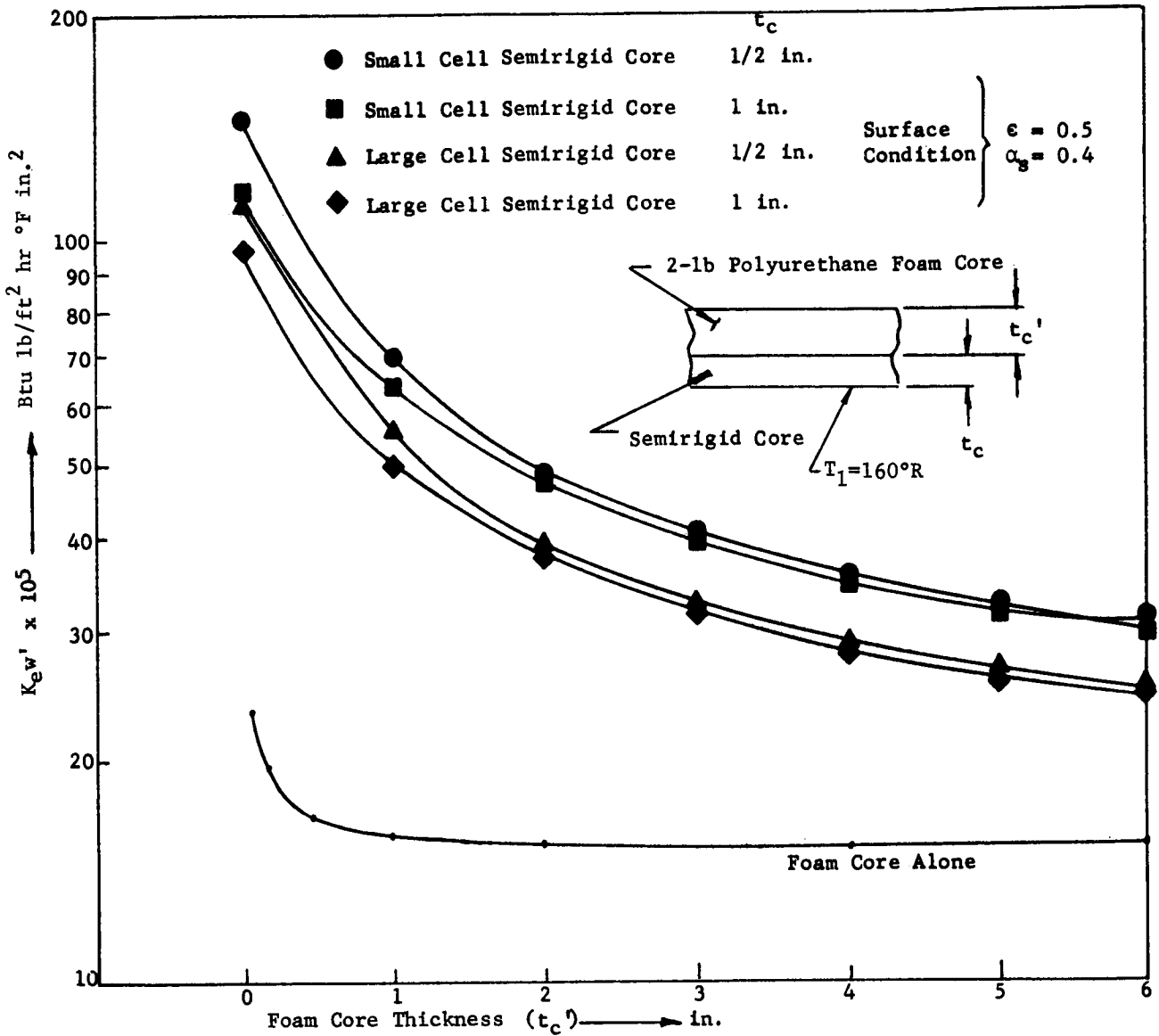


Figure 83 Thermal Efficiency Parameter vs. Flexible Foam Core Thickness for a Rotating Cylinder

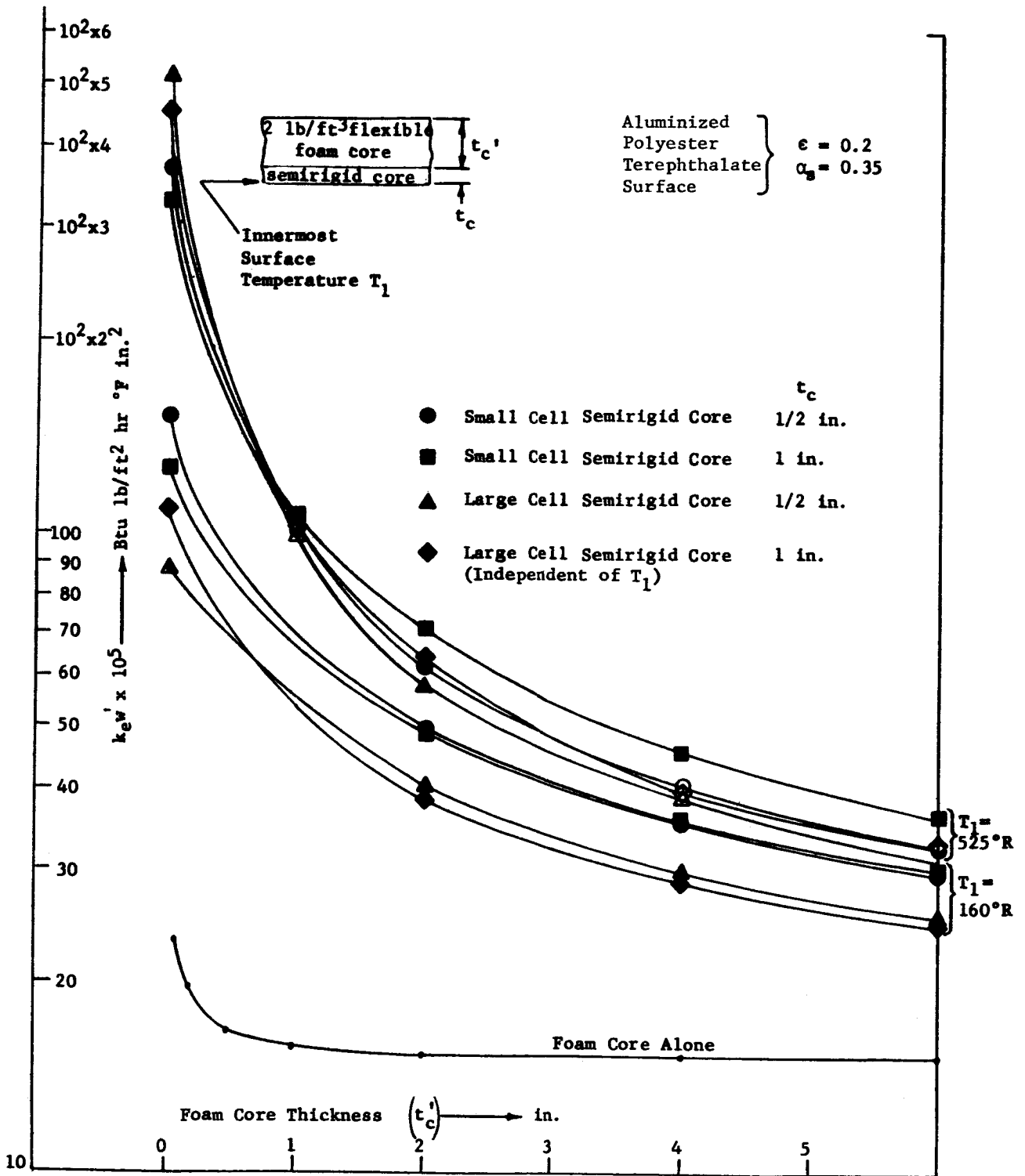


Figure 84. Thermal Efficiency Parameter vs. Flexible Foam Core Thickness for a Rotating Cylinder

Outer Surface Condition

Symbol	ϵ	α_s	T_1
●	0.2	0.35	525°R
■	0.2	0.35	160°R
▲	0.5	0.4	160°R

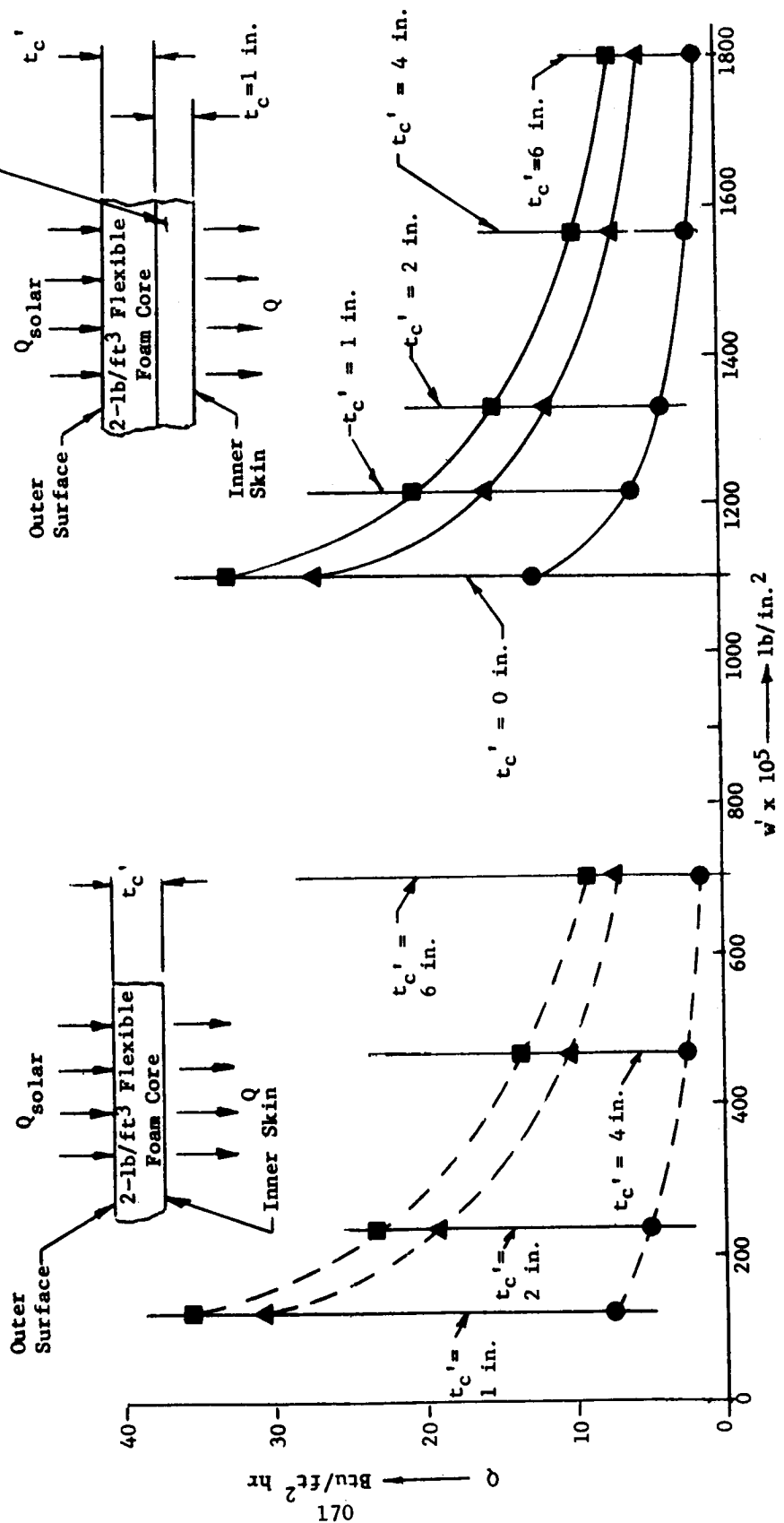


Figure 85. Heat Transfer Rate vs. Weight per Unit Area for a Rotating Cylinder

APPENDIX D

AN ANALYSIS FOR THE METEOROID PROTECTION OF SPACECRAFT UTILIZING THE ELASTIC RECOVERY SANDWICH COMPOSITE WALL CONCEPTS

Abstract

The protective requirements for the elastic recovery composite were determined in this report. Three major areas were studied in this investigation: the types of failure resulting from penetration and spallation, the method of analysis for determining the weight of typical elastic recovery composite, and the comparison of the different wall concepts by weights.

The method of analysis was determined for the composite construction of the elastic recovery concept. For this analysis, each layer performed a function in preventing the meteoroid from penetrating the inner layer. The laminate layers of the composite either fragment or absorb the particle. The foam layers in the composite absorb the smaller fragments. This analysis required many assumptions particularly the strength characteristics of the material and meteoroids under the influence of high impact. This analysis represented the first attempt at obtaining a method for designing a wall for meteoroid protection. The developed curves may be used for different meteoroid mass and velocities.

The results of this analysis indicated that a composite of laminate layers and foam core would provide the necessary protection. This method of analysis does however require experimental verification.

APPENDIX D

AN ANALYSIS FOR THE METEOROID PROTECTION OF SPACECRAFT UTILIZING ELASTIC RECOVERY SANDWICH COMPOSITE WALL CONCEPTS

by

C. E. Thompson

I. INTRODUCTION

One of the environmental hazards of space exploration is possible impact with meteoroids which traverse space at hypervelocities. Numerous investigations have been performed to obtain criteria for the design of a spacecraft against meteoroid impact; however, there are still many areas of uncertainty in the solution of this problem. This fact is illustrated by the following statements:

The meteoroid flux density vs. either mass or velocity for various areas of space is not definitely known. Also, in the area of the mechanics of hypervelocity impact, the knowledge of the exact contribution of the various parameters to penetration is still in a state of flux. For example, Maiden⁽⁴¹⁾ states target strength (S_t) is definitely not a factor in hypervelocity impact, whereas Kinecke and Richards⁽⁴²⁾ indicate target strength (S_t) is a factor up to at least an impact velocity of 15 km/sec. Another important example of a disputed parameter contribution is Bjork's standard work,⁽¹⁸⁾ which shows penetration as a function of $V^{1/3}$, whereas recently Walsh and Tillotson⁽⁴³⁾ state penetration as a function of $V^{0.62}$.

The exact definition of the flux density in space is under intensive investigation. Its complete solution appears to await manned space exploration. The problems in the actual mechanics of hypervelocity impact for the most part have been investigated for single sheet shields. Further, with the average meteoroid velocity range between 11 and 72 km/sec, very little experimental data (which have been in the lower velocity range) have been obtained to substantiate various penetration theories. The largest problem to the theoretical prediction of penetration appears due to the limited knowledge of material

properties (i.e., stress-strain curves) under extremely high loading conditions. (This, of course, ties in with the contribution of the various parameters.) Several years ago, Whipple⁽⁴⁴⁾ suggested the meteoroid bumper concept. This concept, in brief, utilized a thin plate placed at a distance away from the spacecraft primary structure to fracture and break up possible meteoroids upon impact. In this way, the meteoroid energy would be greatly reduced. This in turn reduced the amount of weight required for protection by the spacecraft. The elastic recovery wall composites are ideally suited to use the bumper principle due to their layered construction. Since, at the present, experimental means are not available for use in the evaluation of elastic recovery wall concepts, it is the purpose of this investigation to:

- a. Determine an engineering theory to evaluate sandwich wall concepts for hypervelocity impact through the application of existing theory and experiment
- b. Evaluate Narmco's elastic recovery wall concepts as to efficiency with the above method
- c. Present a plot of the required weight for protection (using the best wall concept) vs. the area of the spacecraft times the time of the mission.

SYMBOLS (NOMENCLATURE)

The following is a list of symbols used throughout this report. Additional symbols will be defined within the actual text as required.

- A - Area of spacecraft, ft^2
- B - Brinell Hardness Number
- C - Velocity of sound
- D_1 - Diameter of spray cone (faster particles) from fracture of meteoroid
- D_2 - Diameter of principal cone (slower particles) from fracture of meteoroid
- E - Modulus of elasticity, psi

- F_1, F_2, F_3 - Facing of sandwich composite
 g - Gravity
 I_1, I_2, I_3, I_4 - Interfaces of the sandwich composite
 K_s - Stiffness factor⁽⁴⁵⁾
 L - Characteristic length of meteoroid
 m_c - Critical mass of meteoroid (largest mass likely for a spacecraft to encounter given the probability requirement, area of spacecraft, and time of mission)
 m_1 - Meteoroid mass
 m_2 - Bumper shield mass
 P_1 - Impact pressure (maximum) on bumper shield at initial impact of the meteoroid, psi
 P_2 - Impact pressure on core c_1 and interface I_2
 P_3 - Impact pressure on facing 2
 P_4 - Impact pressure on core c_2 and interface I_4
 P_5 - Impact pressure on facing 3
 $P(N)$ - Probability of no damaging impacts in N number of damaging impacts of a given mission profile
 S_t - Shear yield stress of target material, lb/in.²
 S_p - Shear yield stress of meteoroid material, lb/in.²
 T - Time of mission, hr
TFM - Typical facing material (facing material of average properties of those material considered for the elastic recovery concept)
 t_p - Penetration depth in a semi-infinite solid, in.
 t_p' - $1.5 t_p$ - penetration depth in a thin plate
 t_f - Thickness of bumper shield required to break up the meteoroid
 V - Velocity of meteoroid or projectile, ft/sec
 V_R - Range of velocity where the formula is applicable
 \bar{V}_c - Volume of meteoroid or fragment of meteoroid, in.³

- V_f - Effective volume of a faster fragment of the shattered meteoroid, in.³
- \bar{V}_{or} - Original volume of meteoroid, in.³
- \bar{V}_s - Effective volume of a slower fragment of the shattered meteoroid, in.³
- V_f^* - Velocity of faster fragments after meteoroid is shattered, ft/sec
- V_s^* - Velocity of slower fragments after meteoroid is shattered, ft/sec
- Z - Bumper parameter = $S_t \rho_t / S_p \rho_p$
- Δ - Densification factor⁽⁴⁵⁾
- ρC - Acoustic resistance
- ρ_c - Density of flexible core material
- ρ_E - Effective density of the shattered meteoroid and shield particles
- ρ_p - Density of meteoroid, lb/in.³
- ρ_t - Density of target material, lb/in.³
- ρ_1 - Density of first material subject to the shock wave in sandwich construction
- ρ_2 - Density of second material subject to the shock wave in sandwich construction
- σ_I - Initial stress or pressure pulse, psi
- σ_R - Reflected stress pulse at interface of two different density materials, psi
- σ_T - Transmitted stress pulse at interface of two different density materials, psi
- φ_c - Flux density rate as given by Whipple⁽⁴⁴⁾

II. METHODS OF ANALYSIS OF IMPACT BY HYPERVELOCITY PARTICLES ON ELASTIC RECOVERY COMPOSITES

To develop a method to analyze a sandwich elastic recovery composite structure for hypervelocity impact we must first look at the possible failure modes a shield has under impact by high-speed particles. The possible modes of failure are penetration, spallation, and combination penetration and spallation. These failure modes are sketched in Figure 86.

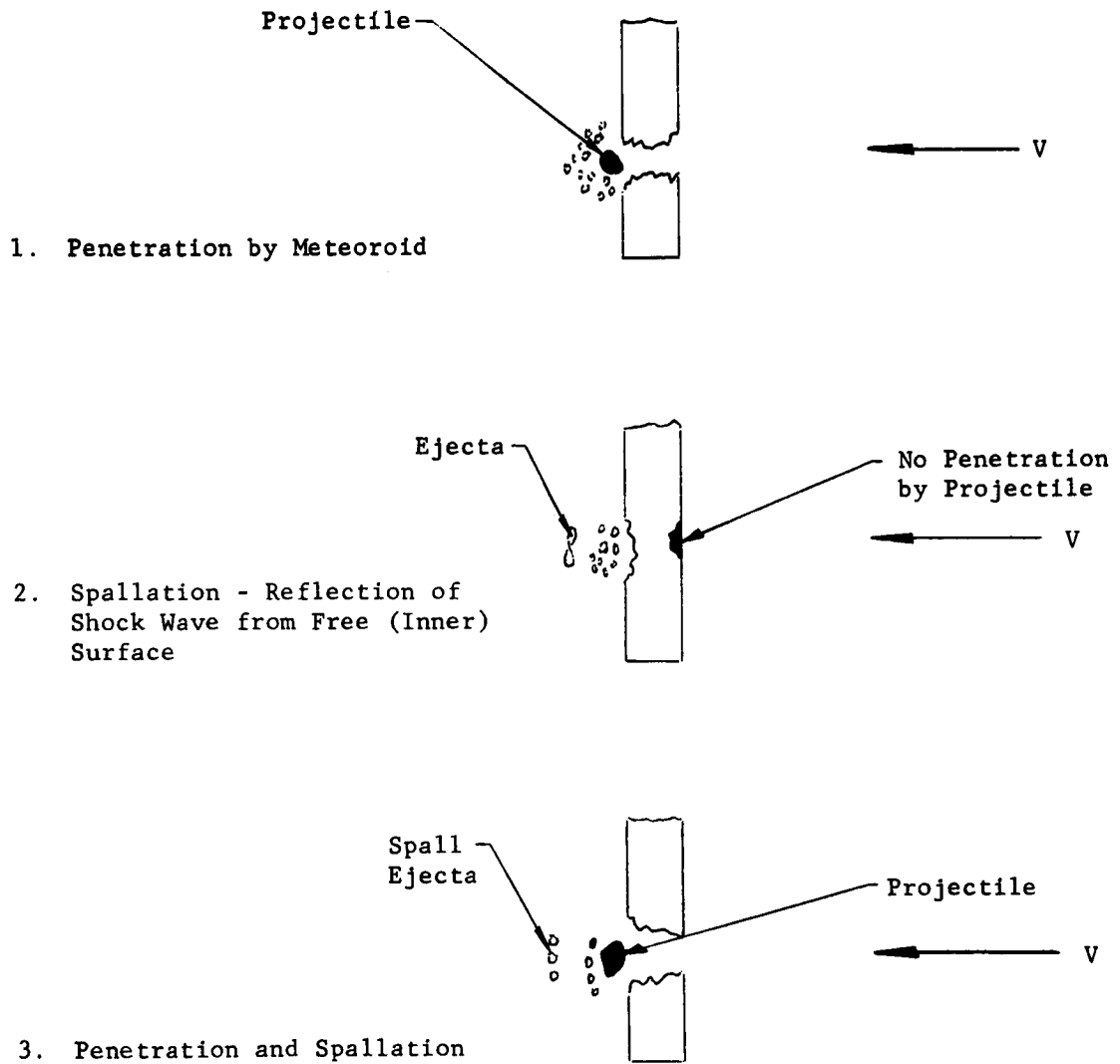
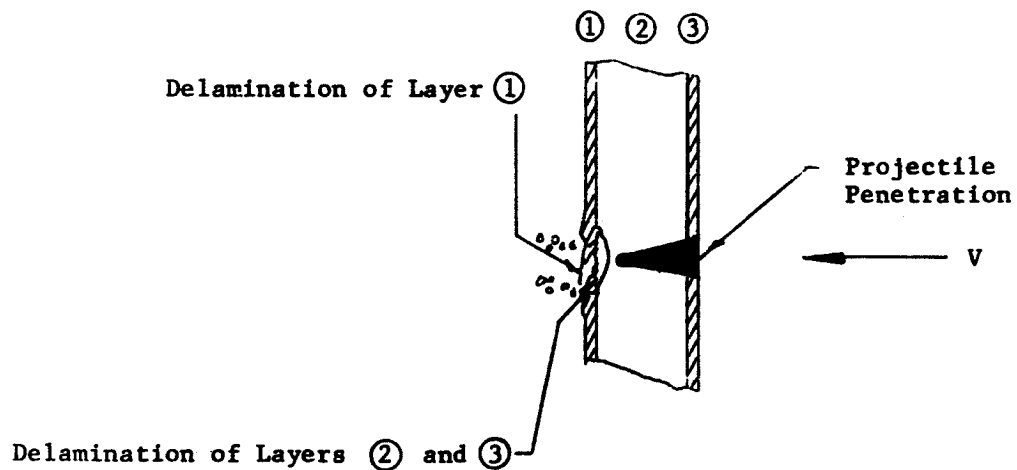


Figure 86. Possible Failure Modes of Shield under Projectile Impact

The sketches of the failure modes are shown for single shields. Basically, the same happens with elastic recovery composites except in the case of spallation. This can also mean delamination of the innermost facing or delamination of the various layers making up the composite; this is illustrated in Figure 87.

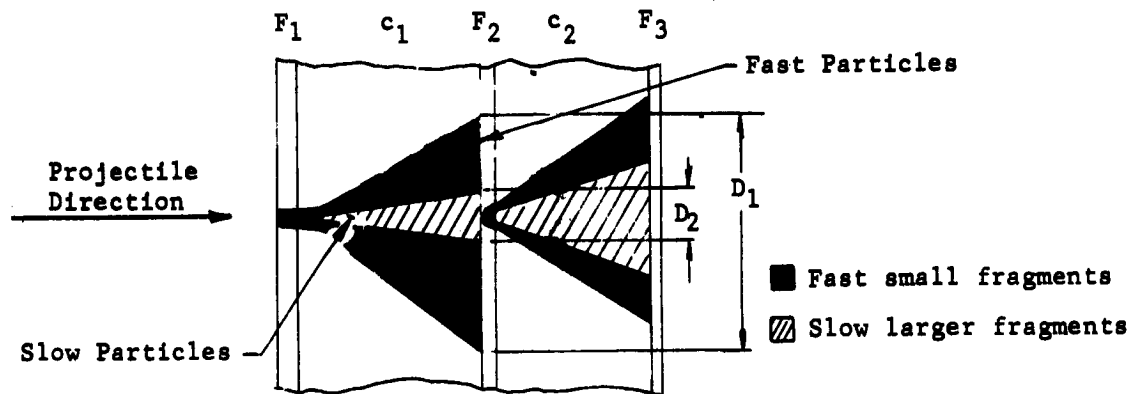


NOTE: Elastic recovery sandwich structure delamination failures, due to reflected shock, occur at the inner surface and at the interface of layers 1 and 2 and layers 2 and 3.

Figure 87. Possible Mode of Failure for Inner Layer of an Elastic Recovery composite under Projectile Impact

A. Penetration

The scheme to analyze a sandwich composite with flexible cores (elastic recovery idea) for the penetration failure mode using the Whipple bumper principle is simple in concept. First, consider a typical elastic recovery wall concept that has been impacted by a meteoroid, but not penetrated (as shown in Figure 88).



- F = Facing
- c = Flexible core
- - Fast small fragments
- ▨ - Slow larger fragments
- D₁ - Dia of spray cone
- D₂ - Dia of principal cone

Figure 88. Typical Elastic Recovery Wall Concept Impacted by a Hypervelocity Particle (Penetration Mode Only)

The meteoroid first impacts facing 1 and fragments. The projectile fragments and the ejecta from facing 1 enter the flexible core c₁. The pieces essentially divide into two parts: one part consists of smaller high velocity particles, the other part the slower and larger particles.

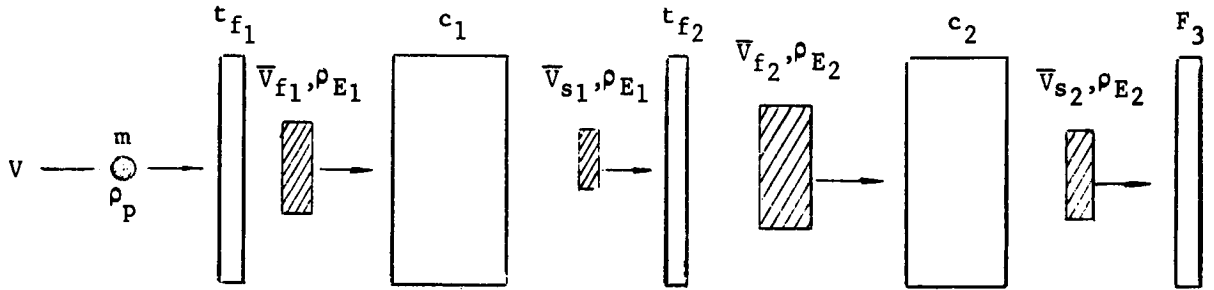
The faster particles are absorbed by the core c_1 ; the slower particles pass through the core c_1 impacting on facing 2, and are either absorbed or are fragmented again by facing 2. In Figure 88, the slow particles from core c_1 are fragmented again by facing 2. Facing 2 then divides the slow particles into two parts: fast and slow. The fast pieces are absorbed by core c_2 , the slow particles are (for this example) absorbed by facing F_3 .

From the above description, an idealized penetration model and a method of analysis was formulated. The idealized model is shown in Figure 89. The development of a method of analysis may be explained in the following steps.

1. Determine the required thickness of facing material to shatter the design meteoroid. (In this particular analysis, reported experimental data were used, and these data plotted vs. the bumper parameter Z .)
2. Assume the density of the fast and slow particles from the shattered meteoroid was an average of the densities of the facing and meteoroid (ρ_E).
3. Assume the velocities of the fast and slow particles (V_f^* , V_s^*) can be determined from Lull's theory as reported by Maiden.⁽⁴⁶⁾
4. Compute \bar{V}_f using a thin plate penetration formula, the information in the above sections, and the penetration depths and core properties reported and estimated respectively from experimental data.⁽⁴⁷⁾⁽⁴⁸⁾
5. Assume that \bar{V}_s can be approximated by $\bar{V}_s = \bar{V}_f \frac{(D_1)^2}{(D_2)^2}$ where D_1 and D_2 are taken from experimental data.⁽⁴⁷⁾
6. Plot sections 4 and 5 vs. bumper parameter (Z) making the necessary extrapolations to ensure a range of required (Z) values is covered.

The procedure of design of a sandwich elastic recovery concept is then clear, knowing the materials to be used and their properties along with the design meteoroid and its properties; i.e.,

1. Determine t_f as per section 1 (from curve).



where ρ_p = Original meteoroid density
 m = Original meteoroid mass
 t_{f1} = Thickness to fracture original meteoroid
 t_{f2} = Thickness to fracture again the slow particles of original meteoroid

$$\rho_{E1} = \frac{\rho_{t_{f1}} + \rho_p}{2} \qquad \rho_{E2} = \frac{\rho_{E1} + \rho_{t_{f2}}}{2}$$

Subscripts 1, 2 = first and second fracture of meteoroid
 c_1, c_2 = core
 F_3 = Facing thickness to absorb projectile of \bar{v}_{s2} and density ρ_{E2}

Figure 89. Idealized Model of Impact Penetration by a Hypervelocity Particle in an Elastic Recovery Sandwich Composite

2. Determine \bar{V}_f , \bar{V}_s , V_f^* , V_s^* , ρ_E from given information and the curves that were developed.
3. Using V_f , V_f^* , ρ_{E1} , compute the thickness c_1 by an applicable thin plate penetration formula.
4. Using \bar{V}_s , V_s^* , ρ_{E1} , compute the thickness of facing number 2 using thin plate formulas or repeat the above process using V_s^* , \bar{V}_s , and ρ_E as the properties of a projectile to be fractured by the second facing. Thus, one may go from layer to layer and obtain the minimum weight for protection.

B. Spallation/Delamination

As shown in the previous discussion of possible failure modes, another mode of failure under impact that must be accounted for in the design of a sandwich composite is spallation/delamination. This type of failure is quite complex and requires much more research to effect a solution. To date, Rinehart⁽⁴⁹⁾ appears to be the only one to attack this problem with a view of finding a practical solution. It is stated in Reference 49 that no really practical solution was found due to the following reasons:

1. Knowledge of material properties (stress-strain) under high loading conditions is quite limited.
2. The shape and time length of a high-speed particle impact pulse is unknown.

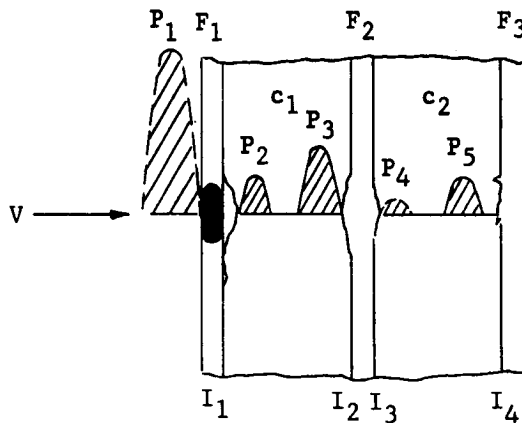
One suggested solution⁽⁴⁹⁾ states that since the shock wave maintains its velocity at all points, the way to change the stress pulse height was by using a composite laminated system such that when a pulse is applied, the amount of stress transmitted and reflected at changes of density can be determined by the following formulas.

$$\sigma_T = \frac{2 \rho_2 C_2}{\rho_2 C_2 + \rho_1 C_1} \sigma_I \quad \sigma_R = \frac{\rho_2 C_2 - \rho_1 C_1}{\rho_2 C_2 + \rho_1 C_1} \sigma_I \quad (1)$$

where subscripts 1 and 2 denote the first and second layers contacted by the shock wave.

It is clear that in this way the stress pulse could be reduced in intensity by grouping several layers of different densities. This method proved unsatisfactory simply because there were not enough types of materials with sufficient difference in acoustic resistance (ρC) to effect a major reduction in stress pulse height without large numbers of layers. A major reduction in stress is required because the impact pressures go into the megabar range (millions of pounds per square inch) for high-speed particles.

It was therefore necessary to propose a design analysis model for spallation/delamination mode of impact failure in the elastic recovery wall concept. Figure 90 depicts this model. Since the shape of the pulse (P_1) is not known, it is assumed for the elastic recovery concept that at interface I_1 , the stress (reflected) will almost immediately rise to a value to break the facing F_1 , away from the core c_1 , which would cause the facing to become a free surface before the full pressure P_1 , is reached at I_1 ; hence, I_1 would not transmit P_1 to the core c_1 .



where

P_1, P_2, P_3, P_4, P_5 = Stress pulses

I_1, I_2, I_3, I_4 = Interfaces


 = Pulse (shape is for illustrative purposes only)

Figure 90. Idealized Model for Spallation/Delamination Analysis of a Sandwich Composite

Thus, as the meteoroid penetrates and fragments in going through facing F_1 (the bumper), the core and the interface I_2 will obtain a stress pulse

proportional to
$$P_2 = P_1 \frac{\bar{v}_{f1}}{\bar{v}_{or}}$$
 and the facing F_2 will receive a stress

pulse proportional to
$$P_3 = P_1 \frac{\bar{v}_{s1}}{\bar{v}_{or}}.$$

The maximum impact pressure (P_1) can be estimated from data given by Reference 6 as

$$P_1 = \sigma_I = E \left\{ \frac{\Delta(\Delta - 1)}{[\Delta - (\Delta - 1) K_s]^2} \right\} \dots \dots \dots (2)$$

If two facings are used (F_1, F_2), then P_2 should be used as the maximum stress reflected and transmitted at I_2 , and P_3 as the maximum stress reflected at the innermost surface of F_2 .

If three facings are used, then the design stress at I_4 (I_3 is assumed to

fail) would be $\left[P_4 = P_3 \left(\frac{\bar{v}_{f2}}{\bar{v}_{s1}} \right) \right]$, and P_5 for the maximum stress

reflected at the innermost surface of F_3 , where $\left[P_5 = \frac{\bar{v}_{s2}}{\bar{v}_{s1}} P_3 \right]$

The formulas of (1) would be used to determine the magnitude of the reflected and transmitted stresses. The criterion of failure (which appears reasonable) would be that due to the reflected stresses, no dangerous ejecta from the innermost surface would be permitted.

C. Combination of Spallation and Penetration

It will be assumed for this analysis that if the elastic recovery wall concept is designed for both penetration and spallation, the design will suffice for the combination spallation-penetration failure mode.

III. PENETRATION FORMULAS

From the method of analysis for the penetration failure mode, it was necessary to choose a thin plate penetration formula. There have been many of these types of equations developed in the literature and are, for the most part, empirical in nature. Most investigators agree that the formula by Herrmann and Jones⁽⁵⁰⁾ and given in the following form (from Reference 51) best fits the experimental data:

$$t_p' = 0.9 m_1^{1/3} \left(\frac{0.6}{\pi} \right)^{1/3} \left(\frac{\rho_p}{\rho_t} \right)^{1/3} \ln \left[1 + \frac{\left(\frac{\rho_p}{\rho_t} \right)^{2/3} \left(\frac{\rho_t v^2}{B g} \right)}{4} \right] \dots (3)$$

The equation, however, was not used in this analysis because the formula requires the Brinell Hardness Number (B). This number would be difficult to obtain for the types of materials considered for the elastic recovery concept. It was assumed a more convenient formula for this analysis would be one where the target strength was a direct factor.

Thus the penetration formulas as taken and extrapolated from APGC TDR 63-22⁽⁵²⁾ appeared more applicable from an engineering viewpoint. These formulas and their applicable velocity ranges are given below as:

$$\left. \begin{array}{l} \underline{v_R \leq 10,000 \text{ ft/sec}} \\ t_p' = (1.5)(0.172) v^{0.893} \rho_p^{0.979} s_t^{-0.457} \rho_t^{-0.35} \bar{v}_c^{0.33} \end{array} \right\} \dots (4)$$

$$\left. \begin{array}{l} \underline{v_R = 20,000 - 30,000 \text{ ft/sec}} \\ t_p' = (1.5)(0.772) v^{0.449} \rho_p^{0.673} s_t^{-0.275} \rho_t^{-0.426} \bar{v}_c^{0.33} \end{array} \right\} \dots (5)$$

$$\left. \begin{aligned} V_R &= 65,000 - 80,000 \text{ ft/sec} \\ t_p' &= (1.5)(0.97) V^{0.21} \rho_p^{0.39} S_t^{-0.10} \rho_t^{-0.46} \bar{V}_c^{0.33} \end{aligned} \right\} \dots \dots (6)$$

$$\left. \begin{aligned} V_R &= 100,000 - 240,000 \text{ ft/sec} \\ t_p' &= (1.5)(0.97) V^{0.18} \rho_p^{0.26} S_t^{-0.04} \rho_t^{-0.46} \bar{V}_c^{0.33} \end{aligned} \right\} \dots \dots (7)$$

A. Development of the Steps in the Method of Analysis for Penetration

The first step as previously stated was to determine the thickness of a given material to shatter the incoming meteoroid. Sandorff⁽¹⁵⁾ and Maiden⁽⁴⁶⁾ have indicated the first theoretical methods to obtain this thickness, t_f . For this analysis, however, it was assumed that a greater advantage might be secured by plotting experimental data of t_f (from Reference 47) vs. the bumper parameter (Z). Thus, Figure 91 shows the required plot by using experimental (t_f) data and the formulas (equations 4 through 7). One important assumption to be noted would be that this curve (Figure 91) represents all velocities. This appears to be reasonable within the state-of-the-art considerations.

The second step was to assume that the shattered fragments of the meteoroid and the ejecta of the facing (t_f) produce slow and fast particles with a density equal to the average densities of the facing and meteoroid.

The third step was to find the velocity at which these fast and slow particles enter the first core. Maiden⁽⁴⁶⁾ gave a convenient discussion and appropriate calculations for these velocities by means of Lull's theory. These formulas for V_s^* and V_f^* are from Reference 46.

$$V_s^* = V \left[\frac{m_1}{m_1 + m_2} - \left(\frac{5}{3}\right)^{1/2} \frac{(m_1 m_2)^{1/2}}{m_1 + m_2} \right] \dots \dots \dots (8)$$

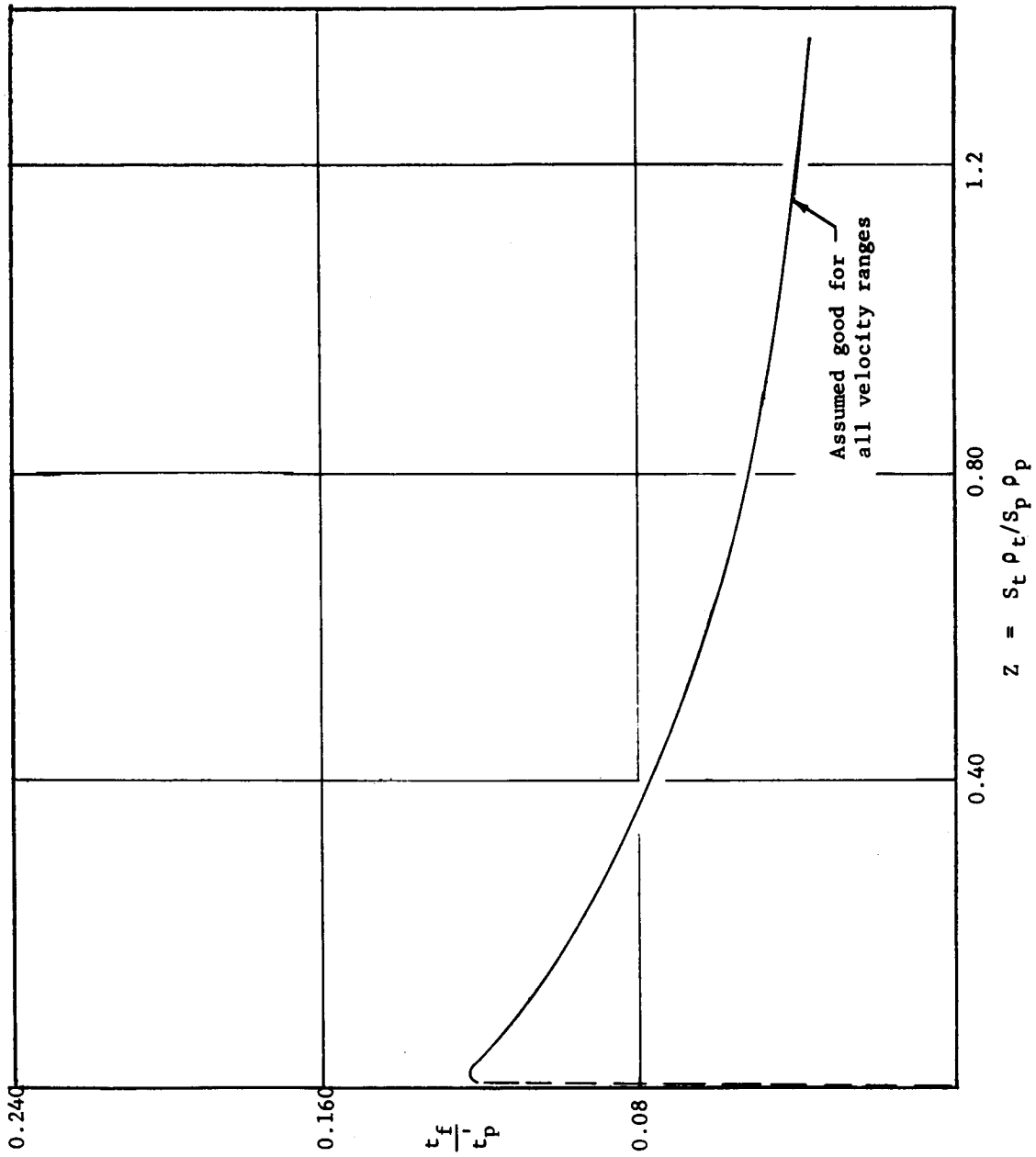


Figure 91. Ratio of Bumper Thickness to $\frac{t_f}{t_p}$ Break Up Meteoroid to Thin Plate Penetration Depth. (For Estimation of Required Meteoroid Fracture Thickness (t_f)).

$$z = S_t \rho_t / S_p \rho_p$$

$$V^*_f = V \left[\frac{m_1}{m_1 + m_2} + \left(\frac{5}{3}\right)^{1/2} \frac{(m_1 m_2)^{1/2}}{m_1 + m_2} \right] \dots \dots \dots (8a)$$

A plot of these formulas is shown in Figure 92 (taken from Reference 46). The dotted lines in Figure 92 show an estimate for conservative design.

As was shown in the idealized model of penetration, the flexible core is effective in absorbing only the smaller, higher velocity (V^*_f) particles from the shattered meteoroid. It appeared reasonable to use this assumption to compute the required volume, \bar{V}_f , that the experimental penetration depth into the flexible core must have had without damage to the innermost facing. Thus, by using the thin plate penetration formulas (equations 4 through 7), the V^*_f as predicted by Figure 92 (with knowledge of the initial impact velocity and shield to projectile weight), the effective density of the fragments entering the core, and reported experimental core penetration depths, \bar{V}_f entering the core was then computed.

The experimental data was chosen from References 47 and 48 for the following reasons:

1. The target specimen consisted of two facings separated by a flexible core.
2. No damage to the innermost facing upon impact of the structure by a high-speed projectile.
3. The initial projectile was shattered by the first facing.
4. The bumper and projectile properties were such to produce different values of Z.
5. The properties of the core could be estimated.

These experimental data were for velocities in the range of 20,000 ft/sec. Then, equation 5 was solved for the volume. Thus

$$t'_p = (1.5)(0.772) V^{0.449} \rho_p^{0.673} S_t^{-0.275} \rho_t^{-0.426} \bar{V}_c^{1/3} \dots (5)$$

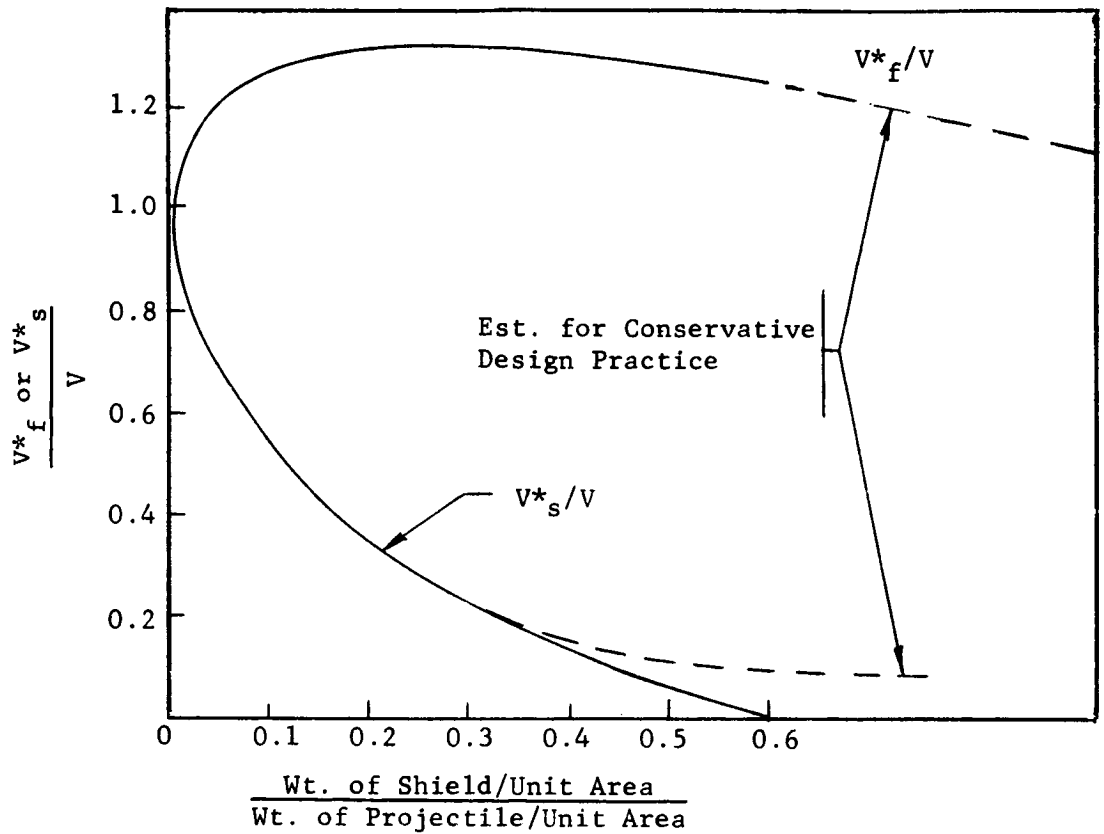


Figure 92. Velocity Ratio vs. Shield/Projectile Weight. V^*_f and V^*_s given after the meteoroid has penetrated and fractured in traveling through the facing (t_f) (Ref. 7)

solving for the volume required by a faster fragment to penetrate the core to a certain depth.

$$\bar{V}_f = \left[\frac{t_p'}{(1.5)(0.772) V_f^* \rho_E^{0.449} S_{c_1}^{0.673} \rho_{E_1}^{-0.275} \rho_{c_1}^{-0.426}} \right]^3 \quad \cdot \cdot \quad (9)$$

- where t_p' = Penetration depth of core from experimental data
 ρ_E = Average density of facing and projectile, used as a "new" projectile into the core
 S_{c_1} = Shear stress for type of core used in the experiment
 ρ_{c_1} = Core density

The use of this formula along with the data taken from References 47 and 48 is summarized in Table 16. These data are plotted in Figure 93.

Three very important assumptions have been made in the determination and subsequent use of Figure 93. The first was the use of the parameter $\frac{t_f V_f}{L V_{or}}$ rather than $\frac{V_f}{V_{or}}$. It was reasoned that V_f was not just a function of the thin plate penetration variables; an account must also be shown of the relative geometric size relationship between the bumper and projectile, which was accomplished by using the parameter $\frac{t_f V_f}{L V_{or}}$. The ratio $\left[\frac{t_f}{L} \right]$ was from the experimental data.

The second assumption was the extrapolation of the data to include a larger range of Z values. This extrapolation was necessary because of the lack of suitable data to extend the Z range in order to evaluate the elastic recovery concepts. It was reasoned that a rough approximation might be made by using a shaped curve (i.e., the slope) similar to that of an experimental core (Figure 21 of Reference 53), where the penetration depth was plotted vs. shield thickness for aluminum shields.

TABLE 16
SUMMARY OF DATA AND CALCULATIONS FOR POINTS ON FIGURE 93

Source	Experimental or Estimated Data																Calculated							
	Bumper				Projectile						Core						V _f [*] ft/sec	ρ _f [*] lb/in. ³	V _f [*] in. ³	ρ _f [*] lb/in. ³	V _f [*] ft/sec	ρ _f [*] lb/in. ³	V _f [*] in. ³	ρ _f [*] lb/in. ³
	Material	S _t [*] psi	ρ _t [*] lb/in. ³	t _f [*] in.	Material	V _p ft/sec	S _p [*] psi	S _p [*] lb/in. ³	L _p in.	Shape	V _{or} in. ³	Material	S _{cl} [*] psi	ρ _{cl} [*] lb/in. ³	t _p [*] in.									
Ref. 8	Aluminum	41,000	0.1	0.063	Steel	18,900	71,000	0.283	0.094	Cylin- drical	0.461 x 10 ⁻²	Tippersul*	135	0.0052	1	24,800	0.192	1.57 x 10 ⁻⁶	0.065	34.8 x 10 ⁻⁶	0.305	0.204		
Ref. 9	Dacron Butyral	2,500	0.04	0.073	Glass	20,000	10,000	0.09	0.063	Sphere	132 x 10 ⁻⁶	Latex	200	0.0035	1.4	20,000	0.065	34.8 x 10 ⁻⁶	0.065	34.8 x 10 ⁻⁶	0.305	0.11		

* Tippersul is a potassium titanate core and is similar to a felted core material

Note: Properties of core, bumper, and projectile were found from data given in Reference 15

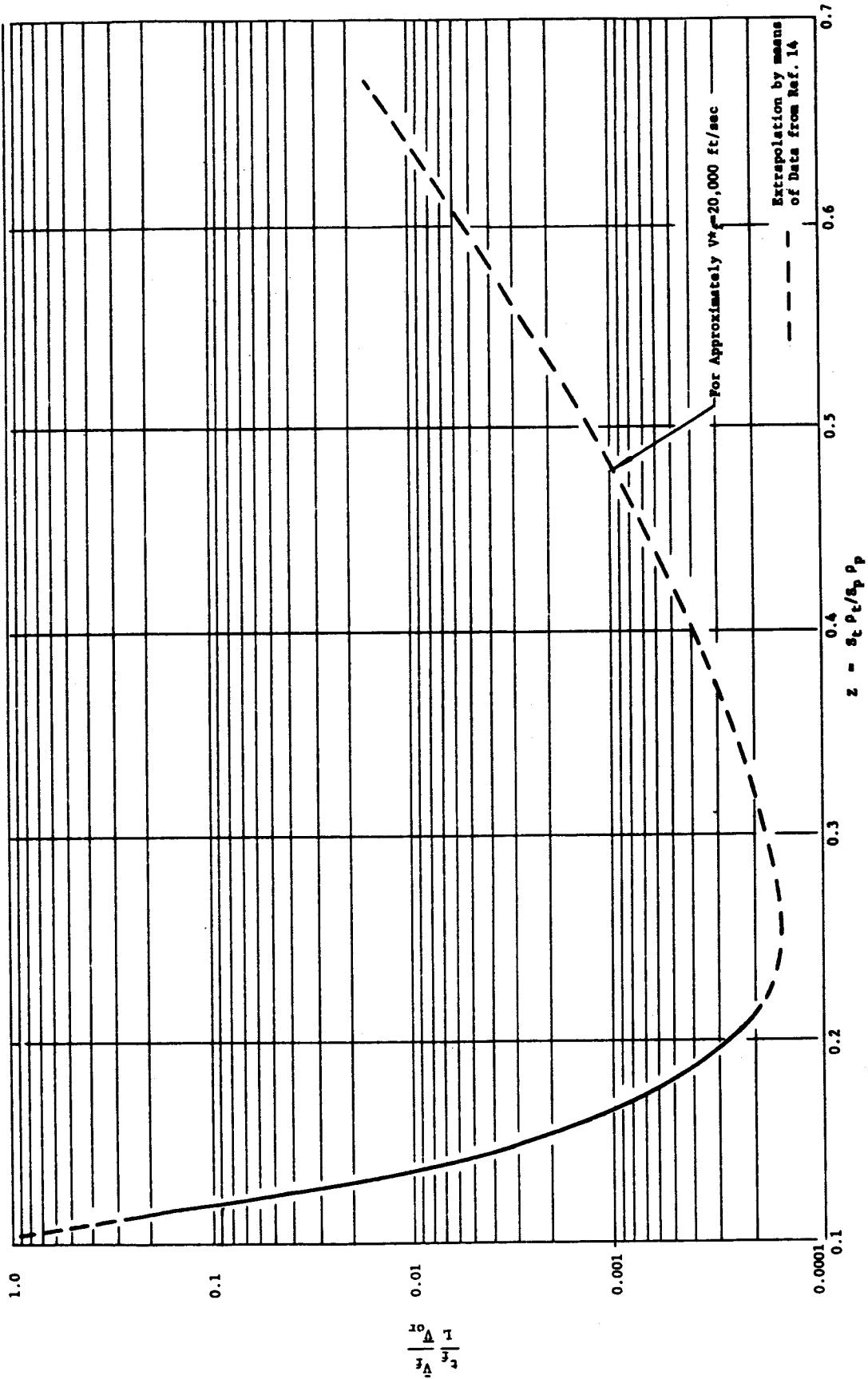


Figure 93. Estimated Variation of \bar{V}_f vs. Bumper Parameter (Z)

The third assumption was that \bar{V}_f taken from the curve of Figure 93 must be redesigned when using the average meteoroid velocity for the initial projectile. This was because it has been shown that as the projectile velocity has been increased, the bumper shield (F_1) becomes more efficient. Thus it can be reasoned by engineering judgment and formulas 4 through 7 that

$$\begin{aligned} @ V_f^* \approx 100,000 \text{ ft/sec} & \\ \text{initial projectile} & \\ \text{velocity range} & \\ & = \bar{V}_f \text{ (Figure 93)} \times \frac{(V_f^*)^{0.18}}{(20,000)^{0.449}} \dots (10) \end{aligned}$$

A second part of this assumption was to assume if $V_f^* \leq 20,000$ ft/sec, then the volume, \bar{V}_f , could be taken directly from the curve.

The next step in the development of the method of analysis for the penetration failure mode was to estimate the volume of the slower fragmented particles (\bar{V}_s). These particles are particularly dangerous, since they readily penetrate the flexible core. It was assumed the role of the second facing (two facing sandwich composite) would be to absorb these slow particles or, in the case of multiple facings, break these slower particles up again (as shown in the idealized model).

An estimate of these slower particles' volume may be obtained by the following formula:

$$\frac{\bar{V}_s}{\bar{V}_f} = \left(\frac{D_1}{D_2} \right)^2 \dots \dots \dots (11)$$

where

D_1 and D_2 are the diameters of faster and slower particle spray cone respectively (see Figure 88) and obtained from experimental data.

\bar{V}_f from Figure 93 and equation (10).

D_1 and D_2 were taken from data in Reference 47 for a combination of the following reasons:

1. The data produced different Z values.

2. There was no penetration of the innermost plate.
3. Two separated plates (facings) with no core between were used as a target specimen.
4. The spacing of these plates was optimum as predicted from experiment (i.e., 1 to 4 in.)

These data are summarized in Table 17.

Again the important assumption was that the $\frac{\bar{V}_s}{\bar{V}_f}$ is not just a function of the Z parameter, but that the geometric relationship between the shield and projectile lengths also play an important role. Thus in Figure 94,

$\frac{t_f \bar{V}_s}{L \bar{V}_f}$ was plotted vs. the Z parameter.

IV. EVALUATION OF NARMCO ELASTIC RECOVERY WALL CONCEPTS FOR METEOROID PROTECTION

Narmco's elastic recovery wall concepts are shown in Figure 95. On the basis of preliminary judgment, concepts (A) and (B) appear to be quite similar for use in meteoroid protection. Concepts (C) and (D) would not be used for design meteoroids (≈ 0.039 -gm wt.) since the thin polyester terephthalate bumper would not break up this type of meteoroid. If (C) and (D) concepts were used for the very small meteoroids ($< 10^{-4}$ gm), they would have more weight (thus less efficiency) than concepts (A) or (B).

It appears, then, that the wall concepts may be essentially formed into two basic ideas: X_1 and X_2 . These ideas are illustrated in Figure 96.

The criterion for judging which wall idea is best when considering penetration was assumed to be weight. Hence, if:

- (1) $t_{p1} < t_{f2} + c_2 + t_{p2}$, X_1 is more efficient
 or
 (2) $t_{p1} > t_{f2} + c_2 + t_{p2}$, then X_2 is more efficient

TABLE 17
 SUMMARY OF EXPERIMENTAL AND CALCULATED DATA* TO ESTIMATE \bar{V}_s

Point	Bumper				Projectile						$\frac{t_f}{L}$	$\left(\frac{D_1}{D_2}\right)^2$	$\frac{t_f}{L} \frac{\bar{V}_s}{\bar{V}_f}$
	Material	ρ_t , lb/in. ³	S_t , psi	t_f , in.	Material	ρ_p , lb/in. ³	S_p , psi	L, in.	$\frac{S_t \rho_t}{S_p \rho_p}$	D_1 , in.			
1	Aluminum	0.10	35,000	0.125	Steel	0.283	75,000	0.094	0.1645	3	1.5	4.0	5.33
2	↑	↑	↑	0.125	↑	↑	↑	↑	↑	4.5	2.25	4.0	5.33
3	↑	↑	↑	0.09	↑	↑	↑	↑	↑	2.75	1.25	4.9	4.68
4	↑	↑	↑	0.09	↑	↑	↑	↑	↑	3.5	1.3	7.28	<u>6.96</u>
													AV. 5.6
5	Aluminum	0.10	35,000	0.09	Copper	0.323	22,000	0.094	0.494	2.25	1.0	5.06	4.85
6	Glass	0.09	10,000	0.094	Steel	0.283	75,000	0.094	0.0424	2	0.5	16	16.0

* Data from Reference 47

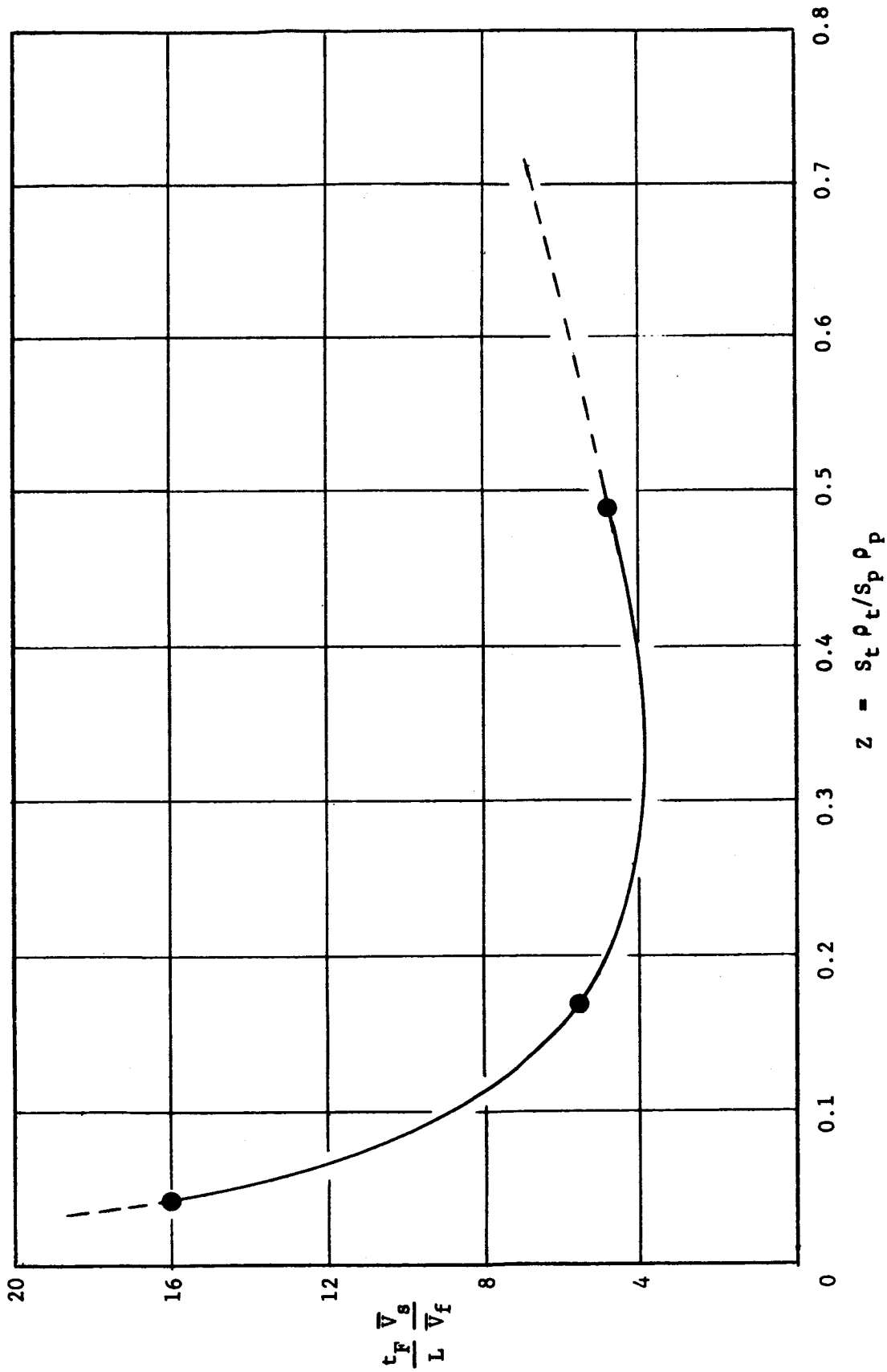


Figure 94. $\frac{t_F \bar{V}_g}{L \bar{V}_f}$ vs. Z as Determined from Table 16

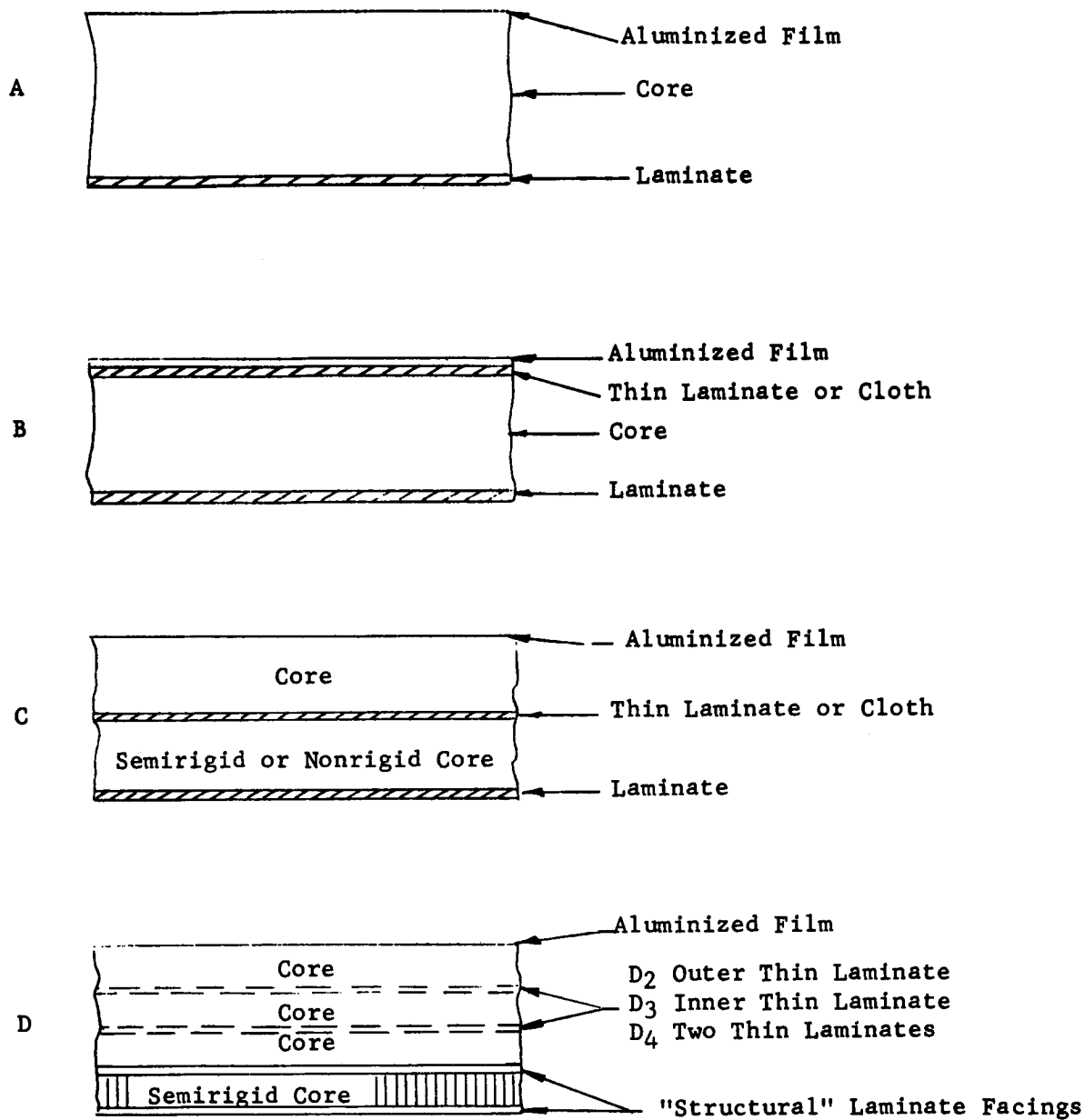
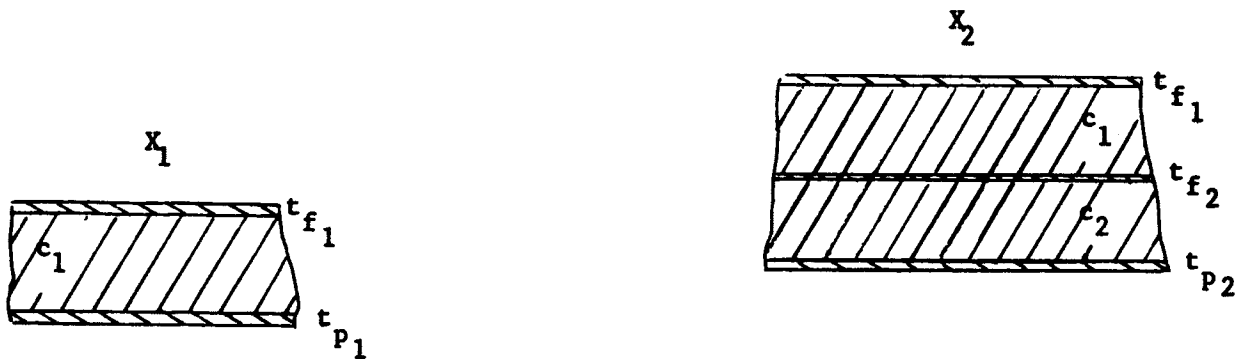


Figure 95. Wall Concepts for Expandable Space Structures



where t_{f1} = Thickness to fracture initial meteoroid

t_{f2} = Thickness required to fracture the \bar{v}_s of the first projectile breakup

t_{p1} = Thickness to absorb \bar{v}_s after first projectile breakup

t_{p2} = Thickness to absorb \bar{v}_s after second fracture by t_{f2}

c_1, c_2 = Cores

Figure 96. Two Basic Narmco Elastic Recovery Wall Concepts for Meteoroid Protection

Next, evaluation of the wall ideas X_1 and X_2 with the previously derived analysis method must be prepared.

1. Design Meteoroid

The design meteoroid was assumed to have the following properties:

$$\rho_p = 2 \text{ grams/cm}^3 = 0.0725 \text{ lb/in.}^3 \text{ (Reference 55)}$$

$$V = 30.5 \text{ km/sec} = 100,000 \text{ ft/sec}$$

$$m_c = \text{critical mass} = 0.039 \text{ gm (0.999 probability) (Reference 53)}$$

$$S_t = 10,000 \text{ psi (assumed for glasslike material)}$$

$$V_c = \frac{m_c}{\rho_p} = \frac{0.039}{454 \times 0.0725} = 1.18 \times 10^{-3} \text{ in.}^3$$

Shape - Sphere (Reference 56)

$$L = \text{meteoroid diameter} = 0.125 \text{ in. (Reference 57)}$$

A. Penetration Failure Mode

1. Compute t_f for the first facing

Assume typical facing material (TFM) properties are

$$S_t = 7700 \text{ psi}$$

$$\rho_t = 0.058 \text{ lb/in.}^3$$

$$\therefore \text{ Using above data } Z = \frac{S_t \rho_t}{S_p \rho_p} = \frac{7700 \times 0.058}{10,000 \times 0.0752} = 0.615$$

$$\text{From Figure 91, } \frac{t_f}{t_p} = 0.06$$

Then, using equation (7),

$$\begin{aligned} t_f &= (0.06)(1.5)(0.97) V^{0.18} \rho_p^{0.26} \rho_t^{-0.46} S_t^{-0.04} \bar{V}_c^{1/3} \\ &= 0.0874(100,000)^{0.18} (0.0725)^{0.26} (0.058)^{-0.46} (7700)^{-0.04} (1.18 \times 10^{-3})^{1/3} \\ t_f &= \underline{0.10 \text{ in.}} \end{aligned}$$

2. Final V_f^* and V_s^*

For Facing 1

$$\frac{\text{wt. of shield/unit area}}{\text{wt. of projectile/unit area}} = 0.64$$

From Figure 92

$$V_f^* = 1.2 \times 100,000 = 120,000 \text{ ft/sec}$$

$$V_s^* = 0.1 \times 100,000 = 10,000 \text{ ft/sec (for conservative design)}$$

3. Find the thickness of the Core C_1

Many factors enter into the selection of the "right" core density. For example, a core which is too dense will not allow the energy to dissipate and therefore increases penetration. On the other hand, a core which is too light will not offer any particle resistance. Core density from approximately 1.5 to 4 lb/ft³ appears optimum.⁽⁴⁸⁾ The core used in the elastic recovery concept averages about 1.35 lb/ft³ which is assumed to be valid for this range. Hence, all the core thickness calculations are based on this density.

Thus, for the core in this analysis,

$$\rho_c = \frac{1.35}{1728} = 0.000783 \text{ lb/in.}^3$$

It will be assumed that this core also is polyurethane with the following shear property:

$$S_{t_c} = 40 \text{ psi (Reference 54)}$$

Thus, the following data are found for computing C_1 :

$$V_f^* = 120,000 \text{ ft/sec}$$

$$S_{t_c} = 40 \text{ psi}$$

$$\rho_E = \frac{\rho_t + \rho_p}{2} = \frac{0.058 + 0.0725}{2} = 0.065 \text{ lb/in.}^3$$

From Figure 93 for $z = 0.615$

$$\frac{t_f \bar{V}_f}{L \bar{V}_{or}} = 8 \times 10^{-3}$$

and $\bar{V}_{or} = 1.18 \times 10^{-3} \text{ in.}^3$

$$0.785 \frac{\bar{V}_f}{1.18 \times 10^{-3}} = 8 \times 10^{-3}$$

$$\therefore \bar{V}_{f_{20,000 \text{ ft/sec}}} = \frac{1.18 \times 8 \times 10^{-6}}{0.785} = 12 \times 10^{-6} \text{ in.}^3$$

$$\bar{V}_f @ V_f\text{-ft/sec} = V_{f_{20,000 \text{ ft/sec}}} \times \frac{V_f^{*0.18}}{(20,000)^{0.449}} \quad \text{From Equation 10}$$

$$\bar{V}_{f_{120,000 \text{ ft/sec}}} = 12 \times 15^6 \times \frac{(120,000)^{0.18}}{(20,000)^{0.449}}$$

$$= 12 \times 10^{-6} \times 0.093$$

$$\bar{V}_{f_{120,000 \text{ ft/sec}}} = 1.12 \times 10^{-6} \text{ in.}^3$$

Then using equation (7),

$$t'_p = (1.5)(0.97) V^{0.18} \rho_E^{0.26} \rho_{t_c}^{-0.46} S_{t_c}^{-0.04} \bar{V}_f^{1/3}$$

$$= (1.5)(0.97)(120,000)^{0.18} (0.065)^{0.26} (0.000783)^{-0.46} \times$$

$$(40)^{-0.04} (1.12 \times 10^{-6})^{1/3}$$

$$= 1.4 \text{ in. of core}$$

4. To find the second facing thickness, assume that it must absorb the slow particles. Then,

$$\frac{t_f \bar{V}_s}{L \bar{V}_f} = 6 \quad (\text{From Figure 94})$$

$$\text{Then } 0.785 \frac{\bar{V}_s}{1.12 \times 10^{-6}} = 6$$

$$\text{Using equation (4), } \bar{V}_{s1} = \frac{1.12 \times 6 \times 10^{-6}}{0.785} = 8.55 \times 10^{-6} \text{ in.}^3$$

$$\text{with } \rho_p = 0.065 \text{ lb/in.}^3$$

$$\rho_t = 0.058 \text{ lb/in.}^3$$

$$S_t = 7700 \text{ psi}$$

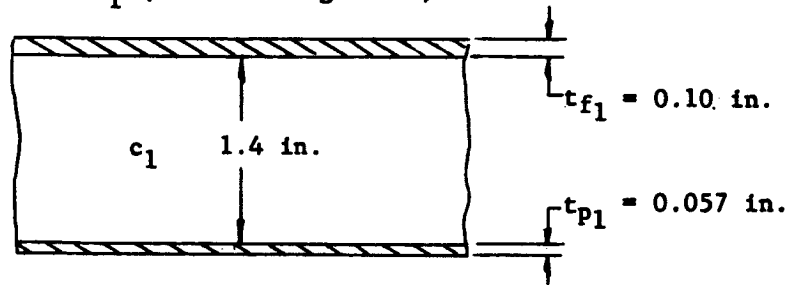
$$V_s^* = 10,000 \text{ ft/sec}$$

$$t_p' = (1.5)(0.772) V_s^{0.893} \rho_p^{0.979} S_t^{-0.457} \rho_t^{-0.35} (\bar{V}_s)^{1/3}$$

$$t_p' = (1.5)(0.772)(10,000)^{0.893} (0.065)^{0.979} (7700)^{-0.457} \times (0.058)^{-0.35} (8.55 \times 10^{-6})^{1/3}$$

$$t_p' = \underline{0.057 \text{ in.}} = t_{p1}$$

This completes the task of finding the weight for meteoroid protection, using the basic idea X_1 (shown in Figure 97).



$$\text{Wt.} = 144 \times 0.157 \times 0.058 = 1.31 \text{ lb/ft}^2$$

$$144 \times 1.4 \times \frac{1.35}{1728} = \underline{0.158 \text{ lb/ft}^2}$$

$$\text{Total } 1.468 \text{ lb/ft}^2$$

$$t_{p1} = 144 \times 0.058 \times 0.057 = 0.476 \text{ lb/ft}^2$$

Figure 97. Basic Idea X_1 and Weight Required for Meteoroid Penetration

5. Find t_{f_2} for basic idea X_2 from the previous calculations

$$\frac{t_{f_2}}{t'_p} = 0.06$$

$$t_{f_2} = 0.06 \times 0.057 = \underline{0.0034 \text{ in.}}$$

6. $V^*_{f_2}$ also using previous calculations

$$V^*_{f_2} = 1.2 \times 10,000 \text{ ft/sec} = 12,000 \text{ ft/sec}$$

7. Assume $\frac{t_{f_2}}{L} =$ same as previous ratio $= 0.785$

8. From Figure 93,

$$\frac{t_f}{L} \frac{V_{f_2}}{V_{s_1}} = 8 \times 10^{-3}$$

$$\bar{V}_{f_2} = \frac{8 \times 8.55 \times 10^{-9}}{0.785} = 87.4 \times 10^{-9} \text{ in.}^3$$

9. Using equation (4), the above data, and $\rho_E = \frac{0.065 + 0.058}{2}$
 $= 0.061 \text{ lb/in.}^3$ to compute the thickness of the core C_1 ,

$$\begin{aligned} t'_p &= 0.258 V^{0.893} \rho_E^{0.979} S_{tc_2}^{-0.457} \rho_c^{-0.350} (\bar{V}_f)^{1/3} \\ &= 0.258 (12,000)^{0.893} (0.061)^{0.979} (40)^{-0.457} (0.000783)^{-0.35} \times \\ &\quad (87.4 \times 10^{-9})^{1/3} \end{aligned}$$

$$\therefore t'_p = \underline{0.728 \text{ in.}}$$

10. To find the volume of the slow particles after the second fracture

$$\frac{t_f \bar{v}_{s_2}}{L \bar{v}_{s_1}} = 6 \text{ (from Figure 94)}$$

$$0.785 \frac{\bar{v}_{s_2}}{87.4 \times 10^{-9}} = 6$$

$$\bar{v}_{s_2} = \frac{87.4 \times 6 \times 10^{-9}}{0.785} = 670 \times 10^{-9} \text{ in.}^3$$

11. To find $v_{s_2}^*$ by using Figure 92

$$v_{s_2}^* = 0.1 \times 10,000 = 1000 \text{ ft/sec}$$

12. Assuming equation (4) applies at the 1000-ft/sec velocity, then

$$\begin{aligned} t_p' &= 0.258 v^{0.893} \rho_E^{0.979} s_t^{-0.457} \rho_t^{-0.350} (v_{s_2})^{1/3} \\ &= 0.258 (1000)^{0.893} (0.061)^{0.979} (7700)^{-0.457} (0.058)^{-0.35} \times \\ &\quad (670 \times 10^{-9})^{1/3} \end{aligned}$$

$$t_p' = 0.0033 \text{ in.} = t_{p_2}$$

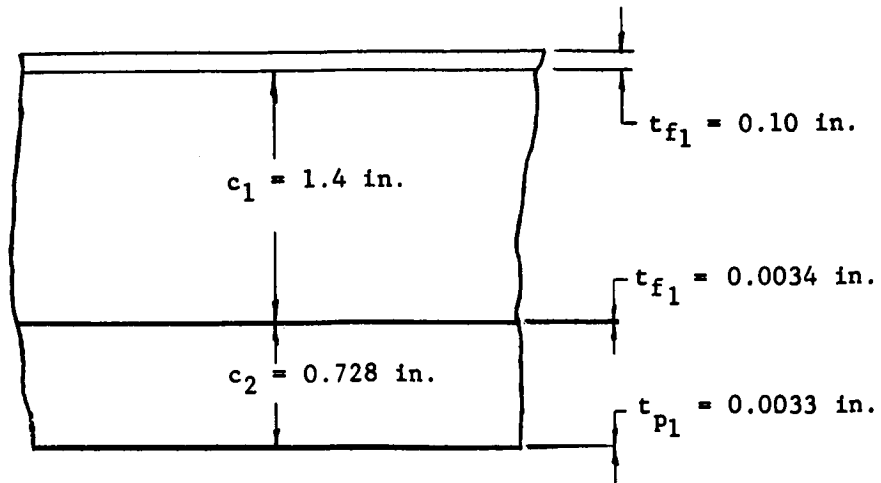
13. The concept X_2 may now be given along with its total weight per ft^2 (see Figure 98).

14. Using weight efficiency as the criterion, the basic idea X_2 is obviously more efficient, from a penetration standpoint. Thus

$$t_{p_2} > t_{f_2} + c_2 + t_{p_2}$$

$$0.476 > 0.146$$

This, of course, would be expected if the meteoroid bumper concept is followed throughout the various layers.



$$\text{Wt.} = 144 \times 0.058 \times 0.1067 = 0.890 \text{ lb/ft}^2$$

$$144 \times 2.128 \times \frac{1.35}{1728} = 0.249 \text{ lb/ft}^2$$

$$\text{Total} = 1.139 \text{ lb/ft}^2$$

$$t_{f_2} + c_2 + t_{p_2} = 0.0067 \times 144 \times 0.058 = 0.056 \text{ lb/ft}^2$$

$$+ 144 \times 0.728 \times \frac{1.35}{1728} = 0.0896 \text{ lb/ft}^2$$

$$\text{Total} = 0.1456 \text{ lb/ft}^2$$

Figure 98. Basic Idea X_2 and Weight Required for Meteoroid Penetration

B. Spallation/Delamination Failure Mode

The basic method of analysis for spallation/delamination has been discussed. The following steps will analyze the basic wall concepts presented in Figure 11.

1. To compute P_1 in Figure 90, using equation (2),

$$P_1 = \frac{E [\Delta (\Delta - 1)]}{[\Delta - (\Delta - 1) K_s]^2} \dots \dots \dots (2)$$

The following have been estimated for a TFM laminate:

- E = 850,000 psi (typical)
- $\Delta = 1.3$
- $K_s = 1.19$ (Reference 45)

$$\begin{aligned} \therefore P_1 &= 0.85 \times 10^6 \frac{1.3(1.3 - 1)}{[1.3 - (1.3 - 1) 1.19]^2} \\ &= 0.85 \times 10^6 \times 0.437 \end{aligned}$$

$$\sigma_I = P_1 = \underline{0.371 \times 10^6 \text{ psi}}$$

2. To compute P_2 ,

$$\frac{\bar{V}_{f1}}{\bar{V}_{or}} = \frac{1.12 \times 10^{-6}}{1.18 \times 10^{-3}} = 0.95 \times 10^{-3}$$

$$\therefore P_2 = P_1 \frac{\bar{V}_{f1}}{\bar{V}_{or}} = 0.37 \times 10^6 \times 0.95 \times 10^{-3} = 0.35 \times 10^3$$

$$P_2 = 350 \text{ psi}$$

3. To compute the reflected and transmitted stresses at I_2 (Figure 87) using P_2 and equations (1)

$$\rho c = \sqrt{E \frac{\rho}{g}}$$

For core:

$$\rho_c C_c = \sqrt{E_c \frac{\rho_c}{g}} = 150 \times \frac{0.000783}{386} = 0.0174$$

For TFM:

$$\rho_{TFM} C_{TFM} = \sqrt{E_{TFM} \frac{\rho_{TFM}}{g}} = \sqrt{850,000 \times \frac{0.058}{386}} = 11.3$$

E_c under impact loading is assumed to be 150 psi for polyurethane core (Reference 54).

At Interface 2 (I_2)

$$\sigma_R = \frac{\rho_2 C_2 - \rho_1 C_1}{\rho_2 C_2 + \rho_1 C_1} \sigma_I = \frac{11.3^{-0.0174}}{11.3^{+0.0174}} \times 350 \approx 350 \text{ psi}$$

$$\sigma_T = \frac{2 \rho_1 C_1}{\rho_2 C_2 + \rho_1 C_1} \sigma_I = \frac{2 (0.0174)}{11.474} 350 \approx 1.0 \text{ psi}$$

The σ_R is a tension wave, and since the core allowable under impact loading in tension is estimated to be 60 psi (Reference 54). The core at interface I_2 will be pulled loose.

4. If the basic two-facing concept, X_1 , is used, then facing 2 will receive a pulse

$$\begin{aligned} P_3 &= P_1 \frac{\bar{V}_s}{\bar{V}_{or}} = 0.371 \times 10^6 \times \frac{8.55 \times 10^{-6}}{1.18 \times 10^{-3}} \\ &= 0.371 \times 10^6 \times 7.24 \times 10^{-3} \\ P_3 &= 2.68 \times 10^3 = 2680 \text{ psi} \end{aligned}$$

This will be reflected at the innermost surface of F_2 as a tension wave. Since it has been estimated that about 3500 psi is required

to delaminate a facing, F_2 will not delaminate or eject dangerous spall particles.

5. It can then be stated that X_1 is safe from the criteria of failure.
6. If the basic idea X_2 is used, then the pressure into the core C_1 (I_3 is assumed to fail) would be

$$\begin{aligned}
 P_4 &= P_3 \frac{\bar{V}_{f_2}}{\bar{V}_{a_1}} = 2.68 \times 10^3 \times \frac{87.9 \times 10^{-9}}{8.55 \times 10^{-6}} \\
 &= 2.68 \times 10^3 \times 10.3 \times 10^{-3} \\
 &= 27.5 \text{ psi}
 \end{aligned}$$

7. At interface I_4

$$\begin{aligned}
 \sigma_R &= \frac{\rho_2 C_2 - \rho_1 C_1}{\rho_2 C_2 + \rho_1 C_1} P_4 = -.975 \times 27.5 = 26.8 \text{ psi} \\
 \sigma_I &= \frac{2 \rho_1 C_1}{\rho_2 C_2 + \rho_1 C_1} P_4 = 0.7 \text{ psi}
 \end{aligned}$$

Since the core is assumed to be good under impact loading up to 60-psi tension I_4 will not fail due to the core failure.

8. At the facing F_3

$$\begin{aligned}
 P_5 &= P_3 \frac{\bar{V}_{s_2}}{\bar{V}_{s_1}} = 2.68 \times 10^3 \frac{670 \times 10^{-9}}{8.55 \times 10^{-6}} \\
 &= 2.68 \times 10^3 \times 78.3 \times 10^{-3} \\
 &= 210 \text{ psi}
 \end{aligned}$$

9. $P_5 = 210$ psi will be reflected as a tension wave and therefore, since 3500 psi is required to delaminate or reject spall, the facing F_3 will not fail.

In summary, the X_1 concept will fail at each of its interfaces, but will not allow dangerous ejecta from the facing F_1 . The X_2 concept was best, of course, since it neither failed at the interface I_4 nor allowed ejecta to be thrown from facing F_3 .

The final conclusion is that the basic idea X_2 is the best method of protection against both the penetration and spallation/delamination failure modes. The X_2 concept shall be used to estimate the spacecraft weight requirements in the next section.

V. FINAL WEIGHT ESTIMATION REQUIRED BY SPACECRAFT USING ELASTIC RECOVERY WALL CONCEPT

In order for the spacecraft designer to predict the amount of protection necessary for meteoroid impact, he must estimate the critical mass the vehicle might encounter, based on the mission time and exposure area. In this analysis, Whipple's estimate of the meteoroid flux is considered to be sufficient. Thus, as given by Reference 53:

$$N = \varphi_c A_1 T \dots \dots \dots (12)$$

where N = Number of damaging impacts that will occur
in mission time T

A_1 = Area of exposure (meters²)

φ_c = Meteor flux rate (Whipple)

Thus from Reference 53

$$N = 1.3 \times 10^{-12} m^{-1} A T \dots \dots \dots (13)$$

where m = Mass of meteoroid (grams)

The probability of no damaging impacts is given as: $P(0) = e^{-N}$.

Then the critical mass (i.e., maximum mass that will occur in given area and mission time) is

$$m_c = \frac{1.3 \times 10^{-12} A T}{-\log e [P(0)]} \dots \dots \dots (14)$$

A range of critical meteoroid masses and the probability of no punctures have been taken from Reference 53 and listed in Table 18. By assuming an exposed spacecraft area of 225 ft², the weight of an aluminum single sheet bumper and the elastic recovery composite wall was also obtained. The results of the calculations were listed in the last two columns of Table 18 and are also plotted in Figures 99 and 100.

Since the design meteoroid and its properties have been chosen, one may calculate the protection weight required if a new critical mass meteoroid is used, provided the density is the same (by ratios of the different meteoroid volume) to that assumed in this analysis; e.g., in Table 18 the critical mass is given as:

$$m_c = 0.00037 \text{ grams} = \frac{0.00037}{454} = 0.815 \times 10^{-6} \text{ lb}$$

The volume of this critical mass is then

$$V_c = \frac{m_c}{\rho_p} = \frac{0.815 \times 10^{-6}}{0.725 \times 10^{-1}} = 1.12 \times 10^{-5} \text{ in.}^3$$

By the ratio of the weights, the volume of the design meteoroid (0.039 gm weight) was found to be

$$V_{c0.039 \text{ g}} = 1.18 \times 10^{-3} \text{ in.}^3$$

The ratio of the volumes then (using equation 7) is

$$\left(\frac{1.18 \times 10^{-3}}{1.12 \times 10^{-5}} \right)^{1/3} = \left(1.08 \times 10^2 \right)^{1/3} = 4.72$$

TABLE 18

DATA FOR FINAL WEIGHT ESTIMATE FOR METEOROID PROTECTION OF A SPACECRAFT

Mission	Duration, Days	Duration, hr (T)	Spacecraft Area, ft ²	AT, ft ² -hr	Probability of No Punctures	Critical Mass, g	Wt. of Best Concept,* lb/ft ²	Wt. of Single Aluminum Shield** Lb/ft ²
Moon	14	336	225	7.35×10^4	0.90	3.7×10^{-4}	0.242	3.02
					0.999	3.9×10^{-2}	1.14	14.2
Venus	320	76.8×10^2	225	1.73×10^6	0.90	8.5×10^{-3}	0.71	8.52
					0.999	9×10^{-1}	3.24	40.6
Mars	500	120×10^2	225	2.71×10^6	0.90	1.3×10^{-2}	0.792	9.94
					0.999	1.4	8.16	46.8

* Elastic recovery concept

** Wt. derived from Reference 53 using Eichelberger-Gehring equations of penetration (Reference 58). It has been ratioed down from Reference 53 to account for the difference in the density of the design meteoroid. This ratio was $(2.8/2)^{1/3} = 1.12$; i.e., the weights in Reference 53 have been divided by 1.12

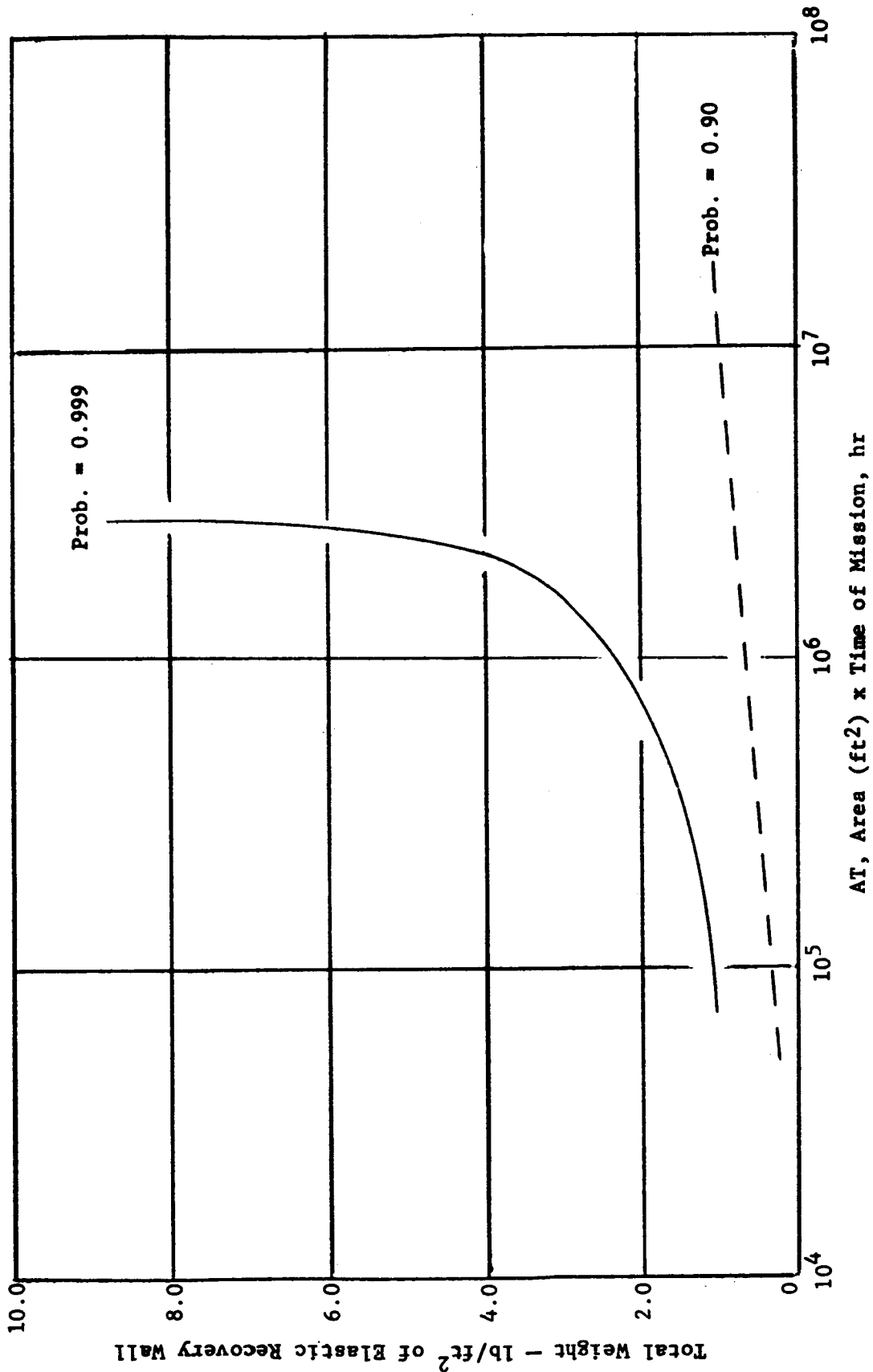


Figure 99. Estimate of Weight Required for Meteoroid Protection Using "Best" Elastic Recovery Wall Concept vs. Exposed Area (ft²) of Spacecraft x Time of Mission (hr)

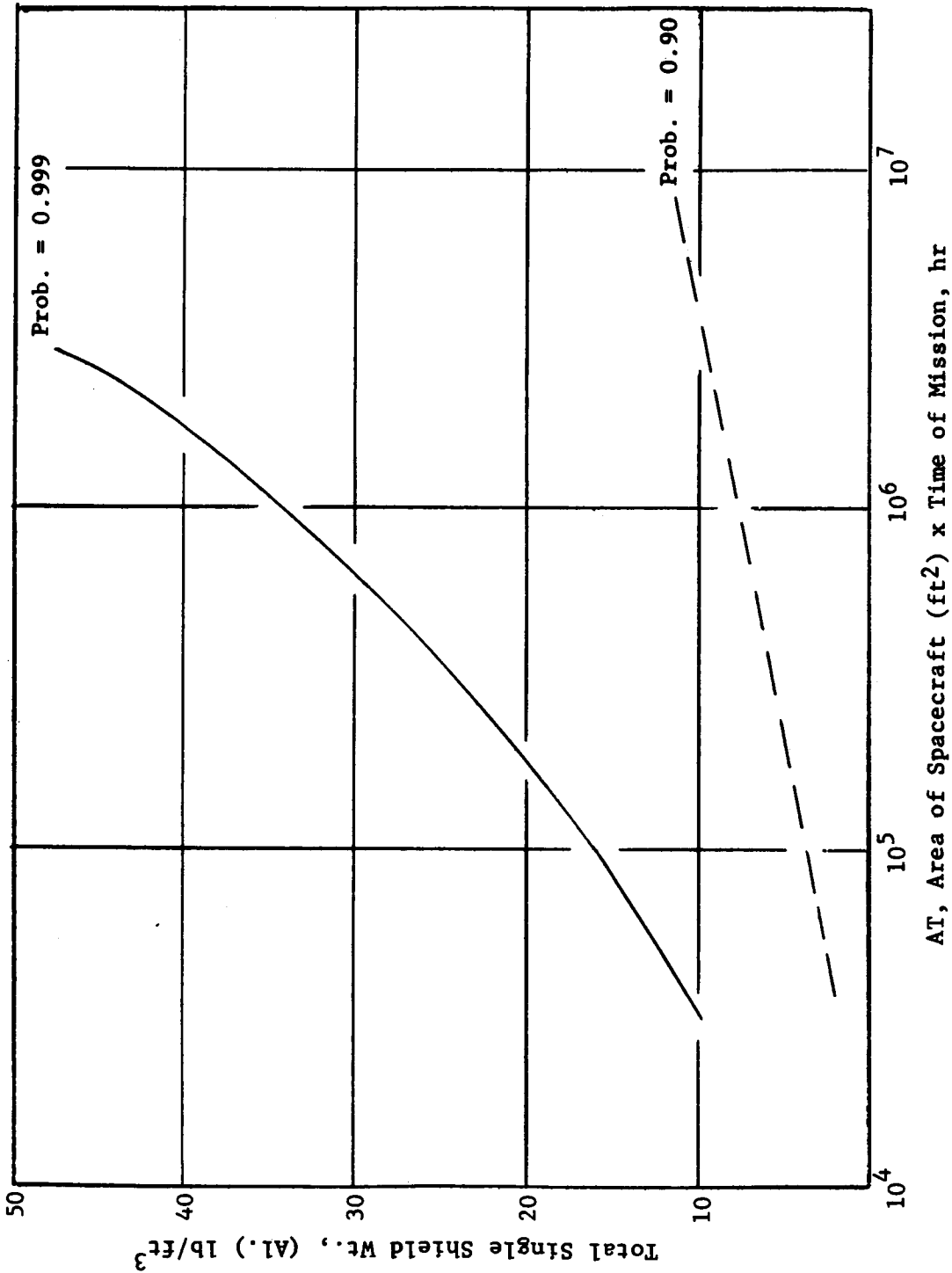


Figure 100. Weight of Single-Sheet Aluminum Required for Meteoroid Protection vs. Area of Spacecraft (ft²) x Time of Mission (hr) Using Eichelberger and Gehring Formulas (Reference 53)

Weight required using 0.039-gm meteoroid for the best wall concept is 1.14 lb/ft² (from Figure 98).

Hence, the weight required for 0.00037-gm meteoroid protection would be

$$\frac{1.14}{4.72} = 0.242 \text{ lb/ft}^2$$

The other values for different weight meteoroids was obtained in the same way.

These data for the weight of the elastic recovery best wall concept are plotted in Figure 99 using the area of the spacecraft (ft²) x mission time in hours.

Figure 100 is presented to show a comparison of sandwich elastic recovery concepts with that of single-sheet aluminum shields.

VI. CONCLUSIONS

The overall conclusions of this analysis are listed as follows:

1. The results of this study indicate that the elastic recovery composite would be lighter and more efficient than single-sheet aluminum shields in preventing a puncture from a critical mass meteoroid.
2. Spallation as such apparently will not occur with the elastic recovery composite. However, local delamination would be expected within the composite.
3. The curves developed during this investigation are adaptable for determining the protection required for different critical mass meteoroids.
4. This analysis on the prevention of meteoroid penetration has been a study only, and as such will require experimental verification.

APPENDIX E

EVALUATION OF SPACE RADIATION SHIELDING PROPERTIES FOR ELASTIC RECOVERY EXPANDABLE MATERIALS

Abstract

The purpose of this report was to determine the effectiveness of materials in the elastic recovery composite when subjected to radiation. A study was made to determine the type of radiation missions in space would encounter. The different types of radiation such as that trapped in the Van Allen belts and from solar flares were discussed.

Due to the complex nature of the various types of radiation, an experimental procedure was developed to obtain the protective characteristics of the elastic recovery material. The equipment used for this procedure included a low pressure chamber, detecting equipment, isotopic sources, and readout equipment. The isotopic sources were used because of the relative simplicity for their use. The sources used include α , β , radiation for calibration and γ radiation for tests.

Each of the components of the elastic recovery composite were tested for their effectiveness against the radiation. The results of the test were based upon an aluminum index since its effectiveness based upon atomic number is well known. The comparison of the material's "effective atomic number" was made as a result of the tests. The tests indicated that the elastic recovery materials and a lower, "effective atomic number" (hence, more effectiveness) than the aluminum index against the proton radiation. A further reduction in the effective atomic number occurred when carbon was added to the foam or laminate resin.

APPENDIX E

EVALUATION OF SPACE RADIATION SHIELDING PROPERTIES FOR ELASTIC RECOVERY EXPANDABLE MATERIALS

by

C. E. Wolcott

I. INTRODUCTION

Because the basic nature and ultimate intended application of elastic recovery expandable structures implies a space environment, it is considered most reasonable to assume this environment will contain some level of harmful radiation. In view of this consideration, Narmco Research & Development has conducted a basic investigation to determine the radiation absorption characteristics of certain elastic recovery materials.

A large number of possible expandable structures uses may necessarily require close scrutiny of radiation shielding properties, particularly where a biological absorbed dose is of concern (e.g., airlocks, lifeboats, connecting tube chambers, work spaces, and personnel shelters). However, the radiation environment will most likely be defined by the particular mission contemplated and the shield effectiveness will thus be defined on mission terms. The very wide range of particle energies and flux density which could be involved in the case missions other than near the earth will undoubtedly require a critical inventory of all mass which may serve as shielding. On the other hand, should the expandable structure be required to serve as an equipment shelter, wall thickness and materials selected in the wall design may adequately limit the allowable radiation to acceptable levels.

Although the radiation absorption coefficients of most basic materials are known, most of these data are not reasonably usable in defining most composite aerospace materials. This is the case with the elastic recovery materials considered for expandable structures. The reason for this lack of reference data is that most materials contemplated for aero-

space applications are composites which vary with manufacturing processes. A manufacturing technique factor is also considered where seemingly similar structural composites are not necessarily identical. Composites such as laminates, which may contain several plastic components as well as glass fabric, is one of the more common examples. A particular fabric selection from the various available fabrics also enters into this consideration.

If all the component ratios, distribution and atomic numbers Z , of a given composite material are known, the effective radiation shield properties of the material can be calculated. In the usual case, however, this is quite difficult and often impractical. For example, determining shield effectiveness by calculation for screening a series of composite materials or a structural assembly of composites is desirable, but becomes impractical when considering other methods available.

In view of the difficulty encountered with calculating shield effectiveness, a more logical approach would be to evaluate by actual simulation. This approach first considers a particle acceleration as a feasible source of radiation. As will be noted in a following discussion, however, radiation energy levels which could be involved would require extrapolation of the data obtainable from available testing facilities. In addition, desirable data should be obtained on the materials tested in a reasonably simulated environment, which in this instance would be very low-pressure atmospheric or space simulation. This approach is not the most economical for screening materials in order to select those most suitable, but would be more applicable to final evaluations.

A fundamental approach to material screening leads to the consideration of radioactive isotopic sources. Although such sources of radiation do not produce the particles to be encountered in space, a method is considered to allow the material relative radiation absorption coefficient index to be established. The establishment of this index thus permits extrapolation for higher radiation energy levels to obtain a relative figure of

merit on the screened composite materials. This basically describes the procedure used to evaluate the radiation shield effectiveness of the elastic recovery materials.

Since it has been reasonably established that the space radiation of most concern is solar flare and Van Allen belt protons, the following investigations shall examine the proton stopping power for each of the elastic recovery materials over the proton energy range from 1.0 MeV to 1.0 BeV. In terms of dose, light elements are the most effective proton shields. Bremsstrahlung dose rates are directly related to the square of the atomic number, Z . A relative composite atomic number \bar{Z} is determined for each of the elastic recovery materials and the effects of carbon loading investigated. This is a particularly significant investigation, since it has been determined that the neutron dose exceeds the proton dose in aluminum hull spacecraft when the hull thickness is greater than 6.6 cm. Considering the proton flux which can be anticipated in the radiation belt, the neutron dose rate is expected to constitute a serious biological hazard. (59)

II: ELEMENTARY CONSIDERATIONS

A. The Radioactive Space Environment

Although the primary intent of this reported study is to present radiation shielding data upon elastic recovery materials investigated by Narmco, some considerations which relate to the practical environmental expectations will be discussed. Because the intended environment could be either those solar areas near the Earth or extended into deep space, environmental extrapolation should consider the various possibilities. Since the primary consideration of the reported material evaluations concerns radiation shielding, the effect of material deterioration due to radiation exposure will be neglected.

Much has been learned about the phenomena of radiation in space through the use of orbital and probe vehicles with monitor instrumentation. These data are hardly sufficient, however, to encompass and adequately relate all of the anticipated space phenomena to fulfill all the requirements for solar radiation shield designs.

Since the Second International Polar Year, numerous data have been collected and theories proffered to relate the various magnetic and radiation phenomena occurrences in space affecting the earth environment. Unfortunately, this extensive effort was limited to those studies and data accumulation which could be accomplished from within Earth's atmosphere. Most of these data concern the record of events by means of radio propagation studies, radio sounding, and sunspot activity studies.

Two instances of solar simulation investigations are known which seemingly appear to reproduce, by simulation, the radiation phenomenon found in space. This approach appears to be a feasible means of simulating the radiation behavior through the entire solar system.

At Bruache AEG in 1928, German physicist Terella simulated energetic particle entrapment by a magnetic dipole representative of Earth's magnetic field.⁽⁶⁰⁾ These investigations concerned the theories of Fredrik Carl Störmer and were conducted by employing a vacuum chamber containing fluorescing gas into which energetic particle streams were injected. Particle entrapment by the Earth dipole simulation occurred in the form of the well-known Van Allen belt configuration. A similar instrumentation approach and simulation was conducted by Dr. Willard H. Bennett of the Naval Research Laboratory with similar results.

Thus, in view of recent experimentation by space instrumentation vehicles, the major influence of magnetic fields upon space radiation appears well founded. An extrapolation of magnetic theory, therefore, could serve as the means of implying radiation event levels throughout the space of our solar system. However, a brief discussion of the magnetic Earth environment should first be considered.

1. The Earth's Magnetic Field

On the basis of potential theory, it may be shown that the Earth's main field rises from sources within the Earth itself. The nature of the source is a continuing enigma, but the most plausible theory is based upon an ordered turbulence within a molten core. A theory has also been considered which develops the field externally by means of great dynamo currents produced cylindrically about the Earth. Theoretically, such currents can be shown to exist.

As the surface of the Earth is penetrated to extensive depths, the composition temperature increases and the density increases greater than 10 times that of water. The plausible theory considers that at about one-half Earth radius, matter becomes molten; thus, the Earth has a liquid core moving in a slow irregular motion. Electric currents are generated in the core by dynamo action to produce molecular orientation resulting in the magnetic field and, consequently, the magnetic dipole.

The external field is generally assumed to approximate a magnetic sphere having its dipole moment located at the sphere center. The axis of the magnetic dipole is inclined approximately 11.4 degrees to the Earth's celestial axis and drifts slowly with time. This drift is referred to as secular variation. Perturbations are observed in the magnetic field near the Earth's surface and may be explained by the nonuniformity in the permeability of the Earth's crust. The observed effect of these perturbations is significant considerably beyond the ionospheric F-region in radio propagation studies.

Due to the surface perturbations, points exist, where the magnetic field is perpendicular to the Earth's surface, which do not coincide with the geomagnetic poles defined by the unperturbed field. These magnetic points of discontinuity are referred to

as dip poles. These anomalies appear constant at a given location; however, by employing a time scale of days, hours, or minutes, and highly sensitive instrumentation, one finds that the field is constantly varying at any point on the Earth's surface. These variations are classified diurnal as occurring in mean solar-day cycles, and are similar in appearance from day to day. It therefore seems reasonable to consider the possible existence of a relation between magnetic perturbation and trapped radiation fluctuation.

2. The Ionospheric Environment

Extensive radio communication studies have been conducted on the Earth's immediate environment, the ionosphere, which begins at about 30 miles above the surface and extends to approximately 300 miles. The ionospheric regions of varying electron densities, known as D, E, and F layer regions respective to the Earth's surface, greatly influence radio propagation. Below the E layer, the air is composed primarily of nitrogen and partly oxygen molecules. At the F_2 layer peak, the primary constituent is atomic oxygen; above the F_2 layer there is a transition from atomic oxygen to atomic hydrogen. The hydrogen layer is partly neutral up to the 30,000-degree isothermal surface, and is almost completely ionized above it. The geomagnetic field reduces the conductive heat flow into the atmosphere in low and middle magnetic latitudes, and in the high magnetic latitudes the heat flows freely, nearly along the lines of magnetic force. This unequal heat flow in different latitudes distorts the isothermal surfaces from a spherical form. Below the noted isothermal surface, however, the neutral atoms of the partly neutral thick layer of gas can conduct heat unaffected by the magnetic field, and the isothermal surface will tend to be spherical.

The Earth's environmental regions have been termed as atmosphere, thermosphere, metasphere, and protosphere, respectively, the protosphere being the outermost region and the region of transition to interplanetary gas. The partly neutral hydrogen layer between the 30,000-degree isothermal surface and the oxygen-hydrogen transition region is known as the metasphere, while actually, the thermosphere encompasses the E and F ionospheric layers, and the metaspheric and photospheric hydrogen layers. The metasphere is believed to be the region where solar gas streams result in the producing of so-called magnetic storms.

3. The Solar Environment

Generally speaking, it is not unusual to think of the Earth as being isolated in stellar space consisting of a vacuum. However, space is known to contain solids in the form of dust particles and meteors, which are themselves surrounded by an interplanetary gas of low density. These solids and gas reflect and scatter sunlight, thus contributing to the zodiacal light. The effective gas particles are primarily electrons or sundered particles separated from neutral atoms and molecules, thus leaving a positive nucleus or ion. The source of the interplanetary gas is generally conceded to be the Sun, although the planets of the solar system no doubt are contributors as gas escapes from their atmosphere.

The Sun, a G2 star, can therefore be assumed to be the emitting source of solar gas throughout the entire solar system, such that the system environment is essentially that of a solar atmosphere that is subject to flux variations (a probable occurrence supported by Earth observations). It is also generally conceded that the Sun has a strong magnetic field and thus constitutes a strong magnetic dipole as a center of the solar system, which is itself in a stellar field of low magnitude.

Due to limited magnetic observations by space probe instrumentation, a contravening magnetic theory has been proposed wherein the Sun's solar atmosphere magnetic field consists of radial-spiral open-ended magnetic lines of force following permeable paths. By correlating Earth observed space phenomena and relating to space instrumentation observations, a more reasonable explanation appears feasible.

It is well known (and recorded) that following a Sun event of any consequence, electromagnetic radiation in the spectrum of visible light, X-ray, ultraviolet light, and radio waves arrive at the Earth in approximately 8 minutes. The transit time is over 1 hour for protons and up to 2 days for electrons. No valid reason exists for assuming that these transits occur in the same magnitude in solar gas of the far reaches beyond the Earth's magnetic field, or that a semidirectional magnetic path does not permanently exist between the Earth and the Sun.

By considering the existence of a closed-loop magnetic path, several extrapolations can be made. The direct magnetic path consisting of linked magnetic lines of force could provide the particle propagation medium. The significant presence of particle flux, however, would result in the localized increase in permeability which should correspondingly increase the flux strength of magnetic path. This implies further particle acceleration due to the presence of the particle itself.

In addition to the above, a magnetic linkage between the Earth and Sun should maintain a more permeable and, therefore, directive path for electromagnetic radiation from a quiescent condition. However, this apparently is not a valid assumption when considering the visible electromagnetic spectrum.

If the existence of a linked magnetic path between the Earth and Sun can be established, however, the probability of such paths could also be established with other planets of the solar system. By this expediency, radiation areas in space of major consequence could feasibly be predicted. Further, predictions pertaining to solar flare events are the greatest influencing factors of concern to the space vehicle designer.

B. A Space Radiation Spectrum Index for Evaluating the Elastic Recovery Materials

Because the radiation shield evaluation for the elastic recovery materials is extrapolation at the various radiation levels, a presumed radiation spectrum based upon readily available data serves as the fundamental foundation. The presumed radiation, therefore, is not necessarily in terms of a maximum established by a particular historical solar event, or a minimum biased by so-called quiet conditions. Instead, it is intended to provide a starting point upon which to base extrapolated evaluations, and a tool to index design considerations when evaluating for a particular mission and application.

The presumed radiation environment is shown by Figure 101, in terms of energy level at various extended Earth radii. Detailing a particular application would require specific background information not necessarily pertinent to this report.

C. Consideration of Particle Accelerators to Evaluate the Radiation Shield Merit of Elastic Recovery Materials

During the initial concept phase of this evaluation study, various testing methods were considered and discussed⁽⁶⁰⁾ from the standpoints of facility requirements, economy, and information obtainable. Basically, the method evaluations consist of determining the extent and relative value of information which can be obtained from various radiation sources in terms of costs. Emphasis is placed on the fact that regardless of the type of source contemplated, the direct simulation of the space radiation spectrum will not be achieved. This

implies, of course, that true simulation can only be achieved in the actual environment under total spectrum conditions and on consideration of a time factor. Such a simulation, therefore, necessitates prior radiation data accumulating missions on promising shield materials in varying space environments.

Useful radiation information can be obtained through the use of particle accelerators, although this method is not exactly representative of space radiation. For example, the spectrum of energetic protons on a passive shield wall in the space environment would be continuous and relatively softer than accelerator-produced monoenergetic protons in the several hundred MeV range. The consequence is a significant reduction in secondary neutron production which emphasizes the effect of proton primaries possibly penetrating the passive wall. In addition, the gamma-ray dose outside of a thick high-energy accelerator shield is normally quite low relative to the neutron dose. This does not necessarily relate to the passive wall in space, however, where the gamma/neutron dose ratio could be effectively greater.

For initial material screening and shield evaluating purposes, it may be concluded that the cost of testing materials at very high energy levels in other than correctly simulated environments cannot be justified. This, then, leads to the consideration of particle accelerators of medium- or low-energy levels.

About the most economical Van de Graaff particle accelerator readily available commercially is in the 400-KeV range. This machine can be employed for certain extrapolation index measurements; however, the obtained information will be greatly limited. A more useful model Van de Graaff accelerator is also available which operates in the 2 MeV range and has greater flexibility through the use of modification kits. In this instance, however, special radiation facility requirements must be met and a means devised to simulate a test environment.

Since in any low- or medium-level radiation test procedure, the obtained information serves only as an index for extrapolation data, the use of isotopic sources is considered.

D. Theoretical Procedure for Radiation Shield Merit Evaluation by the Use of Isotopic Radiation Sources

The major drawback in the use of isotopic radiation sources for material shielding evaluations is the limited type of radiation produced. Since the shielding information required concerns high-energy electrons and protons, as well as gamma radiation, this particle radiation spectrum is not obtainable with the isotopic method.

Because the isotopic method obviously provides the most economical and easily applied approach to testing material shield methods, close consideration is made herein to determine a means of simulation which allows the computing of shielding merit when subjected to space radiation. A further advantage obtainable through the use of an isotope radiation source is the ease of conducting radiation tests in a vacuum environment. In view of test simplicity and economy, the following discussion will consider the basic fundamentals of a method to evaluate the shield effectiveness of composite materials by establishing a relative \bar{Z} number. A vast amount of reference information is readily available on the radiation shield characteristics of various elements which have been conveniently considered for aerospace structures. Currently, the most common of these materials is aluminum. If the radiation absorption characteristics of a material as well as its secondary radiation characteristics can be determined, for a particular radiation spectrum, then the materials may find the same convenience in design considerations as found with aluminum. The isotopic approach requires determining a relative absorption coefficient and relative Z number which are the relative complex absorption (stopping) and \bar{Z} value of a complex composite material.

Fundamentally, the complex occurrence due to the interaction of electromagnetic radiation with matter depends upon the nature of, and

radiation energy, and the atomic number of the material, Z . By increasing the energy, the processes referred to as classical scattering, photoelectric process, Compton process, pair production, and photonuclear reaction occur individually or collectively. In each case, the absorption coefficient or the cross section describes the relative probability of each process. A useful flexibility has been derived to describe the absorption coefficient with certain qualifications.

The linear absorption coefficient μ , a constant of proportionality, is numerically equal to the fractional decrease in radiation intensity resulting from an absorbing material of unit thickness. The term μ has the dimensions of cm^{-1} . The absorption is exponential; therefore, it is convenient to identify the absorber in half-thickness values. Thus,

$$\text{Linear Absorption Coefficient} = \mu \text{ cm}^{-1}$$

To consider a material in terms of its density (ρ), a mass absorption coefficient relation is conveniently used. Thus,

$$\text{Mass Absorption Coefficient} = \mu/\rho \text{ cm}^2 \text{ gm}^{-1}$$

To consider the absorption coefficient in terms of the atomic number (Z), the atomic weight (A), and Avogadro's number ($N = 6.02 \times 10^{23}$), the following relation is used:

$$\text{Atomic Absorption Coefficient} = \frac{\mu}{\rho} \cdot \frac{A}{N} \text{ cm}^2 \text{ atom}^{-1}$$

When it is more useful to express the absorption coefficient independently of a material chemical or physical state, the absorption coefficient per electron is conveniently used, particularly since

radiation interaction with matter concerns the effect upon the electrons and atoms. Thus,

$$\text{Electronic Absorption Coefficient} = \frac{\mu}{\rho} \cdot \frac{A}{N} \cdot \frac{1}{Z} \text{ cm}^2 \text{ electron}^{-1}$$

The instrumented accuracy of determining the true absorption coefficient is dependent upon the instrumentation geometry. This is because the obtained μ has the identity of a total absorption coefficient and the scatter absorption coefficient resulting from the geometry. The true scatter coefficient is not readily obtained unless the detection means is capable of including all the scattered radiation. From a biological standpoint, a distinction is made between the true and total absorption coefficient. This is because a biological effect does not result from the scattered energy from the material. Scatter is defined by Thomson's classical theory and/or the Compton process in terms of the differential cross section per unit solid angle and for electron distributions, wherein a photoelectric process occurs only with bound electrons, the Compton process can occur with free or lightly bound electrons, respectively. A thorough treatment of this subject is beyond the scope of this report; however, the details can be found in The Atomic Nucleus⁽⁶¹⁾ and Handbook of Physics.⁽⁶²⁾

Since the prior discussion has considered radiation of an electromagnetic nature, the absorption process now considered is corpuscular radiation (i.e., radiation possessing a measurable rest mass), the electron and proton. The energy reduction of electrons occurs by multiple inelastic collisions until it achieves thermal levels. The attenuation processes are collisions resulting in ionization, atom excitation, resonance absorption, radiation production, and electrodisintegration of nuclei. Since this report is concerned with the absorption behavior of a material as a radiation shield in space, the radiation energy loss receives close consideration.

At high electron energies, the radiation energy loss through bremsstrahlung, due to negative acceleration (stopping) of electrons, achieves major importance. Negative acceleration due to electron deflection in a nuclear-atomic field must conserve energy by energy radiation. Momentum conservation results usually from activity of the nucleus. The energy lost as radiation by the electron per unit path length is proportionally equivalent to its energy and the square of the nuclear charge. Although the radiation loss process (bremsstrahlung) involves fewer electrons than collision losses, relatively large discrete losses result from the radiation. The probability of radiation energy loss increases with increasing electron energy and varies at the square of the atomic number Z . Additionally, the probability of radiation energy loss relative to the probability of collision energy loss increases directly with electron kinetic energy and directly with the atomic number Z . Therefore, by taking into account the electron scattering by means of the Rutherford equation (which neglects the orbital electron influence) or the Mott relation (which includes this influence), the electron range in a shielding medium as a function of energy, angle, and atomic number Z , can be extrapolated.

Through the above procedure, the complex relative \bar{Z} number of a composite material and absorption coefficient obtained by means of electromagnetic radiation, an index can be related to corpuscular radiation absorption and loss in the same material. As with the energetic electron, similar index relations can be established with energetic protons and neutrons.⁽⁶²⁾

Now consider an instrumentation procedure consisting of a known gamma radiation spectrum, an absorber medium of known local absorption coefficient and Z number and of calibrated half thickness to serve as a calibration index, and a detection means which responds to any radiation which irradiates the medium to interpret the valid dose reading. Assume the geometry of the above arrangement to be optimized

and the monitor system to be capable of high resolution respective to time. One further assumption is that the calibrating absorber medium is not immersed in a second medium (e.g., air at atmospheric pressure).

Consider next that a spectral monitored radiation measurement is made of the total absorption by the calibrating medium (for example, aluminum) of calibrated thickness, and that these data are tabulated. Next, an additional thickness is added to the calibrating medium such that the medium thickness is doubled. Again, the monitor measurements are performed under circumstances identical to those of the first measurement, and these data tabulated. A third measurement is performed with a tripled thickness of the absorber medium identically to the two preceding measurements to complete the calibrating sequence.

By employing the above procedure and by means of readily available cross-reference information on the index calibrating absorber medium, accurate calibration is obtained for the monitor instrumentation for the particular geometrical arrangement. The absorber medium of this calibration, therefore, serves as an instrumentation reference standard because of its prior known absorption coefficient and Z number. Thus, establishing direct index relationships between the monitor calibration and radiation transmission, absorption, cross section, range, and energy (relative to the reference standard Z number in terms of thickness) is achieved.

With the above calibration procedure and reference established, measurements may then be conducted with certain qualifications upon composite absorber materials of unknown complex Z values to obtain a relative \bar{Z} number. This relative \bar{Z} is obtained in relation to the reference standard Z by absorption measurement and, therefore, may be identified in terms of absorption "Figure Of Merit." This is the procedure employed to screen and evaluate the elastic recovery materials.

E. Cross Reference of Units Which Relate to Isotopic Basic Data Acquisition and Extrapolation of Radiation Effect

1. Radiation Classification

Since space radiation shield evaluation primarily concerns biological effects, radiation units should first be considered from a biological point of view. Therefore, the various types of ionizing radiation are grouped into two fundamental phenomena: first, electromagnetic radiations which ionize by virtue of the secondary electrons released when they are absorbed; and second, corpuscular radiations which ionize, either directly as a function of their charge, or indirectly through charge particles set in motion by collision processes.

Electromagnetic radiation "intensity" (dose rate) at any point is precisely defined as the radiation energy in ergs flowing per second through 1 cm^2 of area perpendicular to the propagating direction. This qualification stipulates that the photon energy spectrum and energy flux be known quantities.

2. Roentgen

The international x-ray dose unit, the roentgen, was modified in 1937 to include applicability to radium gamma-ray dosimetry, and reads as follows:

"The roentgen shall be the quantity of x- or gamma radiation such that the associated corpuscular emission per 0.001293 gm of air produces, in air, ions carrying 1 esu of quantity of electricity of either sign."

This wording which includes gamma radiation has led to considerable dissension as to the exact quantity definition. Regardless of the preferred point of view, an amount of ionization is specifically defined which implies an energy absorption per unit mass of air that is almost invariant with photon energy.

The validity of the unit roentgen is questionable when the secondary corpuscular emission is not in equilibrium with the primary quantum radiation. A point of notation is the case where the roentgen is not descriptively adequate for the dose at an air-tissue interface where a finite penetration is required to achieve secondary electronic equilibrium. Thus, the fallacy exists between the true energy absorption in the surface tissue and that implied by the roentgen dose, particularly where the radiation energy is at high levels. In order to alleviate the situation of definitions, several units are conveniently used.

3. Gram-Roentgen

The gram-roentgen as a unit related to the roentgen as equal to the x or gamma energy absorbed when 1 gm of air is exposed to 1 roentgen. Several values have been noted in various literature to describe this unit, each of which are based upon somewhat different assumptions. These values are 87 ergs, 84 ergs and 83.7 ergs. The 87 ergs/gm (air) assumed that the average energy expended per ion pair formed is 5.4×10^{-11} erg (34 electron volts). The 84 ergs value has found use in the determination of the unit roentgen equivalent physical (REP), and either this value or the 83.7 ergs value may be considered valid because they represent a calculated constant. This is considered as follows:

The number of ion pairs produced by the energy absorption in 0.001293 gm of air is $1/e$, where e is the electrostatic unit of charge. Now let W represent the energy lost by a secondary electron per ion pair formed in air; thus, the energy is W/e . W/e represents a near constant energy absorption per roentgen for all photon energies, since W does not depend upon the energy

of the secondary electron except at very low energies. The value of W for air is approximately $32.5e/300$ ergs, the value of W/e is approximately 32.5 ergs, which converted to ergs per gram (air) determines the energy absorption per roentgen in 1 gm of air as 32.5 divided by 300 times 0.001293, or 83.8 ergs. Values of W between 32.2 to 34 electrovolts have been assumed, which result in the unit variation.

4. Roentgen Equivalent Physical (REP)

This unit was invented to define the dose of ionizing radiation which produces an energy absorption of 84 ergs/cm³ in tissue. The value was changed to 93 ergs/cm³ of tissue because this value more accurately represents the energy absorption per cubic centimeter of aqueous tissue which has received a dose of 1 roentgen. The absolute value of this unit is ambiguous, because the precise amount of energy absorbed by tissue from 1 roentgen is unknown. Thus, the radiation absorbed dose unit was devised.

5. Radiation Absorbed Dose (RAD)

The RAD is a measure of the energy imparted to matter (i.e., retained by matter) by ionizing radiation per unit mass of irradiated material at the place of interest. The RAD is thus defined as the unit of absorbed dose* and is 100 ergs/gm.

6. Roentgen Equivalent Man (REM)

As the result of biological experiments it has become evident that the biological damage by radiation is not always proportional

* A point of contravention exists in the use of the term "dose." This is due to the use of the word dose in conjunction with the definition of the roentgen. A "dose" of 1 roentgen implies an "absorbed dose" of approximately 93 ergs/gm in soft tissue or 0.93 RAD in the photon spectrum up to 3 MeV.

to the absorbed energy. Radiations of various types exhibit different biological effects, and the overall biological damage to a system is dependent on the type and energy of the radiation. Therefore, the REM was initially defined as the dose which delivered to a man exposed to any ionizing radiation, is biologically equivalent to the dose of 1 roentgen of x or gamma radiation, not absorbed photoelectrically. Thus, the REM takes into account the Relative Biological Effectiveness (RBE) of different types of radiation. However, because the factors vary both in radiation properties and biological effect, the REM is defined as a biological effect, the REM is defined as a biological unit of dose as follows:

$$\text{Dose in REM} = \text{Dose in REP} \times \text{RBE}$$

where RBE values are given as inverse ratios of energy absorptions of different radiations for particular biological action, and which produce equal biological effect.

7. Integral Absorbed Dose

This unit is defined as the integration of the energy absorbed throughout a given region of interest and is expressed in gram-rads wherein 1 gm-rad = 100 ergs.

8. Frequently Required Definitions

- a. Curie: The curie is a unit of amount of radioactive material and was initially defined as the number of disintegrations per second of 1 gm of radium in equilibrium with its daughter products. The present definition of the curie is "that quantity of a radioactive nuclide disintegrating at the rate of 3.7×10^{10} atoms per second." Thus, if a Co^{60} source is in the amount of 1 curie, the air dose rate at 20-cm distance would be 32.5 roentgen/hour, or at 1-meter

distance, 1.32 roentgen/hour. This unit allows the relating of disintegrating rate of nuclides to dose rate.

- b. Linear energy transfer (LET): This definition defines the linear energy transfer of a particle passing through matter as the energy transferred to the material per unit path length. Units normally used are "electron volts/centimeter" or "electron kilo-volts/micron." The particle energy loss, (dE/dX) , is stated in the same units (e.g., MeV per gm/cm^2).

F. Derivation of Quantities and Extrapolation Procedure for Screening Radiation Shield Materials

Where an incident of radiation ϵ (ergs/cm^2) is required to produce 1 roentgen, the energy absorption in air/gm is $\epsilon(\mu_a/\rho)$ (ergs/gm) where μ_a/ρ is the true mass absorption coefficient of air. Thus,

$$\epsilon(\mu_a/\rho)_{\text{air}} = 83.8 \text{ ergs/gm} \quad (1)$$

The mass absorption coefficient is a summation of several terms. Hence,

$$\mu_a = \tau + \sigma_a + \kappa_a \quad (2)$$

where

- τ - the photoelectric absorption coefficient
- σ_a - that fraction of photon energy imparted to the recoil electron in the Compton absorption process
- κ_a - the photon energy component given to the positron and negatron in pair production

The value κ_a has been calculated from the pair production coefficient κ , as follows:

$$\kappa_a = \frac{\kappa(h\nu - 1.02)}{h\nu} \quad (3)$$

where $h\nu$ is the photon energy in MeV, thus

$$\epsilon = \frac{83.8\rho}{\tau + \sigma_a + \kappa_a} \text{ ergs/cm}^2\text{-roentgen} \quad (4)$$

The validity of results from the above is reliable only to a few MeV, within roentgen meaning, and within the known W value. Thus, when the true mass absorption coefficient of a medium in question and air are known, the medium energy absorption ϵ_M (roentgen/gram) of medium can be defined as:

$$\epsilon_M = \frac{(\mu_a/\rho)_{\text{medium}}}{(\mu_a/\rho)_{\text{air}}} \times 83.8 \text{ ergs/gm-roentgen} \quad (5)$$

The need to examine complex substances, (e.g., water, atmosphere, tissue, plastic, etc.) is often encountered, and in such cases, it may be convenient to examine the composites in terms of an "effective atomic number" which is referred to as relative \bar{Z} . Expressing μ_a/ρ in terms of relative \bar{Z} is considered reasonably valid, as long as the power function is adequately representative of the photoelectric absorption coefficient at photon energies in the range sufficiently above the critical absorption energies of the atoms present in the composite material. However, this approach is not entirely valid for making use of such values to express the pair formation coefficient.

In cases where the atomic number is low, the photon energy ranges do not overlap where τ and κ_a are of consequence. Thus, the number of electrons/gram (n_0) depends on the Z/A ratio (A being the atomic weight). Because this ratio changes in small magnitude with atomic number, n_0 depends very little upon composition, and can be evaluated with reasonable accuracy.

An ionizing particle in passing through material is characterized by its energy loss per unit length of path traversed. This loss

rate is referred to as linear energy transfer (LET), or stopping power $S(E)$. The "stopping number" of a material is conveniently represented by a dimensionless term (B). Thus, the average energy loss by ionization, dE/dx , per centimeter path is given by the well-known relation

$$-\frac{dE}{dx} = \frac{4 \pi e^4 z^2}{mv^2} \bar{N} B \quad (6)$$

- where
- E = the kinetic energy of the particle
 - z = the charge of the incident particle
 - v = the velocity of the incident particle
 - B = Z $\left[\left[\ln \frac{2mv^2}{I} - \ln (1-\beta^2) - \beta^2 \right] - C_{\kappa} \right]$
 - \bar{N} = $\frac{\text{Avogadro's number}}{\text{material atomic weight}}$ density of material and is the number of atoms per cm^3
 - Z = atomic number of the material
 - m, e = electron mass and charge
 - β = v/c where c is electromagnetic velocity
 - I = the average excitation potential for the stopping material conveniently determined empirically (proportionally equivalent to the material atomic number)
 - C_{κ} = correction term for κ -shell binding

To express the rate of energy loss in terms of gm/cm^2 of material, σ_M (mass stopping power) finds convenient use. Thus

$$\sigma_M = -\frac{1}{\rho} \frac{dE}{dx} \quad (7)$$

where ρ represents the material density. Note that the quantity σ_M may be considered independent of the stopping material density because of the previous definition of \bar{N} in the $-dE/dx$ equation.

The stopping power of a composite material may be derived by the addition of contributions of atoms composing the material according to Bragg's rule of additivity. The Bragg approach neglects the effects of the electronic binding in the molecular composite, whereas in the true case, the average excitation potential of the individual atoms may be changed in magnitude of a few percent when it is bound in a molecule. The definition of B in equation (6) shows the excitation potential to be a logarithmic term, and therefore, the resultant stopping power variation of the composite is of low order.

To evaluate the relative mass stopping power ρ_M of a composite material \bar{Z} in relation to a reference standard material Z_{RS} , let p_i be the fraction by weight of the i th element in the composite, and \bar{N}_i representative of the number of atoms of the i th element of the composite per cm^3 and equal to $N p_i \rho / A_i$; N being Avogadro's number, ρ the composite density, and A_i the atomic weight of the i th element, then Bragg's rule states

$$-\frac{dE}{dx} = \frac{4 \pi e^4 z^2}{mv^2} N \rho \sum_i \frac{p_i}{A_i} B_i \quad (8)$$

Thus,

$$\rho_M = \frac{\left(\frac{1}{\rho} \frac{dE}{dx} \right)_{\bar{Z}}}{-\left(\frac{1}{\rho} \frac{dE}{dx} \right)_{Z_{RS}}} = \frac{\sum_i \frac{p_i}{A_i} B_i}{\frac{B_{Z_{RS}}}{A_{Z_{RS}}}} \quad (9)$$

The effective atomic number, relative \bar{Z} , and effective excitation potential, \bar{I} , can be employed in equation (6).

Thus,

$$-\frac{dE}{dx} = \frac{4 \pi e^4 z^2}{mv^2} \bar{N} \bar{Z} \left[\ln \frac{2mv^2}{\bar{I}} - \ln (1-\beta^2) - \beta^2 \right] C_{\kappa} \quad (10)$$

where

$$\ln \bar{I} = \frac{\sum_i N_i Z_i \ln I_i}{\bar{N} \bar{Z}}$$

and

$$\bar{N} \bar{Z} = \sum_i N_i Z_i$$

III. INSTRUMENTATION

A. Environmental Simulation

In the prior discussion pertaining to the principle of instrumentation, the assumption was made that the absorber medium to be tested was not immersed in an additional absorber medium (i.e., the atmosphere). The reasons for this assumption are several and resulted in the development and use of an environmental test chamber from which the air can be greatly reduced or evacuated.

The air itself is a complex absorber and, as such, possesses a relative \bar{Z} number. For example, the earth's atmosphere as an effective absorber is roughly equivalent to 3.66 meters of aluminum. Now since the instrumented monitor data obtained from a complex absorber material require a statistical review, the additional inclusion of the complex medium, air, into the measurement, in a ratio which is quite large, imposes an unnecessary source of error into the measurement interpretation.

Additional reasons for the use of a reduced-pressure environmental chamber are to control spurious emissions and random fluctuations, reduce spectral attenuation due to medium absorption within the irradiation range, and improve background/sensitivity of the detection system.

The use of a reduced-pressure test chamber, however, imposes certain restrictions. The geometrical arrangements for simulated testing are limited by the chamber dimensions and thus establishes certain backscatter conditions. The chamber employed to test the elastic recovery materials does not (nor is intended to) simulate the environmental conditions to be found in space wherein the radiation flux, intensity, thermal and medium density would be individually or compositely reproduced. Instead, the subject chamber serves only to increase instrumentation reliability by reducing the complexity of measurement and data evaluation procedure.

B. Radiation Detection Instrumentation

Perhaps the most important unit of a radiation instrumentation system is the detection component which is sensitive to the incident radiation. Three types of conventional detectors are usually found: ionization chambers, Geiger-Müller tube counters, and scintillation counters. Each of these detection methods have certain advantages determined by the radiation information measurement requirements. The associated methods employed within the instrumentation which interprets the detected radiation also influences the selection of the detection method.

In general practice, the use of a radiation counter is to determine a radiation dose in terms of a counted rate. What is not often recognized is that usual instrumentation does not actually count the occurring event, but instead measures the elapsed time between events. This is due primarily to the nature of circuitry employed in the instrumentation metering.

The selection of a best detection method to be used for shielding material measurements required that careful consideration be given to the advantages and disadvantages of each method. It is highly desirable that the detection method used be responsive to the spectrum of the radiation source which, in this case, was to be 3.22 mg of radium. It was also intended to employ two additional detection systems, one which could be converted easily to serve a multiple purpose, and the other a Geiger-Müller tube. Therefore, two of the detectors employed in the instrumentation were specially constructed chambers of proportional counter type, while the third detector was the Geiger-Müller tube.

Because the Geiger-Müller counter response is not directly proportional to the absorbed radiation energy, it is not an exacting instrument for radiation dose measurement. Its sensitivity to low dose rates, however, is very good and it is possible to calculate the expected counting rate for a particular cathode material and gamma ray dose rate. This detector method was not used as the main detection system for the shield material tests primarily because of its plateau operation, wherein the output pulses have the same relative magnitude.

With the ionization chamber detection system, the higher the electrode potential, the greater will be the energy of the radiation resulting ions, and, consequently, greater the total ionization produced. Therefore, the chamber has a gas amplification factor which increases with voltage and which is approximately constant for different initial ionization particles. The chamber possesses a region of proportionality wherein the greater part of the ionization occurs near the track of the ionizing particle and involves a limited area near the collector electrode.

Proportional chambers are usually operated at a higher pressure than counters in the Geiger-Müller region and a quenching agent is not necessarily required because the discharge does not maintain itself. Consequently, the resolution time (dead time and recovery) is very short and compatible to carefully planned electronic circuitry. The response rate, therefore, can far exceed that of the Geiger-Müller counter.

The proportional counter requires the supplied operating voltage to be very stable and a sensitive means of linear, nonoverloading amplification if pulse height discrimination and analyzing methods are to be employed. This discrimination can be accomplished by means of bias control in counting circuitry following preamplification. The proportional counter, therefore, has a particular application where distinction between particles of different ionization characteristic, or difference in energy level, is desired.

The two chambers which were constructed for absorption measurements on the elastic recovery materials are not necessarily descriptive of conventional proportional chambers found with usual instrumentation. The chamber cases are constructed with a heavy copper wall and are not cylindrical in shape. Instead, each chamber presents a series of windows, based upon the air wall concept, in a plane to the radiation. Each chamber contains forty 1.25-cm area windows set in a thick aluminum shield. In each chamber, the sensitive volume which follows the windows totals 210 cc. The detector element used is 4.5-mil tungsten wire and the total length of all collector elements is 95 cm. (length). The chambers were plastic-lined and heavily coated with Aquadag. Gas sealing was accomplished by the method of attaching the aluminum shield window support such that the chambers could function in a vacuum environment.

The subject detection chambers were not designed to be self-quenching. Instead, it was desired that the chambers have a broad decade response

but not be unnecessarily sluggish at low intensity levels. For this reason, a variable and therefore selective external quench circuit was employed in both chamber circuits.

C. Monitor Instrumentation

The monitor instrumentation used for material evaluation consisted of three high gain linear amplification channels employing triode-connected 6AK5 amplifiers. These were followed by a phase splitter pickoff and video preamplifier for oscilloscope amplifier circuitry employing 6J6 dual triodes, and 6AU6 pentodes in the meter amplifier circuitry.

Since it was desired to obtain pulse height discrimination in the meter count by means of switched, precalibrated bias levels, two methods of counting were tried in order to select that most flexible and stable. The first method made use of a driven, one-shot, 12AU7 dual triode multivibrator circuit in which the input trigger level could be preset by controlling the bias level. The objective of this approach was to allow the multivibrator to be triggered only by pulses which exceeded a predetermined amplitude and by means of bias control establish an amplitude decade. By directly comparing the multivibrator approach to a bias controller driver, bias stabilized dual-diode pulse counter, it was determined that better decade stability and flexibility could be achieved with the driven diode circuitry. With both circuits, it was noted that a source of error could be coincident pulses due to the type of radiation chamber detection used.

The input sensitivity of each instrumentation channel for full-decade meter circuit function, excluding the detector gas amplification factor, was -40 db to a 1-volt reference. The intercostal lines between detectors and the amplifier input quench decades were RG-17/U and RG-8/U coaxial cables as determined by the detector voltage. Background discrimination control was provided for each detection channel prior to the video pickoff circuit.

The monitor instrumentation used was rack-mounted and consisted of the following units as listed from the rack top shown in Figure 102:

- a. Count rate meter panel
- b. Aural monitor with amplitude metering
- c. Video amplifier, delay network and time-pulse generator
- d. Three channel amplifier and count circuitry
- e. 900-volt power supply
- f. 3000-volt and 2000-volt dual power supply
- g. Dual 300-volt plate supply and filament supply for all circuitry
- h. 28-volt relay power supply

The entire arrangement consisting of the detection system and environmental chamber, vacuum pump, instrumentation rack and oscilloscope video monitor, is shown in Figure 102.

D. Radioactive Sources

Due to the wide range of performance which was built into the instrumentation, three different source standards were used during the initial test and calibration phase.

One source used was an α -emitter calibrated to a Pu^{239} standard. This source provided 14,400 disintegrations per minute. This source is shown mounted in Figure 103. An additional source used was a β -emitter calibrated at 32,900 disintegrations per minute. This β source is shown mounted in Figure 104.

As was previously mentioned, the source of γ radiation used to conduct the material tests was 3.22 mg of radium. The roentgen dose rate index assumption is based upon the 1-cm distance rate from 1 mg of radium filtered with 0.5-mm platinum for a value of 8.26 r/hr. The γ -ray emission from 0.180 MeV to 2.198 MeV for radium. The radium source used for tests is shown in Figure 105.

For statistical data reasons, pictorial measurements were performed with the two detection chambers operating, from a practical standpoint, in parallel. This is accomplished by means of a video mixer, then to a Tektronic oscilloscope. From the standpoint of meter monitoring, the chambers were isolated. The parallel equivalence function, however, was relevant to a single 80 window chamber of 420-cm³ sensitive volume, which was desirable, when considering the size of the material samples tested.

The background discriminators were adjusted for quiescent state with the test chamber at atmospheric pressure and the radium source exposed. The chamber background thus was as shown in Figure 106.

With the test chamber sealed, the vacuum pump was activated, and at 15-in. vacuum, the radiation was video-monitored as shown in Figure 107. As the air was exhausted beyond 15-in. vacuum, the level increased rapidly as shown by the Figure 108 photograph taken at 25-in. vacuum.

As shown in Figure 109, the maximum vacuum which could be drawn upon the test chamber was 29.5 in. without resorting to a diffusion pump. Therefore, all material testing was accomplished in 29.5-in. vacuum.

The video-monitored radiation level at 29.5-in. vacuum is shown in Figure 110.

IV. ELASTIC RECOVERY MATERIALS

A. Description of Test Samples and Test Environment

For this test phase of radiation shield evaluation, the test materials selected are those used specifically in the Narmco expandable space structure research concepts. These materials are as follows:

1. Aluminum deposited on polyester terephthalate film
2. Elastic polyurethane foam of 1.90 lb/ft³ density
3. DuPont Type 46971 adhesive

4. Laminate composed of PK-1044 polyvinyl chloride resin and glass fabric
5. Laminate composed of PK-1044 polyvinyl chloride resin and regenerated cellulose fiber fabric

Radiation test samples (1 sq ft) of the above listed materials at appropriate thicknesses were prepared for mounting in a 650-cm² area irradiation window. Since obtaining test samples which were representative of conventional manufacturing technology was desired, the only specification stipulated was that the samples which were similar in construction be near the same thickness. By this expediency, the primary purpose was to obtain samples of realistic composite ratios and dimensional tolerances, as could be expected during their application to article manufactured.

During the performance of absorber measurement, the detected radiation was video-monitored by the technique previously described, and the oscilloscope presentation photographed. The relation between oscilloscope photographs for different test samples may be somewhat misleading if the differences between test sample densities and thicknesses are not taken into consideration. The interpretation of the photographs requires a correlation of monitored data and material physical properties, the results of which are presented by charts in Section IV.C.

Prior to conducting tests upon the elastic recovery materials, an index calibration was made with three calibrated thicknesses of sheet aluminum. This procedure determined the count rate with the previously described instrumentation geometry at 0-, 1-, 2- and 3-thickness in the 29.5-in. vacuum environment. The chamber background setting was as shown in Figure 106 at atmospheric pressure. This procedure allows the expression of exponential absorption in terms of counts per minute vs. material thickness in a semi-log plot. The slope of the line serves to evaluate the absorption coefficient.

The absorption coefficient is plotted as function of gm/cm^2 and as function of atomic number Z . Since these values are previously known, the procedure serves as a reference standard of calibration.

The testing of material samples immediately followed the calibrating index and the test chamber background setting checked with each atmospheric cycle of the chamber. The geometry, irradiation, and monitor procedure were identical for each measurement performed.

The radiation tested samples and the video-monitored radiation level are shown in the photographs of the test sequence (Figures 111 through 122).

B. Elastic Materials of Modified Z

When considering the relative merit of structural materials for use in the known space radiation environment, the fact that the attenuation mechanism for electromagnetic radiation is basically different from the one for heavy nuclei is immediately noted. As described by classical theory, a charge which undergoes acceleration produces radiation. Thus, during the instance in which an incident charged particle is changed in velocity, or undergoes path deflection, it radiates electromagnetic energy of a magnitude proportional to the acceleration.

Since electromagnetic radiation absorption increases with the increase of the absorber atomic number Z , the same does not hold true for heavy charged particles. This is shown where the acceleration produced by a nucleus of charge Z_e on a particle of charge z_e with a mass M is proportional to Zz_e^2/M . The intensity, therefore, is proportional to the square of the magnitude and varies as $Z^2z_e^2/M^2$ and the bremsstrahlung per atom varies as the square of the atomic number Z and inversely with the square of the mass of the incident particle.

In the case of space radiation, both electromagnetic and particle radiation require shielding by the same materials or composite material. In terms of Z number, the shield requirements are contradictory; however, the immediate requirement due to particle radiation of the so-called Van Allen belts and solar flare phenomena must receive due consideration. For this reason, a modification was made to certain of the elastic recovery materials to include carbon in their composite structure. Carbon is found to be the third most effective proton shielding element, the first and second being hydrogen and helium in that order.

Three radiation tests were conducted with carbon-loaded test samples of the elastic recovery materials. The first of these tests was on a laminate made of PK-1044 resin to which 20% carbon by weight had been added and Type 181 glass fabric. The second laminate radiation test was conducted upon a sample fabricated identically to the former except that Fortisan fabric was used in place of the 181 glass.

In each laminate case, the addition of carbon in the stated amount results in no apparent change in the elastic properties of the material. The change in viscosity of the resin due to the carbon addition, however, makes reproduction of conventional nonloaded laminate resin-to-glass or Fortisan fabric ratios considerably more difficult.

The third carbon-loaded sample test was performed upon a carbon-saturated polyurethane foam section similar in dimension to that shown in Figure 115. In this case, mixing the carbon with the foam resin components prior to the foaming operation would have been more desirable, providing an equivalent foam density could be achieved. However, since past experience has shown that density control upon carbon loading requires considerable experimentation, the saturation approach was used.

Figures 123 through 128 present the carbon-loaded test samples and the resulting video-monitored radiation levels. The measurement sequence

of these samples immediately followed the nonloaded sample tests. The correlated absorption data are presented in Section IV.C.

C. Test and Extrapolation Data

The test data presented herein are reduced to charted form in order to provide convenient design information. Because the effectiveness of carbon loading for proton shielding was of primary interest, the mass stopping power for proton radiation is presented by extrapolation for those materials shown in Figures 123, 125, and 127.

The "effective atomic numbers," relative \bar{Z} , resulting from the test evaluations for each of the tested materials are presented in Table 19 below. The lower the relative \bar{Z} number, the more effective the material was in shielding against the corpuscular radiation. Table 19 also lists the material densities ρ .

TABLE 19
EFFECTIVE ATOMIC NUMBER AND DENSITY
OF ELASTIC RECOVERY MATERIALS

Material	Relative \bar{Z}	gm/cm ³
Index reference standard aluminum	13.00	2.700
Aluminum on polyester terephthalate	12.23	1.315
PK-1044 resin/181 glass fabric	11.34	1.680
PK-1044 resin/ regenerated cellulose fiber fabric	10.24	1.380
Polyurethane foam	9.13	0.237
PK-1044 resin-carbon/181 glass fabric	8.80	1.395
Polyurethane foam-carbon	8.24	0.356
PK-1044 resin-carbon/regenerated cellulose fiber fabric	8.02	1.280
DuPont type 46971 adhesive	6.92	1.240

The gamma-ray shielding material coefficient monogram (Figure 129) is indexed to determine the "mass attenuation coefficient" μ/ρ (gm/cm²)

when the "linear absorption coefficient" μ (cm^{-1}) is known. Consequently, the linear absorption coefficient may be determined when the mass attenuation coefficient is known. The charted extrapolation of the mass attenuation coefficient μ_0/ρ as a function of photon energy is given in Figure 130 and may be used with the subject nomogram.

Figures 130 through 137 present the total mass attenuation coefficient, μ_0/ρ , for each of the elastic recovery materials with the exception of those carbon loaded, as a function of photon energy from 0.1 MeV to 100 MeV. The charted data, therefore, are the sum of the three absorption coefficients (i.e., the photoelectric, the Compton, and the pair coefficient).

Figures 138 through 145 present charted extrapolations of the "mass stopping power" for each of the elastic recovery materials evaluated, for proton energies from 1 MeV to 1000 MeV.

V. CONCLUSIONS RESULTING FROM ACCRUED AND EXTRAPOLATED TEST DATA

Although the procedures employed to evaluate the composite elastic recovery materials are not entirely accurate over the extrapolated energy spectrums presented in Section IV.C, the charted data are considered sufficiently accurate for design purposes.

In consideration of bremsstrahlung, and in terms of A/Z ratios, each of the elastic recovery materials tested has a higher figure of merit than aluminum for stopping charged particles. Of particular significance is the carbon-loaded regenerated cellulose fiber fabric laminate for proton shield applications.

Upon consideration of various shielding requirements, the flexibility and practical aspects of employing elastic shielding materials in applications in other than expandable structures are noted. For example, the low \bar{Z} materials could find use in spacecraft compound hull designs where a low \bar{Z} outer shell and high \bar{Z} absorber shell (internally) are desired. Thus, the composite material could serve as a micrometeoroid bumper as well as reduce bremsstrahlung.

In cases where the intended applications apply to auxiliary structures for use in an environment of particle radiation, the relative shielding merit of the elastic recovery materials may be considered very good compared to aluminum. Typical applications would be airlocks, storage shelters, work shelters, short-exposure personnel shelters, etc.

IV. RECOMMENDATIONS

- A. The instrumentation employed to obtain the data was not considered to be "first order" for the following reasons:
1. The test chamber employed for tests does not represent the space environment.
 2. The radiation detection means installed in the chamber are not optimized.
 3. In order to conserve on instrumentation, the present three monitor channels share the circuitry common to the monitor units and, therefore, some interaction is detectable which must be compensated for during testing.
 4. The magnitude and type of radiation used is not sufficient to study deterioration effects upon the materials being tested.
- B. In view of these deficiencies, the following recommendations are made:
1. Redesign the test chamber as a "cold-wall" type such that the thermal spectrum from a carbon arc lamp (solar simulation) can be injected by means of an appropriate window. The chamber diameter should be increased to allow improved radiation test geometry.
 2. Improve the radiation detection to include particle detection systems, particularly neutron detection.

3. Improve the monitor instrumentation by improving channel isolation, improving circuitry, add a count scaler and pulse height monitor, and increase the voltage stability to the detection systems.
4. A Cobalt⁶⁰ source of greater magnitude is a desired replacement for the radium source used in material screening. Following screening, candidate materials should further be evaluated with particle radiation. This source would preferably be a Van de Graaff generator with an analyzing magnet, appropriate modification kits, and provide energies in the 2-MeV range.

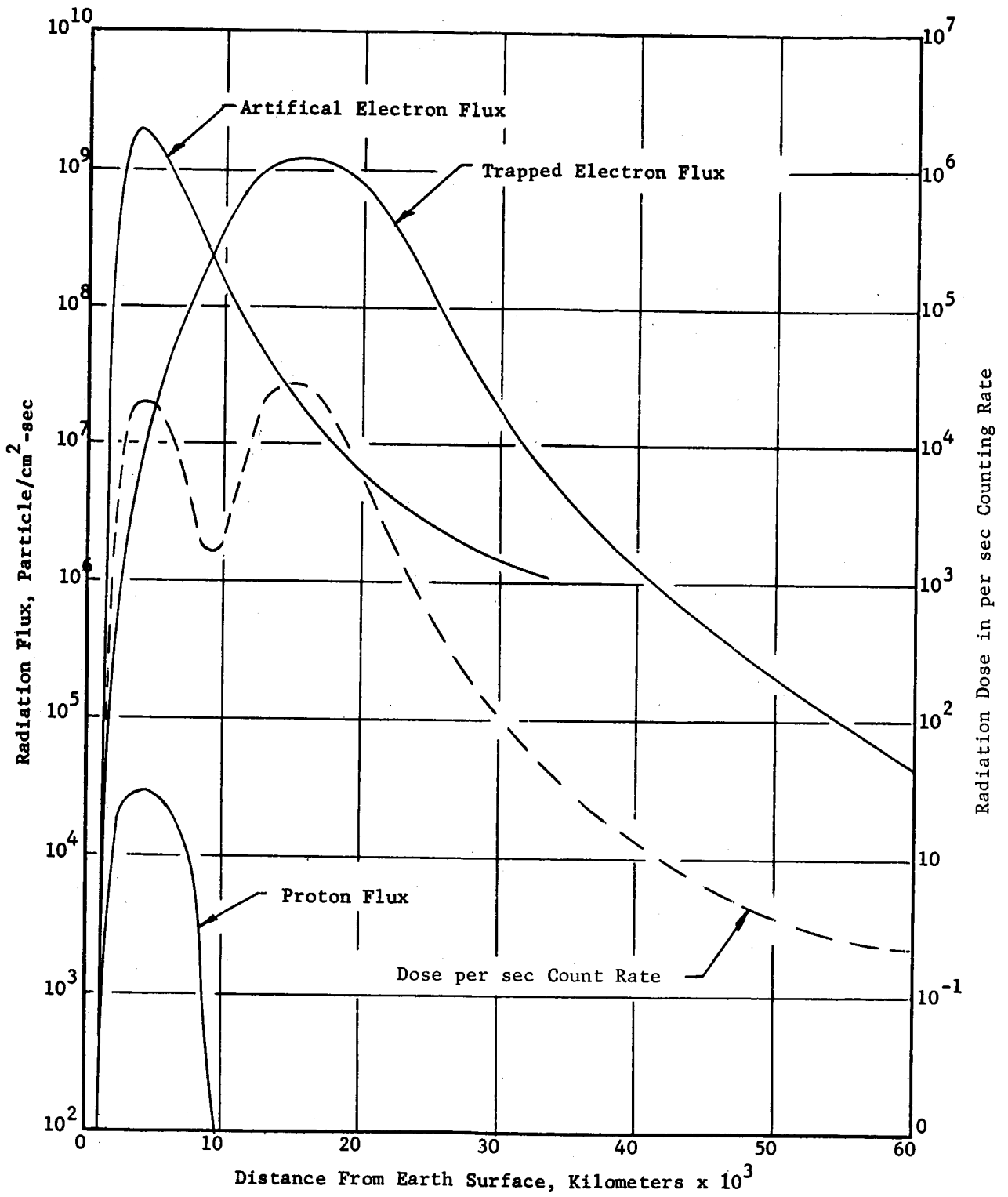


Figure 101. Typical Space Radiation Flux Magnitude

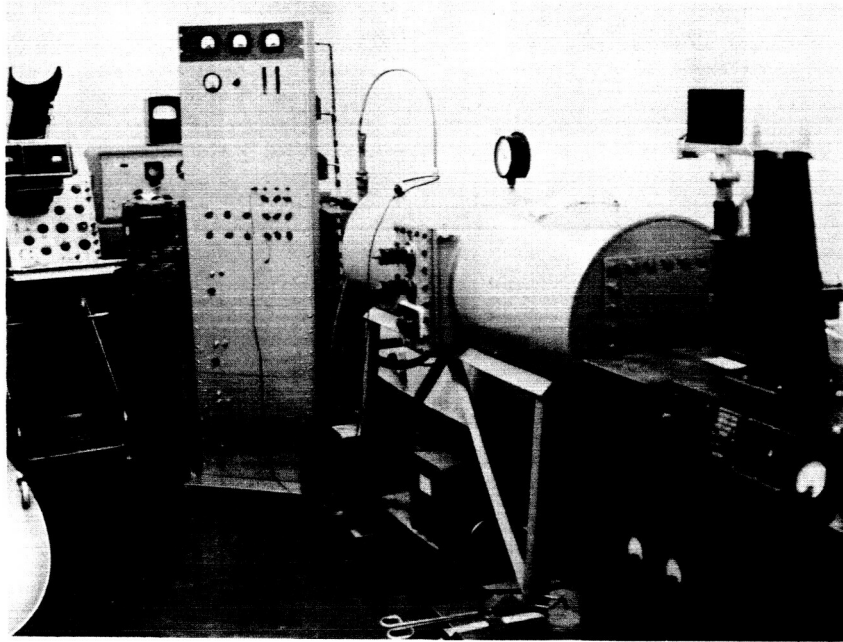


Figure 102. Test Instrumentation Arrangement

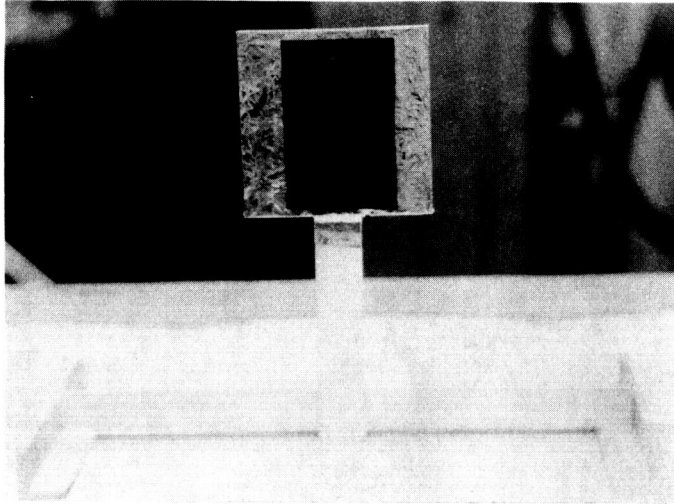


Figure 103. α Radiation Source

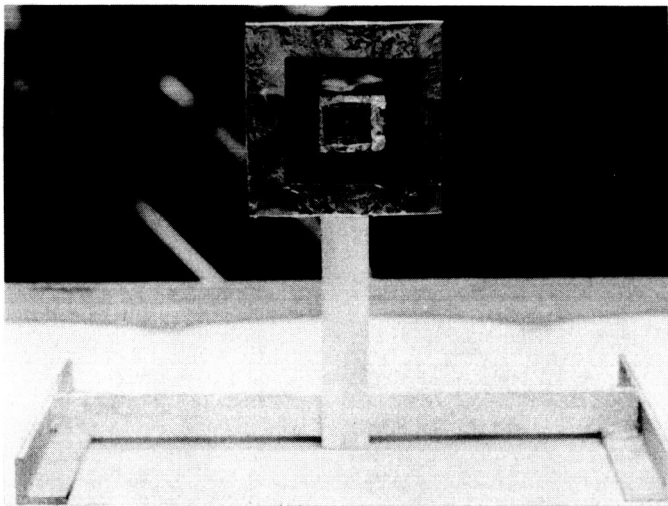


Figure 104. β Radiation Source

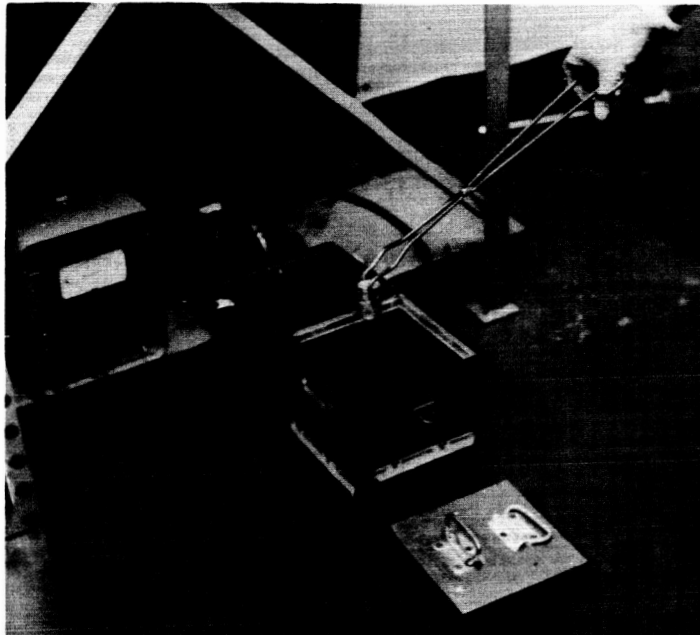


Figure 105. γ Radiation Source

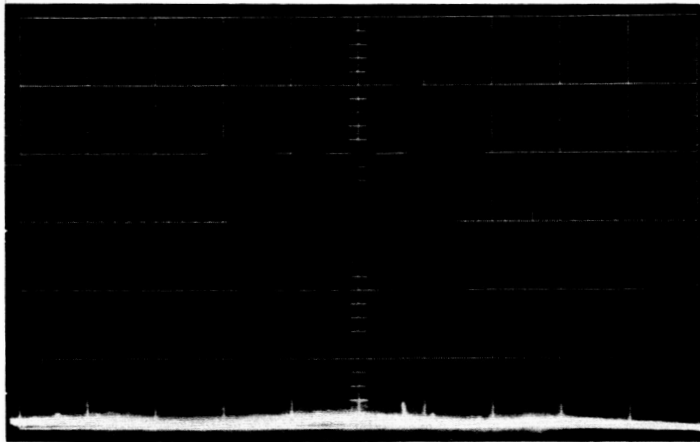


Figure 106. Test Chamber Background Setting
at Atmospheric Pressure

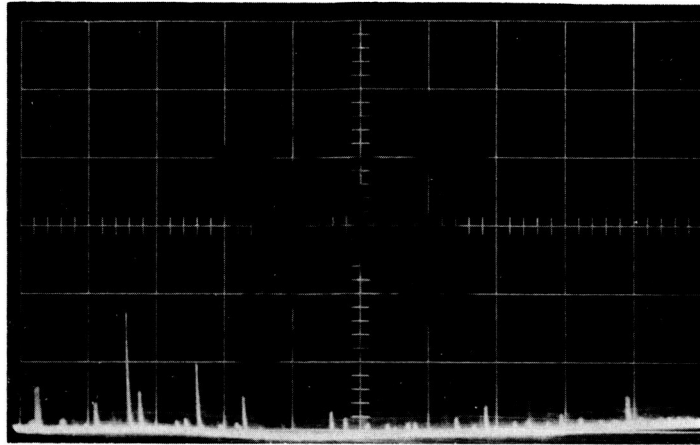


Figure 107. Video-Monitored Radiation Level at 15-in. Vacuum

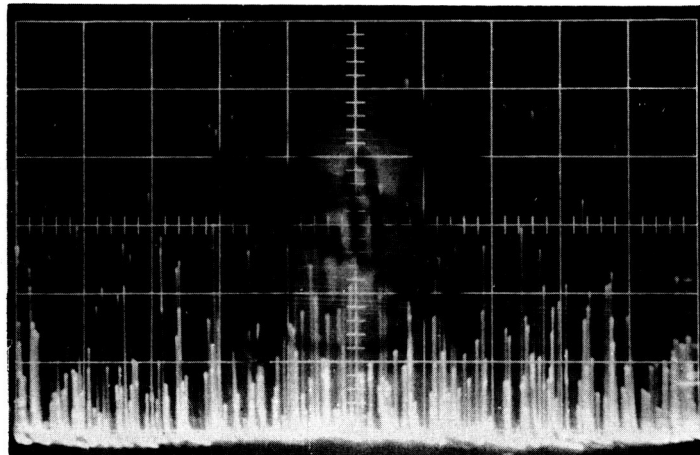


Figure 108. Video-Monitored Radiation Level at 25-in. Vacuum

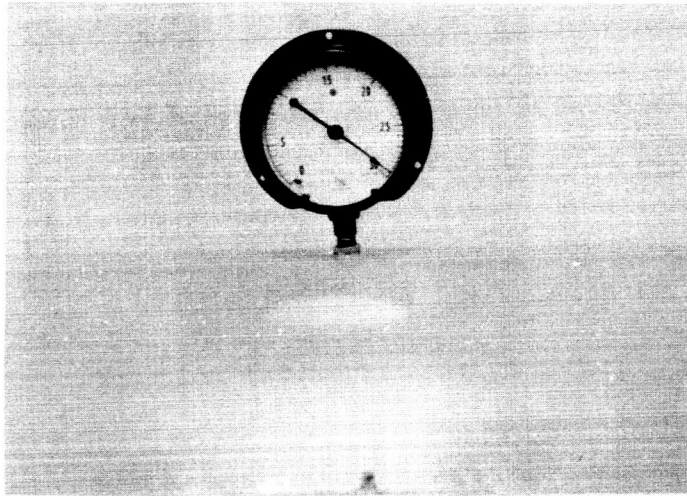


Figure 109. Vacuum Environment During Calibration and Material Tests

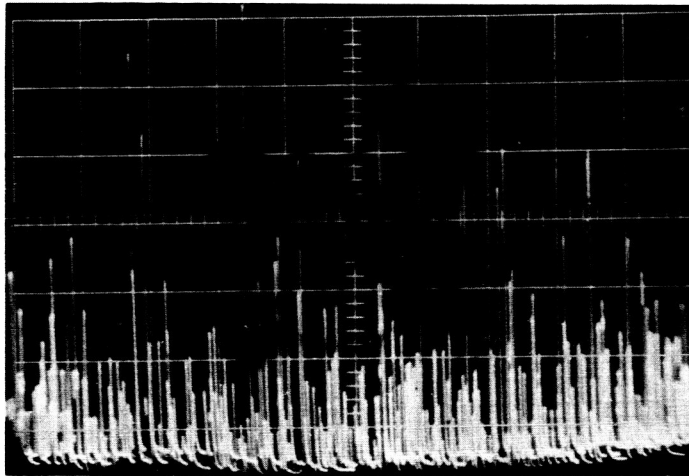


Figure 110. Video-Monitored Radiation Level at 29.5-in. Vacuum

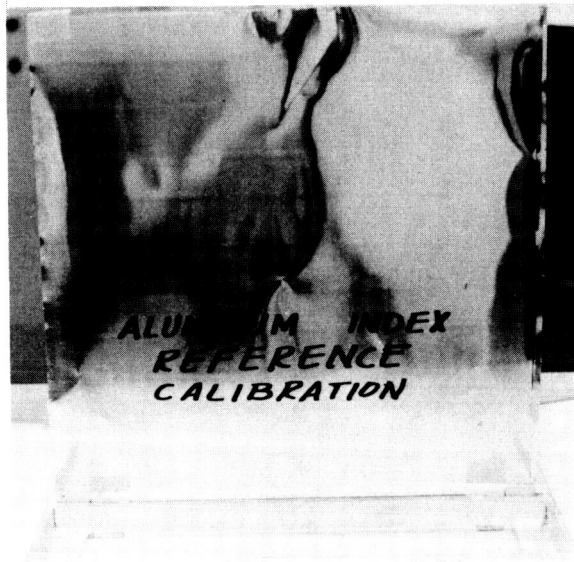


Figure 111. Aluminum Index Reference Standard

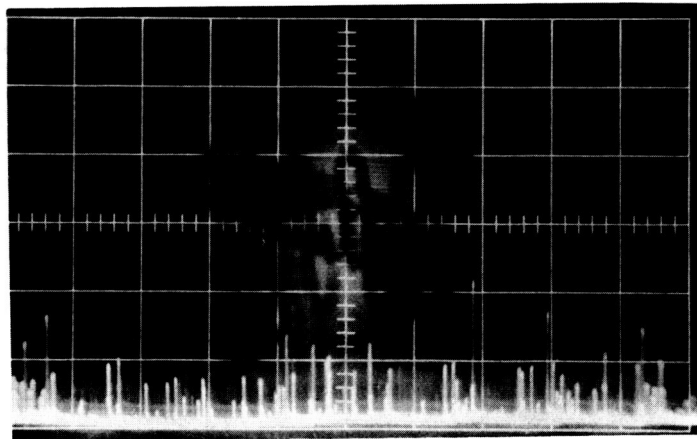


Figure 112. Video-Monitored Radiation Level

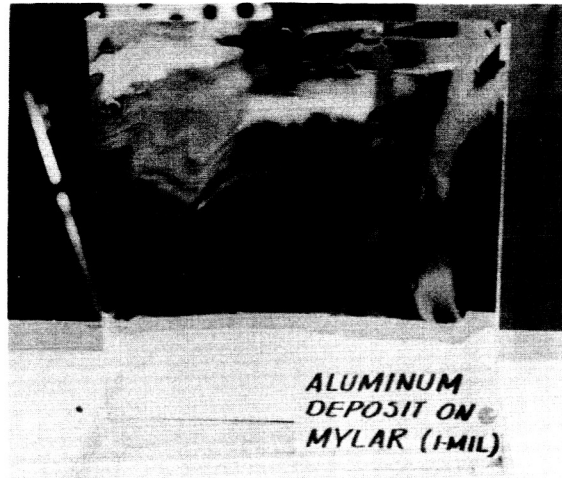


Figure 113. Test Sample of Aluminum Deposited on Mylar

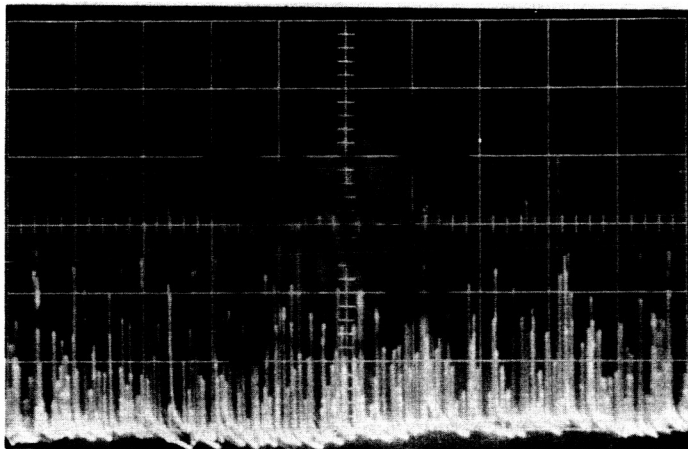


Figure 114. Video-Monitored Radiation Level

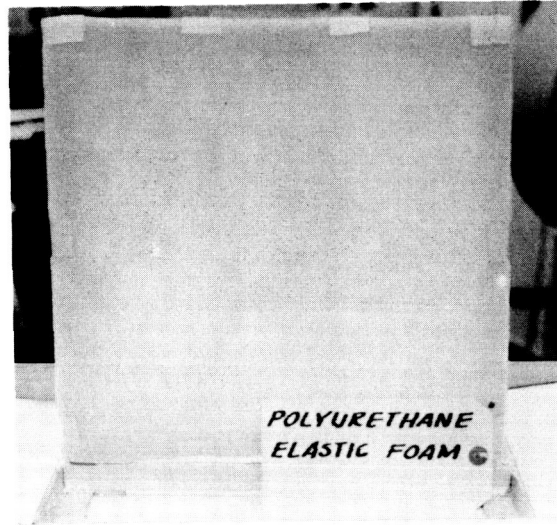


Figure 115. Test Sample of Polyurethane Elastic Foam

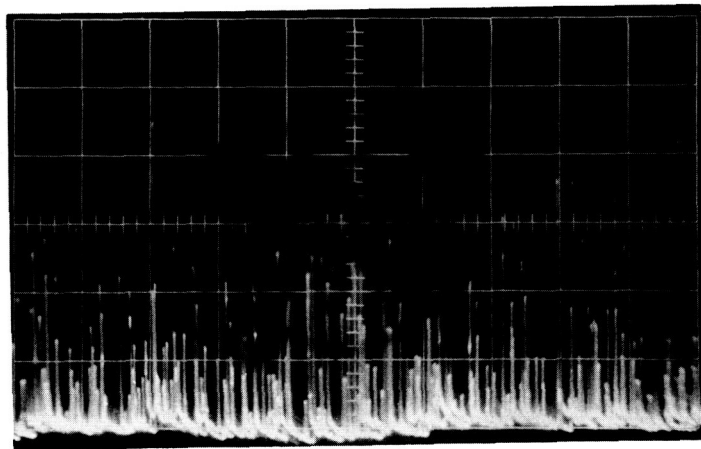


Figure 116. Video-Monitored Radiation Level

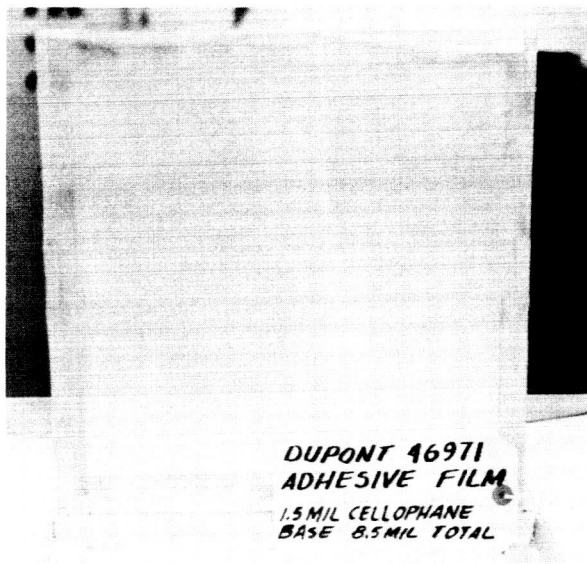


Figure 117. Test Sample of DuPont Type 46971 Adhesive on 1.5-mil Cellophane Base

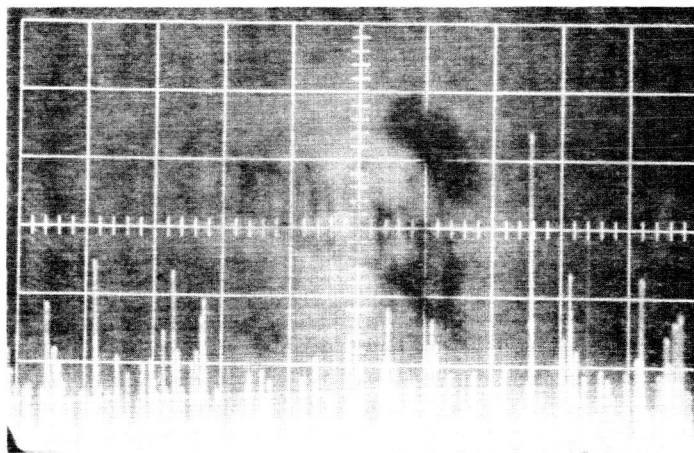


Figure 118. Video-Monitored Radiation Level

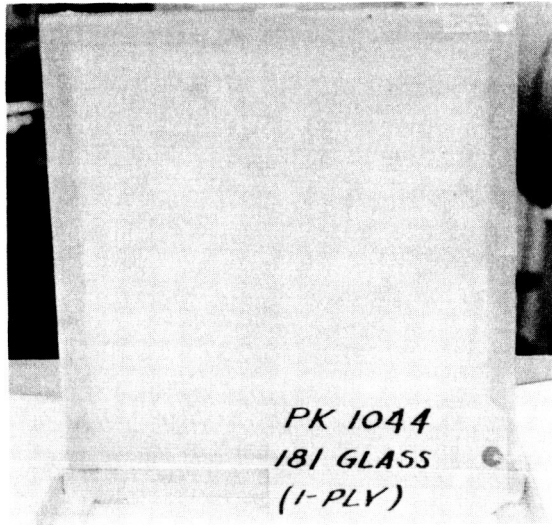


Figure 119. Test Sample of Laminate
(PK-1044 resin and 181
glass fabric)

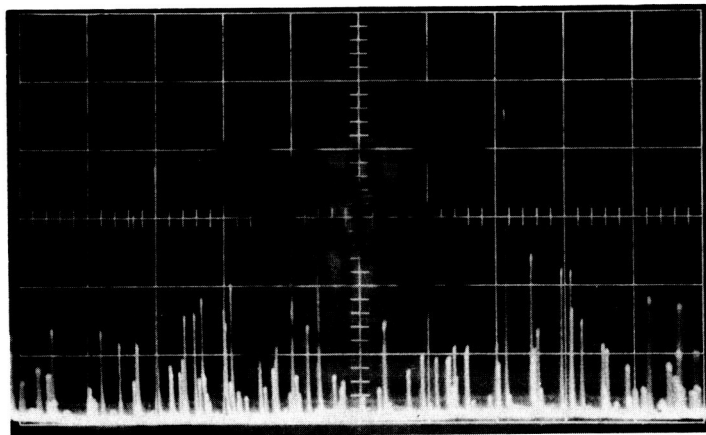


Figure 120. Video-Monitored Radiation
Level

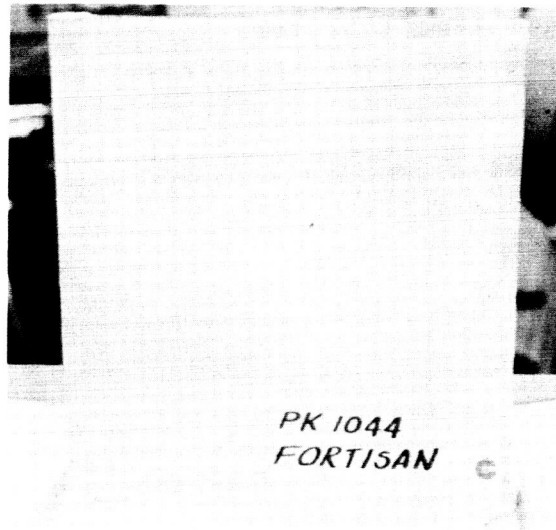


Figure 121. Test Sample of Laminate
(PK-1044 resin and
Fortisan fabric)

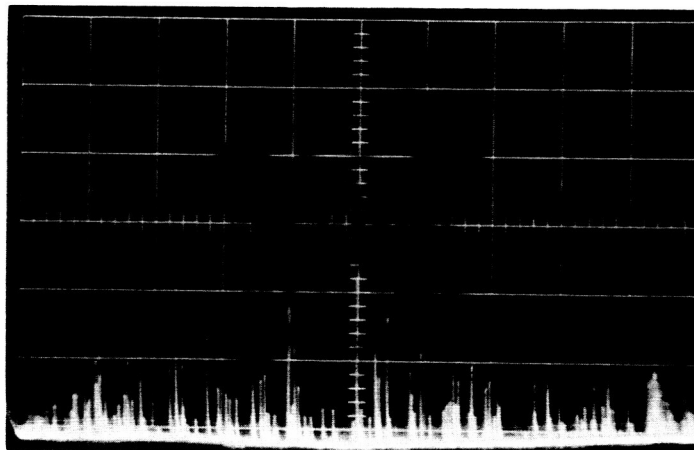


Figure 122. Video-Monitored Radiation
Level

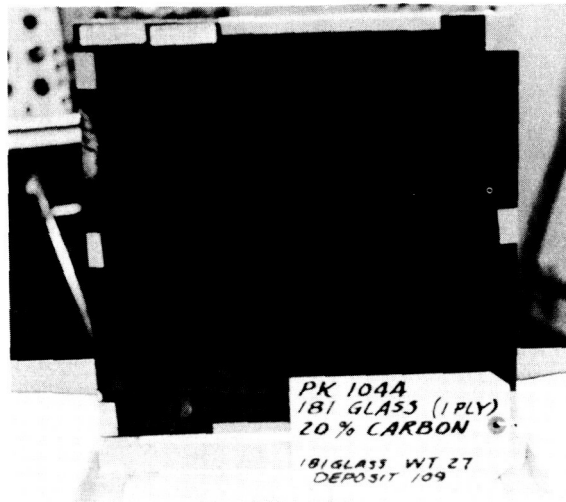


Figure 123. Test Sample of Laminate (PK-1044 resin with 20% by weight carbon loading and type 181 glass fabric)

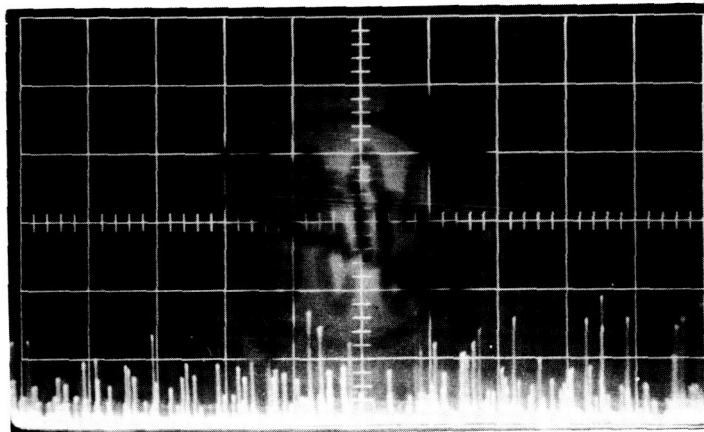


Figure 124. Video-Monitored Radiation Level

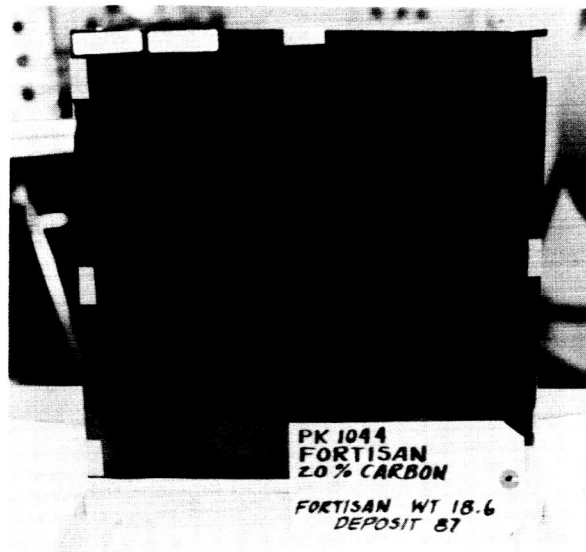


Figure 125. Test Sample of Laminate
(PK-1044 resin with 20%
by weight carbon load-
ing and Fortisan fabric)

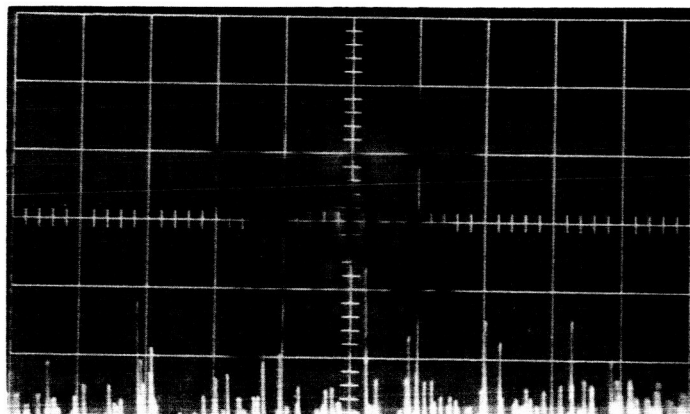


Figure 126. Video-Monitored Radiation
Level

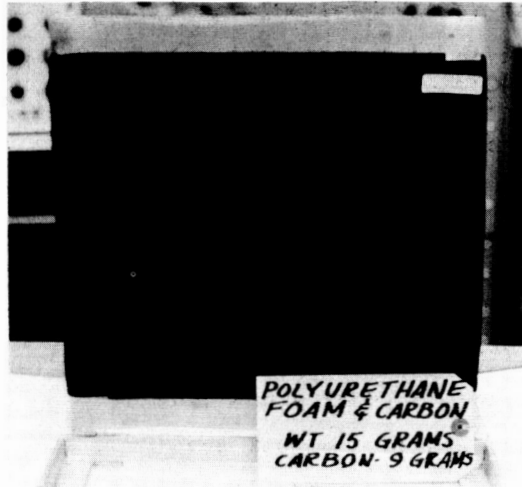


Figure 127. Carbon-Saturated Polyurethane Elastic Foam

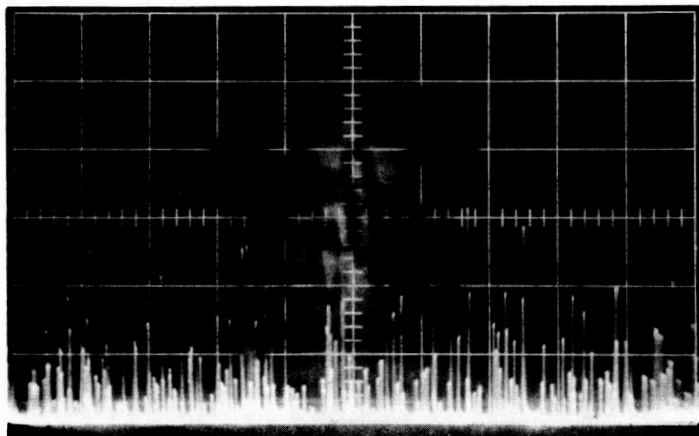
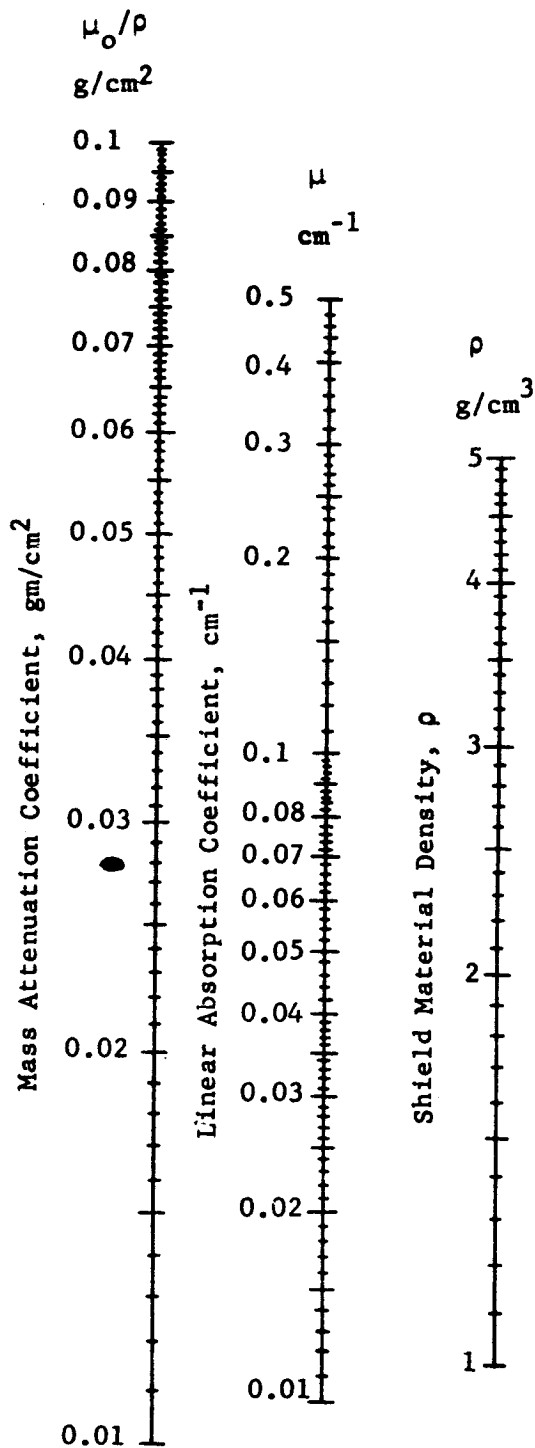


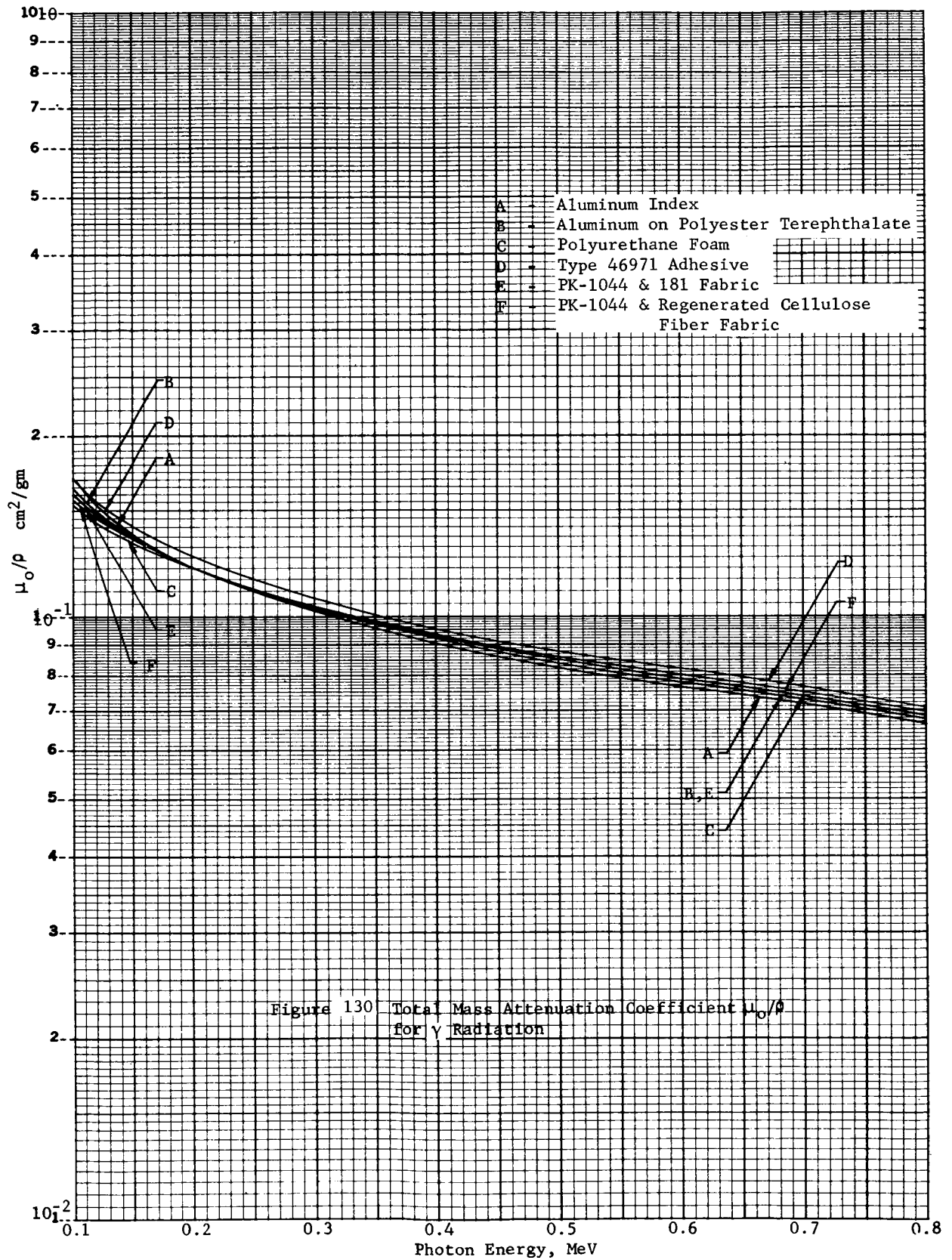
Figure 128. Video-Monitored Radiation Level

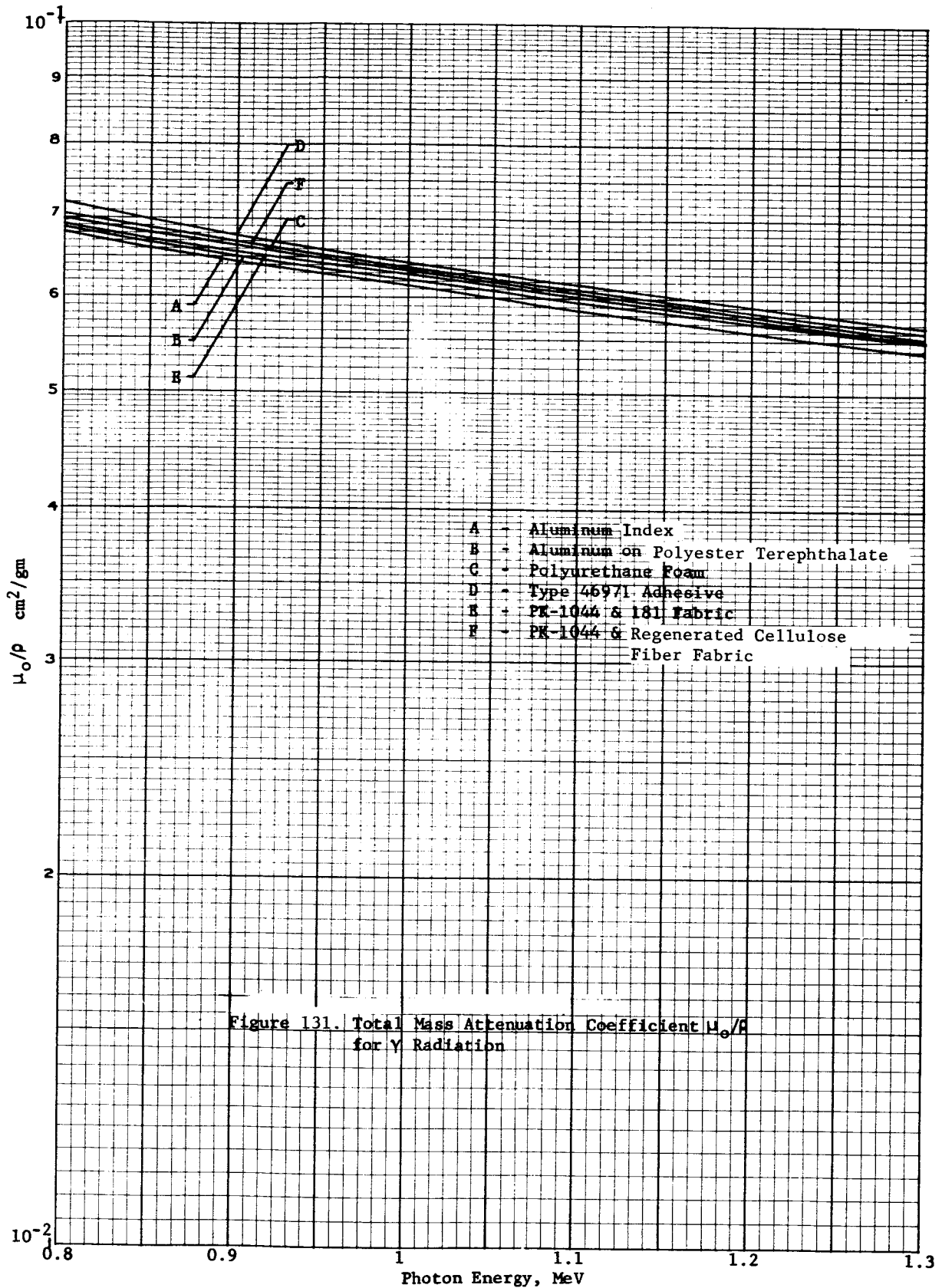


<u>Material</u>	<u>Density, ρ</u>
Aluminum Index	2.70
PK1044/181 Glass	1.68
PK1044/Regenerated Cellulose Fiber	1.38
PK1044-Carbon/181 Glass	1.395
Aluminum polyester Terephthalate	1.315
PK1044-Carbon/Regenerated Cellu- lose Fiber	1.28
DuPont 46971 Adhesive	1.24
Polyurethane Foam	0.237
Polyurethane Foam/Carbon	0.356

* 5.5 MEV energy index

Figure 129. Gamma Ray Shielding Material Coefficients NOMOGRAM





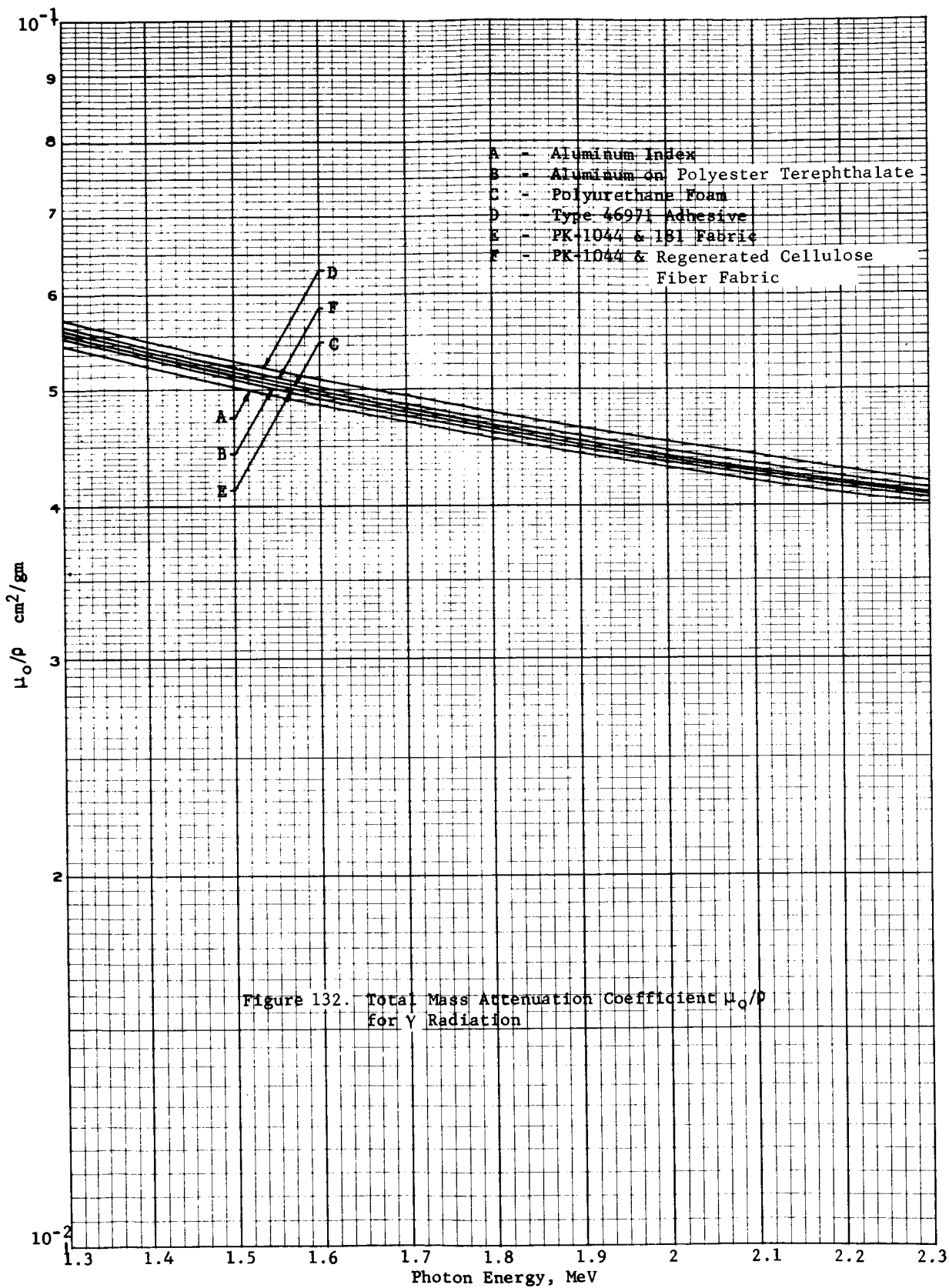
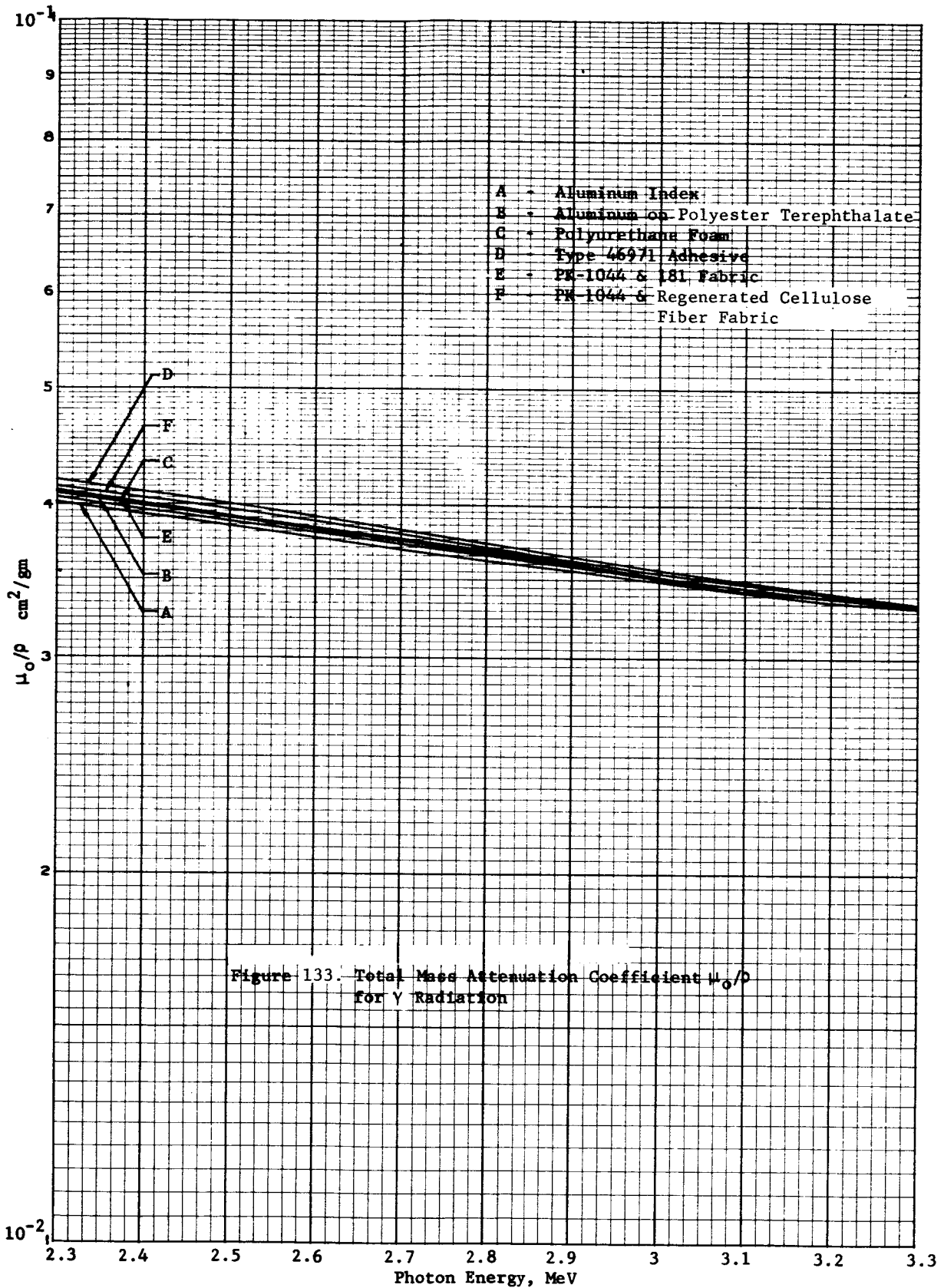


Figure 132. Total Mass Attenuation Coefficient μ_0/ρ for γ Radiation



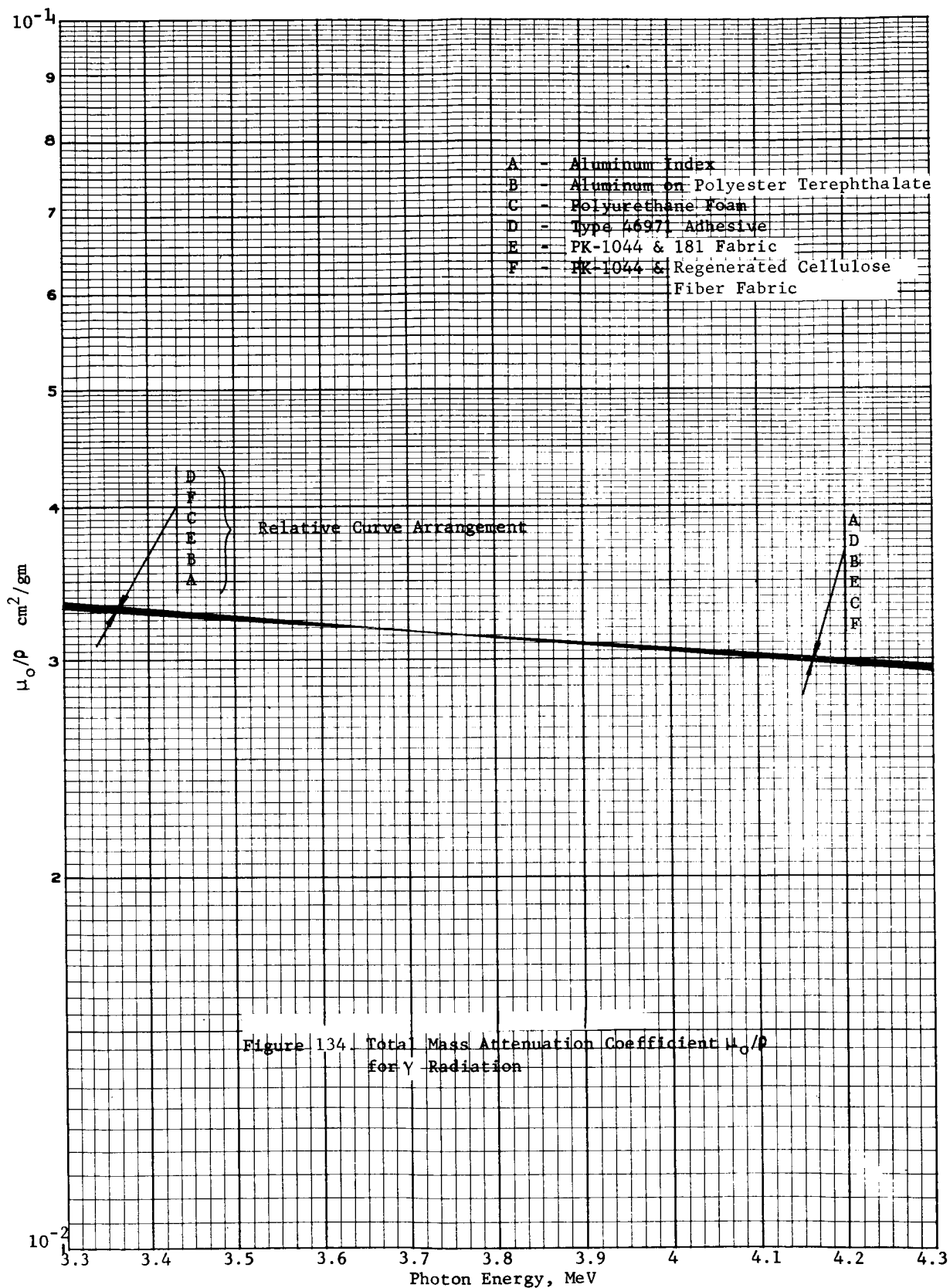


Figure 134. Total Mass Attenuation Coefficient μ_0/ρ for γ Radiation

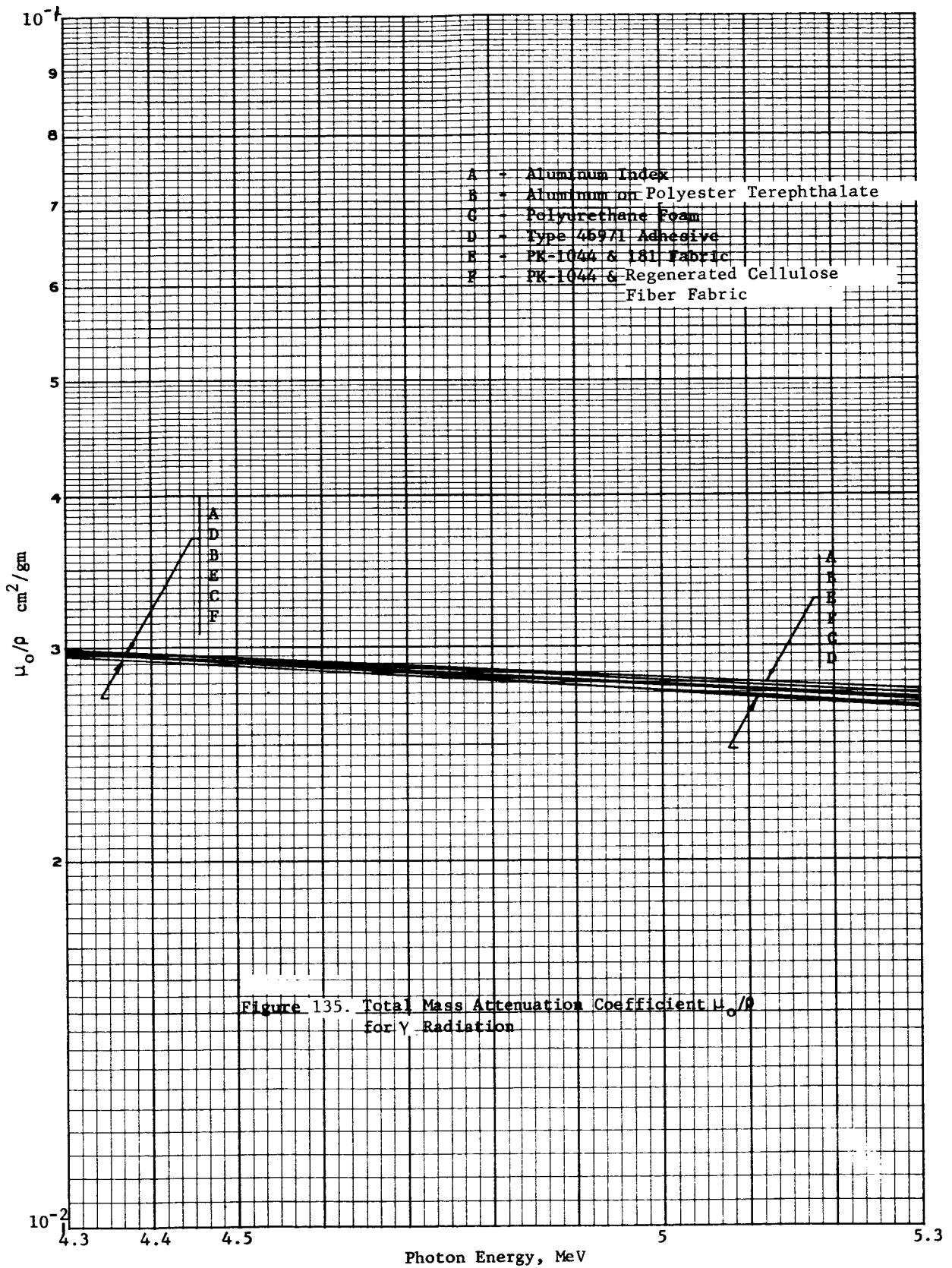


Figure 135. Total Mass Attenuation Coefficient μ_0/ρ For γ Radiation

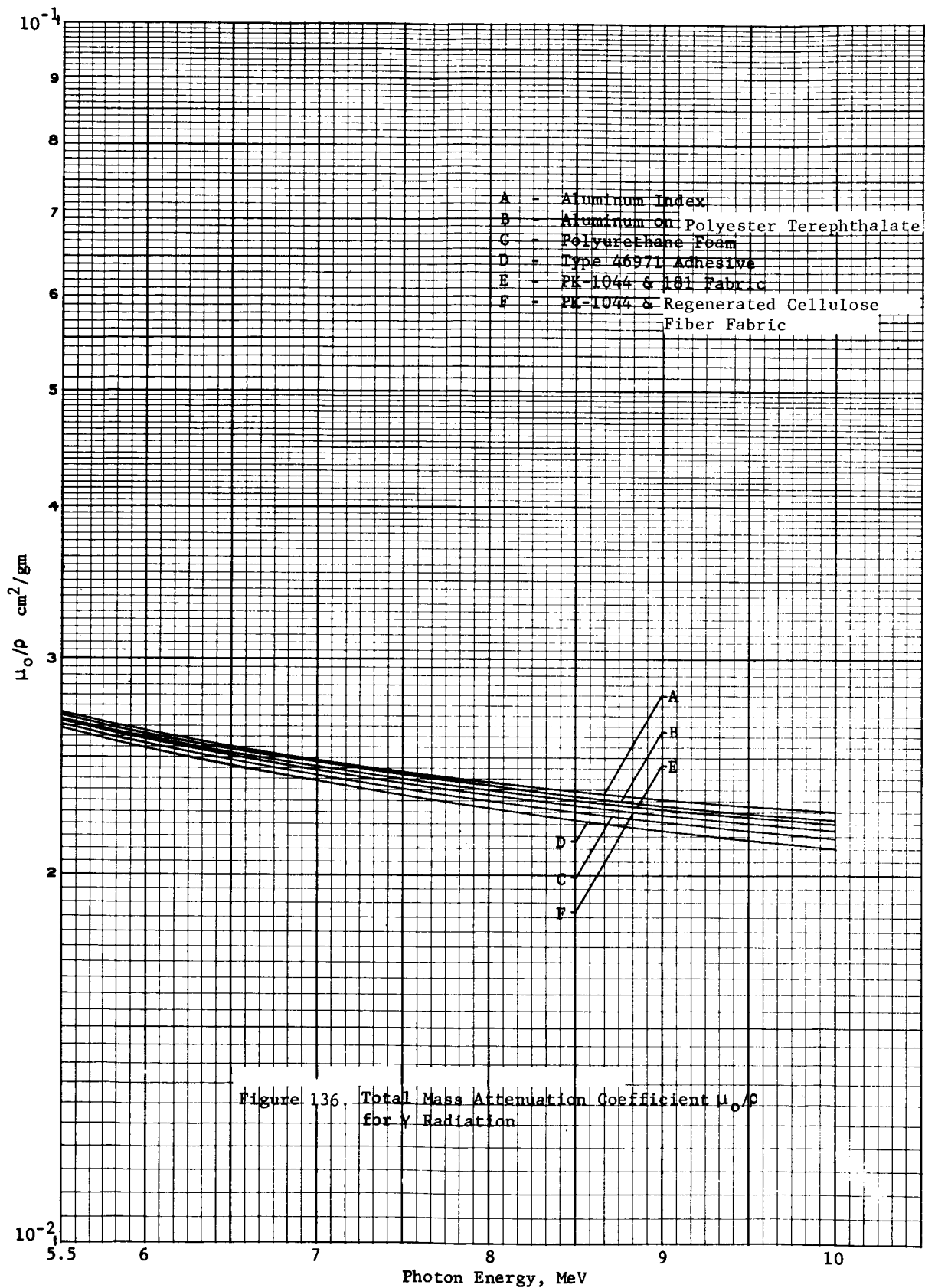
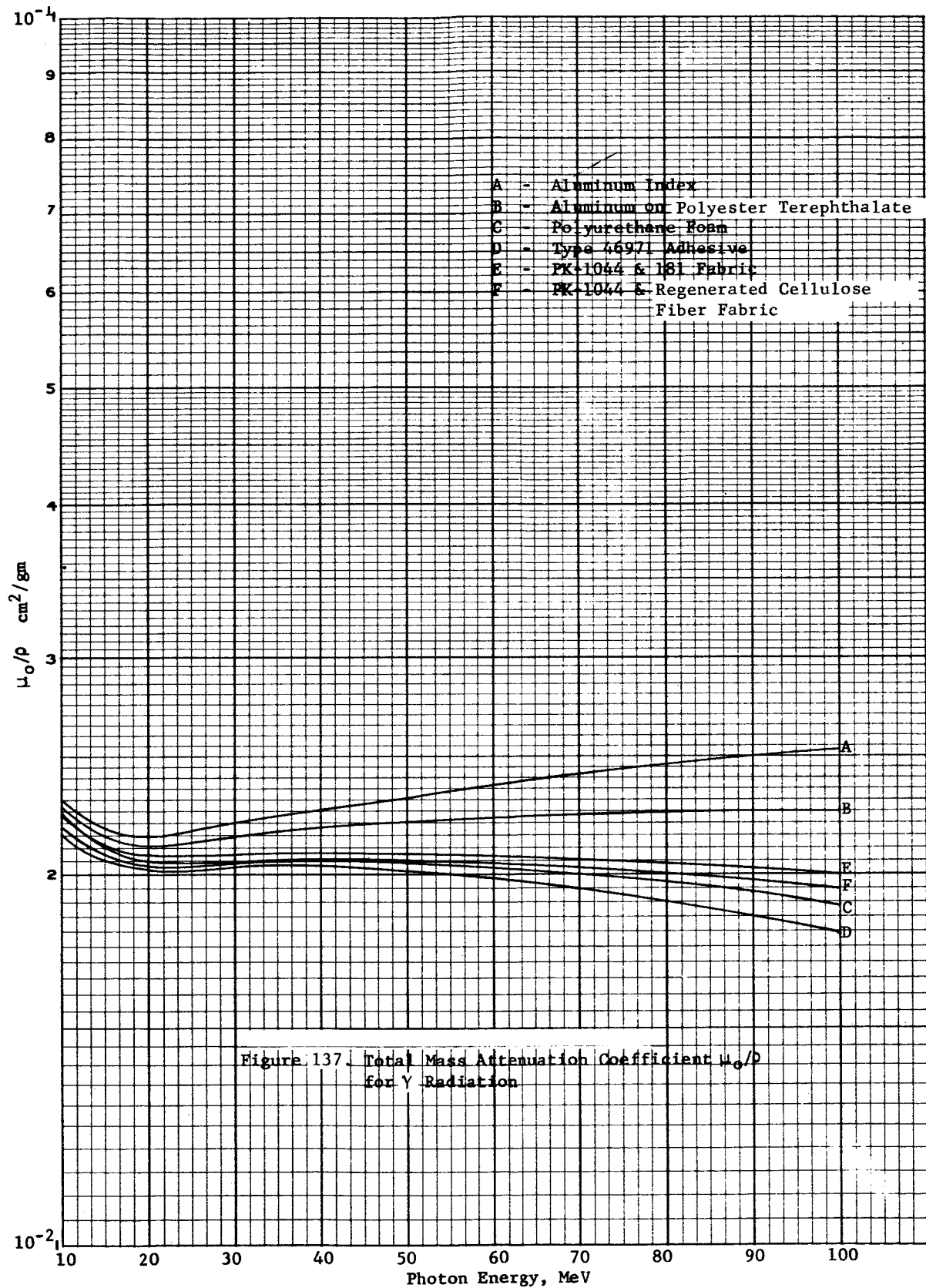


Figure 136. Total Mass Attenuation Coefficient μ_0/ρ for γ Radiation



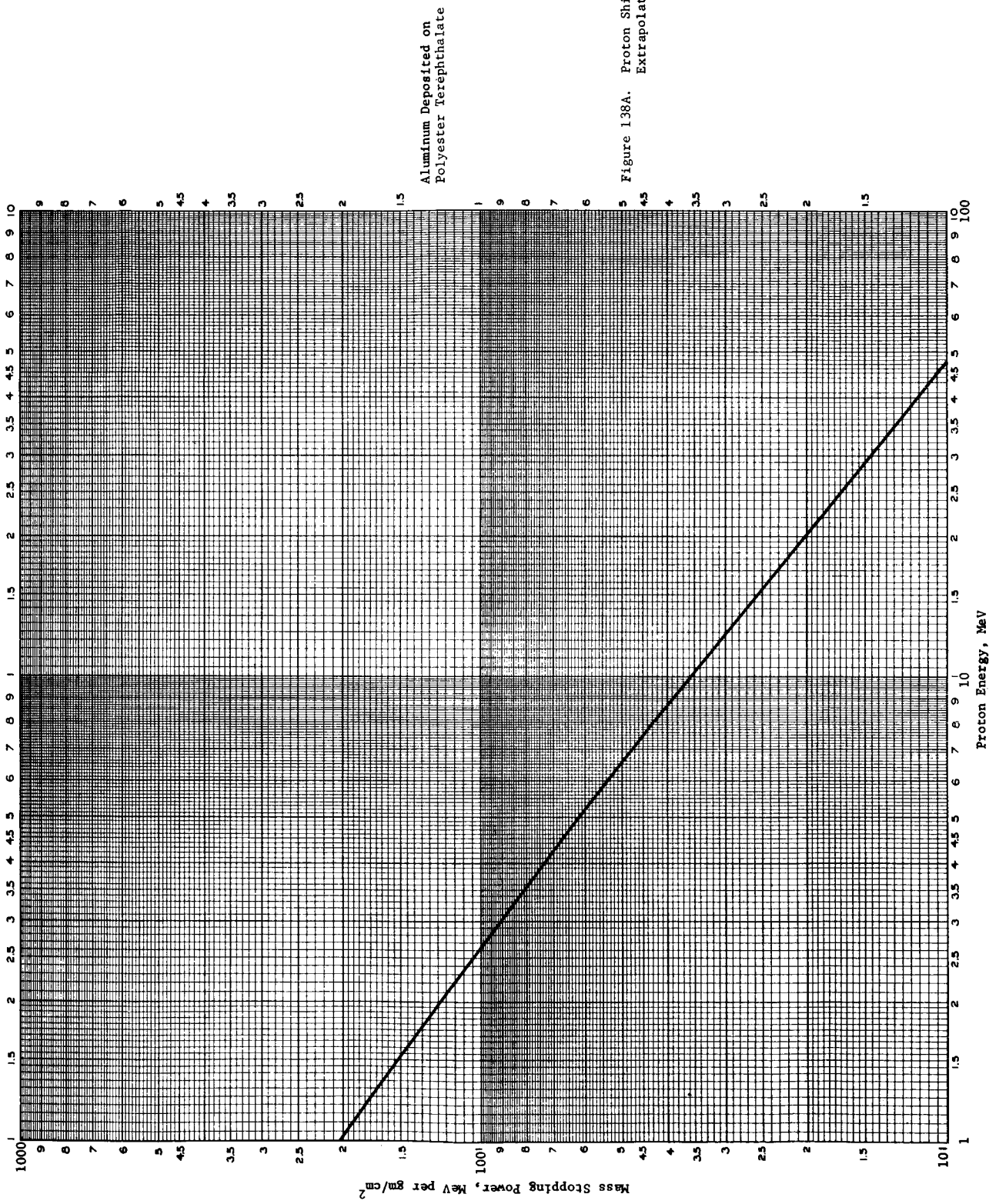


Figure 138A. Proton Shielding Extrapolation

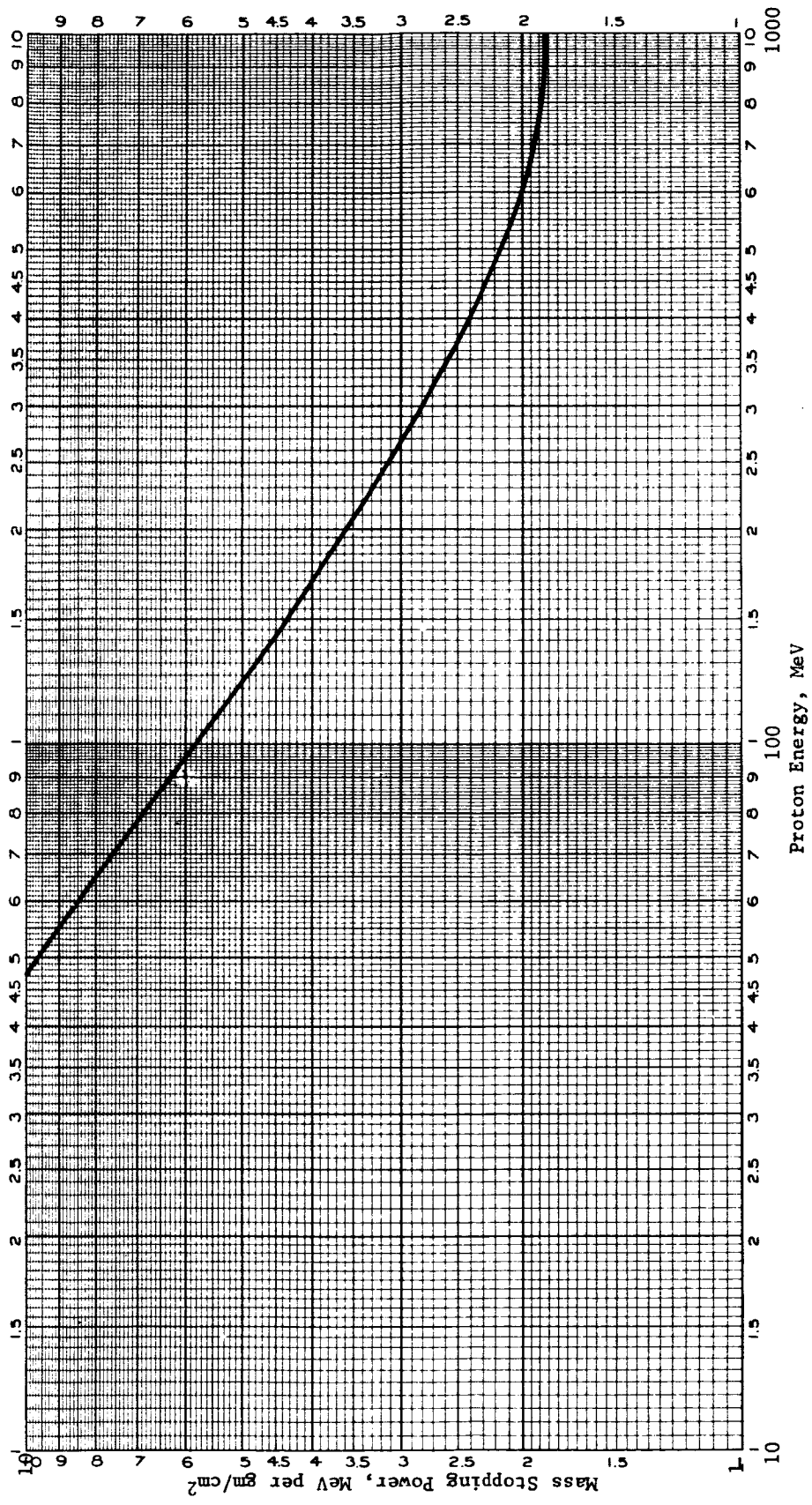


Figure 138B. Proton Shielding Extrapolation
Aluminum Deposited on Polyester
Terephthalate

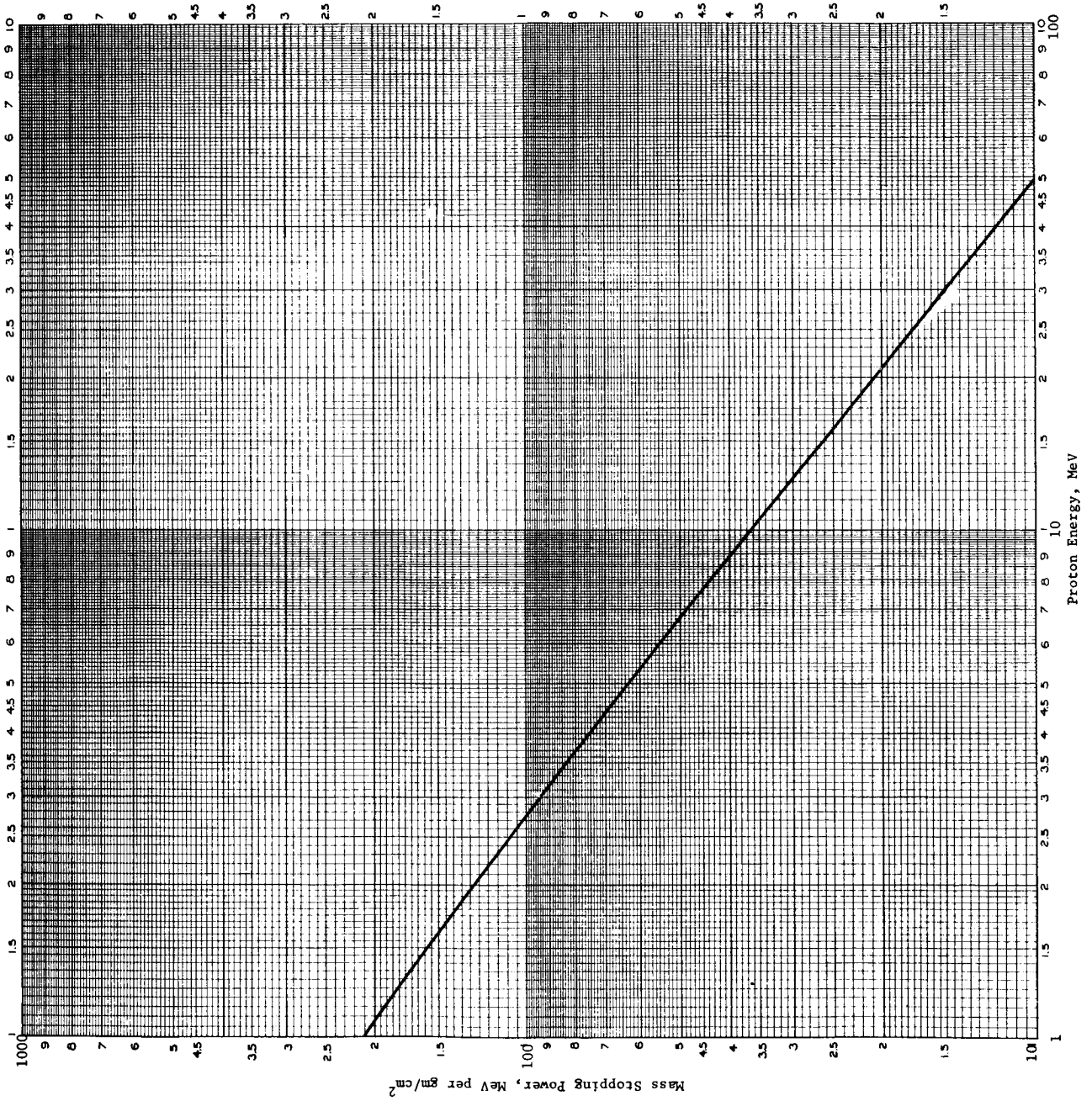


Figure 139A. Proton Shielding Extrapolation

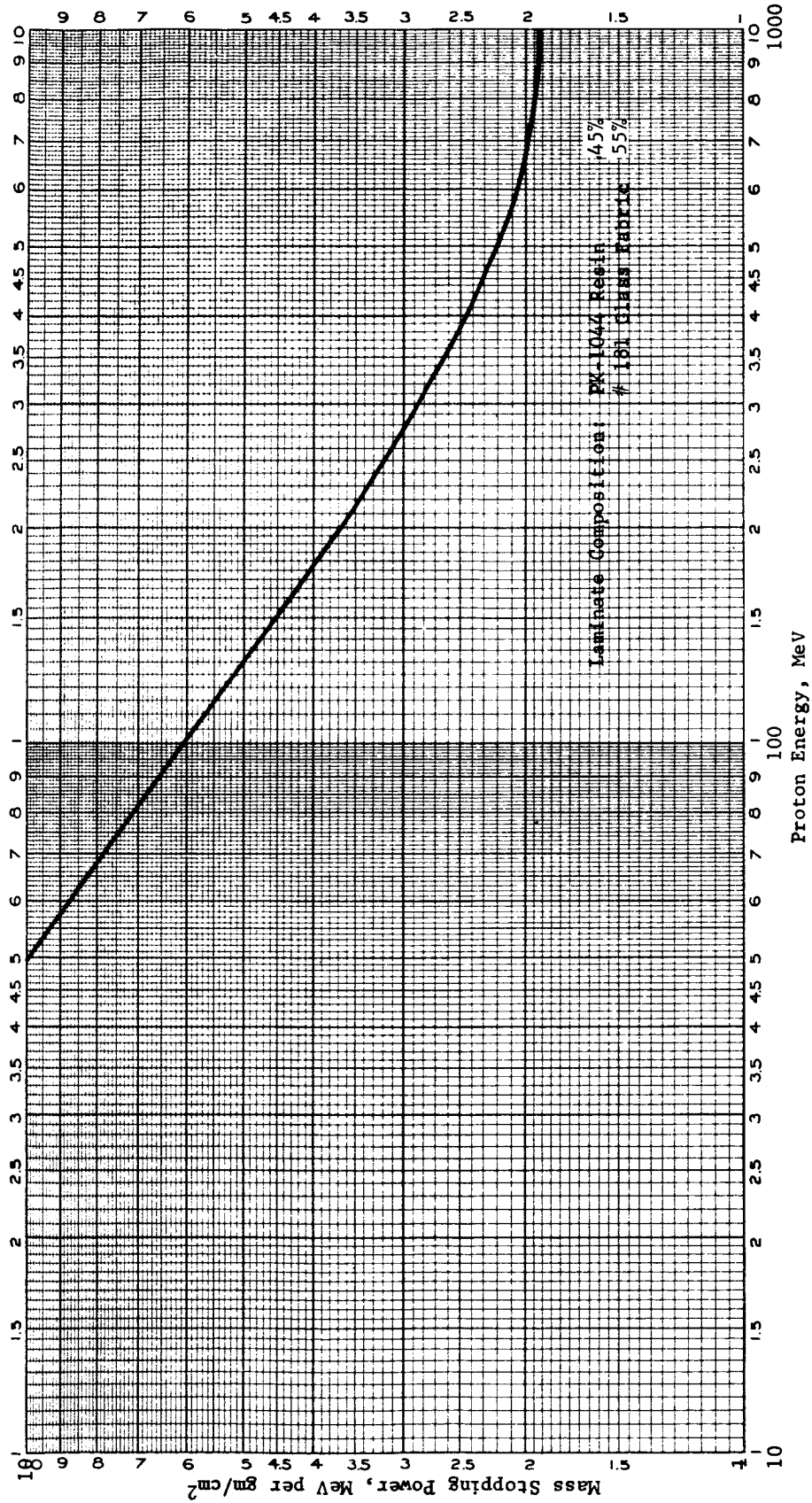
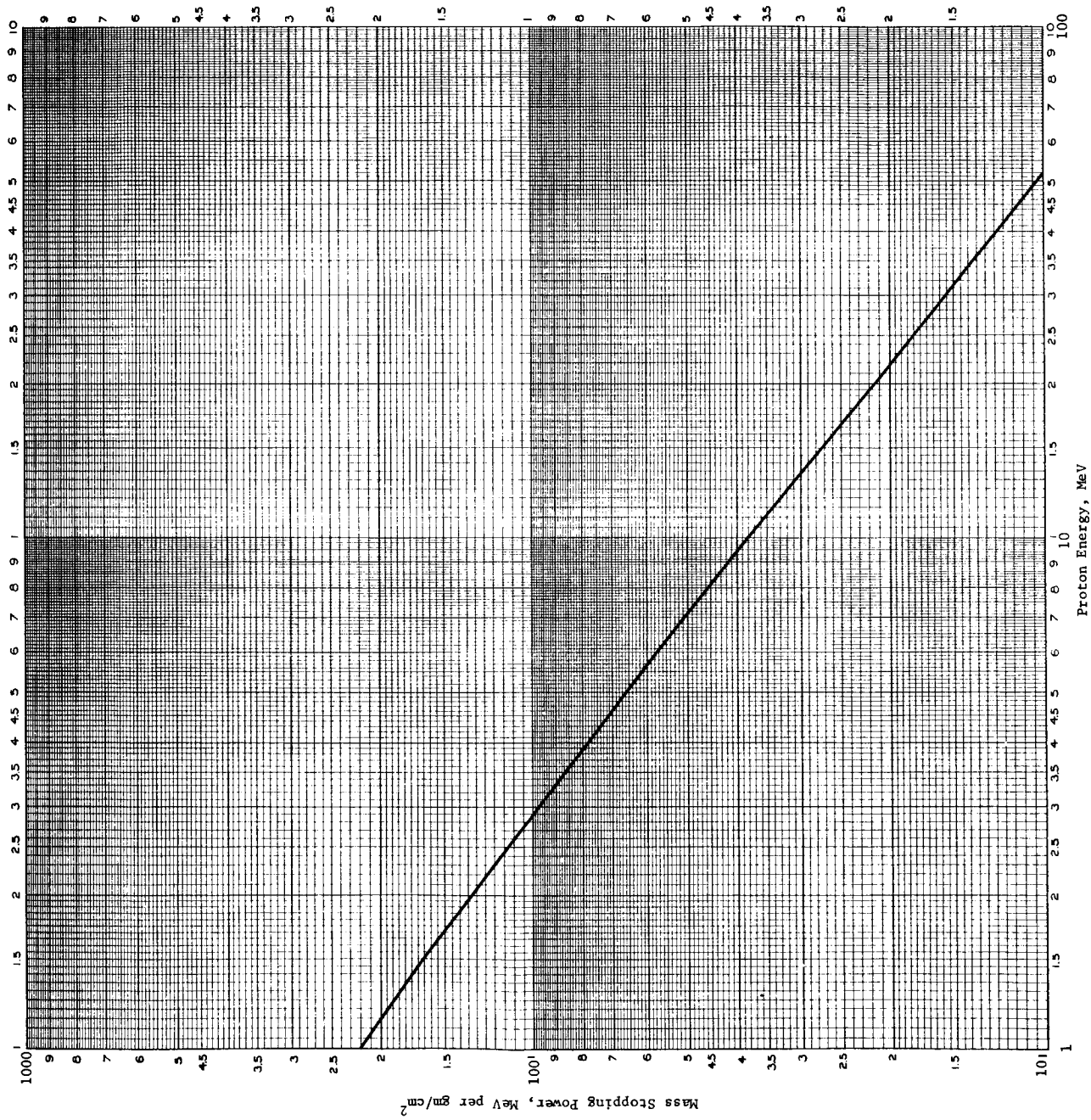


Figure 139B. Proton Shielding Extrapolation



1.5 Laminate Composition
PK-1044 Resin 33%
Regenerated
Cellulose Fiber 67%
Fabric

5 Figure 140A. Proton Shielding
Extrapolation

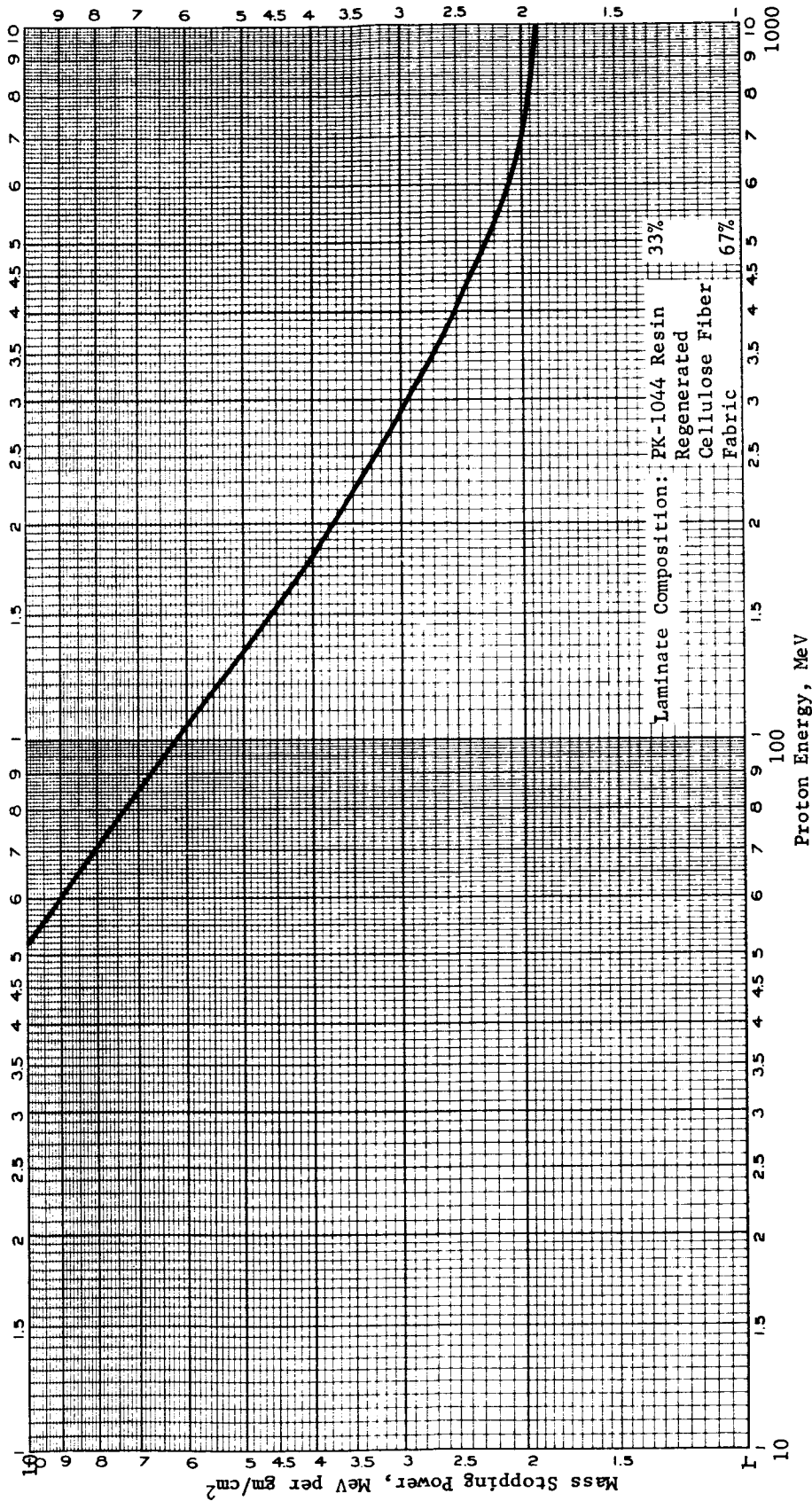
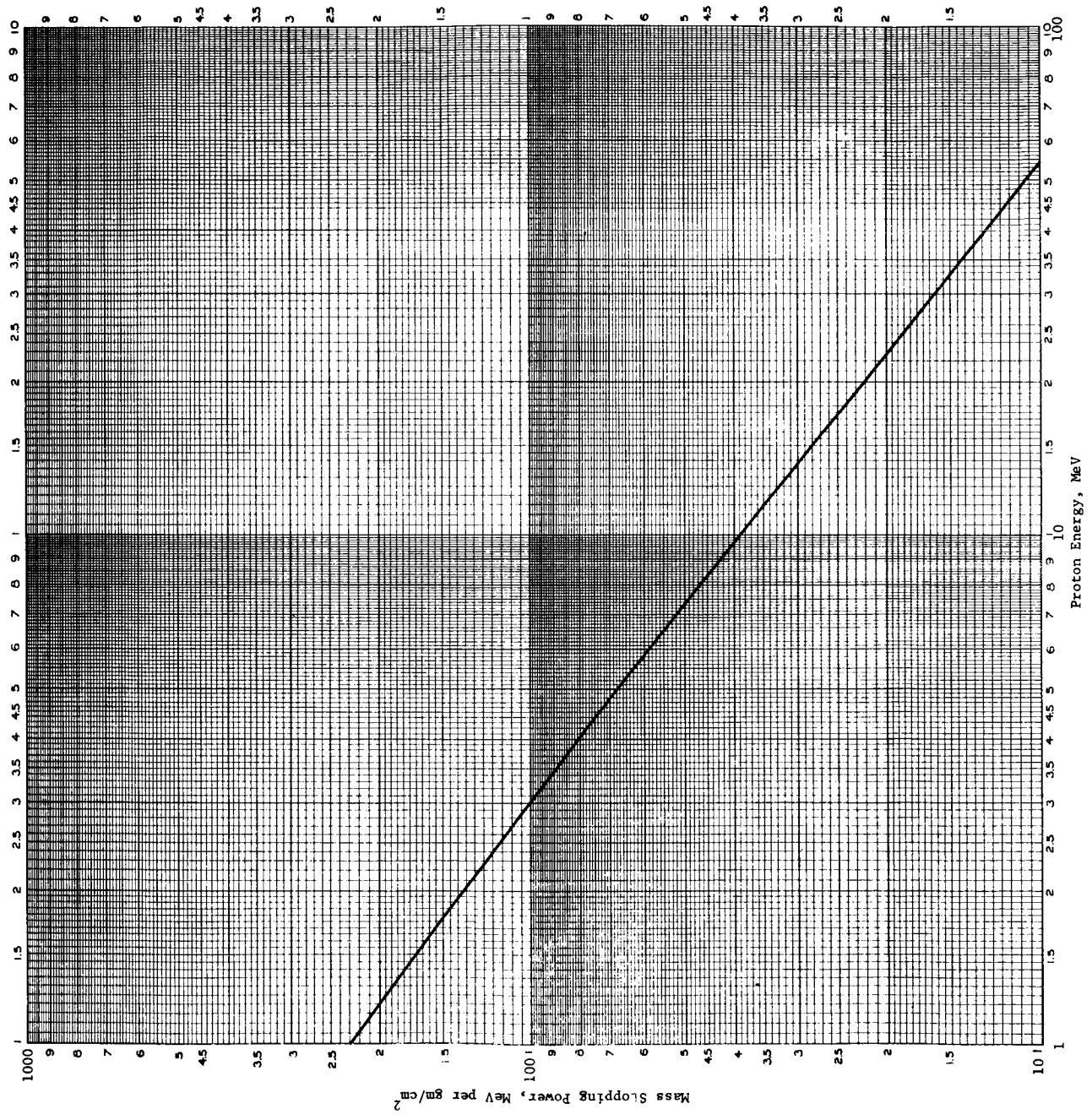


Figure 140B. Proton Shielding Extrapolation



1.5 Polyurethane Foam
Test Sample 1.9 lb/ft³

Figure 141A. Proton Shielding
Extrapolation

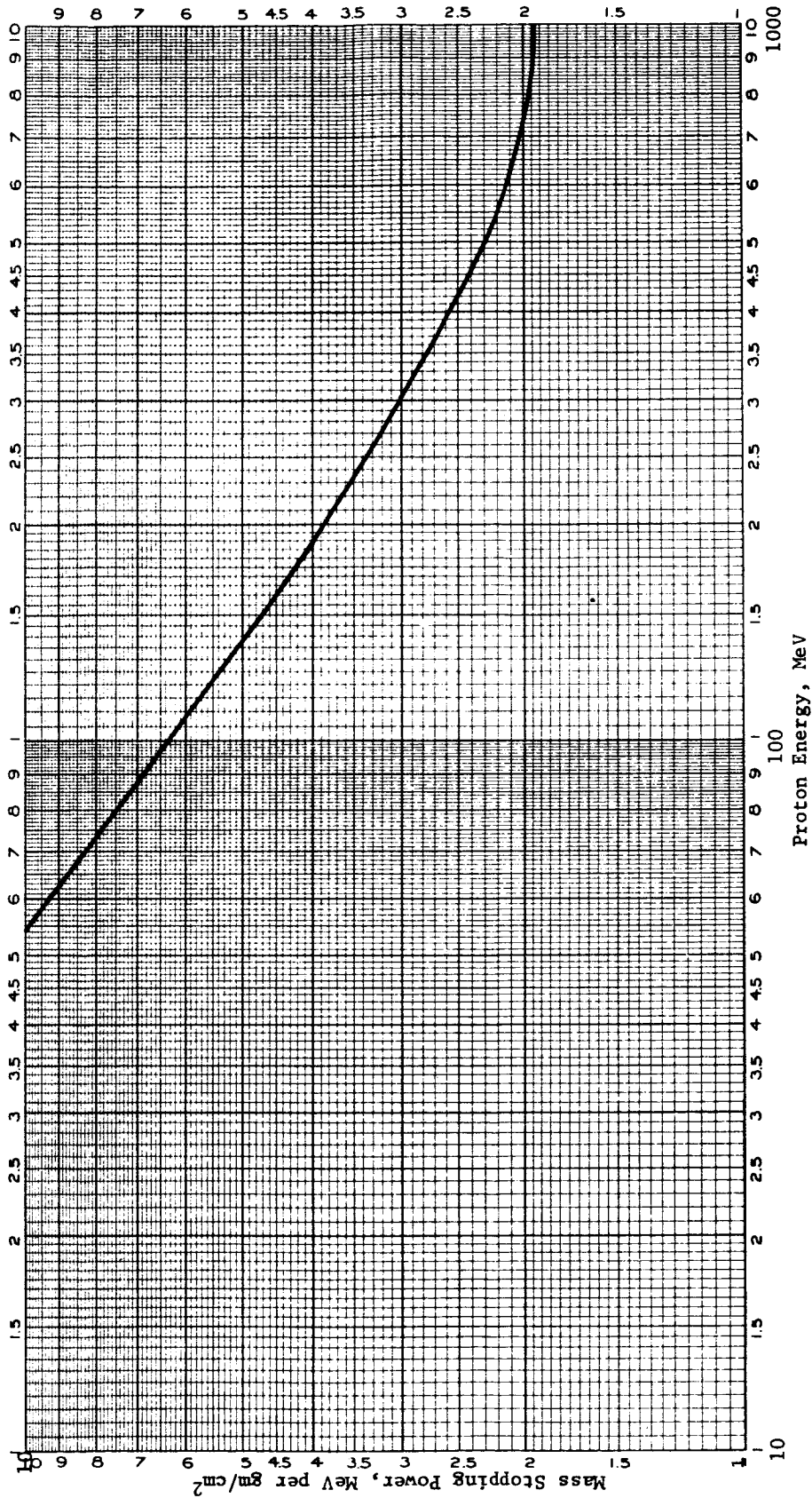


Figure 141B. Polyurethane Foam Test Sample 1.9 lb/ft³
Proton Shielding Extrapolation

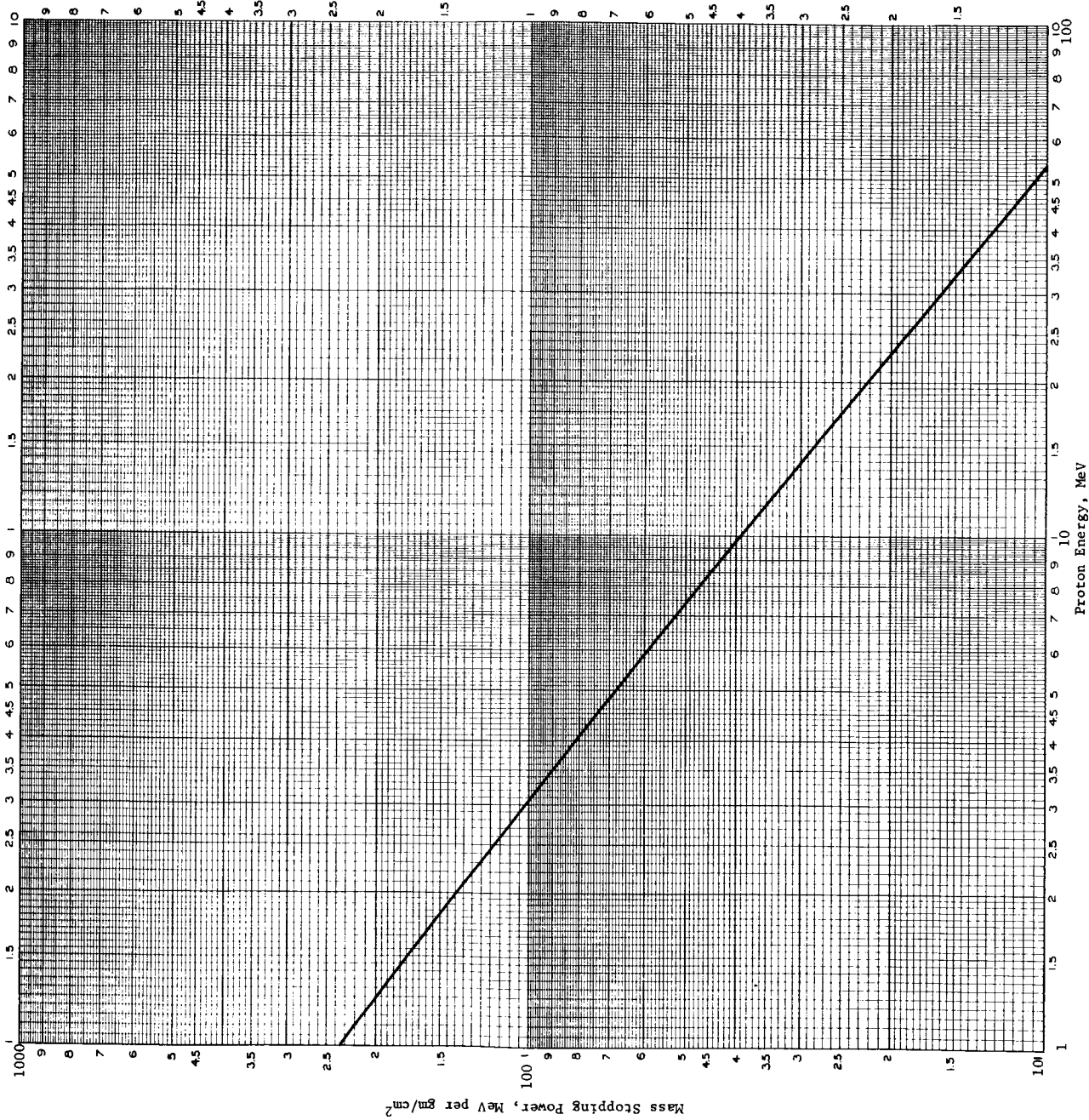


Figure 142A. Proton Shielding Extrapolation

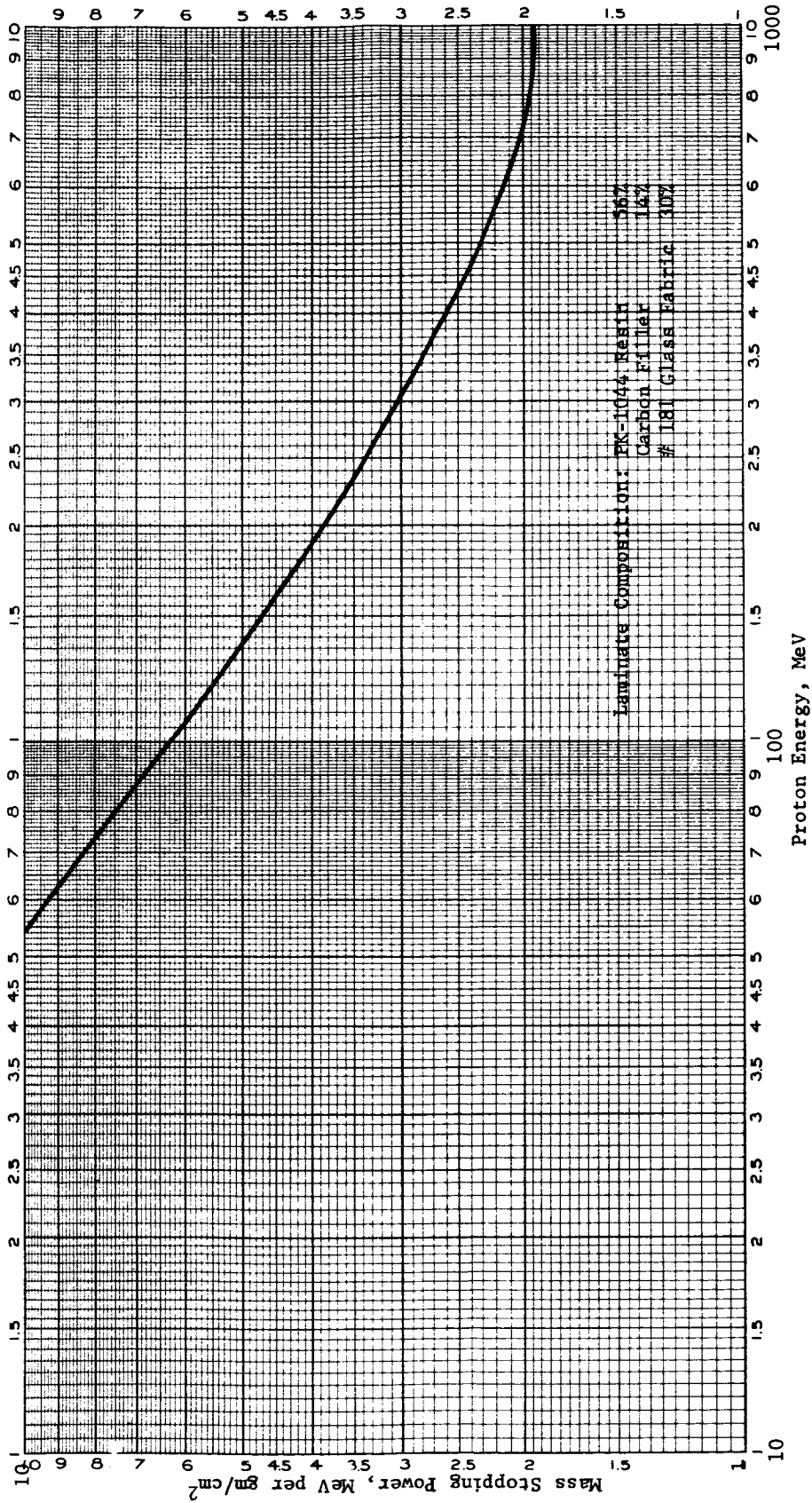
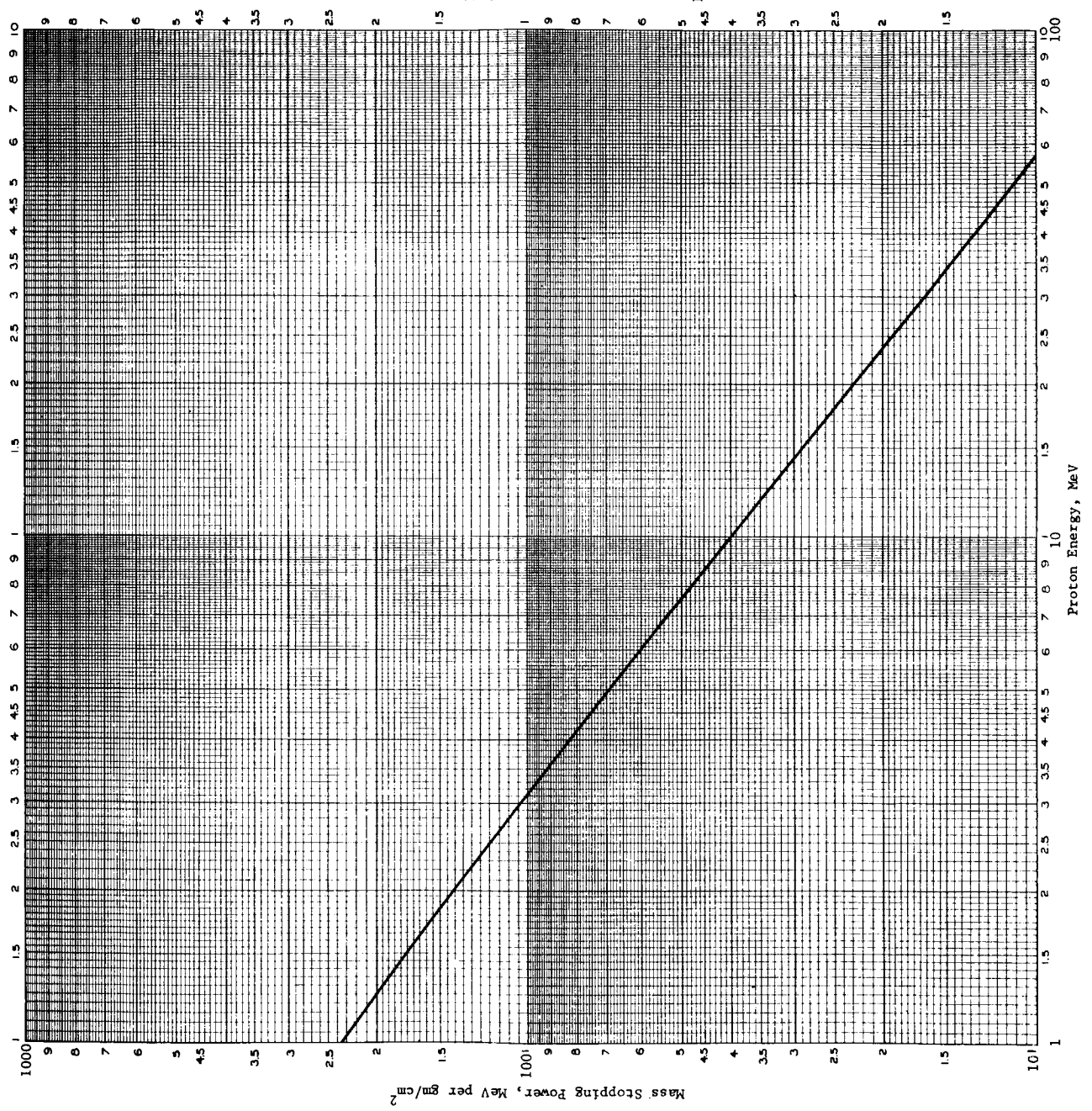


Figure 142B. Proton Shielding Extrapolation



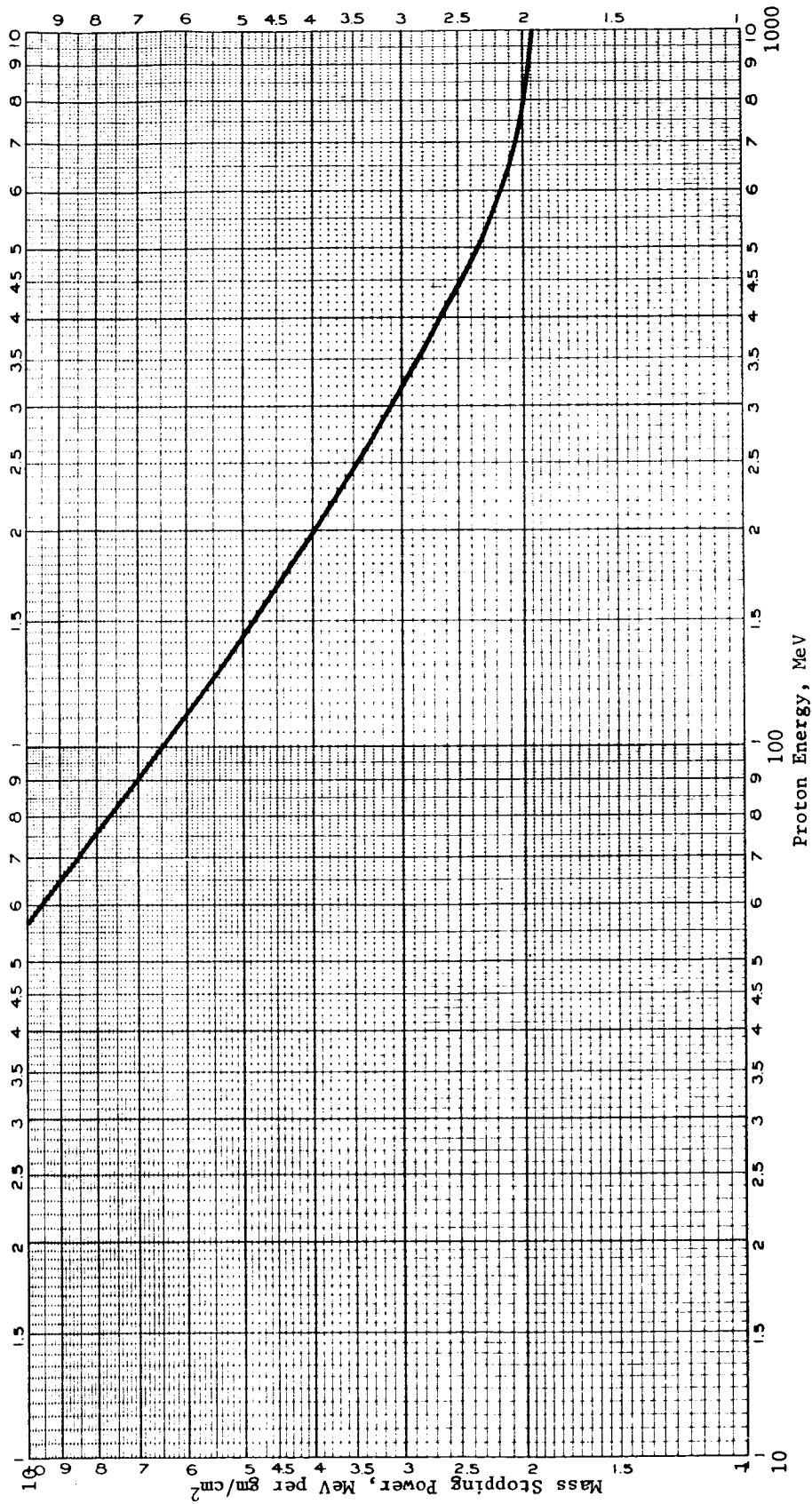
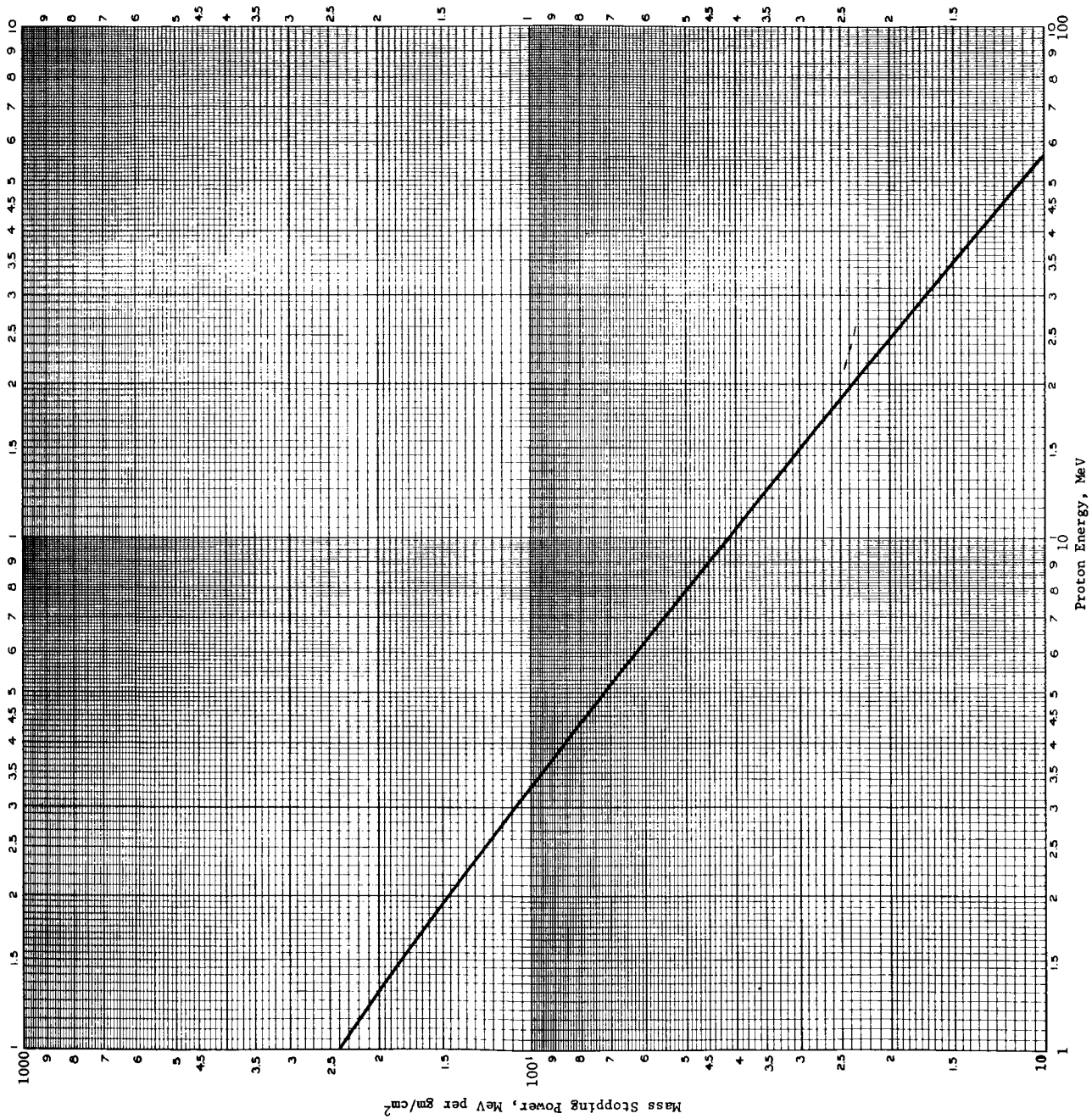


Figure 143B. Proton Shielding Extrapolation
 Polyurethane Foam Test Sample
 1.9 lb/ft³ Carbon Saturated



Laminate Composition
PK-1044 Resin 46.4%
Carbon Filler 11.6%
Regenerated Cellulose Fiber 42 %
Fabric

Figure 144A. Proton Shielding Extrapolation

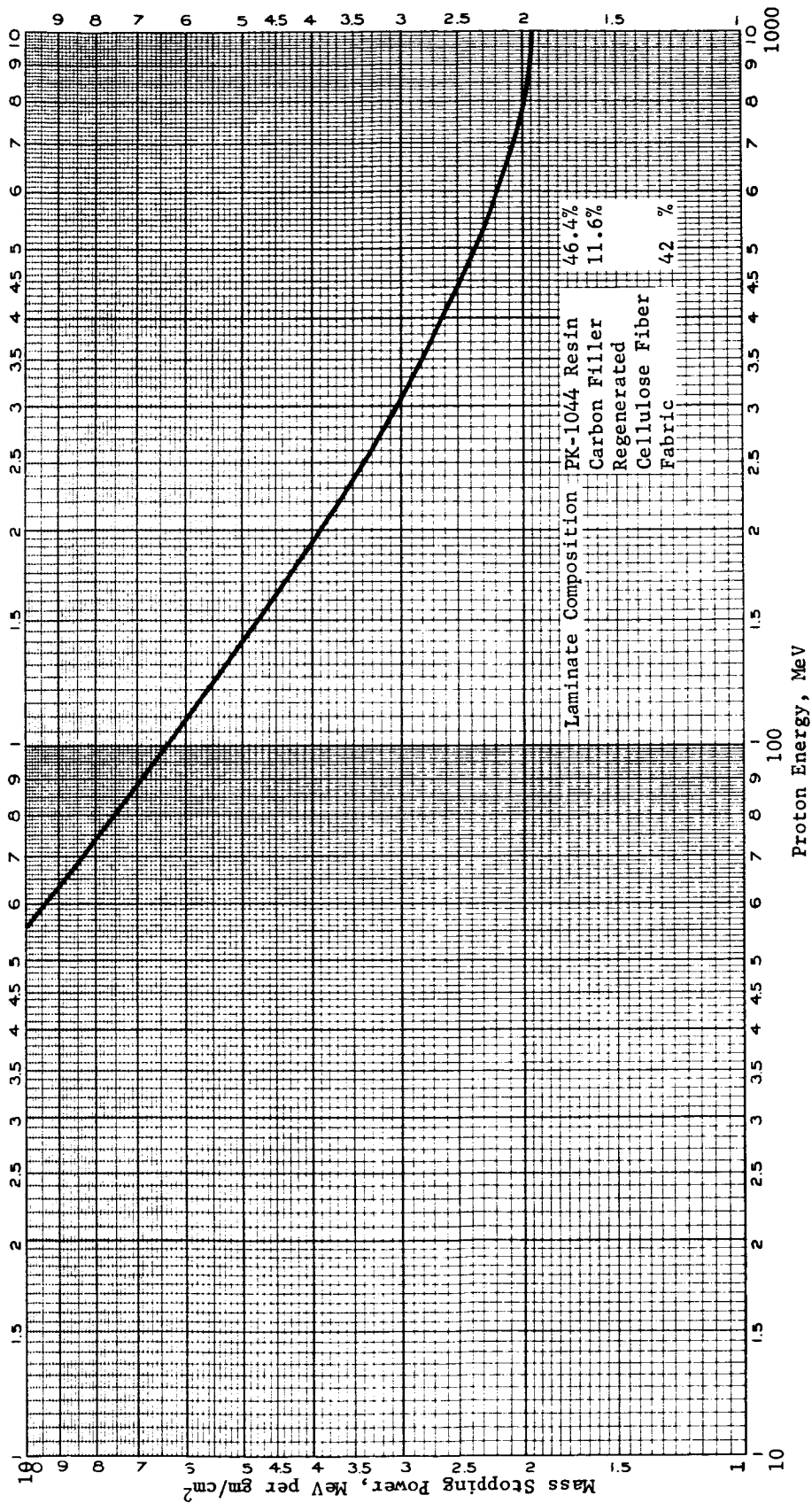
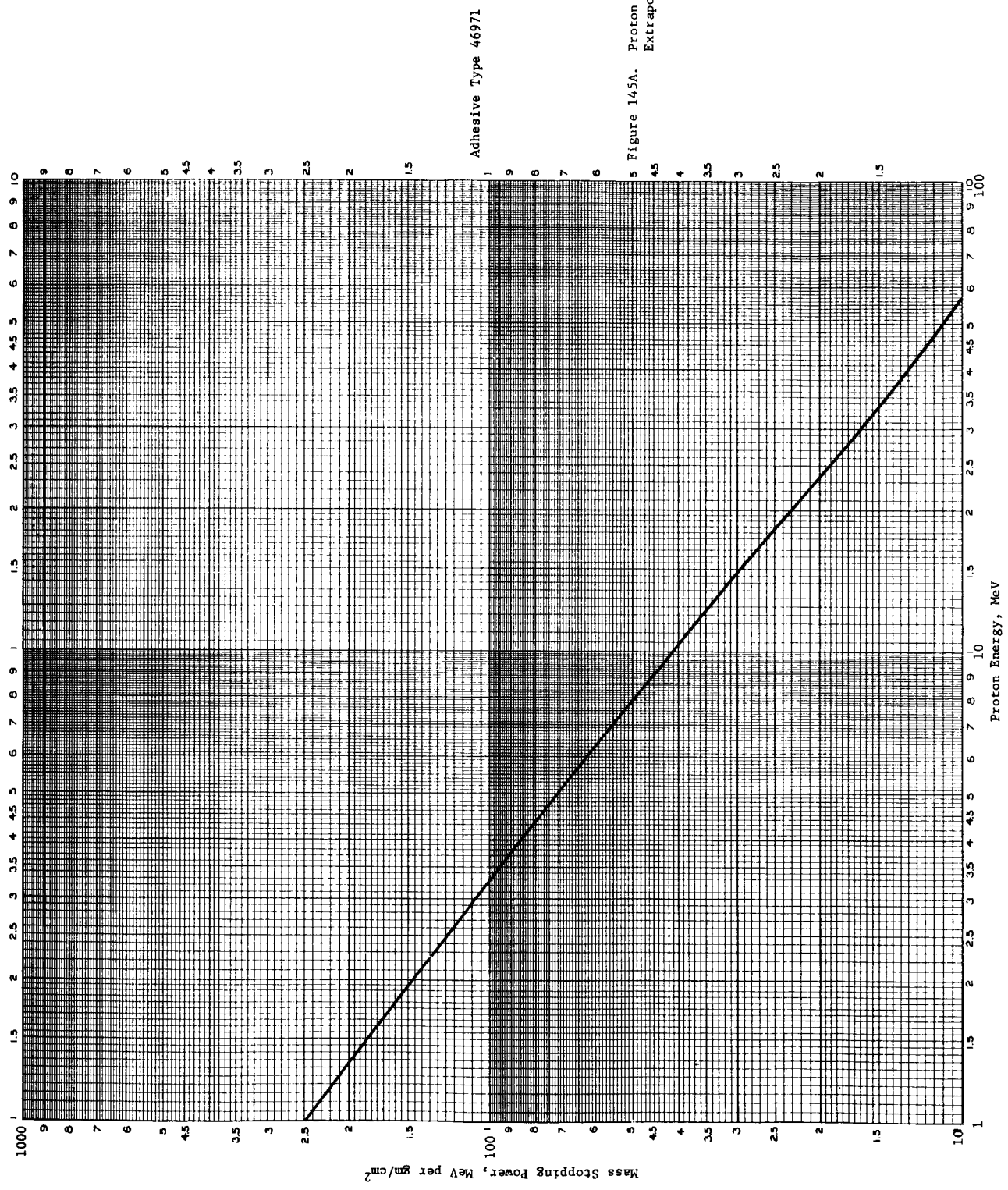


Figure 144B. Proton Shielding Extrapolation



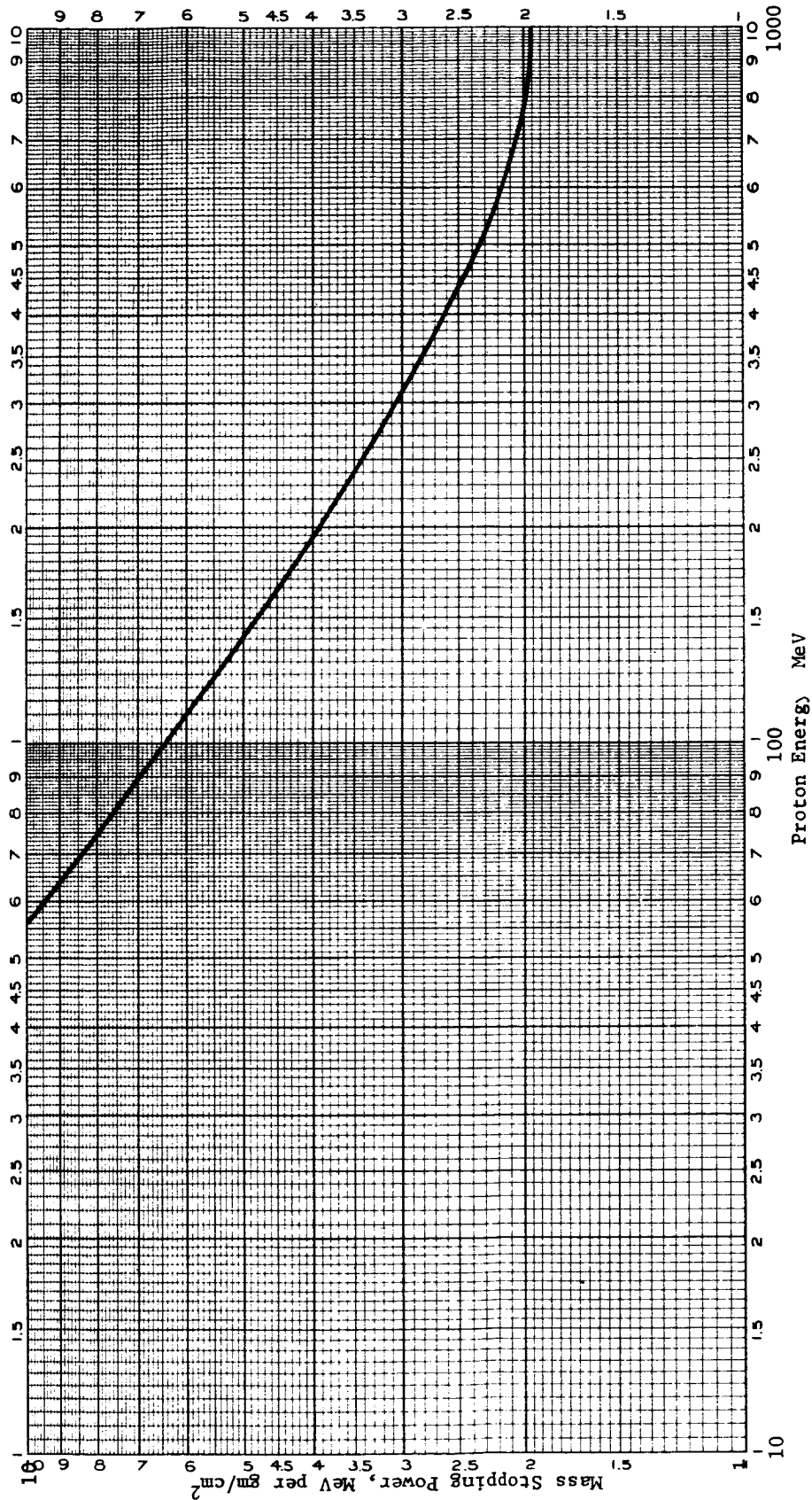


Figure 145B. Proton Shielding Extrapolation
Adhesive Type 46971

APPENDIX F

A STATE-OF-THE-ART REVIEW AND A CONCEPT FOR LARGE, EXPANDABLE SPACE ANTENNAS EMPLOYING ELASTIC RECOVERY MATERIALS

Abstract

This report evaluates those factors of major consequence in the design and construction of large antenna reflecting apertures for use in space environments. The types of antennas considered are those applicable to microwaves in the conventional medium microwave spectrum. The discussions include some of the problems which relate to different construction methods and assembly procedures, as well as the serious effects of environment.

A design is considered to alleviate the construction problems and environmental effects usually encountered in large space antenna designs. This approach is presently the subject of a Narmco patent disclosure, and has resulted from the study of construction and dimensional error problems associated with parabolic reflector antennas. The subject approach makes use of elastic recovery expandable materials in unique applications to achieve structural, environmental, and performance efficiency.

In order to emphasize the problem areas associated with conventional concepts of space antenna design, the discussions detail the current antenna state-of-the-art limitations to show certain areas in concept designs where assumptions made are invalid.

APPENDIX F

A STATE-OF-THE-ART REVIEW AND A CONCEPT FOR LARGE, EXPANDABLE SPACE ANTENNAS EMPLOYING ELASTIC RECOVERY MATERIALS

by

C. E. Wolcott

I. INTRODUCTION

Generally, space antenna concepts may be divided into two basic categories: the class of antennas based upon resonant elements to achieve directivity, and the class of antennas based upon collimation techniques. Antennas in the resonant element class are typified by the use of parasitic, helical, spiral, log-periodic, slot and other forms of elements and are often found in the form of arrays. The class of antennas based upon collimation principles is typified by parabolic reflectors, horns, and lens, and may also be used in arrays.

In functional terms, the directivity of an antenna (gain, G_0) is not necessarily of separate identity from collimation. However, a difference may be recognized in a physical definition between the two classes relating to performance. Where the requirement specifies a very high gain function which can only be satisfied by extremely complex arrays in the resonant element case, using the far less complex collimation principles is found to be advantageous.

Therefore, the following discussions and evaluation for large, highly directive space antennas will pertain to the class of antennas referred to as employing microwave collimating reflectors or lens. Because the antennas are to be considered for use in space, a particular environment is specified, and, therefore, the first consideration should be the evaluation of concepts of construction in terms of the specified environment.

II. CONCEPTS FOR SPACE ANTENNA CONSTRUCTION

A review of practice and proposed space antenna concepts, of the collimating mirror reflector category, shows a general preference for the parabola of revolution. A wide variety of parabola construction methods have been proposed in attempts to achieve relatively light weight, a compact packaging for space vehicle transportation, ease of deployment in space, large aperture areas, and, in a few cases, obtain the required precision reflecting surface mandatory for efficient microwave antenna performance. These concepts have been based upon designs which include the following:

1. Inflatable parabolas of plastic-fabric materials
2. Inflatable tubular structural members which support reflecting membranes
3. Plastic apertures of revolution deployed by inflating members which are then separated
4. Plastic foamed-in-place reflectors
5. Unfolding or unfurling segment "petal" parabolas of revolution
6. Parabola assemblies composed of reflecting panel segments

It is of particular significance that the concepts proposed generally neglect to take into consideration two very important factors, either of which may cause the performance as an antenna to be worthless. These factors are the accuracy as a parabola to which the structure can be deployed, and the accuracy in the solar environment to which the reflecting surface can be maintained as a parabola.

Note the specific requirement for obtaining functional efficiency from a parabolic reflector antenna, wherein the reflective surface deviation shall not exceed $1/8$ wavelength ($\lambda/8$), and preferably no more than $1/16$ wavelength ($\lambda/16$), from that of the equation defined theoretical paraboloid. At a conventional frequency in the midrange of the microwave spectrum (X-band), the dimensional tolerance values of $\lambda/8 = 0.157$ in. or $\lambda/16 = 0.078$ in. are determined allowables consisting of sum-total of realistic values which results from various error contributions. Often, the allowable reflector

surface error is specified in terms of an rms value. This is not a completely accurate definition, since it does not define the error distribution, which should always be specified when the fractional wavelength of allowable error is specified. For example, consider the differences in surface error between a parabola for which the deviation is specified to be 0.078 in. ($\lambda/16$) with a one-sigma gaussian error distribution, and a like parabola specified to be 0.157 in. ($\lambda/8$) with a three-sigma gaussian error distribution. Since it is possible to index the parabola vertex, $x=0$, $y=0$, into an antenna arrangement such that a "best fit" parabola to the antenna arrangement is achieved, obtaining near-equivalent performance from either of the two example reflectors is entirely feasible. The opposite occurs, however, if the specification of error distribution were reversed with the respective reflectors.

The above discussion considers the total deviation error of a parabola surface from that of an equation-defined theoretical parabola. Now in order that the parabolic surface be related to the theoretical or perfect parabola, it is required that an index relation be established between the vertex of the parabola in question, and the vertex of the theoretical parabola. This results in the division of the total allowable error tolerance into positive and negative values referenced to the theoretical parabola coordinates. Thus, the allowable deviation tolerance for the $\lambda/8$ example case is stated as ± 0.078 in. to the theoretical reference and the $\lambda/16$ example as ± 0.039 in. to the theoretical reference, the distribution in each case being specified. Some of the sources which are common contributors to the total allowable deviation error are examined in the subsequent sections.

A. Manufacturing Tolerances

Regardless of the manufacturing technique used or the type of materials employed in fabrication processes, the resulting component or assembly will possess a manufacturing dimensional deviation. This fact is demonstrated by the inability of the manufacturer to produce two or more exactly identical components. The occurrence of error is included in all engineering design by the addition of positive and negative tolerance values to the linear and/or angular dimensions.

B. Assembly Tolerances

If a parabolic reflector is made up of components or component assemblies, a dimensional difference will exist in the relation between one component and another. The primary causes of this are the nonexact uniformity between components and the instrumentation procedures used to establish the component relationships. A further elaboration will be on these error sources in section III of this report.

C. Alignment Tolerances

The case is often encountered with parabolic reflectors wherein assembly of components to dimensions within specified tolerances serves only to index the relation of one component to another. Tolerances are usually found to be accumulative, resulting in dimension amplification. Therefore, alignment is conveniently specified so that the mean sum of assembly and manufacturing tolerances fall within a total specified tolerance value. This dimensional tolerance is of particular significance where an antenna parabolic reflector is of large area and assembled from numerous components.

D. Environmental Tolerances

The false assumption that earth environments have no relation to an antenna in space is a mistake often made by the space antenna designer, who generally assumes that "since the space antenna is used in a weightless environment, the effect of earth's gravity has no bearing upon the antennas design." This assumption can be disproved upon examination of a design which has been favorably received as feasible for parabolic reflectors and solar mirrors, and consists of unfolding or unfurling "petal segments" to form the parabola. Now, in consideration of the weightless space environment, extreme rigidity of the petal is not required, and low vehicle transportation weight being desired results in a petal designed as a thin membrane, or, at best, a relatively light and thin sandwich structure which can be attached at the root end.

During the processes of manufacture and assembly of the petal concept, the question arises as to what procedures may be employed to determine that a parabolic petal segment has been produced, or, that the petals will assemble into a parabolic structure which will satisfy the space antenna requirement.

Because the petal possesses very low stiffness in the gravity environment, the effect of gravity induces bending and, therefore, the petal assumed a contour which is not parabolic. One might assume that a petal contour could be measured horizontally with the surface up, and then rotated 180 degrees to a face-down position for contour measurement, thus allowing the determining of contour as the mean average by subtracting gravity deflections. It will be determined that this is not a valid procedure because the petal will not deflect the same in both directions due to the differences in curvature as defined by the equations for the two surfaces. A classic example of this occurrence, due to gravity, is illustrated in Figure 146, which shows a very rigid parabolic petal segment installed in a deflection fixture, allowing the petal to be rotated in the horizontal attitude. The petal shown is constructed of stretch-formed aluminum skins and aluminum honeycomb core in a sandwich arrangement, and has a very high stiffness-to-weight ratio.

Although the test fixture shown in Figure 146 is constructed of tubular steel and gusseted at all joints, this fixture was found to be inadequate for accurate measurement of petal deflection, because the fixture itself excessively deflected in rotation, such that valid measurements could not be made. A more stringent technique was employed to determine that a petal attitude deflection of 0.024-in. static and 0.007-in. dynamic occurred between the petal-face-up and petal-face-horizontal attitudes.

Now in the case of the space antenna petal which has low stiffness, the problem of demonstrating that a parabolic segment has been produced or that a series of such petals will assemble into an arrangement

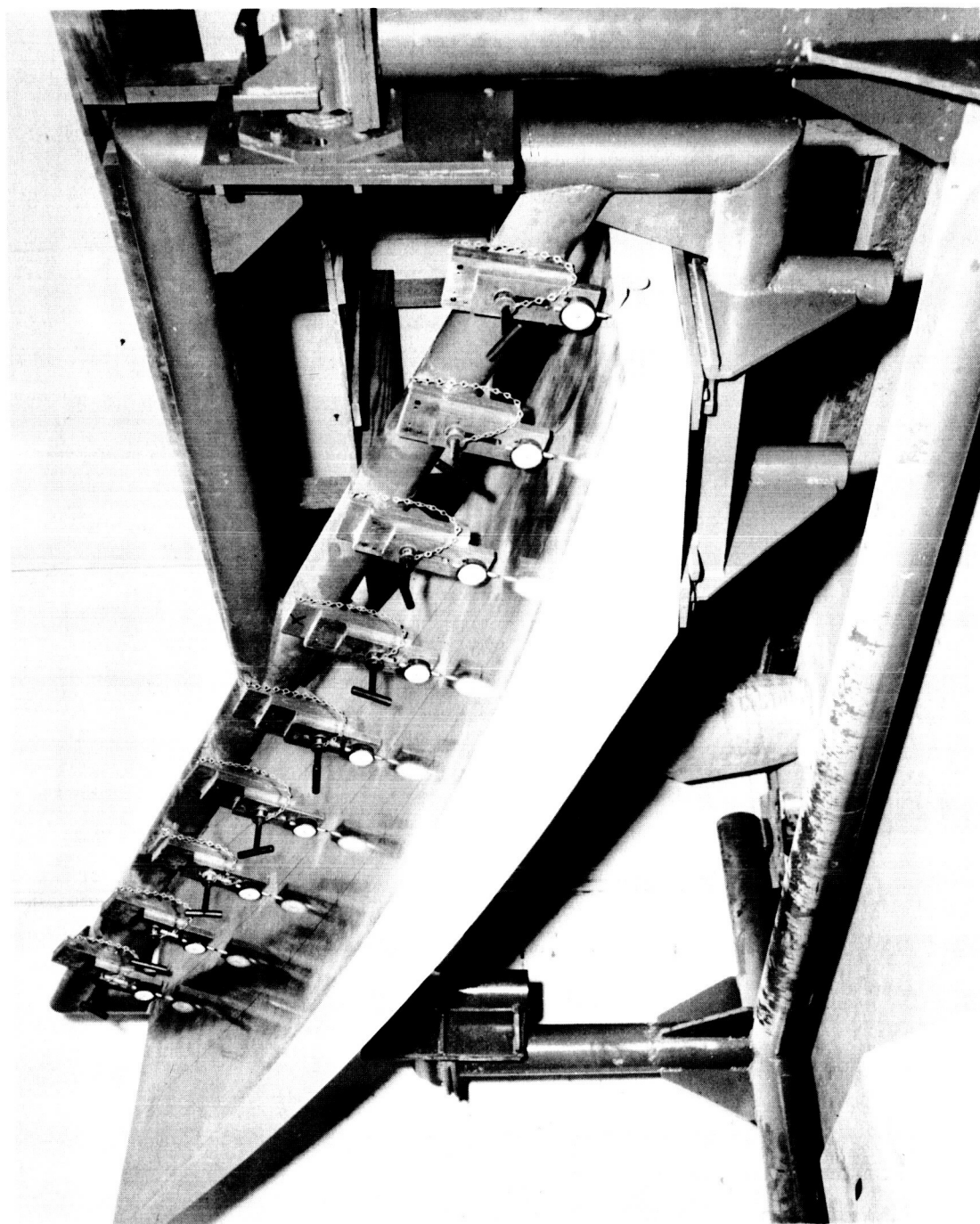


Figure 146. Petal Deflection Test Fixture

which represents a parabola of revolution in a weightless environment becomes a near-impracticable task. This is particularly the case when efficient performance at X-band frequencies (± 0.039 -in. contour) is specified.

The subsequent section will briefly consider the next stringent environmental factor which has extensive effect upon a petal segment of a parabola of revolution, this effect being temperature. In the case of the petal shown in Figure 146, the effect of temperature upon the contour was determined over a temperature range from -40°F to 149°F . The design nominal temperature was 77°F . In order to better understand the full implication of temperature effect, the geometry of the petal is shown in its parabolic arrangement by Figure 147. The illustration thus shows the parabola coordinate system and gives the diameter and F/D ratio.

At -40°F , the petal tip x-coordinate decreases from the 77°F nominal coordinate in the value of -0.0754 in., but at the same time, the decrease in radial y-coordinate is -0.1992 in. At 149°F , the x-coordinate increases, in reference to the 77°F nominal coordinate, by the value of 0.0942 in., and the y-coordinate increases above nominal by the value of 0.1226 in. The actual error of the x-coordinate is 0.1526 in. However, in terms of the parabola coordinates as specified in F/D, the changed position of y must be taken into consideration. Thus, the maximum thermal deviation in contour at -40°F will be 0.0613 in. This exceeds the total allowable ± 0.039 -in. contour deviation for an X-band antenna.

Emphasis must be placed on the fact that the above deviations occurred under conditions of thermal equilibrium in which the petal structure achieved thermal stability. Consider now the condition in the space environment where a thermal solar load of 440 Btu/hr/ft^2 is applied to only one surface of the petal. Adding to this obviously large deviation the cumulative tolerances of manufacture, assembly, and

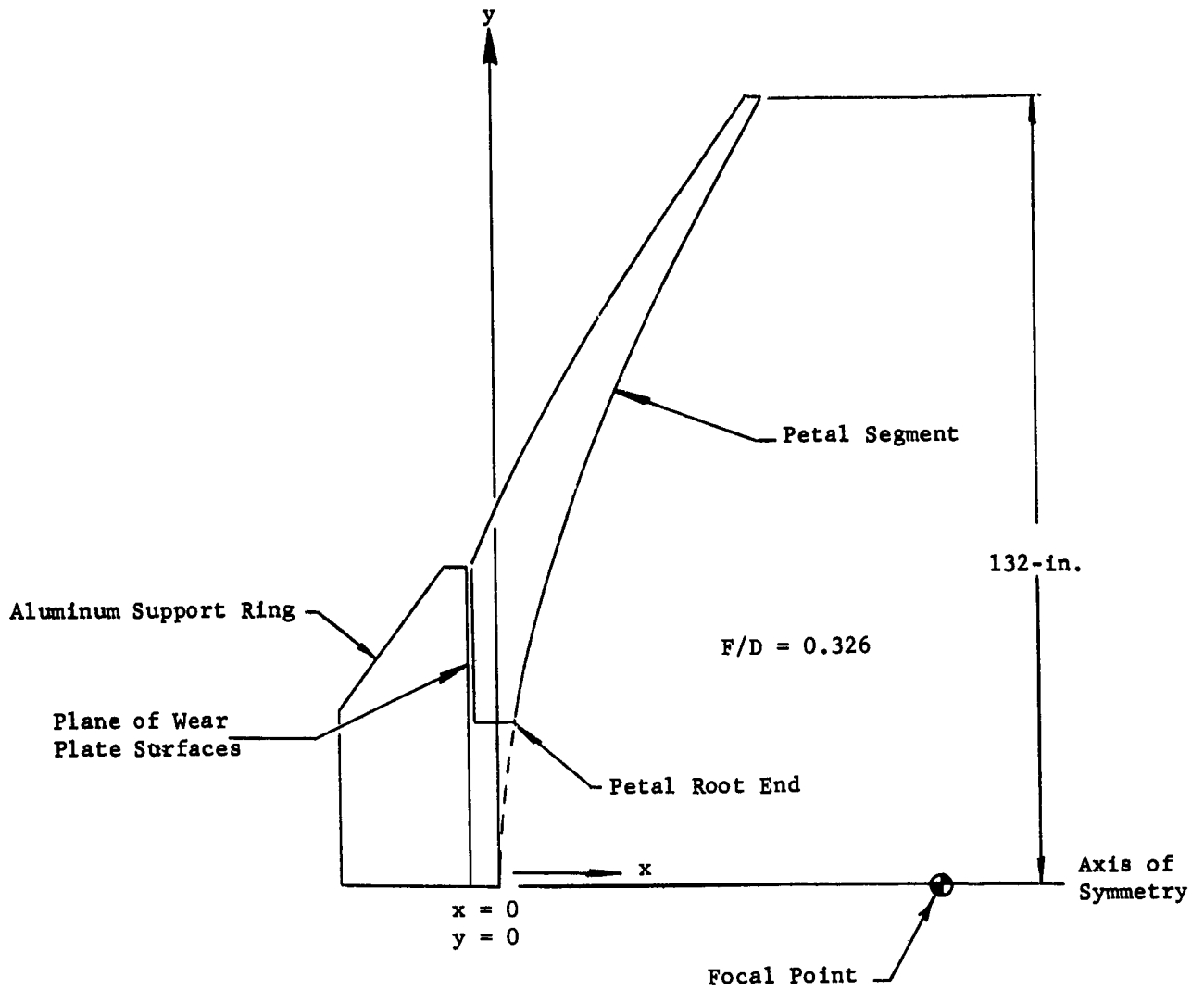


Figure 147. Illustration Showing Petal Segment Location in Parabola of Revolution Arrangement

estimated alignment due to the gravity environment, the petal concept appears as a ridiculous reflector approach for large X-band space antennas. This is not necessarily true, however, if certain objectives are found feasible which make use of the repositioned coordinate x with a corresponding change in the coordinate y. Of course, this approach requires petals of almost perfect "sink" characteristics and probably of unity core/skin weight ratio, very thin petals, and a precise selection of F/D ratio as dictated by the thermal environment.

III. THE FALLACY OF PHYSICAL MEASUREMENTS

The preceding discussions have illustrated that the successful producing of a parabolic reflector for space antennas should require verification by measurement. This discussion, therefore, shall examine the measurement techniques applicable to large precision parabolic reflectors. Since it is inconceivable that such measurements would not be contemplated prior to deployment in space where the measurement penalties are much more severe, the limitations of measurement in the earth environment are those examined. For explicit purposes of illustration, the example antenna reflectors selected for these discussions are each considered to represent the state-of-the-art in their respective applications.

A. Summary of Measurement Methods

Two basic categories of measurement may be employed to obtain the descriptive dimensions of a parabolic reflector in terms of its geometrical coordinates. These two classes of measurement procedure are defined as "optical tooling" and "comparative tooling."

Optical tooling consists of employing the magnified line-of-sight from points of reference to points in question, in geometrical arrangements. The optically established points, in relation to references, may then be used for the geometrical determination of distances. Points of reference or those of question are not always required to possess identity, as in the case where an angle is in question and, as an example, the line of sight is directed to an

autocollimating mirror, prism, or optical square. The most useful items of optical tooling are the tooling telescope with micrometer head, theodolite with optical plumb and collimator light, collimating mirror target, and optical square.

Comparative tooling consists of those forms of physical calibration of geometric dimension which include: tapes, bar scales, templates, dial indicator instruments, protractors, plumblines, and bubble levels. The incremental precision of these measurement instruments are valid only within the limits of calibration and specific modes of use.

1. Comparative Measurement Techniques and Limitations

When dimensional measurements are performed upon parabolic reflectors of relatively small size (up to 20-ft diameter), it has been the general practice in industry to make use of comparative tooling procedures. When the reflector is of large-aperture diameter, convenient use is made of optical tooling because it is considered extremely difficult to precisely measure the linear distance between two points by comparative methods. Consider, for example, the dimensional deviations associated with a precision bar-scale of the type generally accepted in the manufacture of product tooling. The scribe marking of such scales is usually of sufficient accuracy as to permit reading with a magnifier to within 0.010-in. division-to-division, in reference to the dimension being measured. Note, however, that the marking contains width, and therefore an exact measured distance requires interpretation. Further, it is considered that the scale marking and index points are applied to the scale within limits of accuracy containing some tolerance value over which the scribe marking is performed. Finally, because the markings are applied to the scale at some value of temperature, the indexed dimensions may be considered valid only at a calibrating temperature as determined by the thermal coefficient of the material.

As in the case of scales, similar tolerance errors occur with tapes. Conventional tapes sometimes used during the construction of large parabolic apertures are not intended for precision measurement. This may be verified by comparing the full, extended dimension of several 50-ft tapes, particularly if the tapes are of different materials. So-called precision tapes are available, however, some of which are round wire types having low thermal expansion coefficient materials. The finite incremental marking of such tapes is usually only in the end foot, and usually they require that some specified poundage of tension be applied to reduce tape sag over a given length in order to achieve the precalibrated length. The interpretation of measurement is required similarly as that with the scale.

The tape and scale find wide use in the layout and location of coordinate points which, when faired into a curve, identify the surface of index curvature of a parabola template. In the conventional practice of the manufacture of a parabolic reflector, a template is usually prepared which contains the initial layout of parabolic coordinates and serves as the master template to which all following tooling, fixtures, product and check instrumentation is indexed. The problem of dimensional precision begins with the master template. The layout of coordinate points is often accomplished by the use of scales which themselves contain some increment of error; however, to simplify this discussion, the indexing of coordinate points shall be assumed to be perfect. The layout of the parabolic curve between index points is accomplished by a very fine scribe line. Repeating measurements under careful conditions will generally establish the fact that the dimensional reliability of the scribe line, due to the line width and necessary fairing, to be accurate within ± 0.005 in. If care is exercised to trim and finish the surface of curvature so as to only approach and not consume the scribe line, the above tolerance reliability can be halved to $-0.000 +0.005$ in.

Of course a "human factor" tolerance enters into the above, but these have been included in the tolerance values given by assuming an experienced precision toolmaker.

Greater accuracies are generally claimed where the template is cut by means of numerically programmed machines. When attempting to obtain templates of greater accuracy, however, producers generally decline to certify a tolerance of less than 0.005 in., although greater accuracies to as low as ± 0.002 in. are stated without guarantee.

When a contour check template is produced from the curve of the master parabolic template, it contains the inherent 0.005-in. error in a negative direction because of its hyperbolic shape. Because the parabolic surface to be measured contains deviations in both the positive and negative directions from the nominal curvature, a check template of exact contour cannot be used due to the inability of fitting it to a nominal surface. Therefore, the check template requires that some preselected constant offset value be used to establish a reference surface of curvature, at the preselected offset distance from the nominal theoretical parabola as defined by the master template. Note that the offset curvature is no longer defined by the parabola equation, and that if the same layout procedure is used as in the case of the master template, the uncertainty tolerance of the curve is approximately ± 0.005 in. Thus, due to the single tolerance of the master template, the uncertainty tolerance resulting in the check template will be $-0.010 +0.005$ in.

The problem now arises to determine the most exacting procedure of checking the parabola surface with the check template. The template cannot simply be applied to the surface under test because the check template containing the parabolic curve must also contain the axis of revolution. The template axis of

revolution must be exactly coincident with the axis of symmetry of the parabola under test, otherwise measurement error occurs as the template is rotated. Several approaches have been used to overcome this problem and at the same time improve tolerance relationships, two significant examples of which are discussed in the following section.

Figure 148 shows a precision 12-ft K-band antenna reflector with a contour check template installed for test. In this case, the template contains dial indicators which measure only seven points on the reflector panel surface segments and thus does not constitute a template in the true sense. The dial indicators, however, may be preset to a nominal value equal to a nominal contour and thus achieve greater tolerance precision. The test fixture of this example has a post installed into a surface plate to define both the axis of revolution of the template and the axis of symmetry of the reflector being aligned. The reflector petal segments are located to the surface plate by means of their respective attach points and the petal position is then adjusted to obtain the desired template indicator readings.

Because the check template is a beam subject to gravity deflection, bending of the center axis would occur if it were not counterweighted as shown in Figure 148. But since the template must be rotated, some bearing tolerance must be allowed, and this can produce a positive or negative tolerance as a function of radial distance along the template. The possible tolerance errors of this example system are as follows:

- a. Vertical tolerance of axial location
- b. Tolerance due to template bending
- c. Indicator index tolerance
- d. Bending tolerance due to petal attitude
- e. Thermal tolerance of both template and reflector if not maintained at nominal index throughout calibration and alignment sequence
- f. Tolerance due to allowed clearance between the vertical column and template bearing

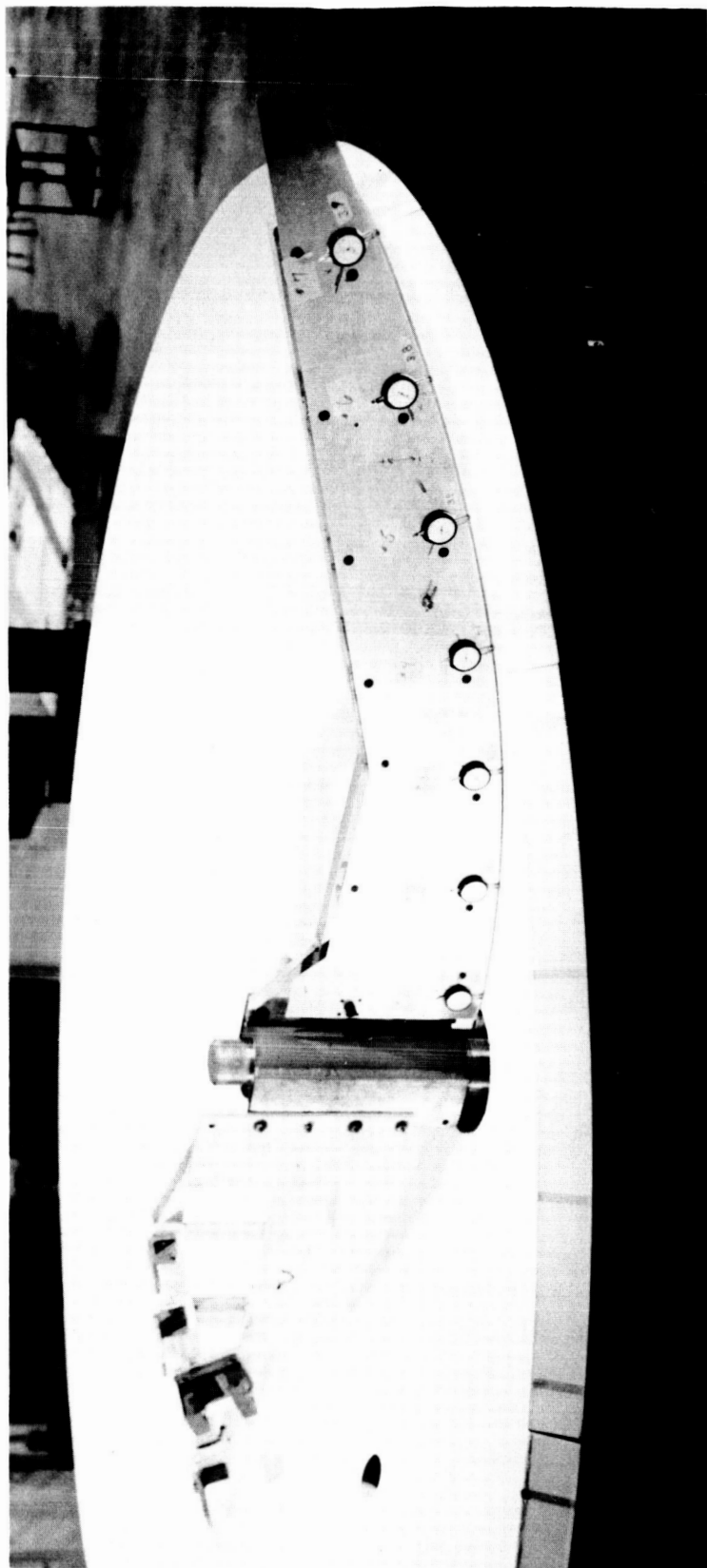


Figure 148. Precision 12-ft K-Band Antenna Reflector with Contour Check Template Installed for Test

These various sources of tolerance deviation are reasonably controllable when the reflector aperture is of small diameter, as shown in Figure 148. However, as the aperture diameter is increased to the order of about 20 ft, the deviations become extremely difficult to control and require that more stringent methods be employed, as will be shown in the following case.

The example antenna shown in Figure 149 is a petal segment concept in the process of contour alignment. Close examination of Figure 149 will show numerous areas where tolerance considerations are made. In this case, the entire reflector assembly is supported on a gigantic rotatable headstock, thus allowing the template to remain fixed relative to index. The attitude of the reflector pointing horizontally is such as to normalize the deflection due to gravity. The contour check template is designed and installed in the vertical position so as to minimize deflection due to gravity, and dial indicators are used to the nominal index setting. The axis of rotation and, in this case, the axis of symmetry are an optical reference established by means of an autocollimated light, telescopic line of sight through the headstock rotating shaft, to a mirror at the far end of the building (not shown). In this example, the reflector, fixtures, and instrumentation environment is controlled by controlling the temperature of the building, thus including temperature control of the concrete floor, which is considered in instrumentation relationships. Although extensive care is exercised to reduce dimensional tolerances, some tolerance value exists in each dimensional relation, within allowable limits. The point is stressed, however, that even though the more than structurally adequate antenna should be adjusted perfectly to a theoretical X-band contour by the procedures shown in Figure 149, it could not adequately maintain this contour within X-band design specified contour deviation limits when placed in a space environment. This is primarily due to thermal change in the structure and its segmented petal design.

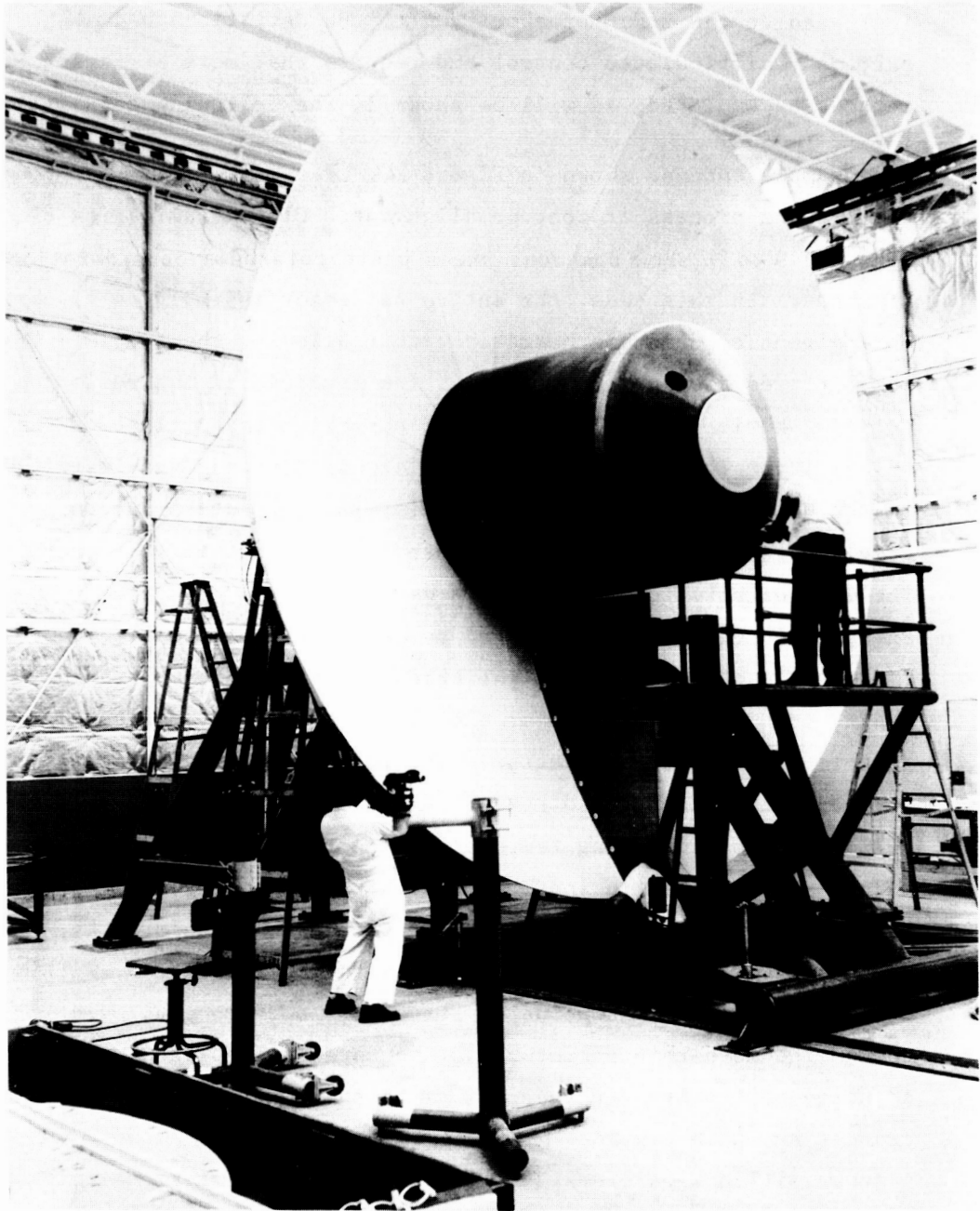


Figure 149. Cassegrain Antenna Employing Segment Petal Concept

2. Optical Measurement Techniques and Limitations

Because dimensional tolerances increase rapidly with increasing dimensions, large-aperture reflector measurements must resort to optical tooling techniques in order to achieve the desired contour accuracy. Unlike the comparative measurement technique, optical tooling does not directly measure the dimension between two points, but instead is used to determine angles of lines of sight so that the dimension may be calculated. When the limitations of the instrumentation are known and fully considered in the optical measurements being performed, the calculated dimensions are reliable within instrumentation tolerances plus the ability of the instrument operator and his interpretation. The important notation is made that when repeating measurements, different instrument operators seldom obtain identical data. For this reason, optical tooling experience is an important prerequisite.

Because the tooling telescope and theodolite make use of the magnified line of sight from point to point, gravity deflections do not occur as in the case of comparative measurement instrumentation between the points. The effect of gravity is not wholly absent as a source of error, however, because of the usual requirement for reference level. Most optical instrumentation used for the measurement of planes, and angles in elevation employ a bubble level which is positioned by gravity. In the case of the theodolite, the bubble is centered according to its case scale calibration, the instrument is rotated 90 degrees, and the bubble is again centered such that by repeating the rotation the bubble does not deviate from its centered position. This centering action establishes the horizontal reference plane for the optic piece and its elevation scale. If the theodolite is a conventional standard model, the readout error could be 0.120 in. in 100 ft. The reason for this error is that the standard theodolite usually employs a bubble which is accurate within 20 seconds of arc. It is therefore

important to remember that 1 second of arc represents 0.006 in. in 100 ft. Theodolites may be obtained which employ a split-coincidence bubble capable of achieving 1 second of arc accuracy. This does not explicitly state, however, that the elevation scale of the optic piece is zero-referenced to this angular accuracy, as verified by the method by which instrument manufacturers state accuracies. Generally the manufacturer states that an instrument will read and repeat to within some value. What is often omitted is the distance over which this stated accuracy is valid; on occasion this has been found to be 1 ft from the instrument optic. One source of bubble error is not often recognized in conducting finite measurement over large distances. This occurs when the instrument is aligned at a facility considerably distant from the area of intended use. Since the instrument calibration is referenced to a bubble centered by gravity, the calibration is directly related to the gravity vector in the facility area. There is no valid reason to assume that the gravity vector will be the same in the area of instrument use. This implies, of course, that a calibration check should always be made in the area of intended use. Confirming the validity of precision theodolites necessary for the alignment of antenna structures can be accomplished by referencing the bubble and elevation scale to a vertical optical axis established by instrument rotation under an autocollimating mirror target. The type of instrument reticle used plays an important part in the precision alignment of large antennas. It is found that when observing the marking of a precision 6-ft tooling scale at 100 ft with a single reticle instrument, the reticle will cover 0.025 in. to 0.030 in. The more suitable instrument has a double reticle and, thus, by employing a white face scale, the double reticle brackets the black marking, permitting precision interpretation. One further instrument tolerance should receive due consideration: this concerns the optic resolving power. Manufacturers generally give the resolving power for instruments of high precision

as 2.9 to 3.5 seconds of arc. Thus, the accuracy tolerance of optical instrumentation is determined by totaling the various values of angular uncertainties in consideration of the distance over which measurement is to be performed.

3. Composite Optical Instrumentation For Antenna Measurement

The use of standard optical instruments to measure and align extremely large precision reflecting surfaces requires that extreme techniques often typified as state-of-art be applied. The technique is not found impractical, however, as verified by the precision alignment of the cornucopia horn antennas used with the Telstar system. Theodolites referenced to a precision bench-mark plot were used to align the horn at Andover Maine to ± 0.040 in. and the one in France to ± 0.080 in. with precise temperature control being considered. For this alignment, however, the horns are inverted in elevation pointing angle so that measurements are performed at ground level with the bench-mark plot actually functioning equivalent to a large optical bench. In the case of large parabolic reflector antennas, the bench mark reference system cannot reasonably be established; thus, it becomes necessary to employ new techniques.

The optical instrument shown in Figure 150 was developed specifically for the alignment of large-aperture diameter X-band antennas. (63) This instrument consists of a precision vertical centerless ground steel column supporting a horizontal optical bench that can be raised and rotated about the column. Lateral and angular adjustment of the column are made at the column base to allow it to be centered and plumbed to within 1 second of arc.

The optical bench supports two alignment telescopes. One sights along a radial line from the column center to orient the optical bench and provide a vertical distance measurement relative to the reflector. The other, which is set at fixed angle and moves along

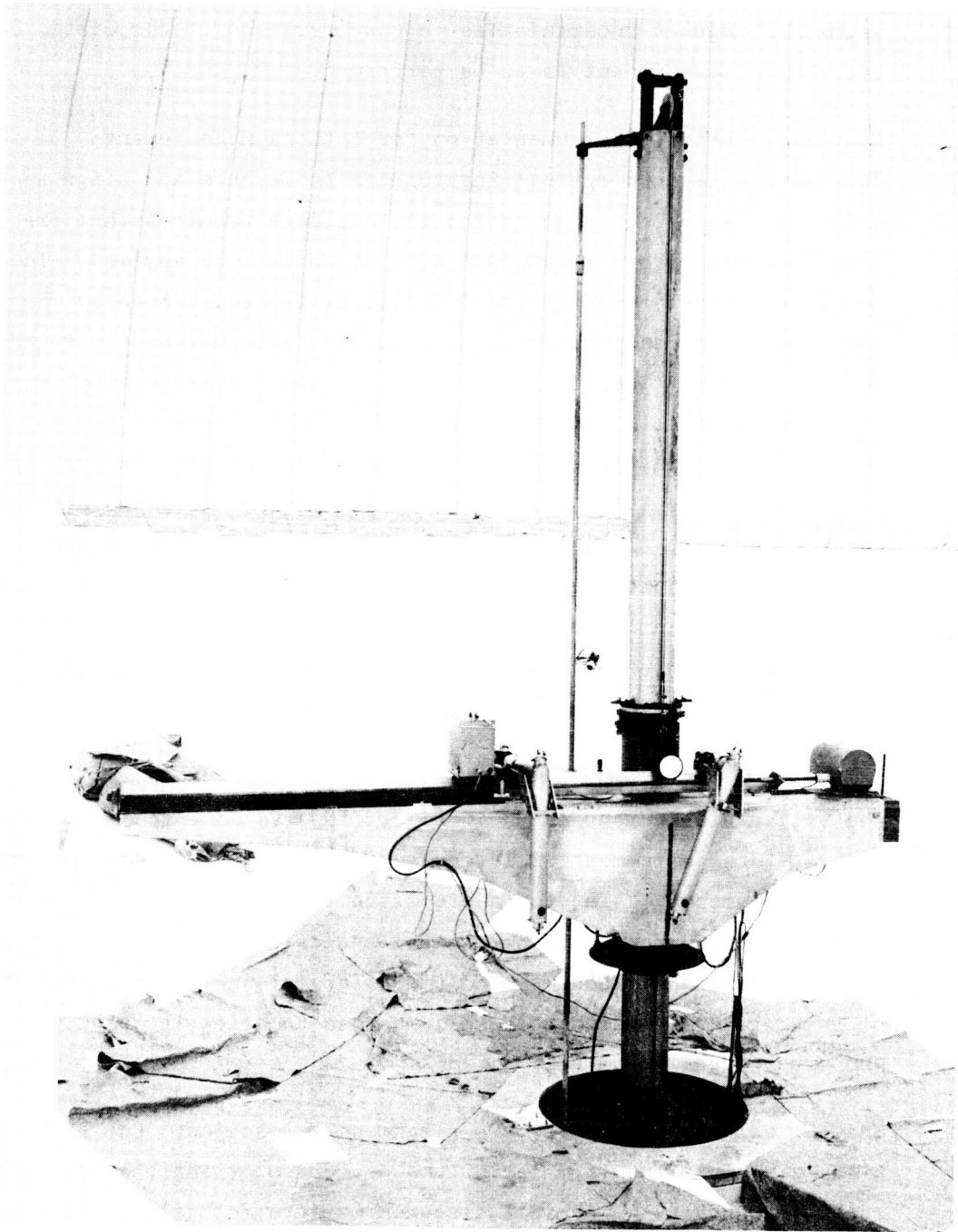


Figure 150. Paraboloscope Rangefinder

the optical bench to provide ranging measurements, is indexed to a linear scale - yielding radial range directly in inches.

Because alignment telescopes have a pointing accuracy of only 3.5 seconds of arc, this could result in a 0.021-in. error in 100 ft, amplified by the 1 second of arc vertical column error as a function of the height of the optical bench. The optical accuracy can be improved to greatly reduce the above error tolerance through the use of paired-line targets. This method relies upon the ability of the observer to center the telescope crosshairs between paired lines on the target. Thus, by this expediency, the telescope accuracy can be increased to less than 1 second of arc. In order to use the paraboloscope rangefinder instrument for the alignment of a large X-band parabola, it is mandatory that thermal environment be controlled. It is necessary to enclose both the optical alignment system and the parabola being measured in a housing, such that the temperature of the instrument and the parabola can be stabilized to $\pm 1^\circ\text{F}$. If the controlled temperature deviates as much as 3°F , the measurement or alignment tolerance error will exceed the allowable for X-band antennas. A convenient type of environmental control housing which has given satisfactory environmental control is shown in Figure 151. The housing is a fabric-plastic enclosure held in its semirigid, erected state by air pressure.

4. The Performance of Antenna Reflector Alignment in the Space Environment

The preceding techniques which describe the precision measurement of parabolic reflectors each have one common requirement; i.e., the establishing of a necessary reference plane through the use of a bubble level reacted upon by gravity.

For those antenna concepts which propose to construct or assemble large parabolic reflectors in space, the present concepts of alignment and measurement will be nearly useless, for the simple reason

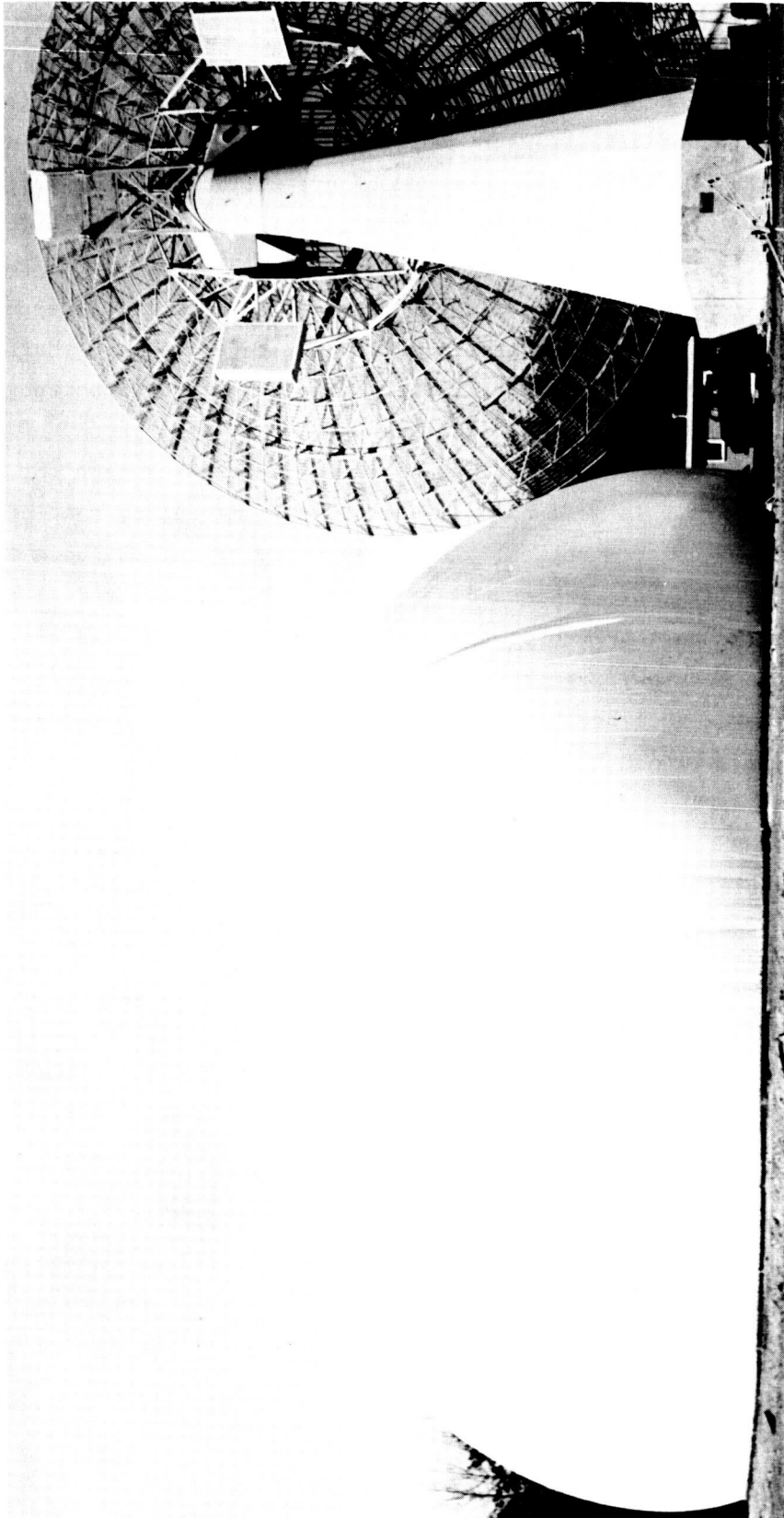


Figure 151. Air-Inflatable Enclosure



Figure 152. X-Band Reflector (60-ft Diameter)

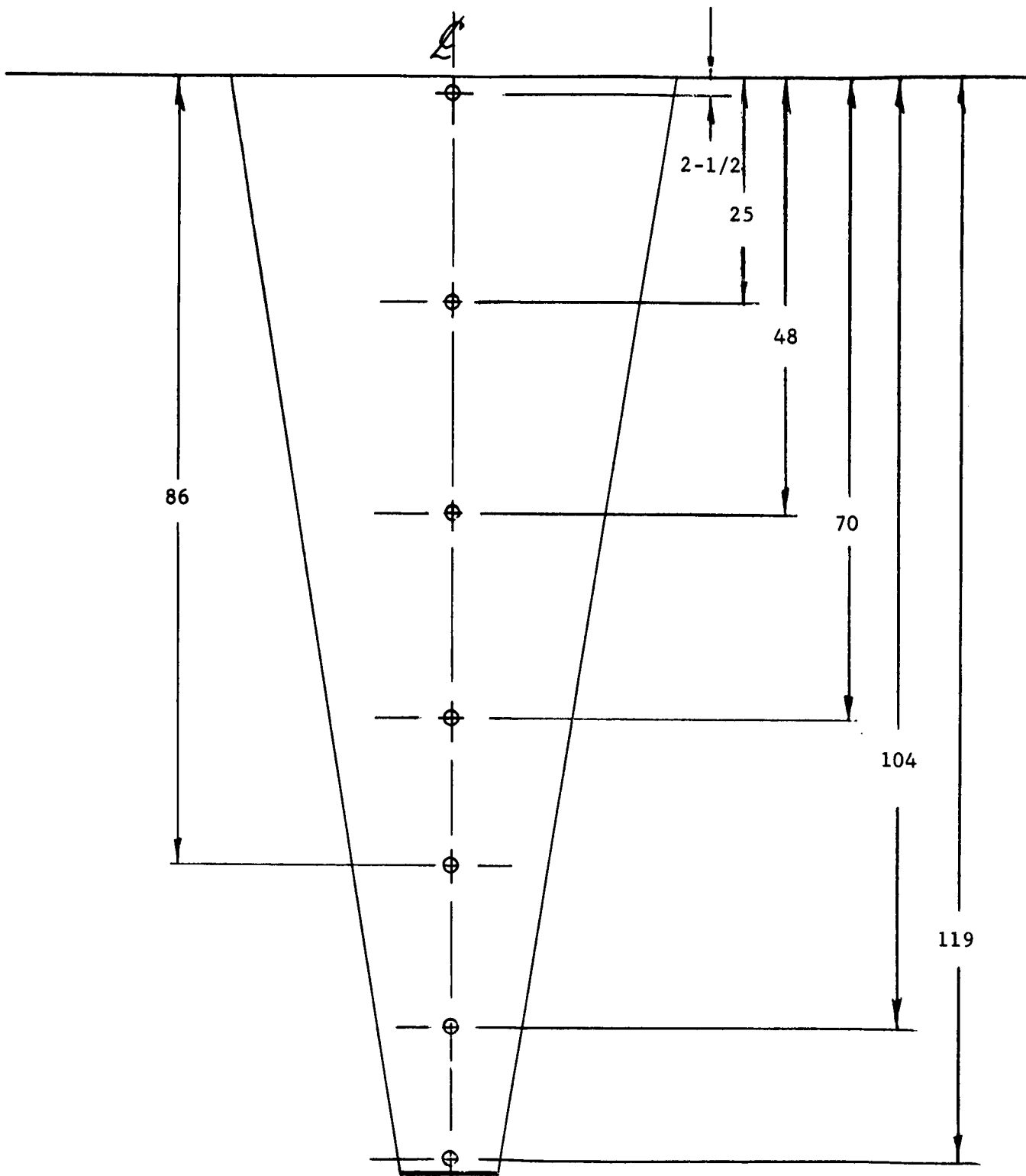


Figure 153. Thermal Gradient Deflection Test; Dial Gage Locations, Top View of Panel. Supports Fixed

that the bubble reference cannot be established. The solution of this problem could constitute the most difficult task in this concept approach, particularly if the requirement is near the microwave X-band region for the resulting reflector. When including best-effort instrumentation error in consideration of the space environment, in addition to the absence or simulation of reference, the concept appears unfeasible.

IV. THE THERMAL DEFORMATION OF ANTENNA REFLECTOR STRUCTURES

Because of the need to demonstrate that a space antenna reflector has been produced which will contain the dimensions required for antenna performance in space, one might assume that a lightweight rigid structure could fulfill the specification. When structural stiffness with very light weight is the criterion, the obvious design approach is to use a sandwich type of construction. Since it can be assumed that the one space environment which will have the greatest effect upon the precision structure is thermal, the designer seeks means of reducing thermal deflections.

If the design divides the parabolic reflector into a multiple of segment panels, and these panels are to be reassembled in space, the design must provide means of isolating the thermal deflection of each panel from the adjacent panels. When the antenna is to be used in areas of space other than directly in the earth's shadow, the effect of unsymmetrical thermal solar loading must be considered. Because the space environment constitutes an excellent insulating medium, and obtaining a perfect sink between sandwich skins is found to be nearly impracticable, the exposed panel surface grows while the shadowed surface contracts, according to the material thermal coefficient. If the segment panels are edge-attached, the error developed in the center panels will be radially transmitted to adjacent panels across the reflector aperture. This leads to the consideration of a design in which each panel is thermally isolated from its neighbor.

Microwave X-band reflectors with large-aperture diameters which contain thermally isolated panels have been produced. An example 60-ft diameter aperture X-band parabolic reflector employing the thermally isolated panel concept is shown in Figure 152. A study of the thermal deflection of the panels which compose a sandwich surface of the type shown in Figure 152 is pertinent to the thermal deflection of panels in space, although the study environment was much less severe.

A. Tests of Parabolic Reflector Panel Deflections Due to Thermal Gradients⁽⁶⁴⁾

A test stand to provide infinite fixity of the supports was designed and manufactured. The stand was equipped with dial gages to indicate its deflection within ± 0.0005 in. and with tension rods for adjustment to its original dimensions. The panels were attached to the stand with special fittings and 3/4-in. diameter studs. For the single supported condition, the studs were removed.

All deflections were measured directly with dial gages. Various types of gages were used. The largest graduation of any gage was 0.001 in. The gages were supported on a frame separate from the test stand to prevent influence by stand movement during adjustment of the stand. Locations of the gages for the various tests are shown in Figures 153 and 154.

A silicone rubber, electric blanket manufactured especially for this test was used to heat the concave surface of the panel to provide the thermal gradients. The blanket is rated at 5.3-kw maximum and was supplied power by a powerstat to obtain stepless control. Power input to the blanket was measured by a voltmeter and ammeter. Since the blanket was measured by resistance element, a unity power factor was assumed.

Temperature was measured by iron-constantan thermocouple probes using the potentiometer null-balance method of determining emf. Locations of probes for all tests are shown in Figure 155.

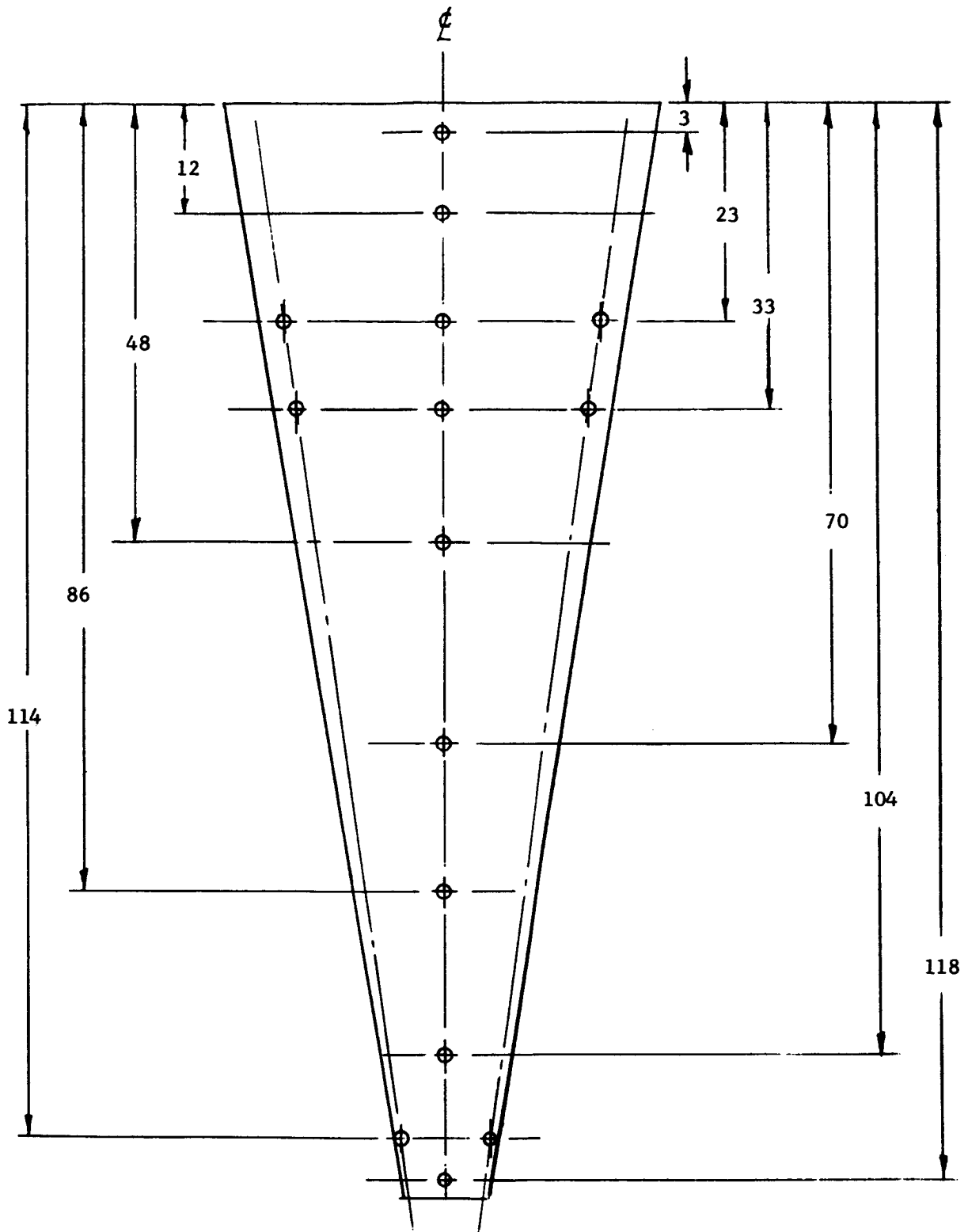


Figure 154. Thermal Gradient Deflection Tests;
Dial Gage Locations, Top View of Panel,
Simply Supported

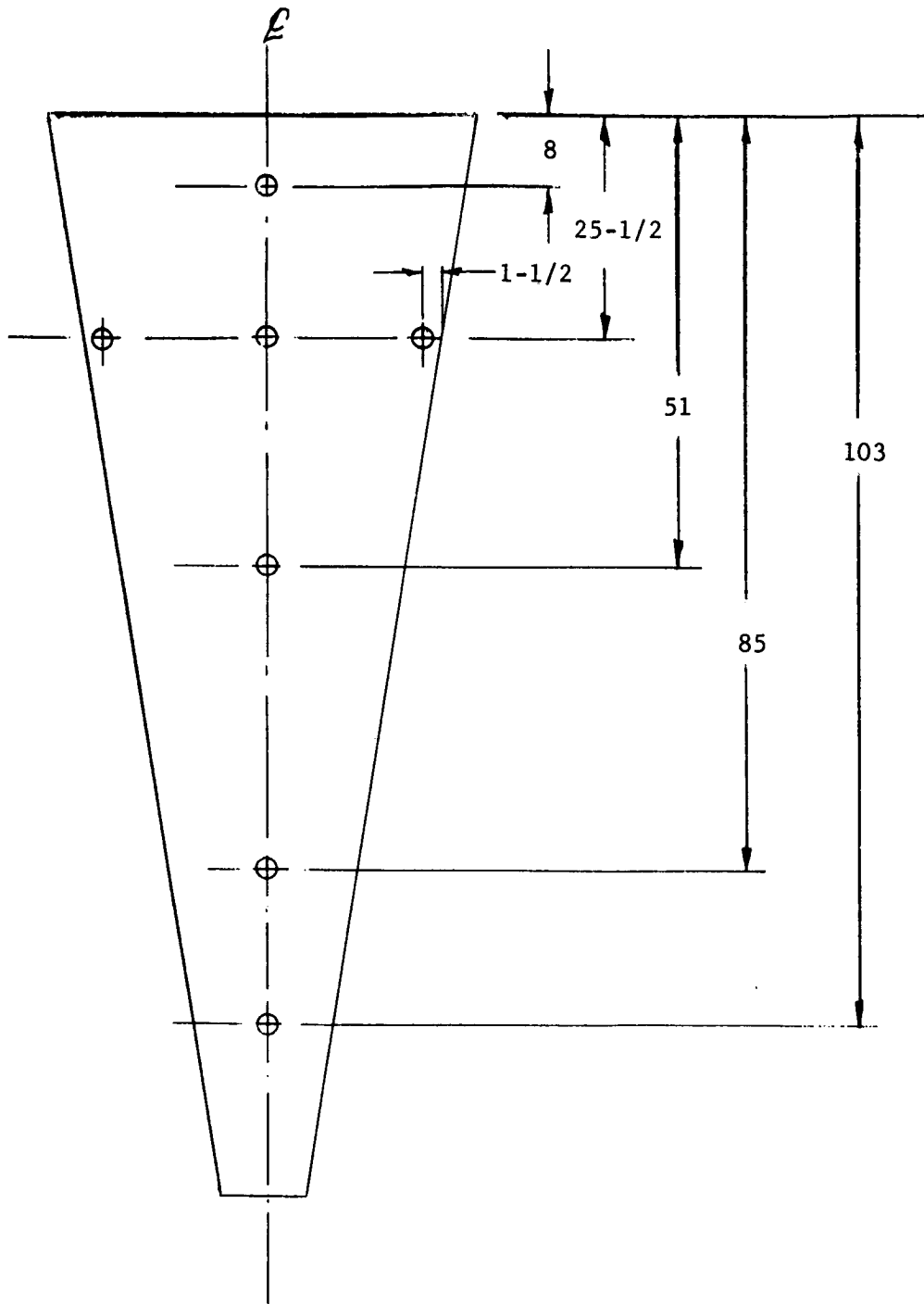


Figure 155. Thermocouple Probe Locations, Both Sides of Panel

Calculation of heat transmitted by the panel was made using known $\frac{K}{X}$ values on thermal conductivity of "Advent" antenna panels.

An approximate value for deflection of the panel due to its own weight was measured. To do this, the panel was simply supported by its end supports and dial gages positioned along the centerline and at the end supports. All gages were set at zero. The center of gravity of the panel was lifted until the gages at the supports showed movement and lowered just until these gages indicated zero. The deflection indicated was assumed to be approximately twice the deflection due to the weight of the panel.

Table 20 lists the maximum deflection, its location, and the corresponding thermal gradient and mean temperature where appropriate. (Data reference numbers are used to indicate corresponding curves and table entries.)

Table 21 contains a summary of temperature and heat data.

For various thermal gradients with the panel in both the fixed and simply supported condition, the deflection characteristics are similar. The deflection of the panel is a function of the temperature gradient, the method of support, and the geometry of the panel. The location of the point of maximum deflection depends on the method of support. Variations in magnitudes of temperature gradients will influence location of this point of maximum deflection. In order to compare data for the two panels, the dimensionless ratio, $\frac{\delta}{L}$, was plotted as a function of $\Delta t/t$, which is also dimensionless. The maximum deflection is δ , the distance from the nearest support to the point of maximum deflection is L , the gradient is Δt , and the mean temperature of the panel is t . Curves for the fixed and simply supported condition are shown in Figure 156. Curves showing deflection as a function of distance along the centerline of the panels are included for the following:

1. Panel No. 1, Supports fixed (Figure 157)
2. Panel No. 2, Supports fixed (Figure 158)

TABLE 20

MAXIMUM DEFLECTION DATA SUMMARY⁽⁶⁴⁾

Max. Deflection, in.	Distance From Large End Along, in.	Distance To Nearest Support in.	Thermal Gradient, °F	Mean Temp, °F	Data Ref. No.
Panel No. 1, Supports Fixed					
0.027	0	24	8.7	145	6-20
0.035	14	27.8	18.3	141	11-20
0.051	25	34.7	30.4	134	4-22
Panel No. 2, Supports Fixed					
0.023	0	24	10.3	117	2-13
0.022	0	24	9.9	132	3-13
0.024	0	24	9.1	143	4-13
0.044	30	38.5	25.6	157	7-13
Panel No. 1, Simply Supported					
0.038	44	50.3	9.5	104	8-5
0.080	52	57.3	16.0	121	9-5
0.104	53	58.2	24.0	146	10-5
0.172	52	57.3	32.1	179	11-5
Panel No. 2, Simply Supported					
0.016	24	34	9.8	130	11-11
0.047	52	57.2	13.0	132	12-11
0.054	52	57.2	15.2	131	13-11
0.063	48	53.6	16.7	141	14-11
0.072	48	53.6	17.0	145	15-11
0.085	50	55.4	17.0	125	2-12
0.106	50	55.4	22.0	148	4-12
Panel No. 1, One Facing Free, Other Facing Fixed					
0.008	0	24	7.5	109	2-6
0.030	26	35.4	15.3	120	3-6
0.032	29	37.6	20.6	134	5-7
0.041	29	37.6	26.0	152	6-7
0.054	26	35.4	32.8	188	7-7

TABLE 21

HEAT AND TEMPERATURE DATA SUMMARY

Ref. No.	Mean Temp of Heated Facing, °F	Mean Temp of Nonheated Facing, °F	Temp Difference, °F	Mean Temp of Panel, °F	Power To Blanket		Heat Through Panel, $\frac{\text{Btu}}{\text{Hr/ft}^2}$	Remarks
					KW	$\frac{\text{Btu}}{\text{Hr/ft}^2}$		
6-20	149.3	140.6	8.7	145	1.375	195.2	78.3	Fan used on nonheated facing Fan circulating air over dry ice under panel Fan used Panel heater covered with cardboard; fan used Fan used Fan used
7-20	150.1	141.4	8.7	145.7	1.375	195.2	78.3	
10-20	150.0	131.6	18.4	140.8	2.065	292.4	165.6	
11-20	150.0	131.7	18.3	140.8	2.065	292.4	165.6	
4-22	149.1	118.7	30.4	133.9	2.560	363	273.6	
8-5	108.3	98.8	9.5	103.5	1.150	163	80.8	
9-5	128.7	112.7	16.0	120.7	2.100	298	144.0	
10-5	158.0	134.0	24.0	146.0	2.560	363	216.0	
11-5	195.4	163.3	32.1	179.3	3.900	516	288.9	
2-6	112.2	104.7	7.5	108.5	.800	113.2	61.75	
3-6	127.5	112.2	15.3	119.8	1.620	230.0	137.7	
5-7	144.0	123.4	20.6	133.7	2.065	292.4	185.4	
6-7	165.4	139.4	26.0	152.4	2.560	363	224.0	
7-7	204.5	171.7	32.8	188.1	2.560	363	295.2	
2-13	122.6	112.3	10.3	117	1.375	195.2	92.7	
3-13	137.3	127.4	9.9	132	1.375	195.2	89	
4-13	147.7	138.6	9.1	143	1.560	203.0	81.8	
7-13	170.1	144.5	25.6	157	2.560	363	230	
11-11	134.6	124.8	9.8	130	1.150	163	88	
12-11	138.3	125.3	13	132	1.560	203	128.8	
13-11	138.5	123.3	15.2	131	1.560	203	137	
14-11	149.8	133.1	16.7	141	2.060	293	150	
15-11	153.8	136.8	16.8	145	2.060	293	152.5	
2-12	133.3	116.5	17	125	2.060	293	153	
4-12	158.3	137.4	21	148	2.560	363	189	

- Panel No. 1.; clamped
- Panel No. 2.; clamped
- △ Panel No. 1.; simply supported
- ▽ Panel No. 2.; simply supported

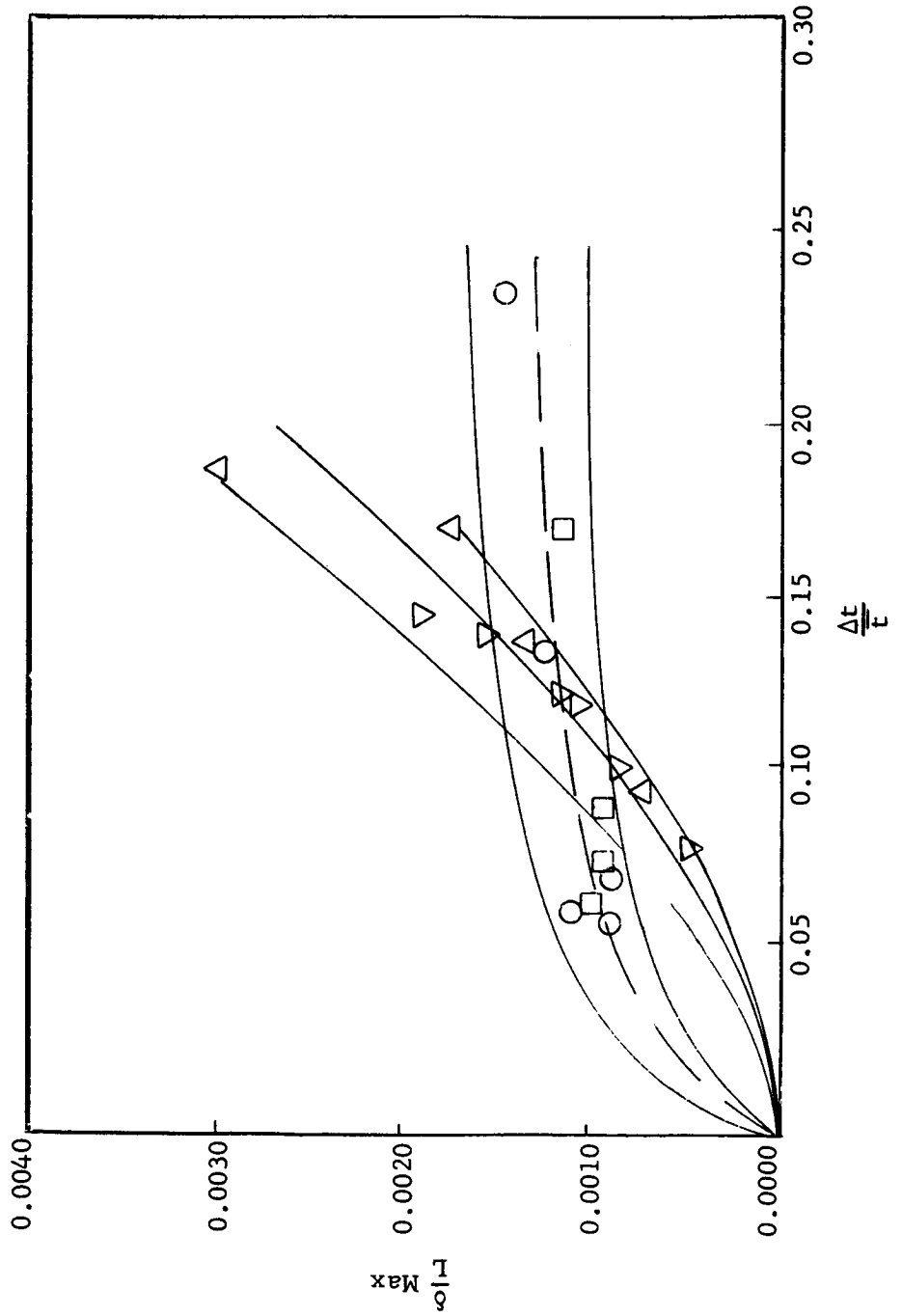


Figure 156. Data Comparison Curves

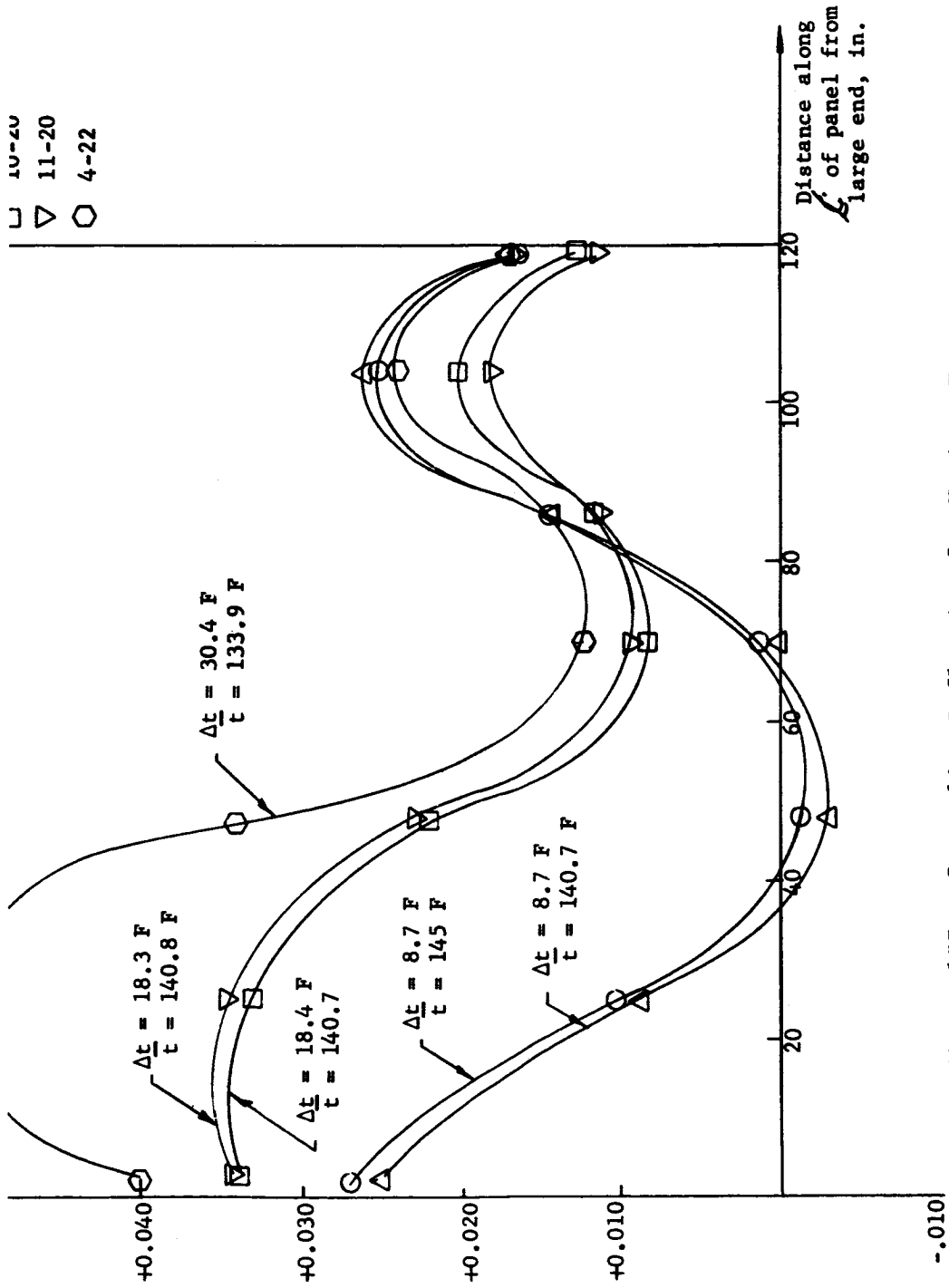


Figure 157. Centerline Deflection for Various Temperature Gradients (Supports Infinitely Fixed; Concave Side Up and Heated; Panel No. 1)

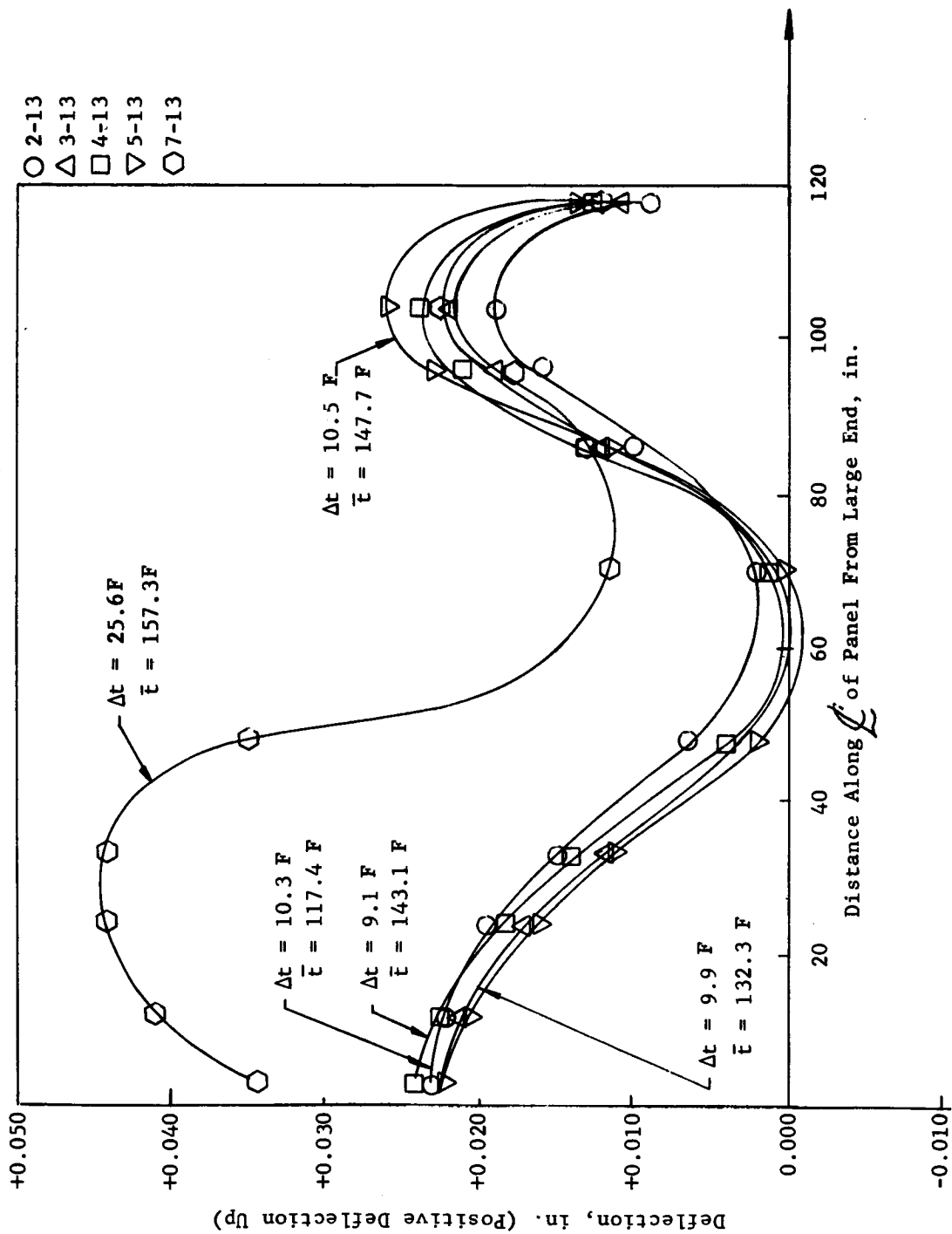


Figure 158. Centerline Deflection for Various Temperature Gradients (Supports Infinitely Fixed; Concave Side Up and Heated; Panel No. 2)

3. Panel No. 1, Simply supported (Figure 159)
4. Panel No. 2, Simply supported (Figure 160)

The data indicate that an intolerable situation for deflection of the panel occurs with a large gradient, large mean temperature, and simple supports. For similar gradients and temperature, the least deflection results with all supports infinitely fixed. However, it should be noted that least deflection does not necessarily mean least local distortion. With all supports fixed, the shorter span of the panel is deflected much more than when only one facing is fixed. The deflection of the longer span is approximately the same for both situations.

The maximum deflection due to a thermal gradient cannot, in general, be added directly to the maximum mechanical deflection. The points of maximum deflection due to the two mechanisms will normally differ. Further, the method of support and the existing reactions at the supports due to the thermal gradient must be considered for an accurate determination of total deflection.

V. CONCLUSIONS RESULTING FROM THE PARABOLIC ANTENNA STATE-OF-THE-ART REVIEW

A. Conclusion Criteria

The conclusions stated in the following are based upon present limitations in manufacturing technology, limits of exactness in measurement techniques, the environmental stability of usable materials, and the present design concepts for microwave antenna reflectors in the medium microwave spectrum wherein surface contour of approximately ± 0.040 in. are desired.

1. To predict the performance of a parabolic reflector in space within reasonable limits of accuracy requires the geometrical relations of the components be measured in the Earth's environment.
2. A parabola of revolution reflector with a constant surface continuity in a large nonuniform thermal environment has a relatively

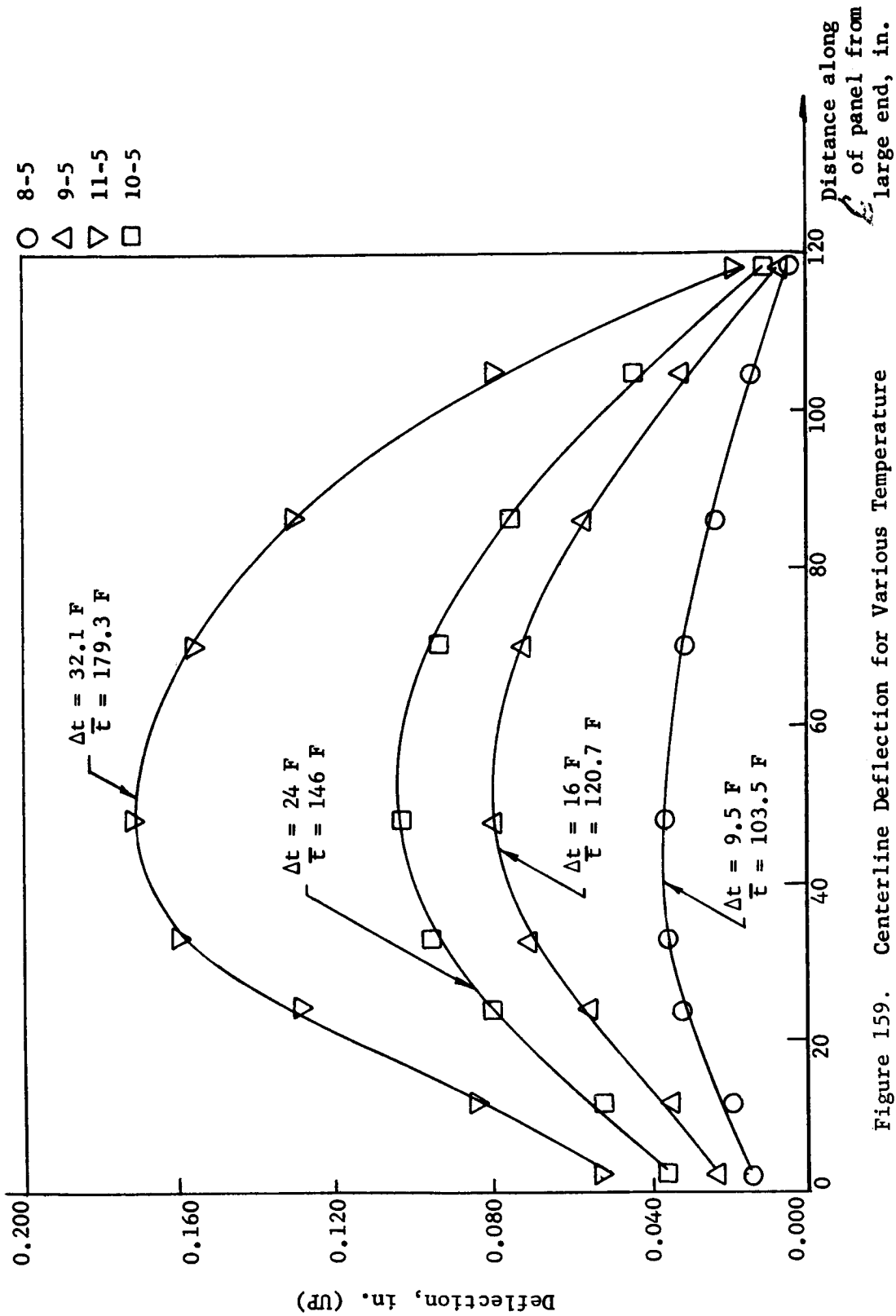


Figure 159. Centerline Deflection for Various Temperature Gradients (Simply Supported; Concave Side Up and Heated, Panel No. 1)

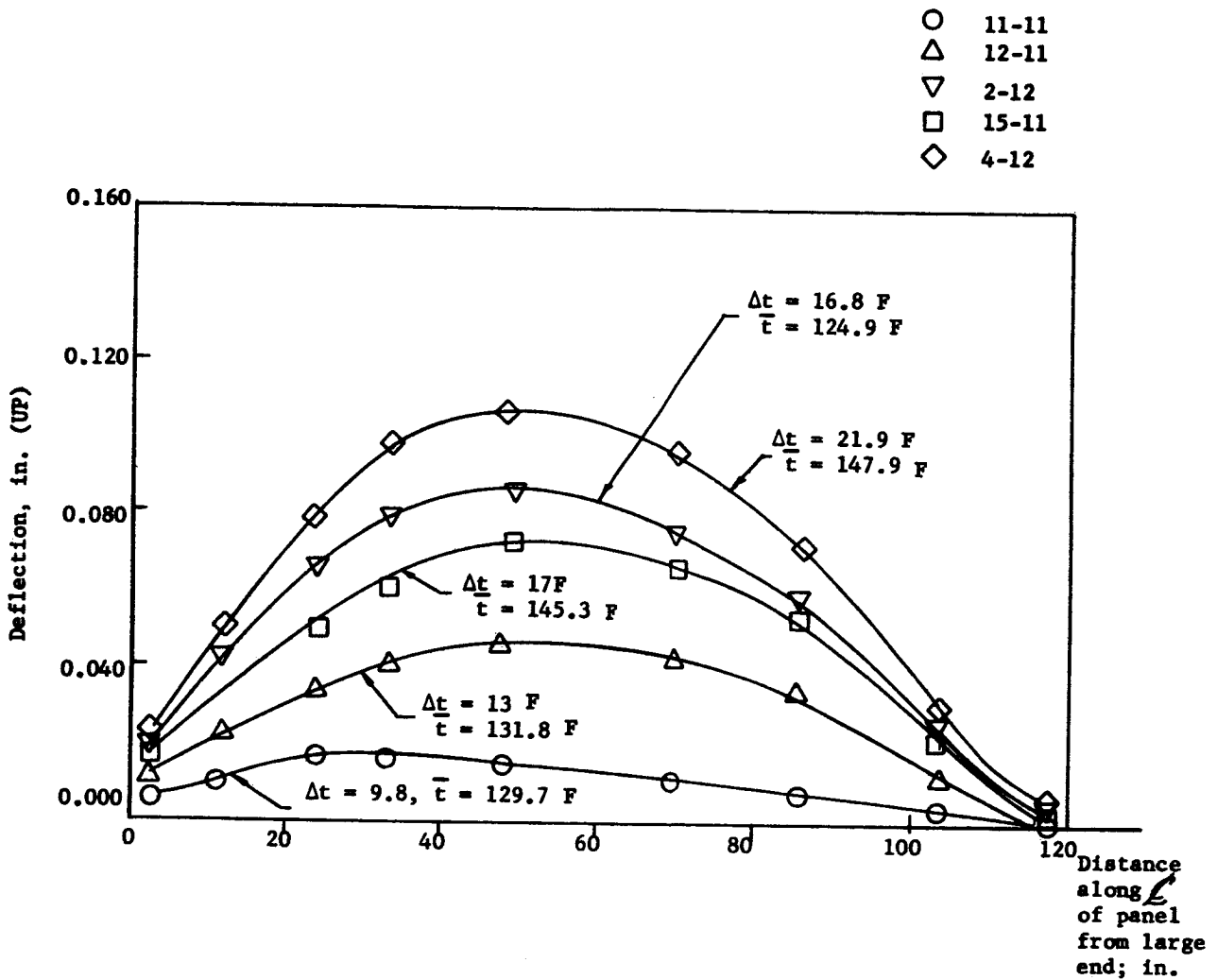


Figure 160. Centerline Deflection for Various Temperature Gradients (Simply Supported; Concave Side Up and Heated; Panel No. 2)

small maximum usable diameter established by its sink stability and the applied service temperature differential. This environmental consequence applies regardless of types of material or construction methods used.

3. When the environmental service temperature range is large, efficient microwave antenna performance cannot be achieved with the large parabolic petal concept of reflector design. This holds true even during conditions where the petal components are in thermal equilibrium.
4. Satisfactory antenna performance can be achieved in solar exposure environments when the parabola used consists of a sandwich having a core/skin ratio in weight approaching unity, sink characteristics to approach equilibrium, and a focal distance-to-diameter (F/D) ratio selection for "best fit" coordinate characteristic of the surface resulting from thermal change.
5. The functional relationships of reflecting surfaces in either a Cassegrainian or Gregorian antenna design arrangement may not excessively deteriorate in a summetrically changing thermal environment.
6. Conventional methods and instruments of dimensional measurement, which require a gravity established reference plane, do not apply to measurement techniques as may be required in space environments.

VI. A NEW CONCEPT FOR LARGE APERTURE PARABOLIC REFLECTORS FOR USE IN SPACE ENVIRONMENTS

A. The Idealized Structural Geometry

A stringent and detailed examination of structural shapes indicates that, with but one exception, the shapes radically change geometrically when subjected to space environments. The excluded shape is the symmetrical sphere which, although it may change in dimension, retains its spherical

geometry. This statement requires qualification by specifying the material which composes the sphere to be elastic. It is assumed that the most severe space environment which results in dimensional change will be thermal; therefore, the following fundamental illustrations depict the basic unsymmetrical thermal effect upon an elastic sphere. Figure 161, illustrating a solar exposed surface area expansion, is exaggerated. Figure 162 shows the same sphere but takes into consideration the elasticity and thermal shrinkage in the shadow area.

Figures 161 and 162 indicate that although thermal distortion can occur to a sphere, the elasticity and contraction which would be induced results in a compromising reaction. The reaction is to reduce thermal distortion in dimension such that spherical geometry is maintained.

The sphere has several advantages in its structural consideration. It is far easier to measure a spherical surface of constant radius than the coordinates of a parabola. A sphere constructed of nonrigid or flexible materials can be measured in the Earth's gravity environment without unknown deflections by employing pressurization. When considering the above and other physical properties of the flexible and elastic spherical structure, the sphere concept has distinct advantages over other concepts for space antenna reflector structures, with the possible exception of electrical characteristics. Therefore, the following discussion examines the feasibility and application of spherical reflecting surfaces to microwave antenna design. In practice, an area on the internal surface of a spherical shell can be used to focus microwave electromagnetic energy precisely the same as a parabolic antenna of the same reflector area. This equivalent function is shown in Figure 163, where the coordinate relationship between a curve of constant radius and a parabolic curve of $F/D = 0.225$ is compared.

In Figure 163, it can be noted that the parabolic curve and the curve of constant radius are coincident over 60% of the radial y-coordinate. This means that for an illustrative 10-ft diameter sphere, a 6-ft

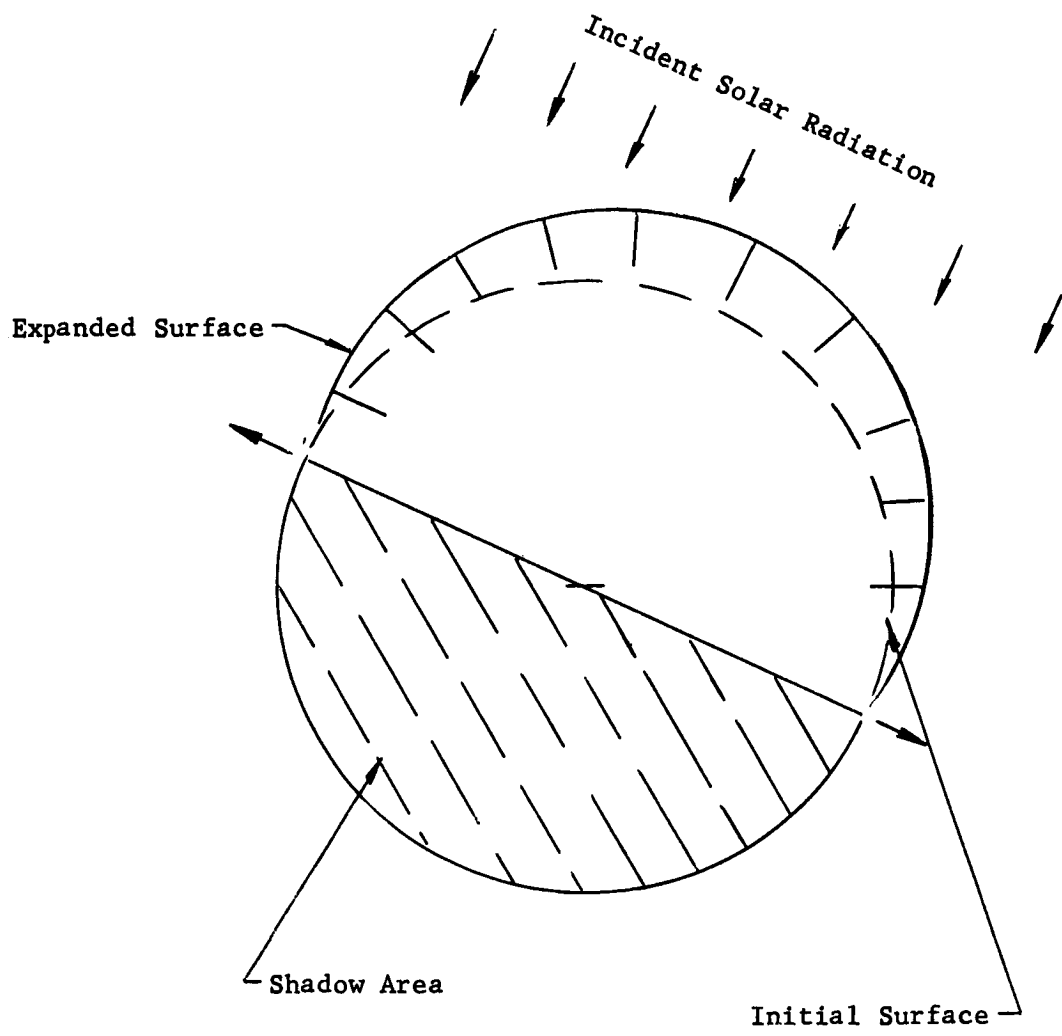


Figure 161. Thermal Distortion of a Sphere
Due to Incident Solar Radiation

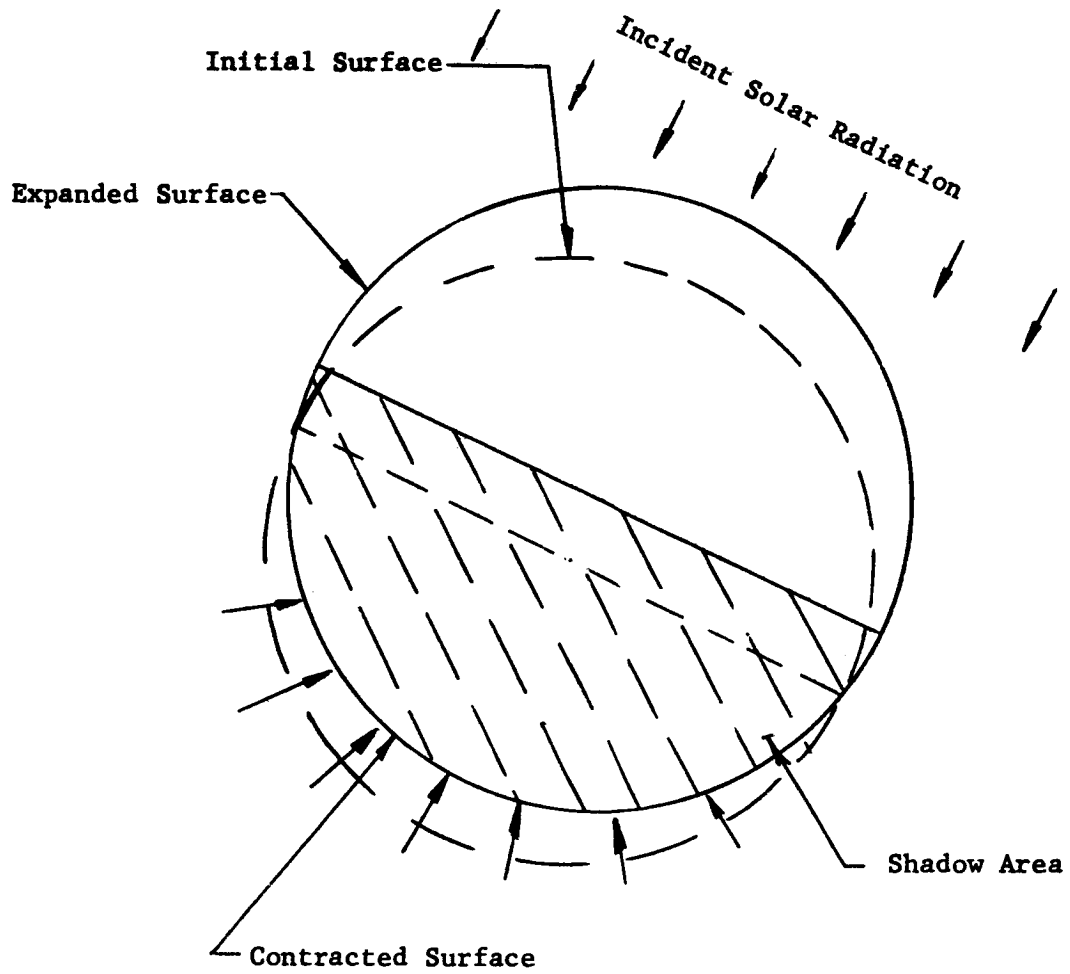


Figure 162. Total Thermal Distortion of a Sphere Due to Incident Solar Radiation and Shadow Areas

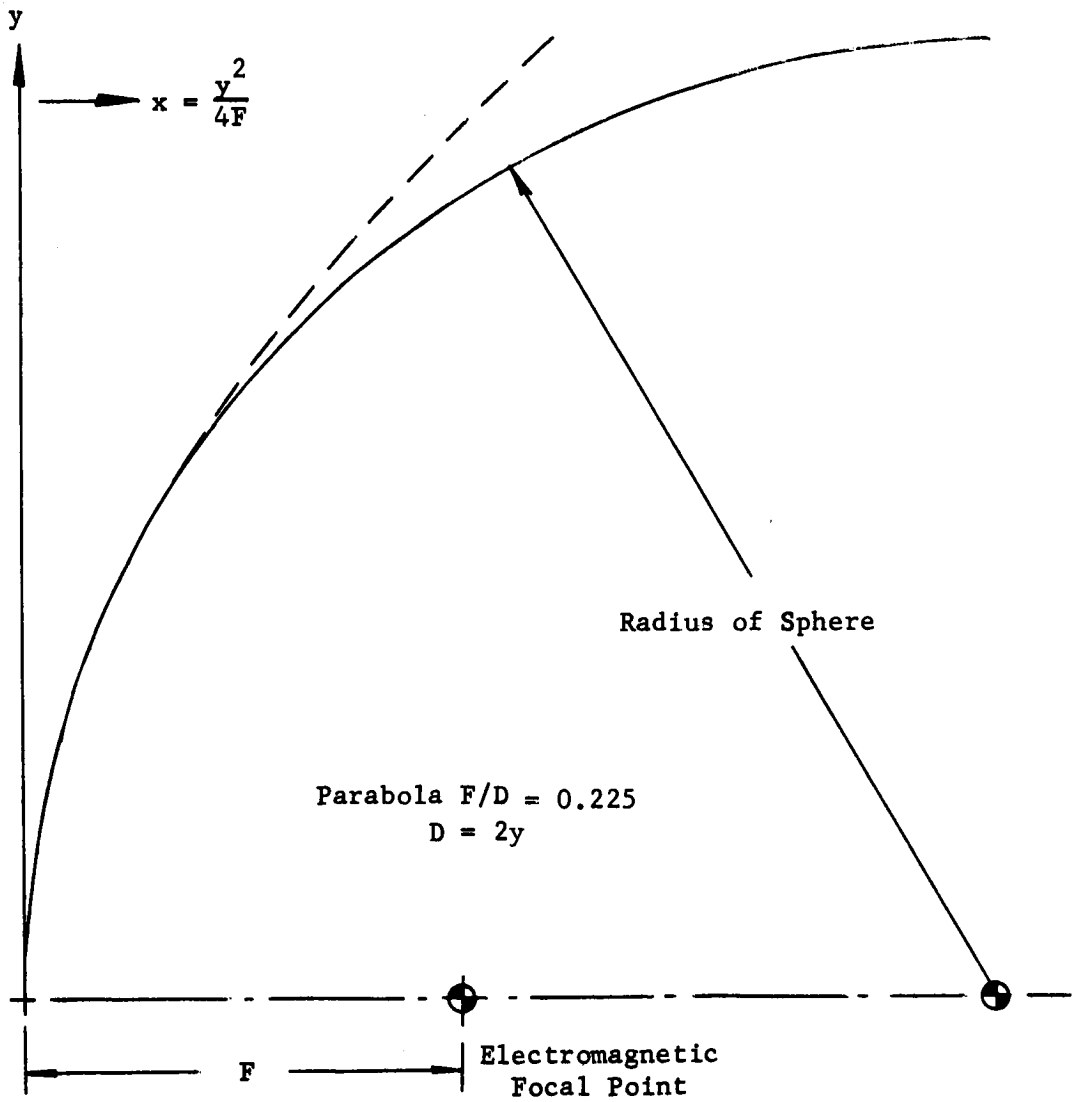


Figure 163. Coordinate Relationship Between a Curve of Constant Radius and a Parabolic Curve of $F/D = 0.225$

diameter area of the sphere could be used as a parabolic reflector. This assumes, of course, that the reflective area is metallic and the balance of the sphere is electromagnetically transparent. It should be noted, however, that the 6-ft diameter reflective surface requires the sphere to be at least 10 ft in diameter, which results in a large part of the sphere's projected area serving no useful purpose. Thus, the sphere's efficiency may be stated in terms of a ratio between the sphere diameter and the useful reflective area. In the example where the sphere diameter required would be of the order of 100 ft, this efficiency is considered to be quite low when considering the sphere diameter required, which serves no contributing purpose.

B. A Spherical Surface Functioning as a Parabolic Electromagnetic Reflector

Because of the obvious advantages offered by an optimized spherical structure for antenna reflectors in a space environment, Narmco has conceived an approach to essentially cause a spherical surface to function as a paraboloid. This conversion is primarily electromagnetic in nature, and is accomplished by the selective application of dielectric materials.

It is well known that a dielectric material retards an electromagnetic wave passing through it, and therefore has an index of refraction defined as the square root of the material's dielectric constant. Just as the parabolic reflector is used as a microwave optical device, a microwave lens constructed of dielectric material may be used to collimate microwave energy. Lenses and reflectors are interchangeable in microwave antennas because both perform the same basic function: modification of phase. Consequently, the two can be compounded as a composite electromagnetic optical device. This, basically, describes Narmco's procedure to convert the spherical surface.

The electromagnetic modification required to increase the projected aperture diameter of a given diameter sphere will be more clearly

understood by referring to Figure 164. Although it has previously been demonstrated that, at an F/D of 0.225, phase correction by dielectric means would be required only in the projected area in excess of 60% from the axis of symmetry, the equivalent parabolic curve in Figure 164 is shown at an example F/D = 0.35 to more clearly show the dielectric use. Indeed, notation should be made of the fact that the current trend in antenna design is toward F/D ratios of approximately 0.35, or less; this is particularly the case for a Cassegrain arrangement.

In Figure 164 dielectric material has been gradiently added to the inner surface of a sphere, increasing in thickness as the diameter of the spherical reflector increases in the y coordinate. The physical thickness of the dielectric, d, is related to the electrical thickness, ϕ , in one-way wave or ray traversal by

$$\phi = \frac{2 \pi d}{\lambda_0} \sqrt{\frac{\epsilon'}{\epsilon_0} - \sin^2 \theta} \quad (1)$$

where:

λ_0 = the electromagnetic free-space wavelength

$\frac{\epsilon'}{\epsilon_0}$ = the complex dielectric constant of the medium

θ = the angle of electromagnetic incidence

Equation (1) does not describe the equation of the refractive surface, but serves only to show the one-way path distance and phase difference. Shell's law describes the optical path due to the refractive index.

Figure 164 indicates that an apparent element of magnification occurs, wherein the actual spherical reflector diameter is less than the equivalent parabolic reflector as described by the electromagnetic ray path. This cannot be regarded as a gain, however, since the projected aperture and a certain dissipation factor of the dielectric material must be taken into consideration.

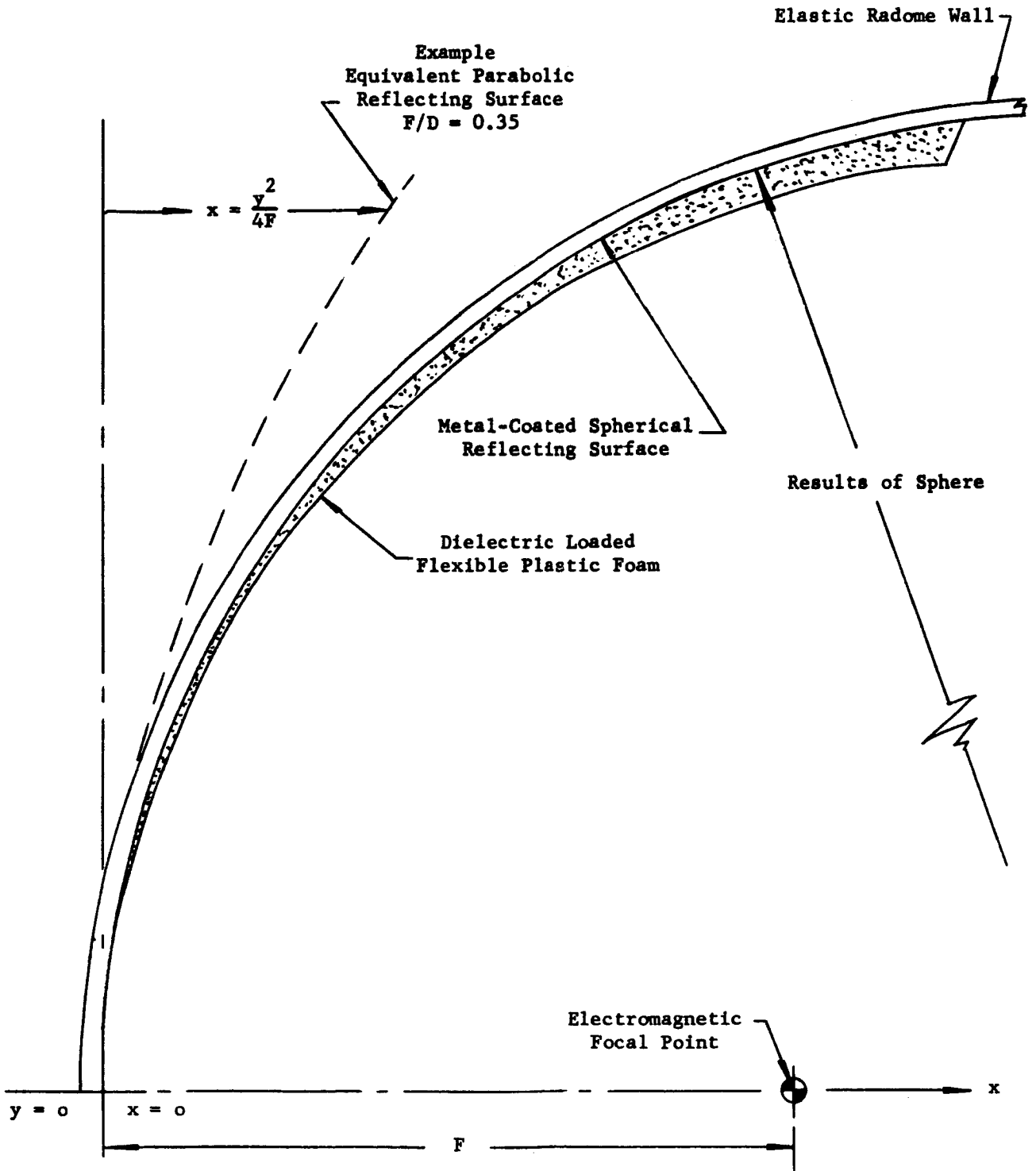


Figure 164. Method to Electromagnetically Change a Spherical Reflecting Surface to an Equivalent Parabolic Reflecting Surface

Now, since the ray correcting refractive medium is a dielectric material, it possesses some value of attenuation due to the dissipation factor which, in plastic foam and titanate materials, is usually quite small.

To better understand the effect of this loss, its relationship to the power distribution across an antenna aperture should be understood. The maximum density of illuminating power from an antenna feed system is directed along the reflector's axis of symmetry toward the reflector vertex. This illuminating power decreases radially in a tapered fashion toward the reflector edge, such that the intensity at the reflector edge is very low in comparison to that at the vertex. It can be seen in Figure 19 that the thickness of the dielectric material in Narmco's concept increases along the spherical surface toward the reflector edge and in the direction of decreasing illuminating power. Thus, the power loss by dissipation has only minor effect upon antenna gain or directivity.

For purposes of simplification, the antenna "gain" can be identified as G , to define the power flow ratio at a distance, in any direction, from the directive antenna. Then, the maximum parabolic antenna gain, assuming a particular illumination, can be stated in the elementary form:

$$G_o = \frac{4 \pi A (F)}{\lambda^2} \quad (2)$$

where:

- A = area of the parabolic reflector aperture
- λ = wavelength of radiation
- F = dimensionless factor resulting from excitation phase and intensity

A complementary property is the receiving cross section, A_r , which relates to gain as follows:

$$A_r = \frac{G \lambda^2}{4 \pi} \quad (3)$$

Since antenna gain is a direct relationship to antenna directivity, it follows that directivity is a function of antenna beamwidth, and radiation intensity at a point some large distance from the antenna is entirely dependent upon antenna beamwidth for a given total power level. The beamwidth is expressed by the approximation derived from the laws of wave optics:

$$\theta \text{ (degrees)} \approx 70 \frac{\lambda}{D} \quad (4)$$

where:

θ = width of beam between directions for half power (3-db down) in a plane passing through the projected parabolic reflector diameter

λ = wavelength

D = projected diameter of the paraboloid antenna reflector

It is therefore shown that, for a given microwave transmitter power level or a receiving microwave signal intensity, the maximum distance in space over which communication can be performed is directly related to the diameter of the parabolic reflector, assuming, of course, that a reflecting surface of sufficient accuracy is maintained.

To consider the proposed phase-modified spherical reflector in terms of antenna gain, it is necessary to evaluate the reflection coefficients of the dielectric material interface, plus the loss tangent ($\tan \delta$), of the dielectric material.

An elementary approach is to simply include a new factor $(D - \gamma)$, into equation (2). Thus,

$$G_o = \frac{4 \pi A (F) (D - \gamma)}{\lambda^2}$$

where:

- A = effective parabola aperture
- F = dimensionless factor ≤ 0.55
- $(D - \gamma)$ = combined attenuation due to dissipation factor and reflection coefficient
- λ = wavelength

C. The Expandable Antenna Structure

The previous discussions have pertained to the functional design of a space antenna by means of a spherical shape. Excellent advantages are also inherent in a sphere's structural and electrical characteristics, as well as its utility in space.

One primary objective of the spherical shell concept is to acquire a highly precise and uniform reflecting surface which has sufficient rigidity to maintain this surface accuracy in a space environment. This can be provided by a perfectly spherical structure which contains an internal pressure to achieve uniformity. This inflated spherical bag approach, however, cannot be effectively utilized in space environments, due to depressurization by meteoroids, as demonstrated in the instance of the Echo I satellite balloon.

Expandable elastic recovery spherical concepts do not depend upon internal pressures to maintain semi-rigidity. However, the elastic recovery structures do not achieve the required uniformity of surfaces necessary for microwave reflectors. This nonuniformity of surface is due to permanent creasing and wrinkling of the structural material when in the folded and collapsed state.

Since it can be shown that a single wall flexible material fabricated to a constant radius will form a perfect sphere when pressure-inflated, and thus can have a precise and uniform surface both internally and externally, it is then apparent that an internal pressure may be utilized to remove the creases and wrinkles from the outer skin surface of an elastic recovery spherical structure. Since the question obviously arises as to the more plausible pressurization of the inside skin surface of an elastic recovery sandwich structure, it is found that a residual restraint is maintained by the outer skin surface and flexible foam core due to remaining creases and wrinkling. Thus, in the event of depressurization, the inside surface will become distorted by continued recovery of the outer material.

In order to alleviate the above condition and achieve uniform spherical surfaces, the concept requires the application of radial smoothing pressures to both the internal and external skin surfaces of an elastic recovery sandwich sphere to approach material yield. This pressurization of both skin surfaces would be accomplished by microscopic perforations included into the inside skin and core material. Thus, radial pressure would first be applied to the inside skin of the spherical structure, and then, as a function of time, traverse the cross section of the sandwich to apply radial pressure to the outside skin. By this expedient a radial pressure would be applied to both sandwich surfaces until, as a function of time, the pressure differential of the surfaces were equalized.

Once full memory of the spheres' elastic material has been restored, the elastic sandwich spherical structure could maintain its spherical geometry precisely in the space environment following perforation and depressurization by meteorites. This ability is mandatory for microwave antenna applications.

By the use of flexible plastic foam, which has a very low dielectric constant and dissipation factor, and flexible plastic laminate skins, which also have a relatively low dielectric constant and dissipation factor, the wall of a spherical shell can be constructed to act as a

radome. This type of radome construction is known as a "symmetrical sandwich," and has excellent electromagnetic transmission characteristics.

Thus, for the "symmetrical lossless sandwich" design, zero-reflection occurs only when the sandwich core thickness $(d_c)_N$ is in the following relations: (65)

For Parallel Polarization of Microwave Energy and Normal Incidence

$$(d_c)_N = \frac{\lambda_o}{2 \pi \sqrt{\alpha_c}} \left[N \pi - \tan^{-1} \frac{2(\alpha_s - 1) \sqrt{\alpha_s \alpha_c} \sin 2\phi_s}{(\alpha_s + 1)(\alpha_c - \alpha_s) + (\alpha_s - 1)(\alpha_s + \alpha_c) \cos 2\phi_s} \right] \quad (6)$$

where $N =$ integer

$(d_c)_N =$ thickness of order N

$\lambda_o =$ free-space wavelength

$\alpha_c = \epsilon_s / \epsilon_o$, specific dielectric constant of core

$\alpha_s = \epsilon_s / \epsilon_o$, specific dielectric constant of skin

$\phi_s = (2 \pi) x$ (electrical thickness of the skin)

For Perpendicular Polarization of Microwave Energy and Arbitrary Incidence

$$\phi_c = N \pi - \tan^{-1} \left[\frac{2 (\alpha'_s - 1) \sqrt{\alpha'_s \alpha'_c} \sin 2\phi_s}{(\alpha'_s - 1)(\alpha'_s + \alpha'_c) \cos 2\phi_s + (\alpha'_c - \alpha'_s)(\alpha'_s + 1)} \right] \quad (7)$$

where $\alpha'_s, \alpha'_c =$ "effective" specific dielectric constants of the skin and core, respectively, for radiation incident at angle θ in air. The actual specific dielectric constants are α_s and α_c .

$$\phi_c = \frac{2 \pi (d_c) N}{\lambda_o} \sqrt{\alpha_c - \sin^2 \theta}$$

$$\phi_s = \frac{2 \pi d_s}{\lambda_o} \sqrt{\alpha_s - \sin^2 \theta}$$

Thus, by employing the above, it is practical to design a space antenna spherical structure that will be transparent to a given band of microwave electromagnetic transmission or reception. A spherical area on the internal skin of the electromagnetically transparent, spherical radome would be metallized to form a spherical antenna reflector. The previously discussed phase-modifying dielectric material, compounded to the spherical reflector to achieve parabolic performance, could also be a flexible, elastic recovery, plastic foam. The dielectric composition of this inner layer could be adjusted to provide an increase in the index of refraction in order to minimize the thickness required as a phase-corrective medium.

Thus, the foam would be loaded with an element which has a very high dielectric constant and low dissipation factor such as barium titanate. The dielectric loading will produce a resultant dielectric constant which is the product of the ratio of dielectrics per unit volume, and is a function of the electromagnetic frequency.

The entire spherical radome structure and the equivalent parabolic reflector can be made flexible and, therefore, collapsible for efficient packaging. When the packaged antenna structure is released, the elastic memory of the materials will expand the sphere into its original shape, thus deploying the antenna, although not into its operating condition. To obtain full elastic recovery, the previously discussed pressurization process is next applied.

Upon full restoration of the sphere's elastic material by the application of this radial-smoothing pressure, the elastic sandwich spherical

structure would precisely maintain its spherical geometry in the space environment following any perforation and depressurization by meteorites. This ability is mandatory for microwave antenna applications.

Various antenna design flexibilities exist through the use of the spherical concept, several of which are shown by Figures 165, 166, and 167. The arrangement shown in Figure 165 could have particular significance in those instances where space atomic radiation and micro-meteoroids are of concern. Characteristically, flexible materials which have low dielectric constants and low dissipation factors are usually of low atomic number. Thus, in instances where damaging space radiation is of corpuscular nature, the bremsstrahlung could be significantly reduced.

Notice that each of the antenna concepts shown may be pointed directly toward the sun without incurring thermal feed damage.

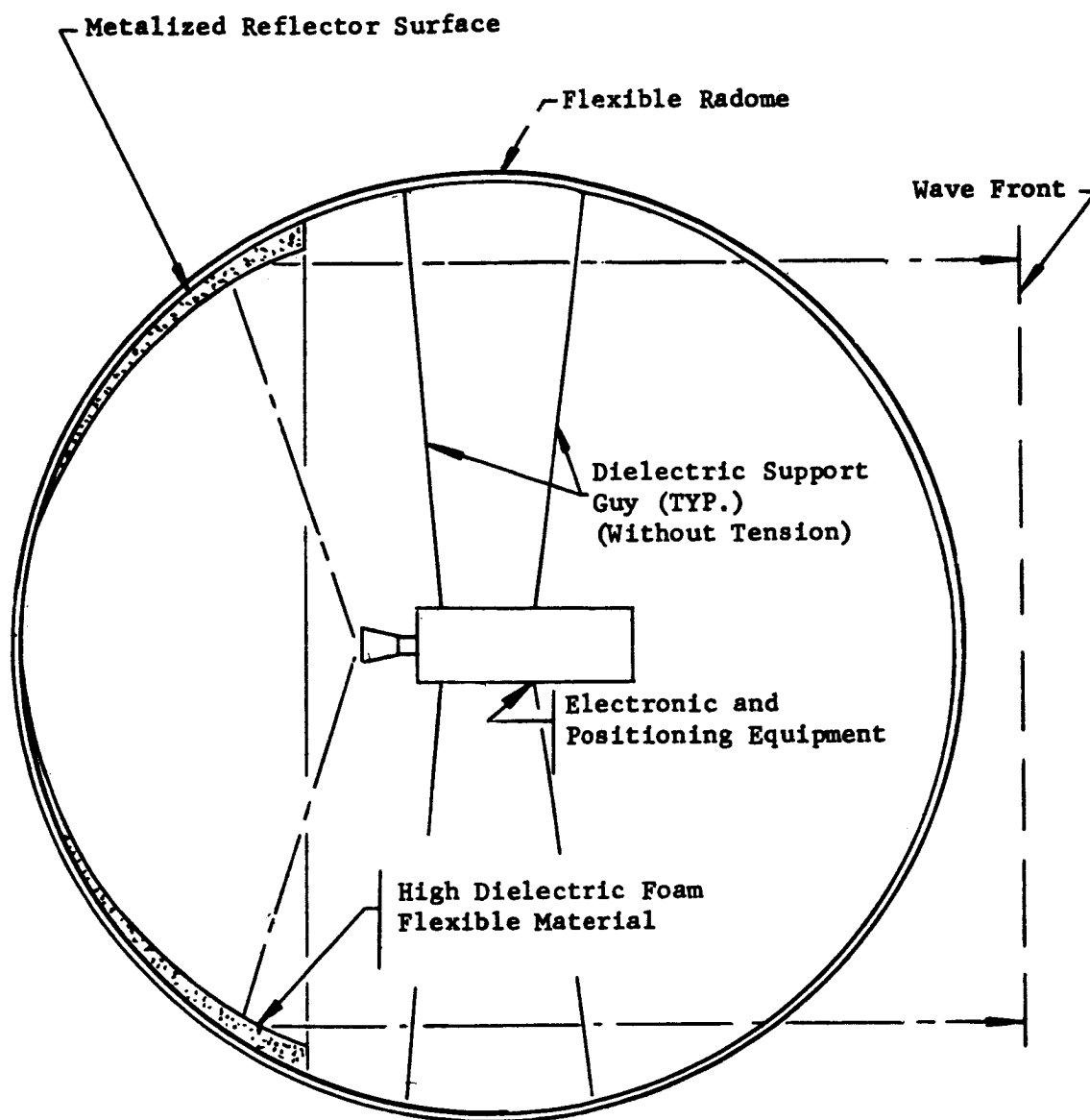


Figure 165. Newtonian Antenna Arrangement Shown With Electronic Equipment Housed in the Spherical Radome Structure

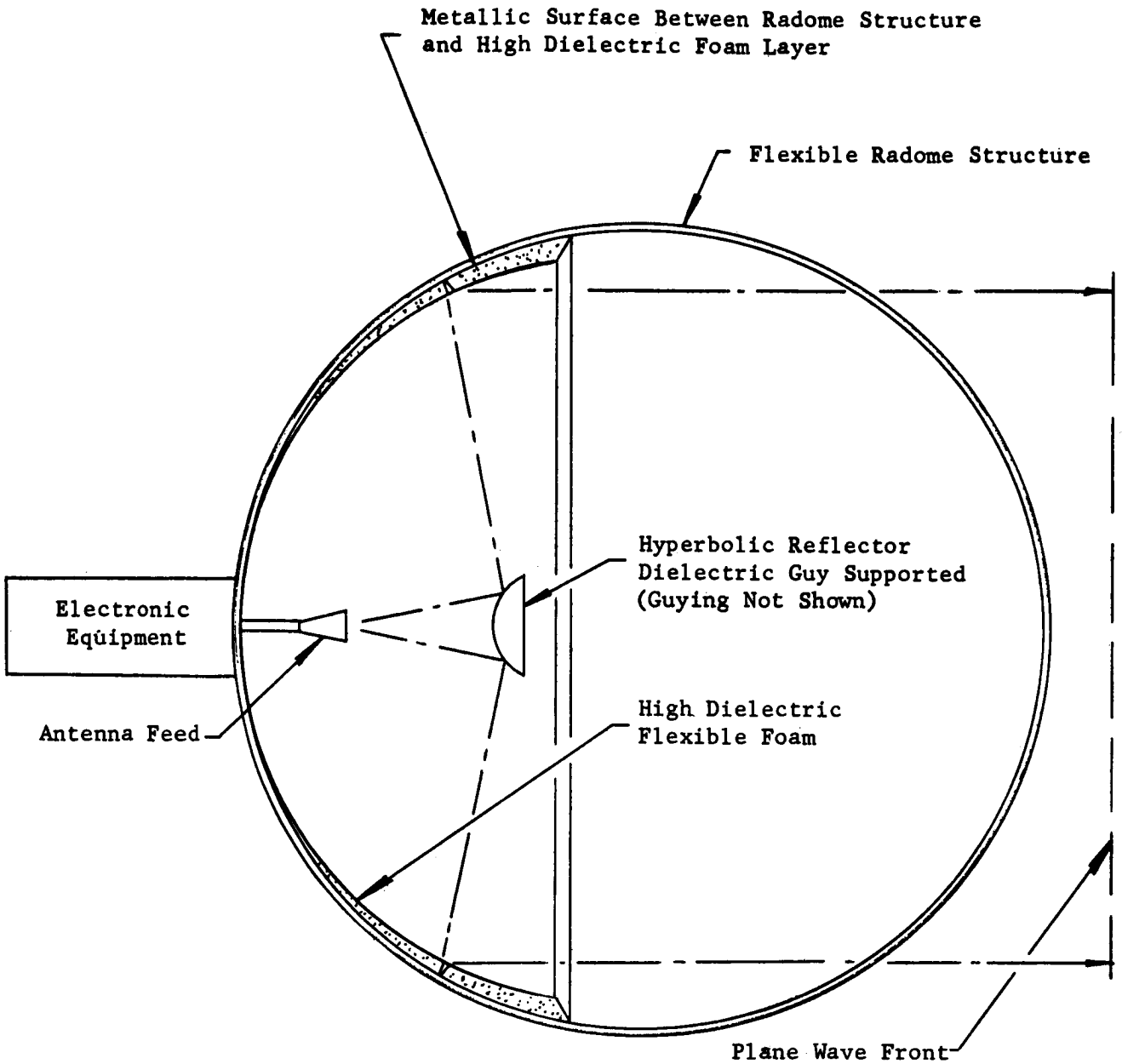


Figure 166. Expandable Cassegrain Antenna Arrangement

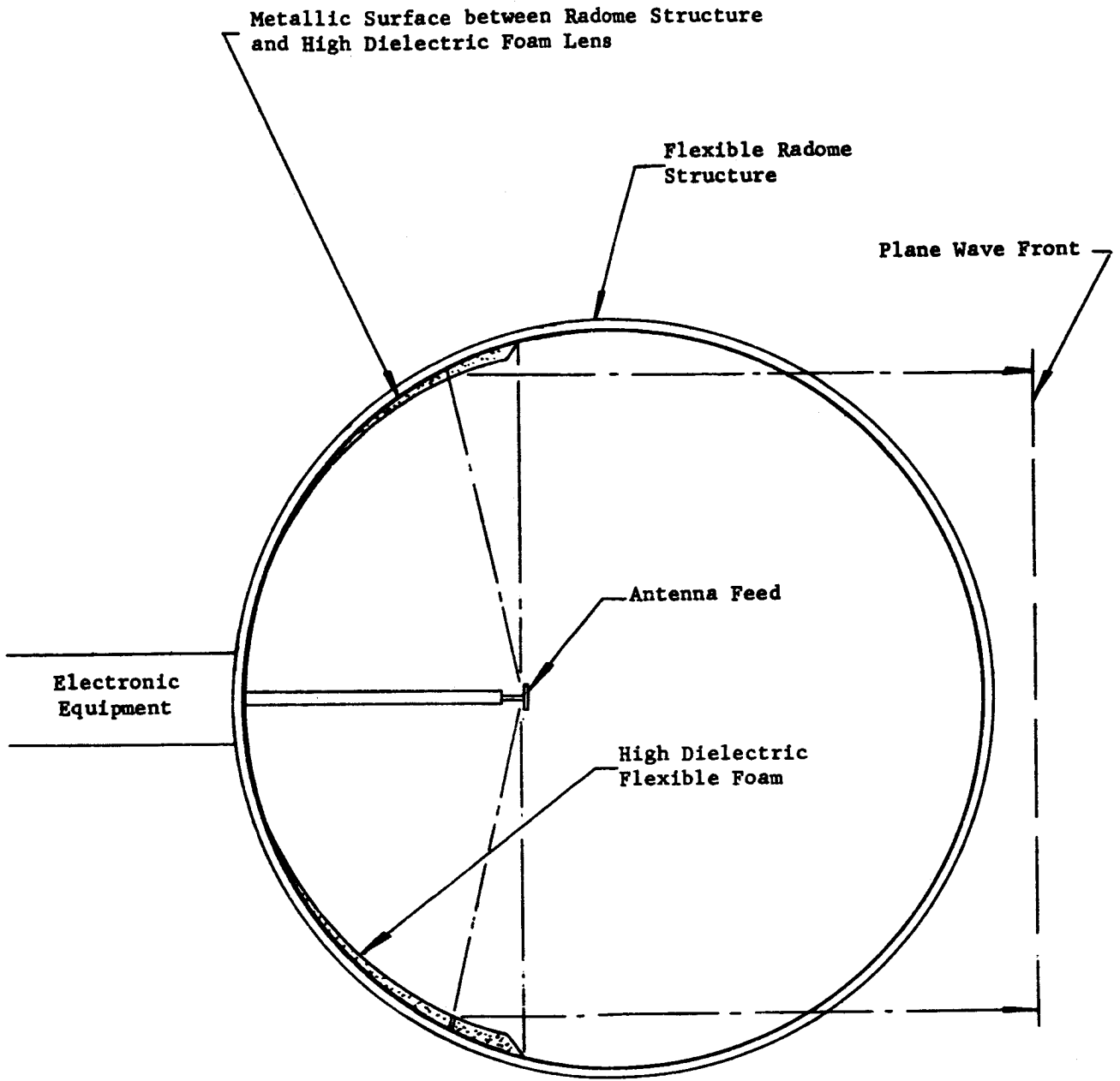


Figure 167. Expandable Newtonian Antenna Arrangement

REFERENCES

- (1) Ford Motor Company, Aeronutronic Division, Nonrigid and Semirigid Structures for Expandable Spacecraft, by D. G. Younger, R. M. Edminston, and R. G. Crum, ASD-TDR-62-568, Newport Beach, Calif., Nov 1962
- (2) Ford Motor Company, Aeronutronic Division, Multiwall Structures for Space Vehicles, by S. Lampert and D. G. Younger, WADD TR 60-503, May 1960
- (3) Langley Research Center Staff, A Report on the Research and Technological Problems of Manned Rotating Spacecraft, NASA TN D-1504, Hampton, Va.
- (4) A. Juzwinski, "A Technique of Evaluating Fuel Losses Due to Meteoroid Puncture and Some Timely Examples" (paper presented at ARS Meeting, Cleveland, Ohio, July 1962)
- (5) T. J. Hart, "Design Criteria and Analyses for Thin-Walled Pressurized Vessels and Interstage Structures" (paper presented at the ARS Meeting, Santa Barbara, Calif., Apr 1960)
- (6) J. Heilfrom and F. H. Kaufman, "Rendezvous and Docking Techniques" (paper presented at the ARS Lunar Missions Meeting, Cleveland, Ohio, July 1962)
- (7) Martin Company, Expandable Space Structures: Interim Technical Documentary Report, by P. M. Knox, Jr., A. Corell, and E. Lane, ASD-TDR-7-943a(I), Denver, Colo., 1 Nov 1962 - 31 Jan 1963
- (8) National Aeronautics and Space Administration, Effect of a Load-Alleviating Structure on the Landing Behavior of a Reentry-Capsule Model, by Edward L. Hoffman, Sandy M. Stubbs, and John R. McGehee, NASA TND-8-11, Washington, D.C., May 1961
- (9) P. H. Bliss, "Status of Lunar Surface Vehicles" (seminar proceedings of Utilization of Extraterrestrial Resources, Jet Propulsion Laboratory, Pasadena, Calif.)
- (10) Robert M. Wood, "Thermostructural Design of Entry Vehicles for Earth, Mars, and Venus" (UCLA Space Exploration Course lecture, Los Angeles, Calif., Dec 1962)
- (11) Hamilton Standard Division of United Aircraft Corporation, Electron Beam Welding in Variable Environments: Interim Technical Documentary Progress Report, by L. G. Foxwell, F. R. Schollhammer, and J. E. Smith, IR-8-243(I), Conn., Oct 1962 - Apr 1963
- (12) D. G. Driscoll, "Cryogenic Tankage for Space Flight Applications," Advances in Cryogenic Engineering, Vol. 5, Plenum Press, New York, 1960
- (13) Goodyear Aerospace Corporation, New and Improved Materials for Expandables, by D. M. Marco, ASD-TDR-62-542 (Part I), Akron, Ohio, 1962

REFERENCES (Continued)

- (14) National Aeronautics and Space Administration, Direct Measurements of Interplanetary Dust Particles in the Vicinity of Earth, C. W. McCracken, W. M. Alexander, and M. Dubin, NASA TN D-1174, Dec 1961
- (15) National Aeronautics and Space Administration, The Explorer XVI Micro-meteoroid Satellite Description and Preliminary Results, by Earl C. Hastings, NASA TM X-810, 16 Dec 1962 - 13 Jan 1963
- (16) Air Force Cambridge Center, Meteoric Dust Measured from Explorer I, by M. Dubin, Mass. (undated)
- (17) E. R. Manring, "Micrometric Measurements from 1958 Alpha and Gamma Satellites," Planetary and Space Science, Vol. 1, p. 27, 1959
- (18) R. L. Bjork, "Meteoroids Versus Space Vehicles," American Rocket Society, New York, 1960
- (19) Rand Corporation, "Effects of a Meteoroid Impact on Steel and Aluminum," by R. L. Bjork, Rand Corp. Paper P-1662
- (20) F. L. Whipple, "Photographic Meteor Orbits and Their Distribution in Space," Astronomical Journal, Vol. 59, p. 201, 1954
- (21) F. G. Watson, "Catalogue of Hourly Meteor Rates," Smithsonian Contributions to Astrophysics, Vol. 4, No. 1, 1960
- (22) California Institute of Technology, Jet Propulsion Laboratory, Behavior of Materials in Space Environments, by L. D. Jaffe and J. B. Rittenhouse, TR No. 32-150, Pasadena, Calif., 1 Nov 1961
- (23) F. L. Whipple and E. L. Fryeman, "Calculation of Erosion in Space from Cosmic Ray Exposure Ages of Meteorites," Nature, Vol. 183, p. 1315, 1959
- (24) D. E. Fisher, "Space Erosion of the Grant Meteorite," J. Geophys. Res 66, pp. 1509-1511, 1961
- (25) National Aeronautics and Space Administration, Radiation Shielding for Manned Space Flight, by L. E. Wallner and H. R. Kaufman, NASA TN D-681, July 1961
- (26) National Aeronautics and Space Administration, Proceedings of Conference on Radiation Problems in Manned Space Flight, NASA TN D-588, Dec 1960 (Conference held 21 June 1960)
- (27) U.S. Air Force, "Space Environmental Criteria for Aerospace Vehicles," U.S. Air Force Bulletin No. 523, 28 Nov 1960
- (28) H. J. Schaefer, "Exposure Hazards from Cosmic Radiation Beyond the Stratosphere and in Free Space," J. Aviation Medicine, Vol. 23, Aug 1952

REFERENCES (Continued)

- (29) University of California, Introduction to the Utilization of Solar Energy, University of California Engineering and Sciences Extension Series, A. M. Zarem and D. D. Erway, editors, McGraw-Hill, New York, 1963
- (30) Martin Company, Expandable Space Structure: Interim Engineering Program Report, by P. M. Knox, Jr., R. O. Moses, and E. Lane, IR-7-9430a(III), Denver, Colo.
- (31) Goodyear Aerospace Corporation, Study on Methods of Structurally Evaluating Expandable Structures Having Potential Space Applications: Final Report, by N. L. Jeppesen et al., Contract No. NASw-471, Akron, Ohio, 23 Aug 1963
- (32) MIL-HDBK-23: Part III, 5 Oct 1959
- (33) Stephen P. Timoshenko, Theory of Elastic Stability, second edition, McGraw-Hill, New York, 1961
- (34) U.S. Department of Agriculture, Forest Products Laboratory, Supplement to Analysis of Long Cylinders of Sandwich Construction under Uniform External Lateral Pressure, FPL Report No. 1844A, Madison, Wis.
- (35) U.S. Department of Agriculture, Forest Products Laboratory, Buckling of Sandwich Cylinders under Uniform External Lateral Pressure, FPL Report No. 1844B, Madison, Wis.
- (36) U.S. Department of Agriculture, Forest Products Laboratory, Design Curves for the Buckling of Sandwich Cylinders of Finite Length under Uniform External Lateral Pressure, FPL Report No. 1869, Madison, Wis.
- (37) Narmco Research & Development, "Thermal Analysis of Elastic Recovery Composites," Narmco Engineering Report No. 64-E14, Apr 1964
- (38) Knoll and Oglebay, "Lightweight Thermal Protection Systems for Space Vehicles Propellant Tank," SAE, 1963
- (39) Langley Research Center, Analysis of Effective Thermal Conductivities of Honeycomb-Core and Corrugated-Core Sandwich Panels, by Robert T. Swann and Claud M. Pittman, NASA TN D-714, Hampton, Va.
- (40) B. E. Gatewood, Thermal Stresses, McGraw-Hill, 1957
- (41) C. J. Maiden and A. R. McMillan, "An Investigation of the Protection Afforded a Spacecraft by a Thin Shield" (AIAA Preprint No. 64-95, subsequently presented at the Aerospace Sciences Meeting, New York, Jan 1964)
- (42) J. H. Kineke and L. G. Richards, "Influence of Target Strength on Hypervelocity Crater Formation in Aluminum" (paper presented at the Sixth Symposium on Hypervelocity Impact, Cleveland, Ohio, Apr 1963)

REFERENCES (Continued)

- (43) General Dynamics/General Atomic, Hydrodynamics of Hypervelocity Impact, by J. M. Walsh and J. H. Tillotson, Report No. GA 3827, Jan 1963
- (44) F. L. Whipple, "The Meteorite Risk to Space Vehicles," Vistas in Astronautics, Vol. 2, Pergamon Press, New York, 1958
- (45) P. E. Sandorff, "A Meteoroid Bumper Design Criteria" (paper presented at the Sixth Symposium on Hypervelocity Impact, Cleveland, Ohio, Apr 1963)
- (46) C. J. Maiden, "Experimental and Theoretical Results Concerning the Protective Ability of Thin Shields Against Hypervelocity Impact" (paper presented at the Sixth Symposium on Hypervelocity Impact, Cleveland, Ohio, Apr 1963)
- (47) General Dynamics/Astronautics, Study of Principles of Meteoroid Protection, by R. F. Rolsten et al., NASA Contract NAS 8-875, San Diego, Calif., Apr 1962
- (48) S. J. Pipitone and B. W. Reynolds, "Meteoroid Protection for Space Vehicles" (paper presented at the AIAA Launch and Space Vehicle Shell Structures Conference, Palm Springs, Calif., Apr 1963)
- (49) Air Force Special Weapons Center, Practical Countermeasures for the Prevention of Spallation, by J. S. Reinhart, TR 60-7, Feb 1960
- (50) W. Herrmann and A. H. Jones, "Hypervelocity Impact - Status of Experiments" (paper presented at the Symposium on Structural Dynamics under High Impulsive Loading, sponsored by ASD and OAR, Dayton, Ohio, 1962)
- (51) California Institute of Technology, Jet Propulsion Laboratory, Space Programs Summary No. 37-24 (Vol. IV), by R. E. Gardner and C. K. Robieland, Pasadena, Calif., Sept 1963 - Nov 1963
- (52) Hayes International Corporation, Study of Target Penetration by High-Speed and Ultrahigh-Speed Ballistic Impact, APGC TDR 63-22, Air Proving Ground Center, Air Force Systems Command, Feb 1963
- (53) General Motors Defense Research Laboratories, Meteoroid Impact, by C. J. Maiden, TM-63-203, Apr 1963
- (54) Reinhold Publishing Corporation, "Materials Selector Guide," Materials in Design Engineering, 1963
- (55) National Aeronautics and Space Administration, Meteoroid Effects on Space Exploration, NASA TND 1839, NASA Headquarters, Washington, D.C., Oct 1963

REFERENCES (Continued)

- (56) J. H. Gehring, D. R. Christman, and A. R. Millan, "Hypervelocity Impact Studies Concerning the Meteoroid Hazard to Aerospace Materials and Structures" (paper presented at the AIAA Structures and Materials Conference, Palm Springs, Calif., Apr 1964)
- (57) National Aeronautics and Space Administration, Preliminary Investigation of Impact on Multiple-Sheet Structures and an Evaluation of the Meteoroid Hazard to Space Vehicles, by C. R. Nysmith and J. L. Summers, NASA TND-1039, 1961
- (58) R. J. Eichelberger and J. W. Gehring, "Effects of Meteoroid Impacts on Space Vehicles," ARS Journal, Vol. 32, No. 10, 1962
- (59) J. P. Martin, L. Witten, and L. Katz (paper presented at the International Symposium on Space Phenomena and Measurement, Detroit, Mich., 1962)
- (60) G. H. Wolter, private communications
- (61) R. D. Evans, The Atomic Nucleus, McGraw-Hill, 1955
- (62) E. U. Condon and H. Odishaw, Handbook of Physics, McGraw-Hill, 1958
- (63) Charles D. LaFond, "Paraboloscope Advances Antenna Art," Missiles and Rockets, 1001 Vermont Ave., N.W., Washington, D.C., 7 Jan 1963 issue
- (64) Advanced Structures, A Division of Telecomputing Corporation, Report 61-015, La Mesa, Calif., 24 July 1961
- (65) Cady, Karelitz, and Turner, Radar Scanners & Radomes, McGraw-Hill, 1948